UNIVERSITÀ
DEGLI STUDI
DI TRIESTE

Università
Ca'Foscari
Venezia

UNIVERSITÀ DEGLI STUDI DI TRIESTE
UNIVERSITÀ CÀ FOSCARI DI VENEZIA

XXXVIII CICLO DEL DOTTORATO DI RICERCA IN CHIMICA

Finanziato dall'Unione europea - NextGenerationEU
Funded by the European Union – NextGenerationEU- Piano Nazionale di Ripresa e Resilienza, Missione4 – Componente 1 – Investimento 4.1 CUP J92B22000930007

METALLO-PORPHYRIN CONJUGATES FOR ARTIFICIAL PHOTOSYNTHESIS OR SINGLE-ATOM CATALYSIS

Settore scientifico-disciplinare:**CHIM/03**

DOTTORANDA
GRETA FOGAR
Greta Fogar

COORDINATORE
PROF. ENZO ALESSIO

SUPERVISORE DI TESI
PROF. ELISABETTA IENGO

CO-SUPERVISORE DI TESI
PROF. SYLVESTRE BONNET

ANNO ACCADEMICO 2024/2025

Finanziato
dall'Unione europea
NextGenerationEU

Ministero
dell'Università
e della Ricerca

Italiadomani
PIANO NAZIONALE DI RIPRESA E RESILIENZA

UNIVERSITÀ
DEGLI STUDI
DI TRIESTE

TABLE OF CONTENTS

Abstract

Chapter 1 provides a concise scientific background of the Thesis, introducing the structural, photophysical, and electrochemical properties of (metallo)porphyrins, with particular emphasis on Sn^{IV}-porphyrins. After outlining the fundamental role of (metallo)porphyrins in natural systems, the Chapter describes their molecular structure, synthetic strategies, and metalation procedures. The coordination chemistry of Sn^{IV}-porphyrins is then discussed, focusing on axial ligand substitution, also as a versatile tool for the obtainment of photoactive conjugates. Few selected literature examples illustrate how these systems can be implemented to control photoinduced energy and and electron-transfer processes. Further address is given to the conjugation of Sn^{IV}-porphyrins with redox-active amino acids. The role of tyrosine and tryptophan as photoactive units for proton-coupled electron transfer (PCET) or simpler electron transfer is summarized. The mechanistic framework and relevance of proton-coupled electron transfer (PCET) in both biological and artificial systems is outlined. Finally, the latest examples of Sn^{IV}-porphyrins conjugates bearing axial tyrosine or tryptophane residues are shortly described as they represent the start point of the work developed in the Thesis. More specific and dedicated introductions will be given at the beginning of each of the following Chapters.

Chapter 2 describes the synthesis, structural characterization, and photophysical study of new metallo-porphyrin phenol conjugates designed to investigate proton-coupled electron transfer, inspired by Photosystem II. The compounds were prepared by conjugating phenolic units to the periphery of a porphyrin scaffold and then inserting either Sn^{IV} or Zn^{II}. NMR, mass spectrometry, X-ray diffraction, and DFT calculations confirm the structures and reveal that the phenol to porphyrin distances are significantly larger than in previously reported axial Sn^{IV}-porphyrin tyrosinate complexes. Photophysical measurements on the Sn^{IV}-porphyrin conjugates, done in collaboration with Prof. Mirco Natali (University of Ferrara, Italy), show that, despite favorable thermodynamics, the increased donor-acceptor distances strongly reduce the kinetic efficiency of the electron transfer. As a result, no photoinduced PCET occurs from the singlet excited state, and the triplet driven PCET pathway is much slower and dominated by bimolecular quenching. Comparison with model compounds highlights that moving the phenol farther apart from the macrocycle suppresses the formation of the desired diradical species. Overall, the results demonstrate that extended chromophore donor distances limit PCET reactivity, providing key insights for the design of future artificial systems that mimic the function of Photosystem II.

Chapter 3 reports the research done during a six-months internship in the laboratories of Prof. Sylvestre Bonnet (Leiden University, The Netherlands). It explores the design, synthesis, and preliminary photophysical characterization of a new Sn^{IV}-porphyrin/peptide conjugate intended to drive photoinduced transmembrane Proton Coupled Electron Transfer (PCET) in lipid bilayers. Inspired by natural photosynthetic charge-separation processes, the work integrates a redox-active Sn^{IV}-porphyrin photosensitizer, tyrosine electron donors, and histidine proton acceptors into a modified $YALP_{23}$ peptide scaffold capable of adopting a transmembrane α-helical structure. Molecular dynamics simulations suggested the optimal insertion position of the chromophore and of the other active components in the peptide sequence. The resulting conjugate (plus the corresponding model peptide and two shorter analogues) were synthesized by combining SPPS and manual coupling and in depth characterized by NMR, MS, CD, and optical spectroscopies. Preliminary quenching experiments were used to select possible operating conditions under which electron- or PCET-type processes may occur. Finally, the conjugate was successfully embedded in DPPC liposomes, without substantial modification of the photophysical properties of the photosensitizer, thus representing a promising platform for future studies on light-driven transmembrane PCET.

Chapter 4 presents the design, synthesis, and surface characterization of a series of functionalized porphyrins aimed at forming tunable two-dimensional metal organic networks (2D-MONs) for single-atom catalysis. Three benzamide-substituted free-base porphyrins and their corresponding cobalt derivatives were synthesized to mimic selected features of enzymatic second coordination spheres. Their structural and photophysical properties were comprehensively determined in solution by 1D and 2D NMR spectroscopy, high-resolution mass spectrometry, and UV-Vis spectroscopy. To investigate the ability of these conjugates to form ordered supramolecular architectures on surfaces, the free-base porphyrin versions were deposited under ultrahigh-vacuum conditions on graphene/Ir(111) and Au(111) substrates using electrospray ionization beam deposition, in collaboration with Prof. Erik Vesselli (University of Trieste, Italy). The resulting layers were analyzed by a combination of IR-visible sum-frequency generation spectroscopy (IR-Vis SFG) and scanning tunneling microscopy (STM). These techniques provided detailed insight into molecular adsorption geometries, thermal stability, intermolecular interactions, and vibrational fingerprints associated with the benzamide functional groups, paving the way for the deposition of the metallo-porphyrin analogues and next studies on the metal single-atom reactivity towards small substrates.

Riassunto

Il *Capitolo 1* fornisce un conciso inquadramento scientifico della Tesi, introducendo le proprietà strutturali, fotofisiche ed elettrochimiche delle (metallo)porfirine, con particolare enfasi sulle Sn^{IV}-porfirine. Dopo aver delineato il ruolo fondamentale delle (metallo)porfirine nei sistemi naturali, il Capitolo ne descrive la struttura molecolare, le strategie sintetiche e le procedure di metallazione. Viene quindi discussa la chimica di coordinazione delle Sn^{IV}-porfirine, con particolare attenzione alla sostituzione dei ligandi assiali, anche come strumento versatile per l'ottenimento di coniugati fotoattivi. Alcuni esempi selezionati dalla letteratura illustrano come questi sistemi possano essere impiegati per attivare processi di trasferimento di energia ed elettroni fotoindotti. La coniugazione di Sn^{IV}-porfirine ad amminoacidi redox attivi viene anche discussa. Viene poi riassunto il ruolo della tirosina e del triptofano come unità fotoattive per processi di trasferimento elettronico accoppiato al protone (Proton Coupled Electron Transfer, PCET) o per più semplici processi di trasferimento elettronico. Sono inoltre delineati il quadro meccanicistico e la rilevanza del PCET sia nei sistemi biologici sia in quelli artificiali. Infine, vengono brevemente descritti i più recenti esempi di coniugati di Sn^{IV}-porfirine aventi tirosina o triptofano o-come leganti assiali , in quanto rappresentano il punto di partenza del lavoro sviluppato nella Tesi. Introduzioni più specifiche e dedicate saranno fornite all'inizio di ciascuno dei Capitoli successivi.

Il *Capitolo 2* descrive la sintesi, la caratterizzazione e lo studio fotofisico di nuovi coniugati metallo-porfirina/fenolo progettati per investigare il PCET, ispirato al Fotosistema II. I composti sono stati preparati coniugando unità fenoliche alla periferia di uno scaffold porfirinico e successivamente metallati con Sn^{IV} o Zn^{II}. NMR, spettrometria di massa, diffrazione a raggi X e calcoli DFT confermano le strutture e rivelano che le distanze tra il fenolo e la porfirina sono significativamente maggiori rispetto a quelle riportate in precedenza per complessi Sn^{IV}-porfirina aventi due tirosinati sulle posizioni assiali. Le misure fotofisiche sulle Sn^{IV}-porfirine, condotte in collaborazione con il Prof. Mirco Natali (Università di Ferrara, IT), mostrano che, nonostante una termodinamica favorevole, l'aumento delle distanze donatore-accettore riduce fortemente l'efficienza cinetica del trasferimento elettronico. Di conseguenza, non si osserva PCET fotoindotto dallo stato eccitato di singoletto, mentre il percorso di PCET guidato dallo stato di tripletto risulta molto più lento ed è dominato da processi di quenching bimolecolare. Il confronto con composti modello evidenzia che l'allontanamento del fenolo dal macrociclo sopprime la formazione della specie diradicalica desiderata. Nel complesso, i risultati dimostrano che distanze estese tra cromoforo e donatore

limitano la reattività PCET, fornendo indicazioni chiave per la progettazione di futuri sistemi artificiali in grado di mimare la funzione del Fotosistema II.

Il *Capitolo 3* descrive la ricerca svolta durante un periodo di ricerca di sei mesi nei laboratori del Prof. Sylvestre Bonnet (Università di Leida, NL). Il Capitolo esplora la progettazione, la sintesi e la caratterizzazione fotofisica preliminare di un nuovo coniugato Sn^{IV}-porfirina/peptide, pensato per indurre un PCET fotoindotto attraverso membrane in doppi strati lipidici. Ispirandosi ai processi naturali di separazione di carica fotosintetica, il lavoro integra un fotosensibilizzatore redox-attivo (Sn^{IV}-porfirina), tirosina come elettron donatore e istidina come base all'interno di uno scaffold peptidico ($YALP_{23}$), capace di adottare una struttura α-elica transmembrana. Simulazioni di dinamica molecolare hanno suggerito la posizione ottimale di inserimento del cromoforo e degli altri componenti attivi nella sequenza peptidica. Il coniugato risultante (insieme al peptide modello corrispondente e a due analoghi più corti) è stato sintetizzato combinando SPPS e coniugazioni in soluzione, ed è stato caratterizzato in modo approfondito mediante NMR, MS, CD e spettroscopie ottiche. Esperimenti preliminari di quenching sono stati utilizzati per selezionare possibili condizioni operative in cui possano verificarsi processi di trasferimento elettronico o di tipo PCET. Infine, il coniugato è stato incorporato con successo in liposomi di DPPC, senza modifiche sostanziali delle proprietà fotofisiche del fotosensibilizzatore, rappresentando così una piattaforma promettente per futuri studi sul PCET fotoindotto transmembrana.

Il *Capitolo 4* presenta la progettazione, la sintesi e la caratterizzazione superficiale di una serie di porfirine funzionalizzate finalizzate alla formazione di network metallo-organici bidimensionali (2D-MONs) modulabili per la catalisi a singolo atomo. Tre porfirine sostituite con un sostituente benzammidico e i corrispondenti derivati del cobalto sono state sintetizzate per mimare specifiche caratteristiche delle seconde sfere di coordinazione enzimatiche. Le loro proprietà strutturali e fotofisiche sono state determinate mediante spettroscopia NMR 1D e 2D, HRMS e spettroscopia UV-Vis. Per investigare la capacità di questi coniugati di formare architetture supramolecolari ordinate su superfici, le versioni free-base sono state depositate, in condizioni di ultra-alto vuoto, su substrati di grafene/Ir(111) e Au(111) mediante deposizione elettrospray, in collaborazione con il Prof. Erik Vesselli (Università di Trieste, IT). I layer risultanti sono stati analizzati combinando IR-Vis SFG e STM. Queste tecniche hanno fornito informazioni dettagliate sulle geometrie di adsorbimento molecolare, sulla stabilità termica, sulle interazioni intermolecolari e sulle impronte vibrazionali associate ai gruppi funzionali benzammidici, aprendo la strada alla deposizione degli analoghi metallo-porfirinici e a studi successivi sulla reattività dei singoli atomi metallici nei confronti di piccole molecole.

CHAPTER 1

Overview

This Chapter provides a concise scientific background of the Thesis, introducing the structural, photophysical, and electrochemical properties of (metallo)porphyrins, with particular emphasis on Sn^{IV}-porphyrins. After outlining the fundamental role of (metallo)porphyrins in natural systems, the Chapter describes their molecular structure, synthetic strategies, and metalation procedures. The coordination chemistry of Sn^{IV}-porphyrins is then discussed, focusing on axial ligand substitution, also as a versatile tool for the obtainment of photoactive conjugates. Few selected literature examples illustrate how these systems can be implemented to control photoinduced energy and electron-transfer processes. Further address is given to the conjugation of Sn^{IV}-porphyrins with redox-active amino acids. The role of tyrosine and tryptophan as photoactive units for Proton Coupled Electron Transfer (PCET) or simpler electron transfer is summarized. The mechanistic framework and relevance of proton-coupled electron transfer (PCET) in both biological and artificial systems is outlined. Finally, the latest examples of Sn^{IV}-porphyrins conjugates bearing axial tyrosine or tryptophane residues are shortly described as they represent the start point of the work developed in the Thesis. More specific and dedicated introductions will be given at the beginning of each of the following Chapters.

List of abbreviations.

DDQ = 2,3-dicloro-5,6-dicianobenzochinone

TPP = 5,10,15,20-(phenyl)porphyrin

Fb = 5-(4benzoic acid)-10,15,20-phenylporphyrin

OEP = 2,3,7,8,12,13,17,18-(octaethyl)porphyrin

FbR = 5-(4-benzoic acid)-15-(3,5-di-*tert*-butylphenyl)-2,8,12,18-tetra-*n*-hexyl-3,7,13,17-tetramethylporphyrin.

TpFP = 5,10,15,20-(pentafluorophenyl)porphyrin

TPyP = 5,10,15,20-tetra-(4-pyridyl)porphyrin

$Sn(OH)_2TPP$ = trans-dihydroxo[5,10,15,20-(phenyl)porphyrinato]-tin(IV)

$Sn(OH)_2OEP$ = trans-dihydroxo[2,3,7,8,12,13,17,18-(octaethyl)porphyrinato]-tin(IV)

Ac-Y = N-Acetyl-*L*-tyrosine

Ac-W = N-Acetyl-*L*-tryptophane

1.1.1 Porphyrins and Metallo-porphyrins in Nature.

(Metallo)porphyrins are widespread in Nature, forming a versatile class of tetrapyrrolic molecules that support essential biological processes. They function as oxygen-transport cofactors in heme-proteins, as prosthetic groups in many metabolic enzymes (such as Cytochrome *C* oxidase),[1–3] and act as ke\y light-harvesting and redox-active pigments within the photosynthetic system (Figure 1.1.1).[4–6] In antennae systems and reaction centres, including the core of Photosystem II, porphyrin assemblies enable efficient light absorption and electron transfer, highlighting their central role in many biological photoinduced processes. The large use of (metallo)porphyrins in natural systems demonstrates their versatility deriving both from their structural and functional properties. The role of porphyrin in PSII is described in detail in Chapter 2.

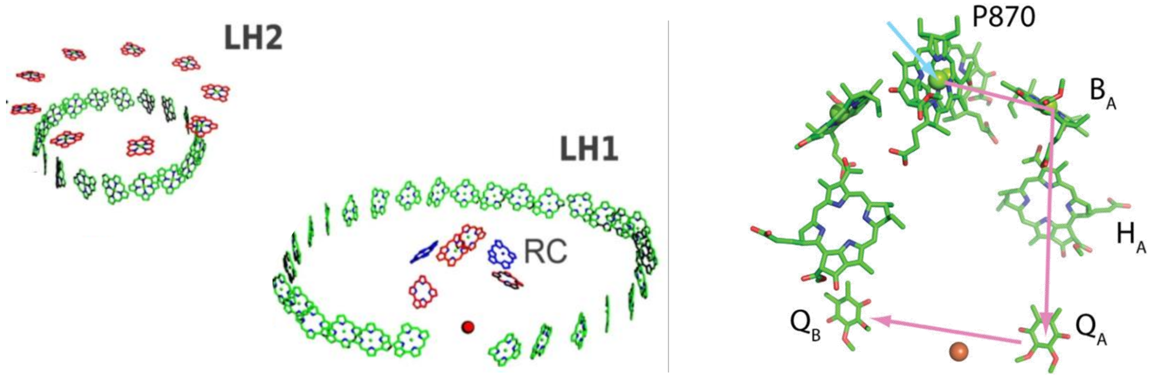

Figure 1.1.1. Schematic representation of two light-harvesting antenna systems (LH) and reaction centre (RC) in purple bacteria. Figure adapted from reference 6 . Right: enlargement of the reaction centre and depiction of the electron transfer.

1.1.2. Porphyrins and Metallo-porphyrins: structure and reactivity.

(Metallo)porphyrins are a versatile and structurally robust family of macrocyclic compounds that plays a central role in both natural biochemical and synthetic chemical fields. In artificial systems these compounds have been widely studied in an endless variety of fields, such as catalysts,[7–9] biomimetic photosynthesis and photodynamic therapy.[10–14] For what concerns artificial photosynthesis the close similarity if not complete identity of these chromophores to the natural dyes make them an obvious choice. Their structural possible diversity is also a key feature in their widespread success. The tetrapyrrolic macrocycle is formed by four pyrrole rings connected to each other by methylene bridges forming a rigid, planar and aromatic structure, as shown in Figure 1.1.2. Accordingly to the IUPAC nomenclature, positions 1, 4, 6, 9, 11, 14, 16, 19 (in black in Figure 1.1.2) are called α-pyrrolic; positions 2, 3, 7, 8, 12, 13, 17, 18 (in blue in Figure 1.1.2) are called β-pyrrolic while the positions 5, 10, 15 and 20 (in red in Figure 1.1.2) are named *meso* positions.

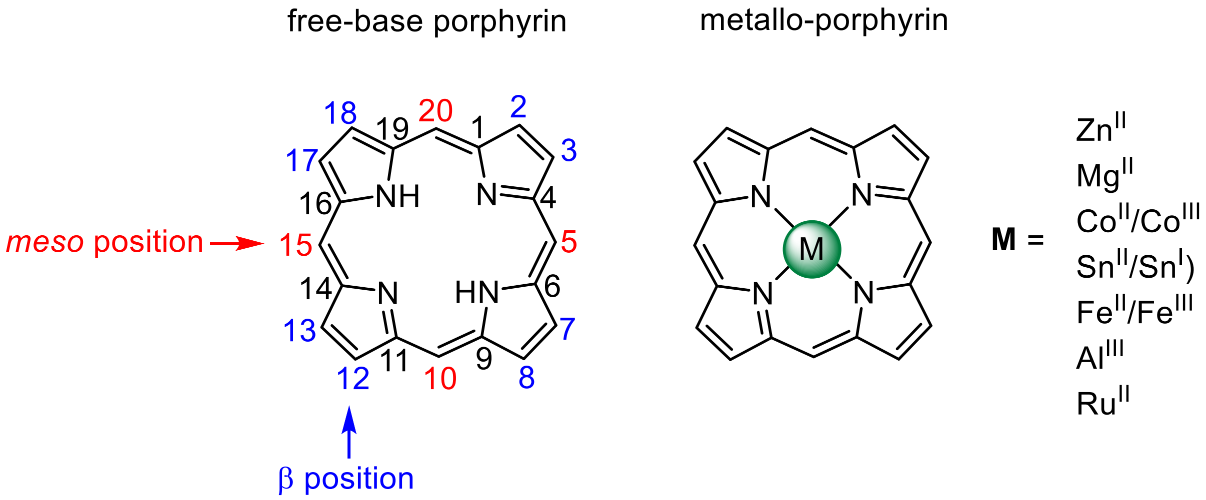

Figure 1.1.2. Chemical structure, IUPAC nomenclature and selection of metal cations that can be inserted in the porphyrin core.

Depending on the position and the nature of the substituents two main synthetic strategies for the porphyrin synthesis can be used. To obtain *meso*-substituted aryl porphyrins the most common used strategy is the Adler-Longo synthesis.[15] With this method pyrrole and one or more aldehydes are mixed in refluxing propionic acid to afford a statistical mixture of *meso*-substituted products. The reaction is not regioselective and the separation of the regio-isomers and undesired by-products (such as oligomers or sub-classes of macrocycles) by column chromatography may be challenging. However, with the Adler-Longo method a variety of mono-, di-, tri-, and tetra *meso*-substituted aryl porphyrin were successfully isolated. An alternative synthetic approach to obtain regiospecific *meso*-substituted porphyrins is the Lindsey method.[16] Here two dipyrromethene units, prepared *via* condensation of pyrrole and the desired aldehyde (or a mixture of two) in acidic conditions, are condensed with another aldehyde and then oxidized with DDQ to form the aromatic ring. The reaction is sensitive to the nature of the used acid and the concentration of reagents, but in general is a convenient method to direct the functionalization towards desired positions. In particular, the Lindsey method allows for the isolation of *trans meso* substituted porphyrins or β-substituted ones. Porphyrins can coordinate a metal centre in their inner cavity, by deprotonation and coordination of the pyrrole nitrogen atoms, with formation of the corresponding metallo-porphyrin (Figure 1.1.2). The porphyrin core can chelate metal cations form both the main groups and the transition series. Generally, the free-base porphyrin precursor are treated with an excess of a metal salt (typically acetate or chloride), in conditions that strongly dependent on the chosen metal cation.[17] For Zn^{II}-porphyrins, complete metalation is typically achieved at room temperature, using $Zn(CH_3COO)_2{\cdot}2H_2O$ as metal source in a chloroform/methanol mixture. Excess metal salt is removed by washing the reaction mixture with methanol or water depending on the solubility of the resulting Zn^{II}-porphyrin. Sn^{IV}-porphyrins have been prepared using two main synthetic strategies, both of which use $SnCl_2{\cdot}2H_2O$ as the metal precursor. The first method makes use of high boiling solvents, such as pyridine, and high temperatures,[18] thus being not advisable for thermo-labile porphyrins. The second milder alternative, reported by Shetti *et al.*,[19] uses a chloroform/ethanol mixture in refluxing conditions and usually is less efficient, thus the unreacted free-base porphyrin needs to be removed by column chromatography. In both procedures, the isolated product should be the dichloro $SnCl_2$-porphyrin derivative. This metallo-porphyrin derivative can be then converted in the corresponding dihydroxo $Sn(OH)_2$-porphyrin species, which serve as the typical building block for the assembling of larger supramolecular conjugates (see next section). The hydrolysis is usually performed in basic conditions, with a variety of procedures spread out on the literature. One of the earliest reports involves treatment of the $SnCl_2$-porphyrin precursor with concentrated ammonia in pyridine,[18] followed by precipitation with water, filtration and purification by column chromatography on deactivated alumina. In 1986, Arnold reported an example in which efficient hydrolysis was attained by simple treatment of the $SnCl_2$-porphyrin precursor with basic alumina, followed by chromatographic purification.[20] More recently, Crossley *et al.* proposed that efficient hydrolysis can be done using an excess of K_2CO_3 in a THF:H_2O mixture under refluxing conditions, as schematically depicted in Scheme 1.1.1.[21]

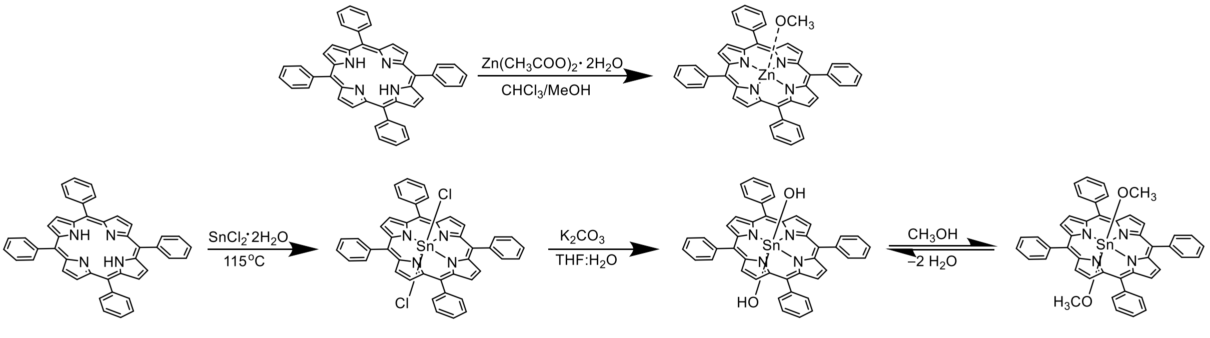

Scheme 1.1.1. Example of metalation processes used for the insertion of Zn^{II} and Sn^{IV} cations in the porphyrin core.

Efficient hydrolysis of $SnCl_2$-porphyrins can be confirmed by ^{1}H NMR spectroscopy. Due to the shielding cone of the porphyrin macrocycle, the resonances of any proton-containing axial ligand are found remarkably upfield shifted. The resonance of the hydroxy groups in $Sn(OH)_2$-porphyrin is found at $\delta \sim -7$ ppm (this signal is normally broad due to exchange with residual water in the solvent of analysis) as shown in Figure 1.1.3. It should be noted that the presence of competing oxygenated ligands inevitably results in partial or complete exchange of the –OH groups with time. For instance, if a $Sn(OH)_2$- or $SnCl_2$-porphyrin is dissolved in either methanol or dimethyl sulfoxide, the formation of $Sn(OCH_3)_2$- or $Sn(OS(CH_3)_2)_2$-porphyrin with time is observed (with faster and complete conversion for the case of methanol, as shown in Scheme 1.1.1). The dialkoxo $Sn(OR)_2$-porphyrins can be directly obtained as pure products from the $Sn(OH)_2$-porphyrins by working in anhydrous conditions in the presence of alcohol as solvent. In addition to the ^{1}H NMR characterization, the ^{119}Sn NMR active nucleus (I = ½) allows for a direct observation of the central metal and for the assignment of its coordination environment. In 1994, Arnold and Bartley reported an exhaustive example on the use of ^{119}Sn NMR to determine the nature of the axial ligands on the metal centre.[22] Due to the low natural abundance of ^{119}Sn (8.6%), 1D ^{119}Sn NMR experiments acquisition times are extremely long. To overcome this issue, ^{1}H-^{119}Sn HMBC (*Heteronuclear Multiple Bond Correlation*) experiments are extremely convenient, as reported by the group of Crossley and by us in the last decades.[18,21,23–27] These experiments allow for indirect determination of δ(^{119}Sn) values with short acquisition times. For *meso*-substituted porphyrins, the ^{1}H-^{119}Sn HMBC spectrum shows correlation peak arising from the ^{4}J coupling between the β-pyrrolic protons and the tin nucleus. This heteronuclear coupling is observed also in the ^{1}H NMR spectrum as the β-pyrrolic protons display characteristic satellite signals (Figure 1.1.3). ^{1}H-^{119}Sn HMBC experiments therefore provide a simple and effective method to assess the purity of the isolated compounds, particularly with respect to the nature of the axial-coordinating ligands, as the ^{119}Sn chemical shift is very sensitive to their nature.[18] Mixed ligands on the apical positions induce an average chemical shift of the ^{119}Sn nucleus (*e.g.* one chloride and one hydroxy are bound to the same tin centre, the δ(^{119}Sn) is the average between those of the dichloro and the dihydroxo corresponding derivatives). Finally, Sn^{IV}-porphyrins are also usually characterized by mass spectrometry. It is rather uncommon to observe the intact molecular species, as the axial ligands are typically lost during the ionization process. Substitution with methoxy groups is also often encountered if methanol is the solvent of analysis (see above and Chapter 2 and 3).

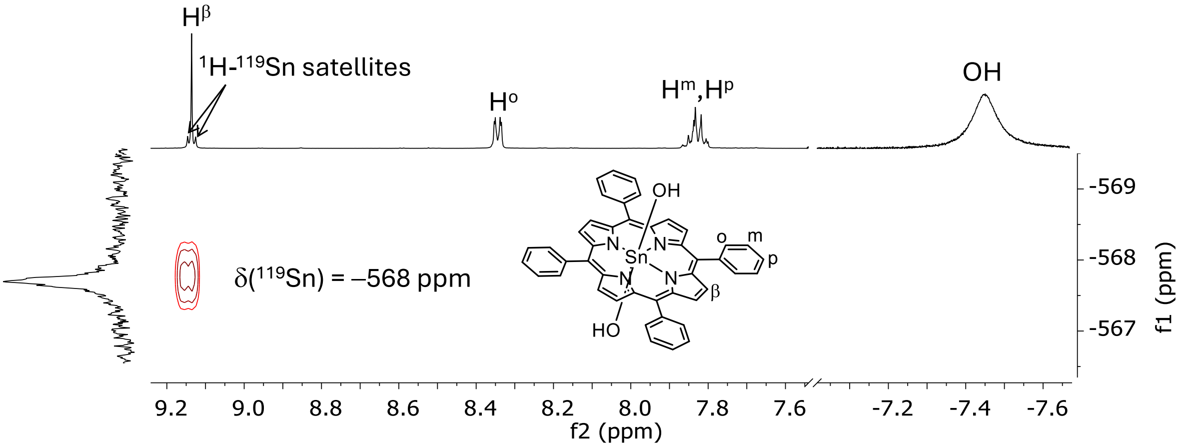

Figure 1.1.3. ^{1}H-^{119}Sn HMBC ($CDCl_3$ 298 K) of **$Sn(OH)_2$TPP**. The signal of the –OH ligands is magnified.

Stability of metallo-porphyrins towards demetallation depends on different factors, like the metal cation size, the degree of covalent bonding and the oxidation state. While Zn^{II}-porphyrins are very sensitive to acid media, Sn^{IV}-porphyrins are surprisingly stable towards demetallation with appreciable demetallation occurring only at H_2SO_4 concentrations close to 100% and high temperatures. However, it is possible to remove the metal cation using basic or reductive conditions, such as lithium in the presence of amines or sodium borohydride in chloroform/ethanol in strict exclusion of air.[18] Porphyrin and metallo-porphyrins present peculiar photo- and electrochemical properties, thus making them interesting systems for a large variety of applications. These chromophores present strong absorption in the visible region due to their extended aromatic conjugation. Considering free-base porphyrins, the absorption spectra present an intense band around 400 – 420 nm ($\varepsilon > 10^5$ M^{-1} cm^{-1}), named Sored band, corresponding to the $S_0 \rightarrow S_2$ $\pi - \pi^*$ transition, and four weaker bands at lower energies, named Q bands, corresponding to the $S_0 \rightarrow S_1$ $\pi - \pi^*$ transition (Figure 1.1.4). Variation of the porphyrin substituents both at the *meso*- or β-pyrrolic positions, induce variations of the energy of the molecular orbitals thus affecting the absorption profile (*i.e.* position and intensity of the Soret and Q bands). The insertion of a metal cation also significantly affects the absorption properties of the porphyrin macrocycle. In general, metallo-porphyrins present a red shift of the Soret band as well as a reduction in the number of the Q bands due to the increased symmetry compared to the free-base porphyrin (Figure 1.1.4).

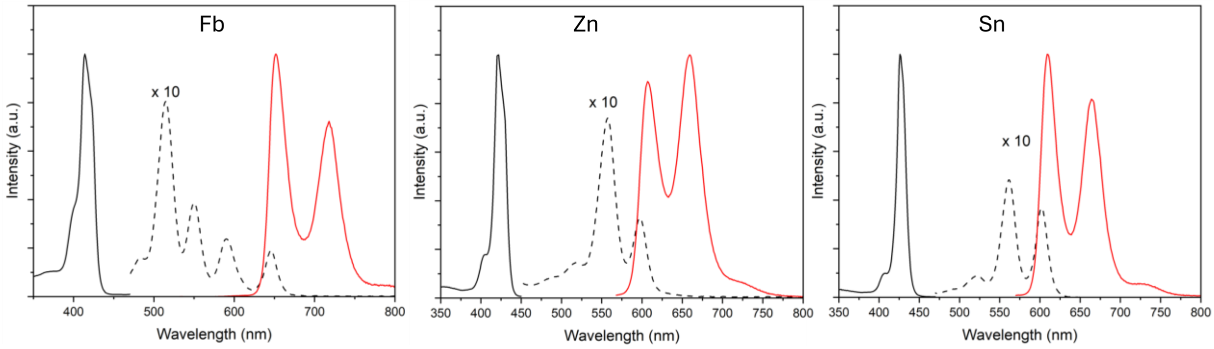

Figure 1.1.4. UV-Vis absorption (black traces) and emission (red traces) spectra of model free-base (Fb, left), Zn- and $SnCl_2$-(tetraphenyl)porphyrins (Zn and Sn, middle and right respectively).

Regarding the emission properties, free-base porphyrins and a large majority of metallo-porphyrins present intense fluorescence emission between 650 – 800 nm (Figure 1.1.4). In the presence of a heavy-metal cation in the inner core the fluorescence emission intensity can be partly or totally quenched, due to an efficient intersystem crossing (ISC) deactivation mechanism of the excited state S_1 and population of the triplet excited state (T_1) caused by the heavy atom effect (and consequent possible phosphorescence emission), as shown in Figure 1.1.5.

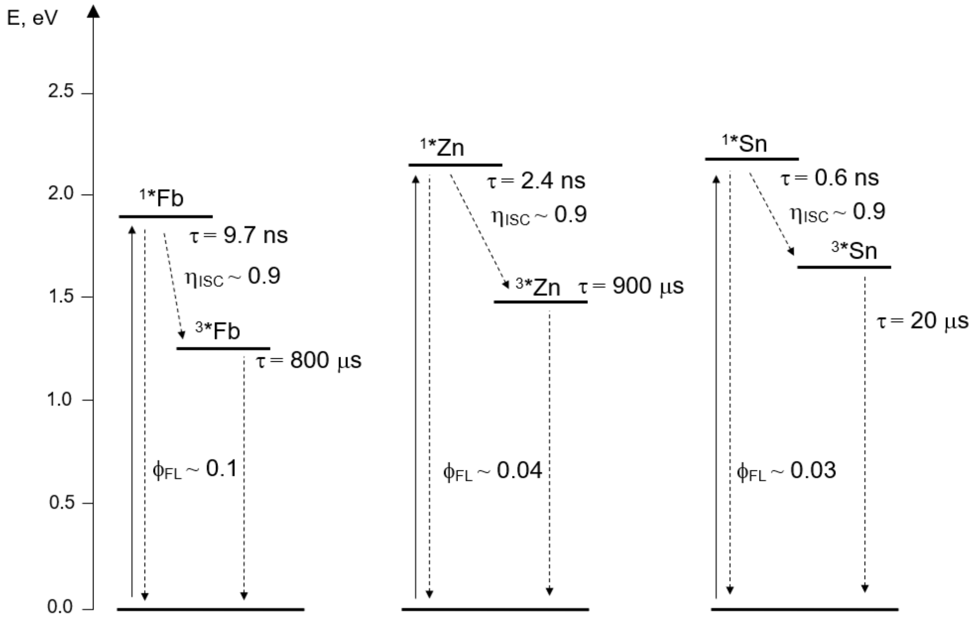

Figure 1.1.5. Energy level diagrams and photophysical deactivation mechanisms for model free-base (Fb), $SnCl_2$- and Zn-porphyrin (Zn). Energy level diagrams taken from compounds **8** – **10** described in Chapter 2.

Considering their electrochemical properties, the porphyrin macrocycle is redox-active and can undergo reversible one- or two-electron reduction and oxidation processes. The presence of the metal centre in metallo-porphyrins may allow also for some metal-centred redox processes, that usually find application in (photo)catalysis.[28–31] Once again, the nature of the metal cation and the substituents at the macrocycle significantly influences the redox potentials of the chromophores. For instance, by comparing electrochemical properties of Zn^{II}- and Sn^{IV}-porphyrins bearing equal peripheral substituents, the latter are more easily reduced than their Zn^{II}- analogues (see also Chapter 2). The redox properties of Sn^{IV}-porphyrins are particularly interesting, as reported by Kadish *et al.*[32] In the case of $SnCl_2$-derivatives, two subsequent one-electron reduction are observed in the Cyclic Voltammetry (CV) experiments recorded in CH_2Cl_2. The first reduction corresponds to the one-electron reduction of the porphyrin macrocycle, forming a Sn^{IV}-porphyrin radical anion (with the $E_{1/2}$ value being also dependent upon the type of axial ligand). The conversion of Sn^{IV} to Sn^{II} is not observed under the electrochemical conditions. From the photophysical and electrochemical properties of (metallo)porphyrins the energy diagrams of the excited states (as well as those of possible charge separated states in the case of (metallo)porphyrin conjugates, if conjugation does not perturb the ground states) can be predicted (see also Chapter 2).

Metallo-porphyrins are often used as scaffolds for the synthesis of supramolecular structures based on coordination chemistry, if the metal cation has a coordination number of at least five, and the apical ligands deriving from the insertion step are sufficiently labile. In this situation, one or both the axial ligands can be substituted by organic fragments, normally in a selective way, regulated by hard/soft discriminations. For example, Zn^{II}-porphyrins preferentially coordinate one nitrogen axial ligand, while Sn^{IV}-porphyrin are selective towards the coordination of two oxygenated ligands. The strength and inertness of the axial bonds depend on the nature of the metal cation and of the ligands.

1.1.3. Axial coordination chemistry of Sn^{IV}-porphyrins.

Preparation of Sn^{IV}-porphyrin supramolecular arrays is widely studied and reported in the literature for many different applications, ranging from photocatalysis to medicinal chemistry.[24,33–43] The typical starting building block is a dihydroxo $Sn(OH)_2$-porphyrin but also the dialkoxo derivatives work well in this regard. In general, the hydroxy ligands can be replaced using acids (HX), if the pK_a of HX is lower than that of water (Scheme 1.1.2). Phenol ligands can also be coordinated as aryloxides from $SnCl_2$- or $Sn(OH)_2$-porphyrins by reaction, in refluxing conditions, with the desired free phenol (two metal-ether bonds are formed).[18] The dicarboxylates Sn^{IV}-$(COOR)_2$-porphyrins are normally prepared by mixing the dihydroxo $Sn(OH)_2$-porphyrin with two equivalents of the carboxylic acid (with formation of two metal-ester bonds). The mechanism for the substitution of hydroxy ligands with carboxylates was studied and reported in 1998 by Sanders *et al.*[44] The isolated Sn^{IV}-(COOR)$_2$-porphyrin conjugates are in general quite stable and inert compounds, in slow exchange on the NMR timescale with excess free carboxylic acid. This feature though prevents the isolation of asymmetric Sn^{IV}-porphyrin conjugates bearing two different axial ligands. From the comparison of the pK$_a$ of phenols and carboxylic acids, the carboxylate derivatives are expected to be more stable to hydrolysis than the aryloxides. It should be mentioned that, in the case of Sn(OH)$_2$-porphyrins, the substitution reaction proceeds with elimination of two water molecules and may therefore require the addition of drying agents (*e.g.* anhydrous Na_2SO_4) to achieve complete coordination of the selected axial ligand. Finally, good solubility of both precursors in the working solvent (or at least in miscible solvents) is found to be essential.

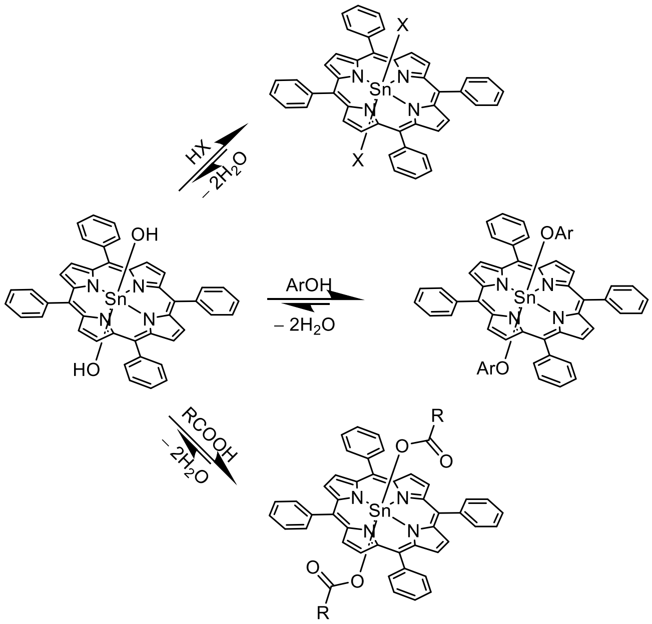

Scheme 1.1.2. Schematic representation of the synthesis of Sn^{IV}-porphyrins with different axial ligands.

1.1.4. Photoactivity of Sn^{IV}-porphyrins and Sn^{IV}-porphyrin conjugates.

Thanks to their interesting photophysical and electrochemical properties, Sn^{IV}-porphyrins have been employed as photoactive units for photocatalytic purposes. Few selected examples are now illustrated. In 2014, Kurz *et al.* reported one of the first examples of SnCl$_2$-porphyrins used as photosensitizers for light-driven proton reduction.[33] They showed that a SnCl$_2$-porphyrin (**SnCl$_2$TPP(COOH)$_4$** in Figure 1.1.6) can act as photosensitiser in a photocatalytic system operating by a reductive quenching mechanism in combination with a PtO_2 heterogenous catalyst, in water solution. The authors also found that the metallo-porphyrin macrocycle behaves as a redox non-innocent ligand in water, as it gets permanently reduced to the corresponding Sn^{IV}-chlorine derivative with time, and the reduction product plays a key role in the photocatalytic cycle. In 2020 Coutsolelos *et al.* reported on the possibility to combine positively, neutral or negatively charged Sn^{IV}-porphyrins photosensitizers (PS) with a cobaloxime-based photocatalyst, to promote efficient hydrogen production.[34] In particular, the two neutral **$SnCl_2TPP$-$(COOMe)_2$** and **$SnCl_2TPP[PO(OEt)_2]_4$** were found to be efficient PSs towards H_2 production (Figure 1.1.6).

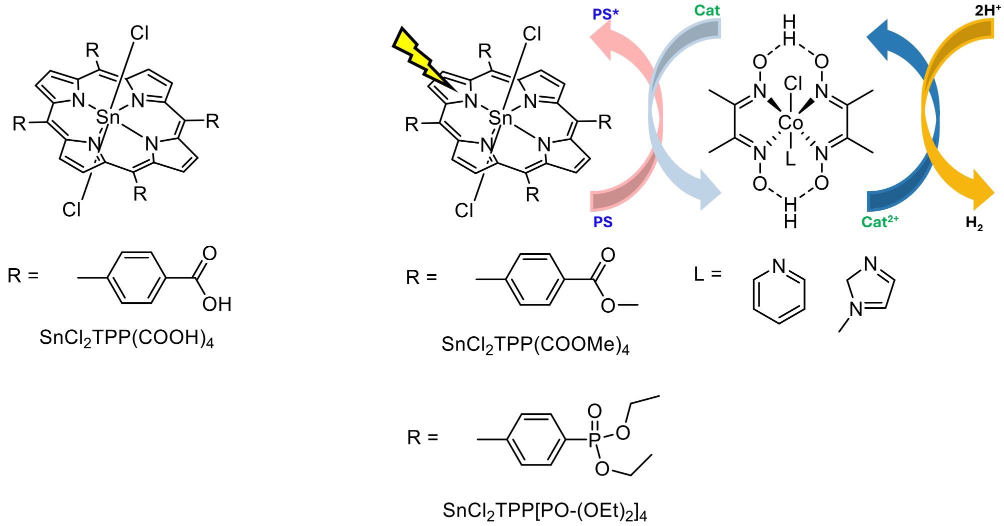

Figure 1.1.6. Left: chemical structure of the $SnCl_2$-porphyrin reported by Kurz *et al.*[33] Right: schematic representation of the photocatalytic reactions reported by Coutsolelos *et al.*[34]

Due to their versatile coordination chemistry, Sn^{IV}-porphyrins have been widely used as supramolecular scaffolds for the construction of light-responsive supramolecular assemblies. The reported examples rely on the axial coordination of either aryloxide or carboxylate ligands. The literature on photoactive Sn^{IV}-porphyrin arrays featuring apical ligands bound through carboxylate (or phenolate) groups is extensive, and a comprehensive description of all the examples lies beyond the scope of this Introduction. Few selected cases will be now presented. One of the first examples of the synthesis of a bis(aryloxo) Sn^{IV}-porphyrin was reported by Maiya *et al.* in 1999.[35] In this system, two free-base porphyrins are axially coordinated to the tin centre of a central metallo-porphyrin (**Fb-SnP-Fb** in Figure 1.1.7). This assembly allowed to perform photoinduced intercomponent processes following selective excitation of either the Sn^{IV}-porphyrin or the free-base units. For instance, the selective excitation of the central Sn^{IV}-porphyrin led to a highly efficient (~ 70%) energy transfer to the free-base porphyrins. The modularity of the synthetic approach of this systems enables the incorporation of a wide variety of porphyrin units, therefore subsequent Sn^{IV}-multiporphyrin arrays have been developed, based on the formation of axial metal-ether bonds.[45]

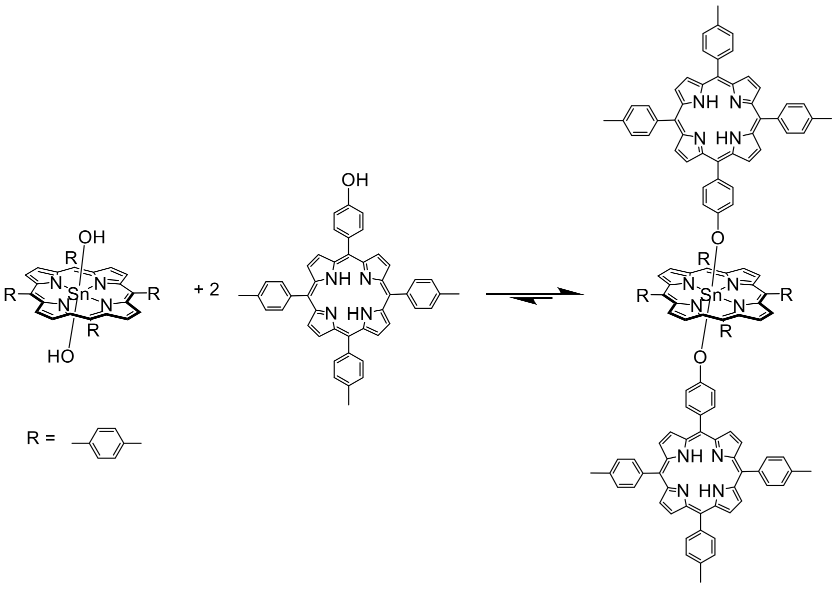

Fb-SnP-Fb

Figure 1.1.7. Schematic representation of the Sn^{IV}-multiporphyrin array reported by Maiya *et al.*[35]

In 2012 Coutsolelos *et al.* reported the synthesis of multichromophore arrays bearing two Bodipy units axially bound to a Sn^{IV}-porphyrin either as carboxylates or as a phenolates (Figure 1.1.8).[38] Different reaction conditions are required for the efficient coordination of the two types of functional groups (see also above). The authors showed that, at room temperature, the type of photoinduced intercomponent processes that take place after the selective excitation of the Bodipy units depends on the presence of either the metal-ether or metal-ester bond. For **SnP1** selective Bodipy excitation results in efficient energy transfer from the Bodipy to the Sn^{IV}-porphyrin unit, leading to sensitized metallo-porphyrin emission. On the other hand, for **SnP2**, selective Bodipy excitation promotes the formation of a charge-separated state *via* electron transfer, yielding to the phenoxyl radical cation and the metallo-porphyrin radical anion. When the excitation is done at 77 K in frozen toluene, the electron transfer is suppressed and both compounds favour population of the metallo-porphyrin singlet excited state *via* energy transfer.

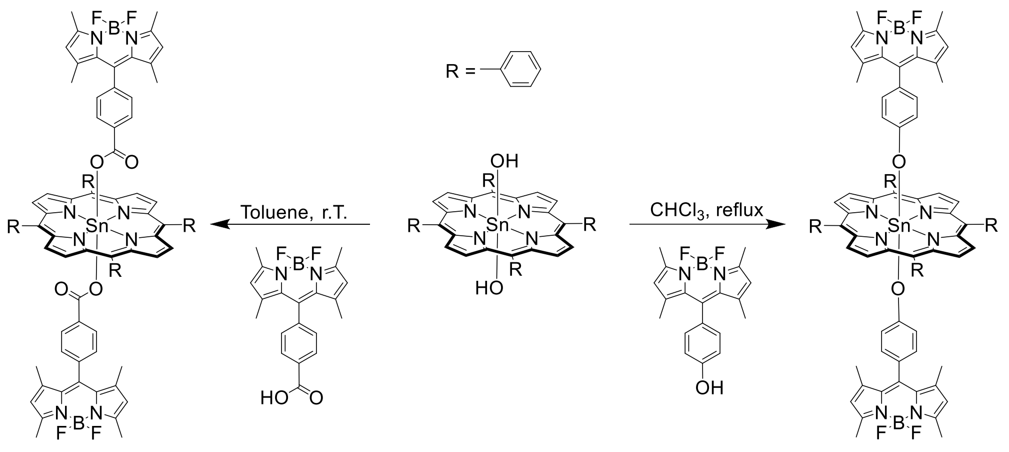

SnP1 SnP2

Figure 1.1.8. Chemical structure of the two Sn^{IV}-porphyrin/Bodipy conjugates reported by Coutsolelos *et al.*[38]

In 2019 Iengo *et al.* reported an elegant example of the synthesis of a library of multiporphyrin arrays based on Sn^{IV}-porphyrin scaffolds and axial carboxylate free-base porphyrins (Figure 1.1.9). In this work the authors highlighted how simple variations of the substituents at the β-pyrrolic or *meso* positions of both the Sn^{IV}-porphyrin units or the free-base ones, significantly influences the photoinduced intercomponent processes promoted by visible light irradiation (it must be noted that for these conjugates completely selective excitation of either of the chromophores is not always feasible). Photophysical studies were done in two different solvents with different polarity: CH_2Cl_2 and toluene. **Sn(Fb)$_2$TPP** and **Sn(Fb)$_2$OEP** exhibited ultrafast energy transfer from the excited Sn^{IV}-porphyrin to the free-base units with unitary efficiency in both solvents. **Sn(FbR)$_2$TPP** showed a neat switch in the photoinduced intercomponent quenching mechanism upon changing the solvent polarity. In the more polar CH_2Cl_2, photoinduced electron transfer occurs upon selective Sn^{IV}-porphyrin excitation, while in the less polar toluene, the mechanism switches to energy transfer. Finally, for **Sn(Fb)$_2$TpFP**, excitation of either of the chromophores results in an ultrafast electron transfer quenching mechanism in both investigated solvents.

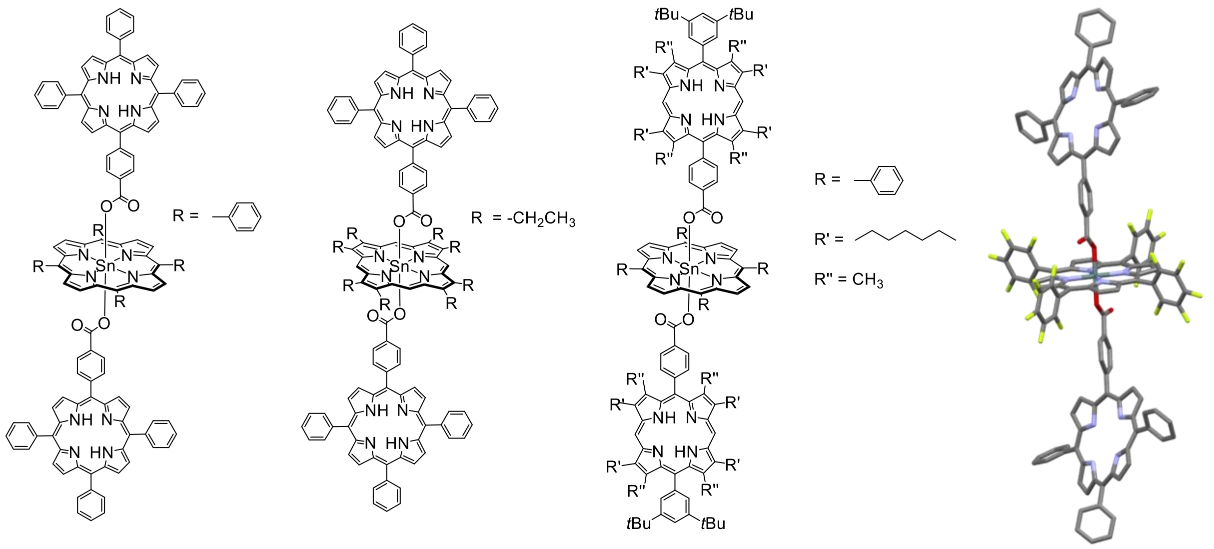

Sn(Fb)$_2$TPP

Sn(Fb)$_2$OEP

Sn(FbR)$_2$TPP

Sn(Fb)$_2$TpFP

Figure 1.1.9. Schematic structures and one selected single crystal X-ray structure (not yet published) of Sn^{IV}-multiporphyrin dyads reported by Iengo *et al.*[24] For the X-ray structure: hydrogen omitted for clarity. Colour code: Sn: dark green; F: yellow; N: purple; O: red; C: grey.

Surprisingly, the strong affinity of Sn^{IV}-porphyrins towards coordination of carboxylates was not much exploited for the combination of this metallo-porphyrins with natural amino acids or peptides. The first example in this sense was reported by Kim *et al.* in 2009.[41] These authors have attached the chiral *L*-proline to a **SnTPyP** (Figure 1.1.10) and fully characterized the system both in solution and in the solid state by single crystal X-ray analysis. Later Coutsolelos *et al.* reported the possibility to coordinate simple dipeptides (*L*-phenylalanine-*L*-phenylalanine = FF) on the apical position of a Sn^{IV}-porphyrin (**Sn(FF)$_2$TPP** in Figure 1.1.10).[42] Taking advantage of the known ability of N-protected di-*L*-phenylalanine peptides to self-assemble into nanostructures, these authors have induced self-assembly of **Sn(FF)$_2$TPP** into spherical nanostructures, as confirmed by SEM images. Finally, our group reported the efficient coordination of either *L*-tyrosinato or *L*-tryptophanato ligands on the apical position of both Sn-(tetraphenyl)porphyrin and Sn-(octaethyl)porphyrin (**Sn(Ac-Y)$_2$TPP**, **Sn(Ac-Y)$_2$OEP**, **Sn(Ac-W)$_2$TPP** and **Sn(Ac-W)$_2$OEP** in Figure 1.1.10).[25–27] The choice of tyrosine and tryptophane was done in view of their key roles as charge transfer promoter in many biological systems. In the natural system tyrosine oxidation is always coupled to proton transfer (Proton Coupled Electron Transfer), while in the case of tryptophane ET-only or PCET pathways can both occur. The photophysical properties of these conjugates is thoroughly described in Section 1.1.7 below and in Chapter 2. Some of the features of tyrosine and tryptophan in the natural systems will be now detailed.[46,47]

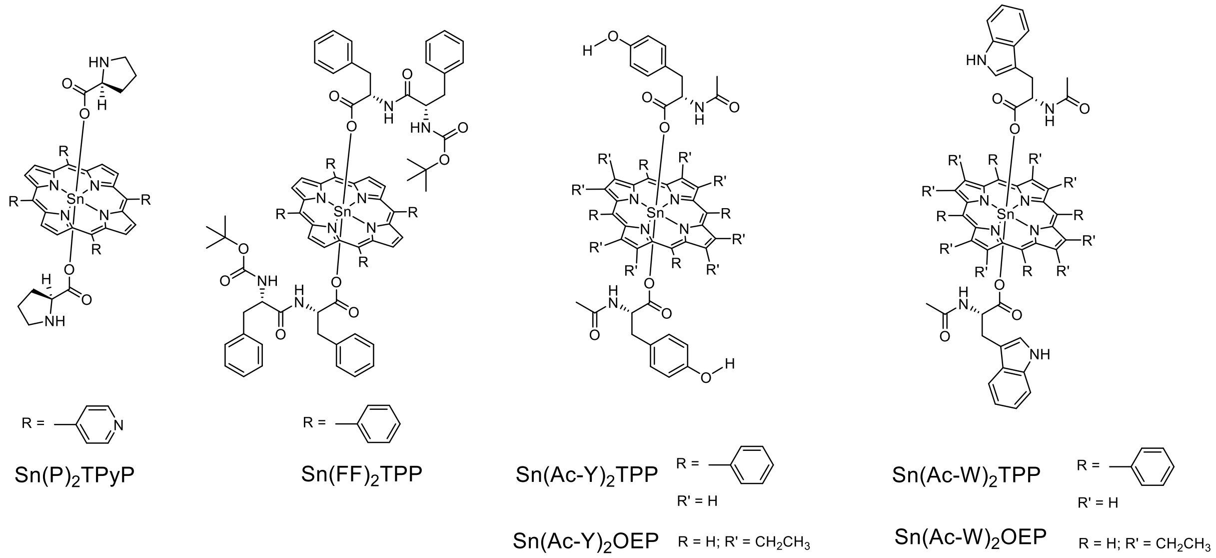

Figure 1.1.10. Chemical structures of the chiral Sn^{IV}-porphyrin/amino acid or peptide conjugates reported by Kim *et al*;[41] Coutsolelos *et al*;[42] and Iengo *et al.*[25–27]

1.1.5. Tyrosine and tryptophane in Natural systems.

Tyrosine (TyrOH) and tryptophane (TrpNH) are key amino acids in natural systems as they are directly involved in many biological processes involving electron transfer (ET). Respiration is a case point: at least fifteen ETs are required to extract reducing equivalents from NADH, deposit them in O_2, and generate the electrochemical proton gradient required to drive ATP synthesis.[46] If ET is coupled with proton transfer (PT) the mechanism is called Proton Coupled Electron Transfer (PCET). Many redox enzymes require transfer of electrons and holes at high potentials, for which the side chain of redox-active amino acids, such as tyrosine and tryptophane, are involved. The different redox and acid-base properties of such amino acids make their reactivity towards ET significantly different. For tyrosine the high oxidation potential of the phenol group (E° ~ +1.5 V *vs.* NHE for the TyrOH/$TyrOH^{\cdot +}$ couple) and the low pK_a of the $TyrOH^{\cdot +}$ species ($pK_a = -2$ in aqueous solution), translates in the fact that tyrosine oxidation is always coupled with proton transfer through a PCET mechanism. On the other hand, for tryptophane the relatively low oxidation potential (E° ~ +1.2 V *vs.* NHE for the TrpNH/$TrpNH^{\cdot +}$ couple) and the higher pK_a of the $TrpNH^{\cdot +}$ ($pK_a = 4.7$ in aqueous solution) are such that, depending on the surrounding conditions, tryptophane oxidation may involve either the $TrpNH^{\cdot +}$ radical cation (*via* ET) or the $TrpN^{\cdot}$ neutral radical species (PCET).[46,47] As an example, tyrosine is known to play a fundamental role in the water oxidation reaction in PSII during plants and bacteria photosynthesis. In particular, tyrosine acts as an electron shuttle to facilitate water oxidation at the Oxygen Evolving Complex (OEC).[48,49] Additionally, tyrosine oxidation is coupled with proton transfer to a close-by histidine *via* PCET (see Chapter 2). On the other hand, tryptophane is a key residue in the photoactivation mechanism of E. Coli DNA photolyase.[50] The first oxidation step is promoted by the excited-state of a flavin adenine dinucleotide followed by an ET only mechanism, with the formation of a $TrpNH^{\cdot+}$ radical cation. The subsequent hole transfer to a second terminal tryptophane residue is accompanied by deprotonation yielding to a neutral $TrpN^{\cdot}$ species *via* PCET mechanism.

1.1.6. Proton Coupled Electron Transfer mechanisms.

Proton Coupled Electron Transfer represents a fundamental class of reactivity in biological, catalytic, and material systems. In these processes the transfer of one or more electrons is intrinsically linked to the transfer of one or more protons, and the two events cannot be treated separately. This coupling may occur either in a single kinetic step or through a sequence of discrete steps, yet the defining characteristic is that electron and proton motions are energetically connected and mechanistically intertwined. In biological systems PCET governs the reactivity of a wide range of oxidoreductases and plays a central role in the water oxidation chemistry of Photosystem II during photosynthesis (see also Chapter 2). Outside biology, PCET underlies key transformations in synthetic catalysis, including hydrogen atom transfer (HAT), oxygen activation, activation of small molecules, and CO_2 reduction. While all electron transfer coupled to proton shifts may be referred to as PCET, the mechanism details can be different. PCET can proceed *via* concerted or stepwise pathways (Scheme 1.1.3). Thermodynamics and kinetics of the two mechanisms are well described in the literature.[46,51–55]

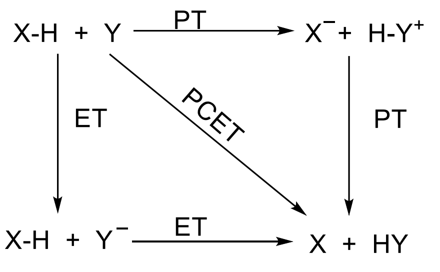

Scheme 1.1.3. Schematic representation of the concerted *vs.* stepwise PCET.

In stepwise PCET the electron and proton are transferred sequentially through ETPT or PTET mechanisms, often involving short-lived, high-energy intermediates that typically do not accumulate and are not detectable. In this mechanism each step is normally endergonic. In contrast, concerted PCET involves the simultaneous transfer of electron and proton in a single kinetic step, thereby bypassing the formation of high-energy intermediates. A related process is hydrogen atom transfer (HAT) in which both the proton and electron are transferred between the same donor and acceptor. HAT is generally adiabatic, with the electronic wavefunction varying smoothly along the proton coordinate resulting in a minimal charge redistribution and low solvent reorganization energy. In contrast, non-adiabatic concerted PCET involves abrupt changes in the electronic wavefunction. Importantly, the distinction between HAT and PCET is not always straightforward. The details on the HAT mechanism will not be described further here. The theoretical description of PCET builds on established frameworks for electron and proton transfer theories. Electron transfer rates are well described by the Marcus theory, in which the rate constant depends on the reaction free energy and the reorganization energy. Proton transfer, in contrast, may require either a classical or quantum mechanical treatment depending on the strength of the coupling. Compared to electrons, protons have higher mass, resulting in more localized wavefunctions and shorter tunnelling distances, typically less than ~1 Å, while electron tunnelling can occur over tens of Å. Hammes-Schiffer and co-workers developed the most used theory for PCET by integrating quantum mechanical descriptions of both electron and proton motion with a classical treatment of the remaining nuclei and the solvent.[54,55] Because protons tunnel over much shorter distances than electrons, proton transfer exhibits a stronger distance dependence, and small changes in donor-acceptor distance can significantly alter PCET rates. The more localized vibrational wavefunctions of deuterons further reduce tunnelling efficiency, giving rise to kinetic isotope effects (KIEs). KIE is defined as $k_{\mathrm{PCET}}(\mathrm{H})/k_{\mathrm{PCET}}(\mathrm{D})$. Although KIEs have been widely used to probe PCET mechanisms, their interpretation is often complex. Large KIE values suggests a concerted PCET, although large values are uncommon. Stepwise PTET pathways may also display significant KIEs, and even some pure electron-transfer reactions exhibit small but measurable KIEs. Consequently, only exceptionally large KIEs provide unambiguous mechanistic information. Concerted PCET can be described as a vibronic transition between reactant and product states in which both the electron and proton tunnel through a shared transition state. In the high-temperature, nonadiabatic regime the rate constant depends on the electronic coupling and on the Franck-Condon overlap between proton vibrational wavefunctions of reactant and product states. Because proton tunnelling is spatially restricted, variations in proton donor-acceptor distances play a dominant role in determining PCET kinetics and often count more than changes in electronic coupling. Assigning whether a PCET reaction proceeds through a concerted or stepwise mechanism requires combining several experimental and theoretical considerations.[53] The thermochemistry of PCET provides a first stage of mechanistic insight. Detailed discussion in this regard has been reported by Mayer *et al.* in 2010.[47] The free energies of the individual ET and PT steps can be estimated from redox potentials, $\mathrm{p}K_{\mathrm{a}}$ values, and bond dissociation free energies (BDFEs), enabling the construction of thermodynamic cycles that predict whether the hypothetical intermediates of stepwise ETPT or PTET pathways would be accessible. When the formation of these intermediates is significantly uphill, a concerted pathway becomes thermodynamically favoured, even before any kinetic data are considered. Thermodynamic exclusion tests represent a first mechanistic probe: by using redox potentials and pK_a values to estimate the free energies of possible ET or PT steps and by comparing them with the experimentally obtained ones, it becomes possible to assess whether a stepwise pathway would require physically unrealistic rate constants. When such inconsistencies arise, a concerted mechanism is strongly supported. This approach, however, depends heavily on the availability of accurate thermodynamic data. Kinetic isotope effects can also provide mechanistic insight, although their diagnostic power is limited by the complexities mentioned above. The most informative probe is the driving-force dependence of the observed rate constant. Plots of $\ln k_{PCET}$ against the driving force for electron transfer ($\Delta G_{ET}°$) or proton transfer ($\Delta G_{PT}°$) reaction allow the identification of characteristic slopes that distinguish between competing mechanisms (Figure 1.1.11).

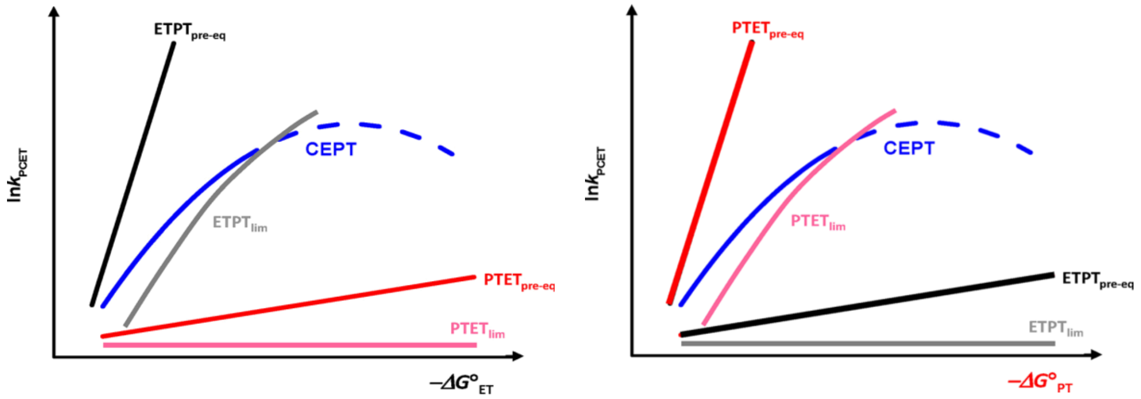

Figure 1.1.11. Qualitative illustration of the different driving force dependencies for the sequential and concerted mechanisms when either $\Delta G_{ET}°$ or $\Delta G_{PT}°$ is varied. In each case, one of the rate-limiting mechanisms has a similar dependence as concerted PCET but lower driving force and larger vibronic coupling. Figure adapted from ref. 53.

Stepwise mechanisms limited by the initial ET or PT step (ETPT$_{lim}$ and PTET$_{lim}$) typically exhibit slopes of about 0.5 in the normal Marcus regime, while pre-equilibrium mechanisms (ETPT$_{pre-eq}$ and PTET$_{pre-eq}$) show slopes near unity because the observed rate constant reflects the equilibrium constant of the initial step. Concerted PCET, in contrast, exhibits a weaker dependence on driving force, with slopes smaller than 0.5, because the reaction exploits the full driving force of the overall process rather than that of an individual elementary step. As a result, concerted PCET is generally favoured at low overall driving force, while ETPT and PTET pathways dominate when the corresponding individual step is strongly exergonic. The competition between concerted PCET, ETPT, and PTET pathways can be visualized through zone diagrams that map the operative mechanism as a function of the driving forces for electron and proton transfer, as reported by Hammarström *et al.* in 2021.[53] These diagrams reveal that concerted PCET predominates when both electron and proton transfer are only weakly favoured, whereas the stepwise mechanisms take over when either ΔG_{ET}° or ΔG_{PT}° becomes more negative. Such representations provide an intuitive and valuable means to rationalize mechanistic trends and to interpret the kinetic and thermodynamic conditions under which each PCET pathway is expected to operate.

1.1.7. State of the art.

The photophysical behaviour of the Sn^{IV}-porphyrins bearing two tyrosinato or tryptophanato residues on the apical positions of the metal centre (Figure 1.1.10), reported by Iengo *et al.*, will be now discussed, as they represents the starting point of the research carried out in this Thesis.[25–27] It was seen that in CH_2Cl_2 solution, for **Sn(Ac-Y)$_2$TPP**, a photoinduced concerted PCET mechanism in the presence of pyrrolidine as external base is activated upon selective visible light excitation of the Sn^{IV}-porphyrin chromophore (see also Introduction of Chapter 2).[25] The mechanism involves a simultaneous electron transfer from the tyrosine to the macrocycle and a proton shift to the external base. The diradical species presents a short lifetime and the recombination to the ground state is quite fast. Different bases with different strength were also tested, showing that replacing pyrrolidine with weaker bases slows the PCET rates and lowers the quenching yields, accordingly with a Marcus-type normal-region dependence.[26] Additionally, moving from **Sn(Ac-Y)$_2$TPP** to **Sn(Ac-Y)$_2$OEP**, it was demonstrated that in the presence of pyrrolidine a photoinduced concerted PCET is active only from the triplet excited state of the chromophore.[26] This result reflects the more negative reduction potential of **Sn(Ac-Y)$_2$OEP** compared to **Sn(Ac-Y)$_2$TPP** in terms of metallo-porphyrin macrocycle and consequent smaller driving force. Moving to the Sn^{IV}-porphyrin/tryptophane conjugates, depending on the nature of the porphyrin macrocycle different photoinduced intercomponent processes are activated in organic solution.[27] For **Sn(Ac-W)$_2$TPP** excitation of the chromophore leads to an efficient electron transfer from the tryptophane residue to the metallo-porphyrin, with consequent formation of a charge separated state ($SnTPP^{\cdot -}$-$TrpNH^{\cdot +}$). In competition with this mechanism an ISC occurs with population of the triplet excited state that is then deactivated *via* concerted PCET thanks to the presence of pyrrolidine. In contrast, for

Sn(Ac-W)$_2$OEP the PCET mechanism is active from both the singlet and triplet excited states of the chromophore, highlighting the peculiar behaviour of tryptophane with respect to tyrosine. As a final remark, it must be noted that all the above photo-active conjugates are chiral and this aspect may open some unique intriguing developments in the future.

1.2. References.

(1) Tsukihara, T.; Aoyama, H.; Yamashita, E.; Tomizaki, T.; Yamaguchi, H.; Shinzawa-Itoh, K.; Nakashima, R.; Yaono, R.; Yoshikawa, S. *Science* **1995**, *269*, 1069.

(2) Tsukihara, T.; Aoyama, H.; Yamashita, E.; Tomizaki, T.; Yamaguchi, H.; Shinzawa-Itoh, K.; Nakashima, R.; Yaono, R.; Yoshikawa, S. *Science* **1996**, *272*, 1136.

(3) Smith, I.; Johnston, M. R.; Jia, Z. *Coord. Chem. Rev.* **2026**, *547*, 217100.

(4) Otsuki, J. *J. Mater. Chem. A* **2018**, *6*, 6710.

(5) Zeng, Y.; Chen, J.; Yu, T.; Yang, G.; Li, Y. *ACS Energy Lett.* **2017**, *2*, 357.

(6) Yang, J.; Yoon, M.-C.; Yoo, H.; Kim, P.; Kim, D. *Chem. Soc. Rev.* **2012**, *41*, 4808.

(7) Wu, Y.; Jiang, Z.; Lu, X.; Liang, Y.; Wang, H. *Nature* **2019**, *575*, 639.

(8) Gu, S.; Marianov, A. N.; Lu, T.; Zhong, J. *Chem. Eng. J.* **2023**, *470*, 144249.

(9) Castro-Cruz, H. M.; Macías-Ruvalcaba, N. A. *Coord. Chem. Rev.* **2022**, *458*, 214430.

(10) Park, J. M.; Hong, K.-I.; Lee, H.; Jang, W.-D. *Acc. Chem. Res.* **2021**, *54*, 2249.

(11) Xu, D.; Duan, Q.; Yu, H.; Dong, W. *J. Mater. Chem. B* **2023**, *11*, 5976.

(12) Abrahamse, H.; Hamblin, M. R. *Biochem. J.* **2016**, *473*, 347.

(13) Ethirajan, M.; Chen, Y.; Joshi, P.; Pandey, R. K. *Chem. Soc. Rev.* **2011**, *40*, 340.

(14) Gunaydin, G.; Gedik, M. E.; Ayan, S. *Front. Chem.* **2021**, *9*.

(15) Adler, A. D.; Longo, F. R.; Finarelli, J. D.; Goldmacher, J.; Assour, J.; Korsakoff, L. *J. Org. Chem.* **1967**, *32*, 476.

(16) Lindsey, J. S.; Schreiman, I. C.; Hsu, H. C.; Kearney, P. C.; Marguerettaz, A. M. *J. Org. Chem.* **1987**, *52*, 827.

(17) Kadish, K. M.; Smith, K. M.; Guilard, R. *The Porphyrin Handbook. Vol. 3, Inorganic, Organometallic and Coordination Chemistry*; Academic: San Diego, Calif., 2000.

(18) Arnold, D. P.; Blok, J. *Coord. Chem. Rev.* **2004**, *248*, 299.

(19) Shetti, V. S.; Ravikanth, M. *J. Porphyr. Phthalocyanines* **2010**, *14*, 361.

(20) Arnold, D. P. *Polyhedron* **1986**, *5*, 1957.

(21) Crossley, M. J.; Thordarson, P.; Wu, R. A.-S. E. *J. Chem. Soc. Perkin 1* **2001**, *18*, 2294.

(22) Arnold, D. P.; Bartley, J. P. Tin Porphyrins. *Inorg. Chem.* **1994**, *33*, 1486.

(23) Brotherhood, P. R.; Luck, I. J.; Crossley, M. J. *Magn. Reson. Chem.* **2009**, *47*, 257.

(24) Amati, A.; Cavigli, P.; Demitri, N.; Natali, M.; Indelli, M. T.; Iengo, E. *Inorg. Chem.* **2019**, *58*, 4399.

(25) Natali, M.; Amati, A.; Demitri, N.; Iengo, E. *Chem. Commun.* **2018**, *54*, 6148.

(26) Natali, M.; Amati, A.; Merchiori, S.; Ventura, B.; Iengo, E. *J. Phys. Chem. C* **2020**, *124*, 8514.

(27) Natali, M.; Amati, A.; Demitri, N.; Iengo, E. *Chem. – Eur. J.* **2021**, *27*, 7872.

(28) Ladomenou, K.; Natali, M.; Iengo, E.; Charalampidis, G.; Scandola, F.; Coutsolelos, A. G. P. *Coord. Chem. Rev.* **2015**, *304–305*, 38.

(29) Silva, R. C. e; Silva, L. O. da; Bartolomeu, A. de A.; Brocksom, T. J.; Oliveira, K. T. *de. Beilstein J. Org. Chem.* **2020**, *16*, 917.

(30) Barona-Castaño, J. C.; Carmona-Vargas, C. C.; Brocksom, T. J.; Oliveira, K. T. D. *Molecules* **2016**, *21*, 310.

(31) Morris, A. J.; Meyer, G. J.; Fujita, E. *Acc. Chem. Res.* **2009**, *42*, 1983.

(32) Ou, Z.; E, W.; Zhu, W.; Thordarson, P.; Sintic, P. J.; Crossley, M. J.; Kadish, K. M. *Inorg. Chem.* **2007**, *46*, 10840.

(33) Manke, A.-M.; Geisel, K.; Fetzer, A.; Kurz, P. A. *Phys. Chem. Chem. Phys.* **2014**, *16*, 12029.

(34) Giannoudis, E.; Benazzi, E.; Karlsson, J.; Copley, G.; Landrou, G.; Angaridis, P.; Nikolaou, V.; Charalambidis, G.; Gibson, E. A.; Coutsolelos, A. G. *Inorg. Chem.* **2020**, *59*, 1611.

(35) Giribabu, L.; Rao, T. A.; Maiya, B. G. *Inorg. Chem.* **1999**, *38*, 4971.

(36) Shetti, V. S.; Ravikanth, M. *Inorg. Chem.* **2010**, *49*, 2692.

(37) Dvivedi, A.; Pareek, Y.; Ravikanth, M. *Chem. – Eur. J.* **2014**, *20*, 4481.

(38) Lazarides, T.; Kuhri, S.; Charalambidis, G.; Panda, M. K.; Guldi, D. M.; Coutsolelos, A. G. *Inorg. Chem.* **2012**, *51*, 4193.

(39) Cavigli, P.; Balducci, G.; Zangrando, E.; Demitri, N.; Amati, A.; Indelli, M. T.; Iengo, E. *Inorganica Chim. Acta* **2016**, *439*, 61.

(40) Indelli, M. T.; Chiorboli, C.; Ghirotti, M.; Orlandi, M.; Scandola, F.; Kim, H. J.; Kim, H.-J. *J. Phys. Chem. B* **2010**, *114*, 14273.

(41) Kim, S. H.; Kim, H.; Kim, K.; Kim, H.-J. *J. Porphyr. Phthalocyanines* **2009**, *13*, 805.

(42) Karikis, K.; Georgilis, E.; Charalambidis, G.; Petrou, A.; Vakuliuk, O.; Chatziioannou, T.; Raptaki, I.; Tsovola, S.; Papakyriacou, I.; Mitraki, A.; Gryko, D. T.; Coutsolelos, A. G. *Chem. – Eur. J.* **2016**, *22*, 11245.

(43) Babu, B.; Mack, J.; Nyokong, T. *Dalton Trans.* **2023**, *52*, 5000.

(44) Hawley, J. C.; Bampos, N.; Sanders, J. K. M.; Abraham, R. J. *Chem. Commun.* **1998**, *6*, 661.

(45) Shetti, V. S.; Pareek, Y.; Ravikanth, M. *Coord. Chem. Rev.* **2012**, *256*, 2816.

(46) Dempsey, J. L.; Winkler, J. R.; Gray, H. B. *Chem. Rev.* **2010**, *110*, 7024.

(47) Warren, J. J.; Tronic, T. A.; Mayer, J. M. *Chem. Rev.* **2010**, *110*, 6961.

(48) Bonin, J.; Robert, M. *Photochem. Photobiol.* **2011**, *87*, 1190.

(49) Styring, S.; Sjöholm, J.; Mamedov, F. T. *Biochim. Biophys. Acta BBA - Bioenerg.* **2012**, *1817*, 76.

(50) Aubert, C.; Vos, M. H.; Mathis, P.; Eker, A. P. M.; Brettel, K. I. *Nature* **2000**, *405*, 586.

(51) Huynh, M. H. V.; Meyer, T. J. *Chem. Rev.* **2007**, *107*, 5004.

(52) Weinberg, D. R.; Gagliardi, C. J.; Hull, J. F.; Murphy, C. F.; Kent, C. A.; Westlake, B. C.; Paul, A.; Ess, D. H.; McCafferty, D. G.; Meyer, T. J. *Chem. Rev.* **2012**, *112*, 4016.

(53) Tyburski, R.; Liu, T.; Glover, S. D.; Hammarström, L. *J. Am. Chem. Soc.* **2021**, *143*, 560.

(54) Hammes-Schiffer, S. *Acc. Chem. Res.* **2009**, *42*, 1881.

(55) Hammes-Schiffer, S.; Stuchebrukhov, A. A. *Chem. Rev.* **2010**, *110*, 6939.

CHAPTER 2

Overview

This Chapter describes the synthesis, structural characterization, and photophysical study of new metallo-porphyrin phenol conjugates designed to investigate Proton Coupled Electron Transfer, inspired by Photosystem II. The compounds were prepared by conjugating phenolic units to the periphery of a porphyrin scaffold and then inserting either Sn^{IV} or Zn^{II}. NMR, mass spectrometry, X-ray diffraction, and DFT calculations confirm the structures and reveal that the phenol to porphyrin distances are significantly larger than in previously reported axial Sn^{IV}-porphyrin tyrosinate complexes. Photophysical measurements on the Sn^{IV}-porphyrin conjugates show that, despite favorable thermodynamics, the increased donor-acceptor distances strongly reduce the kinetic efficiency of the electron transfer. As a result, no photoinduced PCET occurs from the singlet excited state, and the triplet driven PCET pathway is much slower and dominated by bimolecular quenching. Comparison with model compounds highlights that moving the phenol farther apart from the macrocycle suppresses the formation of the desired diradical species. Overall, the results demonstrate that extended chromophore donor distances limit PCET reactivity, providing key insights for the design of future artificial systems that mimic the function of Photosystem II.

The work presented in this Chapter was done in collaboration with Prof. Mirco Natali, University of Ferrara (IT). The DFT calculations were performed by Prof. Federico Berti of the University of Trieste (IT). X-ray analysis was performed by Dr. Gabriele Balducci, University of Trieste (IT).

List of abbreviations.

RC = reaction centre

PQ = plastoquinone

LHCs = light harvesting complexes

OEC = oxygen evolving complex

BIP = benzimidazole-phenol

MV = methyl viologen

TPP = 5,10,15,20-(phenyl)porphyrin

OEP = 2,3,7,8,12,13,17,18-(octaethyl)porphyrin

Ac-Y = N-Acetyl-*L*-tyrosine

TPP-*p*NH$_2$ = 5-(4'-aminophenyl)-10,15,20-triphenylporphyrin;

EDC = N-(3-Dimethylaminopropyl)-N'ethylcarbodiimide hydrochloride

TBAPF$_6$ = tetrabutylammonium hexafluorophosphate

SCE = saturated calomel electrode

SnCl$_2$TPP = *trans*-dichloro[5,10,15,20-(phenyl)porphyrinato]-tin(IV)

Sn(OH)$_2$TPP = *trans*-dihydroxo[5,10,15,20-(phenyl)porphyrinato]-tin(IV)

Ac-A = N-Acetyl-*L*-alanine

TpFP = 5,10,15,20-(pentafluorophenyl)porphyrin

2.1. Introduction.

Proton Coupled Electron Transfer (PCET) plays a fundamental role in many biological processes. To name some of them: cytochrome oxidases,[1–3] ribonucleotide reductase,[4] DNA photolyase,[5] anti-oxidant activity,[6] and C-H activation.[7] Here the focus will be given to the role of PCET in Photosystem II (PSII), a protein complex embedded in the thylakoid membrane of green plants, algae and cyanobacteria, responsible of the water oxidation reaction during oxygenic photosynthesis.[8] Water oxidation splits water into molecular oxygen and protons, forming high-energy electrons that are efficiently transported across the thylakoid membrane to eventually produce NADPH. The produced protons are released in the thylakoid lumen, forming a proton gradient across the membrane that drives ATP production. ATP and NADPH are then used in the dark cycle, also called Calvin-Benson-Bassham cycle, to convert CO_2 into sugars and other organic molecules, called biomass. PSII is a key component of the photosynthetic system responsible for the light-driven oxidation of water and the reduction of plastoquinone. It is a large, multimeric protein complex embedded in the membrane as a dimer, with an overall molecular weight of ~700 kDa as shown in Figure 2.1.1.[9] Interestingly, the structure and function of PSII are highly conserved across photosynthetic organisms, including cyanobacteria, green and red algae, and higher plants. The thylakoid membrane plays an essential role in the efficiency of photosynthetic reactions by spatially separating oxidative and reductive sites, and by facilitating directional electron transfer through the so-called Z-scheme (as described in Chapter 3).

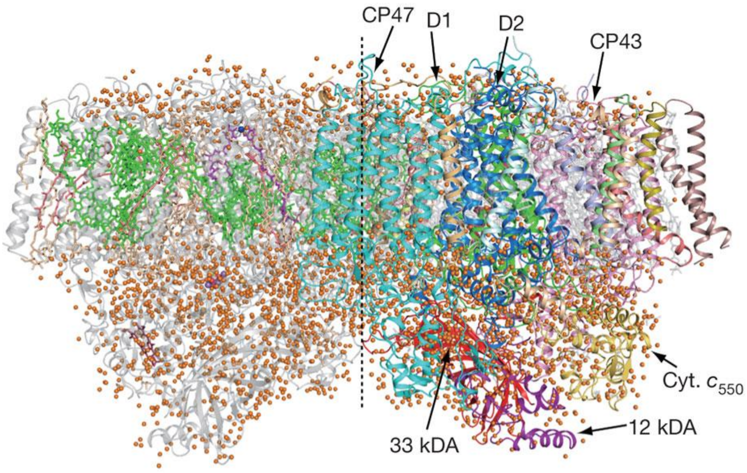

Figure 2.1.1. Overall structure of PSII dimer from *T. Vulcanus* at a resolution of 1.9 Å. View from the direction perpendicular to the membrane normal. The protein subunits are coloured individually in the right-hand monomer and in light grey in the left-hand monomer, and the cofactors are coloured in the left-hand monomer and in light grey in the right-hand monomer. Figure adapted from ref. 9.

All electron transfer processes between the key components in the thylakoid membrane, that are at the basis of oxygenic photosynthesis, are activated by light absorption. Water oxidation reaction driven by PSII can be divided into three sequential steps:

1. Light absorption and excitation energy transfer (EET) within the antenna system, occurring on an ultrafast femtosecond timescale.
2. Charge separation and stabilization in the reaction centre (RC), proceeding on the picosecond to microsecond scale.
3. Chemical reactions, including water oxidation on the donor side and plastoquinone (PQ) reduction on the acceptor side, occurring on much slower millisecond timescales.

The process begins with light absorption by chromophores in the light-harvesting complexes (LHCs), leading to the formation of singlet excited states that are rapidly transferred among pigments of the LHCs and the inner antenna proteins toward the PSII reaction centre. The RC contains four chlorophyll molecules that form the so-called P680 special pair, named for its absorption maximum at ~680 nm.[10] Upon excitation, P680 forms its singlet excited state ($^{1}P680^{*}$), from which one electron is transferred to the primary electron acceptor, pheophytin ($Pheo_{D1}$), within approximately 3 ps.[11] This ultrafast process forms the primary radical pair $P680^{\cdot+}PheoD1^{\cdot-}$. The oxidized species, $P680^{\cdot+}$ has one of the highest known redox potentials in biology (~ +1.25 V),[10] making it a powerful oxidant able to drive the subsequent water oxidation. To prevent charge recombination, which would convert the stored electrochemical energy back into heat, the initial charge separation must be stabilized by a series of secondary electron transfer events. The electron on $Pheo_{D1}^{\cdot-}$ is transferred to a strongly bound plastoquinone molecule (Q_A) within approximately 250 ps, and $P680^{\cdot+}$ is subsequently reduced by the redox-active tyrosine residue Y_Z on the donor side of PSII within 20 ns to 35 µs.[8,12,13] These steps increase the spatial and energetic separation between the positive and negative charges, effectively stabilizing the charge-separated state and allowing the subsequent slower chemical reactions to proceed with high quantum efficiency. On the acceptor side of PSII, first Q_A reduces another quinone, Q_B, that after a second photochemical cycle becomes doubly reduced in concomitance with double protonation to form plastohydroquinone (PQH_2). The reduction of Q_B to PQH_2 requires the sequential transfer of two electrons and two protons. The intermediate semiquinone form ($Q_B^{\cdot-}$) remains tightly bound within its pocket until the next charge separation provides the additional electron and protons. Once fully reduced, PQH_2, having low binding affinity with the pocket, diffuses into the plastoquinone pool within the thylakoid membrane and is replaced by a new Q_B molecule. The overall process is shown in Figure 2.1.2.

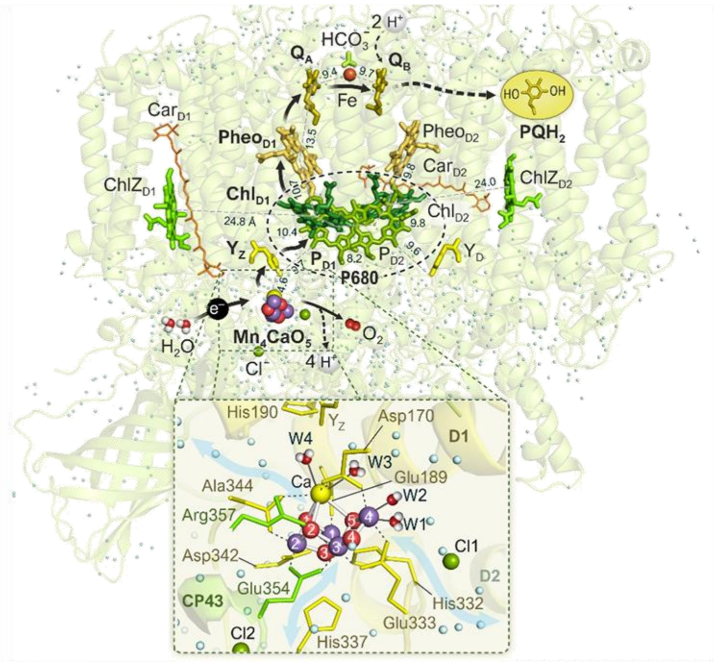

Figure 2.1.2. Arrangement of the electron transfer cofactors in the RC of PSII. The cofactors are shown in colour, and the protein scaffold is shown as a light-green background. The electron transfer direction is indicated by arrows. Figure adapted from ref. 8.

On the donor side, the oxidation of the redox-active tyrosine Y_Z to its radical form ($Y_Z^{\cdot}$) plays a crucial role in the electron transfer process from the Oxygen Evolving Complex (OEC) to the oxidized reaction centre. The oxidation of Y_Z is coupled to a proton release,[14] forming a tyrosyl radical through a Proton Coupled Electron Transfer (PCET) process.[15] This radical is then reduced *via* electron transfer from the manganese cluster of the OEC, resulting in an efficient accumulation of four oxidizing equivalents on the water oxidation catalyst.[16,17] The cluster undergoes stepwise oxidation through four intermediate states ($S_0 – S_4$) in the well-known Kok cycle, with each photochemical event allowing the system to advance of one S-state.[18] During these transitions, the increase in oxidation state of the OEC is compensated by the release of protons in the bulk to maintain charge balance. As already mentioned, a key step in this cycle is the oxidation of Y_Z, which acts as an electron shuttle to transfer electrons between the primary photochemical event at P680 and water oxidation at OEC. Y_Z oxidation implies deprotonation/protonation events, thus rendering the presence of a suitable base crucial. The Y_Z (or Y_{161}) phenolic proton forms a strong hydrogen bond with the imidazole group of a close histidine residue (H_{190} or His_{190}), which plays a fundamental role in helping proton transfer during Y_Z oxidation and reduction, as shown in Figure 2.1.3.

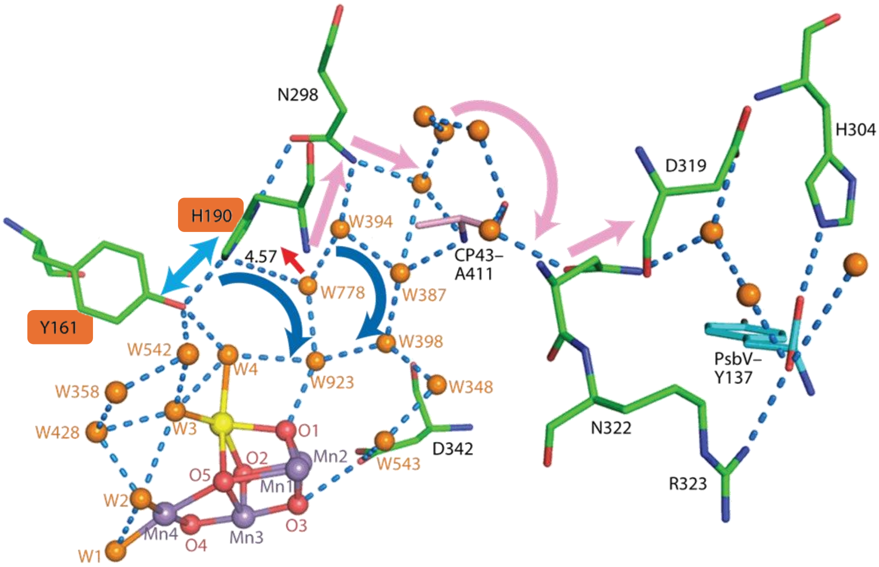

Figure 2.1.3. H-Bond network connecting Mn cluster, Y_{161} (or Y_z) and H_{190}. Figure adapted from ref. 19.

The oxidation of Y_Z is accompanied by a drastic pK_a shift, from ~10 in its reduced form to around −2 in its oxidized radical form, which makes the proton transfer favoured. Y_Z performs multiple fundamental functions within PSII:[20] (i) it drives an ultrafast electron donor to $P680^{\cdot+}$, competing effectively with charge recombination and ensuring nearly unity quantum yield for primary charge separation; (ii) it provides the reducing equivalents necessary to drive water oxidation by maintaining the high redox potential of the donor side; and (iii) through its proton coupled electron transfer behaviour, it prevents the formation of high-energy charged intermediates within the hydrophobic protein matrix, thus maintaining structural and energetic stability. Several mechanistic models have been proposed to describe Y_Z oxidation. The first, known as the hydrogen-atom abstraction model, suggests that the $Y_Z^{\cdot}$ radical abstracts a hydrogen atom from water molecules bound to the Mn cluster, with the released proton transferred *via* a hydrogen-bond network to the bulk solvent.[13,21,22] The second, named the proton-rocking mechanism, proposes that the hydrogen bond between Y_Z and its base (H_{190}) remains intact but shifts upon oxidation, effectively shuttling the proton within the protein environment without full dissociation.[23–26] Kinetic studies have shown that Y_Z oxidation occurs on a complex, multiphasic timescale, with the fastest component (~20 ns) attributed to the reduction of $P680^{\cdot+}$ by Y_Z. The low activation energy (~0.1 eV) and small kinetic isotope effect indicate that proton transfer occurs within a hydrogen bond, consistent with a proton coupled electron transfer (PCET) mechanism rather than stepwise electron-proton (ETPT) or proton-electron (PTET) pathways.[24] Structural and spectroscopic studies further support this view, indicating that in functional PSII, Y_Z is hydrogen-bonded to H_{190}, in line with high-resolution crystal structure data.[9] PCET reactions are not unique to Y_Z oxidation but are also involved in several other steps of the oxygen-evolving cycle, underlying their central importance in the overall mechanism of PSII. Understanding the detailed molecular mechanism of these PCET mechanism is therefore essential for a comprehensive description of photosynthetic water oxidation. For this reason, several artificial systems that try to mimic the chromophore-electron relay assembly of P680-Y_Z-H_{190} have been reported. The aim of these systems is to use simpler, synthetic complexes to allow to artificially mimic natural systems. The reported literature can be divided into two main different approaches: i) study of the PCET mechanism in systems based on the use of hydrogen-bonded imidazole-phenol couples,[27–31] or ii) study of PCET mechanism in chromophore-phenol assemblies in the presence of external bases.[32–39] All the reported systems present three main components:

1) A chromophore unit, able to absorb light thus mimicking natural P680 (shown in orange in Figures 2.1.4, 2.1.5 and Figure 2.1.6).
2) A phenol moiety that acts as electron donor, thus mimicking Y_Z in PSII (coloured in green).
3) An external or internal base with a suitable pK_a able to deprotonate the phenol residue (coloured in light blue).

Here focus is given to the examples based on coordination compounds or porphyrin conjugates. However, it should be noted that several examples based on simple organic molecules have also been reported.[40–44]

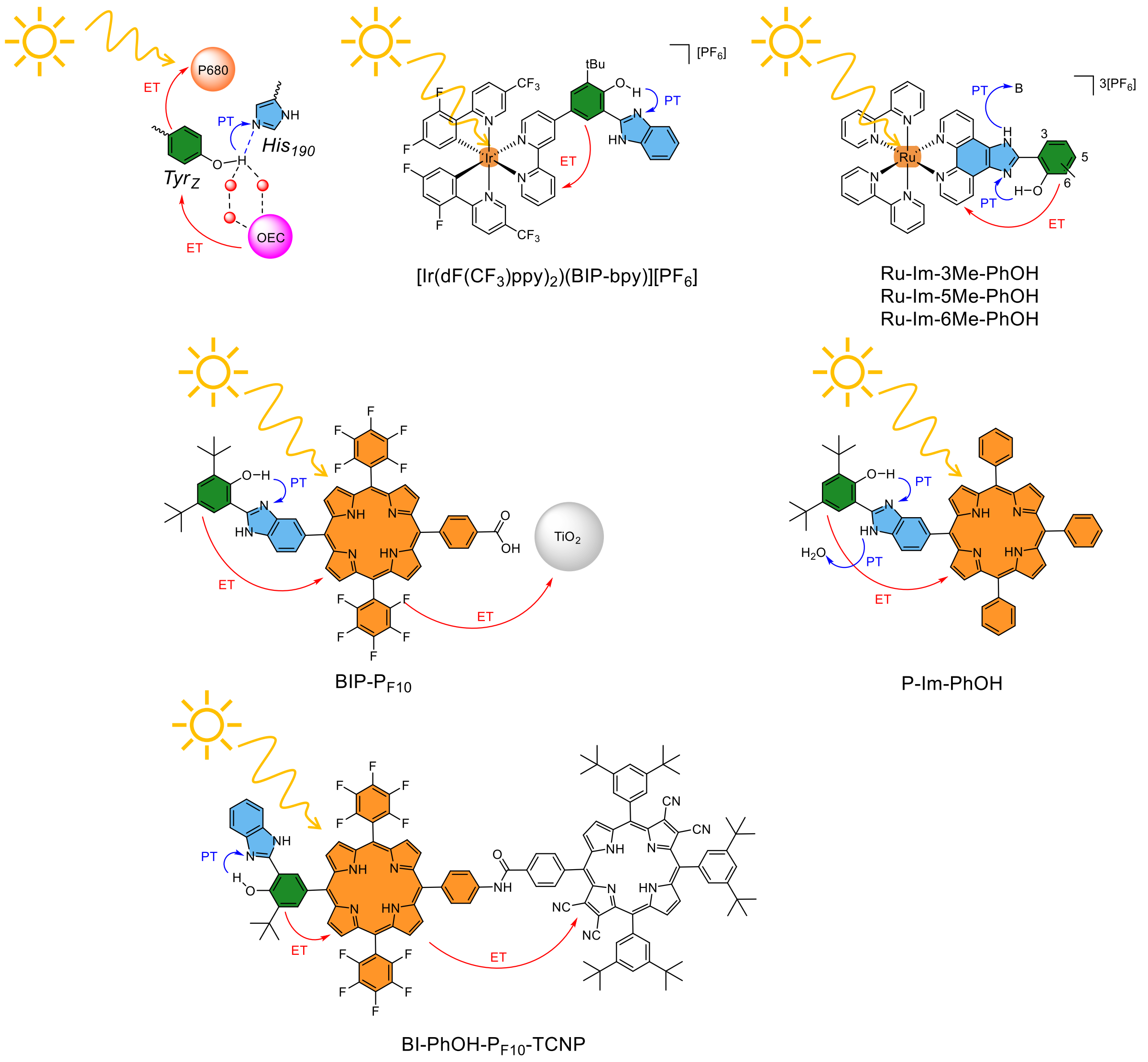

[Ir(dF(CF$_3$)ppy)$_2$)(BIP-bpy)][PF$_6$]

Ru-Im-3Me-PhOH
Ru-Im-5Me-PhOH
Ru-Im-6Me-PhOH

BIP-P$_{F10}$

P-Im-PhOH

BI-PhOH-P$_{F10}$-TCNP

Figure 2.1.4. Concerted PCET in PSII and synthetic mimics with the phenol ligand and the base in the same system, with the structure of the systems described in the main text. For **[Ir(dF(CF$_3$)ppy)$_2$(BIP-bpy)][PF$_6$]** see reference 27. For **Ru-Im-Me-PhOH** see reference 28. For **BIP-PF$_{10}$** see reference 29. For **P-Im-PhOH** see reference 30. For **BI-PhOH-PF$_{10}$-TCNP** see reference 31.

The first example described here was reported by Knowles *et al.* in 2021.[27] They have reported on a Ir(III) complex containing a benzimidazole-phenol (BIP) ligand covalently linked to a 2,2'-bipyridil (bpy) moiety. The molecular structure of the **[Ir(dF(CF$_3$)ppy)$_2$(BIP-bpy)][PF$_6$]** complex is represented in Figure 2.1.4. Upon excitation of the chromophore with blue light, an intramolecular PCET mechanism is activated, involving electron transfer from the phenol to the bpy ligand and a simultaneous proton shift to the adjacent benzimidazole group, with formation of a charge-separated state containing an oxidized BIP. Subsequent reduction of an external methyl viologen dication (MV^{2+}) stabilizes the charge-separated state and significantly lowers the recombination rate. This stabilization was evidenced by the catalytic performance of the complex in the photoreduction of phthalimide esters, which exhibited more than a twofold increase in quantum efficiency compared to the analogous catalyst lacking the BIP moiety. The second example, reported in 2024 by Leibl *et al.*, involves a Ru(III) complex bearing a phenol-imidazole ligand coordinated to the metal centre *via* conjugation to a phenanthroline residue.[28] The authors synthesized a series of ligands with a methyl group at different positions on the phenolic ring (positions 3, 5, or 6), forming **Ru-Im-3Me-PhOH**, **Ru-Im-5Me-PhOH**, or **Ru-Im-6Me-PhOH** (Figure 2.1.4). The study aimed at determining how the methyl position affects the PCET mechanism, particularly considering the steric influence of this substituent on the strength of the intramolecular hydrogen bond between the phenol and imidazole. They observed that the intramolecular oxidation of the ligand by the photogenerated excited Ru(III) species proceeds with a small driving force, like that in photosystem II (PSII). Laser flash photolysis experiments revealed biphasic kinetics for the ligand oxidation. While in **Ru-Im-3Me-PhOH** and **Ru-Im-6Me-PhOH** the fast phase is the dominant one, in **Ru-Im-5Me-PhOH** the slow phase is dominant. The fast phase was attributed to a photoinduced electron transfer leading to oxidation of the phenol moiety, accompanied by proton shift to the imidazole. The slow phase, on the other hand, was found to be highly sensitive to external proton acceptors. Kinetic analyses in the presence of different external bases indicated that this phase corresponds to the deprotonation of the 1-nitrogen of the imidazole, which is not involved in the intramolecular hydrogen bond. Upon PCET at the phenol site, this 1-nitrogen becomes more acidic, and its deprotonation stabilizes the oxidized ligand by compensating the positive charge. These findings highlight the importance of deprotonation of the imidazole 1-nitrogen in facilitating phenol oxidation in systems characterized by low driving force. Several artificial PCET systems have also been developed based on porphyrins. Porphyrins represent valuable artificial analogues of the synthetically demanding and relatively unstable chlorophylls found in natural systems. In 2008, Moore *et al.* reported one example of a porphyrin covalently linked to a BIP ligand (**BIP-PF$_{10}$** in Figure 2.1.4).[29] This system was designed in a way that, upon adsorption on nanostructured TiO_2, rapid primary electron transfer occurs from the photoexcited porphyrin moiety ($^1PF_{10}^*$) to the conduction band of the semiconductor. The covalently linked BIP then undergoes PCET, quenching the high-potential radical cation ($PF_{10}^{\cdot+}$) through electron transfer and a simultaneous proton shift from the phenol to the imidazole site. The resulting charge-separated state, $BIP^{\cdot+}$-PF_{10}-$TiO_2^{\cdot-}$, was confirmed by low-temperature photoinduced EPR spectroscopy. This system is particularly interesting as it features a chlorophyll-like photoactive species, in contrast to the coordination complexes described previously. A very similar system was reported in 2018 by Coutsolelos, Leibl, Aukauloo, Sircoglou *et al.*, namely **P-Im-PhOH** in Figure 2.1.4.[30] In this case, the presence of an intramolecular hydrogen bond between the phenolic proton and the imidazole group was demonstrated by the absence of stretching bands corresponding to the -OH group in the IR spectrum and by the observation of a singlet at $\delta = 12.2$ ppm in the ^{1}H NMR spectrum. Photophysical studies revealed that upon selective excitation of the porphyrin unit, an initial electron transfer occurs between the chromophore and the methyl viologen dication, used as a reversible electron acceptor. The unstable porphyrin radical cation is then stabilized *via* a PCET mechanism involving electron transfer from the phenol to the macrocycle and proton shift from the phenolic -OH to the imidazole. The deprotonated, charge-separated state is subsequently re-protonated at the porphyrin inner core, effectively making the macrocycle a distal base within the system. Finally, the phenoxyl radical is reduced back to its initial form by the oxidized methyl viologen. The last example concerns a very complex porphyrin triad (**BI-PhOH-PF_{10}-TCNP** in Figure 2.1.4) reported by Moore, Gust *et al.* in 2012.[31] This molecular triad was designed with two porphyrin components having redox potentials tuned to reproduce thermodynamic conditions analogous to those of P680 in PSII. This property was obtained by varying the macrocyclic substituents, made possible by the high synthetic modularity of porphyrins (see also Chapter 1). In **BI-PhOH-PF_{10}-TCNP**, the tetra-cyanoporphyrin (TCNP) acts as a strong electron acceptor thanks to the presence of the electron-withdrawing cyano substituents. The pentafluorophenyl-substituted porphyrin (PF_{10}) functions as the primary electron donor, capable of transferring an electron to TCNP upon photoexcitation to form $PF_{10}^{\cdot+}$-$TCNP^{\cdot-}$. This oxidized $PF_{10}^{\cdot+}$ species is thermodynamically able to oxidize the BI-PhOH secondary donor *via* PCET. The resulting phenoxyl radical has the correct redox potential for water oxidation, thereby mimicking the role of Y_Z-His$_{190}$ in PSII. Time-resolved spectroscopic and molecular modelling studies revealed two distinct decay pathways following excitation of PF_{10}: an energy transfer from $^1PF_{10}^*$ to TCNP with subsequent relaxation of $^1TCNP^*$, and a solvent-dependent photoinduced electron transfer forming $PF_{10}^{\cdot+}$-$TCNP^{\cdot-}$. Incorporation of BI-PhOH establishes a redox gradient that provides sufficient driving force for secondary electron transfer from BI-PhOH to $PF_{10}^{\cdot+}$. Oxidation of BI-PhOH substantially increases the acidity of the phenolic proton, generating the potential required for proton transfer to the hydrogen-bonded benzimidazole through a PCET mechanism, forming the final BIH^+-$PhO^{\cdot}$-PF_{10}-$TCNP^{\cdot-}$ species. These results demonstrate that structural and mechanistic features involving PCET in the Y_Z-His$_{190}$ couple of PSII can be effectively reproduced in artificial systems. The next example here discussed regards the use of an external base to drive photoinduced PCET, reported in 2005 by Hammarstrom *et al.* These authors investigated a Ru(II) complex bearing ethyl ester substituents on the bipyridine ligands and one tyrosine residue (**Ru-Tyr**, Figure 2.1.5).[32,33]

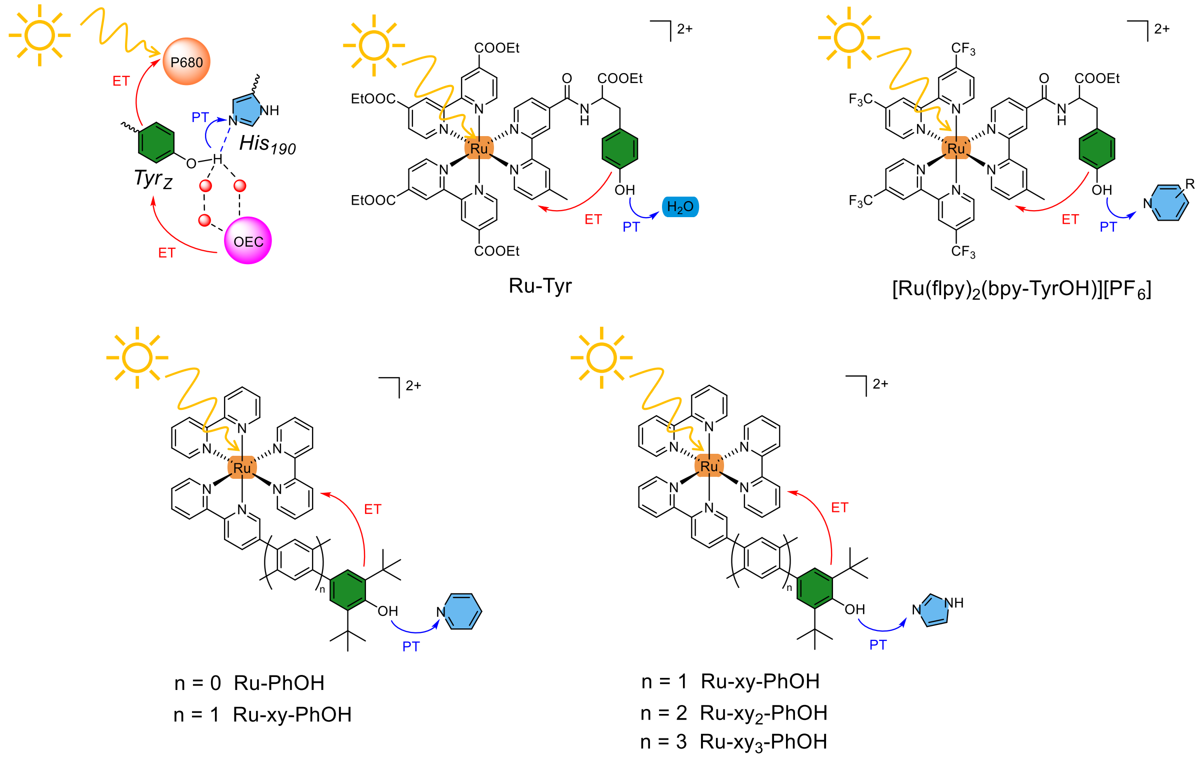

Figure 2.1.5. Concerted PCET in PSII and synthetic mimics working in the presence of an external base. For **Ru-Tyr** see reference 32. For **[Ru(flpy)$_2$(bpy-TyrOH)][PF$_6$]** see reference 34. For **Ru-PhOH** and **Ru-xy-PhOH** see reference 35. For **Ru-xy$_n$-PhOH** see reference 36.

The ethyl ester substituents were introduced to increase the oxidizing potential of the ruthenium complex. A related compound incorporating a redox-active tryptophan residue was also described but will not be discussed here. The present system was studied in buffered aqueous solution (Na_2HPO_4/H_3BO_3), with the buffer acting as a base to facilitate deprotonation of the phenol residue. Two different electron acceptors were employed to generate the initial Ru(III) species: methyl viologen dication and $[Ru(NH_3)_6]^{3+}$. Upon photoexcitation, the Ru(II) complex undergoes oxidative quenching by either one of the electron acceptors, forming the Ru(III) species. Once the Ru(III) complex is generated, it is reduced back to Ru(II) *via* a PCET process involving electron transfer from the amino acid to the metal centre and concomitant proton release in the aqueous phase. The PCET was found to proceed by to competing pathways, a sequential electron transfer and proton transfer (ETPT), and a concerted mechanism in which both transfers occur simultaneously. Moreover, by varying the pH of the solution, the oxidizing strength of the $[Ru(NH_3)_6]^{3+}$, or the nature of the amino acid, the authors demonstrated the possibility of switching between the concerted PCET and the stepwise ETPT pathways. A very similar example was reported in 2017 by Dempsey *et al.*[34] These authors investigated the photophysical behaviour of a Ru(II) complex bearing fluorinated bipyridine ligands and a tyrosine residue (**$[Ru(flpy)_2(bpy\text{-}TyrOH)][PF_6]$**, Figure 2.1.5). The PCET reactivity was studied in acetonitrile in the presence of methyl viologen dication as primary electron acceptor and various pyridine bases as proton acceptors. The five pyridines examined exhibit pK_a values ranging from 10.75 to 14.98 in acetonitrile, *i.e.* intermediate values between those of neutral tyrosine and tyrosyl radical cation. These bases were sufficiently strong to deprotonate the tyrosyl radical cation (pK_a = 6.32) but not the neutral tyrosine (pK_a = 26.35). Transient absorption spectroscopy showed that photoexcitation of the Ru(II) complex followed by oxidative quenching by methyl viologen produces the oxidized Ru(III) species, which then undergoes a PCET quenching. The mechanism proceeds *via* an ETPT sequence: the tyrosine residue first transfers an electron to Ru(III) and then gets deprotonated by the base. This behaviour was found consistent across all tested bases. While the electron-transfer rate constant is independent on the used base, the proton-transfer rate constant varies according to the basicity of the pyridine. These results showed the influence of the proton-transfer driving force on the kinetics of PCET reactions. In 2013, Wenger *et al.* reported one example of a Ru(II) complex bearing three bpy ligands, one of which was modified with a phenol substituent either directly attached to the chromophore or separated by a *p*-xylene spacer (xy in Figure 2.1.5), (**Ru-PhOH** and **Ru-xy-PhOH** in Figure 2.1.5).[35] When studied in pure dichloromethane, neither dyad exhibited photoinduced intercomponent processes. However, upon addition of pyridine and selective photoexcitation of the Ru(II) chromophore, significant quenching of the excited state was observed for both systems, with markedly different rate constants. Transient absorption studies revealed that the photoproducts contained Ru(II) in its ground state and a deprotonated phenol. For **Ru-PhOH**, direct proton transfer to the external base from the photoexcited dyad was proposed as the most plausible pathway. In contrast, for **Ru-xy-PhOH** a sequence of a photoinduced PCET followed by intramolecular (thermal) electron transfer in the reverse direction were proposed to occur. This two-step process involves a reaction intermediate containing a Ru(I) and a phenoxyl radical that converts very rapidly to Ru(II) and phenolate. In both cases, thermal back-reactions restore the initial ground states. A subsequent work of the same group was reported in 2015.[36] In this study three Ru(II) complexes bearing a phenol moiety at progressive increasing distance determined by one, two or three *p*-xylene spacers (**Ru-xy-PhOH**, **$Ru\text{-}xy_2\text{-}PhOH$** or **$Ru\text{-}xy_3\text{-}PhOH$** in Figure 2.1.5) were studied. Photophysical measurements were performed in acetonitrile, with an excess of methyl viologen dication as the primary electron acceptor and imidazole as the external base. Transient absorption spectroscopy revealed that photoexcitation of all dyads induces electron transfer from Ru(II) to methyl viologen, generating the Ru(III) oxidant. The longer the *p*-xylene bridge, the more imidazole is required to accelerate the subsequent PCET step, involving electron transfer from the phenol to the chromophore and proton transfer to imidazole. It is noteworthy that in these triads, PCET competes with an undesired side reaction involving oxidation of the imidazole by Ru(III). For **Ru-xy-PhOH** and **Ru-xy$_2$-PhOH**, the PCET step is faster than the side reaction due to the shorter distance between the chromophore and the phenol, whereas in **Ru-xy$_3$-PhOH**, the larger distance likely hinders efficient electron transfer, making the side reaction dominant. Kinetic analyses demonstrated that in all systems the PCET proceeds *via* a concerted mechanism.

As already introduced in Section 1.1.7 of Chapter 1, our group reported in 2018 and 2020 on the use of Sn^{IV}-porphyrins as building blocks for the assembling of supramolecular dyads or pseudo-triads, designed as artificial models for PCET studies.[37–39] The strong oxophylic nature of the tin centre enabled the axial coordination of two tyrosinate residues *via* their carboxylic functions,[45] as shown in Figure 2.1.6. Focus was given to the photophysical behaviour of two Sn^{IV}-porphyrin adducts bearing the same tyrosinato ligands at the metal apical positions but different substituents on the porphyrin macrocycle, namely **Sn(Ac-Y)$_2$TPP** and **Sn(Ac-Y)$_2$OEP** (Figure 2.1.6). These two conjugates were readily synthesized by reacting the corresponding Sn(OH)$_2$-porphyrin with two equivalents of N-Acetyl-*L*-tyrosine, in mild conditions. The products were isolated in nearly quantitative yields and fully characterized in solution by a variety of techniques (1D and 2D NMR spectroscopy, mass spectrometry, circular dichroism, cyclic voltammetry, and UV-Vis absorption and emission spectroscopies).

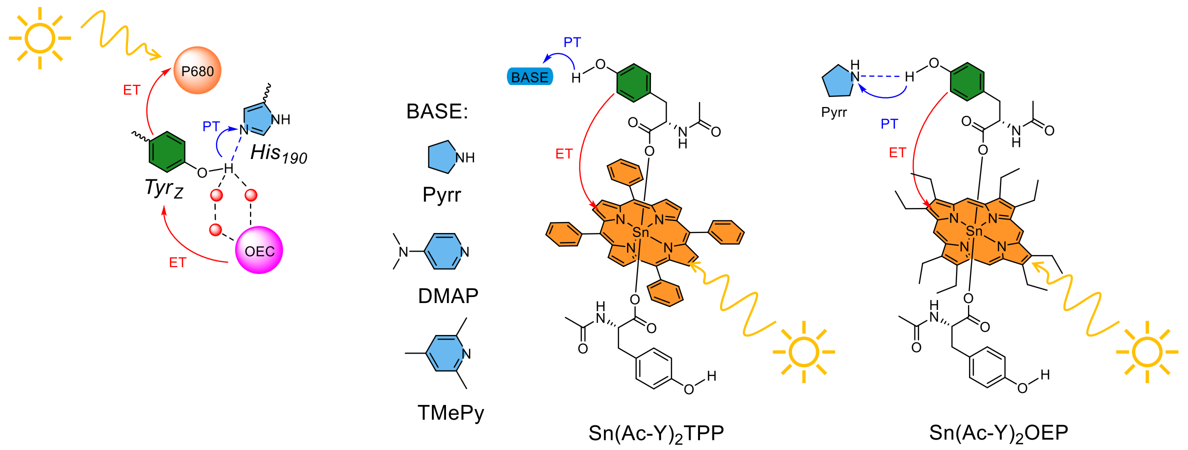

Figure 2.1.6. Concerted PCET in PSII and synthetic mimics reported by us. For **Sn(Ac-Y)$_2$TPP** see references 37 and 38. For **Sn(Ac-Y)$_2$ OEP** see reference 38.

The single crystal X-ray structure of **Sn(Ac-Y)$_2$TPP** is shown in Figure 2.1.7, with highlight on the presence of a hydrogen intermolecular bonding networks involving the phenol groups, and on the distance between the oxygen of the phenol and the closest β-pyrrolic carbon of the porphyrin macrocycle.

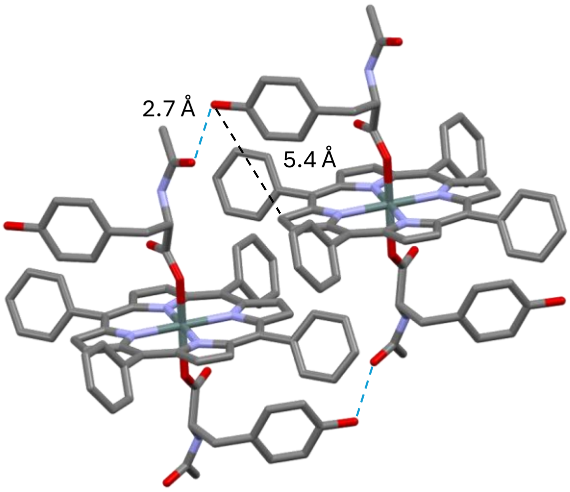

Figure 2.1.7. Single crystal X-ray structure of **Sn(Ac-Y)$_2$TPP**, showing the alignment of two molecules via intermolecular hydrogen bonding. Hydrogen atoms are omitted for clarity. Colour code: Sn: dark green; N: purple; O: red; C: grey.

DFT calculations were later performed to compare the solid-sate and the energy minimized (dichloromethane) solution structures of **Sn(Ac-Y)$_2$TPP**, see Section 2.2.2 and Experimental Part for further details. The DFT model closely matches the structure found in the solid state, with the oxygen of the distance between the phenol and the closest β-pyrrolic carbon being 5.26 Å (see Figure S79 in Appendix A). From a photophysical viewpoint the case of **Sn (Ac-Y)$_2$TPP** will be discussed first. From the photophysical and electrochemical data the corresponding energy level diagram was predicted and is shown in Figure 2.1.8.

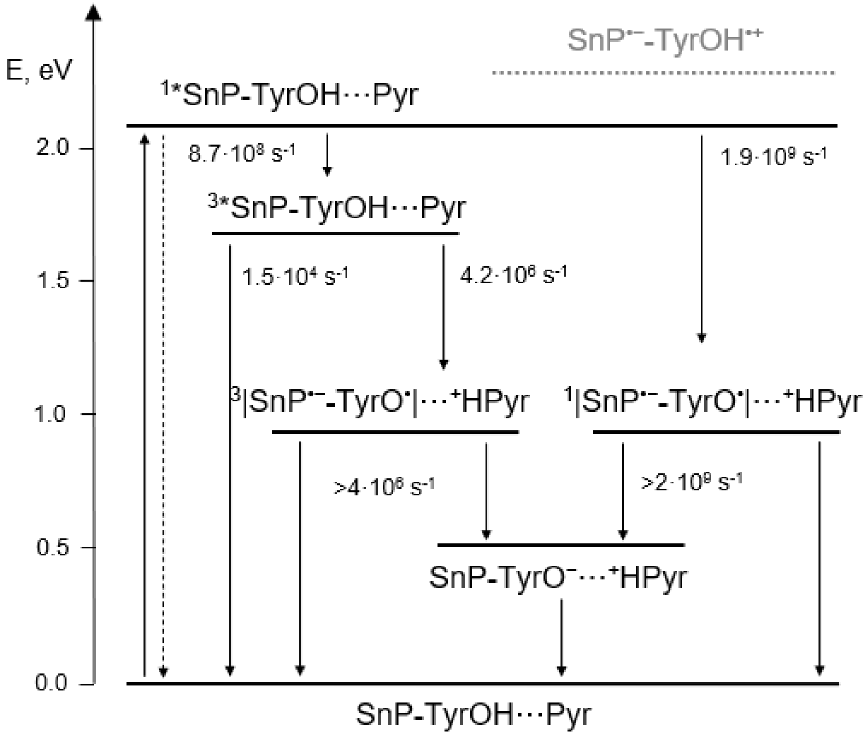

Figure 2.1.8. Energy level diagram of **Sn(Ac-Y)$_2$TPP** with related photoinduced possible processes and rates in CH_2Cl_2, also in the presence of pyrrolidine (for simplicity the same energy is assigned to both singlet and triplet PCET states; the Sn^{IV}-porphyrin unit is named SnP; the tyrosinato ligand is named TyrOH). Figure taken from ref 37.

For metallo-porphyrins, it is well known that visible-light excitation initially populates the singlet excited state, which partly undergoes intersystem crossing to yield a fraction of triplet excited state, depending on the nature of the metal centre (see also Chapter 1). This process is quite relevant for Sn^{IV}-porphyrins, as the efficiency of $^{1*}S \rightarrow {}^{3*}T$ intersystem crossing is known to be quite high.[46] Therefore, subsequent intercomponent processes may occur from both excited states. From the energy level diagram reported in Figure 2.1.8, it is evident that for **Sn(Ac-Y)$_2$TPP** the population of the radical pair state (SnP$^{\cdot -}$-TyrOH$^{\cdot +}$, grey dotted line), in the absence of any external base, is uphill with respect to both the singlet ^{1*}SnP (by 0.12 eV) and triplet ^{3*}SnP (by 0.55 eV) excited states. The energies of the PCET states in the presence of pyrrolidine as a base (|SnP$^{\cdot -}$TyrO$^{\cdot}$|---$^{+}$HPyr) were then estimated considering the energy of the radical pair state in the absence of pyrrolidine and subtracting the contribute of the deprotonation step. This contribution was determined using equation 1, using the pK$_a$ values of the tyrosyl radical cation and of the protonated pyrrolidine (more details on the choice of the pK$_a$ values and the energy differences between singlet and triplet PCET states are given in the Experimental Section).

$$\Delta G_{PT} = 0.059\ \text{eV} \times [\text{p}K_a\ (\text{TyrOH}^{\cdot+}) - \text{p}K_a\ (^{+}\text{HPyr})] \qquad (1)$$

The contribution of the deprotonation step was calculated to be ~ 1.3 eV, yielding an energy level for the PCET states of + 0.9 eV, *i.e.* thermodynamically favoured from both the *SnP states. Accordingly, it was found that a CH_2Cl_2 solution of **Sn(Ac-Y)₂TPP** shows pyrrolidine-dependent fluorescence and triplet deactivation profiles. This behaviour was attributed to the occurrence of parallel photoinduced PCET from the singlet and triplet excited states. These PCET mechanisms involve reduction of the porphyrin macrocycle, oxidation of the phenol of the tyrosine with simultaneous proton shift from the phenol to the base, with formation of diradical species, according to equations 2 and 3.

$$^{1*}\text{SnP-TyrOH --- Pyr} \rightarrow \text{SnP}^{\cdot-}\text{-TyrO}^{\cdot}\ \text{---}\ ^{+}\text{HPyr} \qquad (2)$$

$$^{3*}\text{SnP-TyrOH --- Pyr} \rightarrow \text{SnP}^{\cdot-}\text{-TyrO}^{\cdot}\ \text{---}\ ^{+}\text{HPyr} \qquad (3)$$

The occurrence of concerted PCET is supported by the fact that pyrrolidine is unable to deprotonate the phenol group of the tyrosine (as demonstrated by UV-Vis absorption measurements), and therefore the deactivation of the populated excited states cannot occur *via* a simple ET pathway from a putative phenolate. This observation, on the other hand, strongly support the presence of a pre-association equilibrium between the amino acid and the base, *via* hydrogen bonding. The association constant for this interaction was calculated to be 33.5 (±1.8) M^{-1},[38] and afforded an accurate fitting for the kinetic treatment of the quenching data. The rate constant of the PCET mechanism was then calculated according to equation 4:

$$k_{obs} = k_0 + k_{ET} + k_Q[\text{Pyr}] + k_{PCET}\ [(K_A[\text{Pyr}])/(1+K_A[\text{Pyr}])] \qquad (4)$$

Where k_0 represents the intrinsic deactivation rate of the singlet or triplet excited state, k_{ET} is the rate constant of the electron transfer deactivation mechanism (negligible in the present case due to the higher energy of the $\text{SnP}^{\cdot-}\text{-TyrOH}^{\cdot+}$ state, grey dotted line in Figure 2.1.8), and k_Q derives from the bimolecular quenching reactivity between the excited state and the pyrrolidine base. Being indeed pyrrolidine an amine species, akin to common amines used as sacrificial electron donor,[47] it may behave as an excited state quencher by reductive electron transfer. For the singlet excited state, k_0 was determined from the lifetime of the singlet excited state, while k_Q[Pyr] was neglected by comparison with a model compound. By using the above values, the calculated k_{PCET} from the singlet excited state resulted to be $1.9 \times 10^9\ s^{-1}$. The same equation was employed to determine the PCET rate constant from the triplet excited state. From the lifetime of the triplet excited state k_0 was established, and k_Q was estimated from the triplet quenching data of the model compound in the presence of pyrrolidine. With these data the k_{PCET} from the triplet excited state was calculated to be 4.2×10^6 s^{-1}. Failure to observe the accumulation of photoproduct by transient absorption spectroscopy suggests a short lifetime of the diradical species of both singlet and triplet multiplicity. Likely, rapid recombination occurs from both PCET states by a stepwise proton-transfer, electron-transfer mechanism.[35,48] In a subsequent work, dichloromethane solutions of **Sn(Ac-Y)$_2$TPP** were exposed to bases with distinct basicity. It was concluded that by decreasing the base strength, the concerted PCET process is slowed down, although being still active from both the singlet and triplet excited states. On the contrary, for **Sn(Ac-Y)$_2$OEP** (see Figure 2.1.6. above) the PCET process in the presence of pyrrolidine was found to occur only from the triplet excited state, a thermodynamic limitation resulting from the fact that SnOEP is more difficult to reduce than SnTPP. This observation highlights how simple variations of the porphyrin macrocycle can significantly influence the system's ability to promote photoinduced intercomponent processes, both on a thermodynamic and a kinetic point of view.

From the above State of the Art – expertise in the preparation of Sn^{IV}-porphyrin conjugates and their detailed photophysical characterization – in the present work two novel Sn^{IV}-porphyrin/phenol conjugates, and the corresponding model compounds (**3**, **6** and **9**, **11** in Figure 2.1.9) were designed. The free-base porphyrin analogues (**2**, **5**, **8** in Figure 2.1.9) and Zn^{II}-derivatives (**4**, **7**, **10** in Figure 2.1.9) served as useful intermediates and as comparative models in the photophysical studies. The design aimed at varying the relative position between the chromophore and the redox-active phenol unit by conjugation of the latter at the periphery of the porphyrin macrocycle (in place of by direct coordination at the apical positions of metal centre). Conjugates **3** and **6** should feature roughly the same distance between the porphyrin macrocycle and the phenol group but may differ in the conformational freedom along the alkyl linker, primarily because of the presence or absence of extra H-bonding donor/acceptor sites. As additional bonus, **6** is chiral which may turn advantageous for further applications. Overall, increasing the distance between the porphyrin macrocycle and the phenol unit was intended at slowing down the diradical recombination process, observed for **Sn(Ac-Y)$_2$TPP**, and possibly allowing the accumulation of the PCET photoproducts. From a synthetic viewpoint the decision to covalently link the phenol unit *via* amide-bond formation was also inspired by a previous work from by us, in which a Zn^{II}-porphyrin was covalently attached in the same way to a *fac*-$Re^{I}(CO)_3(bipy)$ fragment carrying a fullerene as sixth ligands, and thus forming a triad.[49,50]

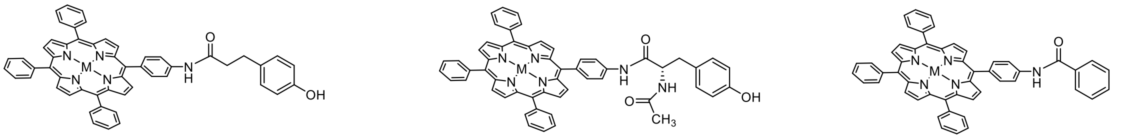

M = H_2; **TPP-*p*PA** (**2**)
M = $SnCl_2$; **$SnCl_2$TPP-*p*PA** (**3**)
M = Zn; **ZnTPP-*p*PA** (**4**)

M = H_2; **TPP-*p*Tyr** (**5**)
M = $SnCl_2$; **$SnCl_2$TPP-*p*Tyr** (**6**)
M = Zn; **ZnTPP-*p*Tyr** (**7**)

M = H_2; **TPP-*p*BA** (**8**)
M = $SnCl_2$; **$SnCl_2$TPP-*p*BA** (**9**)
M = Zn; **ZnTPP-*p*BA** (**10**)
M = $Sn(OH)_2$; **$Sn(OH)_2$TPP-*p*BA** (**11**)

Figure 2.1.9. Molecular structure of the (metallo)porphyrin conjugates described in this Chapter.

2.2. Results and Discussion.

*2.2.1. Synthesis and characterization of **2** – **11**.*

For the synthesis of **$SnCl_2$TPP-*p*PA** (**3**) two different synthetic strategies were explored, both starting from the same free-base porphyrin, **TPP-*p*NH_2**, (**1**) (Scheme 2.2.1). The first approach involved the insertion of Sn^{IV} cation into the free-base porphyrin **1**, followed by conjugation with 3-(4-hydroxyphenyl)propionic acid. In the second approach, the free-base porphyrin **2** was first synthesized and subsequently metalated to yield compound **3**.

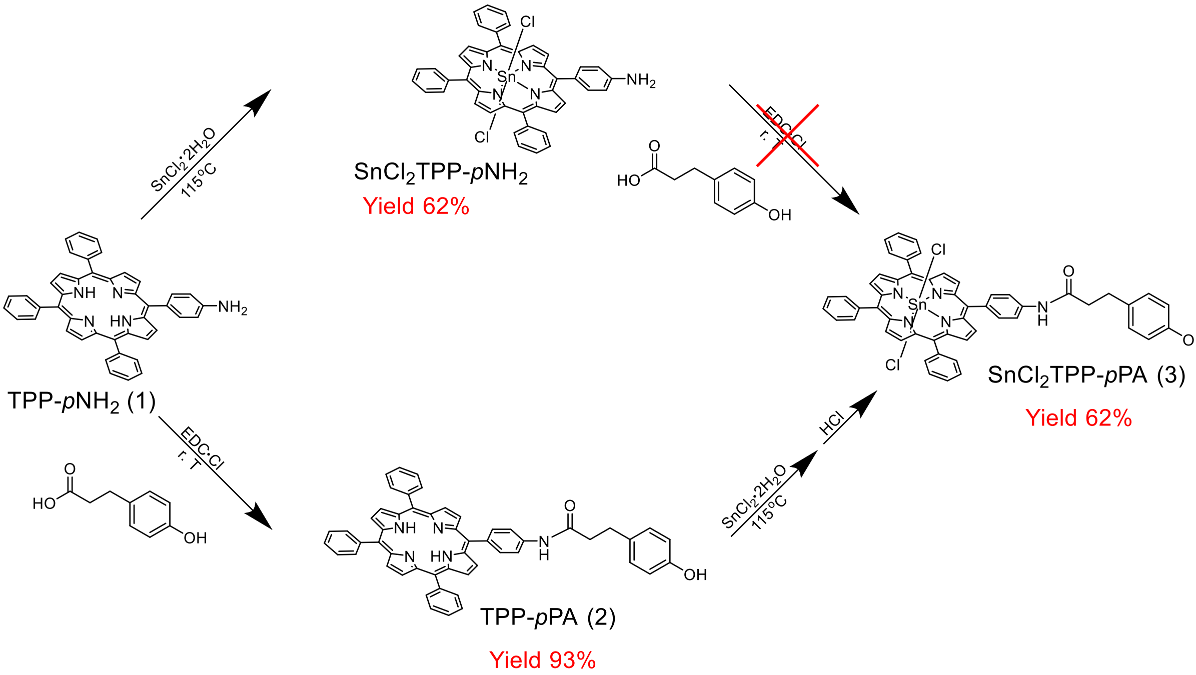

Scheme 2.2.1. Schematic representation of the two synthetic strategies used to obtain **3**.

Due to the poor solubility of **$SnCl_2$TPP-*p*NH_2**, the difficulty in isolating this compound in a pure form, and the consequent very low yield, the second synthetic route was selected. Briefly, compound **1** was prepared from **TPP** following known literature procedures.[50–52] The coupling of 3-(4-hydroxyphenyl)propionic acid was done *via* a classical EDC-mediated amide coupling.[49] The resulting free-base porphyrin **TPP-*p*PA** (**2**) was obtained in 93% yield after isolation by precipitation from a chloroform/*n*-hexane solution. The ^{1}H NMR spectra (CDCl$_3$) of **1**, 3-(4-hydroxyphenyl)propionic acid, and **2** are shown in Figure 2.2.1.

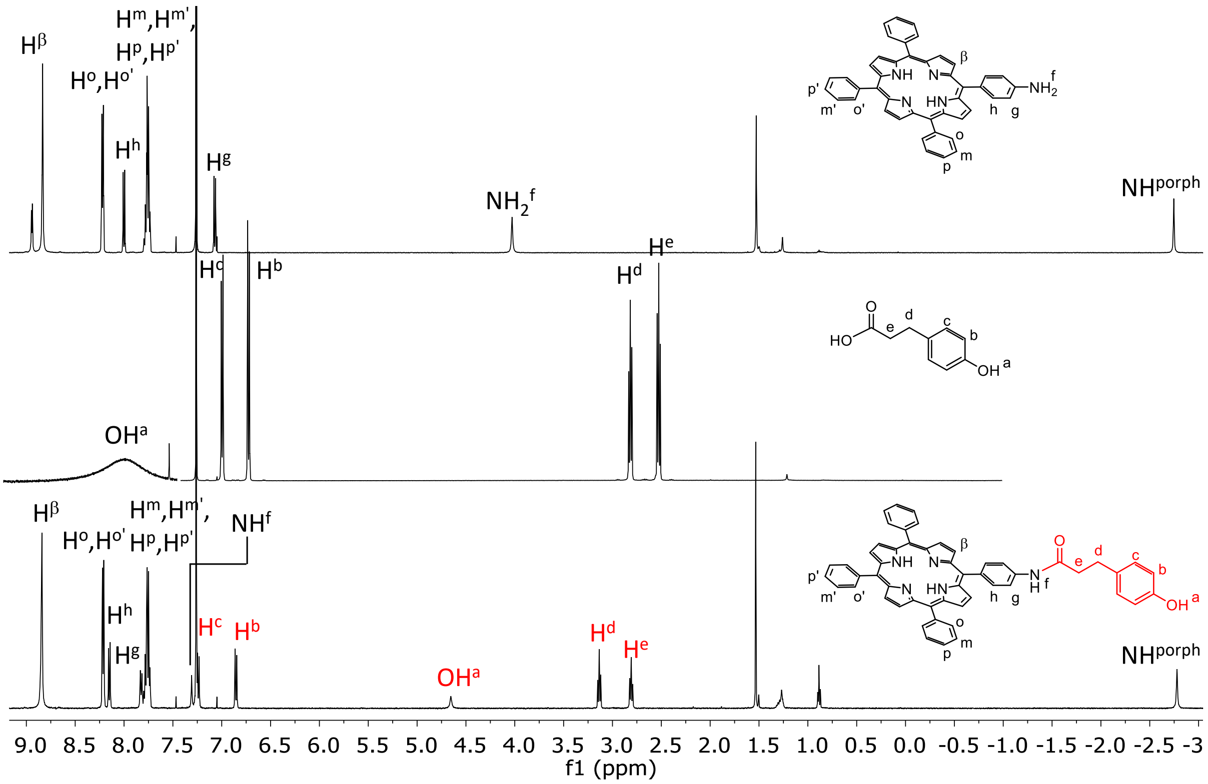

Figure 2.2.1. ^{1}H NMR spectra (CDCl$_3$, 298 K) of **TPP-*p*NH$_2$** (**1**) (top), 3-(4-hydroxyphenyl)propionic acid (middle, signal of OH^{a} magnified) and **TPP-*p*PA** (**2**) (bottom).

The formation of the amide bond is confirmed by the disappearance of the amine resonance at $\delta = 4.03$ ppm and the appearance of the amide signal at $\delta = 7.31$ ppm. The signals corresponding to both aromatic and aliphatic protons of the pendant phenol ligand remain largely unaffected by conjugation to the porphyrin macrocycle, as do the signals belonging to the three *meso* aryl substituents (*ortho*, *meta*, and *para* protons) and to the inner NH pyrrolic protons of the porphyrin. Based on ^{1}H-^{13}C HMBC experiments (Figure S3 in Appendix A) the doublet at $\delta = 7.82$ ppm is assigned to proton H^{g} and, according to the cross-peak observed in the ^{1}H-^{1}H COSY spectrum (Figure S1 in Appendix A), the doublet at $\delta = 8.13$ ppm is attributed to proton H^{h}. Notably, the signal of H^{g} is significantly downfield shifted compared to the starting **TPP-*p*NH$_2$** (**1**) porphyrin, in agreement with the different resonance forms for the phenyl-amino *vs.* the phenyl-amido group. Finally, the singlet at $\delta = 4.91$ ppm is assigned to the phenolic proton, in congruence with the presence of an exchange peak with residual water in the ^{1}H-^{1}H ROESY spectrum in CD$_2$Cl$_2$ (Figure S8 in Appendix A). The nature of compound **2** was further confirmed by ESI-MS (see Figure S13 in Appendix A). The UV-Vis absorption spectrum of **2** presents unvaried features of a typical free-base porphyrin (Figure S23 in Appendix A). The desired Sn^{IV}-porphyrin conjugate **$SnCl_2$TPP-*p*PA** (**3**) was prepared *via* metalation with $SnCl_2 \cdot 2H_2O$ in refluxing pyridine, following classical literature procedures.[53] The progress of the metalation was monitored by UV-Vis absorption spectroscopy, taking advantage of the distinct absorption profiles of a free-base porphyrin compared to its metalated derivative. Initially, the reaction mixture was simply quenched by precipitation upon addition of water, and the resulting purple solid was filtered, thoroughly washed with water to remove excess $SnCl_2 \cdot 2H_2O$ and recrystallized from a chloroform/*n*-hexane mixture. Surprisingly, the ^{1}H NMR spectrum ($CDCl_3$) of the isolated solid presented a very broad general profile, that persisted unvaried by lowering the temperature down to −40 °C, heating up to 50 °C (Figure 2.2.2), by dilution, or by recording the spectrum in CD_2Cl_2 (Figure 2.2.2 and S14 in Appendix A).

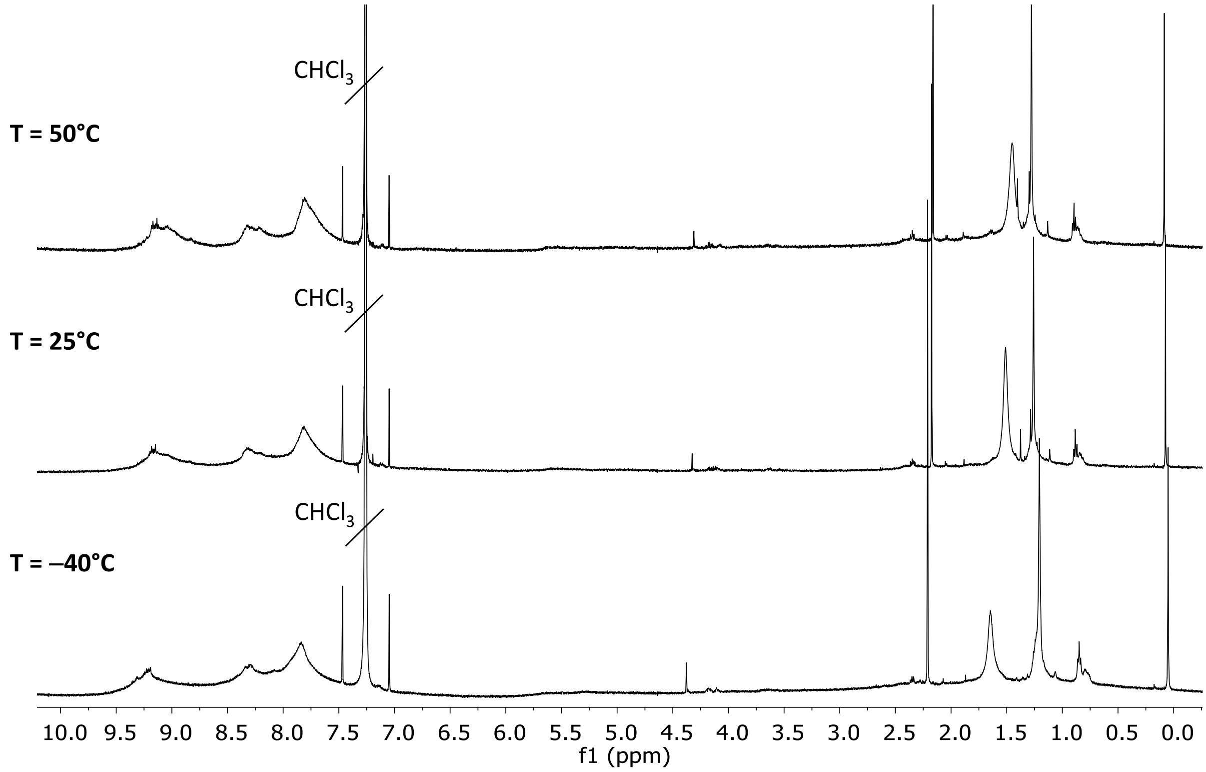

Figure 2.2.2. ^{1}H NMR spectra ($CDCl_3$) the isolated product from metalation (Sn^{IV} cation insertion step) of **2** at three different temperatures (25 °C, middle; 50 °C, top; –40 °C, bottom).

Under the harsh (basic) reaction conditions, the pendant phenol moiety may get deprotonated and coordinate to the Sn^{IV} centre. This would lead to the formation of oligomeric/polymeric species. To exclude the presence of this aggregation phenomena deuterated methanol was added to the $CDCl_3$ solution of the isolated compound. Given the strong preference of the Sn^{IV} centre for oxygen-donor anionic ligands and the large excess of added methanol the formation of the dimethoxy **$Sn(OMe)_2$TPP-*p*PA** porphyrin was expected. This conjugate presents two methoxy groups as apical ligands (see also Chapter 1). Indeed, immediate sharpening of the ^{1}H NMR signals was observed, with the instant and nearly quantitative formation of the expected dimethoxy species (Figure 2.2.3). This was unambiguously confirmed by the chemical shift of the ^{119}Sn observed in the ^{1}H-^{119}Sn HMBC spectrum ($\delta = -564$ ppm, Figure S15 in Appendix A).

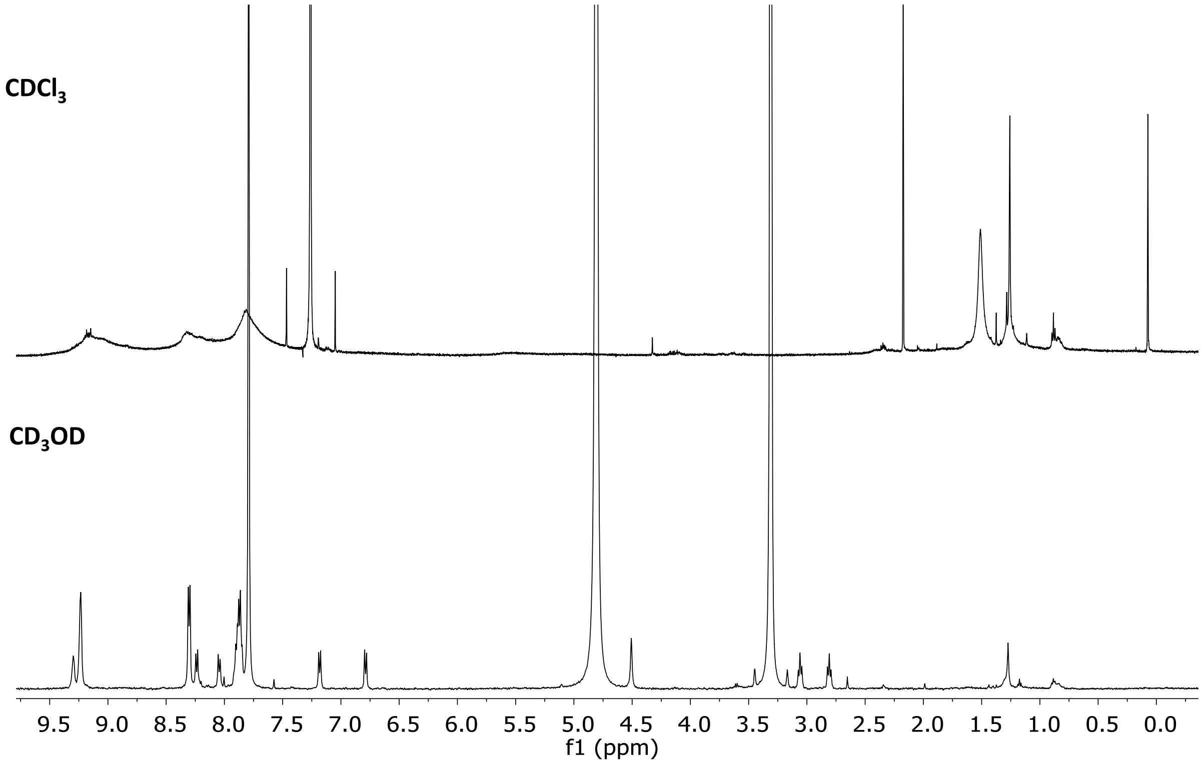

Figure 2.2.3. ^{1}H NMR spectra (298 K) of **3** in $CDCl_3$ (top) and in CD_3OD (bottom).

Pure **$SnCl_2$TPP-*p*PA** (**3**) was successfully obtained (62% yield) by treatment of a chloroform solution of the isolated product with 6 M HCl.[53,54] The ^{1}H NMR spectrum ($CDCl_3$, 298 K) of **3** is reported in Figure 2.2.4.

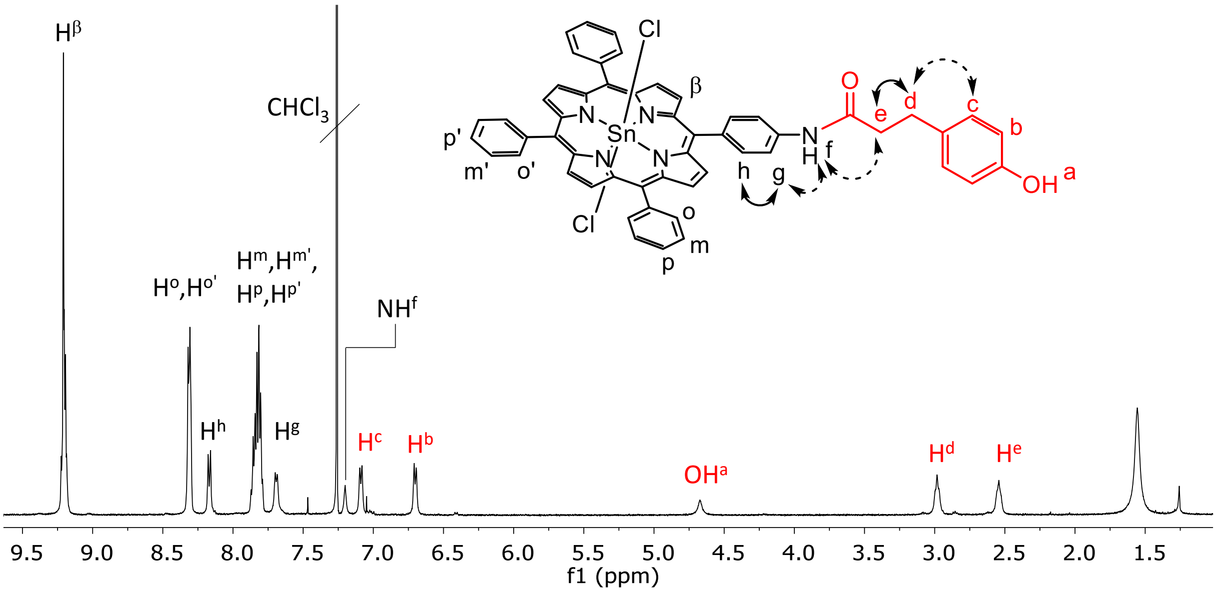

Figure 2.2.4. ^{1}H NMR spectrum ($CDCl_3$, 298 K) of **3**. Dotted arrows indicate nOe correlations, solid arrows indicate bond correlations.

Complete proton assignment was done by combining signal integration, multiplicity, and correlations observed in 1D and 2D NMR experiments (^{1}H-^{1}H COSY, ^{1}H-^{13}C HSQC; ^{1}H-^{1}H ROESY, see Figures S16 – S18 in Appendix A). The presence of a single set of signals indicates that only one species is present in solution. The coordination of the metal centre within the macrocycle is confirmed by the disappearance of the resonance of the inner NH protons at negative ppm values (not shown). Proton assignments were done as follows: the multiplet at $\delta = 9.24 – 9.17$ ppm, integrating for eight protons correspond to the resonances of all β-protons of the porphyrin macrocycle. The doublet of doublets at $\delta = 8.31$ ppm and the multiplets at 7.89 – 7.77 ppm are attributed to the *ortho meta* and *para* aryl protons of the macrocycle. The doublet at $\delta = 8.17$ ppm is assigned to H^{h} by comparison to the ^{1}H NMR spectra of the free-base **2**. Based on ^{1}H-^{1}H COSY correlations the doublet at $\delta = 7.69$ ppm is attributed to H^{g}. This latter resonance presents a nOe cross-peak in the ^{1}H-^{1}H ROESY spectrum with the singlet at $\delta = 7.20$ ppm (not correlated to any carbon in the ^{1}H-^{13}C HSQC spectrum), that is assigned to the amide proton (NH^{f}). The additional nOe cross-peak in the ^{1}H-^{1}H ROESY spectrum between the amide signal and the not resolved resonance at $\delta = 2.54$ ppm, assigns this latter to H^{e}. The close by not resolved signal at $\delta = 2.99$ ppm is attributed to H^{d} by bond correlations. Further nOe peaks with the doublet at $\delta = 7.09$ ppm allows the assignment of the latter to the aromatic proton of the phenol moiety H^{c}. Finally, the doublet at $\delta = 6.70$ ppm is assigned to the remaining aromatic proton of the phenol ligand H^{b}, while the phenolic OH proton, consistent with what observed for the free-base porphyrin **2**, appears as a broad signal at $\delta = 4.67$ ppm. In the ^{1}H-^{119}Sn HMBC spectrum of **3** (Figure 2.2.5), the cross peak at δ = −588 ppm arise from the ^4J correlation between the β-pyrrolic protons and the tin nucleus, consistent with the value reported for the $SnCl_2TPP$ reference system (see also Chapter 1),[53] and therefore with the presence of two chloride anions on the apical positions of the metal centre. The nature of **3** was further validated by ESI-MS analysis (Figure S19 in Appendix A). Photophysical (UV-Vis absorption and emission spectra) and electrochemical properties (CV) of **3** were also investigated and are discussed in Section 2.2.2, below.

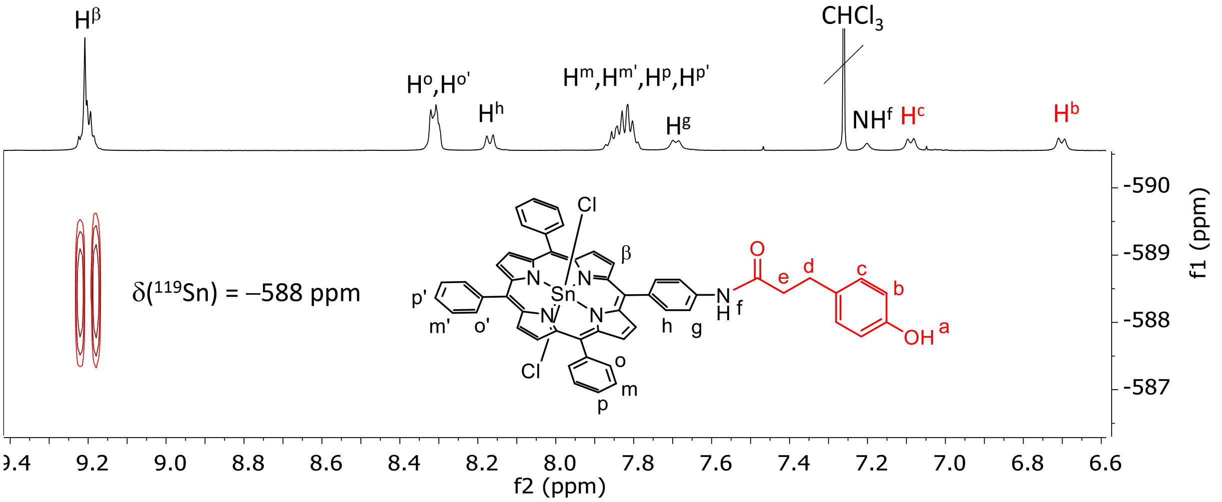

Figure 2.2.5. Aromatic region of the ^1H-^{119}Sn HMBC spectrum ($CDCl_3$, 298 K) of **3**.

For characterization purposes the Zn^{II}-porphyrin analogue, **ZnTPP-*p*PA** (**4**), was also prepared, starting from **2** and using adapted literature procedures, as shown in Scheme 2.2.2.[49] Conjugate **4** was isolated in 80% yield. The product was characterized in solution by 1D and 2D NMR spectroscopy, mass spectrometry and UV-Vis absorption spectroscopy (see also Figures S20 – S23 in Appendix A).

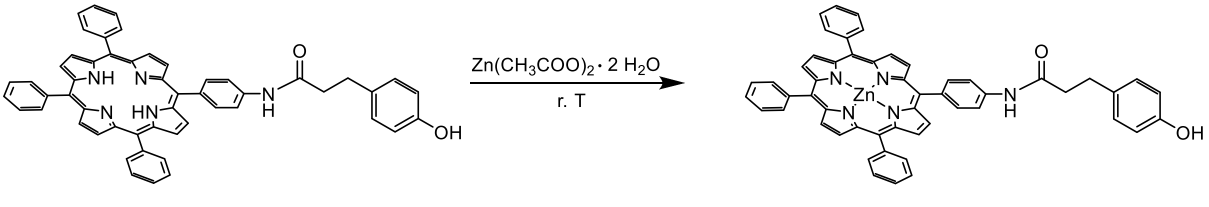

TPP-*p*PA (2)

ZnTPP-*p*PA (4)
Yield 80%

Scheme 2.2.2. Scheme of the preparation of **4**.

The Sn^{IV}-porphyrin conjugate **$SnCl_2$TPP-*p*Tyr** (**6**) was synthesized by adapting the synthetic procedure described above for **3**. Chiral N-Acetyl-*L*-tyrosine was coupled to **1** using a classical EDC-mediated amide coupling, affording the free-base porphyrin **TPP-*p*Tyr** (**5**) in 53% yield, after column chromatography. **5** was then metalated with $SnCl_2 \cdot 2H_2O$ in pyridine at 115 °C, followed by treatment with 6 M HCl (see above) to give the desired conjugate **6** in 65% yield, as schematically represented in Scheme 2.2.3. **5** was characterized in solution mainly by 1D and 2D NMR spectroscopy, the ^{1}H NMR spectrum in dmso-d_6 is reported in Figure 2.2.6, top.

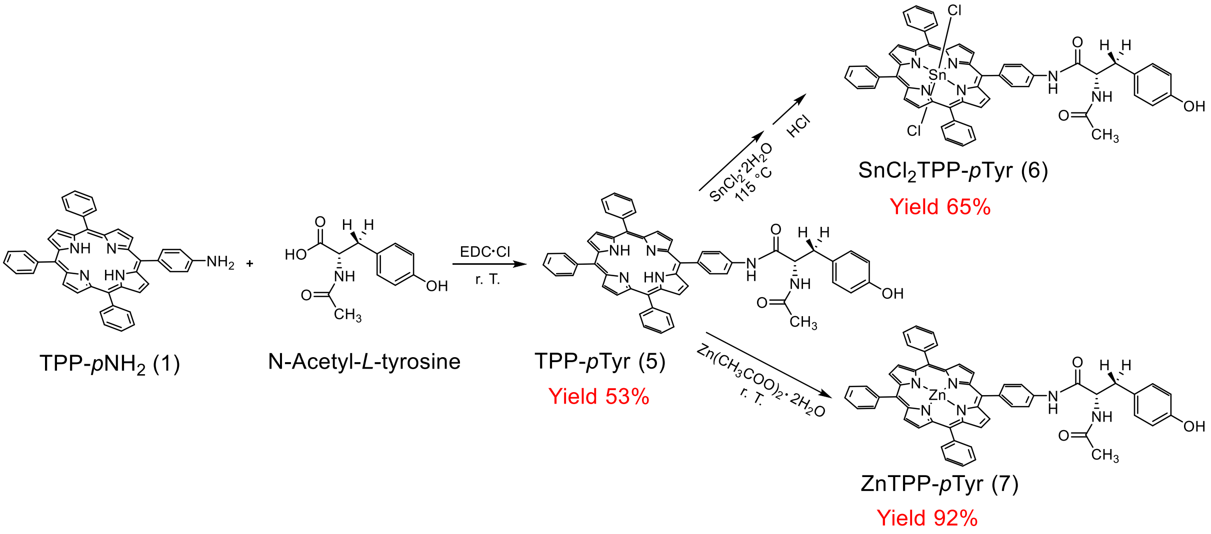

Scheme 2.2.3. Schematic representation of the synthesis of **5**, **6** and **7**.

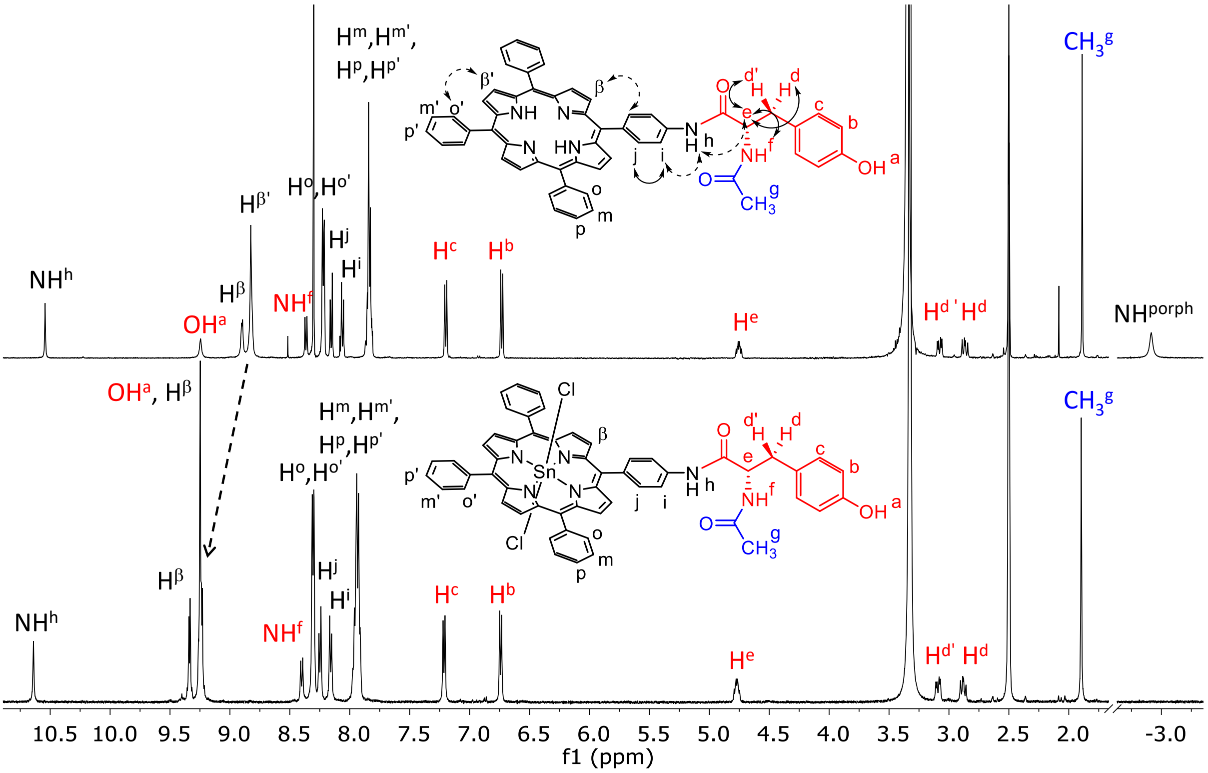

Figure 2.2.6. ^{1}H NMR spectra (dmso-d_6, 298 K) of **5** (top) and **6** (bottom). Dotted arrows indicate nOe correlations, solid arrows indicate bond correlations.

The observation of one single set of signals indicates the presence of only one species in solution; integration and multiplicity confirm the identity of the product. Proton signal assignment was done by a combination of NMR experiments (^{1}H-^{1}H COSY, ^{1}H-^{13}C HSQC,

^{1}H-^{13}C HMBC, and ^{1}H-^{1}H ROESY; see also Figures S24 – S27 in Appendix A). The appearance of a singlet at δ = 10.55 ppm, assigned to the amide proton together with the disappearance of the amine signal, confirm the successful conjugation of the starting molecules. The nOe correlations found in the ^{1}H-^{1}H ROESY spectrum between the NH^{h} singlet and the two resonances at δ = 8.06 ppm and δ = 4.75 ppm allows the assignment of these signals to protons H^{i} and H^{e}, respectively. The mutiplet corresponding to H^{e} presents a correlation in the ^{1}H-^{1}H COSY spectrum with the doublet at δ = 8.37 ppm, which (based also on the absence of a ^{1}J coupling with any carbon in the ^{1}H-^{13}C HSQC spectrum) is assigned to NH^{f}. In addition, the multiplet of H^{e} also couples with the equally intense resonances at δ = 2.87 ppm and δ = 3.08 ppm, that are assigned to the diasterotopic protons H^{d} and H$^{d'}$. The nature of these two protons is confirmed also by the ^{1}H-^{13}C HSCQ spectrum, in which both the corresponding signals exhibit a ^{1}J coupling with the same carbon, thus further validating the chiral nature of the molecule. The nOe correlations found in the ^{1}H-^{1}H ROESY spectrum indicates the spatial proximity of H^{d} to NH^{f}, and of H$^{d'}$ to H^{e}, respectively. The same experiment allowed the assignment of the singlet at δ = 9.24 ppm to OH^{a}, by exchange correlation with residual water. The singlet integrating for three protons at δ = 1.89 ppm is attributed to the methyl group of the N-acetylated tyrosine, as confirmed by the presence of a long-range correlation in the ^{1}H-^{13}C HMBC spectrum with a strongly deshielded carbon resonance (~170 ppm) pertaining to the carbonyl carbon. The aromatic protons of the tyrosine unit are assigned to the two doublets at δ = 7.20 and δ = 6.73 ppm, as H^{c} and H^{b}, respectively, in agreement with the order of proximity to the hydroxyl group. For what concerns the porphyrin fragment, the inner NH protons resonate at δ = – 2.91 ppm; the two multiplets at δ = 8.25 – 8.20 ppm and δ = 7.87 – 7.81 ppm, integrating for six and nine protons, respectively, are assigned to the *ortho* and *meta* + *para* aryl protons. The nOe correlations observed in the ^{1}H-^{1}H ROESY spectrum between the resonance of the *ortho* protons and H$^{\beta'}$, together with the relative integration, allows to discriminate the β-pyrrolic protons close to the amide bond (at δ = 8.90 ppm) and the remaining six β-protons (at δ = 8.83 ppm). A further nOe correlation between the multiplets of H$^{\beta}$ and the doublet at δ = 8.16 ppm (which also shows coupling in the ^{1}H-^{1}H COSY spectrum with the doublet belonging to H^{i}), permits to assign this latter signal to H^{j}. The nature of **5** was further validated by HRMS analysis (Figure 2.2.7, left); chirality of **5** is nicely observed in the CD spectrum in which an induced band in the visible region can be observed (Figure 2.2.7, right). The photophysical and electrochemical properties of **5** are discussed later.

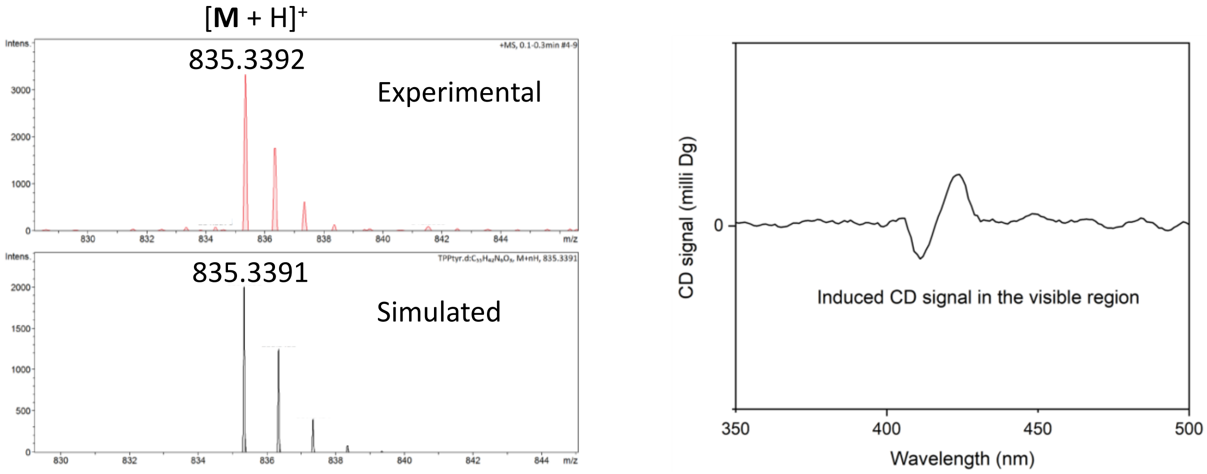

Figure 2.2.7. Left: HRMS spectrum of **5** in CH_3CN, experimental (red) and simulated (black). CD spectrum (CH_2Cl_2, 5 μM) of **5**.

Free-base porphyrin **5** was then metalated in the presence of $SnCl_2{\cdot}2H_2O$, as schematically illustrated in Scheme 2.2.3. After metal insertion, the reaction mixture was quenched by addition of water, the resulting solid was filtered and thoroughly washed with distilled water to remove any excess metal salt. The solid was then re-dissolved in $CHCl_3$ and washed with 6 M HCl to replace any phenolate potentially coordinated to the metal centre with two chloride ions (as discussed above). Conjugate **SnCl₂TPP-*p*Tyr** (**6**) was obtained as a purple solid after isolation by precipitation form a chloroform/*n*-hexane solution, in 65% yield. A thorough NMR analysis confirmed the structure and the coordination environment of **6** (see also Figures S28 – S31 and S33 – S37 in Appendix A). A comparison of the ^{1}H NMR spectra of **5** and **6** in the same solvent (dmso-d_6 chosen for solubility reasons) is reported in Figure 2.2.6. The disappearance of the singlet corresponding to the inner NH protons and the downfiled shift of the signals of the β-protons of the macrocycle found in **6** with respect to **5** (Δδ = +0.40 ppm), confirm the successful metal insertion. It must be noted that dmso-d_6 solutions of **6** are not stable over time, due to progressive displacement of the axial chloride anions by oxygen-bound dmso-d_6 (see the time-evolution of the ^{1}H NMR spectra of **6** in dmso-d_6 in Figure S32, Appendix A). For this reason, the ^{1}H-^{119}Sn HMBC spectrum was recorded in CD_2Cl_2 (Figure

2.2.8), and the chemical shift found for the tin nucleus agrees with that reported for the reference system $SnCl_2TPP$, see also above.

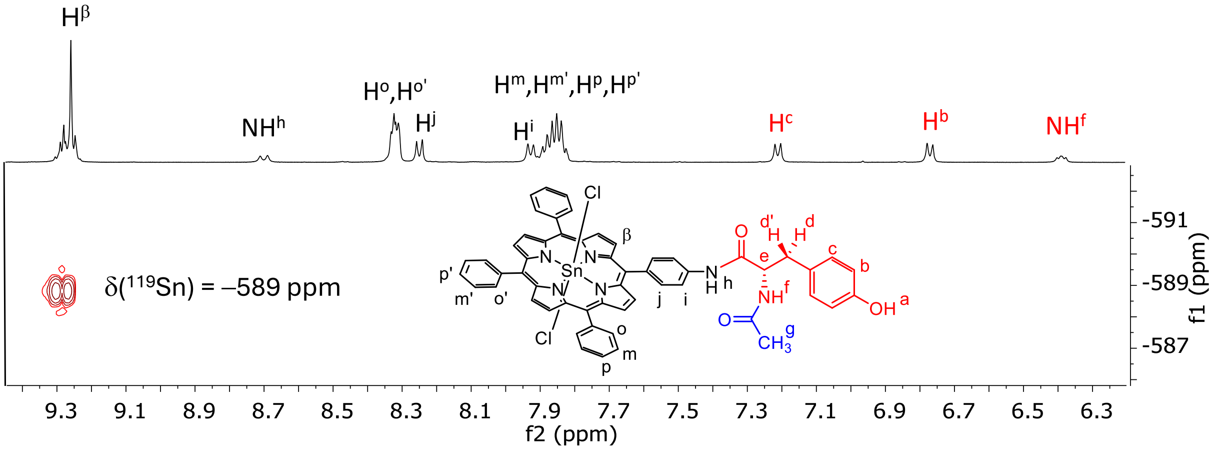

Figure 2.2.8. Aromatic region of the ^{1}H-^{119}Sn HMBC spectrum (CD_2Cl_2) of **6**.

Finally, **6** was also characterized by mass spectrometry and CD analysis (Figure 2.2.9 and Figure 2.2.10, respectively), while the photophysical and electrochemical properties of this novel compound were studied by UV-Vis absorption, emission spectroscopy, and CV (described later), as shown in Figures 2.2.15 and 2.2.16.

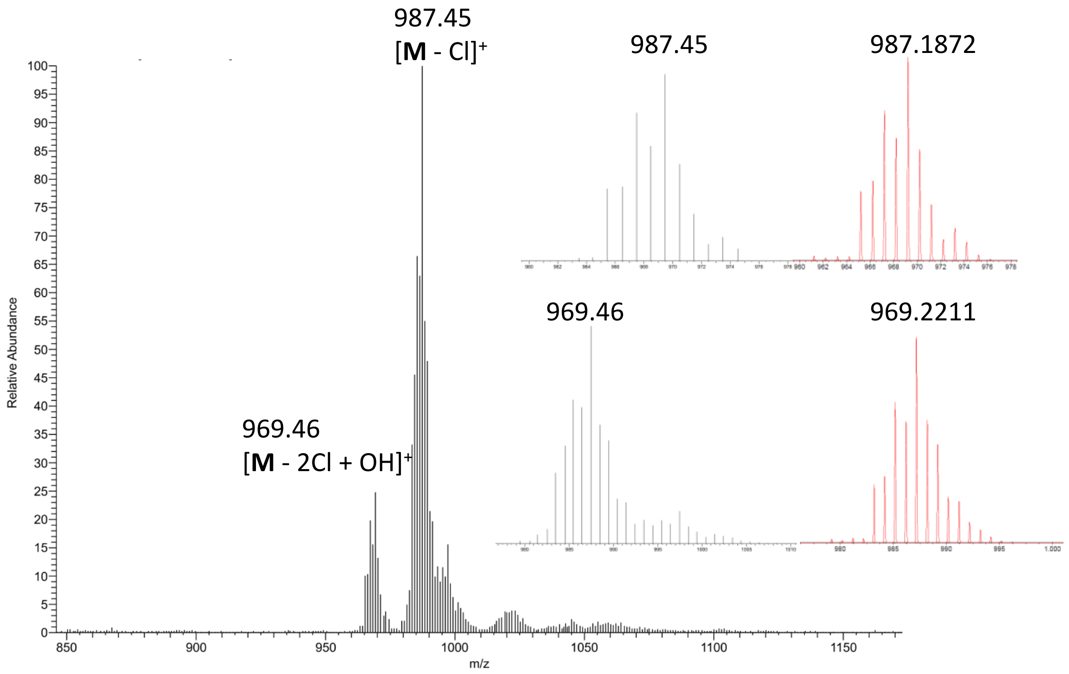

Figure 2.2.9. ESI-MS spectrum of **6** in CH_3CN, experimental (black) and simulated (red).

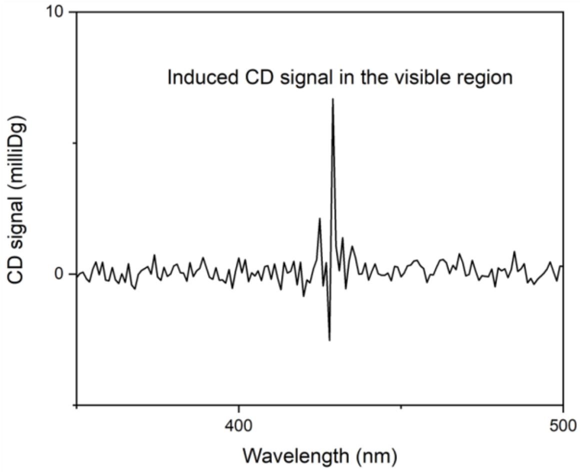

Figure 2.2.10. CD spectrum (CH_2Cl_2, 5 µM, visible region) of **6**.

Single crystals of **6** suitable for the X-ray diffraction analysis were obtained by slow diffusion of *n*-hexane into a 1:1 chloroform/acetonitrile solution of **6**. Details on the crystallization and additional structural data are reported in Experimental Section and in Table S1 and S2 of Appendix A. The X-ray crystal structure confirms the molecular structure and chirality of **6** (Figure 2.2.11).

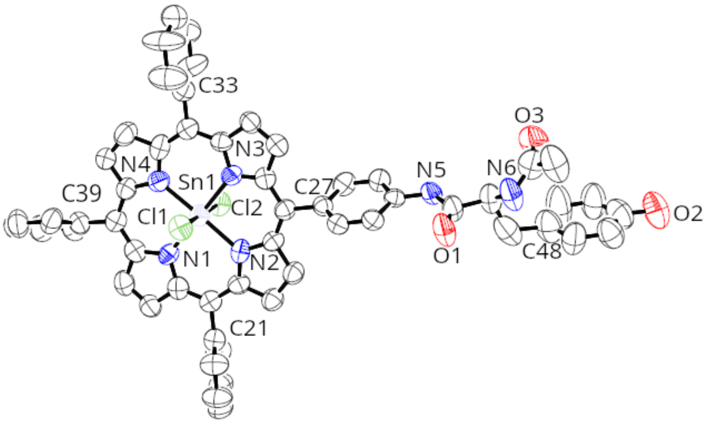

Figure 2.2.11. ORTEP representation of the single crystal X-ray structure of **6**, hydrogens omitted for clarity.

The Sn^{IV}-porphyrin conjugate is 25.2 Å long, length calculated as the distance between the *para*-carbon of the phenyl group in *meso* position 15 (C39 in the Figure) of the macrocycle and the hydroxy oxygen of the tyrosine ligand. The distance between this oxygen and the closest β-pyrrolic carbon is 14.1 Å. All the porphyrin aryl rings are almost perpendicular to the plane defined by the porphyrin macrocycle and the tin centre. There is no significant out-of-plane protrusion of the Sn atom, as its distance from the average plane through the porphyrin macrocycle (0.024 Å) is smaller than the mean distance of the porphyrin carbon and nitrogen atoms from the same plane (0.035 Å). In the crystalline lattice, molecules of compound **6** are packed with all porphyrin planes parallel to each other, in an alternate staggered hydrogen bonded pattern. Each molecule is involved in five intermolecular hydrogen bonds engaging the -NH of the amide and the carbonyl of the protecting group on one side (towards the corresponding complementary sites of a neighbouring molecule), and N-amino acid plus the carbonyl of the amide on the other side (towards the corresponding complementary sites of a second neighbouring molecule). Additionally, each phenol -OH group is hydrogen bonded to one acetonitrile crystallization molecule (Figure 2.2.12).

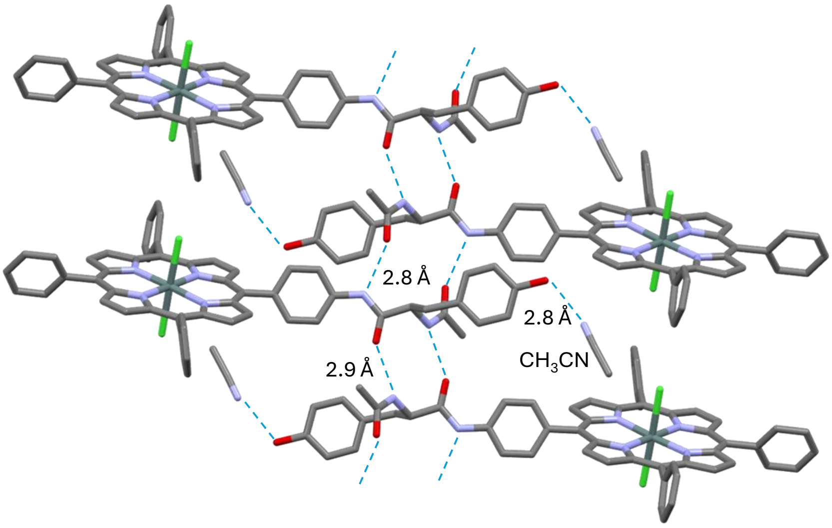

Figure 2.2.12. Hydrogen bond networks found in the crystalline lattice of **6**. Hydrogen bond distances (in Å) are referred to the nitrogen and oxygen atoms of the two amide groups as well as to the oxygen of the phenol group and the nitrogen of the acetonitrile molecule. Hydrogen atoms omitted for clarity. Colour code: Sn: dark green; Cl: light green; N: purple; O: red; C: grey.

Also for this second conjugate, the corresponding Zn^{II}-porphyrin **ZnTPP-*p*Tyr** (**7**) analogue was prepared for characterization purposes, following the same synthetic strategy followed for **4** (Scheme 2.2.3). **7** was isolated, *via* precipitation from a chloroform/*n*-hexane in 92% yield, and fully characterized in solution via 1D and 2D NMR spectroscopy, as well as mass spectrometry (Figures S38 – S42 in Appendix A). Finally, the model compounds **TPP-*p*BA** (**8**), **$SnCl_2$TPP-*p*BA** (**9**) and **ZnTPP-*p*BA** (**10**), Figure 2.2.13, were synthesized in high yields following the same synthetic strategies reported above, by coupling **TPP-*p*NH_2**, (**1**) with benzoic acid, followed by metal insertion and isolated as purple or pink solids in 80%, 70% and 80% yield, respectively (see Experimental part for details).

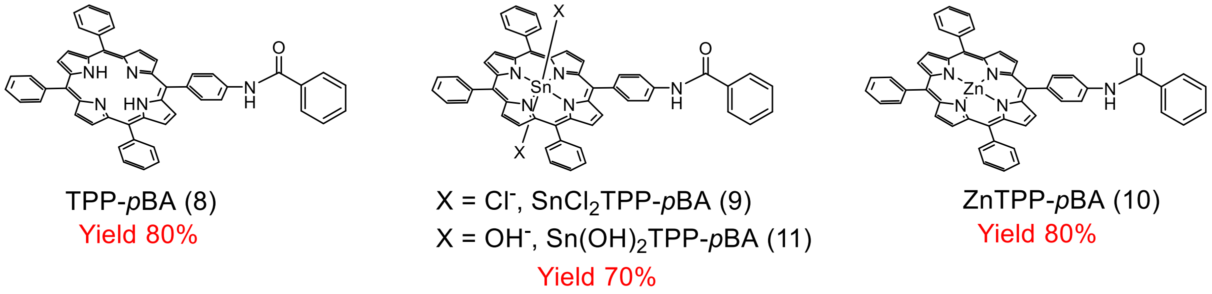
TPP-pBA (8)
Yield 80%

X = Cl$^-$, SnCl$_2$TPP-pBA (9)
X = OH$^-$, Sn(OH)$_2$TPP-pBA (11)
Yield 70%

ZnTPP-pBA (10)
Yield 80%

Figure 2.2.13. Chemical structure of the model compounds **8** – **11.**

Models **8** – **10** were fully characterized in solution by 1D and 2D NMR spectroscopy, as well as mass spectrometry (see Figures S43 – S63 in Appendix A). Single crystals of **10**, suitable for X-ray diffraction analysis were obtained by slow diffusion of *n*-hexane into a $CHCl_3$/ethanol solution of the compound. A preliminary structure is reported in Figure 2.2.14. Metal insertion leads to a distortion of the porphyrin macrocycle, with the zinc being displaced out of the average macrocyclic plane, as typically observed in the X-ray structures of zinc-porphyrins.[55] The apical position of the metal is occupied by one molecule of ethanol, while a second ordered molecule of crystallization of ethanol is also found. Both these molecules are engaged in an extended intermolecular hydrogen bond network (Figure 2.2.14). Each independent molecule of **10** forms two hydrogen bonds on opposite sides: one with the carbonyl group and the ethanol apical to the Zn^{2+} of a second molecule, and one with the amide NH group and a crystallization ethanol molecule, with the formation of an ordered packing of staggered conjugates. The Zn^{II}-porphyrin conjugate **10** is 22.0 Å long (distance calculated between the *para*-carbon of the aryl group in position 15 of the macrocycle and the *para*-carbon on the phenyl group at the opposite end of the conjugate).

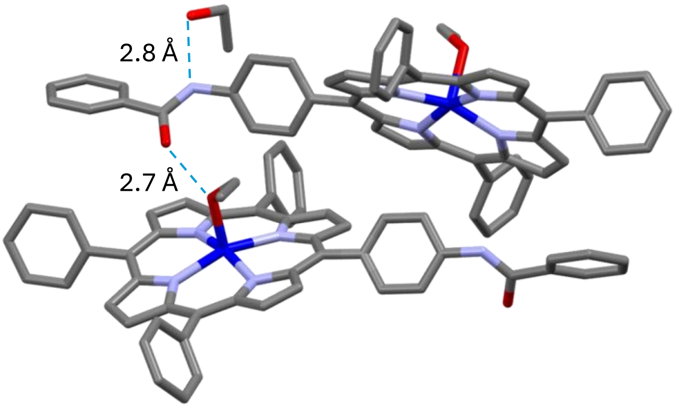

Figure 2.2.14. Hydrogen bond networks found in the crystalline lattice of **10**. Hydrogen bond distances (in Å) are referred to the nitrogen and oxygen atoms of the amidic function and the oxygen atoms of the ethanol units. Colour code: Zn: blue; N: purple; O: red; C: grey.

The absorption, emission, and electrochemical properties of **8** – **10** were measured by UV-Vis absorption and emission spectroscopy, and cyclic voltammetry (see Figures S64 and S65 in Appendix A, and Section 2.2.3 below). Photophysical and electrochemical characterization of these systems served for the subsequent characterization of the Sn^{IV}-porphyrin/phenol conjugates **3** and **6**. The photophysical properties of **TPP-*p*Tyr** (**5**), **ZnTPP-*p*Tyr** (**6**), and **SnCl₂TPP-*p*Tyr** (**7**), with highlights on their similarities and differences are briefly discussed here. The UV-Vis absorption and emission spectra of **5** – **7** are reported in Figure 2.2.15, left and right, respectively.

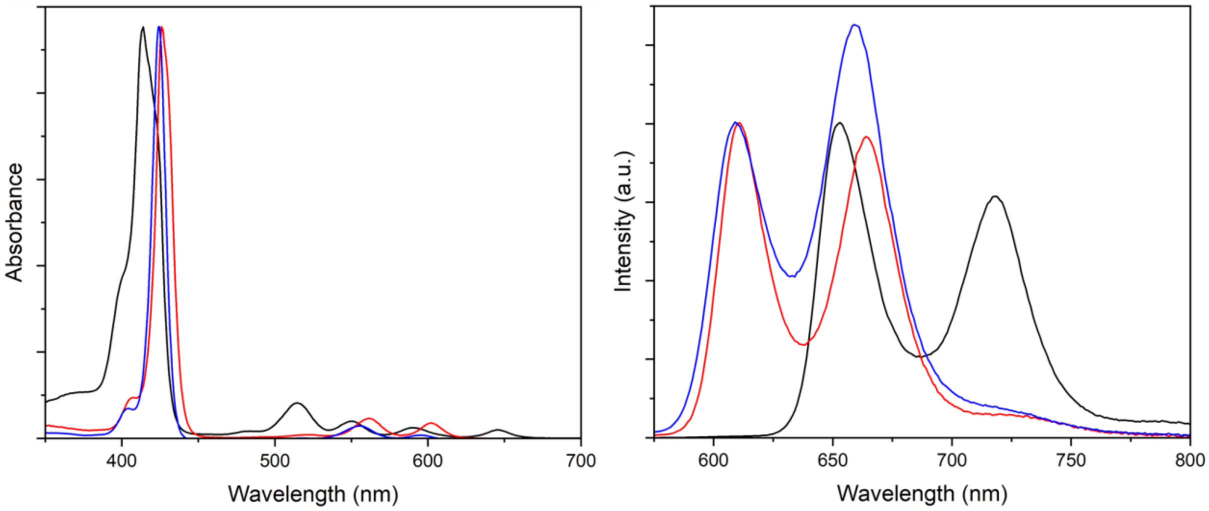

Figure 2.2.15. Left: UV-Vis absorption spectra (CH_2Cl_2, 25 μM) of **5**, **6** and **7**. Right: Emission spectra (CH_2Cl_2, 25 μM, λ_{irr} = 515 nm for **5**, λ_{irr} = 560 nm for **6**, λ_{irr} = 558 nm for **7**) of **5**, **6** and **7** (black, red and blue traces respectively).

For all the conjugates both the UV-Vis absorption and the fluorescence spectra closely match those of simple TPP, ZnTPP and $SnCl_2$TPP analogues, as well as those of the corresponding models **8** and **10** (Figure S64 in Appendix A) and of **9** (Figure 2.2.17). This observation indicates that conjugation of the redox active tyrosine fragment at the periphery of the macrocycle does not influence the ground state electronic interactions (see also next section for further details). As expected, metal insertion causes a red-shift of the Soret band of about 10 nm (maxima at 414, 426 and 424 nm for **5**, **6** and **7**, respectively), and a reduction in the number of the Q bands from four to two, as a consequence of the increased symmetry of the macrocycle (D_{2h} for **5**, D_{4h} for **6** and **7**). In general, all the conjugates exhibit fluorescence emission profiles with two broad bands in the 600 – 800 nm region. Intensity, spectral shape and position of these bands are influenced by the presence/nature of the metal and of the substituents on the porphyrin macrocycle (see also Chapter 1). In **6** and **7** the emission bands are blue-shifted compared to **5**. As already mentioned in Chapter 1, deactivation of the singlet excited state *via* fluorescence competes with ISC, which leads to population of the triplet excited state in both **6** and **7** (see also next section). Finally, the comparison between electrochemical CV data of **5**, **6** and **7** is reported in Figure 2.2.16 and in Table 2.2.1.

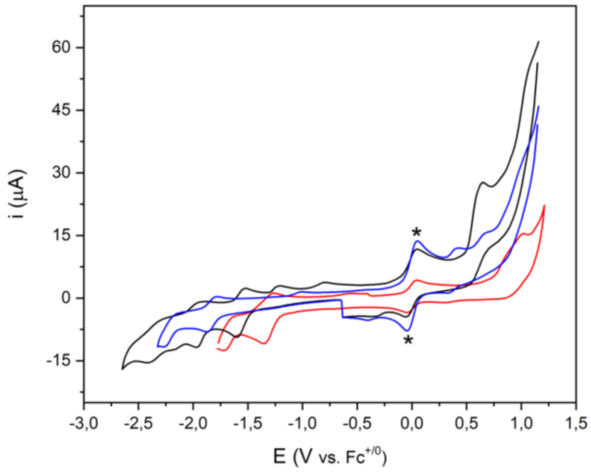

Figure 2.2.16. Cyclic voltammetry (CV) of 1 mM DMF:CH_2Cl_2 or CH_2Cl_2 solution of **5** – **7** (black, red and blue traces respectively) recorded at 0.1 V/s with 0.1 M $TBAPF_6$ as supporting electrolyte under inert atmosphere using a glassy carbon as working electrode, a platinum wire as a counter electrode, SCE (saturated calomel electrode) as reference and ferrocene (*) as internal standard.

In general, the redox properties of porphyrins strongly depend on the nature of the substituents on the porphyrin macrocycle both at the β- or *meso*-positions, while being equal the organic skeleton insertion of different metal cations induce significant differences. Considering conjugates **5** – **7**, and the corresponding models **8** – **10** (Figure S65 in Appendix A and Figure 2.2.16), the first reduction events related to the porphyrin macrocycle are in line with those found for the series TPP, ZnTPP and $SnCl_2TPP$.[56] When comparing Zn^{II}- and Sn^{IV}-porphyrins, the tin derivatives are more easily reduced than their Zn^{II} analogues. This can be attributed to the presence of a highly charged metal ion coordinated within the inner cavity of the macrocycle, resulting in Sn^{IV}-porphyrins having a more pronounced electron-accepting character (Table 2.2.1). This trend is clearly seen in conjugates **6** and **7** as well as in their model compounds **9** and **10**. Additionally, for derivatives **5** – **7** the oxidation of the tyrosine fragment can be detected at positive values, between +0.85 and +1.05 V *vs.* $Fc^{+/0}$.

Table 2.2.1. Photophysical and electrochemical data for **5** – **7** and relative model compounds **8** – **10**.

Compound	**E_{red} (V)**[a]	**E_{ox} (V)**
5 (**8**)	−1.56 (−1.68)	+0.58 (+0.51)
6 (**9**)	−1.30 (−1.26)	+1.01 (+0.99)
7 (**10**)	−1.84 (−1.77)	+0.37 (+0.36)

Redox potentials of **5** – **7** and corresponding model compounds **8** – **10** in brackets. [a]First reduction event related to the porphyrin macrocycle).[56]

Some brief considerations can be done in relation to the choice of the apical ligands on the tin-porphyrin conjugates of interest. Chlorides are surely the best choice for the purposes of the present study for two main reasons: the tin-chloride bond in sufficiently inert and the presence of these ligands move the reduction potential value in the right direction (for instance literature data indicate that $SnCl_2TPP$ is more easily reduced than $Sn(OH)_2TPP$ by ~ 0.15 V and by about 0.10 V, for the first and the second event respectively).[56] On the other hand, the presence of two hydroxyl groups may be valuable in future perspective. In fact, as described in Chapter 1, $Sn(OH)_2$-porphyrins are typically employed as precursors for the obtainment of supramolecular systems by replacement of the -OH groups with carboxylates or phenolates. This may allow in a following study to introduce a third photoactive partner by axial ligation to the metal centre. Therefore, initial attempts to perform basic hydrolysis of the dichloride conjugates **3**, **6** and **9** were performed, by following reported literature procedures also employed by us in previous works ($CHCl_3$:EtOH solvent mixture with excess K_2CO_3, under refluxing conditions).[57] For the model compound **9** the reaction worked well, allowing the isolation of **$Sn(OH)_2$TPP-*p*BA** (**11**) in 70% yield (Figure 2.2.13). The presence of the hydroxyl groups on the metal centre is confirmed both by the presence of a broad signal at the negative chemical shift values (~ $\delta = -7$ ppm) in the ^{1}H NMR spectrum (Figure S66 in Appendix A) and by the chemical shift value for the ^{119}Sn nucleus ($\delta = -570$ ppm). In contrast, for compounds **3** and **6** the isolation of a clean $Sn(OH)_2$-derivative was unsuccessful. For both cases the isolated reaction products presented very broad ^{1}H NMR ($CDCl_3$) spectra, which sharpened upon addition of CD_3OD. This behaviour is very similar to that observed for the isolated solid obtained from metal insertion in free-base porphyrin **2** (see above). For the moment it can be reasonably concluded that under the chosen reaction conditions, the phenol groups of both **3** and **6** gets deprotonated and coordinate as phenolates to any available Sn^{IV} centres, leading to the formation of a mixture of oligomeric/polymeric species. Further investigations on this aspect will be done.

2.2.2. Photophysical studies.

In collaboration with Prof. Mirco Natali (University of Ferrara, Italy), a comprehensive photophysical investigation of **SnCl$_2$TPP-*p*PA** (**3**) and **SnCl$_2$TPP-*p*Tyr** (**6**) in dichloromethane solutions was done, also in the presence of pyrrolidine as external base. The study focused on the selective photoexcitation of the Sn^{IV}-porphyrin unit using steady-state and time-resolved absorption and emission spectroscopies. The photophysical and electrochemical properties of **3** were measured in dichloromethane and compared with those of model compound **SnCl$_2$TPP-*p*BA** (**9**). The UV-Vis absorption spectrum of **3** is superimposable with that of **9** (Figure 2.2.17, left). In the visible region, the spectrum is dominated by the intense absorption of the Sn^{IV}-porphyrin unit, with a strong Soret band centred at 428 nm and two less intense Q bands at 562 and 602 nm.

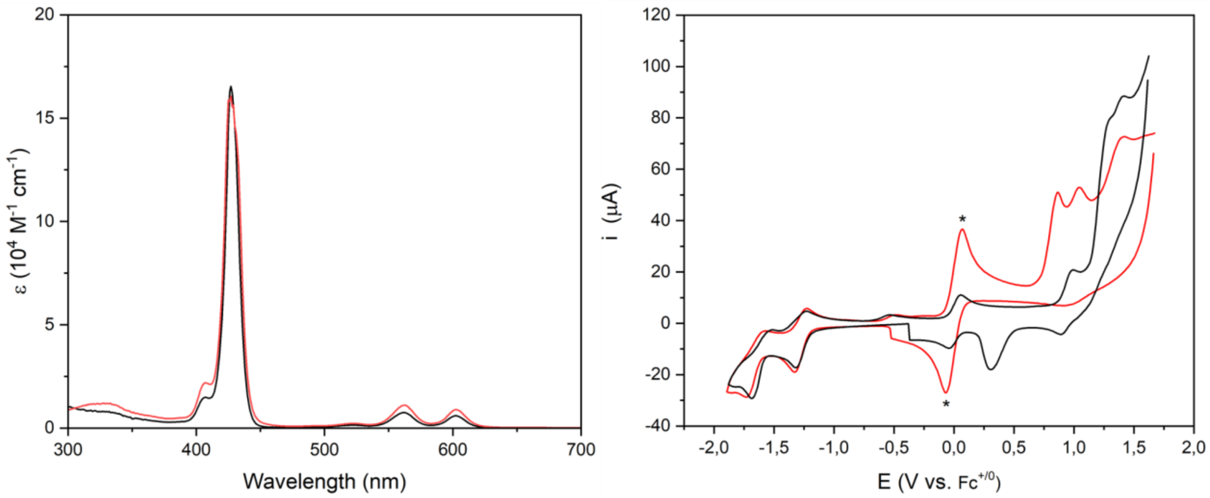

Figure 2.2.17. Left: UV-Vis absorption spectra (CH$_2$Cl$_2$, 25 μM) of **SnCl$_2$TPP-*p*PA** (**3**) and **SnCl$_2$TPP-*p*BA** (**9**) (red and black traces respectively). Right: Cyclic voltammetry (CV) of 1 mM CH$_2$Cl$_2$ solution of **3** and **9** (red and black traces respectively) recorded at 0.1 V/s with 0.1 M TBAPF$_6$ as supporting electrolyte under inert atmosphere using a glassy carbon as working electrode, a platinum wire as a counter electrode, SCE (saturated calomel electrode) as reference and ferrocene (*) as internal standard.

The cyclic voltammetry traces are shown in Figure 2.2.17 and the corresponding values are reported in Table 2.2.2: for both derivatives, two reduction peaks are observed (−1.28 and −1.72 V *vs.* Fc$^{+/0}$ for **3**; −1.26 and −1.69 V *vs.* Fc$^{+/0}$ for **9**). The first reduction is a reversible peak, attributed to the one-electron reduction of the porphyrin macrocycle, while the second is an irreversible peak, corresponding to the two-electron reduction of the same chromophore, in perfect agreement with the literature.[56] Regarding the anodic part of the CV, **9** exhibits a single irreversible peak at +0.99 V, corresponding to porphyrin oxidation, while for **3** two oxidation peaks appear, the first one (+0.87 V) is attributed to the phenol oxidation, and the second (+1.04

V) to the oxidation of the porphyrin macrocycle. These photophysical and electrochemical data confirm that there are no electronic interactions in the ground state between the two components of conjugate **3**. The absorption, emission and electrochemical data (summarized in Table 2.2.2) can be correctly used to estimate the energy level diagram of **3**: the energies of the various states were calculated using the model compounds and literature data, as better described in the Experimental Section.[37,45]

Table 2.2.2. Photophysical and electrochemical data for **$SnCl_2$TPP-*p*PA** (**3**), **$SnCl_2$TPP-*p*Tyr** (**6**) and the relevant models **9** and N-acetyl-*L*-tyrosine (**Ac-Y**).

Compound	**$E_{00}(S_1)$ (eV)**[a]	**$E_{00}(T_1)$ (eV)**[b]	**E_{red} (V)**	**E_{ox} (V)**
3	2.05	1.65	−1.28, −1.73	+0.87,[c] +1.05
9	2.08	1.65	−1.26, −1.69	+0.99
6	2.05	1.65	−1.30, −1.72	+0.88,[c] +1.01
Ac-Y	--	--	--	+0.83[c,d]

[a]Taken from the intersection between normalized absorption and emission spectra. [b]Taken from the SnTPP analogue.[58] [c]Phenol. [d]Taken form ref. 37.

As shown in Figure 2.2.18, the energy of the diradical state in the absence of any external base is uphill with respect to both the singlet (by ~0.1 eV) and the triplet excited state (by ~0.5 eV) of the tin-porphyrin in **3**, thus no intercomponent charge-transfer processes are expected to occur in the absence of external bases.

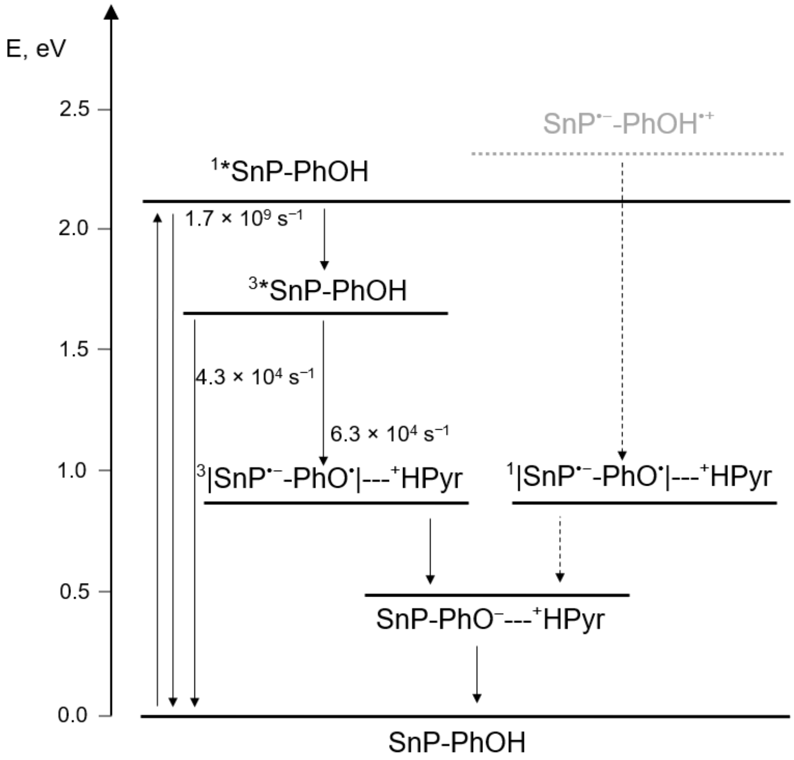

Figure 2.2.18. Energy level diagram in **3** with related photoinduced processes and estimated rates in CH_2Cl_2, also in the presence of pyrrolidine (for simplicity the same energy is assigned to both singlet and triplet PCET states). Solid lines indicate the active mechanisms, while dotted arrows indicate the non-active pathways. For simplicity the Sn^{IV}-porphyrin unit is named SnP, while the phenol ligand is named PhOH.

Indeed, comparable emission profiles in terms of relative intensities and spectral shape were observed upon visible-light excitation of optically matched CH_2Cl_2 solutions of **3** and **9** (Figure 2.2.19, left). Similarly, the fluorescence lifetimes of the two systems were found to be comparable ($\tau = 0.59$ ns for **3** and $\tau = 0.62$ ns for **9**, Figures S72 and S73 in Appendix A). Also, the kinetic profile of the triplet decay measured by laser flash photolysis for **3** and **9** were found identical, affording the same rate constant $k_0 = 4.3 \times 10^4$ s^{-1} (in Figure 2.2.20 the kinetic traces of the deactivation of the triplet excited state in the presence of pyrrolidine and the derived rate constants for **3** are shown).

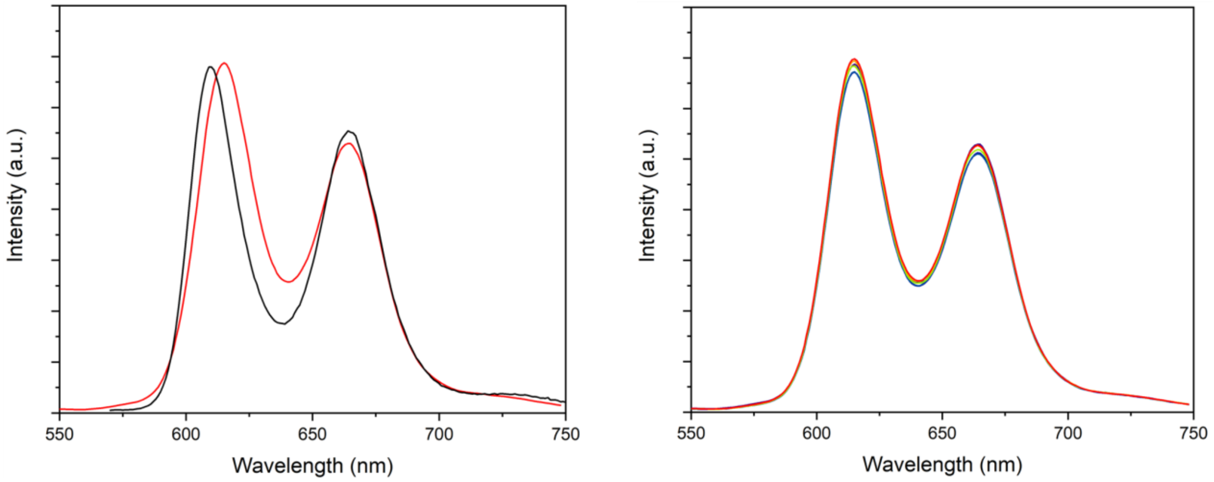

Figure 2.2.19. Left: Emission spectra (CH_2Cl_2, 25 mM, $\lambda_{irr} = 560$ nm) of **3** and **9** (red and black traces respectively). Right: Emission spectra ($\lambda_{irr} = 560$ nm) of CH_2Cl_2 solutions containing 25 μM of **3** and increasing amounts of pyrrolidine, from 0.00 M to 0.084 M.

As already stated in the Introduction, the energy levels of the PCET states in the presence of pyrrolidine ($^{1}|SnP^{\cdot-}$-$PhO^{\cdot}|$---$^{+}HPyr$ and $^{3}|SnP^{\cdot-}$-$PhO^{\cdot}|$---$^{+}HPyr$) were predicted by subtracting the contribution of the deprotonation step from the energy of the diradical pair state. For simplicity the same energy was assigned to both singlet and triplet PCET states. As briefly described above and previously reported by us,[37] the energy contribution associated with the deprotonation of a phenol promoted by pyrrolidine (in organic solvent) was calculated to be ~1.3 eV. It must be noted that this value was obtained applying several approximations - for instance, protonation data were measured in acetonitrile in place of dichloromethane and using a different phenol derivative (see Experimental Section for further details). The resulting PCET states are found lower in energy than both the singlet and triplet excited states (ΔG ~1.2 eV and ~0.8 eV, respectively). Therefore, based on pure thermodynamic considerations, photoinduced PCET processes may be feasible in the presence of pyrrolidine. Surprisingly, upon visible-light excitation of the SnP chromophore the fluorescence emission profile (Figure 2.2.19, right) and the singlet excited-state lifetime of **3** were found to remain unchanged by addition of increasing amounts of pyrrolidine. On the other hand, the behaviour of the triplet excited state revealed significantly different (Figure 2.2.20).

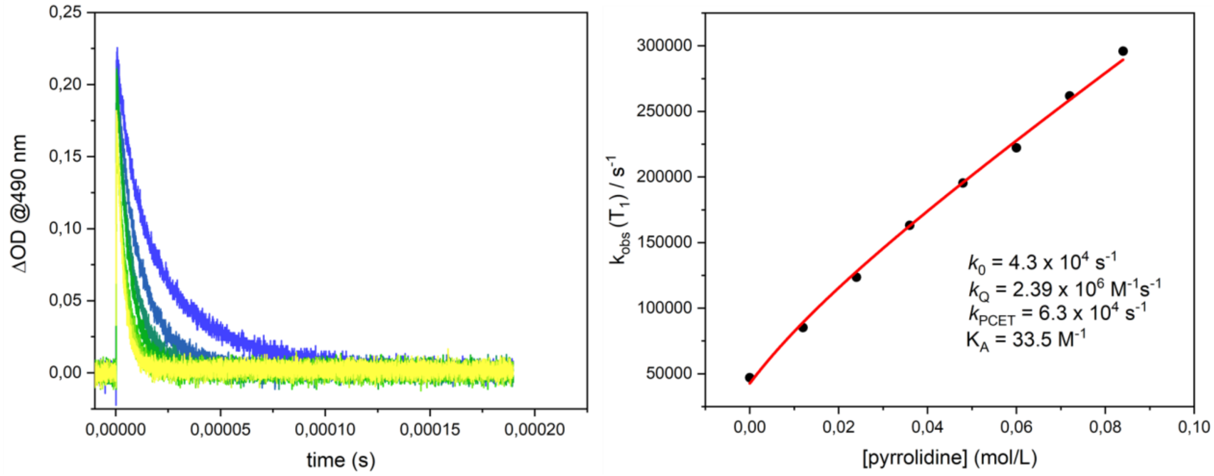

Figure 2.2.20. Left: Kinetic traces at 480 nm obtained by laser flash photolysis (λ_{irr} = 532 nm) in oxygen-free CH_2Cl_2 solutions containing 25 μM of **3** and increasing amounts of pyrrolidine, from 0.00 M (blue trace) to 0.084 M (yellow trace). Right: Mathematical fitting of the observed rate for the triplet excited state decay according to our previous reports (see also Section 2.1).[37]

The fraction of triplet excited state in **3**, formed *via* intersystem crossing from the singlet excited state, showed a deactivation kinetics at 490 nm that depends on pyrrolidine concentration, as monitored by transient absorption spectroscopy (Figure 2.2.20, left). Addition of increasing amounts of pyrrolidine causes the quenching of this state, with a decrease of lifetime from 23 to 4.3 μs in the concentration range tested. These data were fitted using the same formalism previously adopted for the axial systems (equation 4 in Introduction) assuming the occurrence of a PCET from the triplet excited state of **3**, that involves simultaneous oxidation of the phenol residue, reduction of the porphyrin macrocycle and proton shift from the phenol to the pyrrolidine, with formation of a diradical anion species according to equation 3:

$$^{3*}\text{SnP-PhOH --- Pyr} \rightarrow \text{SnP}^{\cdot-}\text{-PhO}^{\cdot}\text{ --- }^{+}\text{HPyr} \qquad (3)$$

For the fitting, we assume the following key points: (i) pyrrolidine is not able to deprotonate the phenol, as previously found by us (see also Section 2.1), thereby ruling out the occurrence of a two-step process, *i.e.* proton abstraction followed by electron transfer from the phenolate to the metallo-porphyrin; (ii) a pre-association equilibrium between the phenol group and pyrrolidine occurs *via* hydrogen-bond formation with a $K_A = 33.5\ M^{-1}$ (see also Experimental Section);[38] (iii) the presence of a competitive bimolecular reductive electron transfer between the pyrrolidine and the tin-porphyrin was considered.[47] The bimolecular rate constant of this latter process was determined using a classical Stern-Volmer treatment to the model Sn^{IV}-porphyrin **9** in the presence of increasing amounts of pyrrolidine (affording a $k_Q = 2.39 \times 10^6$

M^{-1} s^{-1}, see Experimental Section). Overall, a $k_{PCET} = 6.3 \times 10^4$ s^{-1} was derived from the fitting (Figure 2.2.20, right). Due to the small rate constant for the PCET process, the dominating deactivation channel of the triplet excited state of the Sn-porphyrin component in **3** in the presence of pyrrolidine involves the bimolecular quenching by the added base. This evidence precludes the possibility to gain experimental insight into the recombination event taking place from the PCET state and to assess whether the increased distance between the chromophore and phenol units is beneficial to enhance the corresponding lifetime.

The photophysical and electrochemical properties of **SnCl₂TPP-*p*Tyr** (**6**) were investigated in CH_2Cl_2, also in comparison with model compounds **9** and N-acetyl-*L*-tyrosine. The analysis of the data allowed for the construction of the energetic diagram, in analogy with what previously described for **3**. Figure 2.2.21 shows the UV-Vis absorption spectra (perfectly superimposable) and CV of **6** and **9**, and Table 2.2.2 contains the relevant redox potentials. The energy level diagram of **6** is reported in Figure 2.2.22.

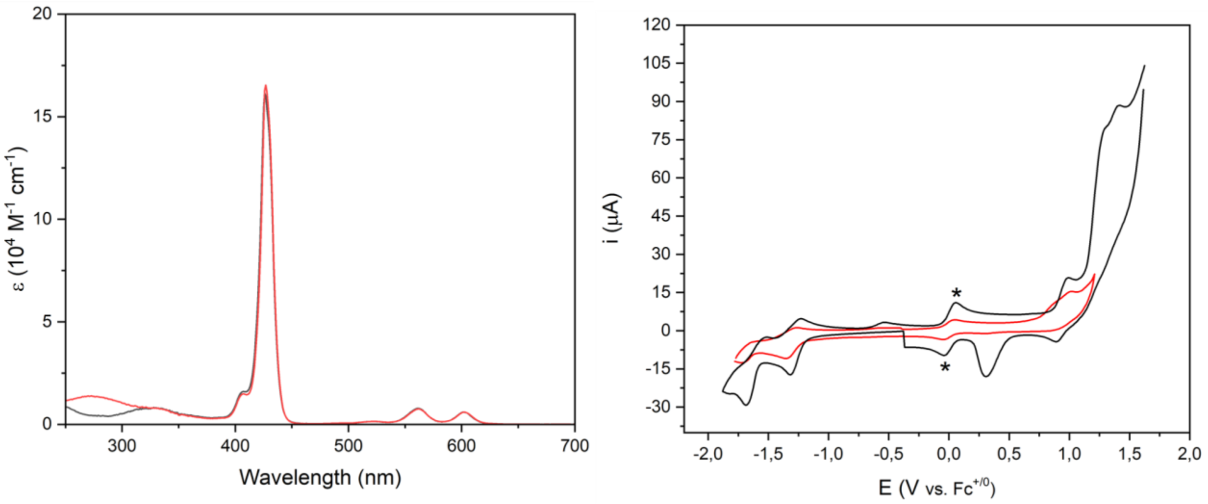

Figure 2.2.21. Left: UV-Vis absorption spectra (CH_2Cl_2, 25 μM) of **SnCl₂TPP-*p*Tyr** (**6**) and **SnCl₂TPP-*p*BA** (**9**) (red and black traces, respectively). Right: Cyclic voltammetry (CV) of 1 mM CH_2Cl_2 solution of **6** and **9** (red and black traces, respectively) recorded at 0.1 V/s with 0.1 $TBAPF_6$ as supporting electrolyte under inert atmosphere using a glassy carbon as working electrode, a platinum wire as a counter electrode, SCE (saturated calomel electrode) as reference and ferrocene (*) as internal standard.

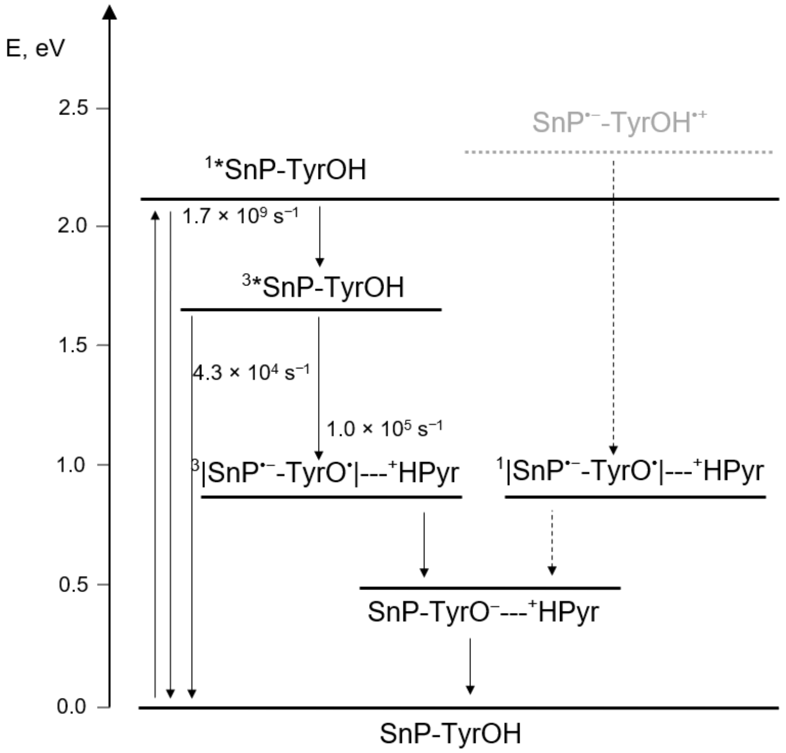

Figure 2.2.22. Energy level diagram in **6** with related photoinduced possible processes and rates in CH_2Cl_2, also in the presence of pyrrolidine (for simplicity the same energy is assigned to both singlet and triplet PCET states). Solid lines indicate the occurring PCET mechanism from the singlet excited state, while dotted arrows indicate the non-active pathways. For simplicity the Sn^{IV}-porphyrin unit is named SnP, while the peripheral amino acid is named TyrOH.

The energy of the diradical species in the absence of external base (SnP$^{\cdot-}$-TyrOH$^{\cdot+}$, shown in grey dotted line in Figure 2.2.22) lies above both the singlet and triplet excited states of the SnP unit (by ~0.1 eV and ~0.5 eV respectively), thereby ruling out the possibility of photoinduced intercomponent processes in the absence of an external base. The energy of the PCET states deriving from the singlet and the triplet excited state of the SnP unit of **6** (^{1}|SnP$^{\cdot-}$-TyrOH$^{\cdot}$|---$^+$HPyr and ^{3}|SnP$^{\cdot-}$-TyrOH$^{\cdot}$|---$^+$HPyr, respectively) were determined as previously described and indicate that the corresponding PCET processes are downhill also for this conjugate. In agreement with the thermodynamics of the energy level diagram, the emission spectra of optically matched CH_2Cl_2 solutions of **6** and **9** are superimposable (Figure 2.2.23 left), and closely matching singlet excited-state lifetimes were also measured (τ = 0.60 ns and 0.62 ns for **6** and **9**, respectively, see also Figure S74 and S72, Appendix A). Akin to what observed for conjugate **3**, the fluorescence of **6** showed no quenching upon addition of increasing amounts of pyrrolidine (Figure 2.2.23 right), and substantially unvaried lifetimes were found in the absence and in the presence of pyrrolidine (0.60 ns and 0.58 ns, respectively, see also Figures S76 in Appendix A).

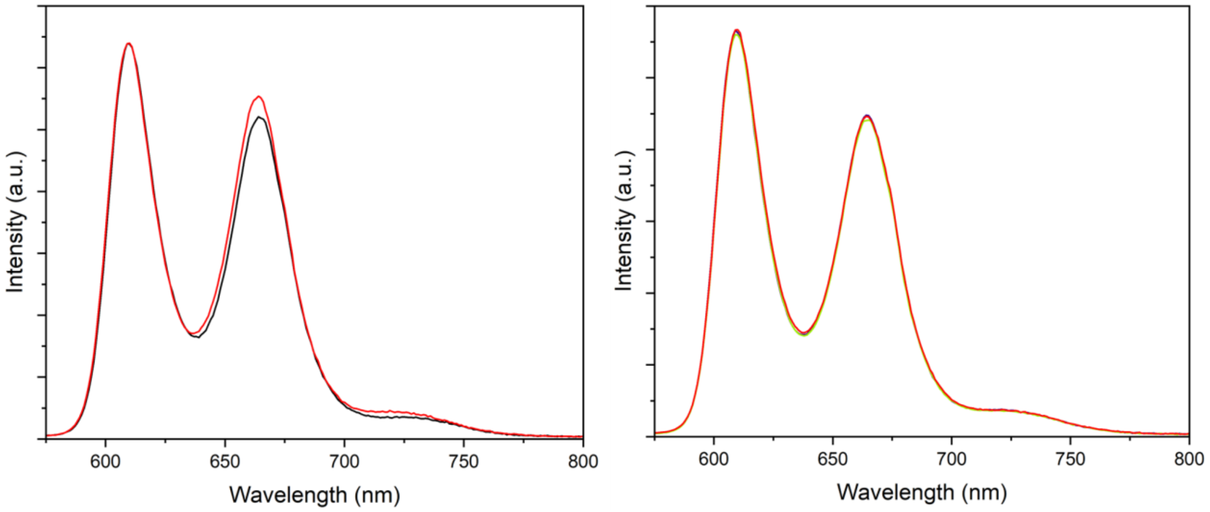

Figure 2.2.23. Left: Emission spectra (CH_2Cl_2, 25 mM, λ_{irr} = 560 nm) of **6** and **9** (red and black traces respectively). Right: Emission spectra (λ_{irr} = 560 nm) of CH_2Cl_2 solutions containing 25 µM of **6** and increasing amounts of pyrrolidine, from 0.00 M to 0.084 M.

In similarity to conjugate **3**, the triplet excited state of **6** exhibited a markedly different behaviour upon addition of pyrrolidine. The population of the triplet excited state, formed *via* intersystem crossing from the singlet excited state, displayed pyrrolidine-dependent deactivation profiles at 490 nm (Figure 2.2.24, left). Increasing concentrations of pyrrolidine led to efficient quenching of this state without the accumulation of photoproducts, as confirmed by transient absorption spectroscopy (Figure S77 in Appendix A). Accordingly, the triplet lifetime was found to decrease from 23 µs to 4.1 µs in the concentration range tested. By following the same analysis and data fitting (Figure 2.2.24, right and Experimental Section) described above in detail for **3**, it was possible to conclude that photoinduced PCET can occur from the triplet excited state of the metallo-porphyrin involving simultaneous tyrosine oxidation and proton shift from the phenol to the base, yielding the diradical species $SnP^{\cdot-}$-$TyrO^{\cdot}$, with a $k_{PCET} = 1.0 \times 10^5\ s^{-1}$ (Figure 2.2.24 right). Similar as above, the dominating deactivation pathway involving the triplet is the bimolecular reaction with pyrrolidine, still precluding experimental investigation of the diradical recombination mechanism.

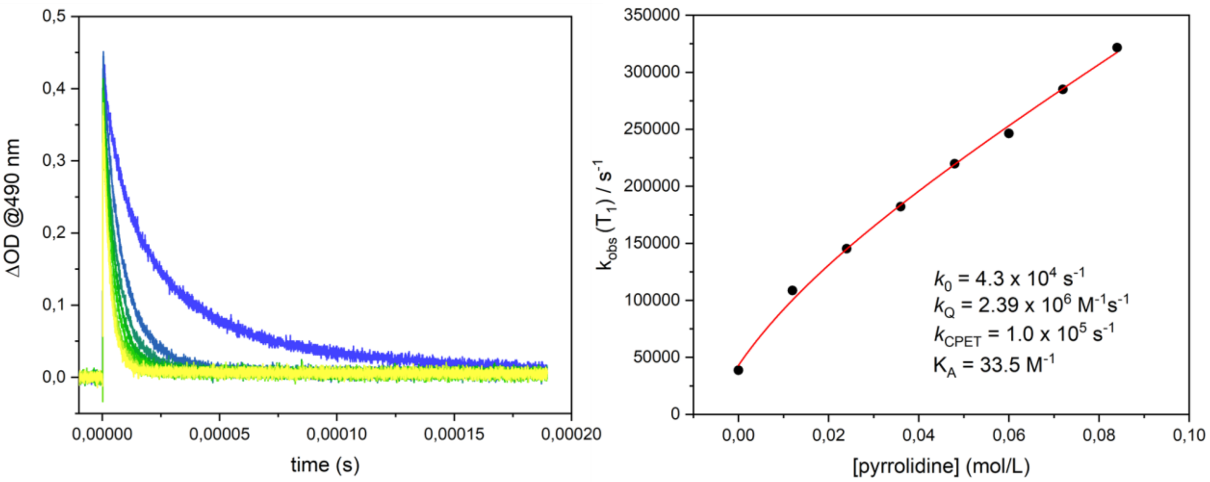

Figure 2.2.24. Left: Kinetic traces at 490 nm obtained by laser flash photolysis (λ_{irr} = 532 nm) in oxygen-free CH_2Cl_2 solutions containing 25 μM of **6** and increasing amounts of pyrrolidine, from 0.00 M (blue trace) to 0.084 M (yellow trace). Right: Kinetic treatment of the observed rate for the triplet excited state decay.

The markedly different behaviour of these two novel conjugates compared to **Sn(Ac-Y)$_2$TPP**, *i.e.* absence of photoinduced PCET from the ^{1*}SnP and significant slower rates of photoinduced PCET from the ^{3*}SnP, can be attributed to the increased distance between the phenol unit and the porphyrin macrocycle in **3** and **6**, as compared to **Sn(Ac-Y)$_2$TPP**. This is anticipated to reduce the electronic coupling thereby slowing down the overall PCET process. This situation thus disfavours the intended intercomponent processes from a kinetic viewpoint despite the similar thermodynamics. A similar effect was previously attained with **Sn(Ac-Y)$_2$OEP**, in response to a variation of the substituents at the porphyrin macrocycle (see above). In that case, however, with virtually identical electronic coupling values, the different thermodynamics (consequent to the presence of ethyl chains in the β-positions in place of phenyl rings in the *meso* positions) was the main factor governing the difference in kinetics. Here, the choice of positioning of the active phenol further apart from the metallo-porphyrin (see also the X-ray crystal structures of **Sn(Ac-Y)$_2$TPP** and **SnCl$_2$TPP-*p*Tyr** (**6**) in Figures 2.1.7 and 2.2.11 – 2.2.12 of the previous Sections) was done with the idea of increasing the lifetime of the diradical species by slowing down the recombination to the ground state. Opposite to what was envisaged, the conjugation of the phenol unit at the periphery of the macrocycle seems detrimental towards the formation of the PCET photoproduct. We therefore decided to perform some DFT calculations to better visualize the conformations assumed by **SnCl$_2$TPP-*p*PA** (**3**) and **SnCl$_2$TPP-*p*Tyr** (**6**) in dichloromethane solution. DFT simulations were performed in collaboration with Prof. Federico Berti (University of Trieste, Italy). Geometry optimization was done using a DFT B3LYP-D3/def2-SVP calculation with Schrödinger suite (see also

Experimental Section).[59,60] The obtained DFT models show that both **3** and **6** adopt extended conformations, corresponding to phenol-macrocycle distances between 14 – 15 Å (Figures 2.2.25 and 2.2.26).

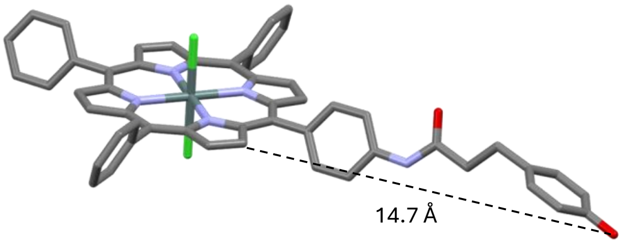

Figure 2.2.25. DFT model of **3** in CH_2Cl_2 showing the distance between the phenol oxygen and the closest β-pyrrolic carbon of the porphyrin macrocycle. Hydrogen atoms omitted for clarity. Colour code: Sn: dark green; Cl: light green; N: purple; O: red; C: grey.

For **6** two conformers, slightly differing in energy by 2.2 kcal/mol, were obtained (Figure 2.2.26). The two conformers differ from each for the presence (in the more stable conformer) or the absence (in the less stable one), of an intramolecular hydrogen bond between the amide proton and the carbonyl group of the N-acetyl protecting group. Overall, both the DFT conformers, at least in terms of useful distances, closely resemble the X-ray crystal structure obtained for **6** (Figures 2.2.11 and 2.2.12). **6** adopts an extended conformation that positions in average the redox-active tyrosine 14.35 Å far from the porphyrin macrocycle. The presence of two conformers in solution is compatible with the ^{1}H NMR spectrum in CD_2Cl_2 (Figure S33 in Appendix A), where the proton signals of the two amide groups are both split into two resonances of roughly equal intensities. This observation reflects the presence of two non-equivalent NH protons per amide function, which may be consistent with the presence in this solvent of two conformers in slow exchange on the NMR time-scale. Additional experiments to confirm this hypothesis are currently underway.

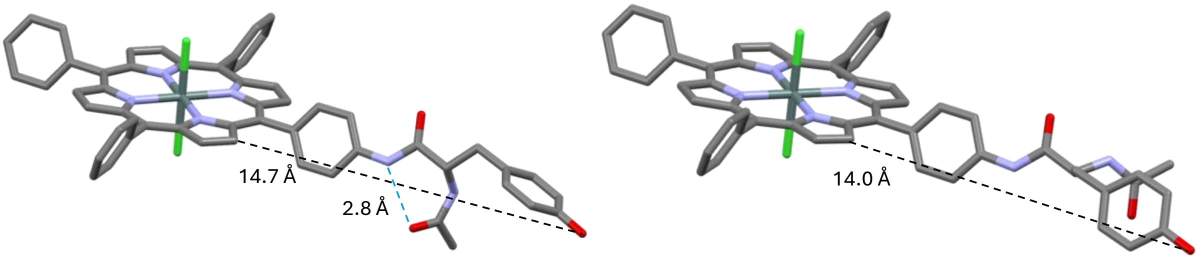

Figure 2.2.26. DFT models of **6** in CH_2Cl_2 showing the distance between the phenol oxygen and the closest β-pyrrolic carbon of the porphyrin macrocycle as well as the distance of the H-bond (left). Hydrogen atoms omitted for clarity. Colour code: Sn: dark green; Cl: light green; N: purple; O: red; C: grey.

The slightly lower distance (on average) between the chromophore and the phenol unit measured for **6** with respect to **3**, is consistent with the slightly faster kinetics for the PCET process as experimentally observed. These results thus support the crucial role of the distance between the molecular units involved in PCET to achieve fast rates.

2.3. Conclusions and future perspectives.

In this Chapter, the synthesis and complete characterization of the two new Sn^{IV}-porphyrin/phenol conjugates, **SnCl$_2$TPP-*p*PA** (**3**) and **SnCl$_2$TPP-*p*Tyr** (**6**), along with their Zn^{II} analogues and corresponding models, were reported and discussed in detail. For conjugate **6** a preliminary single crystal X-ray structure was also presented. Highlight was given to some critical points regarding the Sn^{IV} insertion step, the role of the solvent as competing ligand, and the usefulness of 2D ^{1}H-^{119}Sn heteronuclear NMR experiments to unambiguously ascertain the nature of the metal apical ligands. The photophysical properties of **3** and **6** were studied in CH_2Cl_2 solution, also in the presence of pyrrolidine as an external base, to evaluate their ability to promote photoinduced PCET. Their behaviour was compared with that of the previously reported **Sn(Ac-Y)$_2$TPP** system, which is known to promote such a photoinduced process activated by visible light excitation of the chromophore. Simultaneous proton transfer from the phenol group of the tyrosinato apical ligand (Ac-Y) to the base and electron transfer from the same residue to the metallo-porphyrin, with the generation of a (short-lived) diradical anion species was observed in that case.[37,38] Compounds **3** and **6** were then designed to activate a similar photoinduced PCET process, but possibly with a more favourable kinetic scenario in terms of diradical pair lifetime, according to the larger distance between the phenol fragment and the metallo-porphyrin chromophore. The photophysical studies on compounds **3** and **6** revealed, for both conjugates, transient absorption kinetic profiles dependent on the base concentration were observed from the triplet excited state. Kinetic analysis of the quenching data revealed that the dominating deactivation pathway of the triplet excited state is the bimolecular reaction with pyrrolidine, while the simultaneous concerted PCET process from the same excited state has a lower rate constant, thus hampering the accumulation of the desired diradical species. Energy minimized models of the derivatives in dichloromethane (obtained by DFT calculations) show for both systems extended structures with average distances between the chromophore and the phenol between 14 – 15 Å. This constitutes a kinetic barrier that limits the efficiency of the electron transfer, rather than slowing down the recombination step. Useful insights were therefore gained on the effect of geometrical structural variations on the kinetics governing PCET for these types of Sn^{IV}-porphyrin/phenol conjugates. In order to address the kinetic or the thermodynamic weakness of the so-far developed dyads, current and future studies are now focused on two novel conjugates, namely **SnCl$_2$TPP-*o*OHBA** and **Sn(Ac-Y)$_2$TpFP** (Figure 2.3.1, left and middle respectively). The Sn^{IV}-porphyrin/2-hydroxybenzoylamide derivative **SnCl$_2$TPP-*o*OHBA** became readily available by metalation of one of the target molecules developed in the parallel project discussed in Chapter 4, on single-atom catalysis. In this derivative, the nature of the photoactive components and the chemical connectivity between them are quite unvaried with respect to **3**, but their relative distance and orientation is dramatically different. Scale-up preparation of **SnCl$_2$TPP-*o*OHBA**, as well as full characterization in solution with special attention on structural details, is in due course. In contrast, **Sn(Ac-Y)$_2$TpFP** is a very close analogue of the original **Sn(Ac-Y)$_2$TPP** system in terms of geometrical disposition and connection of the active components but presents completely different electronic features (consequent to the perfluorinated aryl rings on the metallo-porphyrin). This substantial structural change should stabilize the reduced form of the chromophore. Efforts in the obtainment of clean samples of **Sn(Ac-Y)$_2$TpFP** are ongoing, meanwhile a preliminary single crystal X-ray structure was obtained (Figure 2.3.1, right). A through photophysical investigation for these novel dyads, also in the presence of an appropriate base, is planned to determine the effect of the geometrical and structural changes over possible photoinduced PCET processes. In parallel, screening of alternative bases, that may act only as deprotonating agents while not competing for electron transfer, in also currently ongoing. Finally, the chiral nature of some of the past, present and future derivatives will be addressed in terms of polarized light emission.

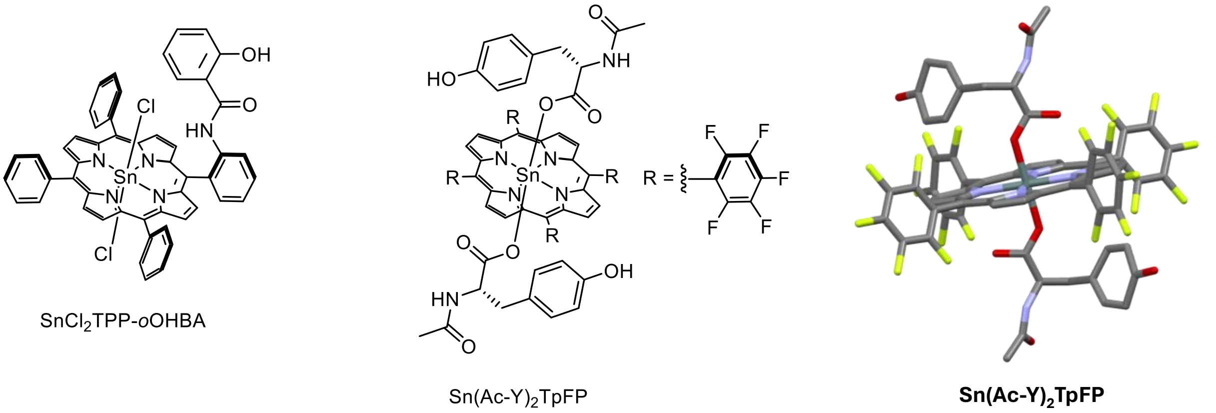

SnCl$_2$TPP-*o*OHBA

Sn(Ac-Y)$_2$TpFP

Sn(Ac-Y)$_2$TpFP

Figure 2.3.1. Schematic representation of the structures of **SnCl$_2$TPP-*o*OHBA** and **Sn(Ac-Y)$_2$TpFP**, left and middle respectively, objects of current and future investigations. Right: preliminary single crystal X-ray structures of **Sn(Ac-Y)$_2$TpFP**. Hydrogen atoms are omitted for clarity. Colour code: Sn: dark green; F: yellow; N: purple; O: red; C: grey.

2.4. Experimental Section.

Materials and reagents:

All reagents were obtained from commercial sources and used without further purification, unless otherwise stated. Deuterated solvents $CDCl_3$ and dmso-d_6 were purchased from Sigma-Aldrich, while CD_2Cl_2 from Cambridge Isotope Laboratories (CIL). Silica Gel (Supelco, pore size 60 Å, mesh 230-400) was used for the chromatographic purification of the porphyrins. **TPP-*p*NH$_2$ (1)** was synthesized as described in literature.[50–52] Porphyrins conjugates were synthesized as previously reported in literature.[49,50] Sn^{IV}-and Zn^{II} metal insertion were carried out adapting previous procedures.[49,53] Basic hydrolysis of the $SnCl_2$-porphyrin derivatives was done using reported literature procedures.[37,57]

Instrumentation:

NMR. 1D and 2D experiments (^{1}H; ^{1}H-^{1}H COSY; ^{1}H-^{13}C HSQC; ^{1}H-^{13}C HMBC; ^{1}H-^{119}Sn HMBC; ^{1}H-^{1}H ROESY) were recorded on a *Varian Inova* 500 spectrometer at 25 °C unless otherwise stated, operating at 500 MHz (^{1}H), 126 MHz (^{13}C), and 187 MHz (^{119}Sn). Resonances are expressed in ppm (δ) and are referenced to the peak of the residual non-deuterated solvents: $\delta = 7.26$ ppm (^{1}H) and 77.16 ppm (^{13}C) for $CDCl_3$; 2.50 ppm (^{1}H) and 39.52 ppm (^{13}C) for dmso-d_6; 5.32 ppm (^{1}H) and 53.84 ppm (^{13}C) for CD_2Cl_2. ^{119}Sn chemical shift is referenced to the internal standard $Sn(CH_3)_4$ at 0.00 ppm. Processing was done using MestreNova© program. Multiplicity of the signals is expressed as follows: s = singlet; d = doublet; t = triplet; q = quartet; m = multiplet; dd = doublet of doublets; br. s = broad signal.

UV-Vis Absorption Spectroscopy. All absorption spectra were recorded in CH_2Cl_2 or in a DMF:CH_2Cl_2 mixture, for solubility reasons. The spectra were recorded at 298 K using standard 3 mL quartz cuvette (light path: 1 cm) with a Agilent Technologies spectrophotometer with W/I_2 and H_2/D_2 lamps for the NIR/Vis and the UV irradiation.

Emission Spectroscopy. Photoluminescence spectra were recorded in CH_2Cl_2 or in DMF:CH_2Cl_2 mixtures, with a Edinburgh Instrument spectrophotometer equipped with a monochromatized Xe arc-lamp and a Hamamatsu R3896 photomultiplier tube as excitation source and detector, respectively. The spectra were recorded at 298 K using standard 3 mL quartz cuvette (light path: 1 cm). Cut-off filters have been used either after the excitation monochromator or before the emission one to remove higher-order diffraction phenomena that may affect the obtained spectra. All reported emission spectra have been corrected for the wavelength dependent phototube response.

Mass Spectrometry. Electrospray ionization mass spectrometry (ESI-MS) measurements were always performed starting from 1 mg/mL $CHCl_3$ solutions, then diluted 100 times with CH_3OH or CH_3CN. Experiments were performed with an electrospray ionization (ESI) source and a Thermo Scientific Orbitrap Exploris 250 Instrument. by Dr. Fabio Hollan, Department of Chemical and Pharmaceutical Sciences, University of Trieste (IT).

Circular Dichroism. Circular Dichroism measurements were recorded in CH_2Cl_2 mixture at 298 K using standard 3 mL quartz cuvette (light path: 1 cm) and a JASCO J-815 CD spectrometer.

X-ray Analysis. Data collections were performed by Dr. Gabriele Balducci, Department of Chemical and Pharmaceutical Sciences, University of Trieste (IT) Data collections were performed at the X-ray diffraction beamline (XRD1) of the Elettra Synchrotron in Trieste (Italy), equipped with a Pilatus 2M image plate detector. Collection temperature was 100 K (nitrogen stream supplied through an Oxford Cryostream 700); the wavelength of the monochromatic X-ray beam was 0.700 Å and the diffractograms were obtained with the rotating crystal method. The crystals were dipped in N-paratone and mounted on the goniometer head with a nylon loop. The diffraction data were indexed, integrated and scaled using XDS.[61] The structures were solved by the dual space algorithm implemented in the SHELXT code.[62] Fourier analysis was performed by the full-matrix least-squares methods based on F^2 implemented in SHELXL.[63] The Coot and SHELXLE programs were used for modeling.[64,65] Anisotropic thermal motion was allowed for all non-hydrogen atoms. Hydrogen atoms were placed at calculated positions with isotropic factors $U = 1.2 \times U_{eq}$, U_{eq} being the equivalent isotropic thermal factor of the bonded non hydrogen atom.

DFT Calculations. Geometry optimizations were done with a DFT B3LYP-D3/def2-SVP calculation with suite Schrödinger (suitable for Sn^{IV}-complexes according to the literature)[59,60] and a polarizable continuum model (pcm) for the CH_2Cl_2 solvent. All calculations were done by Prof. Federico Berti, Department of Chemical and Pharmaceutical Sciences, University of Trieste (IT).

Cyclic Voltammetry. Electrochemical experiments were done using a PC-interfaced Eco Chemie Autolab/Pgstat 30 Potentiostat. A conventional three-electrode cell setup was adopted: a saturated calomel electrode (SCE Amel) was used as reference electrode and a Pt electrode was used as a counter electrode, both separated from the test solution by a frit. A glassy carbon (GC) electrode was used as working electrode using a scan rate (ν) of 0.1V/s. All experiments were performed in a nitrogen-purged CH_2Cl_2 (or DMF:CH_2Cl_2) solutions (2 mL) containing 0.1 M $TBAPF_6$, used a supporting electrolyte, and 1 mM of the target compound. All potentials are referenced vs. Fc/Fc^+ couple added as internal standard.

Time-Correlated Single Photon Counting (TC-SPC). Time-correlated single photon counting was used to measure lifetimes of emitting excited stated. All experiments were done using 25 μM CH_2Cl_2 (or DMF:CH_2Cl_2) solutions. Experiments were recorded using a TC-SPC apparatus (*PicoQuant Picoharp 300*) equipped with sub-nanosecond LED sources (280, 380, 460 and 600 nm, 500-700 ps pulse width) powered by a *PicoQuantPDL 800-B* variable (2.5 – 40 Hz) pulsed power supply. Detection is performed by a photomultiplier (*Hamamatsu PMA 185*) equipped with a monochromator. The decays were processed by an integrated Time-to-Digital Converter (TDC) and analysed by means of *PicoQuant FluoFit* Global Fluorescence Decay Analysis Software.

Nanosecond laser flash photolysis. Nanosecond laser flash photolysis was used for time-resolved absorption measurements in a time window from 6 – 8 ns up to ms. The measurements were dome with a custom laser spectrometer comprised of a Continuum Surelite II Nd:YAG laser (1064 nm, FWHM = 6 – 8 ns) equipped with a frequency doublet (532 nm), triplet (355 nm) or quadruplet (266 nm) options, an Spplied Photophysics Xe light source including a mod. 720 150 W lamp housing, a mod. 620 power-controlled lamp supply and a mod. 03 – 102 arc lamp pulser. Laser excitation is provided at 90° with respect to the white light probe beam. This latter is controlled by means of an Oriel 71445 shutter, which opens only for ca. 100 ms during the measurements, thus preventing continuous irradiation of the sample. Light transmitted (transient absorption measurements) by the sample is focused onto the entrance slit of a 300 mm focal length Acton SpectraPro 2300i triple grating, flat field, double exit monochromator equipped with a photomultiplier tube detector (Hamamatsu R3896), used for kinetic studies at fixed wavelength, and a Princeton Instruments PIMAX II gated intensified CCD camera, used for spectral detection at fixed time-delays, employing a RB Gen II intensifier, a ST133 controller and a PTG pulser. Singal from the photomultiplier is processed by means of a LeCroy 9360 (600 MHz, 5 GS/s). Excitation source, lamp and shutter are computer-controlled by a LabVIEW (National Instruments) software routine.

Synthesis.

TPP-*p*PA (**2**):

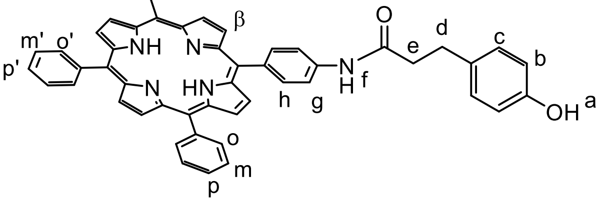

3(4-hydroxyphenyl)propionic acid (52.8 mg, 0.318 mmol, 2.00 eq) and 1-(3-Dimethylaminopropyl)-3-ethylcarbodiimide hydrochloride (61.0 mg, 0.318 mmol, 2.00 eq, EDC·Cl) were dissolved in dry pyridine (5.0 mL) in an oven dried round bottom flask and the solution stirred for 10 min at room temperature under argon atmosphere. **TPP-*p*NH$_2$**, **1** (100.0 mg, 0.159 mmol, 1.00 eq) was added and stirring was maintained at room temperature. The reaction was monitored by TLC (silica gel, $CHCl_3$). After 5 hours 20 mL of distilled water were added, the purple precipitate collected by filtration, washed with distilled water, re-dissolved in $CHCl_3$ and dried over anhydrous Na_2SO_4. The product was obtained as a purple powder by precipitation from chloroform/*n*-hexane solution. Yield 93.0 mg (75%).

^{1}H NMR (δ, 500 MHz, CD_2Cl_2): 8.87 ppm (br. s, 8H, H^{β}), 8.22 ppm (d, J = 6.9 Hz, 6H, H^{o}, $H^{o'}$), 8.13 ppm (d, J = 7.9 Hz, 2H, H^{h}), 7.84 – 7.75 ppm (m, 11H, H^{g}, H^{m}, $H^{m'}$, H^{p}, $H^{p'}$), 7.43 ppm (s, 1H, NH^{f}), 7.21 ppm (d, J = 7.9 Hz, 2H, H^{c}), 6.80 ppm (d, J = 7.9 Hz, 2H, H^{b}), 4.91 ppm (s, 1H, OH^{a}), 3.07 ppm (t, J = 7.5 Hz, 2H, H^{d}), 2.75 ppm (t, J = 7.5 Hz, 2H, H^{e}), −2.83 ppm (s, 2H, $NH^{porphyrin}$). ^{13}C from ^{1}H-^{13}C HSQC (δ, 126 MHz, CD_2Cl_2): 135.4 ppm (C^{h}),135.0 ppm (C^{o}, $C^{o'}$), 129.9 ppm (C^{c}), 128.0 – 127.0 ppm (C^{m}, $C^{m'}$, C^{p}, $C^{p'}$), 118.2 ppm (C^{g}), 115.6 ppm (C^{b}), 40.0 ppm (C^{e}), 30.9 ppm (C^{d}).

^{1}H NMR (δ, 500 MHz, $CDCl_3$): 8.87 – 8.82 ppm (m, 8H, H^{β}), 8.24 – 8.18 (m, 6H, H^{o}, $H^{o'}$), 8.15 ppm (d, J = 8.3 Hz, 2H, H^{h}), 7.82 ppm (d, J = 8.1 Hz, 2H, H^{g}), 7.78 – 7.71 ppm (m, 9H, H^{m}, $H^{m'}$, H^{p}, $H^{p'}$), 7.31 ppm (s, 1H, NH^{f}), 7.24 ppm (d, J = 8.3 Hz, 2H, H^{c}), 6.85 ppm (d, J = 8.3 Hz, 2H, H^{b}), 4.65 ppm (s, 1H, OH^{a}), 3.14 ppm (t, J = 7.5 Hz, 2H, H^{d}), 2.81 ppm (t, J = 7.5 Hz, 2H, H^{e}), −2.78 ppm (s, 2H, $NH^{porphyrin}$). ^{13}C from ^{1}H-^{13}C HSQC (δ, 126 MHz, $CDCl_3$): 135.1 ppm (C^{h}),134.6 ppm (C^{o}, $C^{o'}$), 129.7 ppm (C^{c}), 127.6 – 126.6 ppm (C^{m}, $C^{m'}$, C^{p}, $C^{p'}$), 117.9 ppm (C^{g}), 115.5 ppm (C^{b}), 39.9 ppm (C^{e}), 30.7 ppm (C^{d}).

^{1}H NMR (δ, 500 MHz, dmso-d_6): 10.35 ppm (s, 1H, NH^{f}), 9.21 ppm (s, 1H, OH^{a}), 8.91 – 8.84 ppm (m, 8H, H^{β}), 8.26 – 8.21 ppm (m, 6H, H^{o}, $H^{o'}$), 8.15 ppm (d, J = 7.9 Hz, 2H, H^{h}), 8.06 ppm (d, J = 7.9 Hz, 2H, H^{g}), 7.87 – 7.83 ppm (m, 9H, H^{m}, $H^{m'}$, H^{p}, $H^{p'}$), 7.15 ppm (d, J = 7.6 Hz, 2H, H^c), 6.75 ppm (d, J = 7.6 Hz, 2H, H^b), 2.95 ppm (t, J = 7.7 Hz, 2H, H^d), 2.76 ppm (t, J = 7.7 Hz, 2H, H^e), −2.90 ppm (s, 2H, $NH^{porphyrin}$). ^{13}C from ^{1}H-^{13}C HSQC (δ, 126 MHz, dmso-d_6): 134.4 ppm (C^h), 134.0 ppm (C^o, $C^{o'}$), 130.0 ppm (C^c), 127.9 – 126.8 ppm (C^m, $C^{m'}$, C^p, $C^{p'}$), 117.1 ppm (C^g), 114.9 ppm (C^b), 38.4 ppm (C^e), 29.9 ppm (C^d). UV–Vis (λ_{max}, nm, CH_2Cl_2): 420, 515, 551, 590, 646. ESI-MS: (*m/z*) (positive mode) for $C_{53}H_{40}N_5O_2$ ($[M + H]^+$) calculated 778.93, found 778.58.

$SnCl_2$TPP-*p*PA (3):

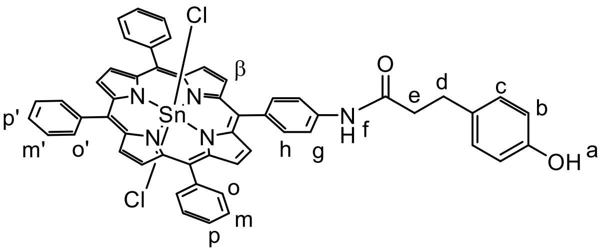

TPP-*p*PA, **2** (50.0 mg, 0.0643 mmol, 1.00 eq) was dissolved in 3.0 mL of pyridine. $SnCl_2 \cdot 2H_2O$ (36.3 mg, 0.161 mmol, 2.50 eq) was added to the solution and the reaction mixture was refluxed at T = 115 °C. The reaction was monitored both by TLC (silica gel, $CHCl_3$:MeOH 95:5) and UV-Vis absorption spectroscopy. After 2 h the reaction mixture was cooled to room temperature and 50 mL of distilled water were added. The purple precipitate was filtered and washed several times with water to remove the excess $SnCl_2 \cdot 2H_2O$. The product was dissolved in chloroform and treated with 6 M HCl, dried over anhydrous Na_2SO_4, and isolated by precipitation from a chloroform/*n*-hexane solution. Yield 38.5 mg (62%).

^{1}H NMR (δ, 500 MHz, $CDCl_3$): 9.24 – 9.17 (m, 8H, H^β), 8.31 (dd, J = 6.8, 3.8 Hz, 6H, H^o, $H^{o'}$), 8.17 (d, J = 7.7 Hz, 2H, H^h), 7.89 – 7.77 (m, 9H, H^m, $H^{m'}$, H^p, $H^{p'}$), 7.69 (d, J = 5.3 Hz, 2H, H^g), 7.20 (s, 1H, NH^f), 7.09 (d, J = 7.9 Hz, 2H, H^c), 6.70 (d, J = 7.9 Hz, 2H, H^b), 4.67 (s, 1H, OH^a), 2.99 (br. s, 2H, H^d), 2.54 (br. s, 2H, H^e). ^{13}C from ^{1}H-^{13}C HSQC (δ, 126 MHz, $CDCl_3$): 135.4 ppm (C^h), 134.9 ppm (C^o, $C^{o'}$), 132.7 ppm (C^β), 129.5 ppm (C^c), 128.6 – 127.1 ppm (C^m, $C^{m'}$, C^p, $C^{p'}$), 118.2 ppm (C^g), 115.5 ppm (C^b), 39.7 ppm (C^d), 30.6 ppm (C^e). ^{119}Sn from ^{1}H,^{119}Sn-HMBC (δ, 180 MHz, $CDCl_3$): −588 ppm. UV–Vis (λ_{max}, nm, CH_2Cl_2): 428, 562, 602. ESI-MS: (*m/z*) (positive mode) in CH_3OH for $C_{54}H_{50}N_5O_3Sn$ ($[M - 2Cl + OCH_3]^+$) calculated 926.2147, found 926.50.

ZnTPP-*p*PA (4):

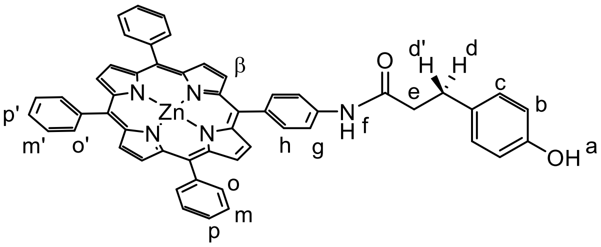

TPP-*p*PA, **2** (20.0 mg, 0.026 mmol, 1.00 eq) was dissolved in $CHCl_3$, then a methanol solution of $Zn(CH_3COO)\cdot 2H_2O$ (16,9 mg, 0.077 mmol, 3.00 eq) was added and the mixture was stirred at room temperature. The reaction was monitored by UV-Vis absorption spectroscopy. After 1h the solvent was removed by evaporation, the product re-dissolved in $CHCl_3$ and washed several times with distilled water. The organic phase was dried over anhydrous Na_2SO_4 and the pure product was isolated by precipitation from chloroform/*n*-hexane solution. Yield 17.1 mg (80%).

^{1}H NMR (δ, 500 MHz, $CDCl_3$:CD_3OD 6:1): 8.86 – 8.82 ppm (m, 8H, H^{β}), 8.18 ppm (d, *J* = 6.8 Hz, 6H, H^{o}, $H^{o'}$), 8.11 ppm (d, *J* = 7.9 Hz, 2H, H^{g}), 7.87 ppm (d, *J* = 7.9 Hz, 2H, H^{h}), 7.70 ppm (m, 9H, H^{m}, $H^{m'}$, H^{p}, $H^{p'}$), 7.16 ppm (d, *J* = 8.0 Hz, 2H, H^{c}), 6.79 ppm (d, *J* = 7.9 Hz, 2H, H^{b}), 3.05 ppm (t, *J* = 7.8 Hz, 2H, H^{d}), 2.77 ppm (t, *J* = 8.0 Hz, 2H, H^{e}). UV–Vis (λ_{max}, nm, CH_2Cl_2): 425, 555, 595. ESI-MS: (*m/z*) (positive mode) for $C_{53}H_{38}N_5O_2Zn$ ($[M + H]^+$) calculated 840.2311, found 840.51; for $C_{54}H_{42}N_5O_3Zn$ ($[M + CH_3OH]^+$) calculated 872.2574, found 872.50.

TPP-*p*Tyr (**5**):

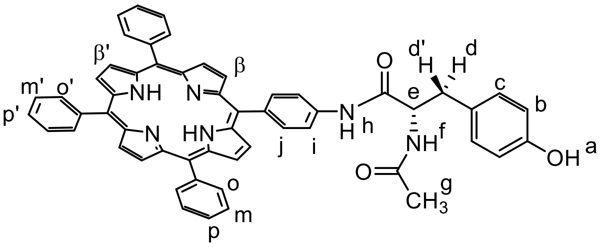

5 was synthesized using same synthetic procedure described for **2**, starting from 50.0 mg of **1**. **5** was isolated as a pure product by column chromatography on silica gel (eluent $CHCl_3$:EtOH 97:3). Yield 35.0 mg (53%).

^{1}H NMR (δ, 500 MHz, dmso-*d*$_6$): 10.55 ppm (s, 1H, NH^{h}), 9.24 ppm (s, 1H, OH^{a}), 8.90 ppm (s, 2H, H^{β}), 8.83 ppm (s, 6H, $H^{\beta'}$), 8.37 ppm (d, *J* = 8.1 Hz, 1H, NH^{f}), 8.25 – 8.20 ppm (m, 6H, H^{o}, $H^{o'}$), 8.16 ppm (d, *J* = 8.2 Hz, 2H, H^{j}), 8.06 ppm (d, *J* = 8.2 Hz, 2H, H^{i}), 7.87 – 7.81 ppm (m, 9H, H^{m}, $H^{m'}$, H^{p}, $H^{p'}$), 7.20 ppm (d, *J* = 8.3 Hz, 2H, H^{c}), 6.73 ppm (d, *J* = 8.3 Hz, 2H, H^{b}), 4.75 ppm (q, $J = 8.4$ Hz, 1H, H^{e}), 3.08 ppm (dd, $J = 13.6, 5.2$ Hz, 1H, H$^{d'}$), 2.87 ppm (dd, $J = 13.6, 9.5$ Hz, 1H, H^{d}), 1.89 ppm (s, 3H, CH$_3$^{g}), −2.92 ppm (s, 2H, NH^{porphyrin}). ^{13}C from ^{1}H-^{13}C HSQC (δ, 126 MHz, dmso-d_6): 134.7 ppm (C^{j}),134.3 ppm (C^{o}, C$^{o'}$), 130.2 ppm (C^{c}), 128.1 – 127.1 ppm (C^{m}, C$^{m'}$, C^{p}, C$^{p'}$), 117.7 ppm (C^{i}), 115.0 ppm (C^{b}), 55.6 ppm (C^{e}), 37.1 ppm (C^{d}, C$^{d'}$), 22.5 ppm (CH$_3$^{g}). UV–Vis (λ$_{max}$, nm, DMF diluted in CH_2Cl_2): 414, 515, 550, 590, 646. ESI-MS: (*m/z*) (positive mode) for $C_{55}H_{42}N_6O_3$ $[M + H]^+$ = 835.3391 found 835.3392.

SnCl$_2$TPP-*p*Tyr (**6**):

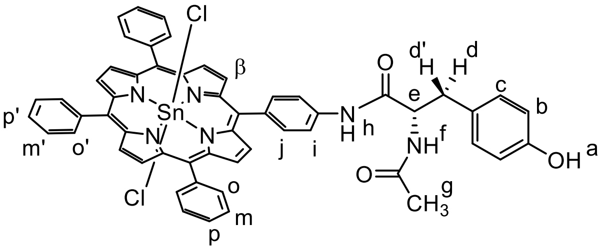

6 was synthesized using the same synthetic procedure described for **3**, starting from 23.0 mg of **5**, and was isolated by precipitation from a chloroform/*n*-hexane solution. Yield 20.0 mg (65%). ^{1}H-NMR (δ, 500 MHz, dmso-d_6): 10.65 ppm (s, 1H, NH^{h}), 9.30 – 9.16 ppm (m, 9H, H^{β}, OH^{a}), 8.40 ppm (d, $J = 8.1$ Hz, 1H, NH^{f}), 8.36 – 8.21 ppm (m, 8H, H^{o}, H$^{o'}$, H^{j}), 8.16 ppm (d, $J = 8.2$ Hz, 2H, H^{i}), 7.94 ppm (m, 9H, H^{m}, H$^{m'}$, H^{p}, H$^{p'}$), 7.21 ppm (d, $J = 8.0$ Hz, 2H, H^{c}), 6.74 ppm (d, $J = 8.0$ Hz, 2H, H^{b}), 4.77 ppm (q, $J = 8.1$ Hz, 7.5 Hz, 1H, H^{e}), 3.09 ppm (dd, $J = 13.6, 5.2$ Hz, 1H, H$^{d'}$), 2.88 ppm (dd, $J = 13.5, 9.5$ Hz, 1H, H^{d}), 1.90 ppm (s, 3H, CH$_3$^{g}). ^{13}C from ^{1}H-^{13}C HSQC (δ, 126 MHz, dmso-d_6): 135.0 ppm (C^{j}), 134.3 ppm (C^{o}, C$^{o'}$), 133.0 – 132.7 ppm (C^{β}), 129.9 ppm (C^{c}), 128.7 – 127.3 ppm (C^{m}, C$^{m'}$, C^{p}, C$^{p'}$), 117.8 ppm (C^{i}), 114.7 ppm (C^{b}), 55.4 ppm (C^{e}), 36.8 ppm (C^{d}, C$^{d'}$), 22.1 ppm (CH$_3$^{g}).

^{1}H NMR (δ, 500 MHz, CD_2Cl_2): 9.32 – 9.21 ppm (m, 8H, H^{β}), 8.70 ppm (d, $J = 10.6$ Hz, 1H, NH^{h}) , 8.33 – 8.24 ppm (m, 6H, H^{o}, H$^{o'}$), 8.25 (d, $J = 8.1$ Hz, 2H, H^{j}), 7.92 (d, $J = 8.0$ Hz, 2H, H^{i}), 7.92 – 7.80 ppm (m, 9H, H^{m}, H$^{m'}$, H^{p}, H$^{p'}$), 7.21 (d, $J = 8.0$ Hz, 2H, H^{c}), 6.77 (d, $J = 8.0$ Hz, 2H, H^{b}), 6.40 – 6.37 ppm (m, 1H, NH^{f}) , 4.94 – 4.88 ppm (m, 1H, H^{e}), 3.23 ppm (dd, $J = 13.9, 7.2$ Hz, 1H, H$^{d'}$), 3.14 – 3.06 ppm (m, 1H, H^{d}), 2.07 ppm (s, 3H, CH$_3$^{g}). ^{13}C from ^{1}H-^{13}C HSQC (δ, 126 MHz, CD_2Cl_2): 135.9 ppm (C^{j}), 135.3 ppm (C^{o}, C$^{o'}$), 133.1 ppm (C^{β}), 131.0 ppm (C^{c}), 129.0 – 127.6 ppm (C^{m}, C$^{m'}$, C^{p}, C$^{p'}$), 118.9 ppm (C^{i}), 116.0 ppm (C^{b}), 56.3 ppm (C^{e}), 37.6 ppm (C^{d}, C$^{d'}$), 24.1 ppm (CH$_3$^{g}). ^{119}Sn from ^{1}H-^{119}Sn HMBC (δ, 187 MHz, CD_2Cl_2): −589 ppm. UV–Vis (λ$_{max}$, nm, CH_2Cl_2): 426, 562, 602. ESI-MS: (*m/z*) (positive mode) in CH_3CN for

$C_{55}H_{41}N_6O_4Sn$ ([M - 2Cl + OH]$^+$) calculated 969.2211, found 969.46; for $C_{55}H_{40}ClN_6O_3Sn$ ([M - Cl]$^+$) calculated 987.1872, found 987.45. In CH_3OH for $C_{56}H_{43}N_6O_4Sn$ ([M – 2Cl + OCH_3]$^+$) calculated 983.2368, found 983.51.

ZnTPP-*p*Tyr (**7**):

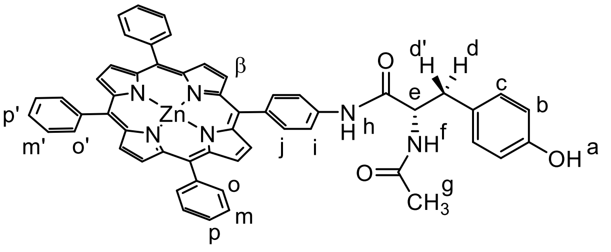

7 was synthesized as described for **4**, starting form 20.0 mg of **5** and was isolated by precipitation from a chloroform/*n*-hexane solution. Yield 19.8 mg (92%).

^{1}H NMR (δ, 500 MHz, $CDCl_3$:CD_3OD 6:1): 8.82 ppm (m, 8H, H^β), 8.16 ppm (d, *J* = 6.7 Hz, 6H, H^o, H$^{o'}$), 8.10 ppm (d, *J* = 8.0 Hz, 2H, H^j), 7.79 ppm (d, *J* = 8.0 Hz, 2H, H^i), 7.74 – 7.64 ppm (m, 9H, H^m, H$^{m'}$, H^p, H$^{p'}$), 7.14 ppm (d, *J* = 8.0 Hz, 2H, H^c), 6.79 ppm (d, *J* = 8.0 Hz, 2H, H^b), 4.77 ppm (t, *J* = 7.2 Hz, 1H, H^e), 3.16 ppm (dd, *J* = 13.7, 7.3 Hz, 1H, H$^{d'}$), 3.01 ppm (dd, *J* = 13.8, 7.1 Hz, 1H, H^d), 2.02 ppm (s, 3H, CH_3^{g}). ^{13}C from ^{1}H-^{13}C HSQC (δ, 126 MHz, $CDCl_3$:CD_3OD 6:1): 134.7 ppm (C^j), 134.3 ppm (C^o, C$^{o'}$), 131.4 ppm (C^β), 130.2 ppm (C^c), 127.0 – 126.1 ppm (C^m, C$^{m'}$, C^p, C$^{p'}$), 117.9 ppm (C^i), 115.2 ppm (C^b), 55.3 ppm (C^e), 37.5 ppm (C^d, C$^{d'}$), 22.4 ppm (CH_3^{g}). UV–Vis (λ_{max}, nm, DMF diluted in CH_2Cl_2):424, 555, 595. ESI-MS: (*m/z*) (positive mode) for $C_{55}H_{40}N_6O_3Zn$ ([M + H]$^+$) calculated 896.24479, found 896.54; for $C_{56}H_{45}N_6O_4Zn$ ([M + CH_3OH + H]$^+$) calculated 929.27883, found 929.32.

TPP-*p*BA (**8**):

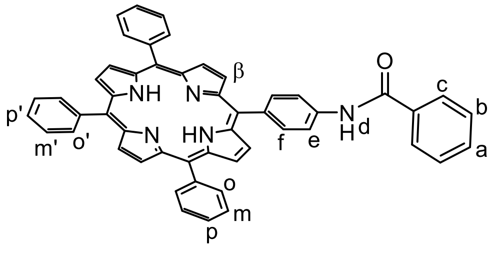

The same synthetic procedure described for **2** was followed, starting from 100.0 mg of **1**. **8** was isolated as a pure product by precipitation from a chloroform/*n*-hexane solution. Yield 89.0 mg (80%).

^{1}H NMR (δ, 500 MHz, CDCl$_3$): 8.98 – 8.77 ppm (m, 8H, H$^\beta$), 8.31 – 8.20 ppm (m, 8H, H^o, H$^{o'}$, H^f), 8.16 ppm (s, 1H, NH^d), 8.11 – 8.00 ppm (m, 4H, H^e, H^c), 7.84 – 7.69 ppm (m, 9H, H^m, H$^{m'}$, H^p, H$^{p'}$), 7.69 –7.55 ppm (m, 3H, H^a, H^b), –2.76 ppm (s, 2H, NH^{porphyrin}). ^{13}C from ^{1}H-^{13}C HSQC (δ, 126 MHz, CDCl$_3$): 135.5 ppm (C^f), 134.5 ppm (C^o, C$^{o'}$), 132.0 ppm (C^a), 128.9 ppm (C^b), 127.6 – 126.6 ppm (C^m, C$^{m'}$, C^p, C$^{p'}$), 127.0 – 118.3 ppm (C^e, C^c). UV–Vis (λ$_{max}$, nm, CH$_2$Cl$_2$): 414, 515, 550, 590, 646. ESI-MS: (*m/z*) (positive mode) for $C_{51}H_{36}N_5O$ ([M + H]$^+$) calculated 734.2914, found 734.43

SnCl$_2$TPP-*p*BA (**9**):

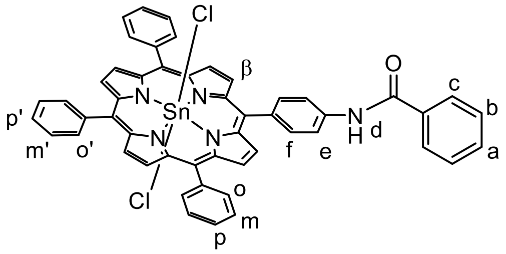

The same synthetic procedure described for **3** was followed, starting from 50.0 mg of **8**. Yield 43.0 mg (70%).

^{1}H NMR (δ, 500 MHz, dmso-*d$_6$*): 10.85 ppm (s, 1H, NH^d), 9.46 – 9.17 ppm (m, 8H, H$^\beta$), 8.42 – 8.38 ppm (m, 2H, H^e), 8.35 – 8.26 ppm (m, 8H, H^o, H$^{o'}$, H^f), 8.13 ppm (m, 2H, H^c), 8.02 – 7.87 ppm (m, 9H, H^m, H$^{m'}$, H^p, H$^{p'}$), 7.73 – 7.59 ppm (m, 3H, H^a, H^b). ^{13}C from ^{1}H-^{13}C HSQC (δ, 126 MHz, dmso-*d$_6$*): 134.9 ppm (C^f), 134.3 ppm (C^o, C$^{o'}$), 132.9 – 132.7 ppm (C$^\beta$), 131.6 ppm (C^a), 128.3 ppm (C^b), 128.7 – 127.3 ppm (C^m, C$^{m'}$, C^p, C$^{p'}$), 127.6 ppm (C^c), 118.7 ppm (C^e).

^{1}H NMR (δ, 500 MHz, CD$_2$Cl$_2$): 9.37 – 9.21 ppm (m, 8H, H$^\beta$), 8.36 – 8.28 ppm (m, 6H, H^o, H$^{o'}$), 8.29 ppm (d, *J* = 8.1 Hz, 2H, H^f), 7.98 ppm (s, 1H, NH^d), 7.94 ppm (d, *J* = 8.0 Hz, 2H, H^e), 7.91 – 7.84 ppm (m, 9H, H^m, H$^{m'}$, H^p, H$^{p'}$), 7.82 ppm (d, *J* = 7.4 Hz, 2H, H^c), 7.62 ppm (t, *J* = 7.4 Hz, 1H, H^a), 7.50 ppm (t, *J* = 7.6 Hz, 2H, H^b). ^{13}C from ^{1}H-^{13}C HSQC (δ, 126 MHz, CD$_2$Cl$_2$): 135.8 ppm (C^f), 134.6 ppm (C^o, C$^{o'}$), 133.7 ppm (C$^\beta$), 132.4 ppm (C^a), 129.2 ppm (C^b), 129.1 – 127.6 ppm (C^m, C$^{m'}$, C^p, C$^{p'}$), 127.6 ppm (C^c), 118.9 ppm (C^e). ^{119}Sn from ^{1}H,^{119}Sn-HMBC (δ, 187 MHz, CD$_2$Cl$_2$): –589 ppm. UV–Vis (λ$_{max}$, nm, CH$_2$Cl$_2$): 426, 562, 602. ESI-MS: (*m/z*) (positive mode) for $C_{51}H_{34}N_5O_2Sn$ ([M – 2Cl + OH]$^+$) calculated 868.1734, found 868.1740.

ZnTPP-*p*BA (10):

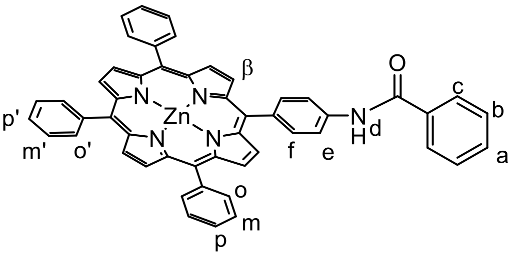

The same synthetic procedure described for **10** was followed, starting from 20.0 mg of **8**, the product was isolated by precipitation from a chloroform/*n*-hexane solution. Yield 17.2 mg (80%).

^{1}H NMR (δ, 500 MHz, CD_3OD): 9.00 – 8.75 ppm (m, 8H, $H^β$), 8.32 – 8.15 ppm (m, 8H, H^f, H^o, $H^{o'}$), 8.10 ppm (m, 4H, H^e, H^c), 7.84 – 7.69 ppm (m, 9H, H^m, $H^{m'}$, H^p, $H^{p'}$), 7.69 – 7.54 ppm (m, 3H, H^a, H^b). ^{13}C from ^{1}H-^{13}C HSQC (δ, 126 MHz, $CDCl_3$:CD_3OD 6:1): 135.4 ppm (C^f, C^o, $C^{o'}$), 132.8 ppm ($C^β$), 132.7 ppm (C^a), 129.5 ppm (C^b), 128.1 – 126.5 ppm (C^m, $C^{m'}$, C^p, $C^{p'}$), 128.5 – 120.0 ppm (C^e, C^c). UV–Vis ($λ_{max}$, nm, CH_2Cl_2): 422, 557, 598. ESI-MS: (*m/z*) (positive mode) for $C_{51}H_{34}N_5O_1Zn$ ($[M + H]^+$) calculated 796.2049, found 795.33.

$Sn(OH)_2$TPP-*p*BA (11):

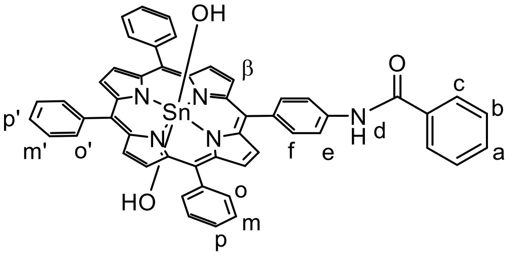

9 (50.0 mg, 0.0543 mmol, 1.00 eq) was dissolved in 50 mL of a THF:H_2O mixture. Excess K_2CO_3 was added, and the reaction was allowed to react over-night under refluxing conditions. THF was then evaporated under reduced pressure, the aqueous phase extracted with CH_2Cl_2, then the organic phase was dried over anhydrous Na_2SO_4. The product was isolated by precipitation from chloroform/*n*-hexane. Yield 33.6 mg (70%).

^{1}H NMR (δ, 500 MHz, $CDCl_3$): 9.15 – 9.07 ppm (m, 8H, $H^β$), 8.41 – 8.31 ppm (m, 6H, H^o, $H^{o'}$), 8.01 ppm (d, J = 8.0 Hz, 2H, H^f), 7.92 – 7.80 ppm (m, 9H, H^m, $H^{m'}$, H^p, $H^{p'}$), 7.47 ppm (s, 1H, NH^d), 7.34 ppm (t, J = 7.5 Hz, 2H, H^a), 7.06 ppm (t, J = 7.7 Hz, 2H, H^b), 6.87 – 6.81 ppm (br. s, 4H, H^c, H^e), −7.19 ppm (s, 2H, OH). ^{13}C from ^{1}H-^{13}C HSQC (δ, 126 MHz, $CDCl_3$): 135.7 ppm (C^f), 135.0 ppm (C^o, $C^{o'}$), 132.6 ppm ($C^β$), 131.0 ppm (C^a), 128.3 – 127.0 ppm (C^m, $C^{m'}$,

C^p, $C^{p'}$), 128.0 ppm (C^b), 126.7 ppm (C^c), 118.3 ppm (C^e). ^{119}Sn from ^{1}H-^{119}Sn HMBC (δ, 187 MHz, $CDCl_3$): −570 ppm.

Energy level diagrams.

The energy level diagrams shown in Section 2.2.2 have been predicted from photophysical, electrochemical and protonation data using literature procedures.[37] For simplicity here we will refer to 3-(4-hydroxyphenyl) propionic acid and N-Acetyl-L-tyrosine as PhOH and TyrOH respectively; additionally, the levels described later on are referred to PhOH but same considerations were done for TyrOH.

1) **SnP-PhOH --- Pyr** level: it corresponds to the ground energy ant its energy has been set at 0.0 eV.

2) **^{1*}SnP-PhOH** level: it corresponds to the lowest energy of the singlet excited state (S_1) of the Sn^{IV}-porphyrin, and its value (+2.05 eV for both **3** and **6**) has been estimated from the wavelength at the intersection between normalized absorption and fluorescence spectra.

3) **^{3*}SnP-PhOH** level: it corresponds to the lowest energy of the triplet excited state (T_1) of the Sn^{IV}-porphyrin. Its value (+1.65 eV for both **3** and **6**) has been taken from literature data.[58]

4) **SnP$^{\cdot-}$PhO$^{\cdot+}$** level (grey dotted line): correspond to the di-radical anion pair state in the absence of external bases. Its energy has been calculated from the difference between the first reduction potential of Sn^{IV}-porphyrin and the oxidation potential of the phenolic residue (Table 2.2.1 in Results and Discussion). Its value is 2.15 eV for **3** and 2.18 eV for **6**.

5) **^{1}|SnP$^{\cdot-}$TyrO$^{\cdot}$ --- $^+$HPyr|** level: correspond to the PCET state in the presence of pyrrolidine as external base. Its value has been estimated considering the energy of the di-radical anion pair state in absence of pyrrolidine (point 4) and subtracting the contribution of the deprotonation step. This contribution has been calculated according to equation 1. For simplicity the energy difference between the singlet and triplet di-radical anions pair states, which is related to the spin-exchange integral, has been neglected and the same energy was considered for both states.

$$\Delta G_{PT} = 0.059\ \text{eV} \times [\text{p}K_a\ (\text{TyrOH}^{\cdot+}) - \text{p}K_a\ (^+\text{HPyr})] \qquad (1)$$

In the absence of suitable pK_a data for TyrOH$^{\cdot+}$ and PhOH$^{\cdot+}$ in organic solvents such as CH_2Cl_2, we decided to consider pK_a values for both acids in CH_3CN. Additionally, the literature reported pK_a value for an analogue tri-substituted phenol (2,4,6-tri-tert-butylphenol, tBuPhOH$^{\cdot+}$) was used.[66]

The used data are: pK$_a$ ($^+$HPyr) = 19.65;[67] pK$_a$ (tBuPhOH$^{\cdot+}$) = −3. With these data it turns out that the value for ΔG_{PT} is ~1.3 eV, thus giving an energy for the singlet and triplet PCET states of 0.85 eV for **3** and 0.88 eV for **6**. These data are, therefore, to be taken with caution as several approximations has been taken (e.g. different phenol derivative, pK$_a$ values in acetonitrile) and should be considered, with quite confidence, as a lower limiting value. The energies of the singlet and triplet PCET states should, therefore, be considered as ≥ 0.85 eV for **3** and ≥ 0.88 eV for **6**.

6) **SnP-PhO$^-$ --- $^+$HPyr** level: it corresponds to the state where the backward reaction has already occurred by only an ET from the Sn^{IV}-porphyrin radical anion to the phenol radical while the proton is still on the base. It has been estimated considering, similarly to the previous case, the pK$_a$ value of tBuPhOH (28) and the pK$_a$ of $^+$HPyr (19.65) in CH_3CN. Using the same equation described above (S1) this value has been estimated to be +0.5 eV. For the same reasons as above, this value should be taken in consideration with caution and should be considered as a lower limiting one (≥ + 0.5 eV).

Kinetic treatment and determination of k_{PCET}.

The observed rate constant for the decay of the triplet excited state can be split into several different contributions, deriving from all the potential pathways available to the triplet excited state, as shown in equation 4.

$$k_{obs} = k_0 + k_{ET} + k_Q[Pyr] + k_{PCET}\,[(K_A[Pyr])/(1+K_A[Pyr])] \qquad (4)$$

In the case of the triplet excited state decay, simple electron transfer can be neglected, thus equation 4 is reduced to 5.

$$k_{obs} = k_0 + k_Q[Pyr] + k_{PCET}\,[(K_A[Pyr])/(1+K_A[Pyr])] \qquad (5)$$

The bimolecular rate constant (k_Q) was determined by the triplet quenching data of **9** in the presence of pyrrolidine, using a classical Stern-Volmer treatment. This fitting yielded a $k_Q = 2.39 \times 10^6$ M^{-1} s^{-1}.

For the Sn^{IV}-porphyrin conjugate **3**, by using a k_0 value of 4.3×10^4 s^{-1}, obtained from the lifetime of the triplet excited state in the absence of pyrrolidine, and a K_A value of 33.5 M^{-1} (as already done by us),[38] fitting process yielded the following result:

$k_{PCET} = 6.3 \times 10^4$ s^{-1}.

For the Sn^{IV}-porphyrin conjugate **6**, by using a k_0 value of 4.3×10^4 s^{-1}, obtained from the lifetime of the triplet excited state in the absence of pyrrolidine, and a K_A value of 33.5 M^{-1} (as already done by us),[38] fitting process yielded the following result:

$k_{PCET} = 1.0 \times 10^5$ s^{-1}.

2.5. References.

(1) Okamura, M. Y.; Paddock, M. L.; Graige, M. S.; Feher, G. *Biochim. Biophys. Acta BBA - Bioenerg.* **2000**, *1458*, 148.

(2) Babcock, G. T. *Proc. Natl. Acad. Sci.* **1999**, *96*, 12971.

(3) Kaila, V. R. I.; Verkhovsky, M. I.; Wikström, M. *Chem. Rev.* **2010**, *110*, 7062.

(4) Stubbe, J.; Nocera, D. G.; Yee, C. S.; Chang, M. C. Y. *Chem. Rev.* **2003**, *103*, 2167.

(5) Aubert, C.; Vos, M. H.; Mathis, P.; Eker, A. P. M.; Brettel, K. *Nature* **2000**, *405*, 586.

(6) Litwinienko, G.; Ingold, K. U. *Acc. Chem. Res.* **2007**, *40*, 222

(7) Roth, J. P.; Yoder, J. C.; Won, T.; Mayer, J. M. *Science* **2001**, *294*, 2524.

(8) Shevela, D.; Kern, J. F.; Govindjee, G.; Messinger, J. *Photosynth. Res.* **2023**, *15*, 279.

(9) Umena, Y.; Kawakami, K.; Shen, J.-R.; Kamiya, N. *Nature* **2011**, *473*, 55.

(10) Barber, J. In *Encyclopedia of Biological Chemistry (Second Edition)*; Lennarz, W. J., Lane, M. D., Eds.; Academic Press: Waltham, 2013; 512.

(11) El-Khouly, M. E.; El-Mohsnawy, E.; Fukuzumi, S. *J. Photochem. Photobiol. C Photochem. Rev.* **2017**, *31*, 36.

(12) Babcock, G. T.; Barry, B. A.; Debus, R. J.; Hoganson, C. W.; Atamian, M.; McIntosh, L.; Sithole, I.; Yocum, C. F. *Biochemistry* **1989**, *2*, 9557.

(13) Tommos, C.; Babcock, G. T. *Biochim. Biophys. Acta BBA - Bioenerg.* **2000**, *1458*, 199.

(14) Bonin, J.; Robert, M. *Photochem. Photobiol.* **2011**, *87*, 1190.

(15) Styring, S.; Sjöholm, J.; Mamedov, F. T. *Biochim. Biophys. Acta BBA - Bioenerg.* **2012**, *1817*, 76.

(16) Dau, H.; Iuzzolino, L.; Dittmer, J. *Biochim. Biophys. Acta BBA - Bioenerg.* **2001**, *1503*, 24.

(17) Dau, H.; Zaharieva, I. *Acc. Chem. Res.* **2009**, *42*, 1861.

(18) Sugie, K.; Kato, Y.; Nagao, R.; Noguchi, T. *J. Phys. Chem. B* **2025**, *129*, 6172.

(19) Shen, J.-R. *Annu. Rev. Plant Biol.* **2015**, *66*, 23.

(20) Debus, R. J.; Barry, B. A.; Sithole, I.; Babcock, G. T.; McIntosh, L. *Biochemistry* **1988**, *27*, 9071.

(21) Tommos, C.; Babcock, G. T. *Acc. Chem. Res.* **1998**, *31*, 18.

(22) Hoganson, C. W.; Babcock, G. T. A *Science* **1997**, *277*, 1953.

(23) Rappaport, F.; Lavergne, J. *Biochim. Biophys. Acta BBA - Bioenerg.* **2001**, *1503*, 246.

(24) Eckert, H.-J.; Renger, G. *FEBS Lett.* **1988**, *236*, 425.

(25) Hays, A.-M. A.; Vassiliev, I. R.; Golbeck, J. H.; Debus, R. J. *Biochemistry* **1999**, *38*, 11851.

(26) Barber, J.; Anderson, J. M.; Junge, W.; Haumann, M.; Ahlbrink, R.; Mulkidjanian, A.; Clausen, J. *Philos. Trans. R. Soc. Lond. B. Biol. Sci.* **2002**, *357*, 1407.

(27) Sayre, H.; Ripberger, H. H.; Odella, E.; Zieleniewska, A.; Heredia, D. A.; Rumbles, G.; Scholes, G. D.; Moore, T. A.; Moore, A. L.; Knowles, R. R. *J. Am. Chem. Soc.* **2021**, *143*, 13034.

(28) Sheth, S.; Gotico, P.; Herrero, C.; Quaranta, A.; Aukauloo, A.; Leibl, W. *Chem. – Eur. J.* **2024**, *30*, e202400862.

(29) Moore, G. F.; Hambourger, M.; Gervaldo, M.; Poluektov, O. G.; Rajh, T.; Gust, D.; Moore, T. A.; Moore, A. L. *J. Am. Chem. Soc.* **2008**, *130*, 10466.

(30) Chararalambidis, G.; Das, S.; Trapali, A.; Quaranta, A.; Orio, M.; Halime, Z.; Fertey, P.; Guillot, R.; Coutsolelos, A.; Leibl, W.; Aukauloo, A.; Sircoglou, M. *Angew. Chem. Int. Ed.* **2018**, *57*, 9013.

(31) Megiatto, J. D.; Antoniuk-Pablant, A.; Sherman, B. D.; Kodis, G.; Gervaldo, M.; Moore, T. A.; Moore, A. L.; Gust, D. *Proc. Natl. Acad. Sci.* **2012**, *109*, 15578.

(32) Sjödin, M.; Styring, S.; Wolpher, H.; Xu, Y.; Sun, L.; Hammarström, L. *J. Am. Chem. Soc.* **2005**, *127*, 3855.

(33) Irebo, T.; Zhang, M.-T.; Markle, T. F.; Scott, A. M.; Hammarström, L. *J. Am. Chem. Soc.* **2012**, *134*, 16247.

(34) Lennox, J. C.; Dempsey, J. L. *J. Phys. Chem. B* **2017**, *121*, 10530.

(35) Kuss-Petermann, M.; Wenger, O. S. *J. Phys. Chem. A* **2013**, *117*, 5726.

(36) Chen, J.; Kuss-Petermann, M.; Wenger, O. S. *J. Phys. Chem. B* **2015**, *119*, 2263.

(37) Natali, M.; Amati, A.; Demitri, N.; Iengo, E. *Chem. Commun.* **2018**, *54*, 6148.

(38) Natali, M.; Amati, A.; Merchiori, S.; Ventura, B.; Iengo, E. *J. Phys. Chem. C* **2020**, *124*, 8514.

(39) Natali, M.; Amati, A.; Demitri, N.; Iengo, E. *Chem. – Eur. J.* **2021**, *27*, 7872.

(40) Odella, E.; Jimena Mora, S.; L. Wadsworth, B.; J. Goings, J.; A. Gervaldo, M.; E. Sereno, L.; L. Groy, T.; Gust, D.; A. Moore, T.; F. Moore, G.; Hammes-Schiffer, S.; L. Moore, A. *Chem. Sci.* **2020**, *11*, 3820.

(41) Moore, G. F.; Hambourger, M.; Kodis, G.; Michl, W.; Gust, D.; Moore, T. A.; Moore, A. L. *J. Phys. Chem. B* **2010**, *11*, 14450.

(42) Odella, E.; Secor, M.; Elliott, M.; Groy, T. L.; Moore, T. A.; Hammes-Schiffer, S.; Moore, A. L. *Chem. Sci.* **2021**, *12*, 12667.

(43) Guerra, W. D.; Odella, E.; Secor, M.; Goings, J. J.; Urrutia, M. N.; Wadsworth, B. L.; Gervaldo, M.; Sereno, L. E.; Moore, T. A.; Moore, G. F.; Hammes-Schiffer, S.; Moore, A. L. *J. Am. Chem. Soc.* **2020**, *142*, 21842.

(44) Glover, S. D.; Parada, G. A.; Markle, T. F.; Ott, S.; Hammarström, L. *J. Am. Chem. Soc.* **2017**, *139*, 2090.

(45) Amati, A.; Cavigli, P.; Demitri, N.; Natali, M.; Indelli, M. T.; Iengo, E. *Inorg. Chem.* **2019**, *58*, 4399.

(46) Manke, A.-M.; Geisel, K.; Fetzer, A.; Kurz, P. *Phys. Chem. Chem. Phys.* **2014**, *16*, 12029.

(47) Pellegrin, Y.; Odobel, F. *Comptes Rendus Chim.* **2016**, *20*, 283.

(48) Wenger, O. S. *Coord. Chem. Rev.* **2015**, *282*, 150

(49) Cavigli, P.; Da Ros, T.; Kahnt, A.; Gamberoni, M.; Indelli, M. T.; Iengo, E. *Inorg. Chem.* **2015**, *54*, 280.

(50) Gianferrara, T.; Bratsos, I.; Iengo, E.; Milani, B.; Oštrić, A.; Spagnul, C.; Zangrando, E.; Alessio, E. *Dalton Trans.* **2009**, *48*, 10742.

(51) Bettelheim, A.; White, B. A.; Raybuck, S. A.; Murray, R. W. *Inorg. Chem.* **1987**, *26*, 100.

(52) Luguya, R.; Jaquinod, L.; Fronczek, F. R.; Vicente, M. G. H.; Smith, K. M. *Tetrahedron* **2004**, *60*, 2757.

(53) Arnold, D. P.; Blok, J. T. *Coord. Chem. Rev.* **2004**, *248*, 299.

(54) Gouterman, M.; Schwarz, F. P.; Smith, P. D.; Dolphin, D. *J. Chem. Phys.* **1973**, *59*, 676.

(55) Iengo, E.; Zangrando, E.; Bellini, M.; Alessio, E.; Prodi, A.; Chiorboli, C.; Scandola, F. *Inorg. Chem.* **2005**, *44*, 9752.

(56) Ou, Z.; E, W.; Zhu, W.; Thordarson, P.; Sintic, P. J.; Crossley, M. J.; Kadish, K. M. *Inorg. Chem.* **2007**, *46*, 10840.

(57) Crossley, M. J.; Thordarson, P.; Wu, R. A.-S. *J. Chem. Soc. Perkin 1* **2001**, *18*, 229.

(58) Indelli, M. T.; Chiorboli, C.; Ghirotti, M.; Orlandi, M.; Scandola, F.; Kim, H. J.; Kim, H.-J. *J. Phys. Chem. B* **2010**, *114*, 14273.

(59) Bochevarov, A. D.; Harder, E.; Hughes, T. F.; Greenwood, J. R.; Braden, D. A.; Philipp, D. M.; Rinaldo, D.; Halls, M. D.; Zhang, J.; Friesner, R. A. *Int. J. Quantum Chem.* **2013**, *113*, 211.

(60) Laun, J.; Vilela Oliveira, D.; Bredow, T. *J. Comput. Chem.* **2018**, *39*, 1285.

(61) Kabsch, W. *Acta Crystallogr. D Biol. Crystallogr.* **2010**, *66*, 125.

(62) Sheldrick, G. M. *Acta Crystallogr. Sect. C Struct. Chem.* **2015**, *71*, 3.

(63) Sheldrick, G. M. *Acta Crystallogr. A* **2008**, *64*, 112.

(64) P. Emsley, K. Cowtan, *Acta Cryst. D* **60**, *2004*, 2126.

(65) Hübschle, C. B.; Sheldrick, G. M.; Dittrich, B. *J. Appl. Crystallogr.* **2011**, *44*, 1281.

(66) Warren, J. J.; Tronic, T. A.; Mayer, J. M. *Chem. Rev.* **2010**, *110*, 6961.

(67) Kaljurand, I.; Kütt, A.; Sooväli, L.; Rodima, T.; Mäemets, V.; Leito, I.; Koppel, I. A. *J. Org. Chem.* **2005**, *70*, 1019.

Appendix A.

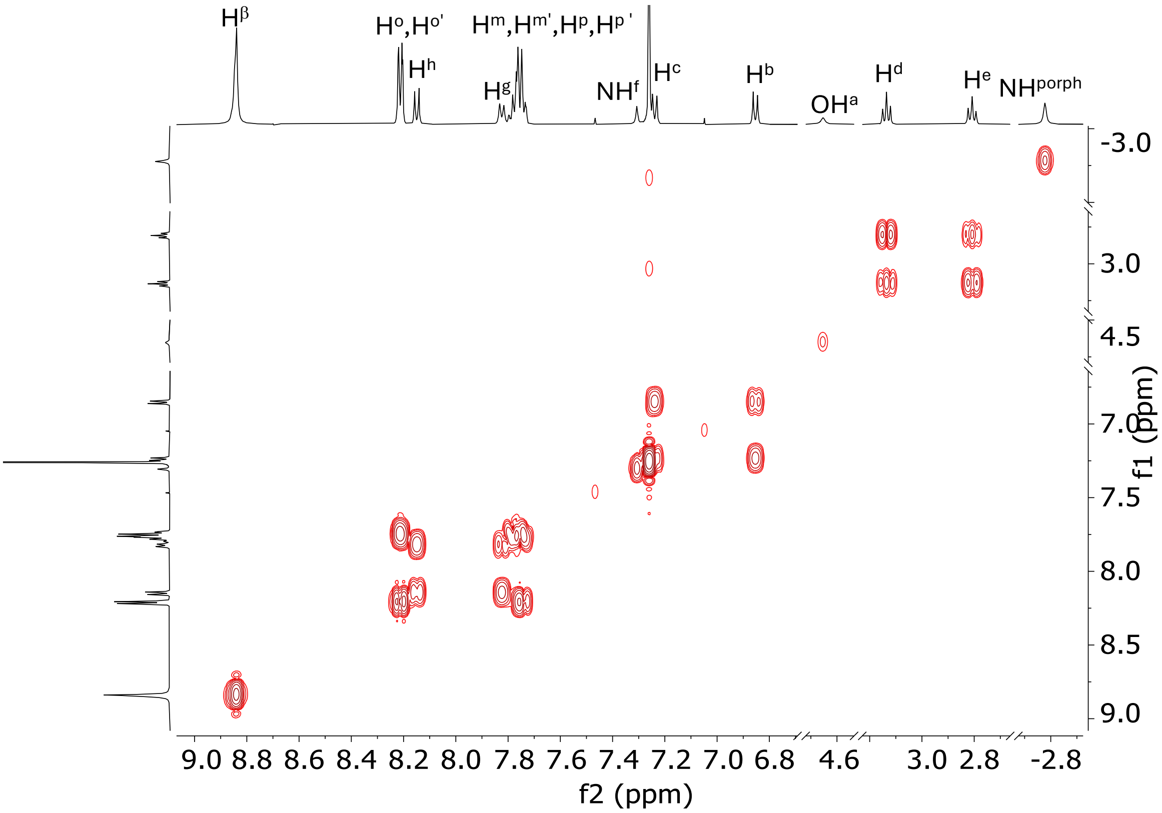

Figure S1. ^{1}H-^{1}H COSY spectrum (CDCl$_3$, 298 K) of **TPP-*p*PA** (**2**). For proton labelling see below.

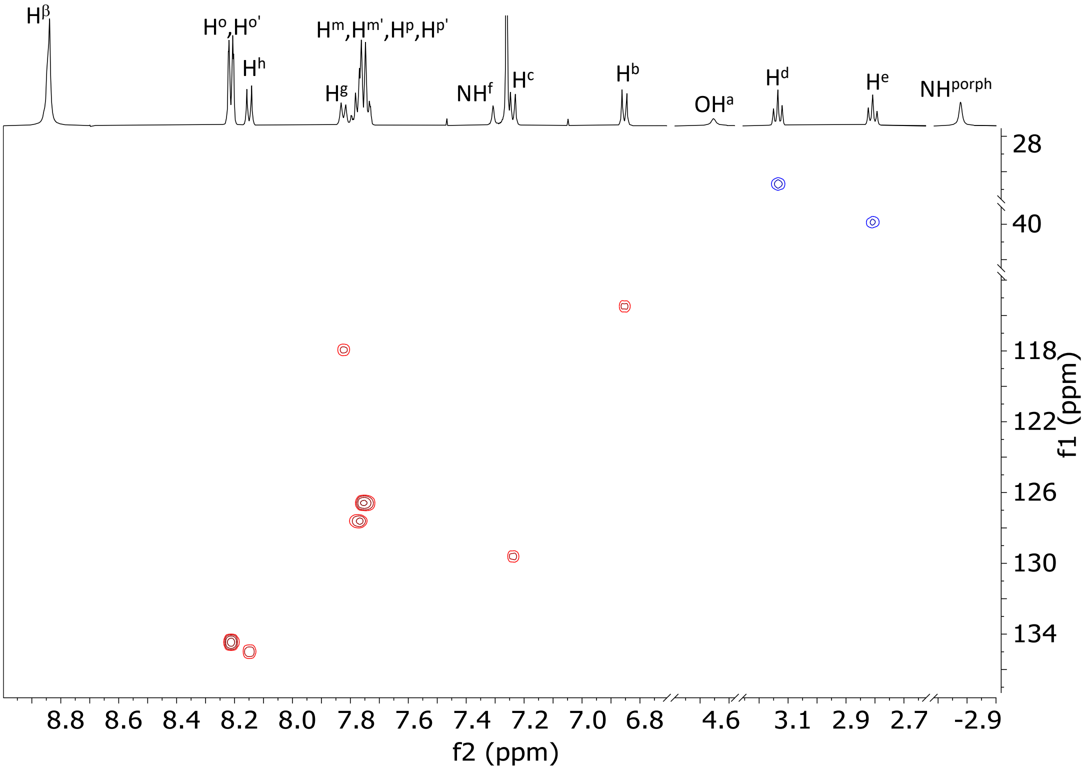

Figure S2. ^{1}H-^{13}C HSQC spectrum (CDCl$_3$, 298 K) of **2**.

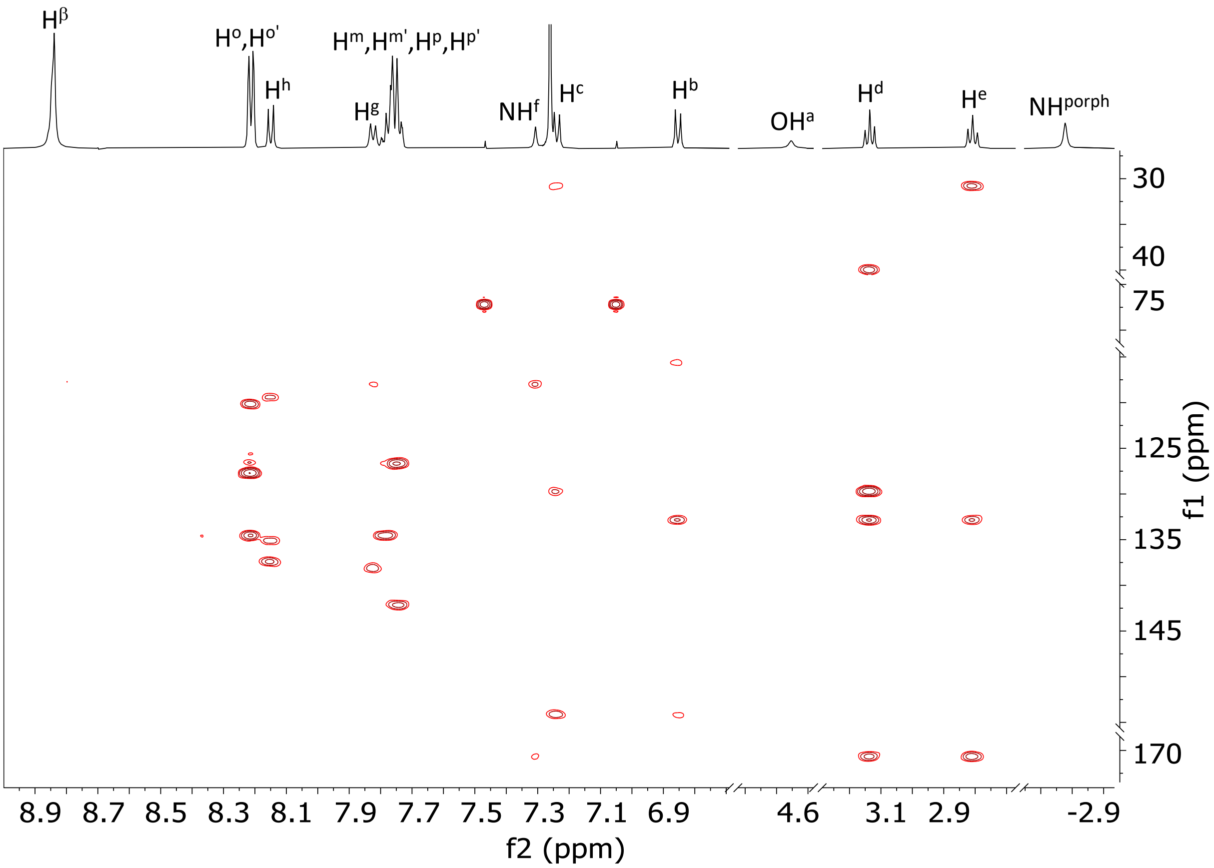

Figure S3. ^{1}H-^{13}C HMBC spectrum ($CDCl_3$, 298 K) of **2**.

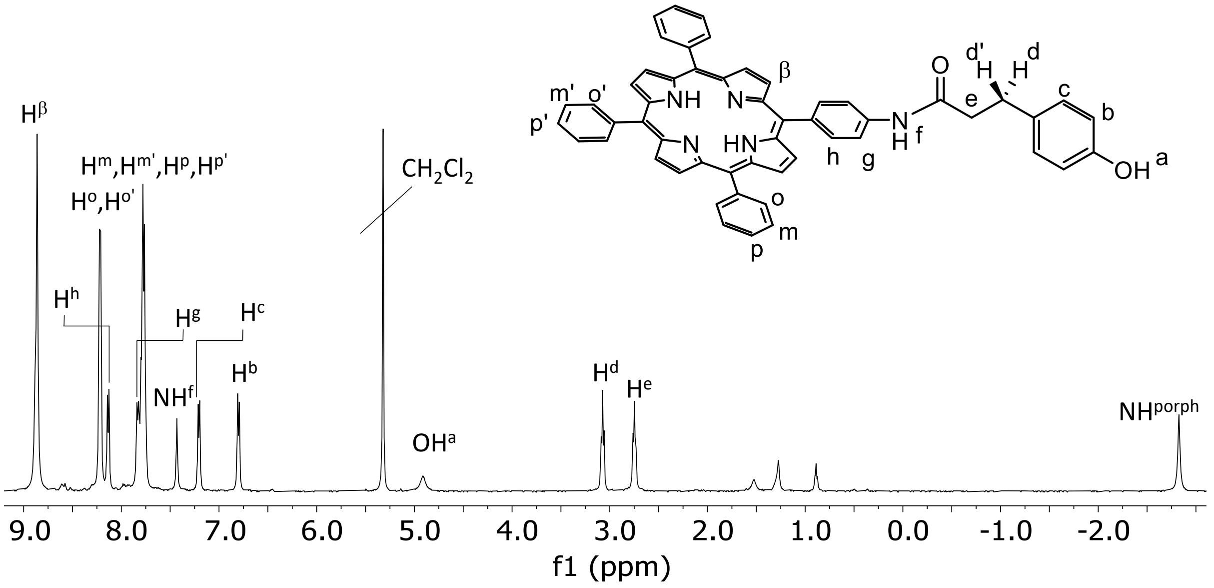

Figure S4. ^{1}H-NMR spectrum (CD_2Cl_2, 298 K) of **2**.

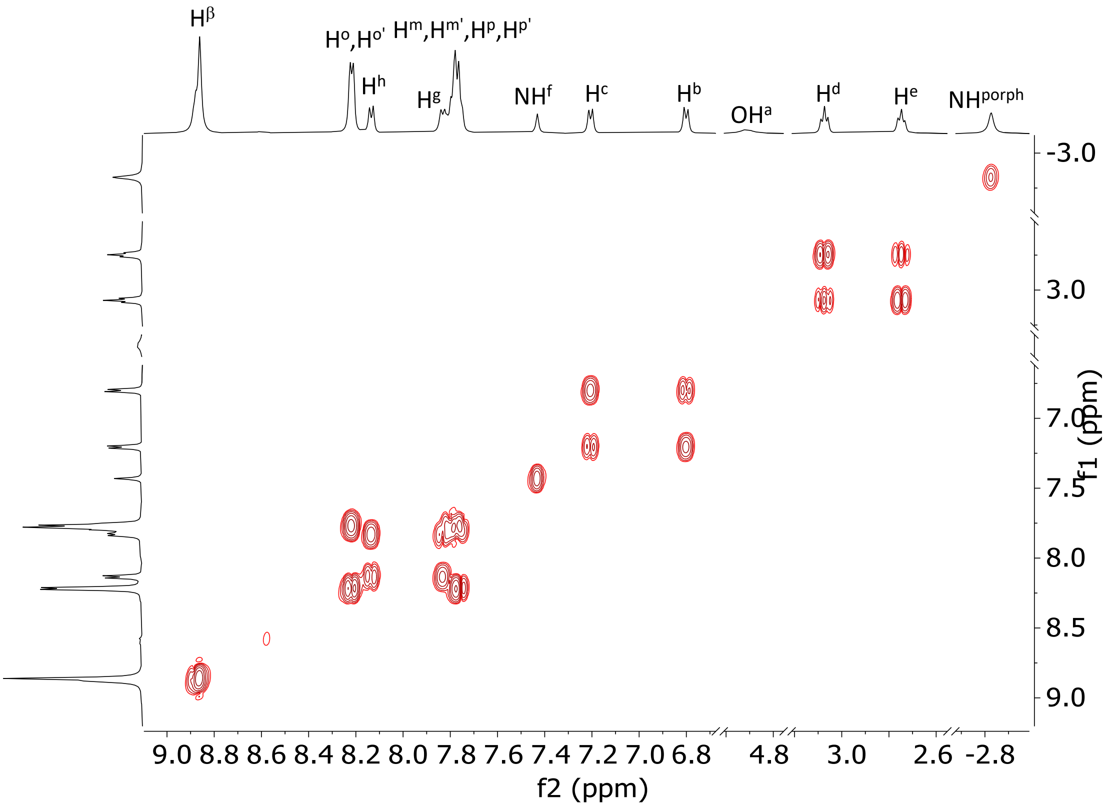

Figure S5. ^{1}H-^{1}H COSY spectrum (CD_2Cl_2, 298 K) of **2**.

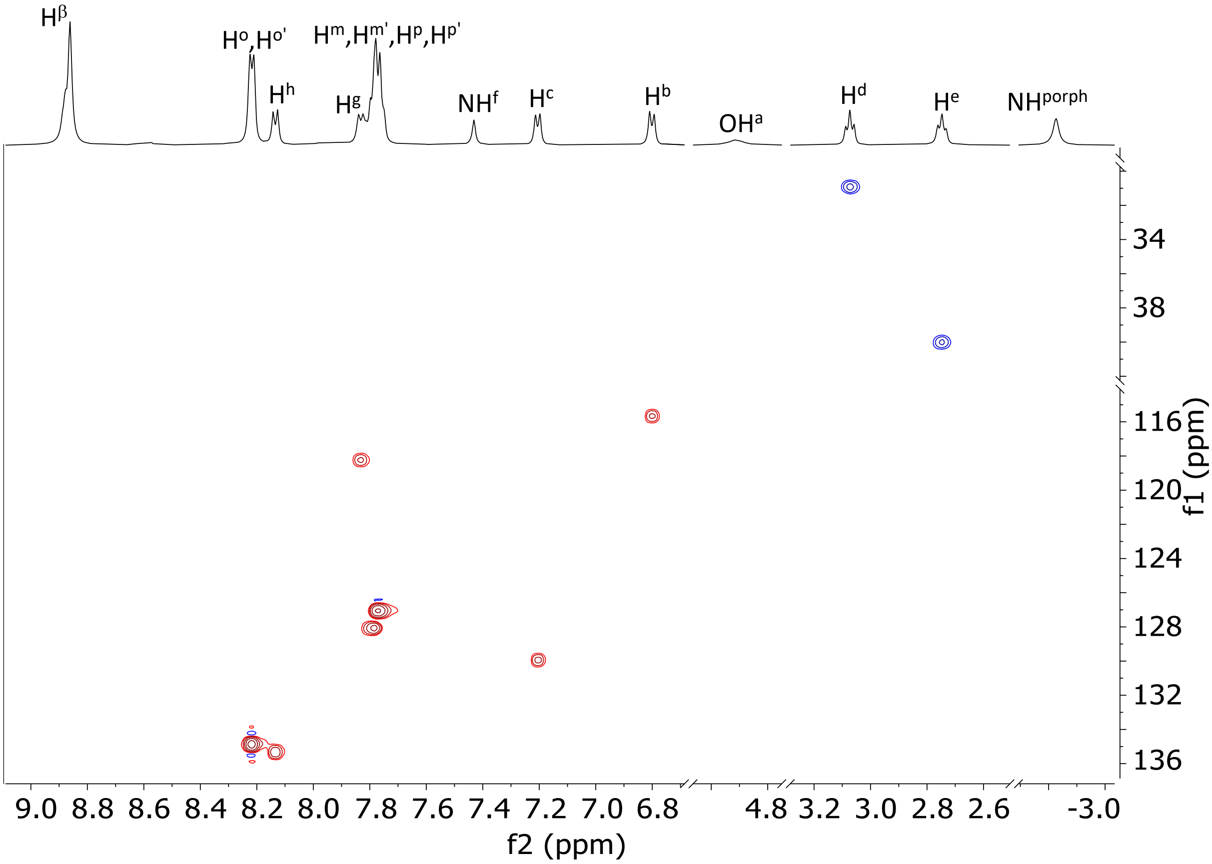

Figure S6. ^{1}H-^{13}C HSQC spectrum (CD_2Cl_2, 298 K) of **2**.

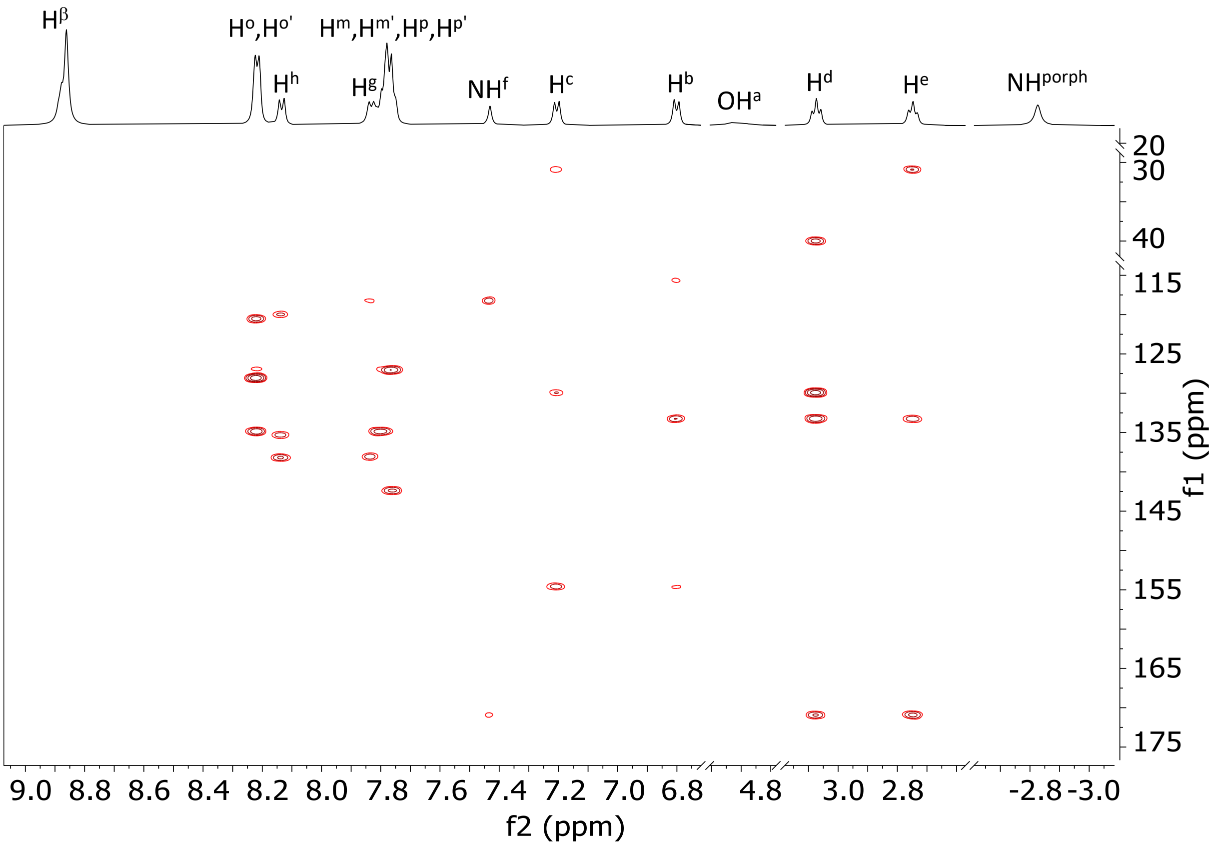

Figure S7. ^{1}H-^{13}C HMBC spectrum (CD_2Cl_2, 298 K) of **2**.

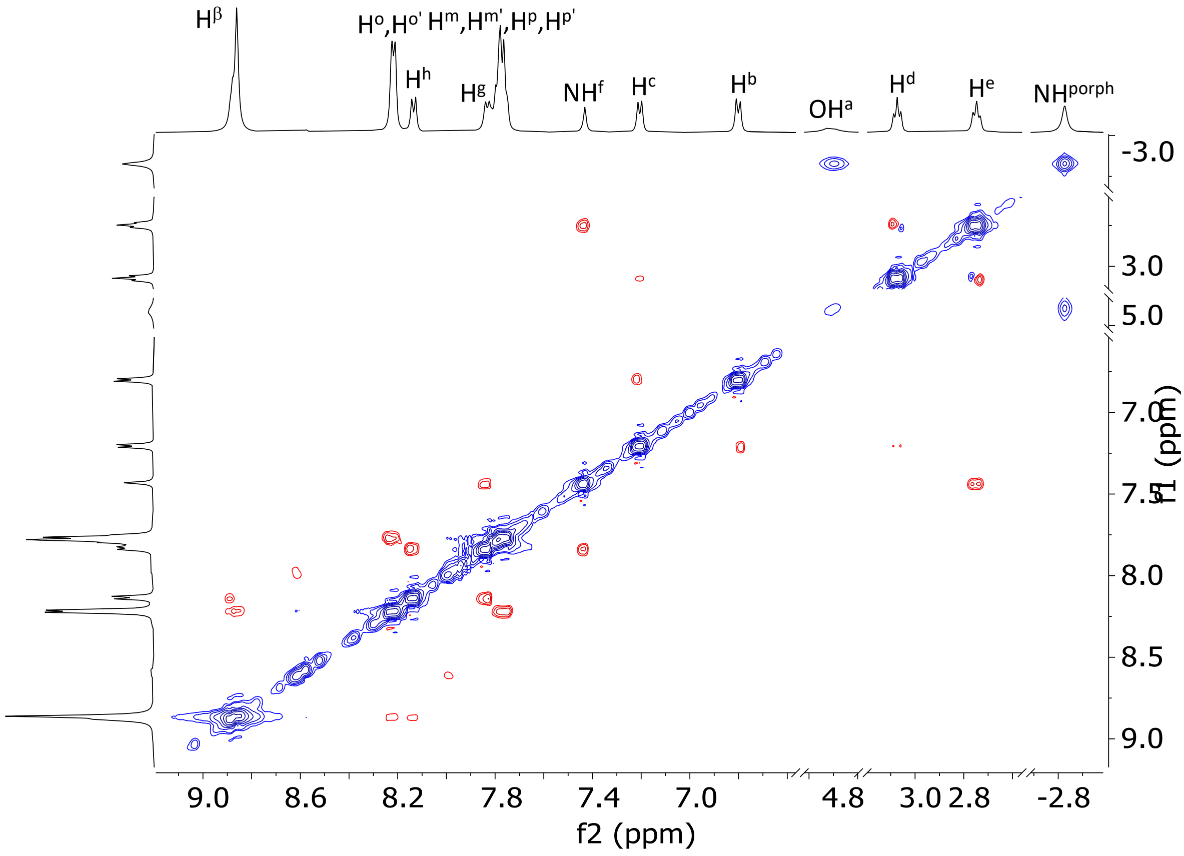

Figure S8. ^{1}H-^{1}H ROESY spectrum (CD_2Cl_2, 298 K) of **2**.

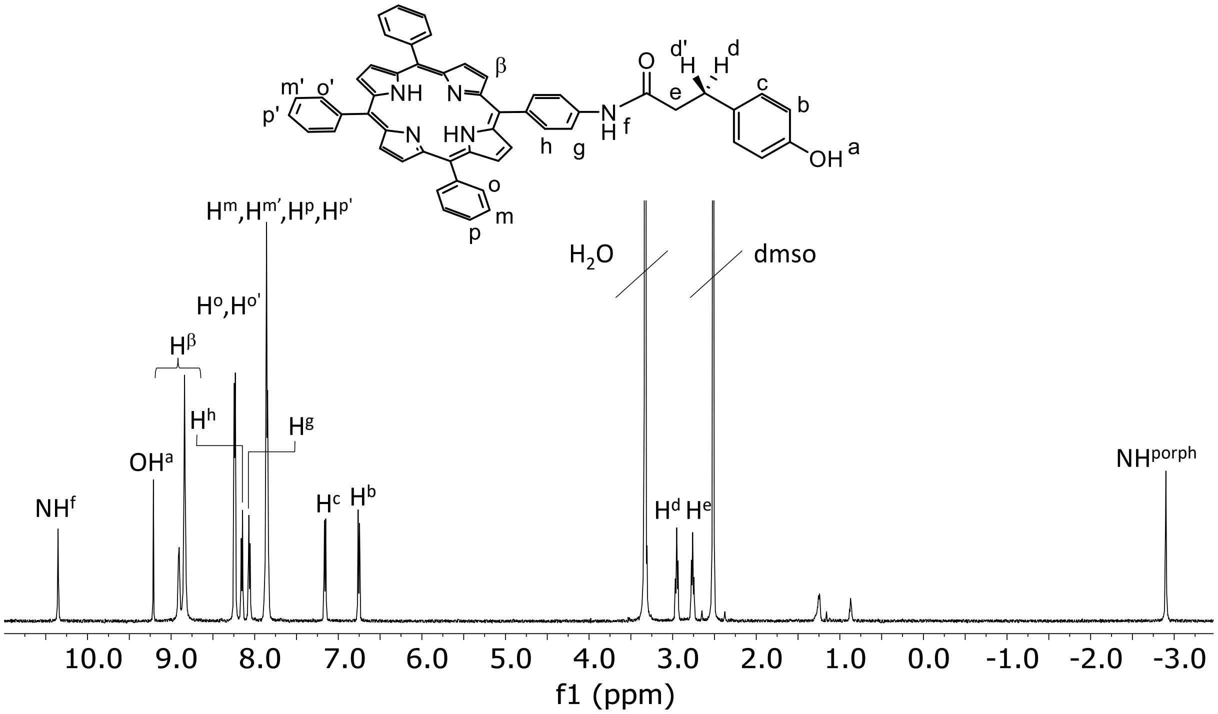

Figure S9. ^{1}H NMR spectrum (dmso-d_6, 298 K) of **2**.

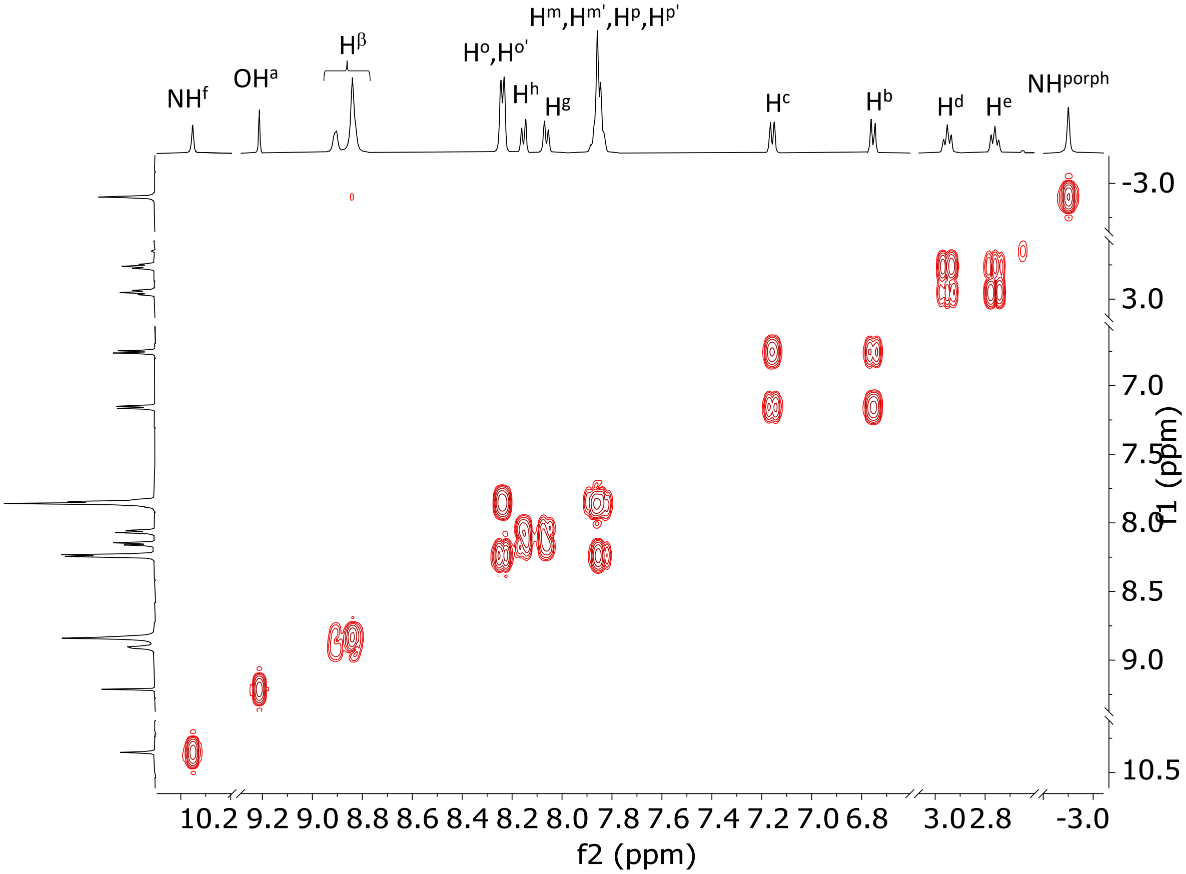

Figure S10. ^{1}H-^{1}H COSY spectrum (dmso-d_6, 298 K) of **2**.

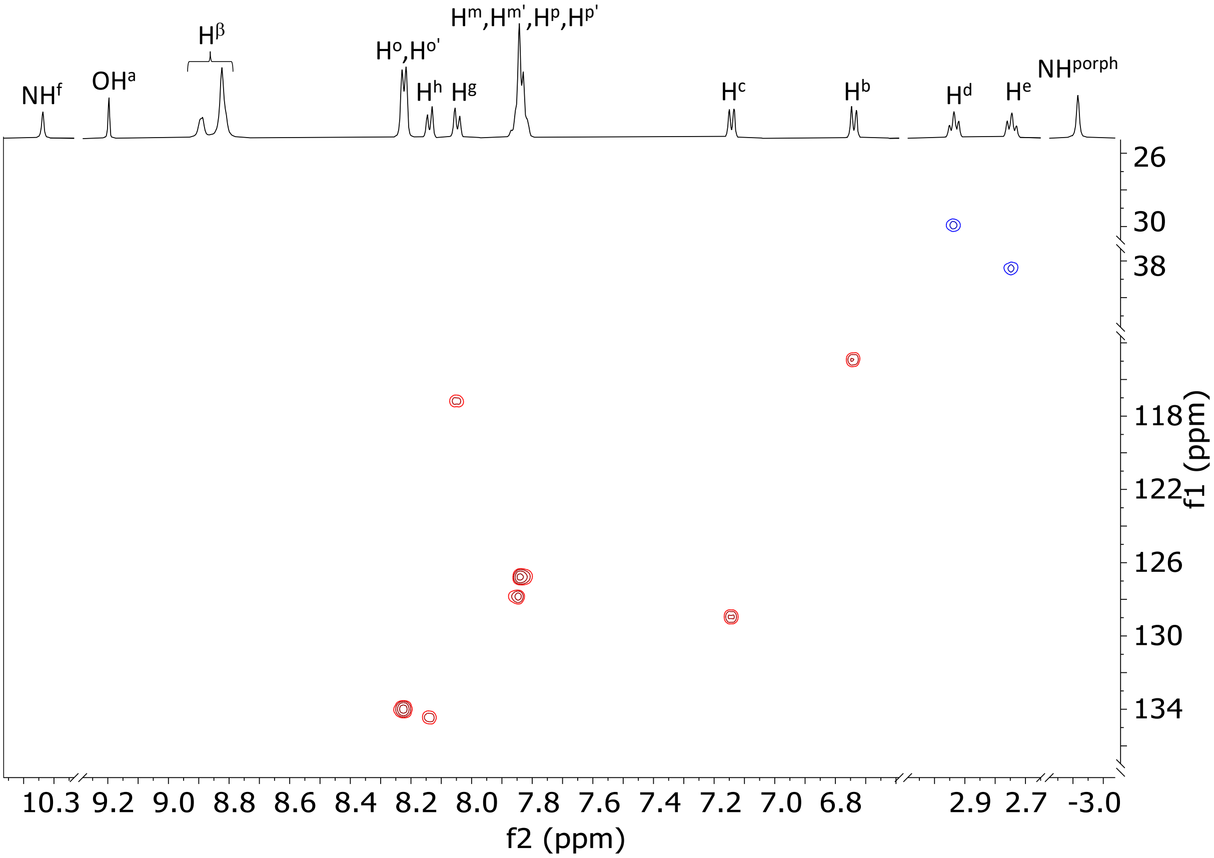

Figure S11. ^{1}H-^{13}C HSQC spectrum (dmso-d_6, 298 K) of **2**.

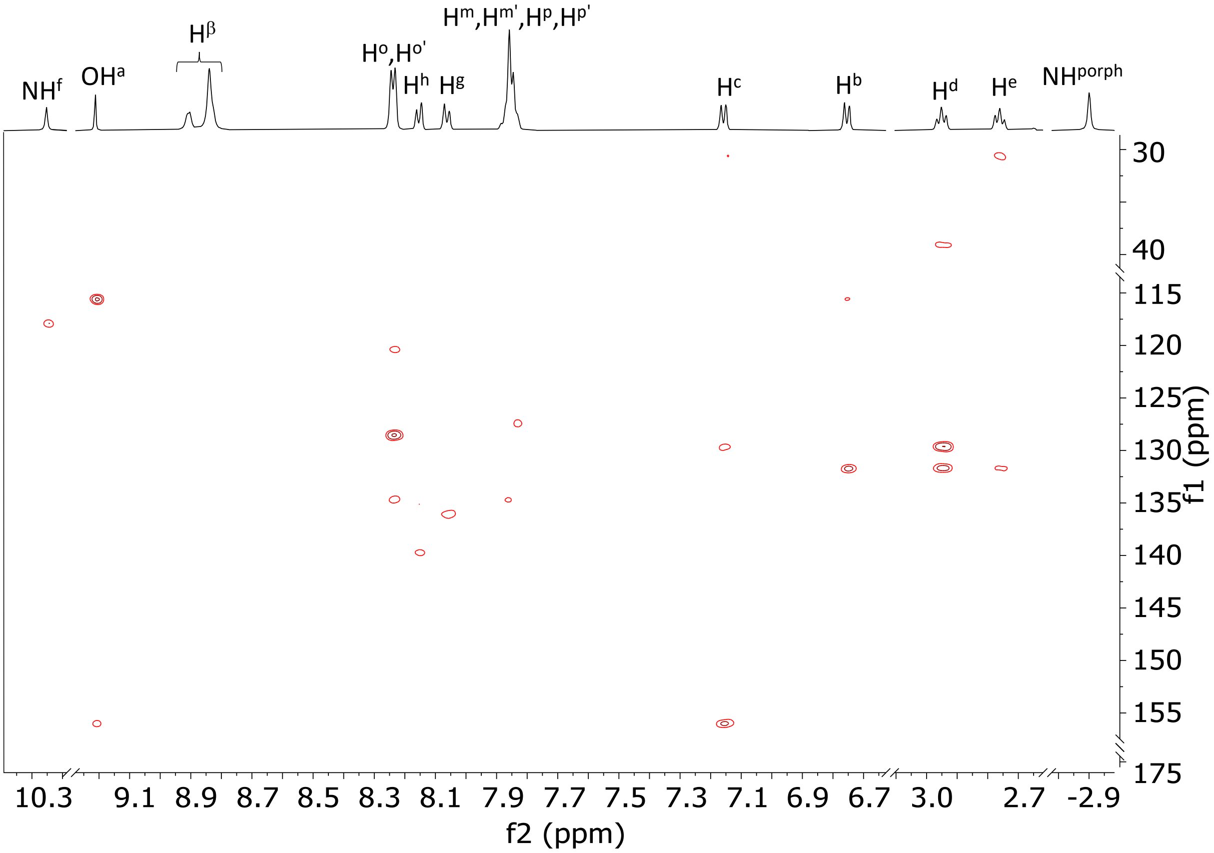

Figure S12. ^{1}H-^{13}C HMBC spectrum (dmso-d_6, 298 K) of **2**.

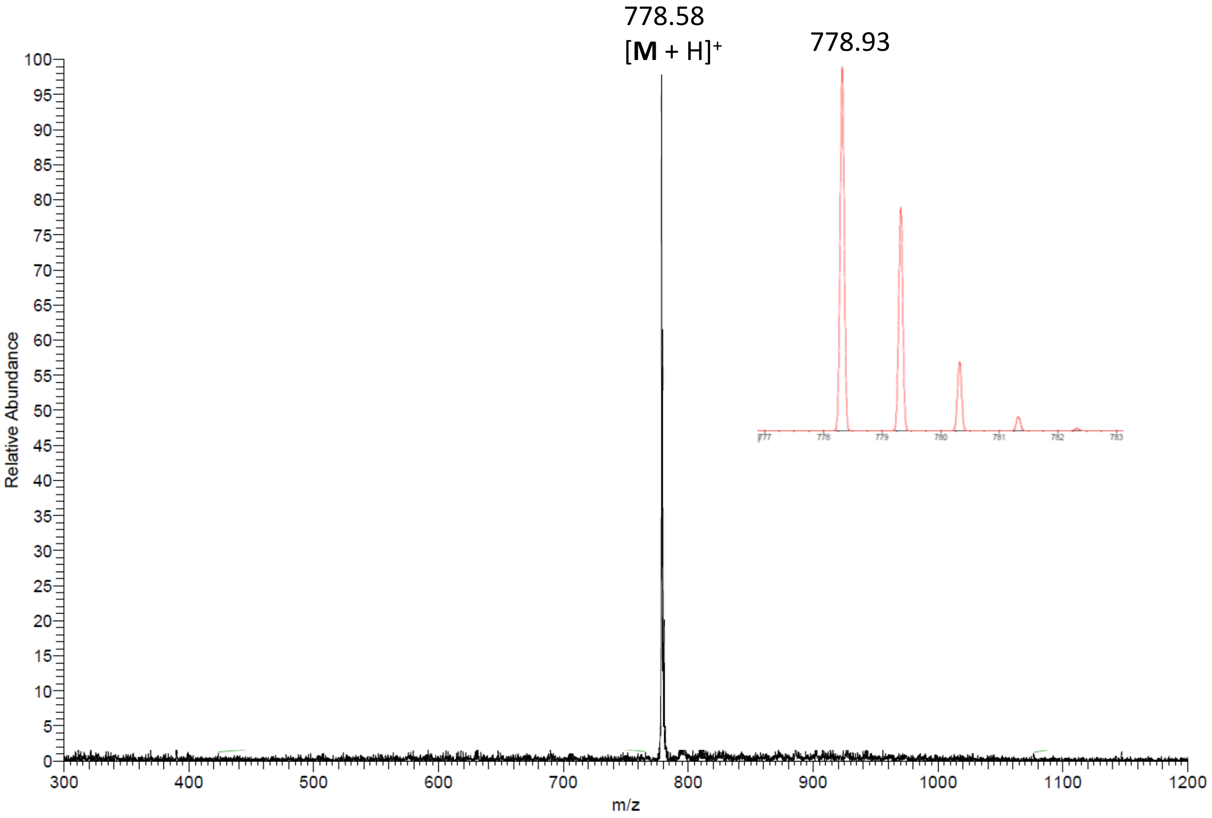

Figure S13. ESI-MS of **2** in CH_3OH, experimental (black) and simulated (red).

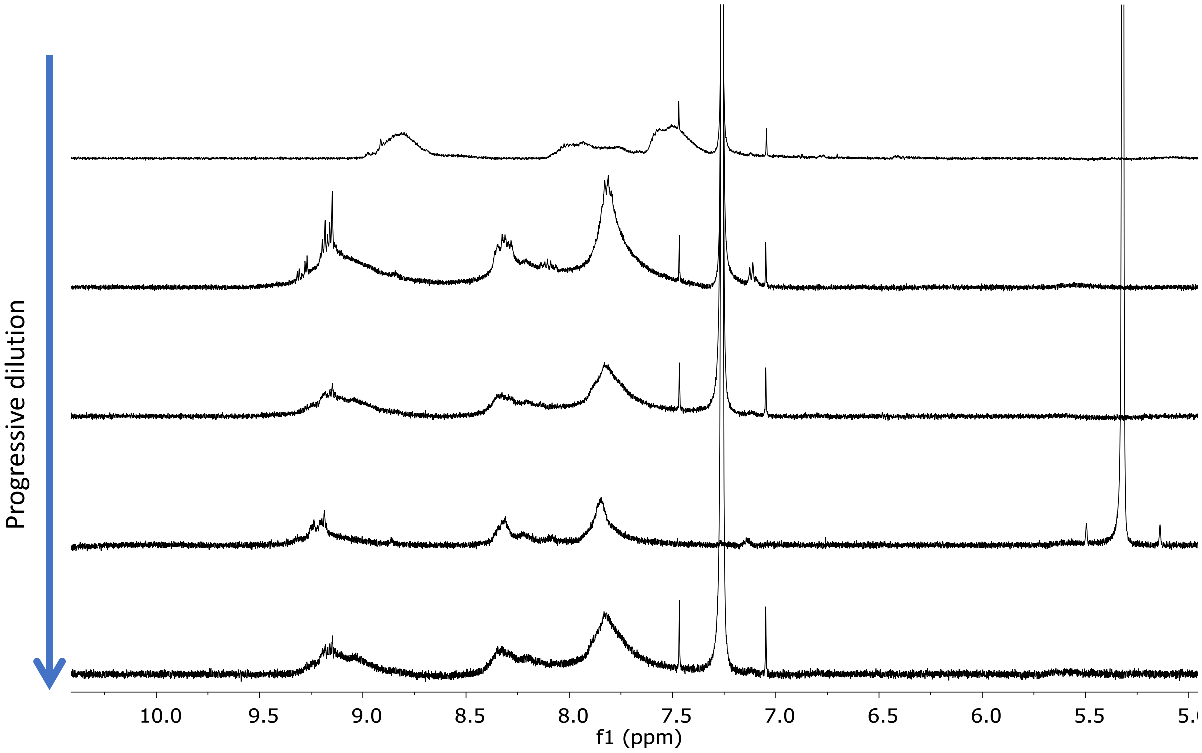

Figure S14. Aromatic region of the ^1H NMR spectra ($CDCl_3$, 298 K) of the isolated product from the metalation step of **2** with $SnCl_2 \cdot 2H_2O$ at different concentrations.

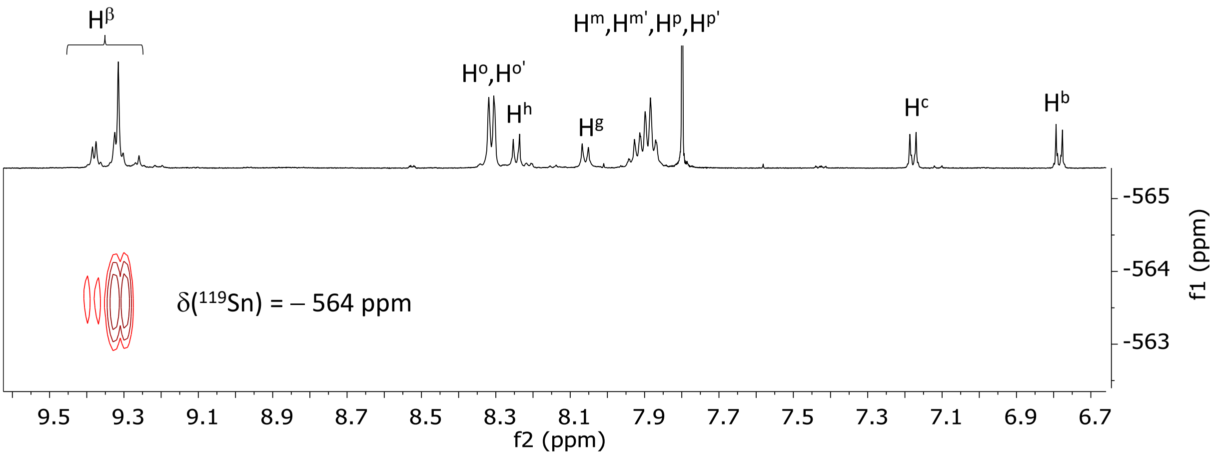

Figure S15. ^{1}H-^{119}Sn HMBC spectrum (CD$_3$OD, 298 K) of the isolated product from the metalation step of **2** with SnCl$_2$·2H$_2$O.

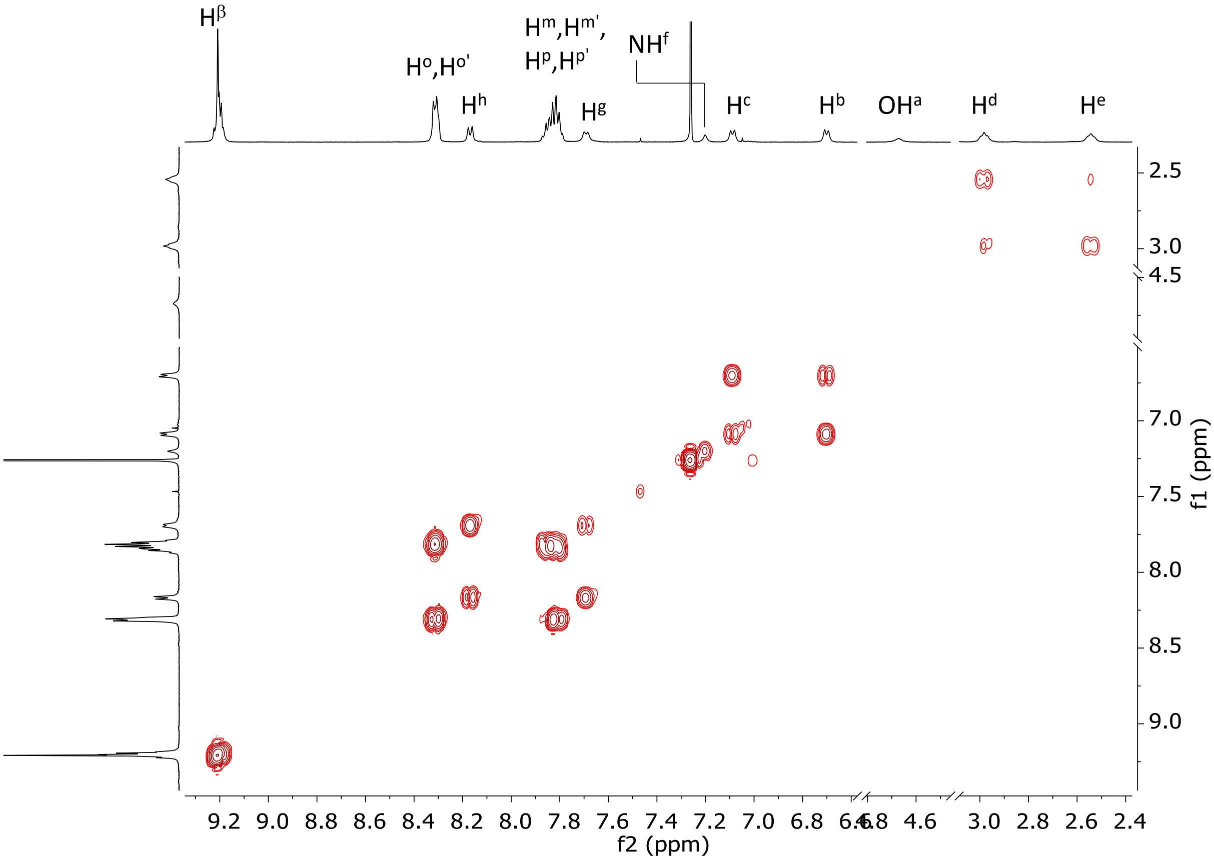

Figure S16. ^{1}H-^{1}H COSY spectrum (CDCl$_3$, 298 K) of **3**. For labelling see Experimental Section.

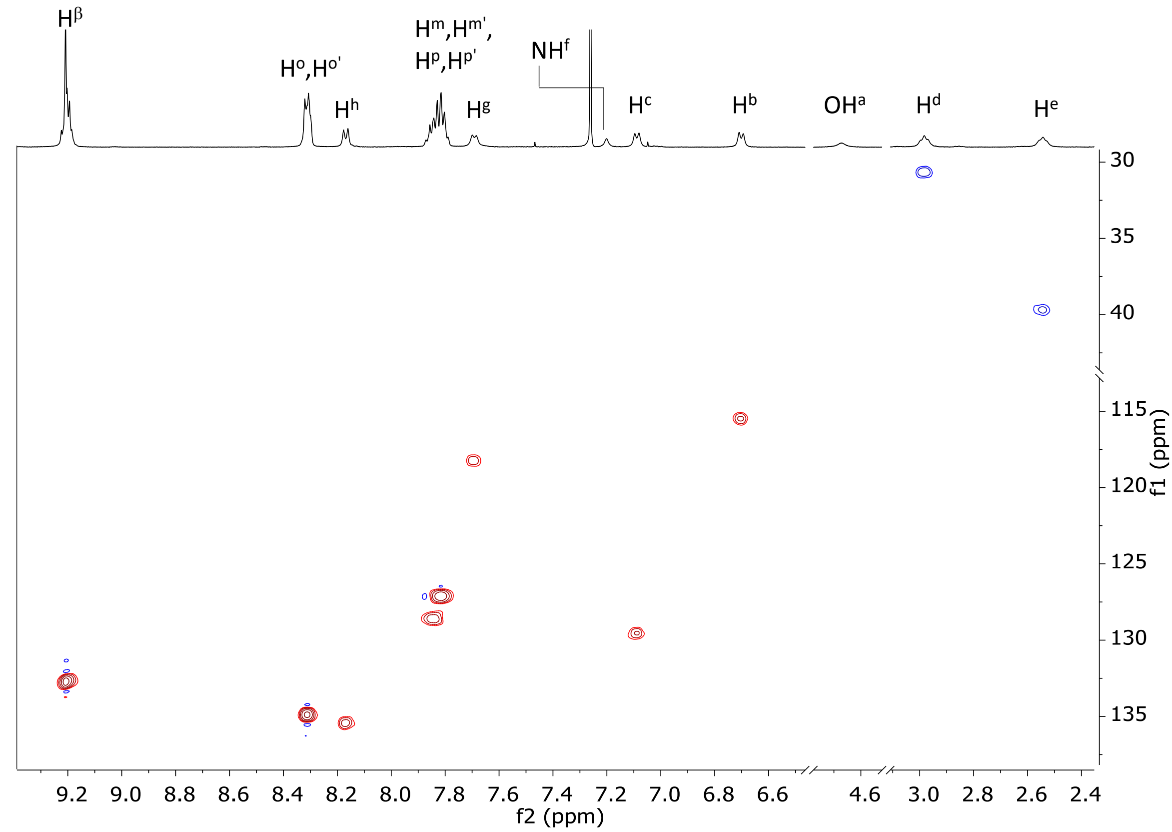

Figure S17. ^{1}H-^{13}C HSQC spectrum (CDCl$_3$, 298 K) of **3**.

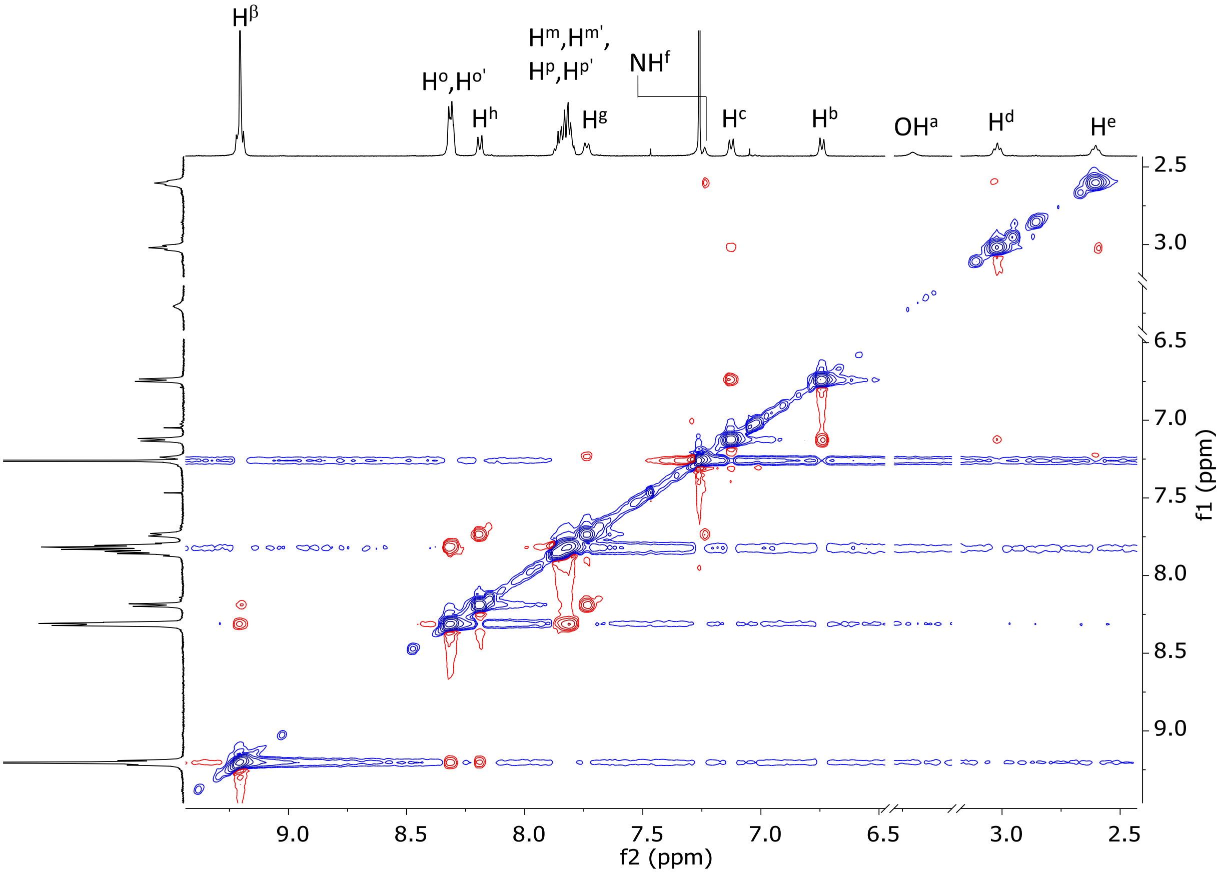

Figure S18. ^{1}H-^{1}H ROESY spectrum (CDCl$_3$, 298 K) of **3**.

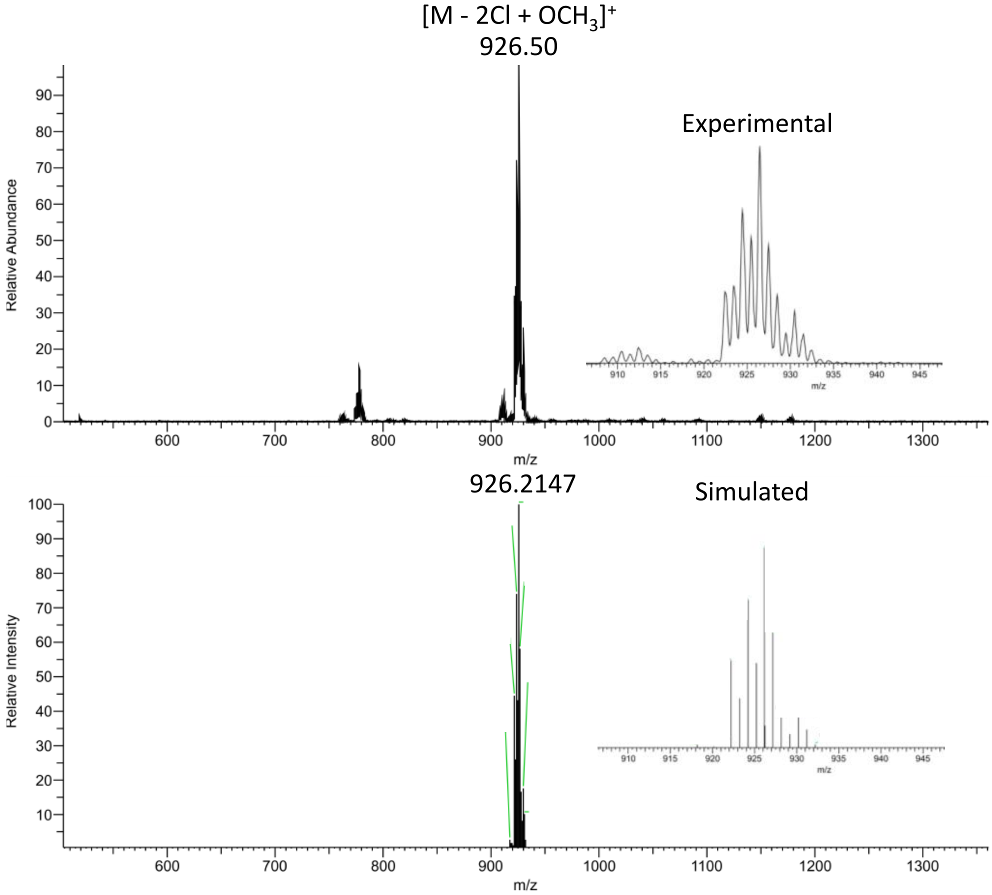

Figure S19. ESI-MS of **3** in CH_3OH, experimental (top) and simulated (bottom).

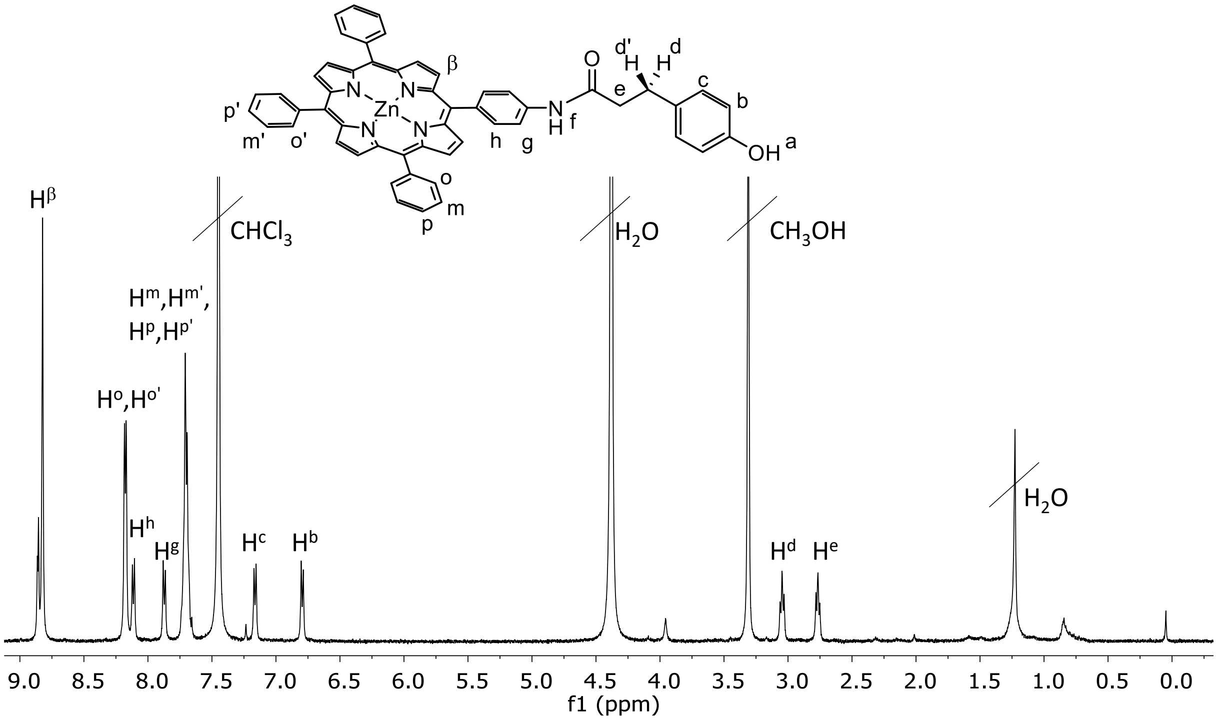

Figure S20. ^{1}H NMR spectrum ($CDCl_3$:CD_3OD 6:1, 298 K) of **ZnTPP-*p*PA** (**4**).

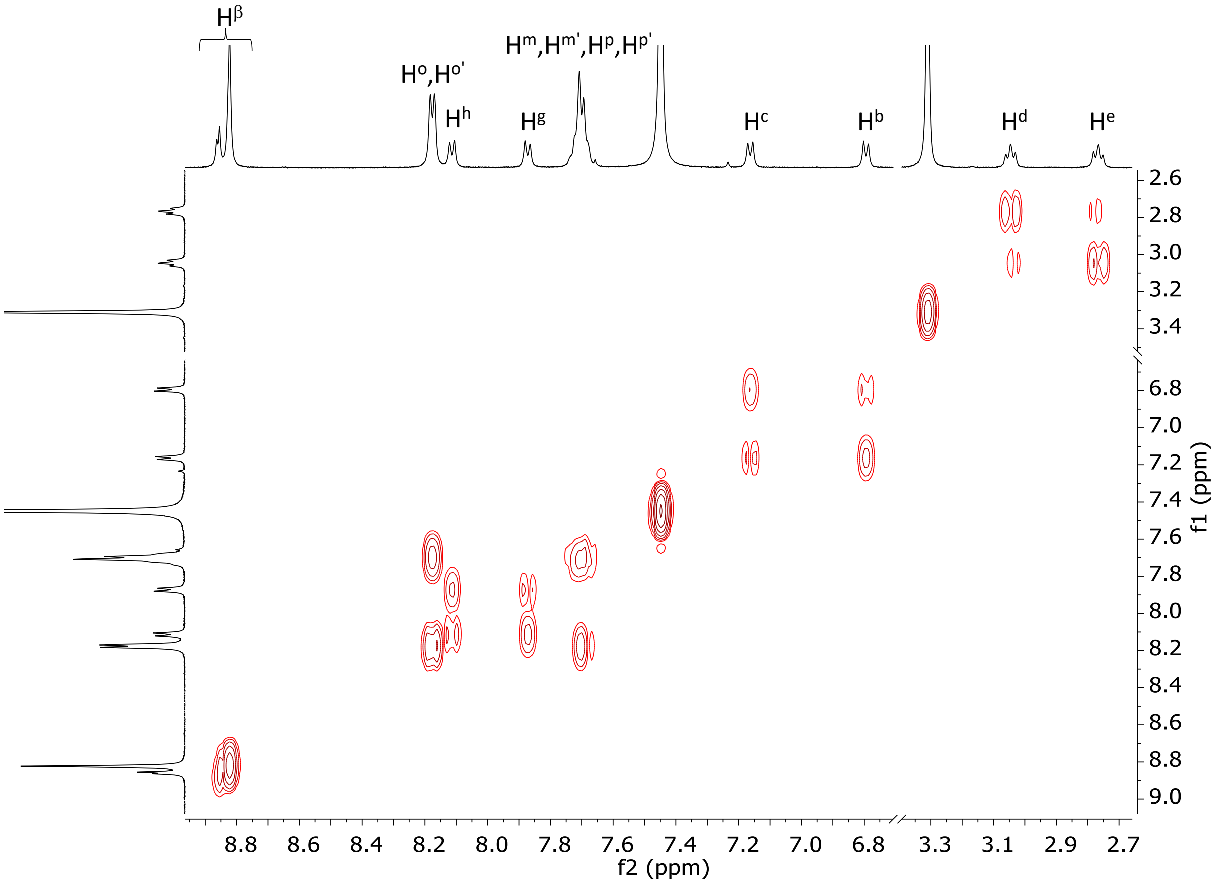

Figure S21. ^{1}H-^{1}H COSY spectrum ($CDCl_3$:CD_3OD 6:1, 298 K) of **4**.

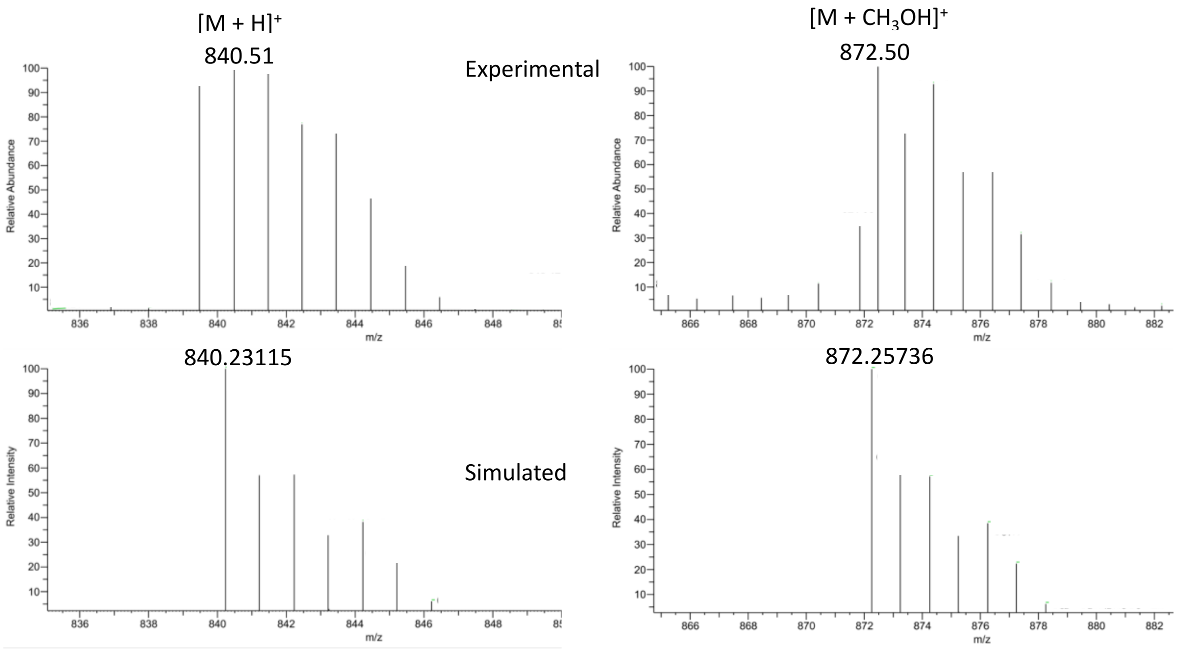

Figure S22. ESI-MS of **4** in CH_3OH, experimental (top) and simulated (bottom).

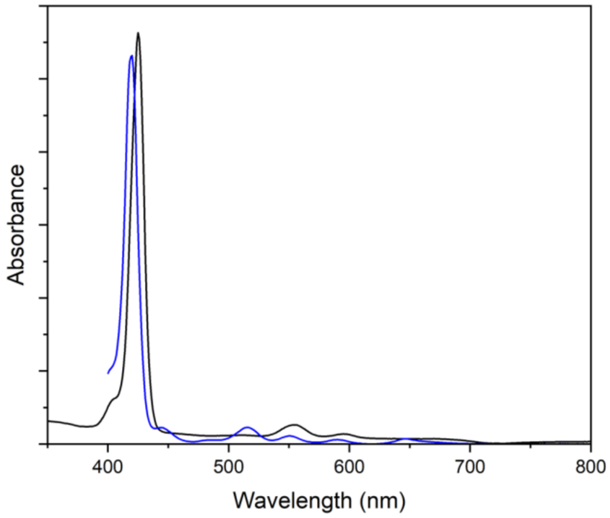

Figure S23. UV-Vis absorption spectra (CH_2Cl_2, 25 µM) of **2** and **4** (black and blue traces, respectively).

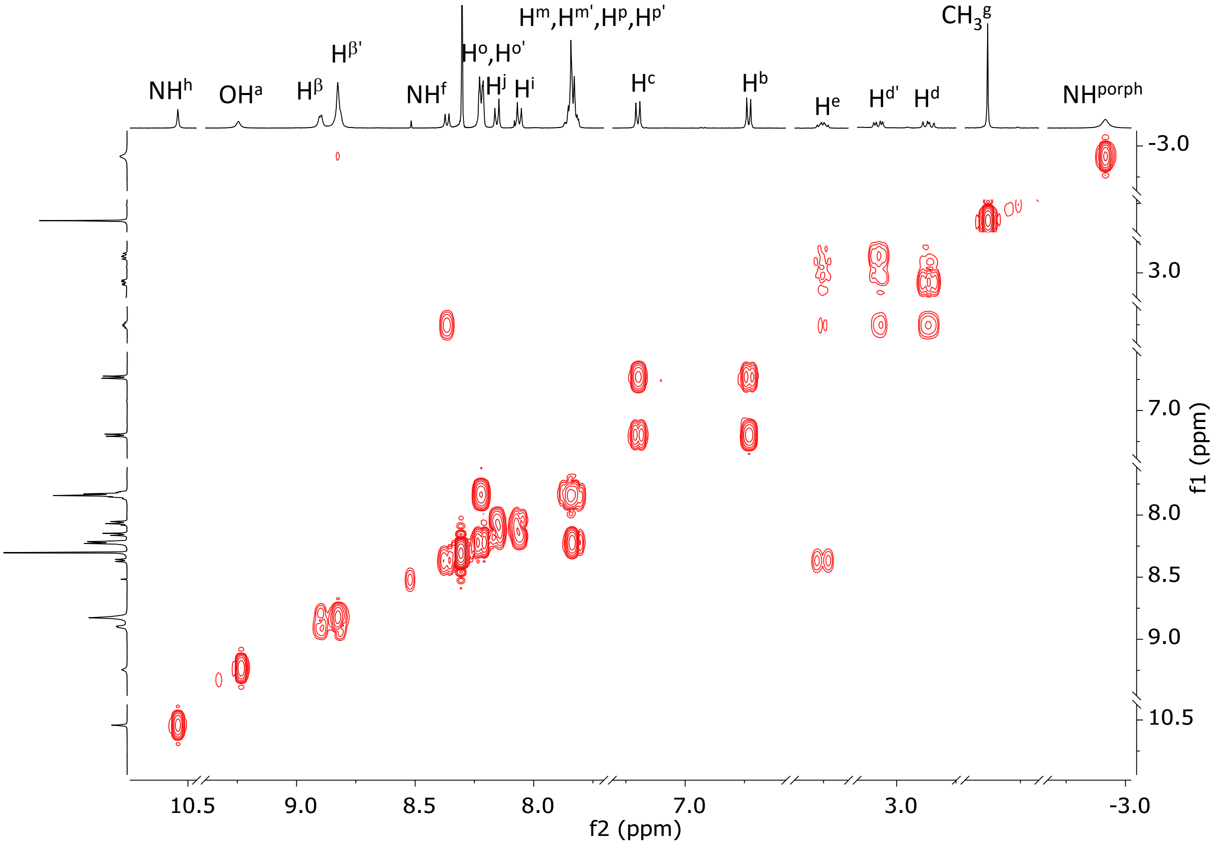

Figure S24. ^1H-^1H COSY spectrum (dmso-d_6, 298 K) of **TPP-*p*Tyr** (**5**). For labelling see Experimental Section.

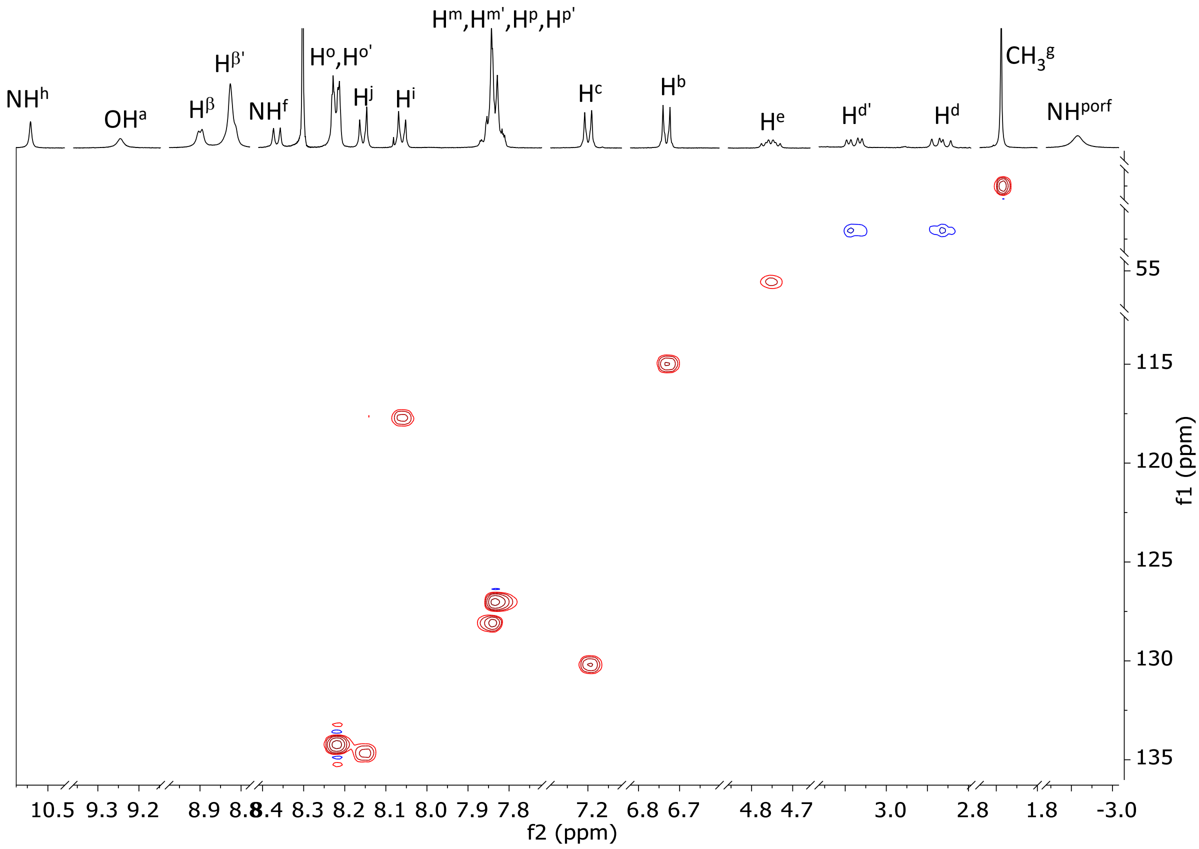

Figure S25. ^{1}H-^{13}C HSQC spectrum (dmso-d_6, 298 K) of **5**.

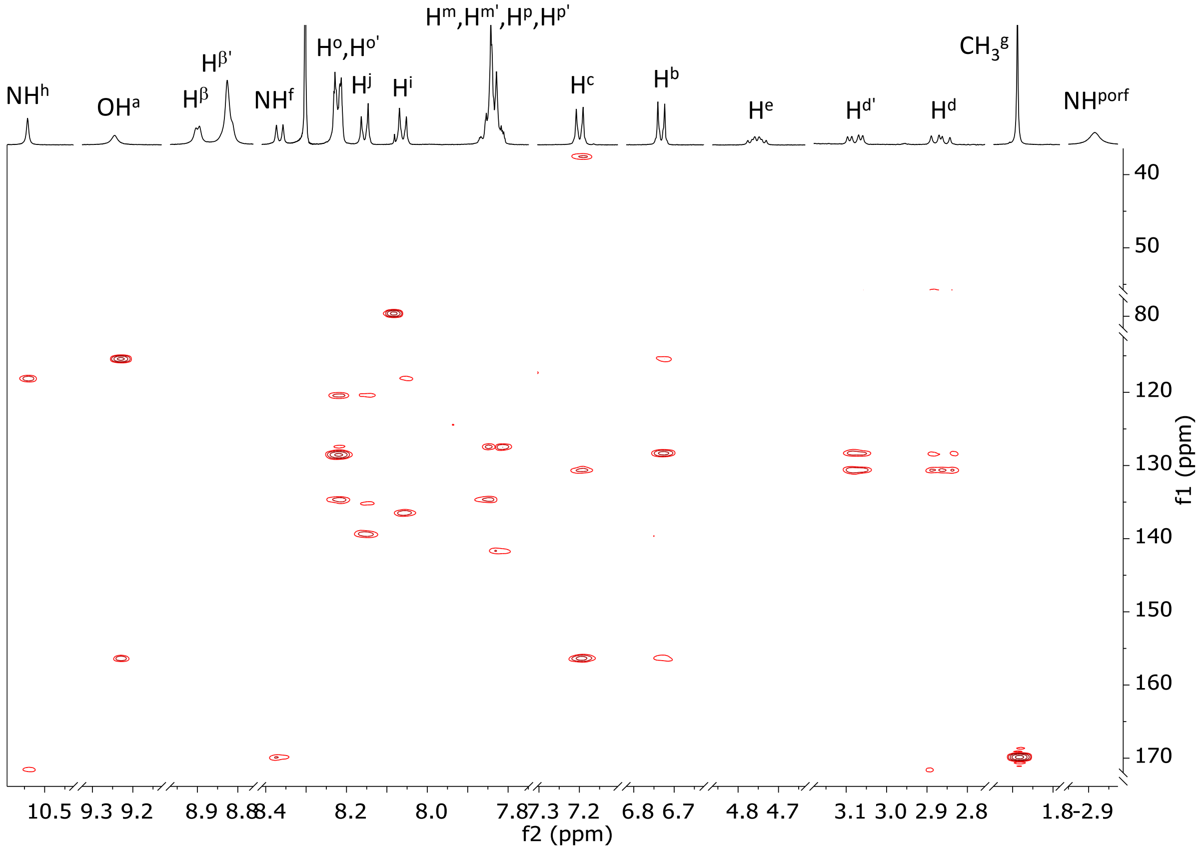

Figure S26. ^{1}H-^{13}C HMBC spectrum (dmso-d_6, 298 K) of **5**.

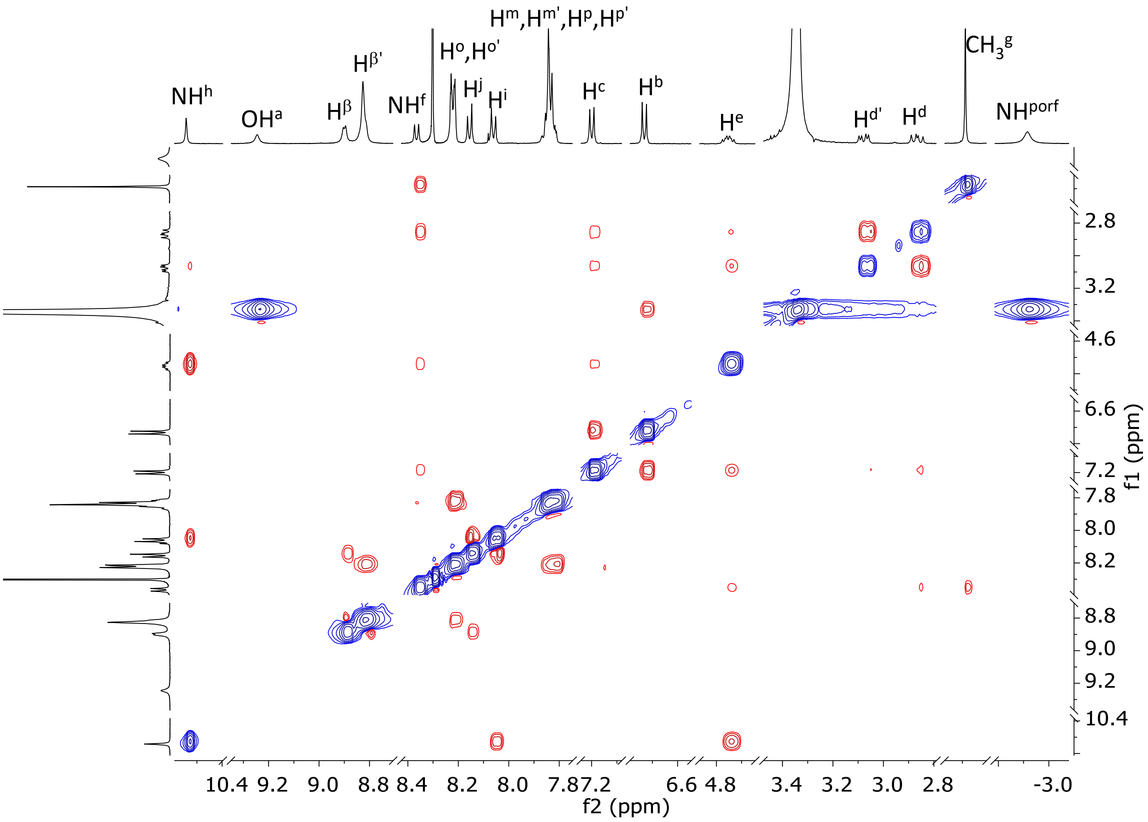

Figure S27. ^1H-^1H ROESY spectrum (dmso-d_6, 298 K) of **5**.

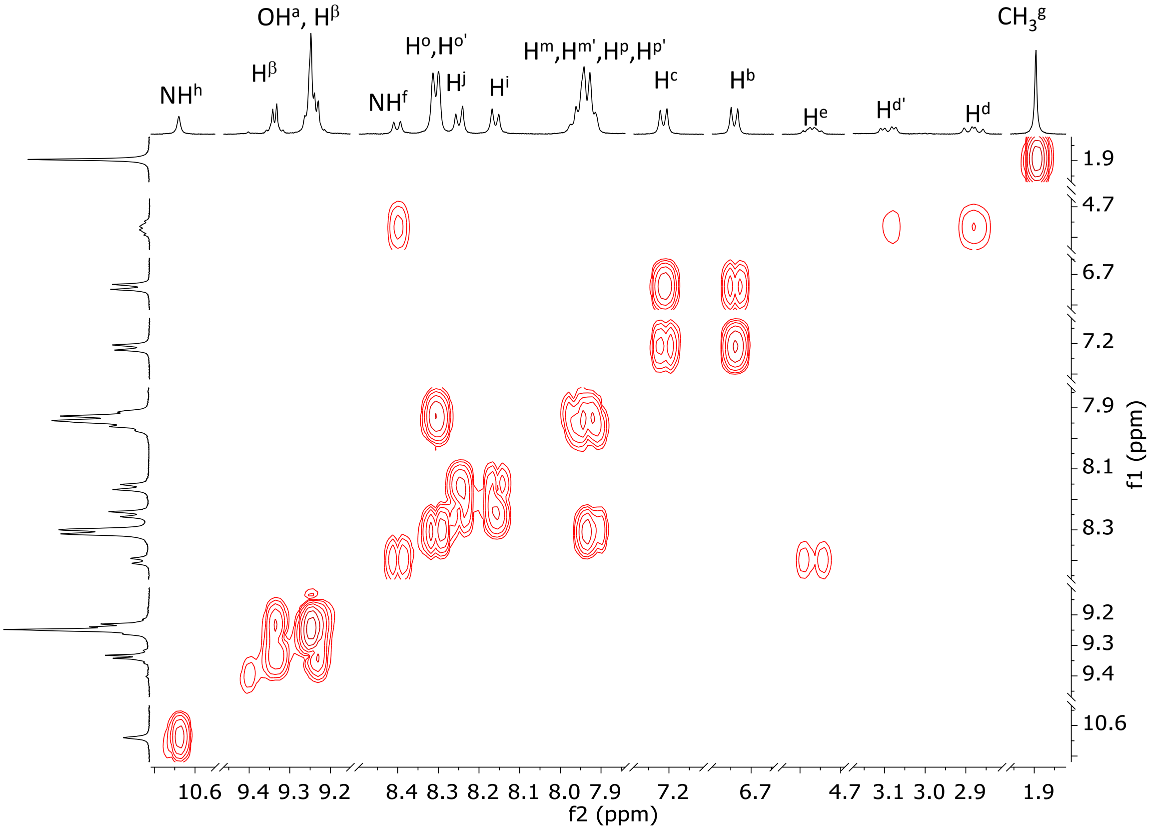

Figure S28. ^1H-^1H COSY spectrum (dmso-d_6, 298 K) of **SnCl$_2$TPP-*p*Tyr** (**6**). For labelling see Experimental Section.

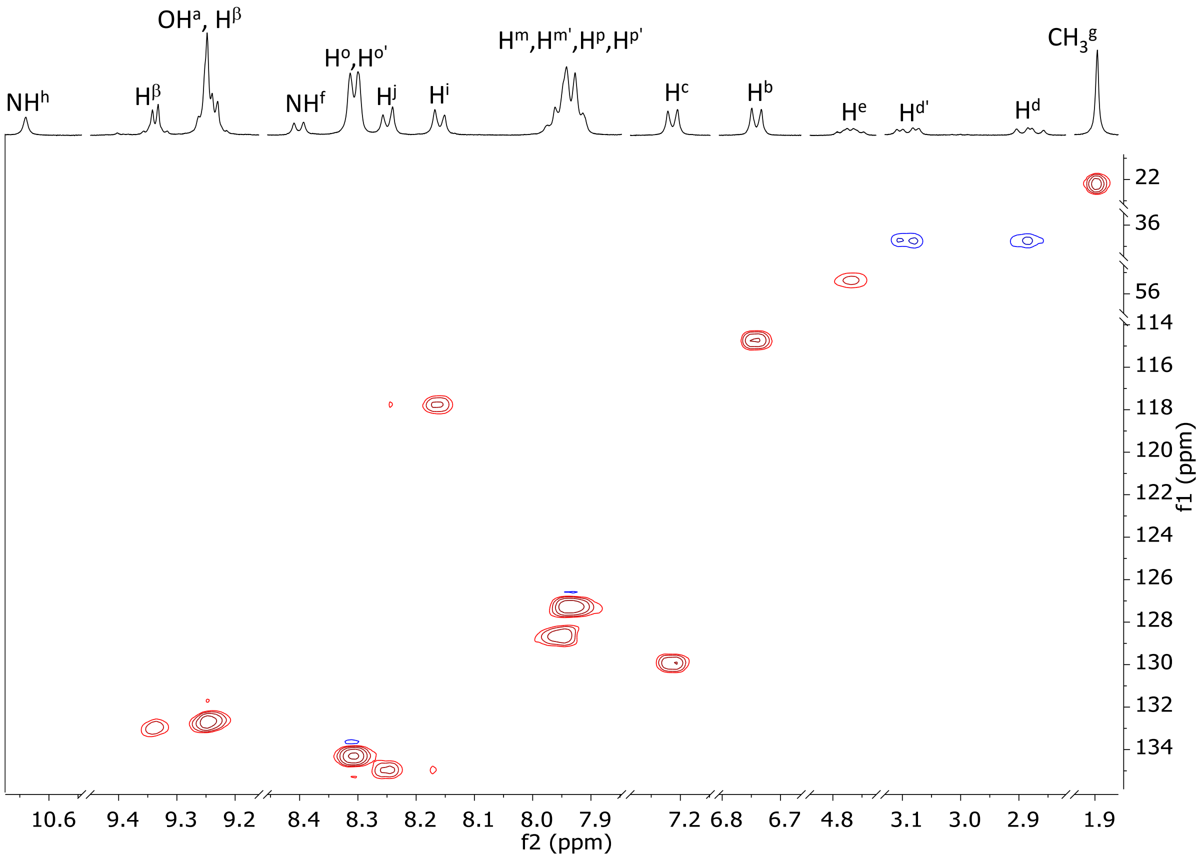

Figure S29. ^{1}H-^{13}C HSQC spectrum (dmso-d_6, 298 K) of **6**.

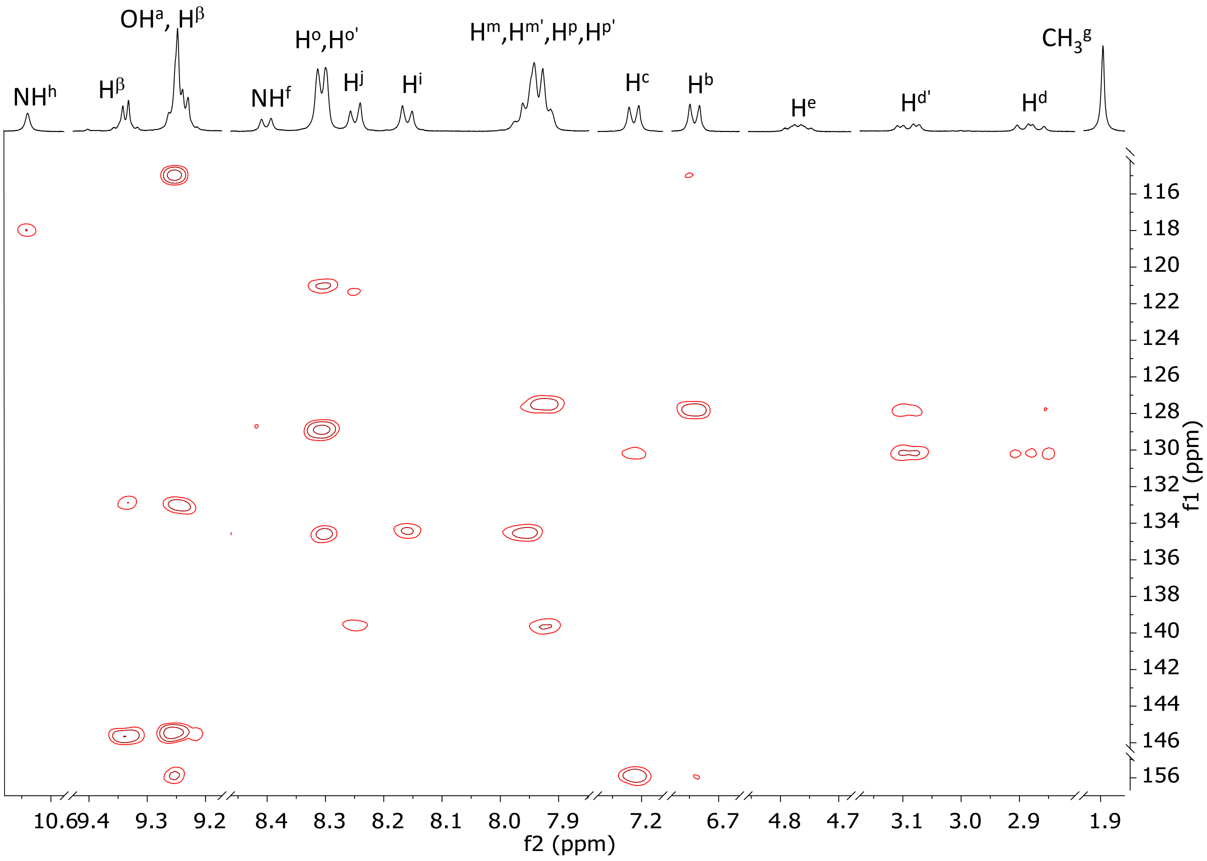

Figure S30. ^{1}H-^{13}C HMBC spectrum (dmso-d_6, 298 K) of **6**.

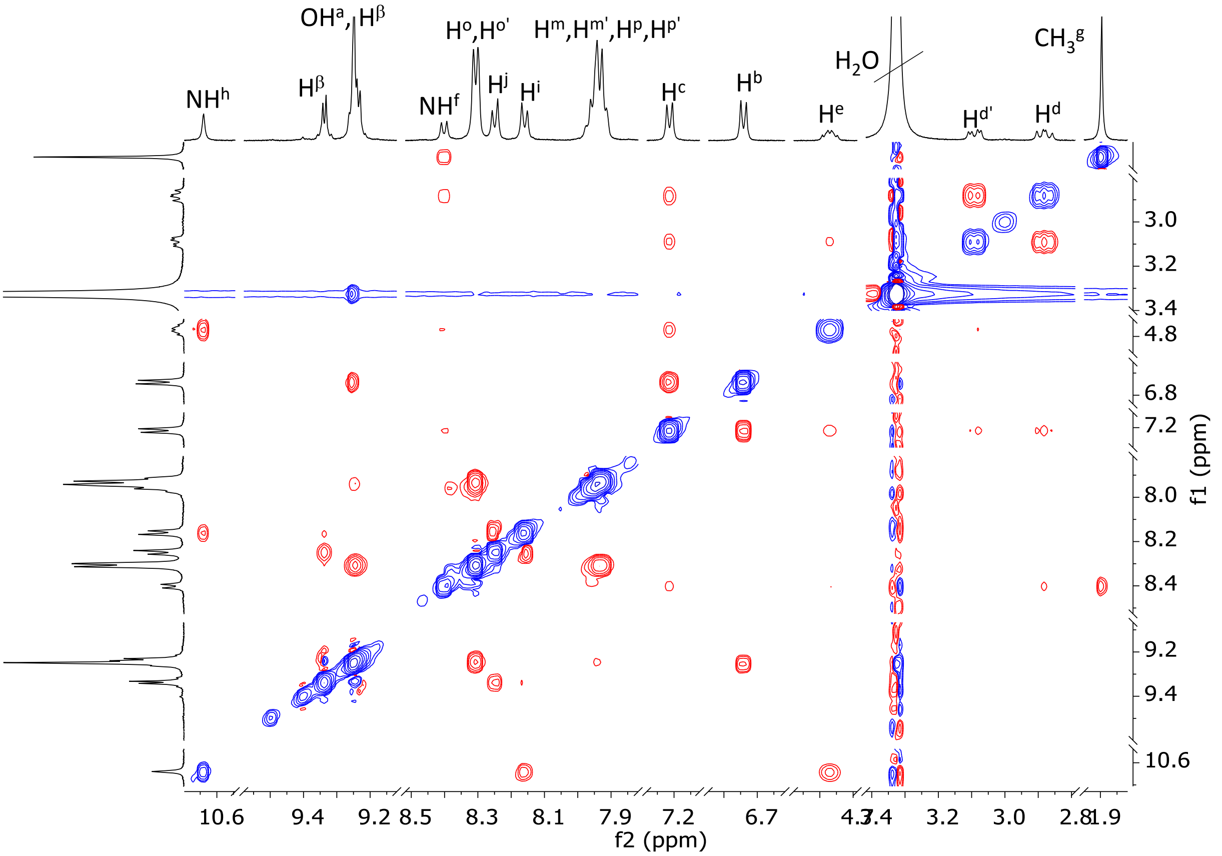

Figure S31. ^{1}H-^{1}H ROESY spectrum (dmso-d_6, 298 K) of **6**.

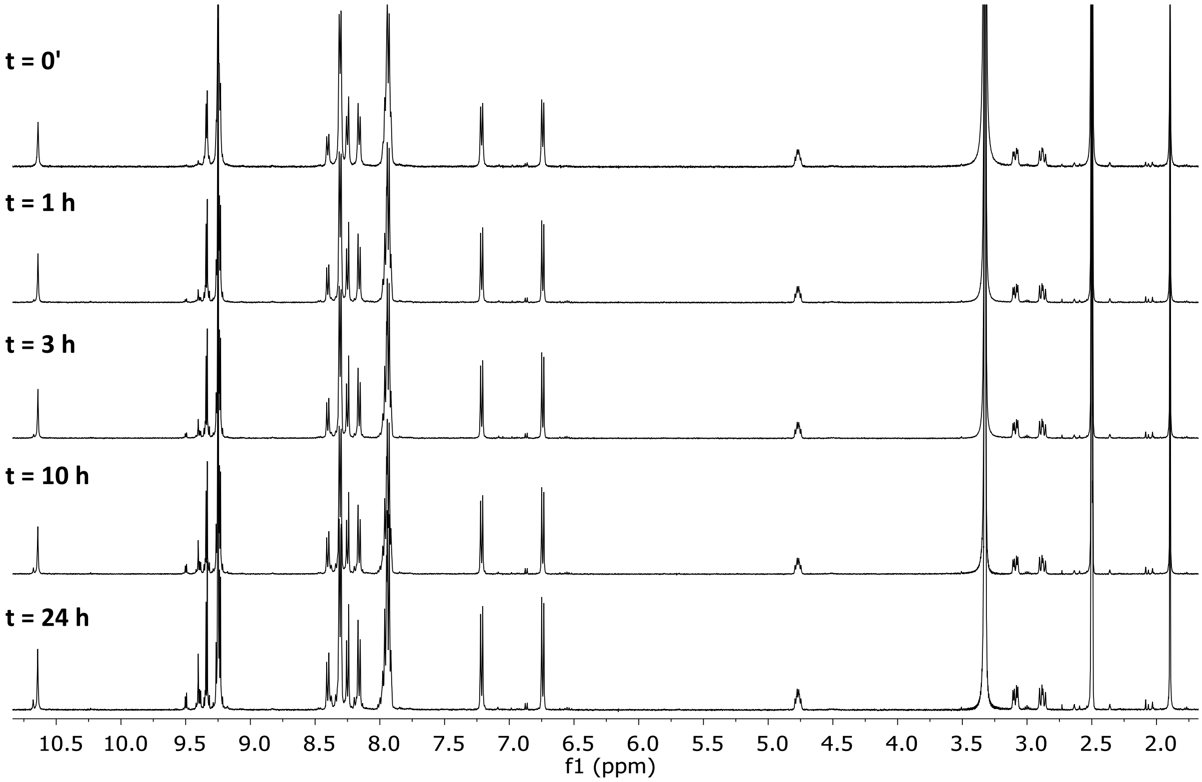

Figure S32. Time evolution of the ^{1}H NMR spectrum (dmso-d_6, 298 K) of **6**.

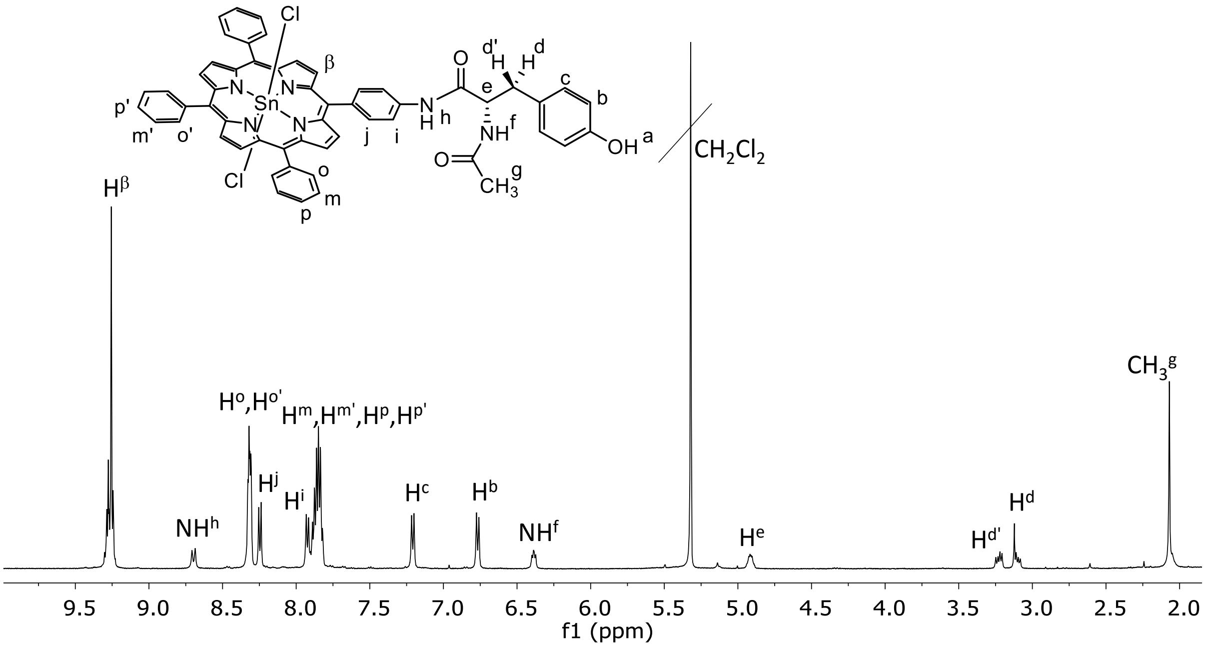

Figure S33. ^{1}H NMR spectrum (CD_2Cl_2, 298 K) of **$SnCl_2$TPP-*p*Tyr** (**6**).

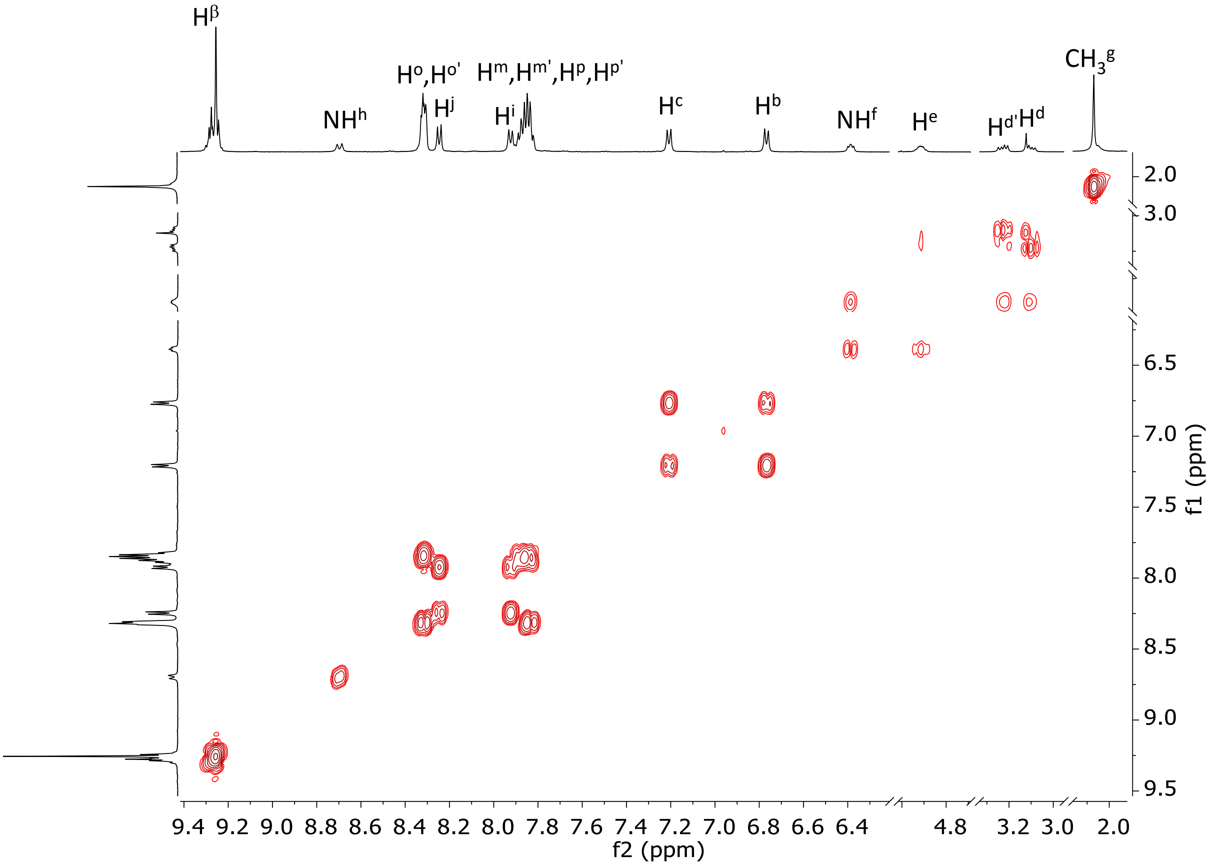

Figure S34. ^{1}H-^{1}H COSY spectrum (CD_2Cl_2, 298 K) of **6**.

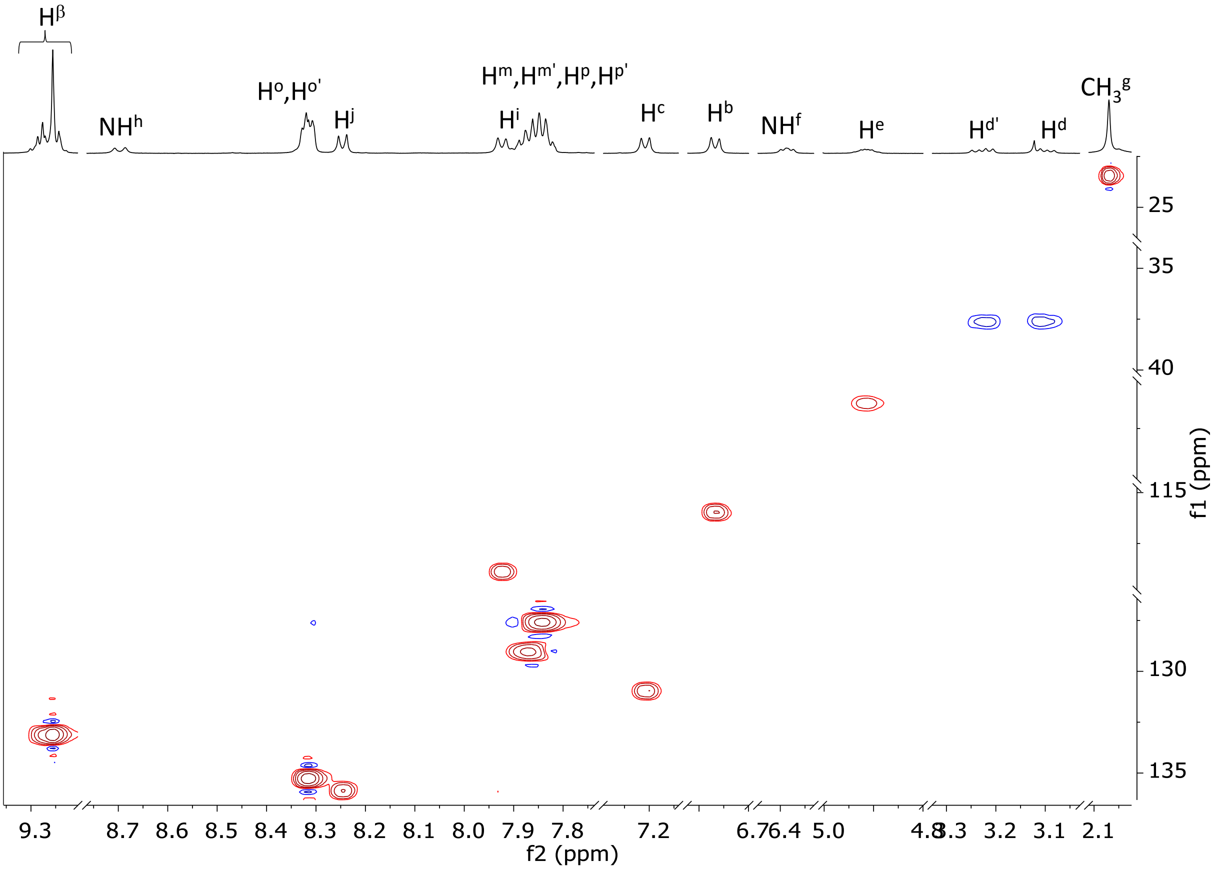

Figure S35. ^{1}H-^{13}C HSQC spectrum (CD_2Cl_2, 298 K) of **6**.

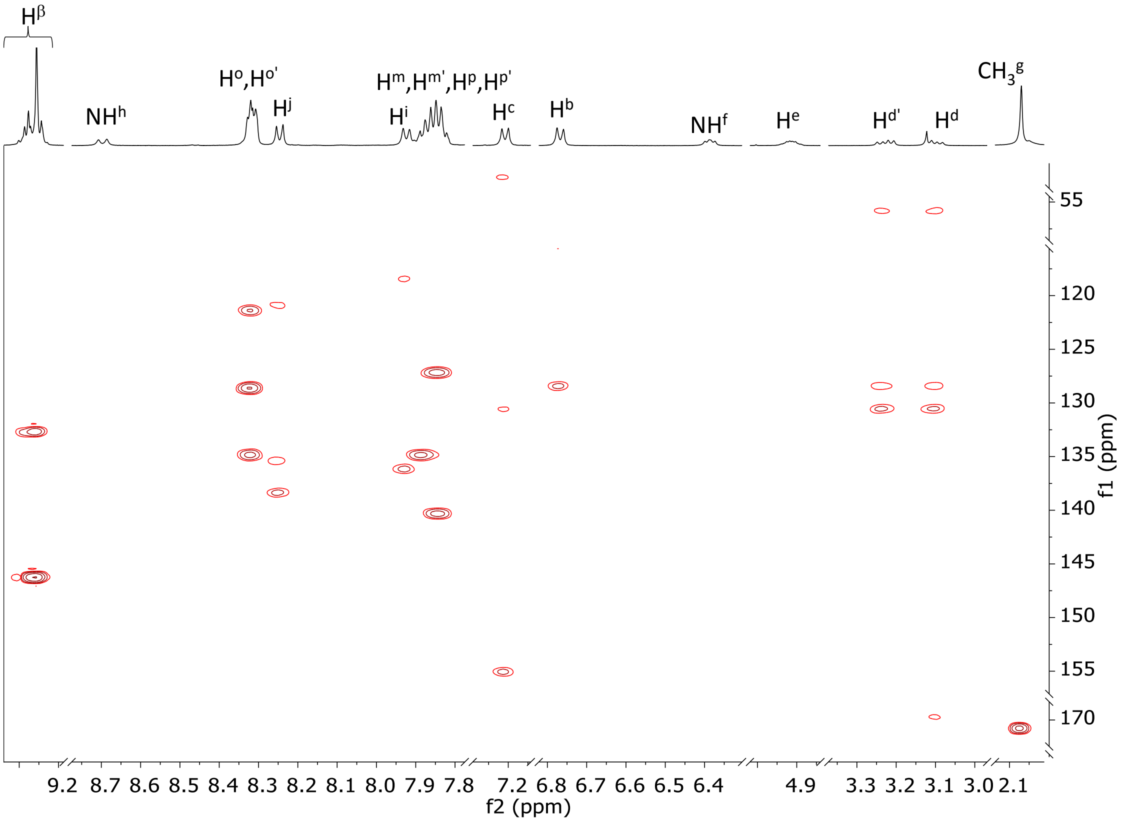

Figure S36. ^{1}H-^{13}C HMBC spectrum (CD_2Cl_2, 298 K) of **6**.

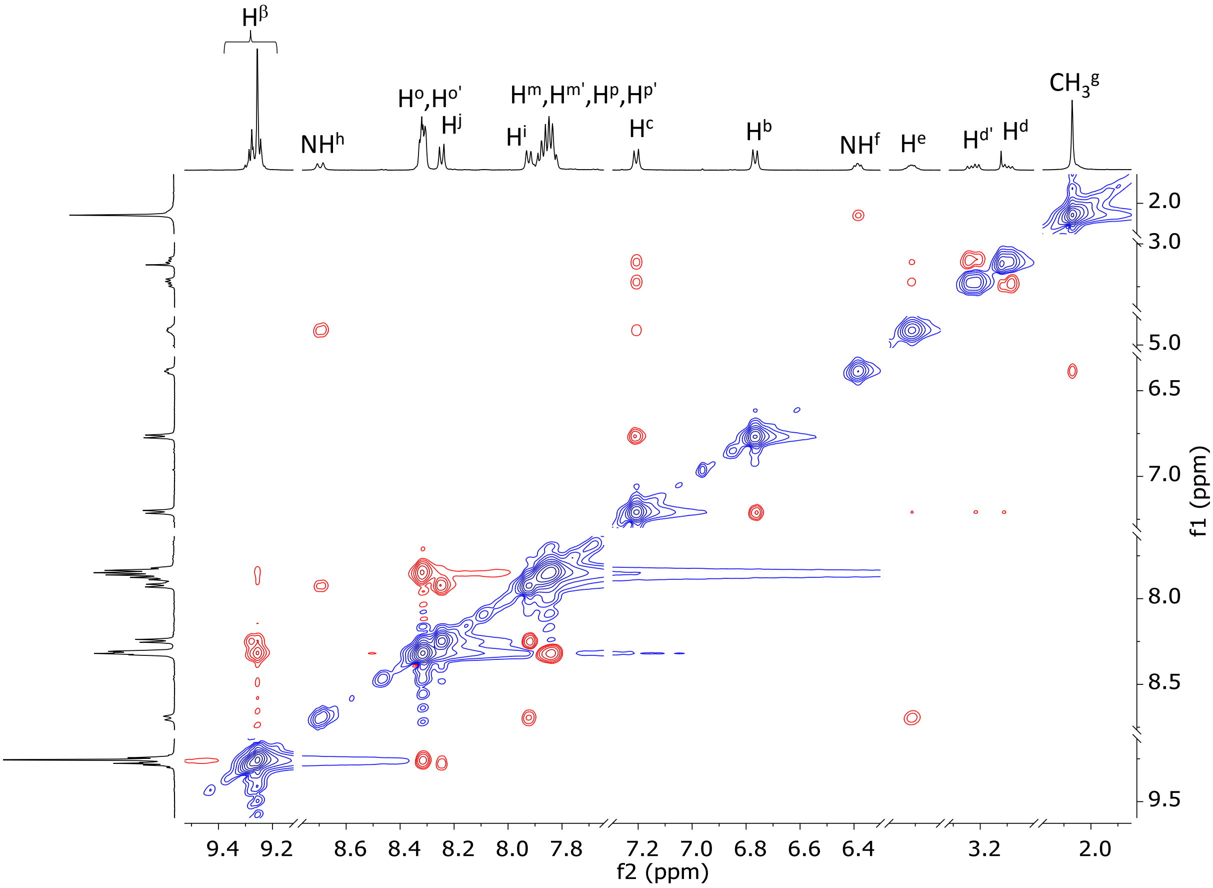

Figure S37. ^{1}H-^{1}H ROESY spectrum (CD_2Cl_2, 298 K) of **6**.

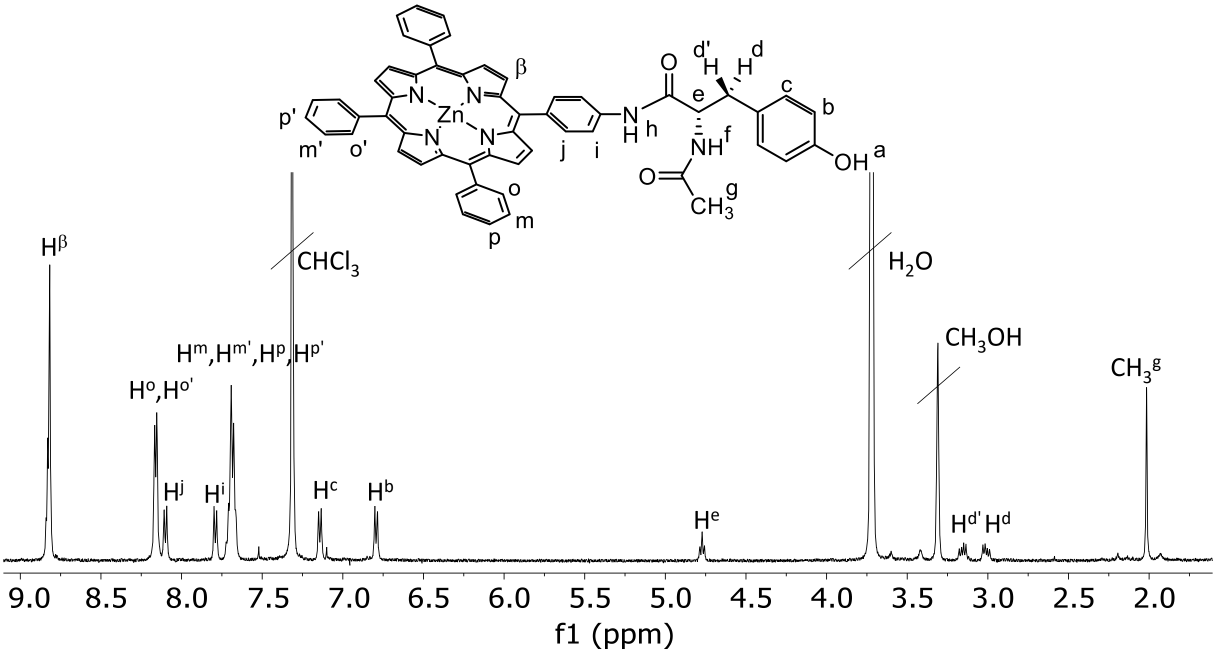

Figure S38. ^{1}H NMR spectrum ($CDCl_3$:CD_3OD 6:1, 298 K) of **ZnTPP-*p*Tyr** (**7**).

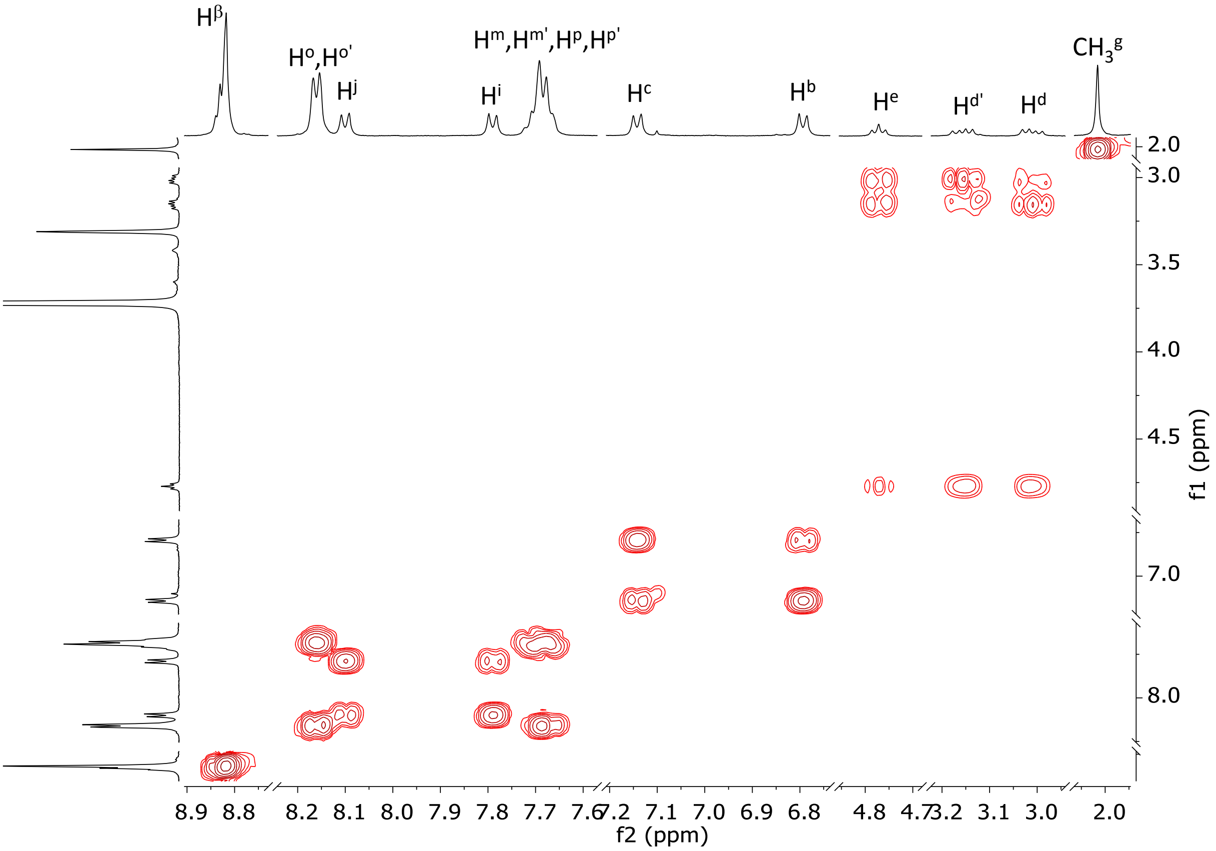

Figure S39. ^{1}H-^{1}H COSY spectrum (CDCl$_3$:CD$_3$OD 6:1, 298 K) of **7**.

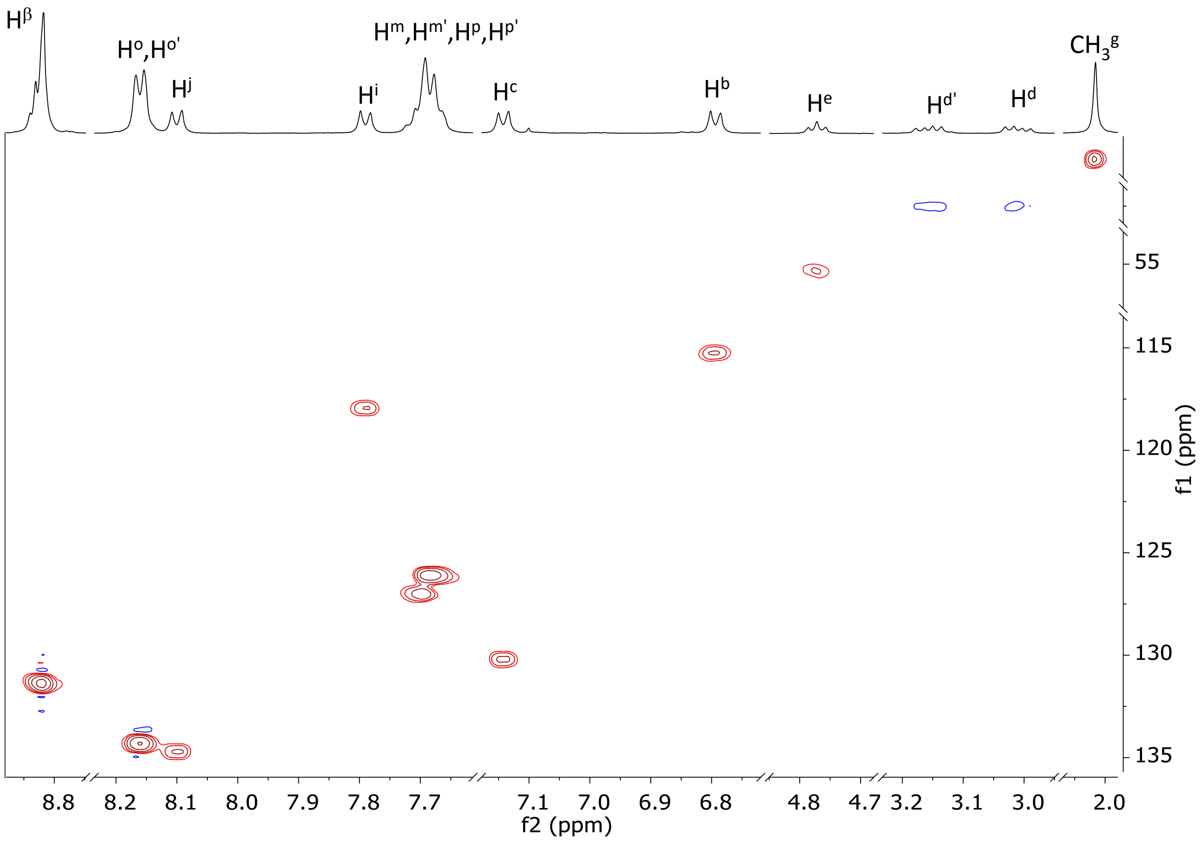

Figure S40. ^{1}H-^{13}C HSQC spectrum (CDCl$_3$:CD$_3$OD 6:1, 298 K) of **7**.

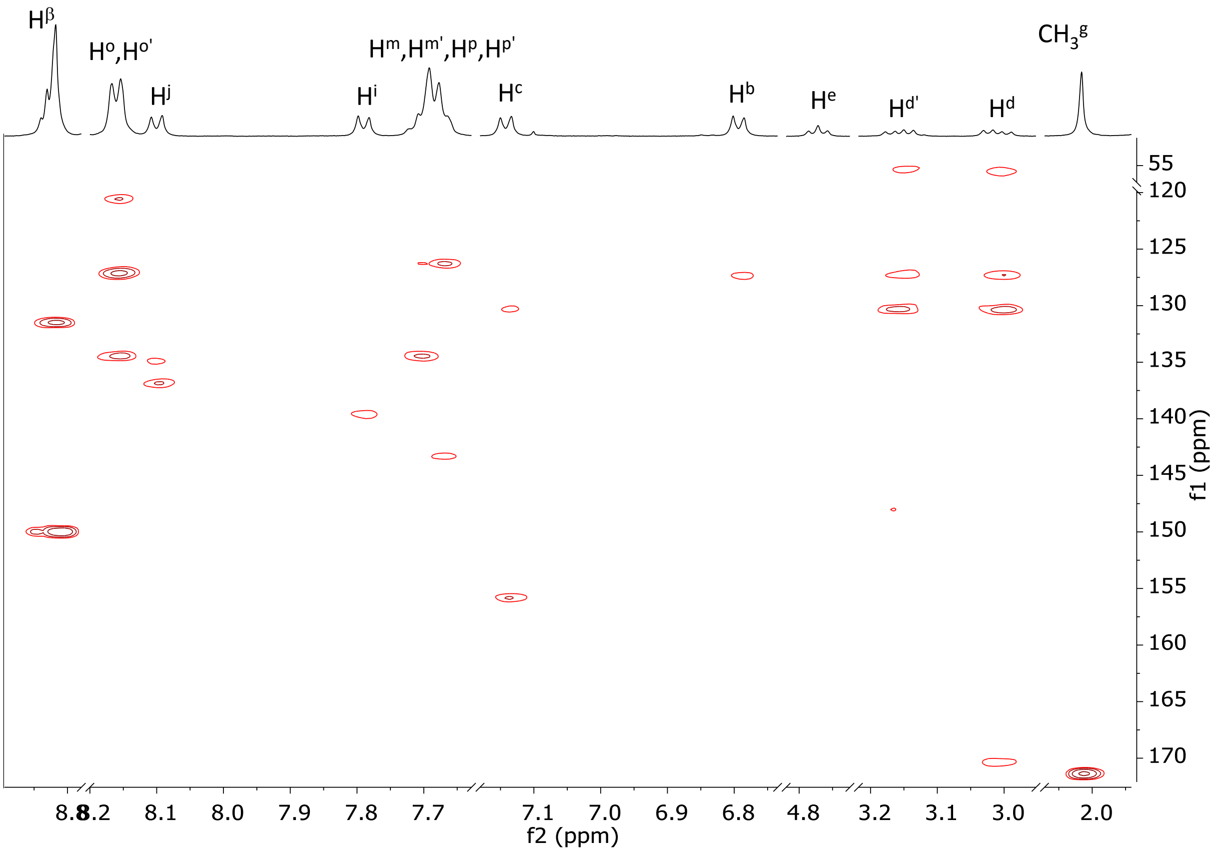

Figure S41. ^{1}H-^{13}C HMBC spectrum (CDCl$_3$:CD$_3$OD 6:1, 298 K) of **7**.

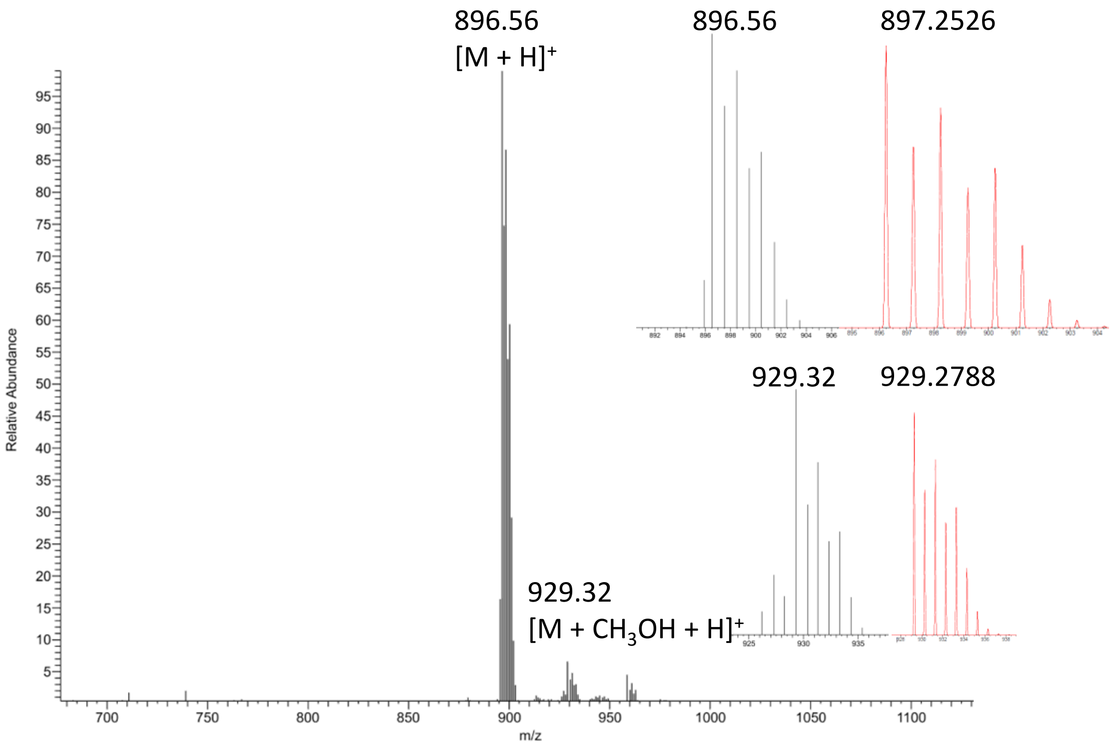

Figure S42. ESI-MS of **7** in CH$_3$OH, experimental (black) and simulated (red).

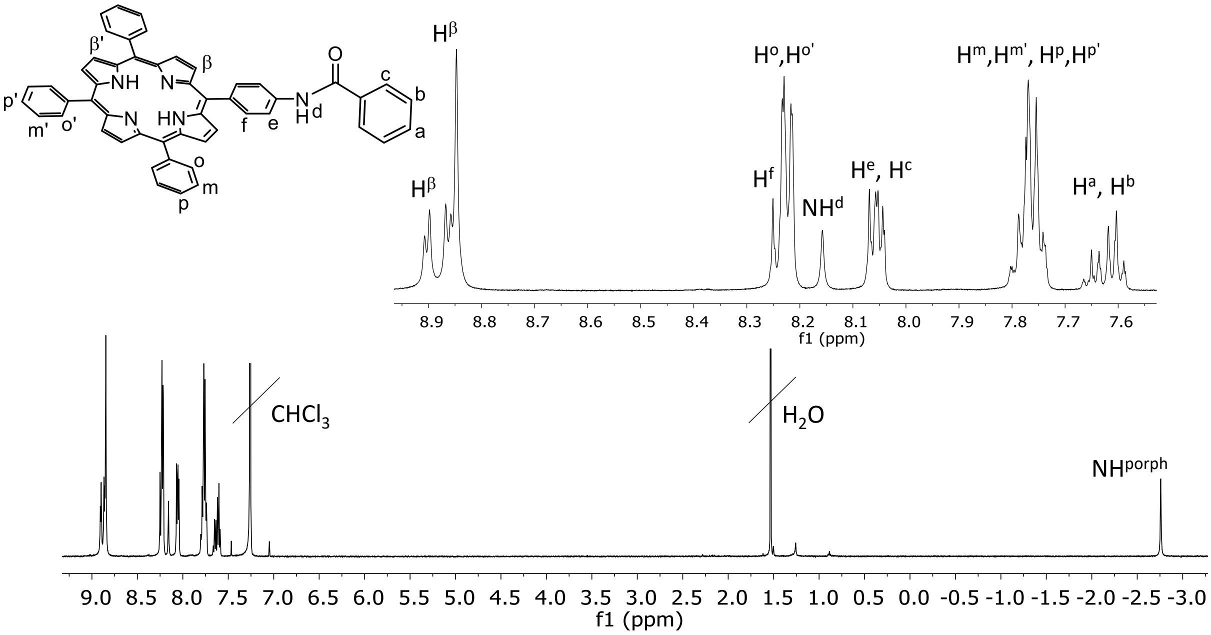

Figure S43. ^{1}H NMR spectrum (CDCl$_3$, 298 K) of **TPP-*p*BA** (**8**). Inset: enlargement of the aromatic region.

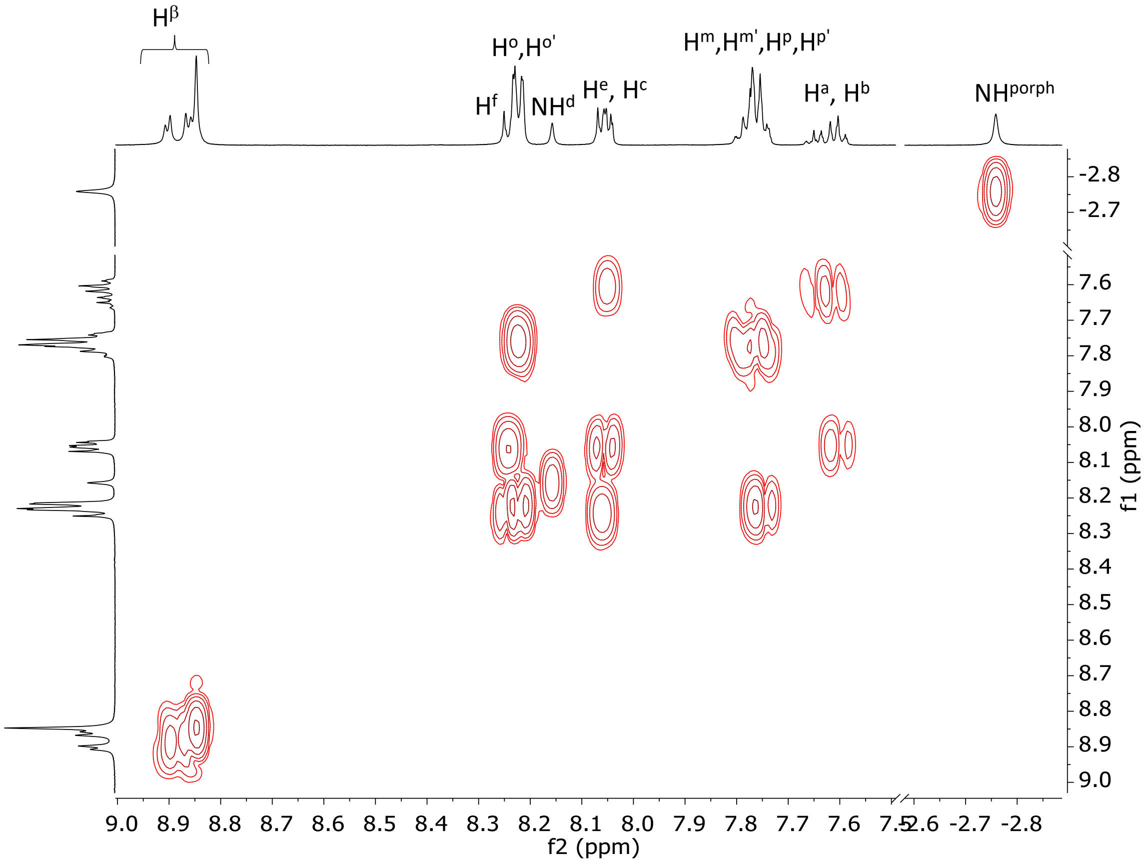

Figure S44. ^{1}H-^{1}H COSY spectrum (CDCl$_3$, 298 K) of **8**.

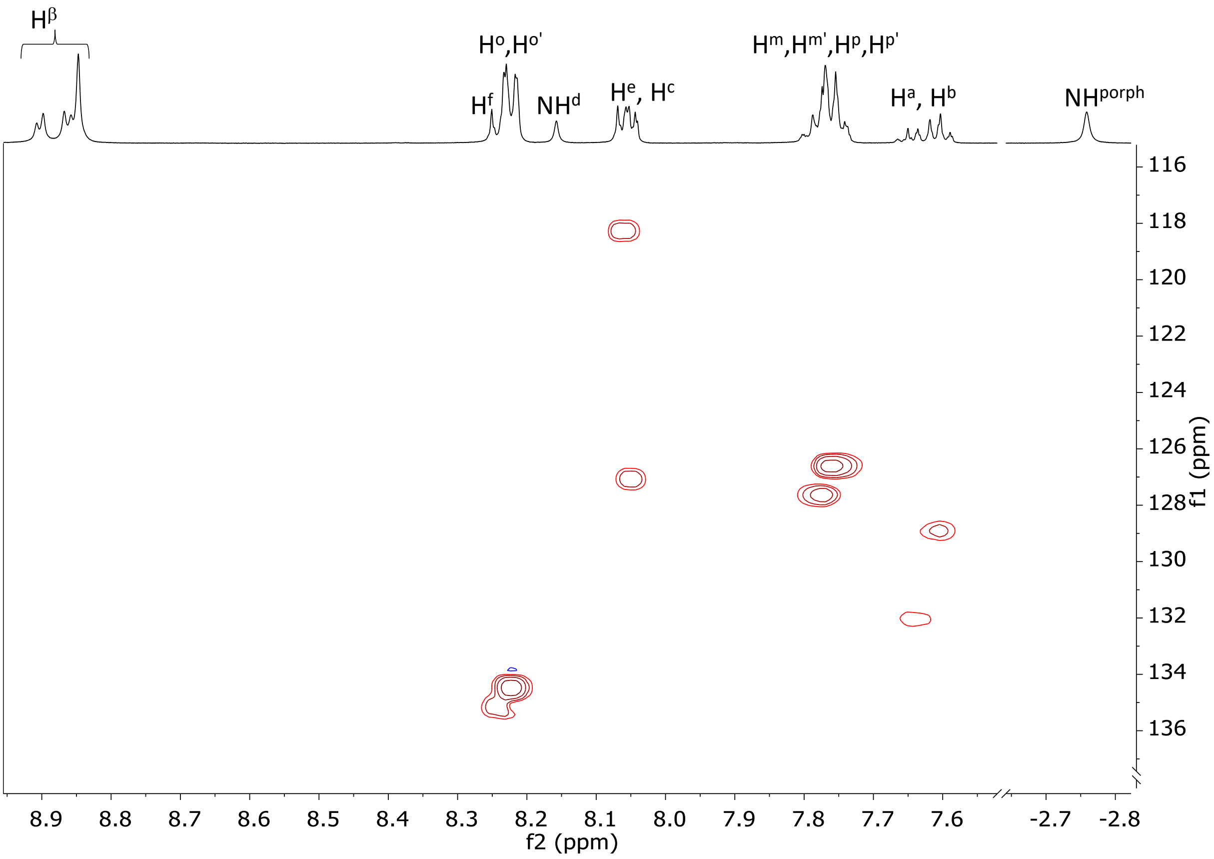

Figure S45. ^{1}H-^{13}C HSQC spectrum (CDCl$_3$, 298 K) of **8**.

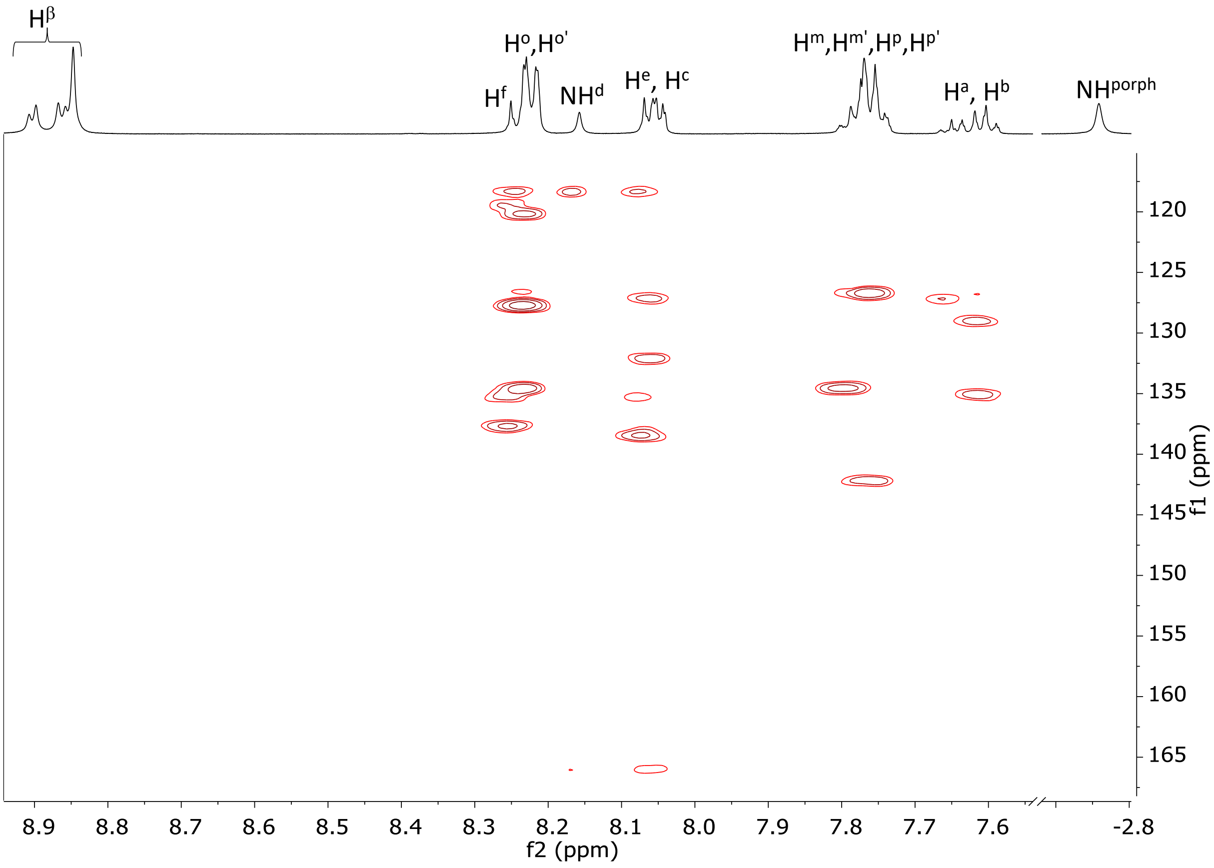

Figure S46. ^{1}H-^{13}C HMBC spectrum (CDCl$_3$, 298 K) of **8**.

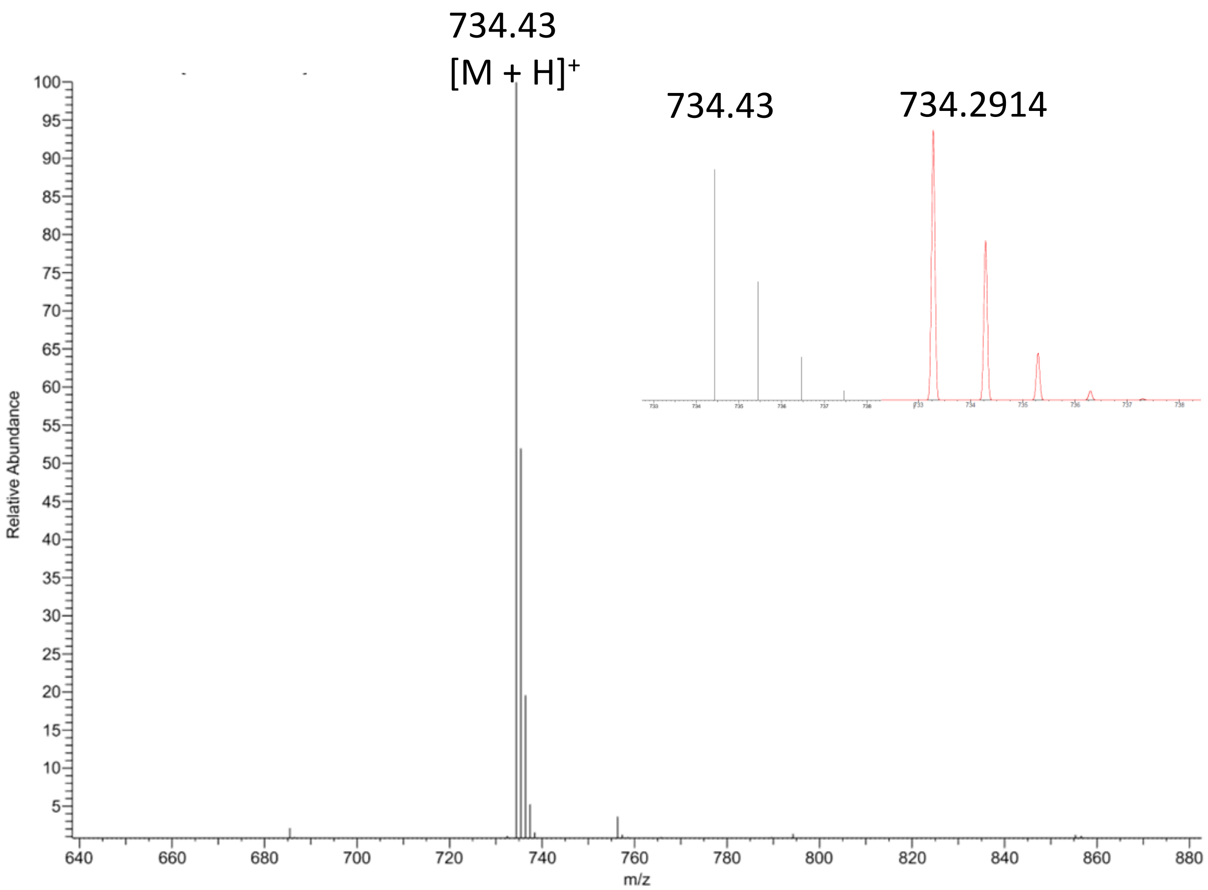

Figure S47. ESI-MS of **8** in CH_3OH, experimental (black) and simulated (red).

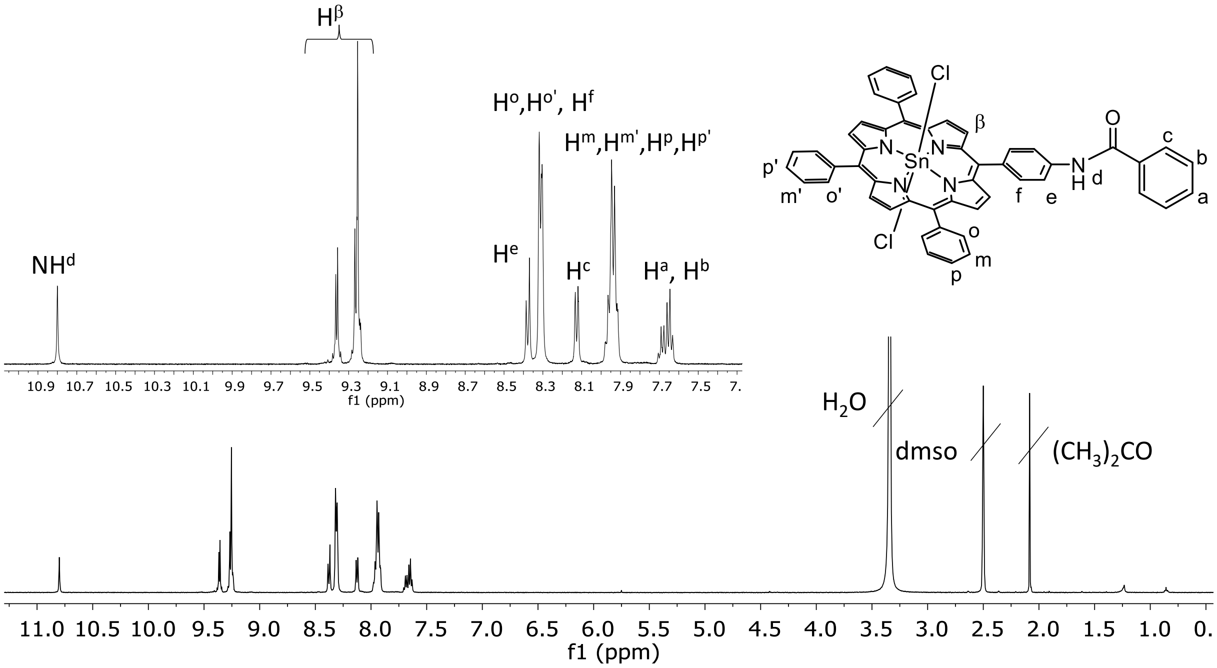

Figure S48. ^1H NMR spectrum (dmso-d_6, 298 K) of **$SnCl_2$TPP-*p*BA** (**9**). Inset: aromatic region.

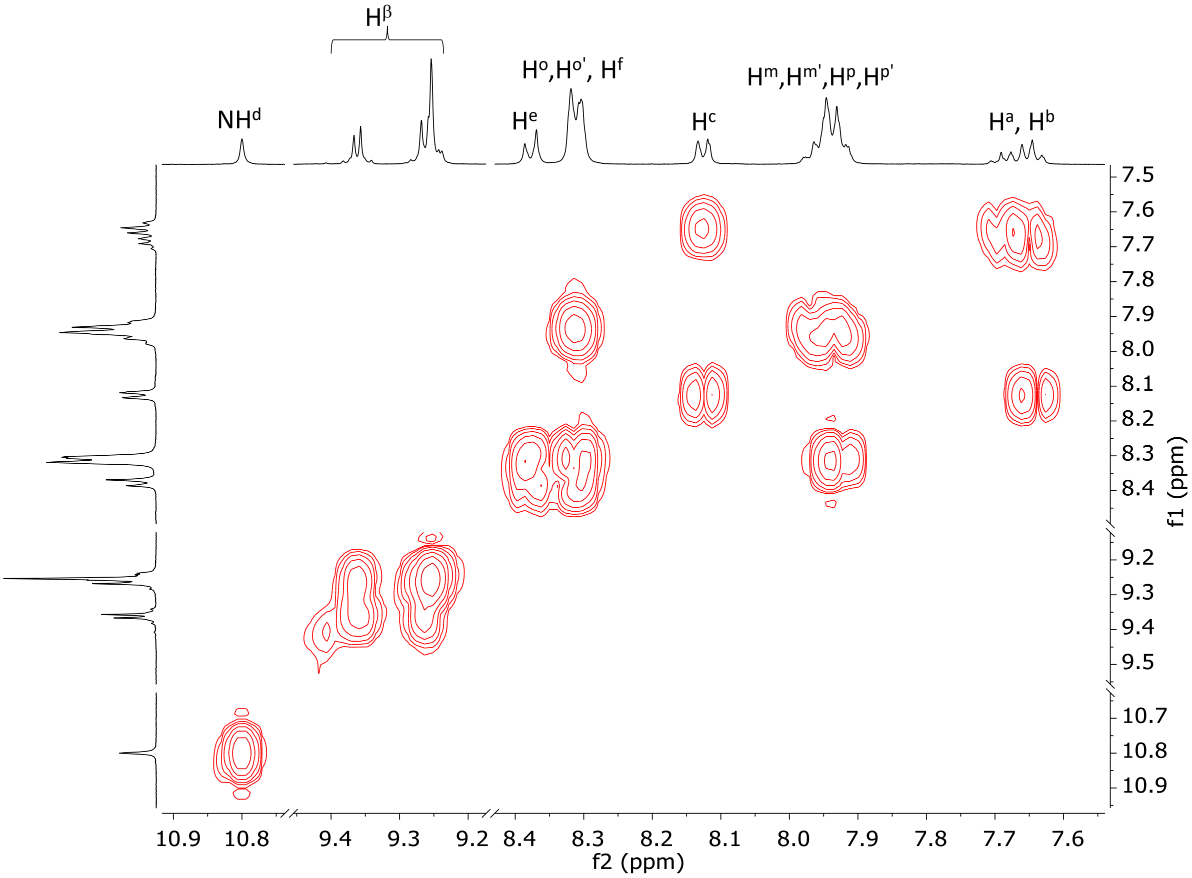

Figure S49. Aromatic region of the ^{1}H-^{1}H COSY spectrum (dmso-d_6, 298 K) of **9**.

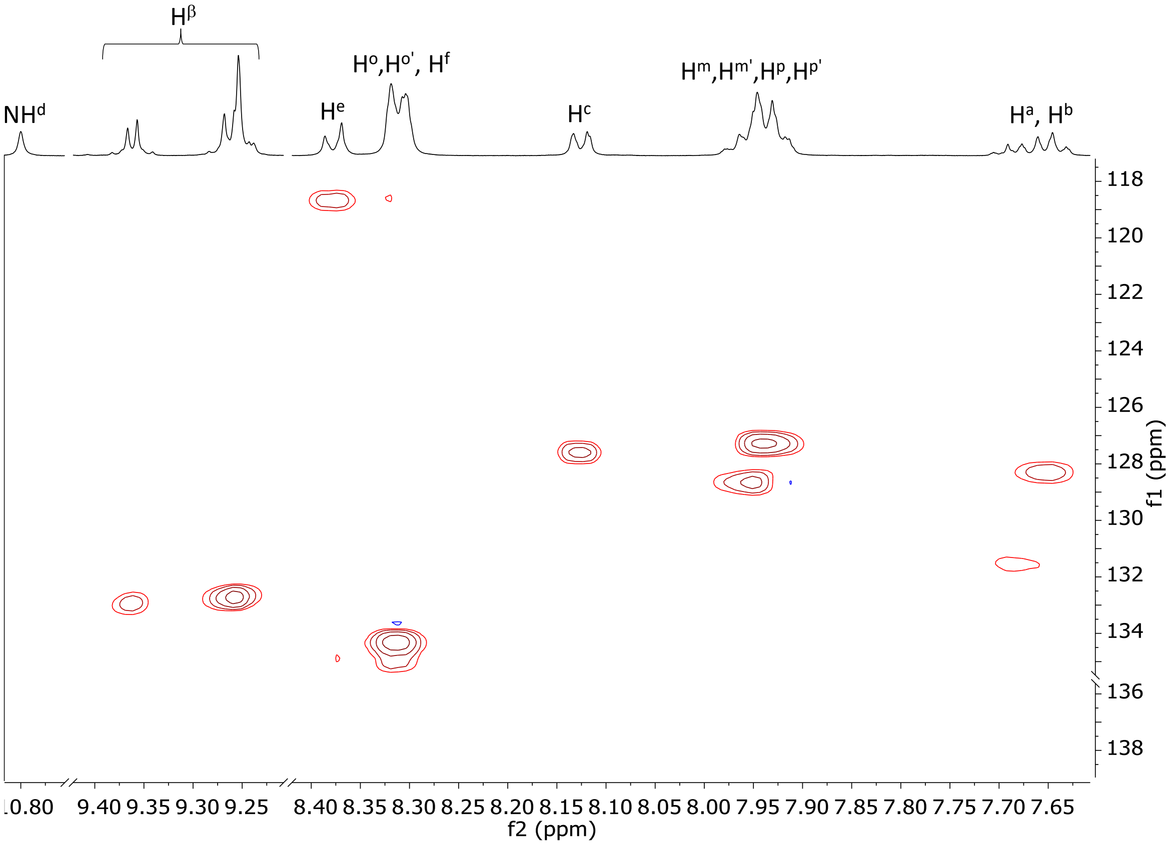

Figure S50. Aromatic region of the ^{1}H-^{13}C HSQC spectrum (dmso-d_6, 298 K) of **9**.

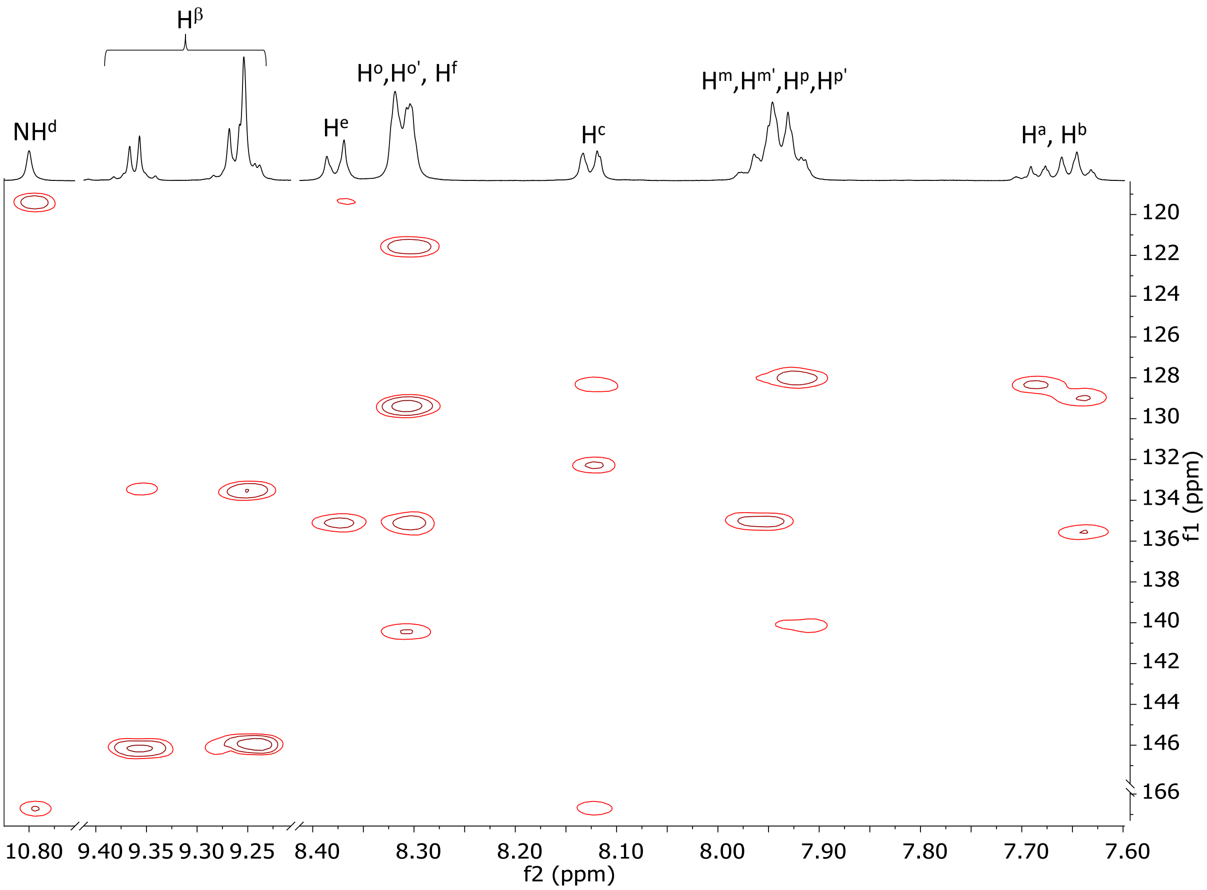

Figure S51. Aromatic region of the ^{1}H-^{13}C HMBC spectrum (dmso-d_6, 298 K) of **9**.

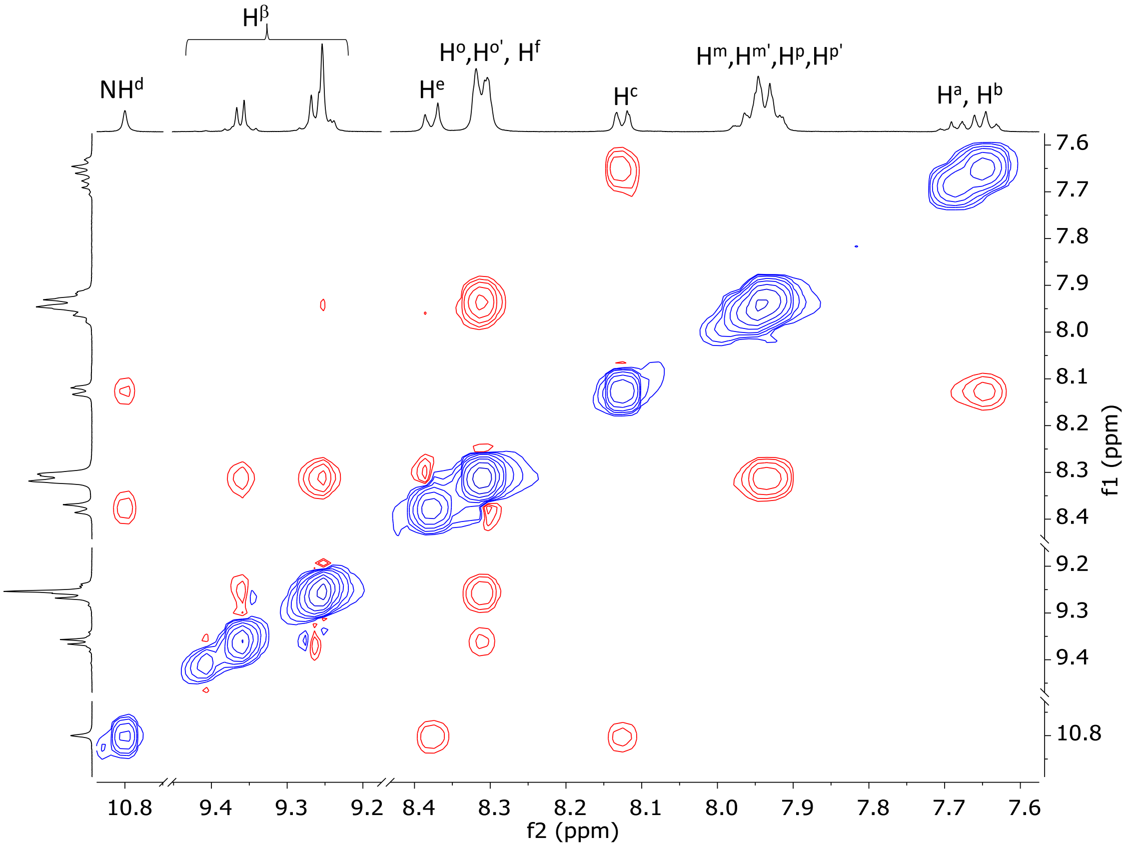

Figure S52. Aromatic region of the ^{1}H-^{1}H ROESY spectrum (dmso-d_6, 298 K) of **9**.

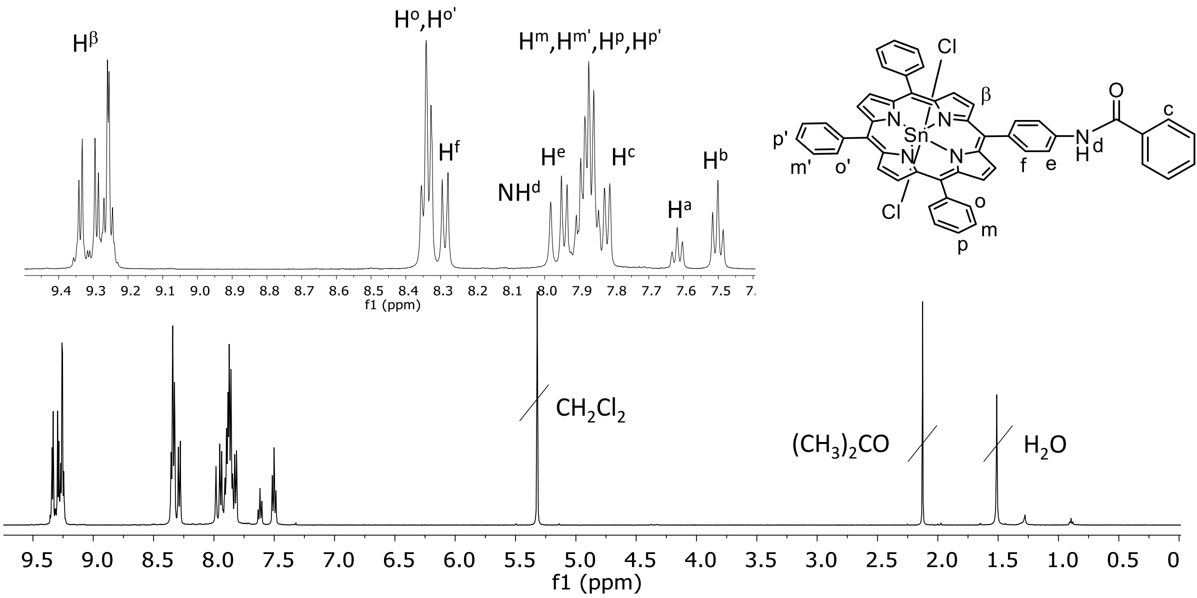

Figure S53. ^1H NMR spectrum (CD_2Cl_2, 298 K) of **9**. Inset: Aromatic region.

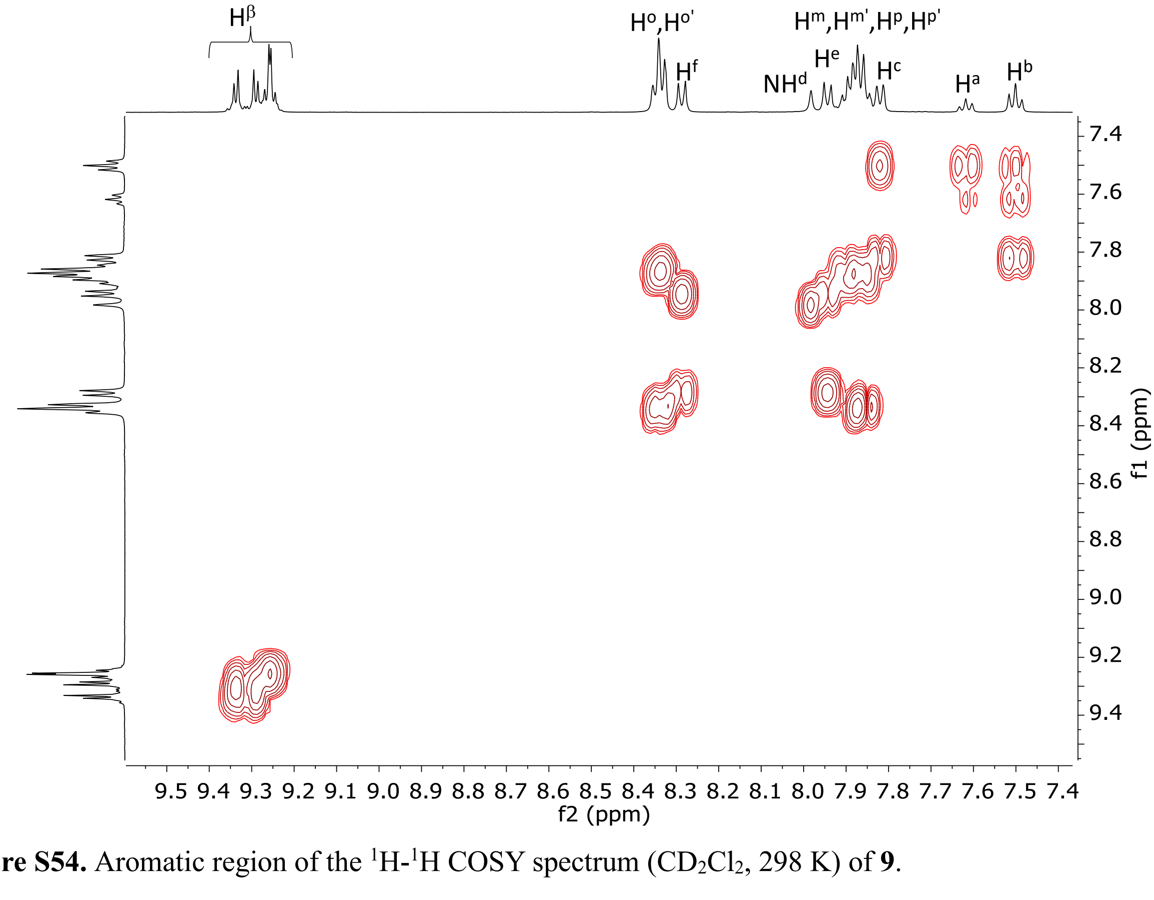

Figure S54. Aromatic region of the ^1H-^1H COSY spectrum (CD_2Cl_2, 298 K) of **9**.

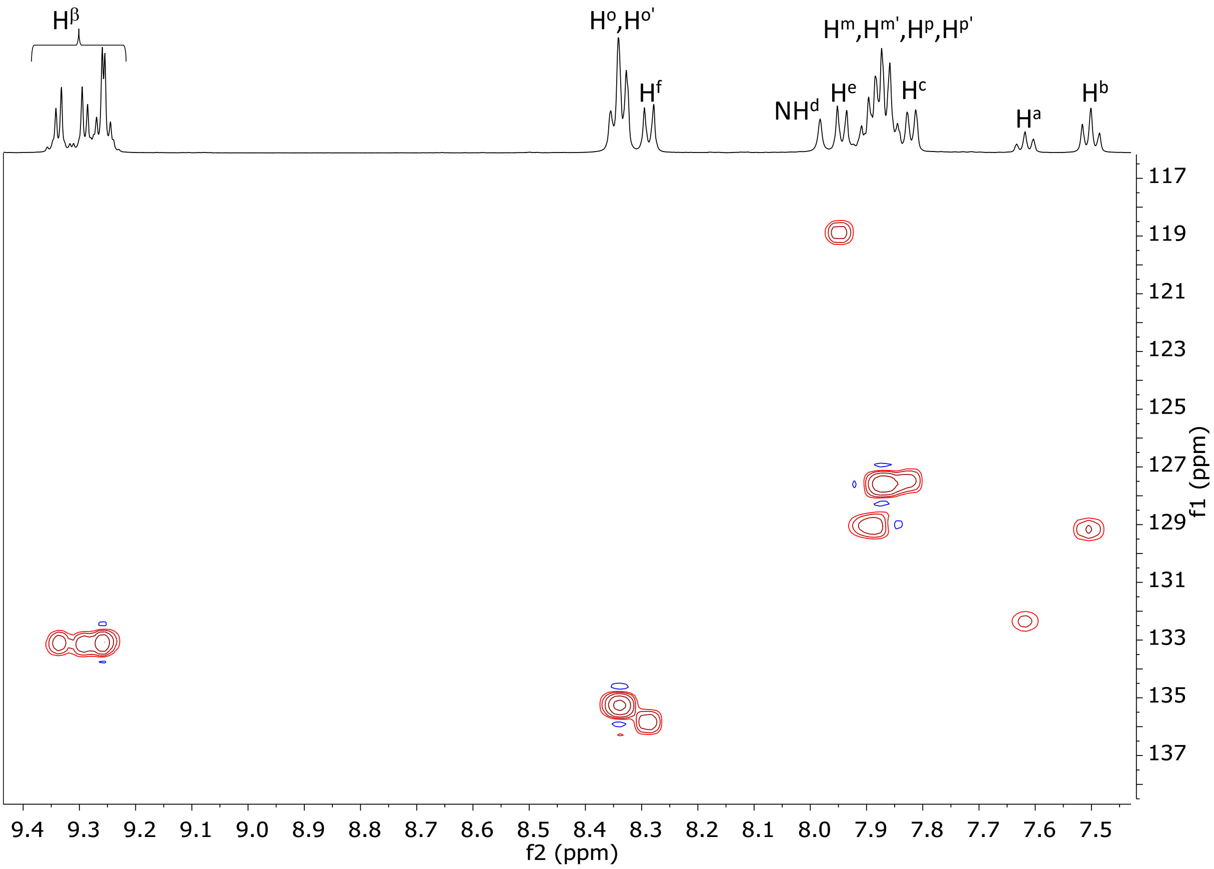

Figure S55. Aromatic region of the ^{1}H-^{13}C HSQC spectrum (CD_2Cl_2, 298 K) of **9**.

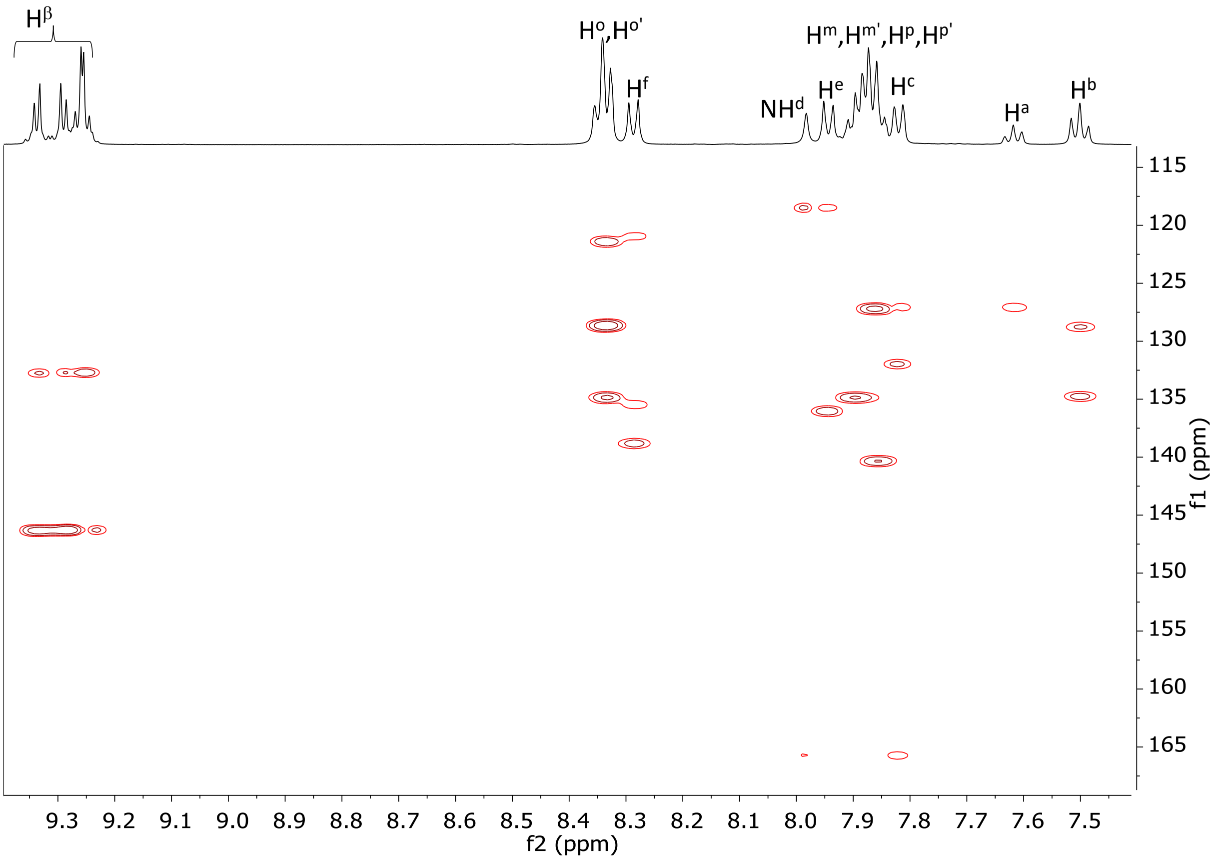

Figure S56. Aromatic region of the ^{1}H-^{13}C HMBC spectrum (CD_2Cl_2, 298 K) of **9**.

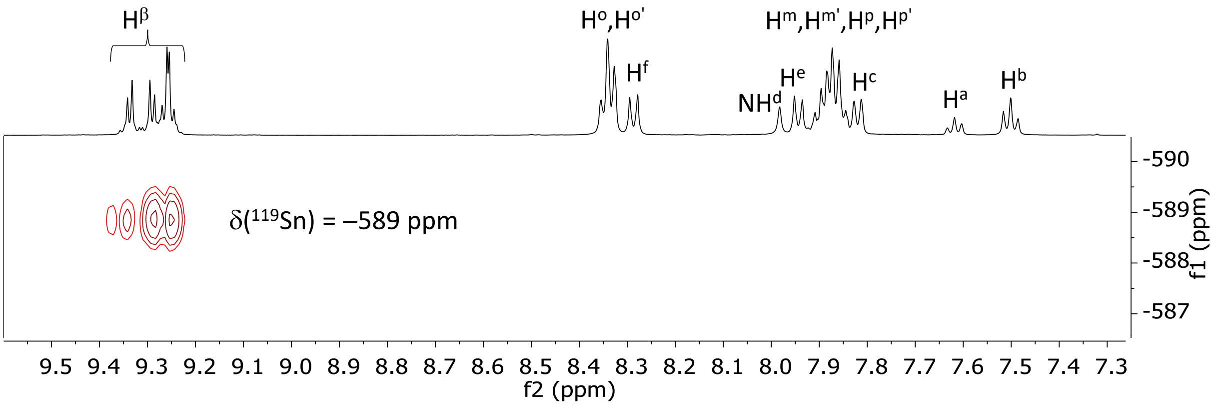

Figure S57. Aromatic region of the ^{1}H-^{119}Sn HMBC spectrum (CD_2Cl_2, 298 K) of **9**.

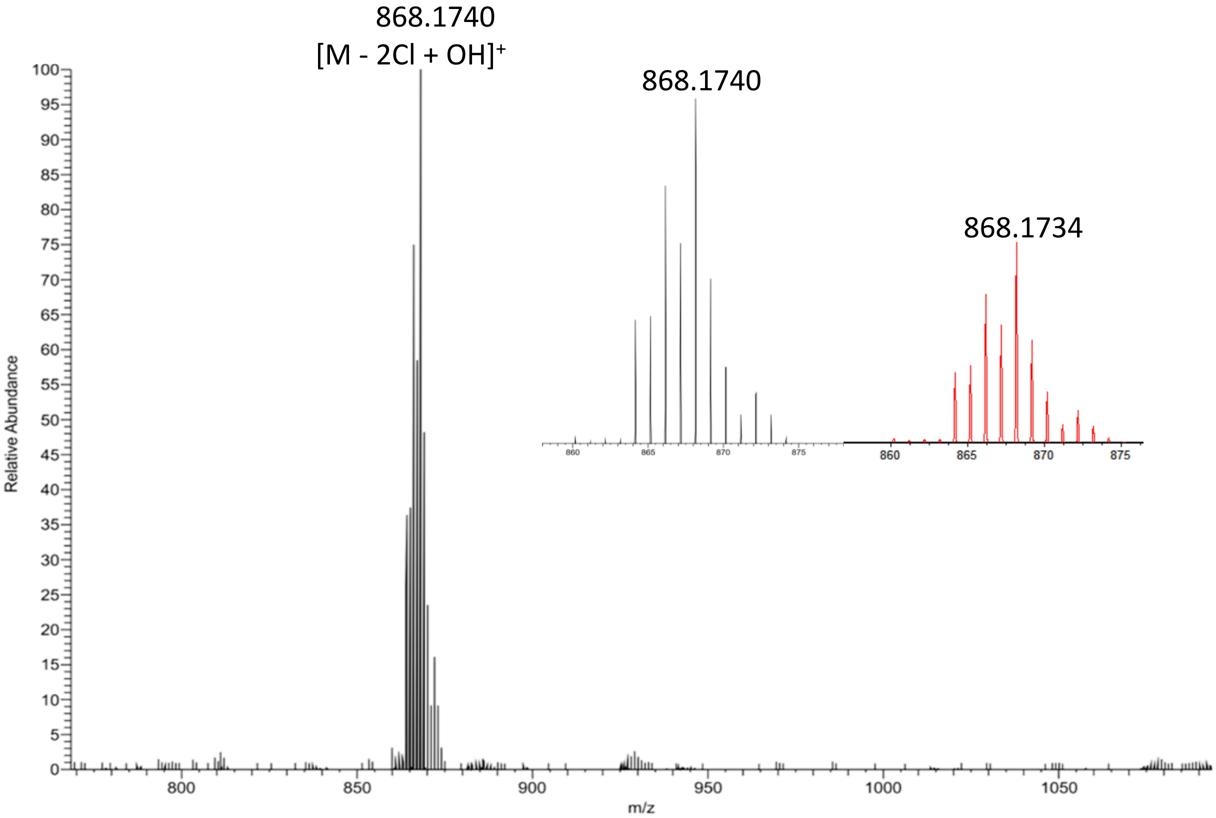

Figure S58. ESI-MS of **9** in CH_3OH, experimental (black) and simulated (red).

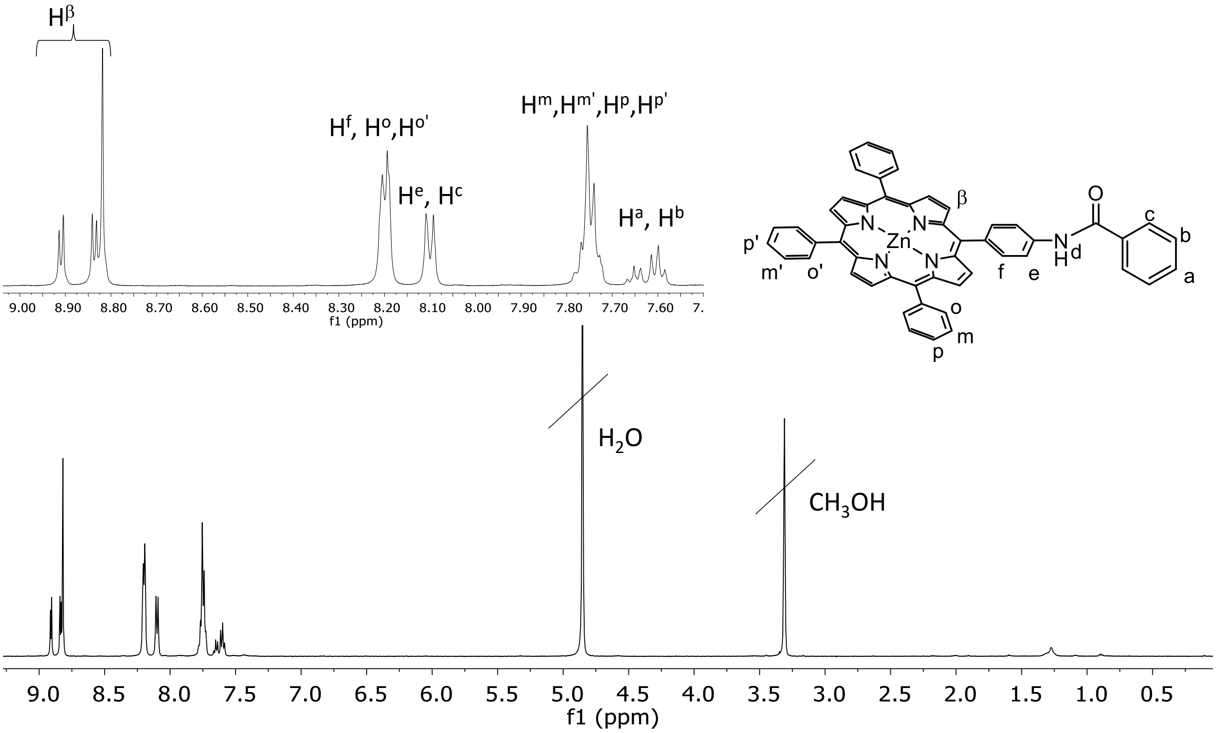

Figure S59. ^{1}H NMR spectrum (CD_3OD, 298 K) of **ZnTPP-*p*BA** (**10**). Inset: Aromatic region.

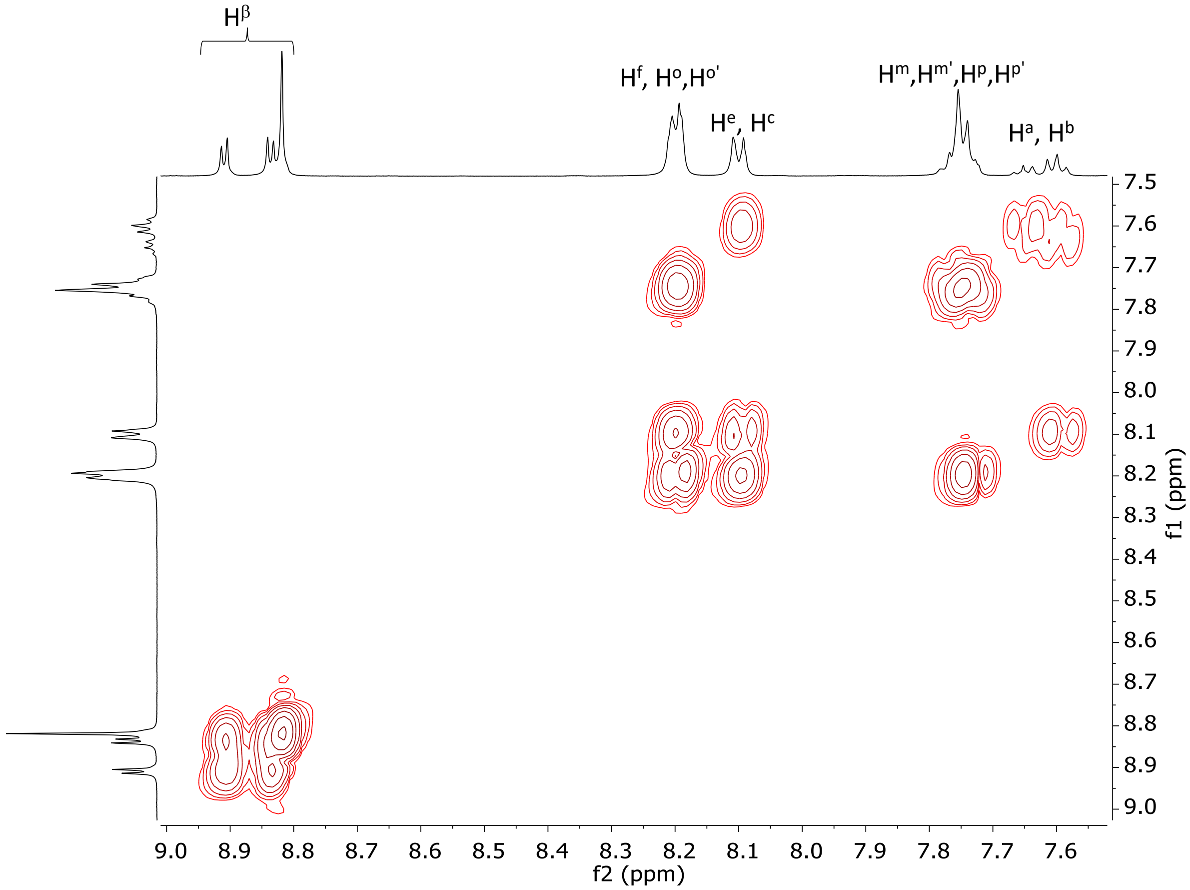

Figure S60. Aromatic region of the ^{1}H-^{1}H COSY spectrum (CD_3OD, 298 K) of **10**.

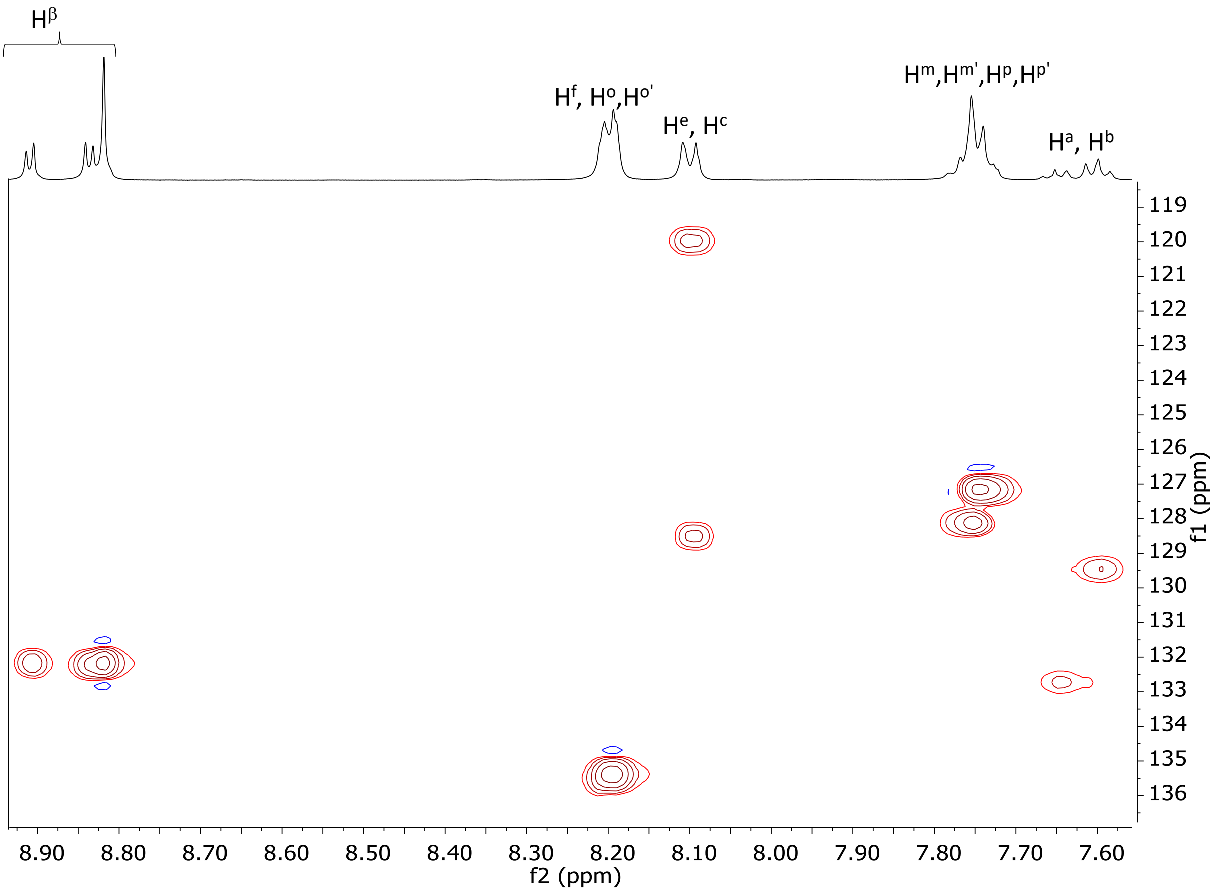

Figure S61. Aromatic region of the ^{1}H-^{13}C HSQC spectrum (CD$_3$OD, 298 K) of **10**.

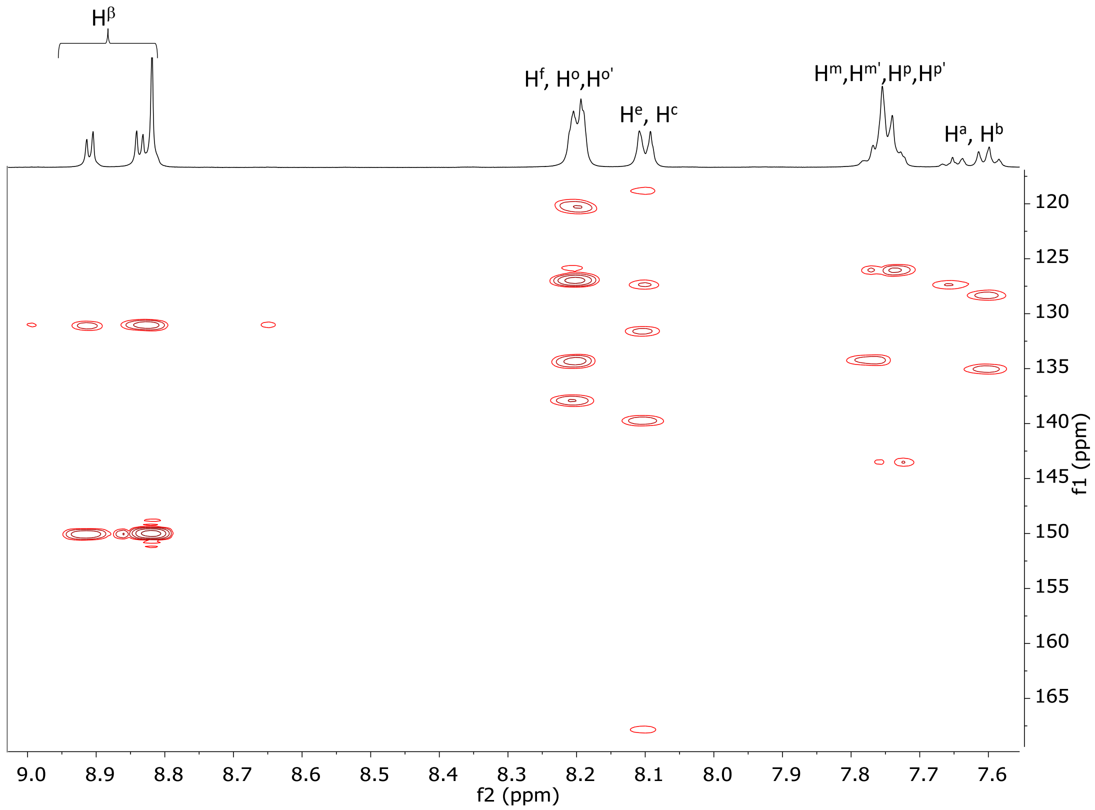

Figure S62. Aromatic region of the ^{1}H-^{13}C HMBC spectrum (CD$_3$OD, 298 K) of **10**.

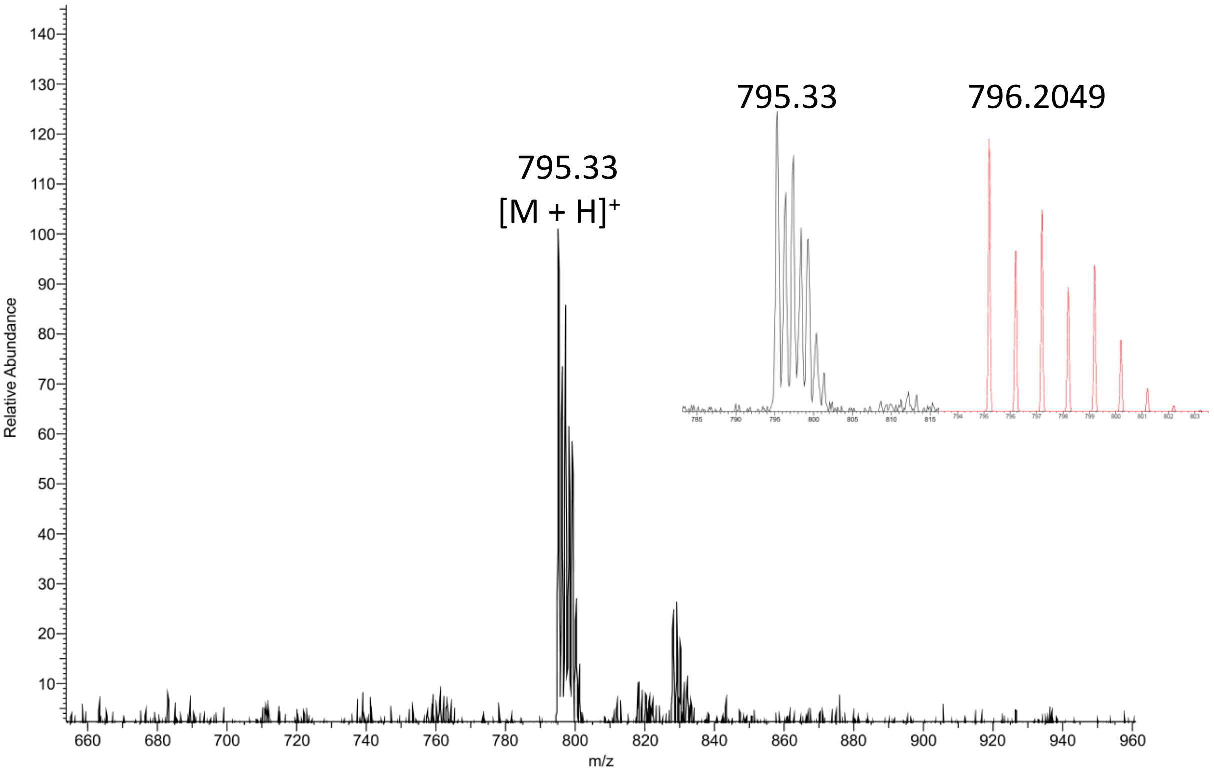

Figure S63. ESI-MS (m/z) (positive mode) of **10** in CH_3OH, experimental (black) and simulated (red).

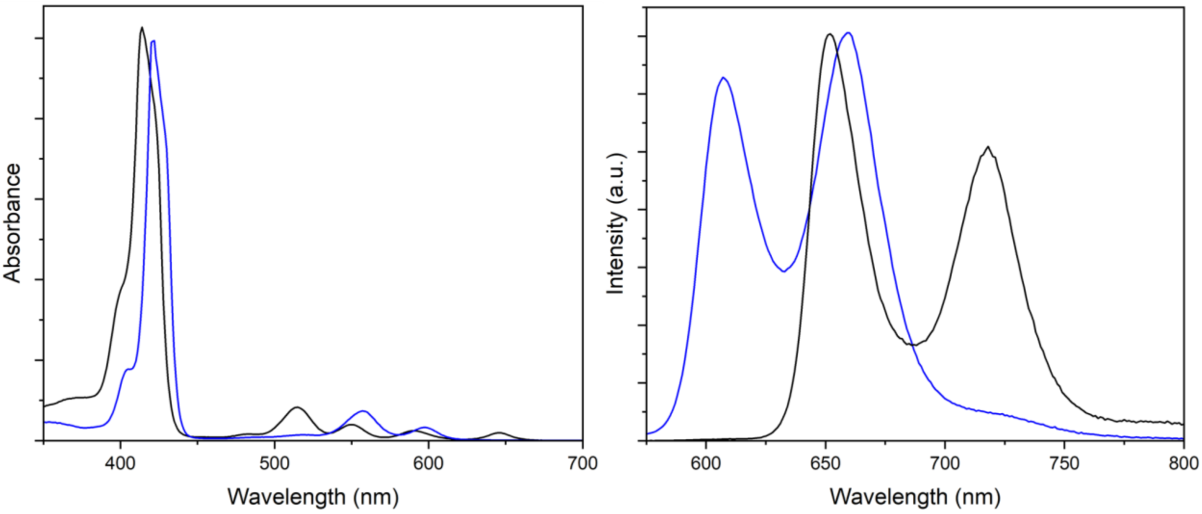

Figure S64. Left: UV-Vis absorption spectra (CH_2Cl_2, 25 μM) of **TPP-*p*BA** (**8**) and **ZnTPP-*p*BA** (**10**). Right: Emission spectra of **8** and **10** (CH_2Cl_2, 25 μM, λ_{irr} = 515 nm for **8**, λ_{irr} = 558 nm for **10**, black and blue traces respectively).

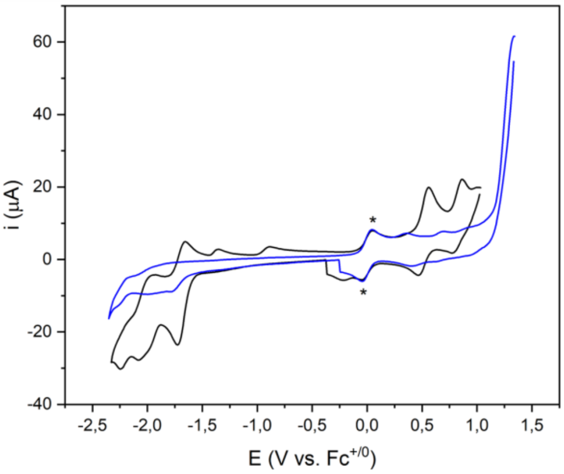

Figure S65. Cyclic voltammetry (CV) of 1 mM CH_2Cl_2 solutions of **8** and **10** (black and blue traces, respectively) recorded at 0.1 V/s with 0.1 M $TBAPF_6$ as supporting electrolyte under inert atmosphere using a glassy carbon as working electrode, a platinum wire as a counter electrode, SCE (saturated calomel electrode) as reference and ferrocene (*) as internal standard.

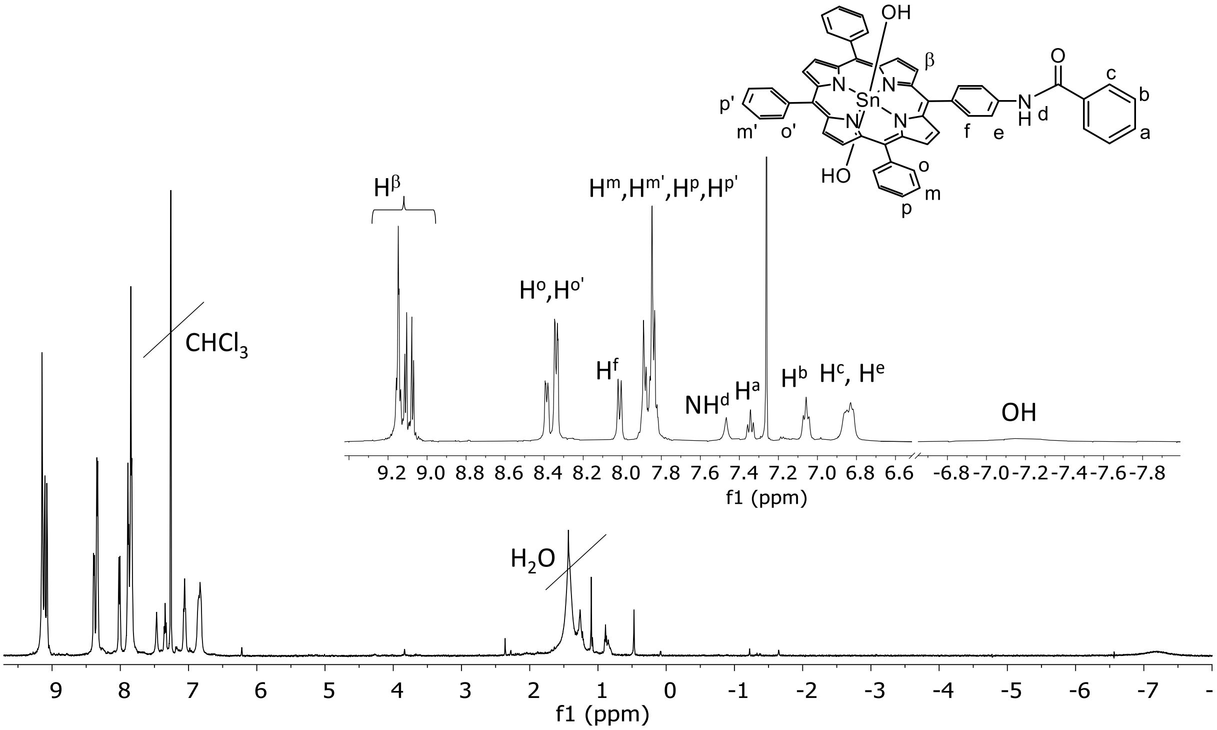

Figure S66. ^1H NMR spectrum ($CDCl_3$, 298 K) of **$Sn(OH)_2$TPP-*p*BA** (**11**). Inset: enlargement of the aromatic and up-field regions.

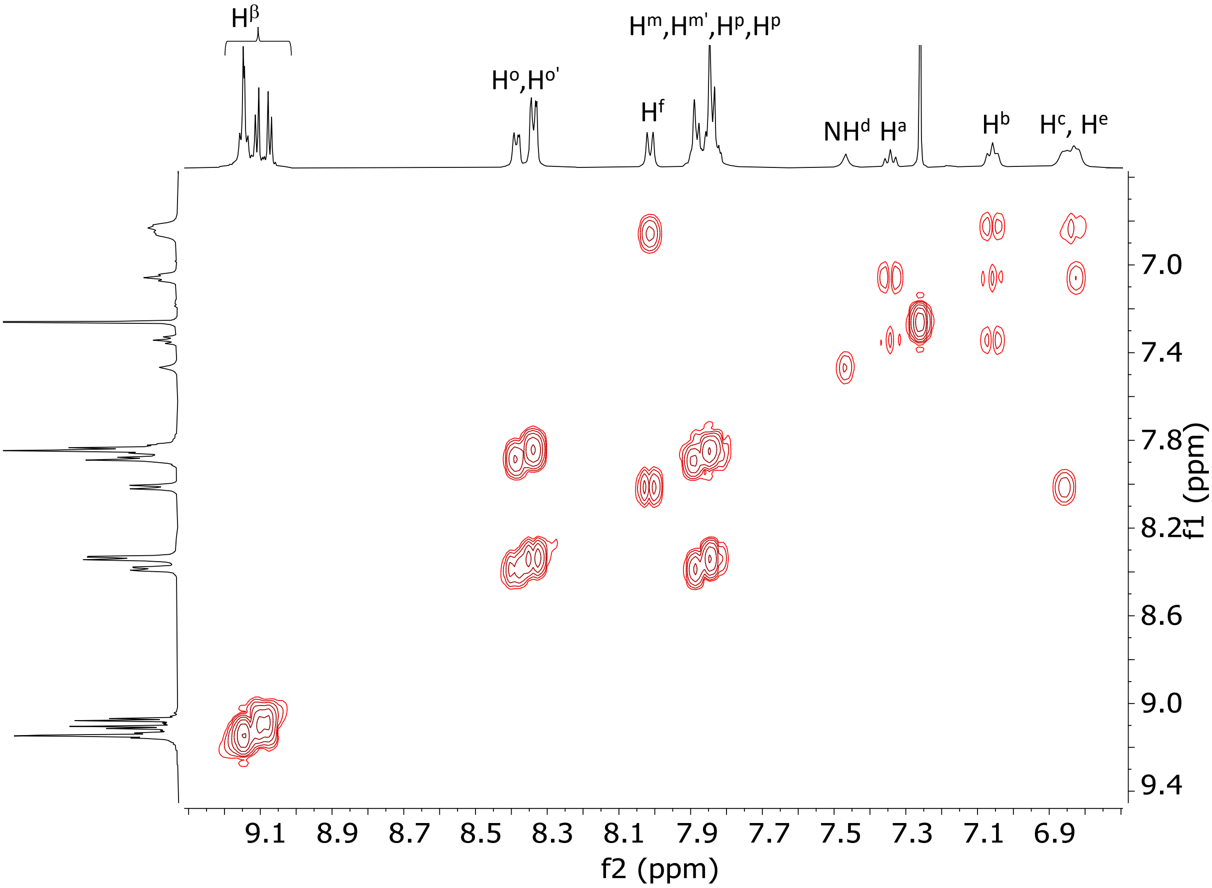

Figure S67. Aromatic region of the ^{1}H-^{1}H COSY spectrum (CDCl$_3$, 298 K) of **11**.

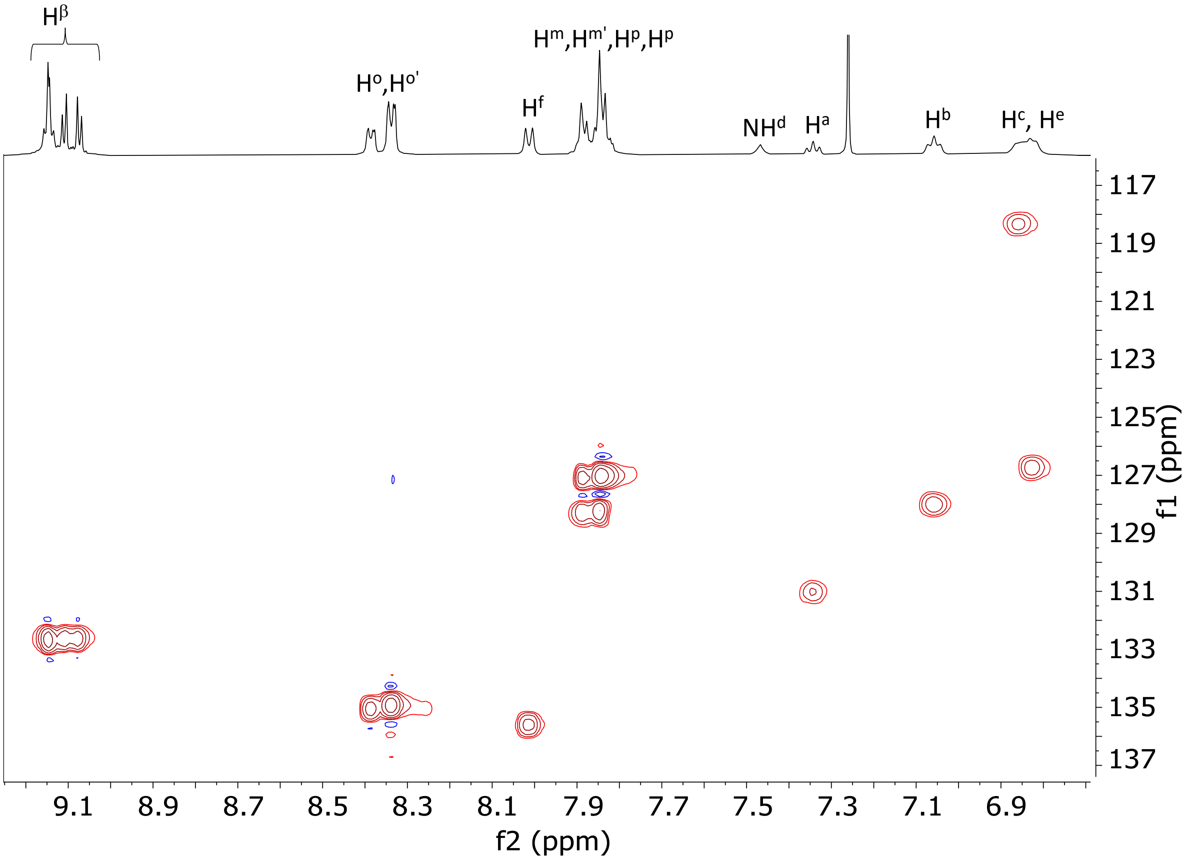

Figure S68. Aromatic region of the ^{1}H-^{13}C HSQC spectrum (CDCl$_3$, 298 K) of **11**.

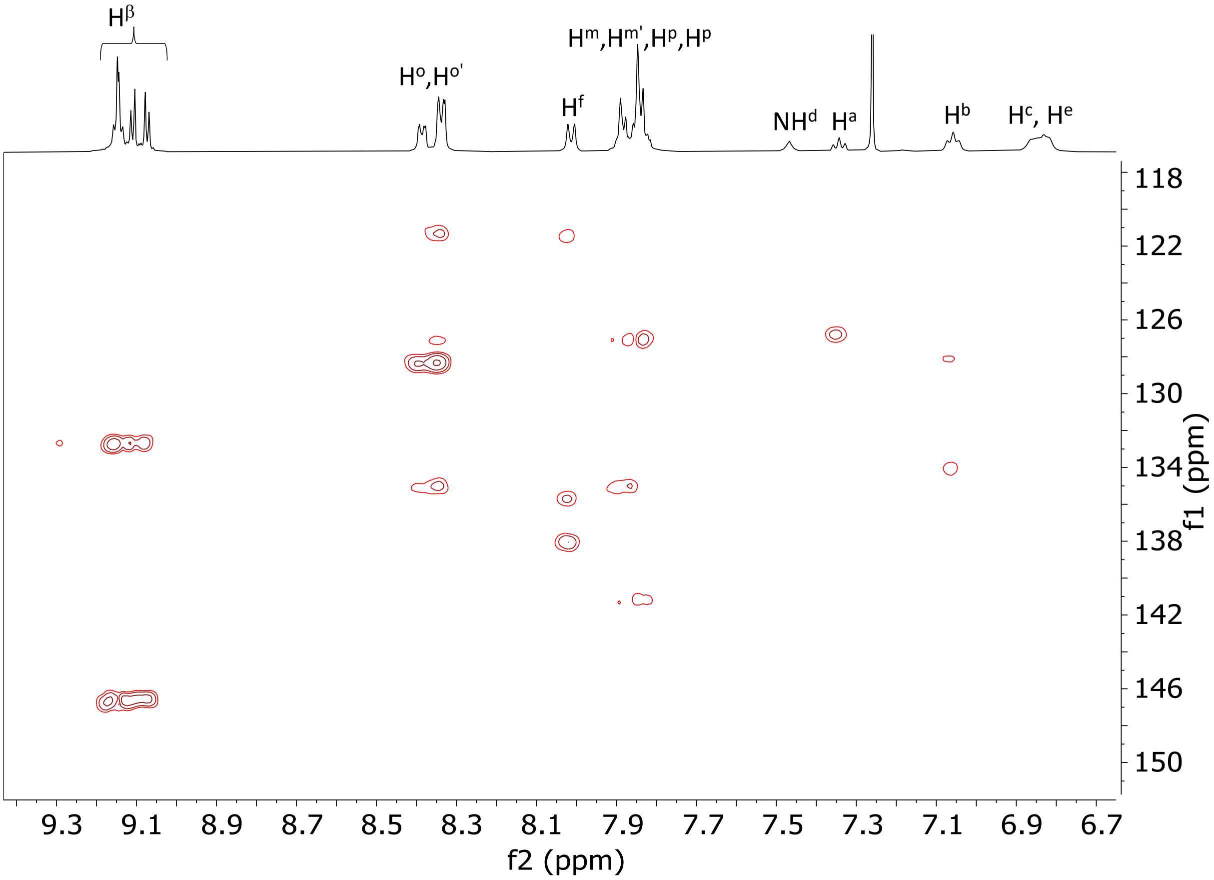

Figure S69. Aromatic region of the ^{1}H-^{13}C HMBC spectrum ($CDCl_3$, 298 K) of **11**.

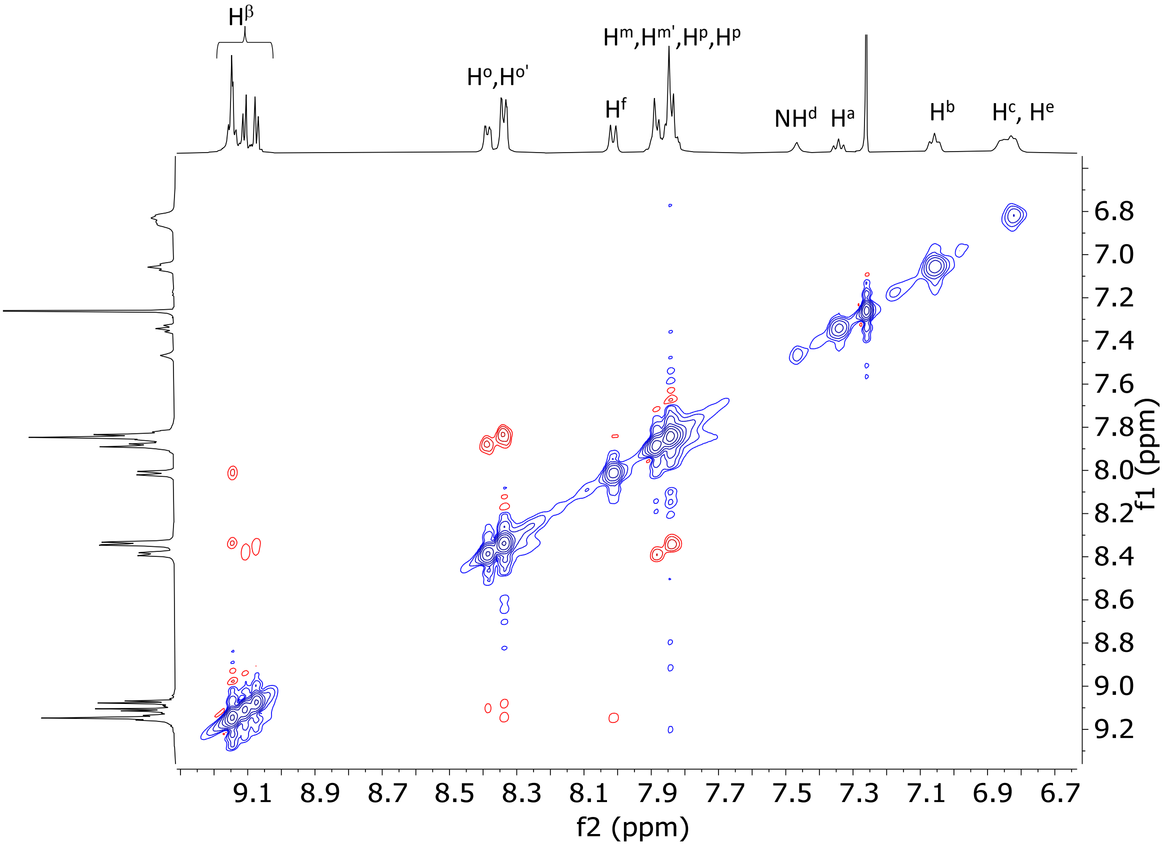

Figure S70. Aromatic region of the ^{1}H-^{1}H ROESY spectrum ($CDCl_3$, 298 K) of **11**.

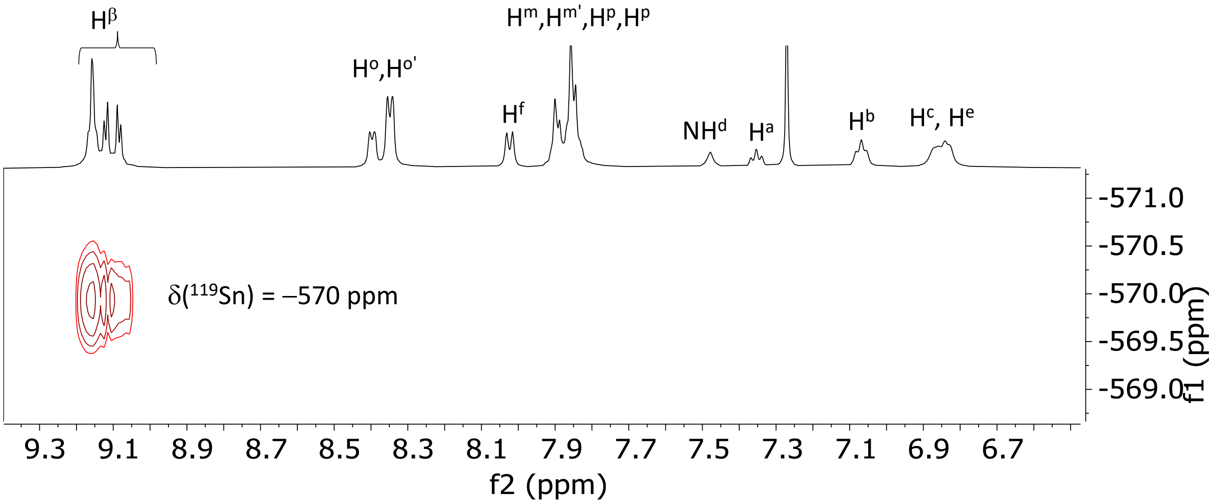

Figure S71. Aromatic region of the ^{1}H-^{119}Sn HMBC spectrum ($CDCl_3$, 298 K) of **11**.

Table S1. Crystallographic data and refinement details for **6**.

Compound name	$SnCl_2$TPP-*p*Tyr (**6**)
Formula	$C_{59}H_{58}Cl_2N_8O_9Sn$
Formula weight (Da)	1212.72
Temperature (K)	100(2)
Wavelength (Å)	0.700
Crystal System	Monoclinic
Space Group	P 21/n
a (Å)	19.331(8)
b (Å)	9.403(8)
c (Å)	34.459(13)
α (°)	90
β (°)	91.245(7)
γ (°)	90
V (Å^{3})	6262(6)
Z	4
ρ (g cm^{-3})	1.286

Table S2. Selected bond distances, angles and dihedral angles for **6**.

Selected distances (Å)		Selected angles (°)		Selected dihedral angles (°)	
Sn1 Cl1	2.448(3)	Cl1 Sn1 Cl2	178.65(8)	[C21] [Sn1]	76.8(3)
Sn1 Cl2	2.466(3)	N1 Sn1 Cl1	90.2(2)	[C27] [Sn1]	62.4(3)
Sn1 N1	2.078(8)	N1 Sn1 Cl2	90.7(2)	[C33] [Sn1]	83.4(4)
Sn1 N2	2.120(8)	N1 Sn1 N2	89.9(3)	[C39] [Sn1]	71.5(3)
Sn1 N3	2.100(8)	N1 Sn1 N3	179.3(3)	[C27] [C48]	9.8(9)
Sn1 N4	2.094(8)	N1 Sn1 N4	88.8(3)		
		N2 Sn1 Cl1	90.3(2)		
		N2 Sn1 Cl2	88.7(2)		
		N3 Sn1 Cl1	89.1(2)		
		N3 Sn1 Cl2	90.0(2)		
		N3 Sn1 N2	90.3(3)		
		N4 Sn1 Cl1	91.4(3)		
		N4 Sn1 Cl2	89.6(3)		
		N4 Sn1 N2	177.8(3)		
		N4 Sn1 N3	91.0(3)		

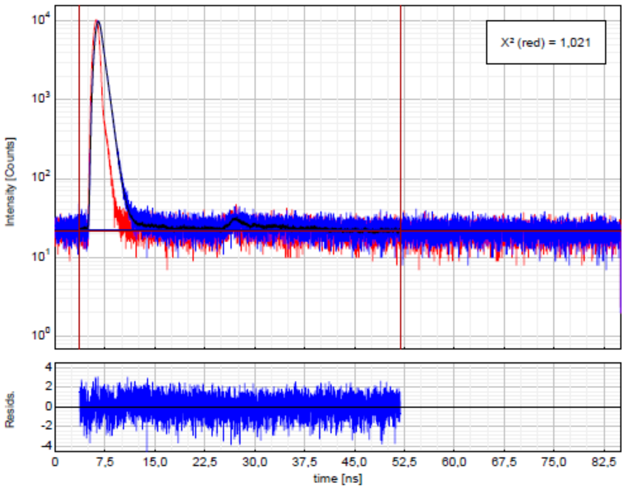

$$I(t)=\int_{-\infty}^{t} IRF(t')\sum_{i=1}^{n} A_i\, e^{-\frac{t-t'}{\tau_i}}\, dt'$$

Parameter	Value	Conf. Lower	Conf. Upper	Conf. Estimation
A_1 [Cnts]	3681	-39	+39	Fitting
τ_1 [ns]	0,5884	-0,0048	+0,0048	Fitting

Figure S72. Time-resolved emission decay (excitation at 600 nm, analysis at 610 nm) of **$SnCl_2$TPP-*p*PA** (**3**) in CH_2Cl_2 solution as measured by TC-SPC (a lifetime of 0.59 ns was estimated from the fitting procedure).

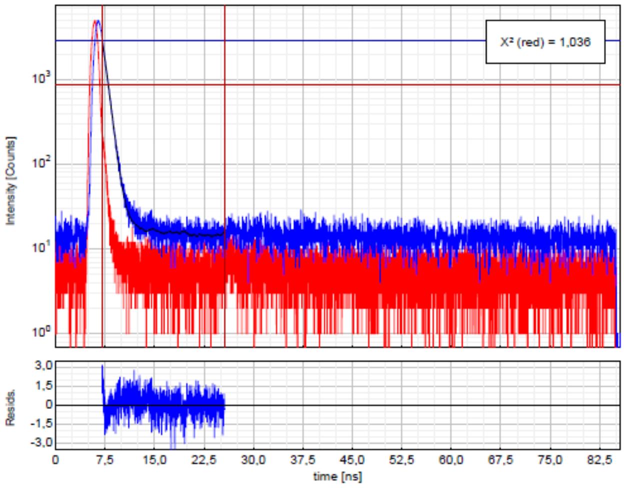

$$I(t)=\int_{-\infty}^{t} IRF(t')\sum_{i=1}^{n} A_i\, e^{-\frac{t-t'}{\tau_i}}\, dt'$$

Parameter	Value	Conf. Lower	Conf. Upper	Conf. Estimation
A_1 [Cnts]	30174,5	-7,8	+7,8	Fitting
τ_1 [ns]	0,61625	-0,00016	+0,00016	Fitting

Figure S73. Time-resolved emission decay (excitation at 600 nm, analysis at 665 nm) of **$SnCl_2$TPP-*p*BA** (**9**) in CH_2Cl_2 solution as measured by TC-SPC (a lifetime of 0.62 ns was estimated from the fitting procedure).

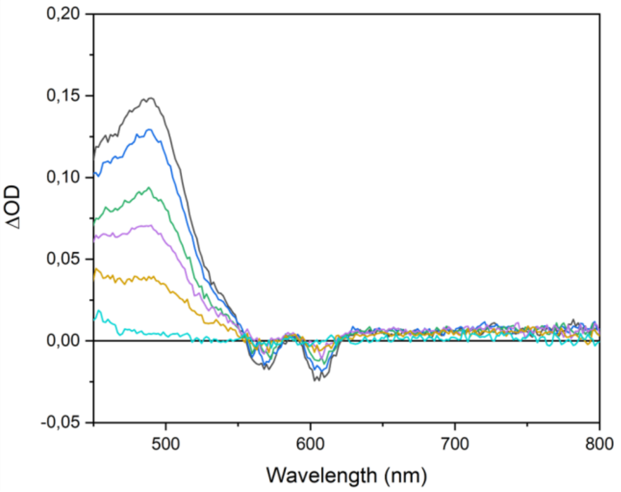

Figure S74. Spectral evolution of the transient absorption spectra (time delay: 0.2 μs, black trace – 30 μs, light blue trace) obtained by laser flash photolysis (λ_{exc} = 532 nm) in oxygen-free CH_2Cl_2 solution of 25 μM **SnCl$_2$TPP-*p*PA** (**3**) and 0.084 M pyrrolidine.

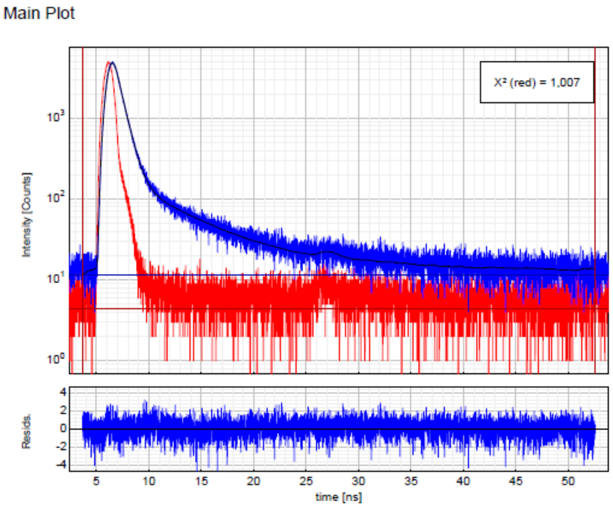

$$I(t) = \int_{-\infty}^{t} IRF(t') \sum_{i=1}^{n} A_i \, e^{-\frac{t-t'}{\tau_i}} \, dt'$$

Parameter	Value	Conf. $_{Lower}$	Conf. $_{Upper}$	Conf. $_{Estimation}$
A_1 [Cnts]	1863	-25	+25	Fitting
τ_1 [ns]	0,6045	-0,0071	+0,0071	Fitting

Figure S75. Time-resolved emission decay (excitation at 600 nm, analysis at 650 nm) of **SnCl$_2$TPP-*p*Tyr** (**6**) in CH$_2$Cl$_2$ solution as measured by TC-SPC (a lifetime of 0.60 ns was estimated from the fitting procedure).

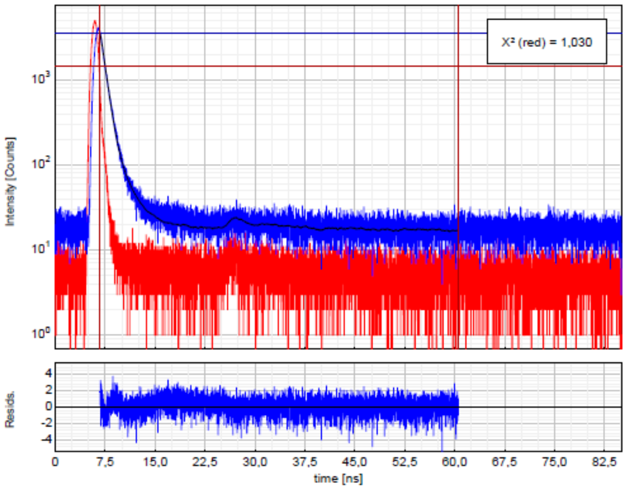

$$I(t) = \int_{-\infty}^{t} IRF(t') \sum_{i=1}^{n} A_i \, e^{-\frac{t-t'}{\tau_i}} \, dt'$$

Parameter	Value	Conf. $_{Lower}$	Conf. $_{Upper}$	Conf. $_{Estimation}$
A_1 [Cnts]	21297,7	-5,2	+5,2	Fitting
τ_1 [ns]	0,57855	-0,00014	+0,00014	Fitting

Figure S76. Time-resolved emission decay (excitation at 600 nm, analysis at 650 nm) of **TPP-*p*Tyr** (**5**) in CH$_2$Cl$_2$ solution in the presence of 0.084 M pyrrolidine as measured by TC-SPC (a lifetime of 0.58 ns was estimated from the fitting procedure).

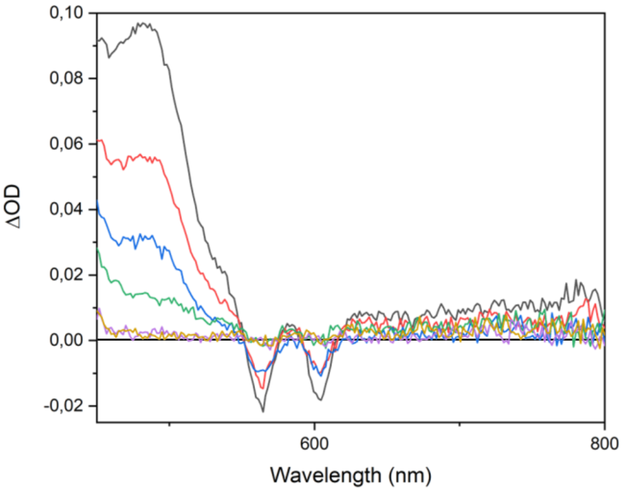

Figure S77. Spectral evolution of the transient absorption spectra (time delay: 1 µs, black trace – 50 µs, dark yellow trace) obtained by laser flash photolysis (λ_{exc} = 532 nm) in oxygen-free CH_2Cl_2 solution of 25 µM of **$SnCl_2$TPP-*p*Tyr** (**6**) and 0.084 M pyrrolidine.

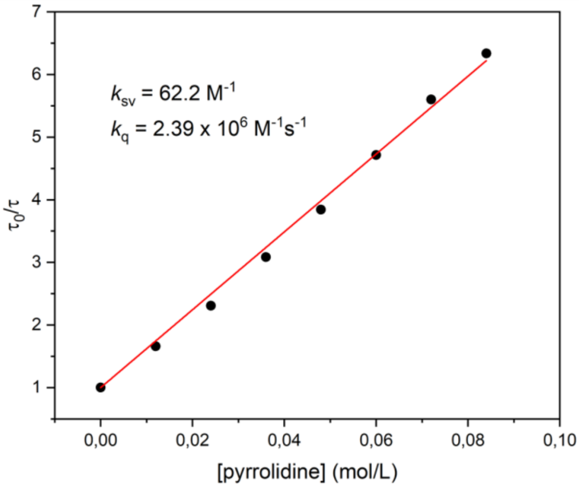

Figure S78. Stern-Volmer treatment of the quenching process of a CH_2Cl_2 25 µM solution of **$SnCl_2$TPP-*p*BA** (**9**) and 0.00 M – 0.084 M pyrrolidine to obtain the bimolecular rate constant (k_Q).

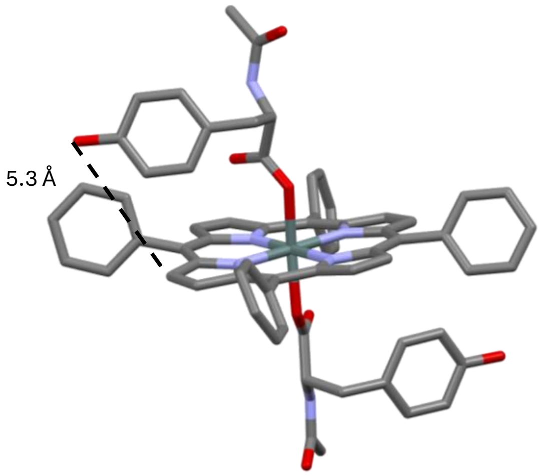

Figure S79. DFT model of **Sn(Ac-Y)$_2$TPP** in CH$_2$Cl$_2$ showing the distance between the oxygen of the phenol group and the closest β-pyrrolic carbon of the porphyrin macrocycle. Hydrogen atoms omitted for clarity. Colour code: Sn: dark green; Cl: light green; N: purple; O: red; C: grey.

CHAPTER 3

Overview

This Chapter explores the design, synthesis, and preliminary photophysical characterization of a new Sn^{IV}-porphyrin/peptide conjugate intended to drive photoinduced transmembrane Proton Coupled Electron Transfer (PCET) in lipid bilayers. Inspired by natural photosynthetic charge-separation processes, the work integrates a redox-active Sn^{IV}-porphyrin photosensitizer, tyrosine electron donors, and histidine proton acceptors into a modified $YALP_{23}$ peptide scaffold capable of adopting a transmembrane α-helical structure. Molecular dynamics simulations suggested the optimal insertion position of the chromophore and of the other active components in the peptide sequence. The resulting conjugate (plus the corresponding model peptide and two shorter analogues) were synthesized by combining SPPS and manual coupling and in depth characterized by NMR, MS, CD, and optical spectroscopies. Preliminary quenching experiments were used to select possible operating conditions under which electron- or PCET-type processes may occur. Finally, the conjugate was successfully embedded in DPPC liposomes, without substantial modification of the photophysical properties of the photosensitizer, thus representing a promising platform for future studies on light-driven transmembrane PCET.

The work presented in this Chapter was done in collaboration with Prof. Sylvestre Bonnet, Leiden Institute of Chemistry, Leiden University (The Netherlands), where the candidate spent six months. The peptide synthesis was performed in collaboration with Dr. Dmitri Filippov and Drs. Nico Meeuwenoord from the same Institute.

List of abbreviations.

DPPC = 1,2-dipalmitoyl-*sn*-glycero-3-phosphocholine

NaDMPG = 1,2-dimistroyl-*sn*-glycero-3-phosphonete(1'-*rac*-glycerol) (sodium salt)

TEA = triethyl amine

TEOA = triethanolamine

EDTA = ethylenediaminetetraacetic acid

DMPC = 1,2-dimyristoyl-*sn*-glycero-3-phosphocholine

TPP = 5,10,15,20-(phenyl)porphyrin

DSPC = 1,2-distearoyl-*sn*-glycero-3-phosphocholine

Bpy = bipyridine

MMP$^+$ = 1-methoxy-N-methylphenazinium cation

WST1$^-$ = 2-(4-iodophenyl)-3-(4-nitrophenyl)-5-(2,4-disulfophenyl)-2H-tetrazolium anion

XTT = 2,3-Bis(2-methoxy-4-nitro-5-sulfophenyl)-2H-tetrazolium-5-carboxanilide solium salt

TPP-*p*NH$_2$ = 5-(4'-aminophenyl)-10,15,20-triphenylporphyrin

EDC = *N*-(3-Dimethylaminopropyl)-*N'*-ethylcarbodiimide hydrochloride

FmocGluOMe = (*S*)-4-((tert-Butoxycarbonyl)amino)-5-methoxy-5-onopentanoic acid

FmocGluO*t*Bu = (*S*)-4-((((9H-Fluoren-9-yl)methoxy)carbonyl)amino)-5-(tert-butoxy)-5-oxopentanoic acid

PEA = phosphatidylethanolamine

DIC = *N,N'*-Diisopropylcarbodiimide

TFA = Trifluoroacetic acid

NaDSPE-PEG2K = 1,2-diasteroyl-*sn*-glycero-3-phosphoethanolamine N-(carbonyl-methoxy polyethylene glycol-2000

3.1. Introduction.

Photosynthesis represents one of the most important processes in Nature, enabling plants and bacteria to convert solar energy into chemical fuels. This transformation relies on a finely tuned sequence of light-induced charge separation and redox reactions, ultimately driving water oxidation. The latter provides the electrons and protons required for the synthesis of the biological reductant nicotinamide adenine dinucleotide (phosphate), in its reduced form [NAD(P)H], together with the energy carrier adenosine triphosphate (ATP). These compounds are then employed in the Calvin cycle to convert CO_2 into carbohydrates.[1,2] The high efficiency of photosynthesis stems from the extraordinary spatial organization of its key components - namely Photosystem II (PSII), Photosystem I (PSI), and the Oxygen Evolving Complex (OEC) - within the thylakoid membrane. This membrane is a supramolecular assembly of lipids and plays a crucial role in separating oxidative from reductive sites, thereby preventing detrimental charge recombination reactions. Central to this process is a Proton Coupled Electron Transfer (PCET) mechanism, essential for efficient water oxidation at the PSII OEC. By coupling proton and electron transfer, energy losses are minimized and multi-electron chemistry is enabled under mild conditions.[3] Mimicking natural photosynthesis with artificial systems represents one of the most promising strategies for solar fuel storage and production. At a molecular level, considerable progress has been achieved through the rational design of photosensitizers and catalysts, often integrated into supramolecular assemblies such as micelles, nanoparticles and liposomes.[4–6] Liposomes are spherical assemblies of lipids that generate three distinct environments: two aqueous phases (the inner and outer compartments), separated by a hydrophobic bilayer. They form spontaneously in aqueous media by self-assembly of amphiphilic lipids, *i.e.* lipids formed of a polar hydrophilic headgroup and a nonpolar hydrophobic alkyl chain. At concentrations above the critical micelle concentration (CMC) in water, lipids aggregate into supramolecular structures such as micelles, reverse micelles, bilayers, and vesicles. The driving forces behind these assemblies include dipole-dipole or ion-dipole interactions of the polar headgroups with water, and hydrophobic interactions among alkyl chains. Generally, lipids can be classified according to their polar or charged head groups: zwitterionic, anionic, cationic and non-ionic. Very commonly used examples of lipids for each class are reported in Figure 3.1.1: 1,2-dipalmitoyl-*sn*-glycero-3-phosphocholine (DPPC) for the zwitterionic class; 1,2-dimistroyl-*sn*-glycero-3-phosphonete(1'-*rac*-glycerol) (sodium salt) (NaDMPG) for the anionic class; 1,2-dioleoyl-*sn*-glycero-3[phosphor-*rac*-(3-lysyl(1-glycerol))] (chloride salt) (O-Lysyl PG) for the cationic class, and 1-palmitoyl-2-oleoyl-3-

bis(β-D-glucosyl)-*sn*-glycerol (16:0 – 18:1 GlcGlcDAG) for the non-ionic class. Other types of classification of phospholipids can be done considering the nature of the counterion (Cl^-, Br^-, Na^+, K^+, *etc*) or the chemical nature of the alkyl chain (hydrocarbon, fluorocarbon, saturated, unsaturated, *etc*).

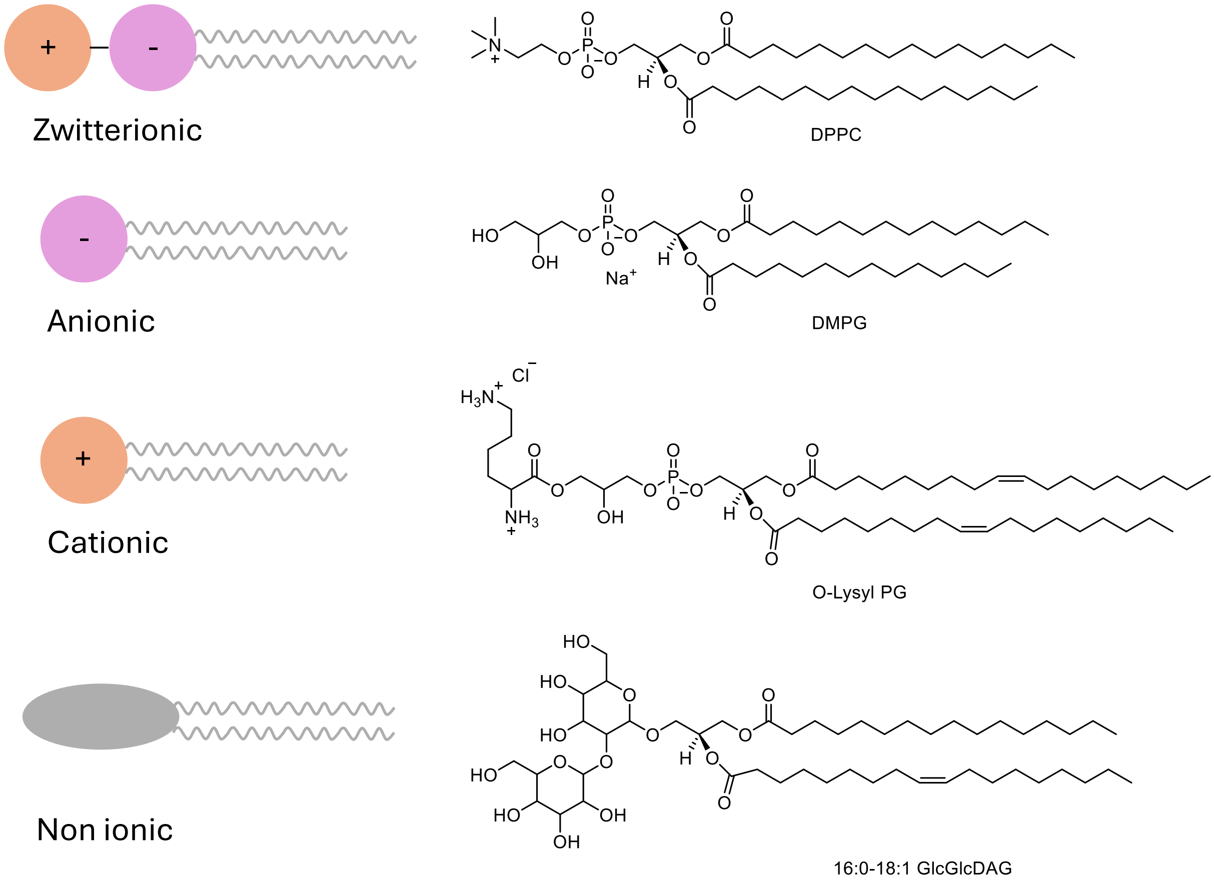

Figure 3.1.1. Examples of the most used lipids for liposome preparation, and corresponding classifications.

Typically, lipids organize into bilayers or vesicles. Such bilayer-based structures are highly attractive for artificial photosynthesis, as the compartmentalization can be exploited to spatially separate water-soluble components (*i.e.* electron donors from electron acceptors, or water oxidation catalysts from water reduction ones), minimizing side reactions and charge recombination (as ideally depicted in Figure 3.1.2).

Several strategies can be employed to target specific molecules to different regions of the lipid bilayer to build more complex photocatalytic membranes. Depending on the nature of both the lipid and the photosensitizer/catalyst, four main synthetic approaches can be adopted: i) covalent linkage of the functional group to the polar head of a lipid that inserts into the membrane; ii) electrostatic interaction between charged functional molecules and the charged head groups of the membrane; iii) incorporation of the functional group into an amphiphilic molecule that preferentially localizes at the interface between the hydrophobic region of the bilayer and the bulk aqueous phase; iv) synthesis of molecules having a sufficiently large hydrophobic portion to allow their embedding within the hydrophobic region of the lipid bilayer. The ability of liposomes to generate a micro-heterogeneous environment, together with the precise control over the spatial localization of different molecules within the liposomal system, enables the organization of an increased number of photoactive units, that are held in proximity at the liposome interfaces. This spatial arrangement enhances intermolecular interactions and helps to overcome some of the limitations typically found in homogeneous photocatalytic reactions.

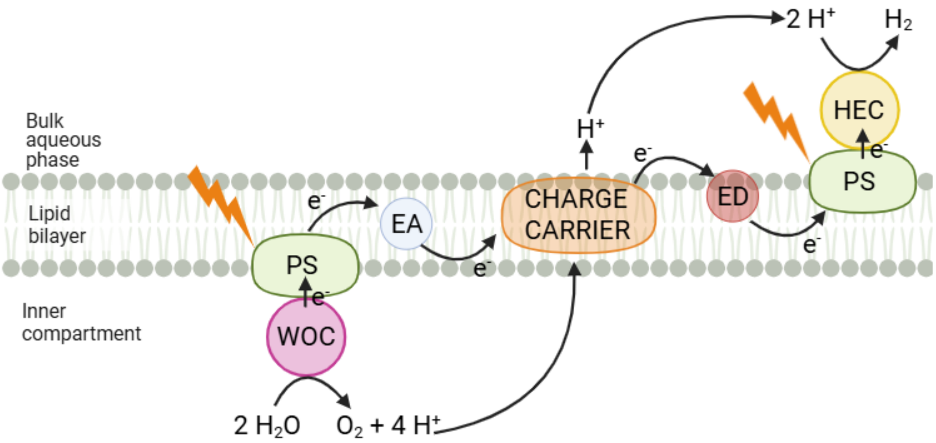

Figure 3.1.2. Scheme of a portion of a synthetic vesicle used as a platform for an artificial photosynthetic assembly: the various components, *i.e.* photosensitizer, charge carrier and electron donor/acceptor, are spatially organized within the lipid bilayer.

When working with liposomes, the aqueous phase consists of buffered aqueous solution, which may also contain electron donors, electron acceptors and photosensitizers, if required. Typical buffers include phosphate, acetate, ascorbate, carbonate and Tris-HCl, that are adjusted at the desired pH values. Liposomal solutions remain stable over a broad pH range (from 3 to 10). An important parameter that must be carefully controlled when working with liposomes with different solute compositions in the inner and outer aqueous phases is the osmotic pressure. Osmotic pressure is defined as the pressure required to stop water diffusion across the lipid bilayer. In dissymmetric liposomes, three different scenarios can occur: (i) hypotonic, (ii) hypertonic, and (iii) isotonic conditions. In the hypotonic case, the osmotic pressure of the outer aqueous phase is lower than that of the inner phase, leading to a net influx of water into the liposome. This causes swelling, which may eventually result in liposome disruption and release of the encapsulated species. The hypertonic condition presents the opposite situation: the osmotic pressure of the bulk aqueous phase is higher than that of the inner compartment, causing water to flow outward. This flow induces liposome shrinkage and may also result in liposome rupture. The isotonic condition is the most favourable one for keeping dissymmetric membranes intact, as equal osmotic pressures in the inner and outer phases result in zero net water flow, thus maintaining a constant liposome size over time.

Mimicking natural photosynthesis with artificial systems requires the integration of synthetic or biological components, which can be broadly categorized into four classes: (i) photosensitizers (PS), (ii) catalysts, (iii) sacrificial agents, and (iv) charge carriers.[6] The photosensitizer initiates the photocatalytic cycle by absorbing light. Key properties for this unit include ability to absorb light (high extinction coefficient at wavelengths that fit the light source), sufficiently long excited states lifetime, appropriate redox potentials, as well as photostability under photocatalytic conditions. To minimize competition for photon absorption, the spectrum of the PS should not overlap significantly with that of other components of the system. Among the studied PS classes are ruthenium-based metal complexes and (metallo)porphyrins, due to their well-defined photophysical properties and, in the case of porphyrins, their similarity to natural light-harvesting systems (see examples below). The catalyst is responsible for solar fuel production and is often based on redox-active metal centre capable of charge accumulation and bond-breaking/forming reactions. Examples include alkylated cobaloximes for H_2 evolution in zwitterionic vesicles,[7] alkylated rhenium complexes for CO_2 reduction,[8] and alkylated Ru-based complexes for water oxidation.[9] While numerous catalysts have been reported, their choice has to consider several performance parameters such as catalyst stability (quantified by turnover number, TON), catalytic activity (quantified by the turnover frequency, TOF), product selectivity and stability. Biological catalysts such as hydrogenases ($H^+ \leftrightarrow H_2$), formate dehydrogenases ($CO_2 \leftrightarrow$ formate), carbon monoxide dehydrogenases ($CO_2 \leftrightarrow CO$), and photosystem II (PSII) for light-driven water oxidation have also been explored.[1,2,10] Despite their high activity, these enzymes are costly to isolate, structurally fragile, and often highly oxygen-sensitive, which limits their practical applicability. Sacrificial electron donors (EDs) or electron acceptors (EAs) are frequently employed to investigate individual half-reactions or electron transfer reactions. They function as reductive or oxidative quenchers of the excited PS, or as regenerators of the PS after a reductive or oxidative quenching step by a catalyst. Their selection largely depends on their redox potential. Common EDs include triethylamine (TEA), triethanolamine (TEOA), and ethylenediaminetetraacetic acid (EDTA) (Figure 3.1.3).[11] It should be noted that all these molecules are amines, and therefore they may also act as bases and vary their redox potentials depending on the pH window, *i.e.* the ammine nitrogen(s) gets protonated at pH < pK_a. In addition to this, the water-soluble EDTA (also named H_4EDTA) has two amino and four carboxylic acid groups (for a total of six pK_a values). This implies that even small variations in the working pH window can lead to different protonation states of this molecule. At around pH = 8, which is a frequent experimental condition (see also below), the predominant species is the trianoinc form, often referred to as $HEDTA^{3-}$ (Figure 3.1.3). Finally, EDTA can act as a very strong multidentate chelating agent for divalent and trivalent metal cations, which may interfere with its electron-donor properties.

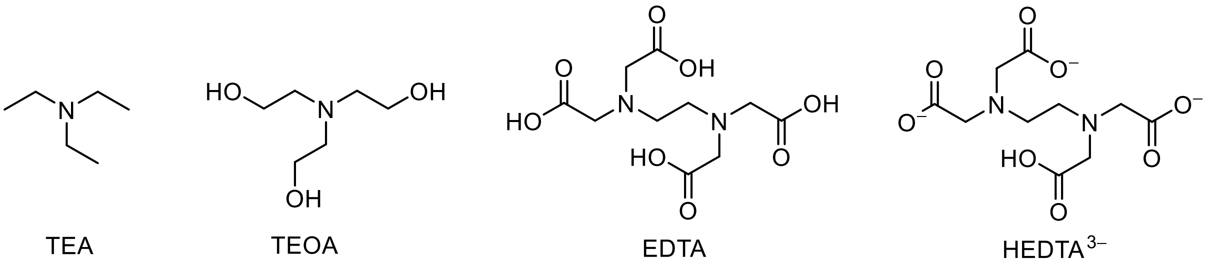

Figure 3.1.3. Chemical structure of frequently used EDs in liposome artificial photosystems.

Common EAs includes sodium thiosulfate ($Na_2S_2O_8$),[12] and tetrazolium anions such as $WST1^-$ and XTT (the sulfonate groups are usually deprotonated). These compounds can be reduced by two electrons to their coloured formazan corresponding derivatives ($Fz1^{2-}$ and FZ, respectively, Figure 3.1.4 and examples below). [13,14]

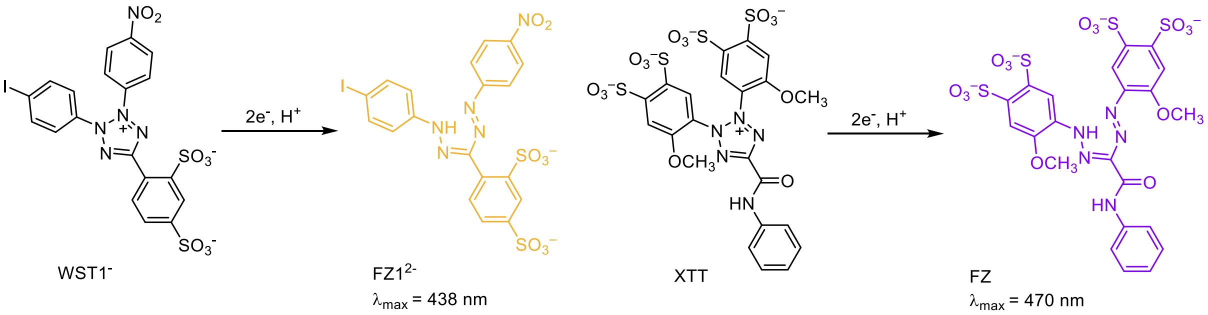

Figure 3.1.4 Chemical structure of two frequently used EAs in liposome artificial photosystems and their corresponding (coloured) reduced form.

Charge carriers are redox-active species that shuttle reducing or oxidizing equivalents between the photoactive components. A representative example is methyl viologen (MV^{2+}), which undergoes one-electron reduction to the stable radical cation $MV^{\cdot+}$. In some cases, charge carriers can undergo proton coupled electron transfer and carry both electrons and protons across lipid membranes. Good examples are the membrane-soluble 1-methoxy-N-methylphenazinium cation (MMP^+), or the quinones 2,5-diphenyl-1,4-benzoquinone (Q_S) and decyl-ubiquinone (dQ) (Figure 3.1.5, and selected examples below). If the protonation or the deprotonation event occurs singly in one of the two compartments of the liposome, the result is the formation of a pH gradient.

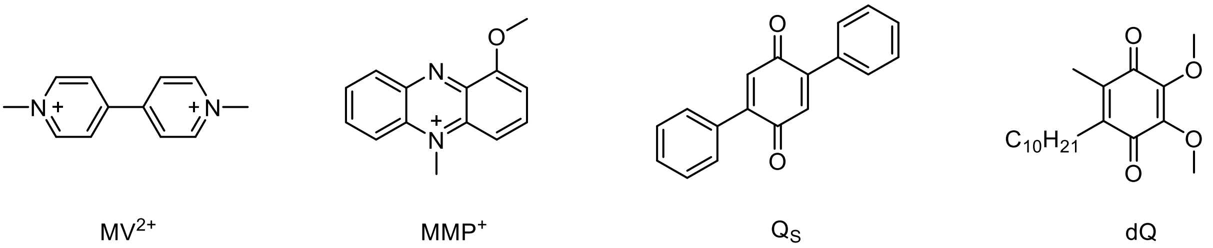

Figure 3.1.5 Chemical structures of the most recurring charge carriers in liposome artificial photosystems.

The choice of charge carrier is critical under several aspects. It is important to determine whether the molecule is “innocent” (transporting only electrons) or “non-innocent” (capable of undergoing side reactions that affect catalytic efficiency). Also, the chemical stability and solubility of the charge carrier must be high in the relevant redox and protonation states. Finally, it must be noted that the effect of membrane environments can tune features of the embedded components, such as their redox potentials, which are typically measured electrochemically in bulk organic solutions. Several studies have reported the use of liposomes as supramolecular scaffolds for photocatalysis. In 2014, König *et al.* reported the first example of co-embedding a molecular water oxidation catalyst and a photosensitizer into lipid membranes.[15] A ruthenium polypyridyl amphiphilic complex and a ruthenium-based water oxidation catalyst were used to achieve oxygen production in aqueous buffer. Remarkably, efficient water oxidation under light irradiation ($\lambda_{irr} = 455$ nm) was obtained at catalyst concentrations significantly lower than those required for homogeneous photocatalysis, offering a new strategy for artificial photosynthesis. In 2016, Bonnet *et al.* incorporated a tris(bipyridine)ruthenium(II) photosensitizer and Ru-, Co-, or Ir-based water oxidation catalysts modified with alkyl chains, for a better bilayer incorporation into DMPC or NaDMPG liposomes.[9] Using $Na_2S_2O_8$ as EA, they demonstrated the occurring of photocatalyzed O_2 production. This study highlighted some clear advantages of liposomal photocatalysis: despite a lower O_2 production, an increased stability and greater tolerance to variations in light intensity and EA concentrations were observed compared to the homogeneous photocatalysis. One of the earliest reports on photocatalytic hydrogen production in liposomes was published in 1983 by Parmon *et al.*, where lecithin vesicles were used with EDTA as ED (in the inner aqueous phase), Zn^{II}-TPP as photosensitizer, and a natural hydrogenase enzyme as catalyst.[16] In 2016, König *et al.* demonstrated efficient hydrogen production using vesicles featuring hydrophilic [FeFe]-hydrogenase mimic adsorbed on surface and a Ru-based photosensitizer embedded in the membrane.[17] Upon blue light irradiation, H_2 production in the liposomal system exceeded that observed in homogeneous solution under acidic aqueous conditions. The key finding of this work was that the spatial proximity of the catalytic subunits at the membrane interface significantly enhanced the H_2 production. In 2014, the same group reported the use of vesicles to overcome solubility issues of hydrogen-evolving catalysts, enabling hydrogen production in purely aqueous solutions.[7] Here, an alkylated Ru^{II}-polypyridyl complex or an organic xanthene derivative served as photosensitizers, together with a modified cobaloxime catalyst with apolar groups to facilitate incorporation into the lipid membrane. TEOA was employed as ED. More recently, in 2022, Bonnet *et al.* described photocatalytic hydrogen evolution using an alkylated polypyridyl Co^{II}-complex immobilized on DMPC, DPPC, or DSPC vesicles.[18] An alkylated Ru-based photosensitizer was used in combination with a 1:1 mixture of sodium ascorbate and tris(2-carboxyethyl)phosphine hydrochloride (TCEP) as EDs. Under deoxygenated conditions and blue light irradiation, efficient H_2 production was observed. The possibility to couple a water oxidation catalyst with a hydrogen evolving one in a liposomal environment is considered as one of the holy grails in the field of artificial photosynthesis. To accomplish this ambitious goal, it is necessary to develop a system that can efficiently transport electrons across the lipid bilayer, *i.e.* to promote the movement of electrons unidirectionally from one compartment to the other, and thus couple water oxidation reaction with water reduction. The main difficulty is that the lipid bilayer is an insulator and too thick (30 – 35 Å) to allow electrons to be transported in one single step.[6,19] To mimic natural transmembrane electron processes several examples have been reported in the literature,[20] which are based on three main strategies: (i) incorporation of a biological component into the lipid bilayer;[21–23] (ii) use of molecular charge carriers able to diffuse across the membrane;[24] (iii) synthesis of covalent transmembrane molecules spanning the lipid bilayer.[25–28] It has to be mentioned that, among the extensive research done on artificial photosynthesis in the last decades, the number of liposomal systems that can effectively perform transmembrane electron transfer are still quite limited. Here some selected examples of each of the above-mentioned strategies will be briefly described. Regarding the first strategy, Mavelli *et al.* reported in 2017 on the inclusion of a photosynthetic reaction center (RC) extracted from *Rhodobacter sphareoides* in a phosphatidylcholine/phosphatidylglycerol giant vesicle (GV), with a very high grade of orientation, using a droplet transfer synthetic method (about 90% of the photosensitizers RC head-sites were found to face the aqueous bulk solution of the vesicles and 90% of the quinone tail-sites were located towards the inner compartment, Figure 3.1.6A).[21,22] This system (RC@GV) was photo-irradiated in the presence of the natural water-soluble ED cytochrome C_2, combined with ferrocyanide $[Fe(CN)_6]^{4-}$ in the outer bulk aqueous phase, and an additional quinone (dQ, see also Figure 3.1.5) in the inner bilayer of the vesicle, acting as EA. By irradiation with red light a proton gradient across the lipid bilayer was generated. Later, Jeuken *et al.* used an icosa-heme transmembrane protein, MtrCAB, to transfer electrons across the lipid bilayer (Figure 3.1.6B).[23] MtrCAB is a heterotrimeric protein (MtrA, MtrB and MtrC) found in the bacterium *Shewanella oneidensis MR1*, where it forms a 20 heme long conductive molecular wire that transports electrons across the insulating membrane to external minerals. In the reported system TiO_2 nanoparticles photosensitized with a $[Ru(bpy)_3]^{2+}$ dye (bpy = 2,2′-bipyridine) and different types of carbon dots (amorphous and graphitic) were used as light harvesting systems (LHNP). To prove the efficient electron transfer across the membrane, an EA dye (RR120) was placed in the inner compartment of the liposome, while EDTA was added as sacrificial ED in the outer aqueous phase. The electron transfer process was monitored via UV-Vis absorption spectroscopy, since RR120 is red-colored in the oxidized-state form but becomes colorless once reduced. The bleaching of the absorption band of RR120 after light irradiation of the LHNP demonstrated the occurring of an electron flow across the membrane, with concomitant re-generation of the holes left in the light harvesting nanoparticles by EDTA. The rate limiting step of the entire process was found to be the electron transfer between the light-harvesting nanoparticles and the electron relay MtrCAB.

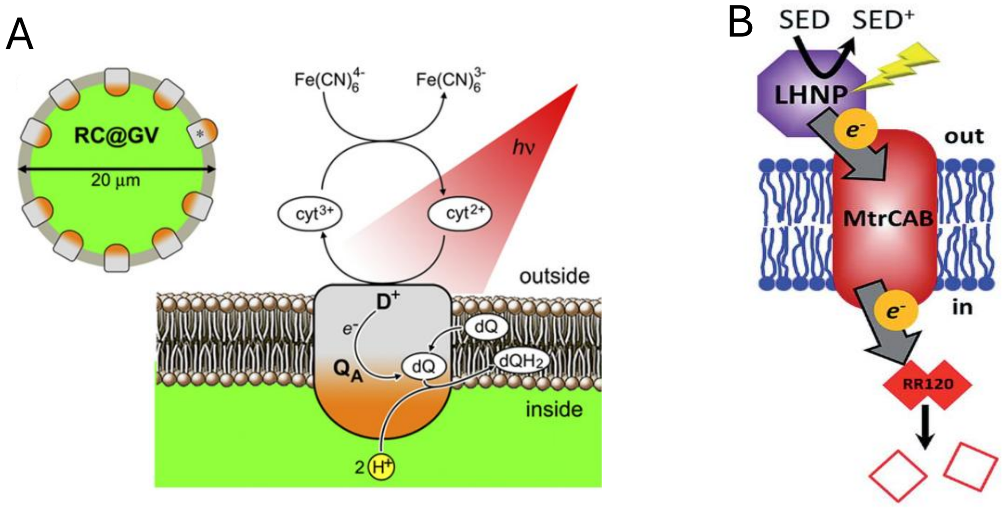

Figure 3.1.6. Schematic representation of incorporation of biological components in the lipid bilayer to drive photoinduced proton gradient (A)[21] or photoinduced electron transfer (B).[23] Figures adapted from refs. 21, 23.

The second strategy is based on the use of molecular charge carriers for an efficient transport of electrons through the insulating membrane. In 2015 Bonnet *et al.* reported an example on the use of the membrane-soluble charge carrier $MMPH/MMP^+$ (see Figure 3.1.5) to perform photoinduced transmembrane unidirectional electron transfer from EDTA, used as the ED in the inner aqueous phase, to the WST1$^-$ EA placed in the bulk solution, in the presence of a cationic Zn^{II}-porphyrin as photosensitizer (Figure 3.1.7).[24] The electron transfer process was easily monitored via UV-Vis absorption spectroscopy since the EA presents a typical absorption band with a maximum at 438 nm when reduced by two electrons to the Fz1^{2-} opened form (see also Figure 3.1.4).[13] Under anaerobic conditions, after irradiation of the metallo-porphyrin embedded close to the water interfaces of the lipid bilayer, the carrier transports photoelectrons across the membrane without limiting the overall rection rate. The compartmentalization of the components involved in the process allows for a low charge recombination rate. The main limit of the process is that unidirectional electron transport was found to be active only under anaerobic conditions.

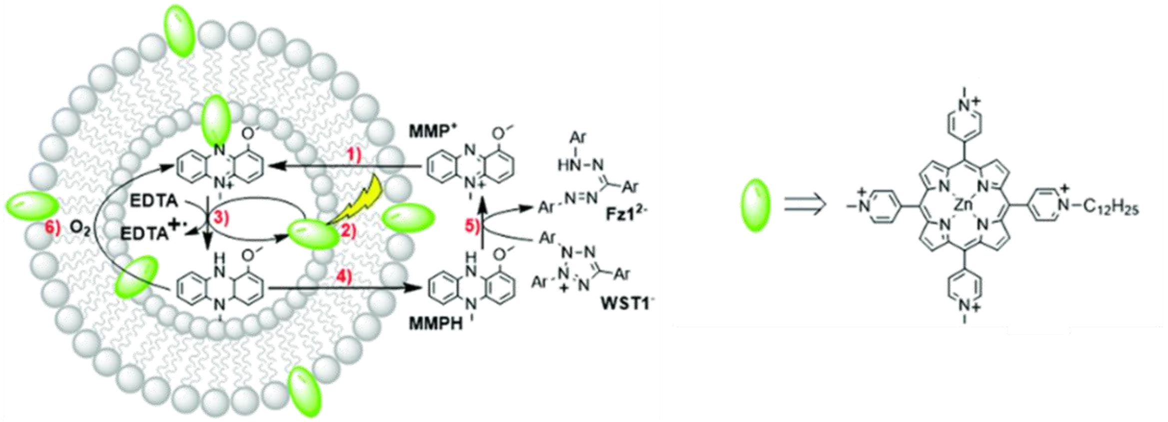

Figure 3.1.7. Schematic representation of the use of a molecular charge carrier for photoinduced transmembrane electron transfer.[24] Figure adapted from ref. 6.

Finally, in the third strategy fully synthetic systems were developed to couple transmembrane electron and proton transfer. One of the first examples was reported by Moore *et al.* These authors prepared a molecular triad (C-P-Q, Figure 3.1.8A) consisting of a tetra-arylporphyrin (P) covalently bound on one side to a naphthoquinone moiety (Q, acting as EA) fused to a norbornene system with a terminal carboxylic group, and on the other side to a carotenoid polyene (C, acting as ED).[25,29] In homogeneous solution the triad undergoes a photoinduced electron transfer from the porphyrin excited state to the quinone acceptor, forming a charge-separated state of the type C-P$^{\cdot+}$-Q$^{\cdot-}$, with a quantum yield of ~1. The molecular triad was also embedded in a lipid bilayer, and it demonstrated to be able to transport electrons across the membrane upon light irradiation. One of the drawbacks of this system is the possible lack of control on the way the asymmetric triad gets inserted in the lipid membrane. Thanks to a series of control experiments the authors proved that most of the triads are oriented with the quinone moiety facing the bulk aqueous compartment, while the carotenoid chain crosses the lipid bilayer to end up facing the inner aqueous compartment. Irradiation of the porphyrin ($\lambda_{irr} = 430$ nm, Soret band) induces the formation of a diradical charge separated state of the type $C^{\cdot+}$-P-$Q^{\cdot-}$ in ~0.1 quantum yield, as detected by the transient absorption band of the carotenoid radical cation at 930 nm. The lifetime of this diradical species was found to be 110 ns or 60 ns, in the absence or in the presence of an additional quinone embedded in the bilayer (Q_s, see also Figure 3.1.5), respectively. The freely diffusing Q_s was demonstrated to establish a reduction potential close to the outer aqueous phase and an oxidation potential near the inner compartment, as well as a pH gradient. In fact, Q_s accepts an electron from the reduced naphthoquinone, generating the reduced negatively charged form $Q_s^{\cdot-}$ that gets protonated and crosses the bilayer, then releasing the proton in the internal compartment and reducing the oxidized carotenoid. In a follow-up study the same group coupled this same generated proton gradient to a membrane-bound ATP synthase complex introduced in the same vesicle. The overall system was able to drive ATP photoinduced production.[30] An elegant example of the use of secondary interactions (such as π-π stacking) to self-assemble supramolecular structures to drive transmembrane electron transfer was reported in 2006 by Matile *et al.*[26] In this study rigid *p*-octiphenyl rods were used to create helical tetrameric π-stacks of blue, red-fluorescent naphthalene diimides able to span the lipid membrane (Figure 3.1.8B). The vesicles were loaded inside with a quinone acceptor and surrounded by the electron donor EDTA. A fast electron transport across the supramolecular array of chromophores was promoted, upon visible light excitation, driving the two-fold reduction and protonation of the quinone. As a result, an oxidative and a reductive potential were generated close to the outer and the inner surface of the vesicle, respectively, as well as a proton gradient across the membrane. A very recent example on the use of liposomes for unidirectional electron transfer was reported by Pannwitz *et al.*[27] They described a rigid oligoaromatic molecular wire used to electronically couple the oxidative and reductive sites that are physically separated by the membrane (Figure 3.1.8C). The molecular wire spanning the membrane presents a simple and symmetric structure and was obtained by relatively facile covalent linkage of a central benzothiadiazole with fluorene moieties. To perform electron transfer studies this system was embedded in DPPC liposomes with NADH as electron donor in the inner compartment and XTT as electron acceptor in the external bulk solution. XTT was used as EA as it forms a strongly colored formazan dye upon reduction (see also Figure 3.1.4).[14] Upon light irradiation of the system, an absorption band at $\lambda_{max} = 470$ nm, characteristic of the reduced form of XTT, gradually increased, while simultaneously the NADH absorption band at 340 nm decreased, indicating oxidation of the ED and reduction of the EA. Overall, the authors demonstrated that with an appropriate fluorescent molecular wire it is possible to drive photoinduced electron transfer across the lipid membrane with a quantum yield of 0.045% in anaerobic conditions (the yield drops down to 0.020% under oxygenated conditions).

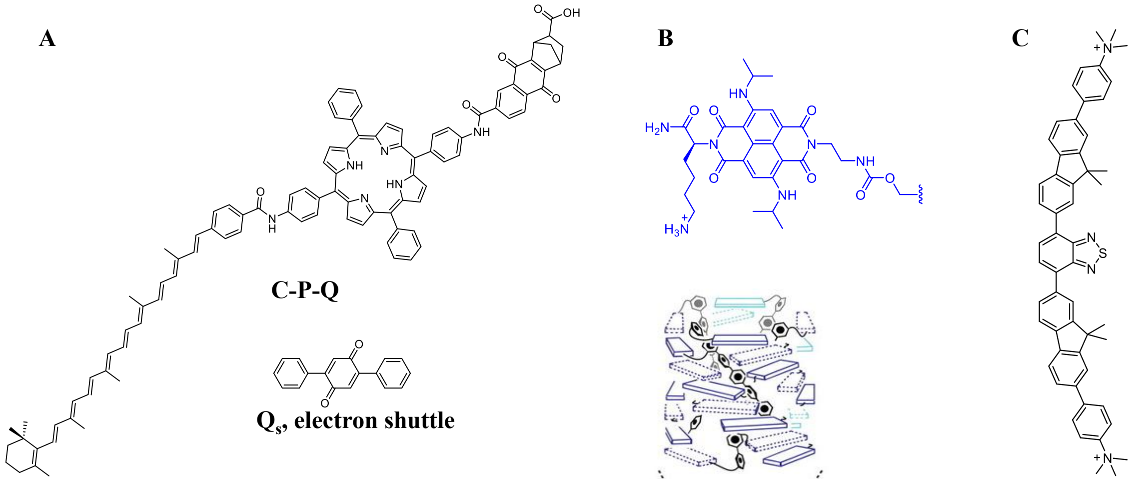

Diffusion-based electron trasnfer

Supramolecular channels

Rigid, covalent, symmetric wire

Figure 3.1.8. Reported chemical structure of: A) a molecular triad;[25] B) building block for the formation of supramolecular assemblies;[26] C) covalent rigid molecular wire, able to span the lipid bilayer and to drive photoinduced electron transfer.[27] For more details see related references.

In the last example Bonnet *et al.* reported on the preparation of two new (metallo)peptides, WALP$_{23}$-Re$_2$ and WALP$_{23}$-Ru$_2$ that were embedded in a DPPC lipid bilayer to perform photoinduced transmembrane electron transfer (Figure 3.1.9).[28] WALP$_n$ peptides are centro-symmetrical hydrophobic α-helical peptides, formed by an initial charged portion of amino acids, followed by an aromatic region and a central hydrophobic sequence of alanine and leucine residues. These peptides were reported for the first time by Killian *et al.* as mimic models for the hydrophobic transmembrane proteins found in nature.[31–33] Bonnet *et al.* modified the WALP$_n$ sequence by replacing two alanine residues by two unnatural alanine featuring one pendant bipyridyl group each (named bipyridylalanines, A$_{bpy}$) that can chelate metal ions. The peptide sequence was synthesized using classical solid phase peptide synthesis (SPPS), while the unnatural amino acid was manually coupled. At the end, after cleavage from the resin, the bpy-modified peptide (WALP$_n$-bpy$_2$) was metalated in the presence of a Ru^{II}- or Re^{I}- precursor to give the final desired (metallo)peptides (WALP$_{23}$-Ru$_2$ and WALP$_{23}$-Re$_2$, respectively). The authors envisioned that by incorporating at least two metal centers in desired selected positions within the WALP$_n$ peptide chain, a fast multi-step transmembrane photoinduced electron transfer may be achieved. More specifically, after light excitation, one of the excited photosensitizers is expected to initiate the transmembrane charge separation either by photoinduced reductive quenching from the ED at the inner aqueous interface, and subsequent electron transfer to the EA present in the bulk phase (*via* charge migration to the next-by PS in the peptide sequence), or by oxidative quenching from EA at the external water interface, and hole transfer towards the inner compartment (again *via* charge migration), with the same overall result. For the photoirradiation studies the vesicle was loaded with EDTA as ED in the inner compartment, and $WST1^{-}$ as EA in the outer bulk solution. $WST1^{-}$ is a tetrazolium salt and it was chosen because it is known that lipid membranes are impermeable to it and as it presents a very characteristic absorption band at 438 nm in its reduced $Fz1^{2-}$ formazan form (see also Figures 3.1.4 and 3.1.7).[13,24] Upon light excitation of the chromophore (either $[Re(bpy)(CO)_3Cl]$ or $[Ru(bpy)_3]^{2+}$) for $WALP_{23}$-Re_2 a genuine transmembrane photoinduced electron transfer was demonstrated to occur, while for $WALP_{23}$-Ru_2 the formation of $FZ1^{2-}$ was attributed to photoinduced leakage of the ED to the bulk aqueous phase, followed by photoinduced electron transfer on one side of the vesicle (Figure 3.1.9). The reported system is one of the most recent examples in literature that demonstrates the ability to drive unidirectional photoinduced transmembrane electron transfer. This work introduces an approach that is highly modular. In fact, various modifications can be made into amino acids lateral sidechains to incorporate specific functional groups into the peptide scaffolds. Moreover, the intrinsic modularity of peptide synthesis enables the preparation of different peptides with varied sequences, and the introduction at the desired positions of unnatural functionalized amino acid(s), without requiring substantial changes in the overall coupling procedure. Finally, this and some recent works by others,[34–36] has validated the use of YASARA (YASARA - Yet Another Scientific Artificial Reality Application, see also below) to perform molecular dynamics to model the folding of the target peptides or synthetic wires across the lipid membrane, with a certain extent of accuracy.

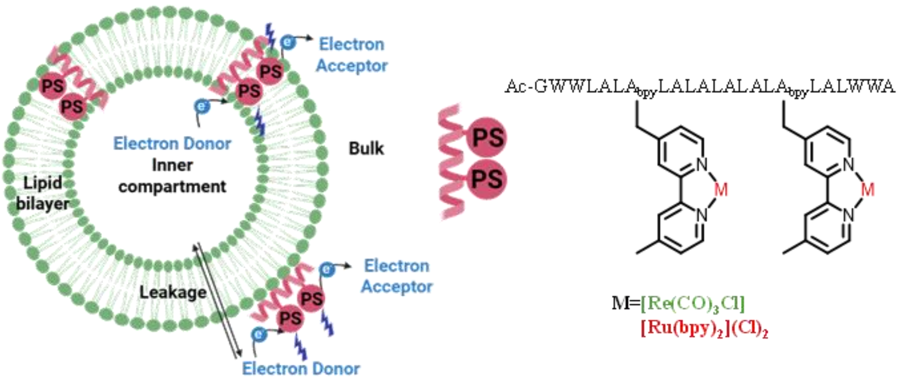

Figure 3.1.9. Schematic representation of the reported (metallo)peptides embedded in the lipid bilayer to give photoinduced transmembrane electron transfer. Figure adapted from ref. 28.

Taking advantage of this background and of the complementary expertise in the preparation and photophysical study of Sn^{IV}-porphyrin/tyrosine conjugates for PCET (see Chapter 2), a collaboration was initiated on a joint project developed by the candidate during a six-months stay at the laboratories of Prof. Sylvestre Bonnet (Leiden Institute of Chemistry, University of Leiden, The Netherlands). The idea was to design and synthesize a new Sn^{IV}-porphyrin/peptide conjugate, and the analogue model peptide (**P1**, **P2** and **P3**, Figure 3.1.10), intended for incorporation into a lipid bilayer, with the ambitious goal of activating a photoinduced transmembrane PCET.

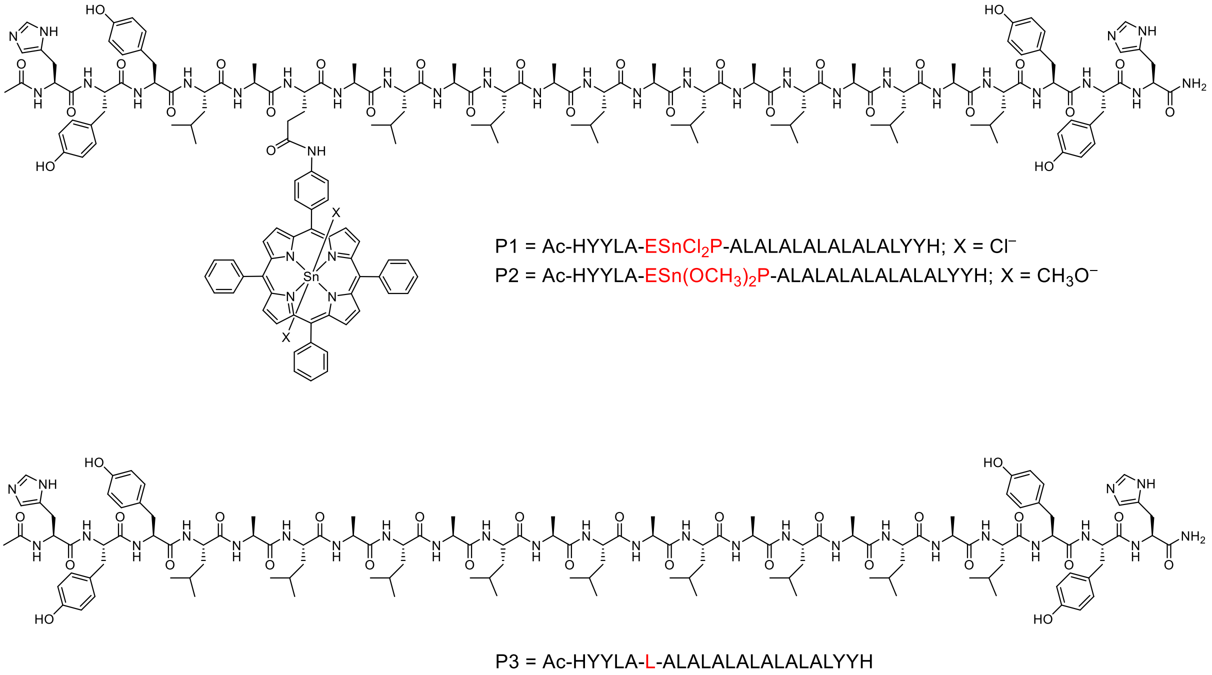

P1 = Ac-HYYLA-ESnCl$_2$P-ALALALALALALALYYH; X = Cl$^-$
P2 = Ac-HYYLA-ESn(OCH$_3$)$_2$P-ALALALALALALALYYH; X = CH$_3$O$^-$

P3 = Ac-HYYLA-L-ALALALALALALALYYH

Figure 3.1.10. Chemical structures of the target **P2** and **P3** peptides, prepared and described in this Chapter.

YALP23, compared to WALP23, presents four tyrosine residues at positions 2, 3, 21, and 22 in place of tryptophans,[37–39] and emerged as ideal scaffold to be derivatized with a pendant Sn^{IV}-porphyrin photosensitizer unit, by inserting an appropriate unnatural amino acid in the peptide sequence. In fact, as discussed more in details in Chapter 2, previous work by us has demonstrated that $Sn^{IV}(Ac\text{-}Y)_2$-tetraphenylporphyrins (Ac-Y = acetyl N-protected-*L*-tyrosine) can promote photoinduced PCET in the presence of pyrrolidine as external base.[40,41] On these premises, it was decided to introduce in the YALP sequence two terminal histidine residues (positions 1 and 23, in place of glycines), as they may act as internal bases towards the proximal tyrosine residues. In this way the resulting peptide (**P2** in Figure 3.1.10) should present all the key components required to drive transmembrane photoinduced PCET: a Sn^{IV}-porphyrin photosensitizer, tyrosine electron donors, and a histidine residue as possible internal base. When embedded in a lipid bilayer, for statistical reasons, **P2** will in part form relatively close dimers of opposite sequence sense, resulting in facing PSs couples. Upon visible-light excitation of the metallo-porphyrin a photoinduced PCET may be activated: electron transfer from the tyrosine to one excited Sn^{IV}-porphyrin mediated by concomitant deprotonation of the same residue by the histidine (or by an external base in the inner compartment), followed by hole scavenging from the inner ED; the other excited PS would by quenched by the external EA, thus allowing electron shuttling between the coupled PSs (as very schematically represented in Figure 3.1.11). This design aims at mimicking the natural Tyr_Z-His_{190} pair found in photosystem II (see Chapter 2).

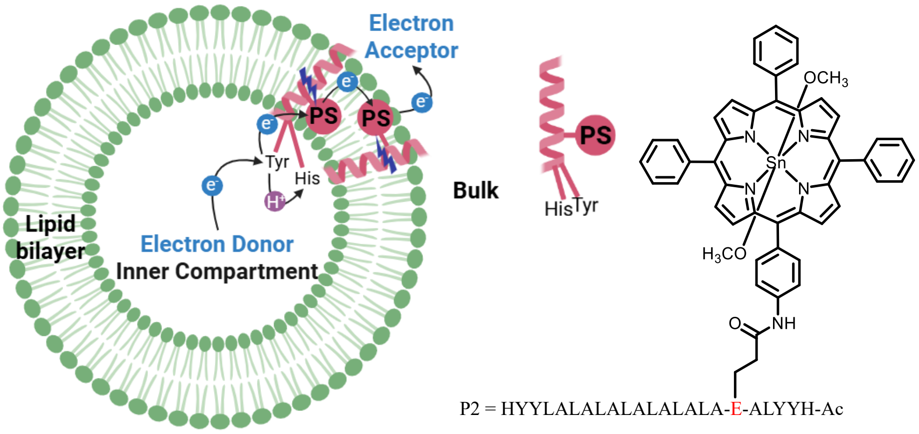

Figure 3.1.11. Schematic representation of the photoinduced transmembrane PCET and the Sn^{IV}-porphyrin/peptide conjugate **P2** described in this Chapter.

The preparation strategy followed the approach described in the previous example: an unnatural glutamic amino acid residue was conjugated (by amide-bond formation) to a pendant tin-porphyrin chromophore, then this residue was used in place of a leucine in the peptide synthesis.

The idea of inserting only one chromophore in the peptide sequence was decided from some observations done in the previously reported example by Bonnet *et al.*[28] These observations relate to the fact that the presence of two chromophores on a single peptide strand leads to slow charge migration due to a limited driving force. In addition, a single-chromophore sequence is certainly less synthetically demanding. The position at which to insert this unnatural amino acid was chosen to be number six, based on modelling using YASARA, taking into consideration the peptide folding within the membrane and the relative distances of the key active components. Two shorter heptapeptides, featuring only a portion of **P2** and **P3** were also prepared as model compounds to be used in organic solvents (instead of lipid membranes), to gain insights into the feasibility of photoinduced electron/proton processes (**P5** and **P6**, Figure 3.1.12). It must be clearly noted here that in the experimental conditions used for the purification and study of these peptides, the chloride apical ligands anions on the tin center are most certainly replaced by two methoxy ligands, so reference will always be given to **P2** and **P5**, while **P1** and **P4** will be neglected.

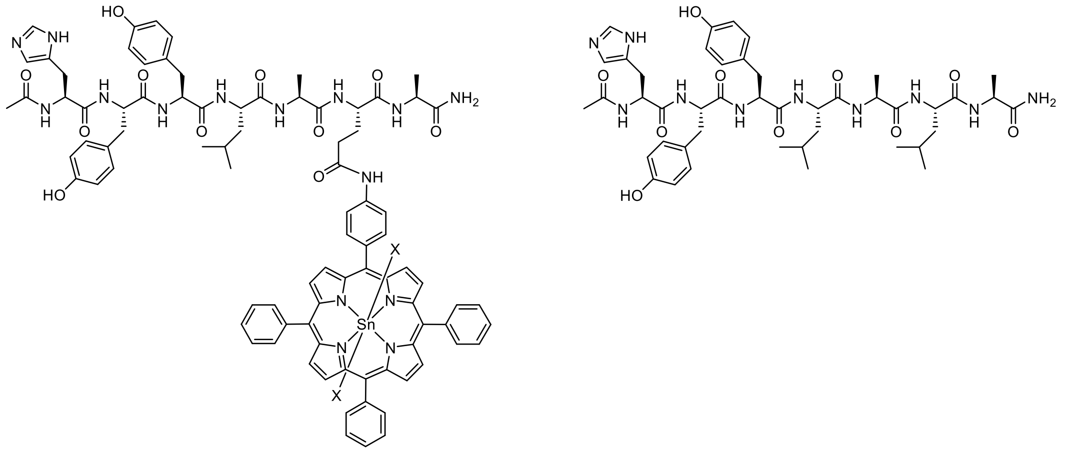

P4 = Ac-HYYLA-ESnCl$_2$P-A; X = Cl$^-$
P5 = Ac-HYYLA-ESn(OCH$_3$)$_2$P-A; X = CH$_3$O$^-$

P6 = Ac-HYYLA-L-A

Figure 3.1.12. Chemical structure of the shorter peptides synthesized and described in this Chapter.

3.2. Results and Discussion.

*3.2.1. Synthesis and characterization of the Sn^{IV}-porphyrin building block **5**.*

Prior to the synthesis of the Sn^{IV}-porphyrin/peptide conjugate, it was necessary to choose the strategy for the introduction of the chromophore into the target YALP$_{23}$ peptide. Several strategies of (metallo)porphyrin conjugation to biomolecules (such as sugars, DNA, peptides, and proteins) have been reported.[42] For the synthesis of chromophore-modified peptides, three main conjugation strategies are used: i) bioorthogonal reactions (Staudinger ligation; Copper

Catalyzed Alkyne-Azide Cycloaddition, CuAAC; Strain Promoted Alkyne-Azide Cycloaddition, SPAAC; or olefin metathesis); ii) cysteine-based ligations (thio-maleimide and thiol-haloacetamide ligations); and iii) amino-group based ligations (thiourea formation or amide coupling). The cysteine-based approach was excluded because the final target peptide does not contain cysteine residues, while the other strategies remained viable. The straightforward idea was to take advantage of the availability of the mono-amino porphyrin, **TPP-*p*NH_2** (**1**) (see Chapter 2), and to couple it to a carboxylic pendant group of an N- and C-protected natural amino acid, following adapted literature procedure.[43,44] This porphyrin-bearing unnatural amino acid was used for the peptide synthesis (see also Section 3.2.3). *L*-glutamic acid (E) was selected as the optimal residue for conjugation with the amino-porphyrin unit **1**. The choice was motivated by the presence in E of two carboxylic functions: the γ-carboxyl group, suitable for the covalent coupling of the chromophore, and the α-carboxyl group, available for peptide synthesis. The alternative option, *i.e. L*-aspartic acid (D) was excluded as it would provide a too short spacer between the pendant chromophore and the peptide chain. Also, the unnatural amino acid resulting from the conjugation between D and **1** may undergo intramolecular cyclization or isomerization unwanted reactions.[45,46] The preparation of the selected building block **5** is outlined in Scheme 3.2.1. First, the precursor **TPP-*p*NH_2** (**1**) was synthesized using previous reported procedures, adapted by us (see also Chapter 2).[47–49] After nitration of TPP, the nitro group is reduced working in concentrated HCl in the presence of $SnCl_2·2H_2O$. **1** was obtained as a pure purple solid after purification *via* column chromatography in 50% yield. **5** was then synthesized *via* a multi-step protocol by adapting a literature procedure,[43] and some of the methods described by us in Chapter 2. An alternative synthetic strategy for the obtainment of the free-base analogue of **5** was also pursued and is described later in this Section.

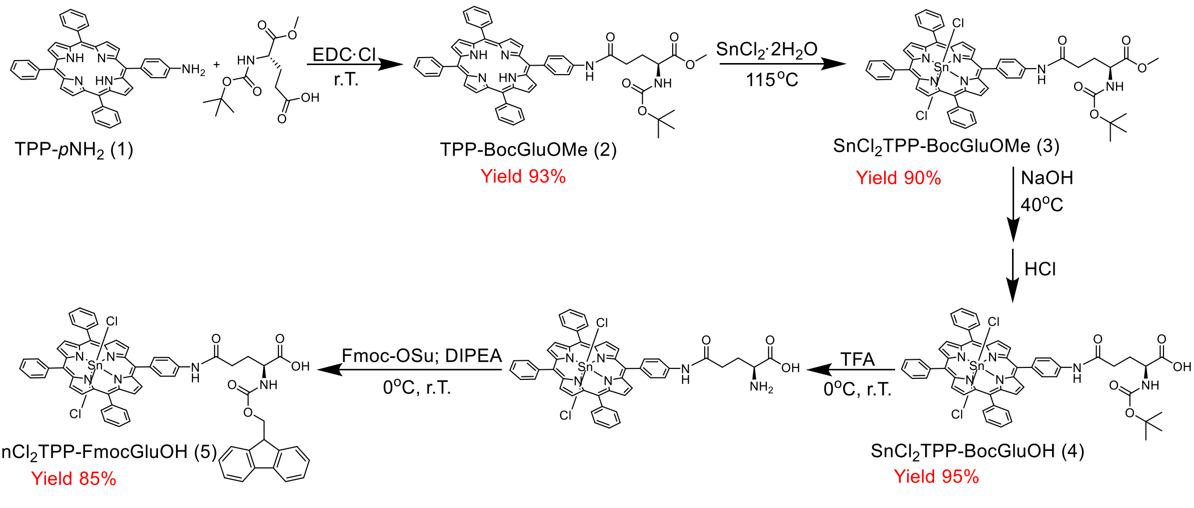

Scheme 3.2.1. Synthetic scheme followed for the preparation of **$SnCl_2$TPP-FmocGluOH** (**5**).

TPP-*p*NH$_2$ (**1**) was first coupled with the N- and C-protected *L*-glutamic acid (BocGluOMe) using a classical EDC-mediated amide coupling, yielding the porphyrin-amino acid intermediate **2**. This free-base porphyrin was metalated with $SnCl_2{\cdot}2H_2O$,[50] affording **3** in 90% yield. The methyl-ester was then hydrolyzed to give **4** and, finally, the N-protecting Boc group was replaced with a Fmoc group, affording the Sn^{IV}-porphyrin building block **5**, suitable for solid-phase peptide synthesis (SPPS). All the intermediates and the final product were isolated in very good yields and fully characterized in solution by 1D and 2D NMR spectroscopy, ESI-MS, HRMS and UV-Vis absorption spectroscopy (see also Appendix B). For simplicity only the characterization of derivative **5** will be given here. In Figure 3.2.1 the ^{1}H NMR (dmso-*d$_6$*) is reported. Complete proton assignments were done by signal integration, multiplicity, correlation peaks in the 2D spectra (see Figures S19 – S21 in Appendix B), and comparison with known similar compounds (Chapter 2). The broad singlet at $\delta = 12.79$ is assigned to the carboxylic proton while the singlet at $\delta = 10.52$ ppm to the amidic proton close to the macrocycle. The non-equivalent β-pyrrolic protons of the porphyrin resonate as a partially resolved multiplet centered at $\delta = 9.35 – 9.17$. The resonances at $\delta = 8.33 – 8.27$ ppm and $\delta = 8.02 – 7.88$ ppm are attributed to the *ortho*, *meta* and *para* protons of the porphyrin aryl groups and to two of the aromatic protons of the Fmoc protecting group. The remaining six aromatic protons of the protecting group resonate as a doublet at 7.79 ppm and as two multiplets of equal intensities between 7.48 – 7.33 ppm. The signals of the aliphatic protons of the same group give rise to a multiplet at $\delta = 4.41 – 4.24$ ppm. The two resolved doublets at $\delta = 8.23$ and 8.16 ppm, both integrating for two protons, are relative to H^g and H^f, respectively. The amide group formed in the last step (NH^h) is found as a doublet at $\delta = 7.84$ ppm, while the amino acid fragment proton resonances are attributed as follows: H^b (4.15 ppm), H^d (2.66 ppm), $H^{c'}$ (2.26 ppm) and H^c (2.01 ppm). It must be noted that protons next to the stereogenic center are diasterotopic and thus appear split into two multiplets of equal intensity.

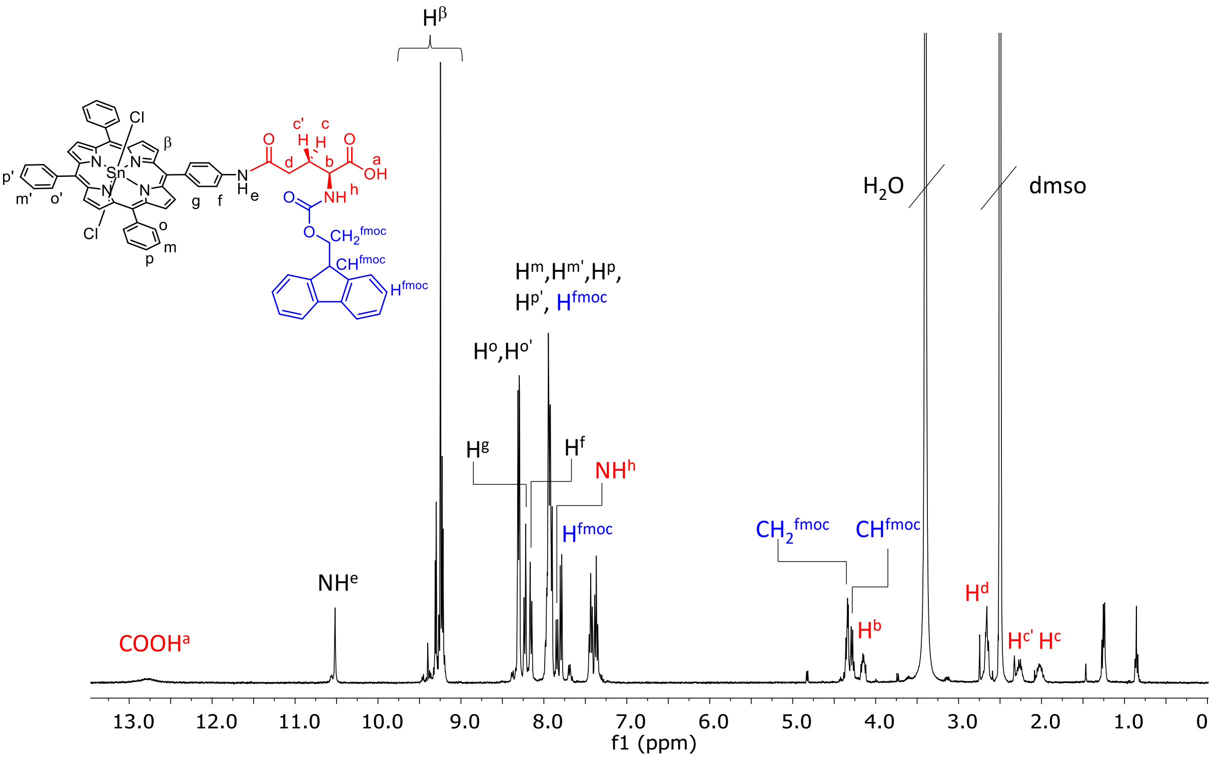

Figure 3.2.1 ^{1}H NMR spectrum (dmso-d_6, 298 K) of **5**, with colored labeling scheme.

In the ^{1}H-^{119}Sn HMBC spectrum of **5**, the cross peak found, due to the ^4J correlation between the β-pyrrolic protons and the tin nucleus, has a chemical shift (–590 ppm) in perfect agreement with the reference SnCl$_2$-tetraphenylporphyrin (SnCl$_2$TPP) and the analogous conjugates discussed in Chapter 2, thus demonstrating the presence of two chloride anions on the apical position of the metal center (Figure 3.2.2).

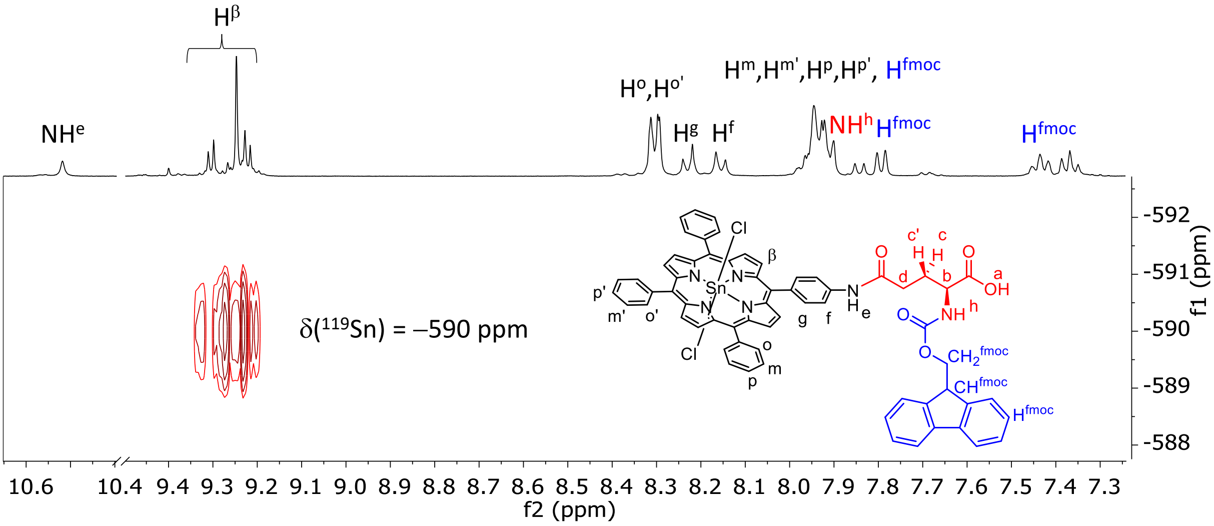

Figure 3.2.2 Aromatic region of the ^{1}H-^{119}Sn HMBC spectrum (dmso-d_6, 298 K) of **5**.

Further confirmation of the nature of **5** was obtained by HRMS data. Due to the strong oxophylicity of Sn^{IV} centre, the SnCl$_2$-porphyrin is rarely directly observed in the mass spectrum (see also Chapter 1). The peak found for the $[\mathbf{5} - 2Cl + OH]^+$ species is fully consistent with the coordination properties of the metal centre (Figure 3.2.3, left). A distinguished feature of **5** is that of being chiral, as nicely observed by the induced CD signal in the visible absorption region of the Sn^{IV}-porphyrin (Soret-Band, Figure 3.2.3, right). The UV-Vis absorption and fluorescence emission spectra of **5** in dichloromethane present the typical features of a $SnCl_2TPP$ porphyrin (Figure 3.2.4, see also Chapter 2).

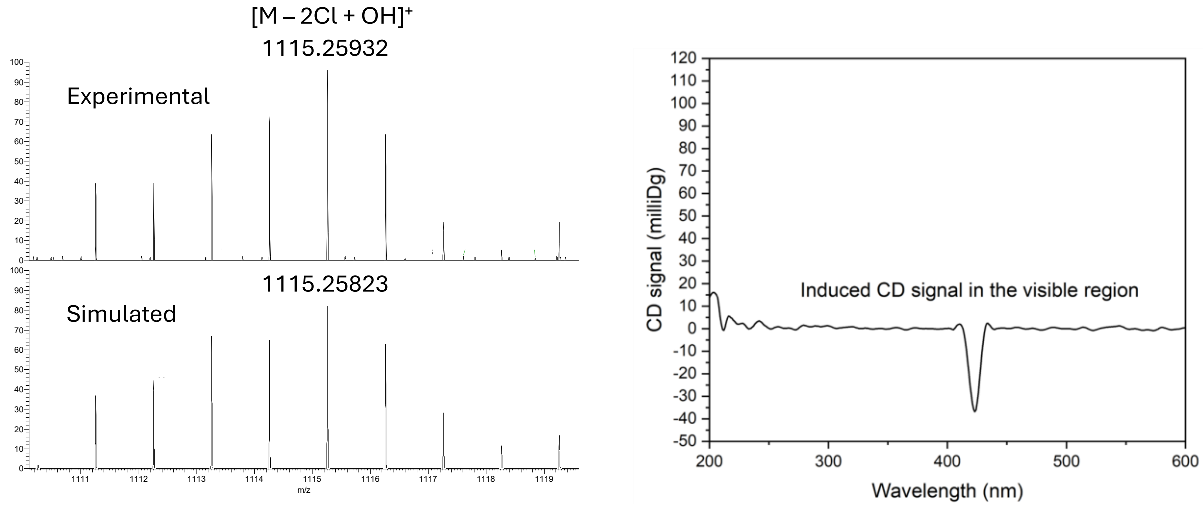

Figure 3.2.3. HRMS of **5** in $CH_3CN:H_2O$ 1:1, experimental (top) and simulated (bottom). Right: CD spectrum (CH_2Cl_2, 25 μM) of **5**.

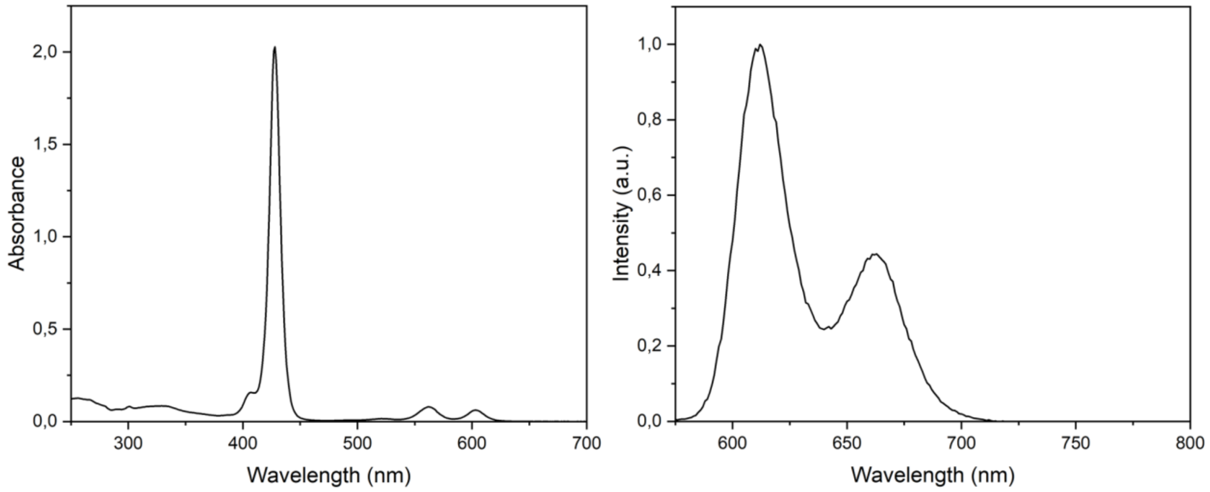

Figure 3.2.4. Left: UV-Vis absorption spectrum (CH_2Cl_2, 5 μM) of **5**. Right: Emission spectrum (CH_2Cl_2, 25 μM, $\lambda_{irr} = 562$ nm) of **5**.

Figure 3.2.5 shows the cyclic voltammogram of **5** in CH_2Cl_2, at room temperature. Within the window -2.0 V < E < 1.2 V *vs.* $Fc^{+/0}$, conjugate **5** presents one reversible reduction wave at -1.28 V *vs.* $Fc^{+/0}$, attributed to the first one-electron reduction of the porphyrin macrocycle and one irreversible wave at -1.75 V *vs.* $Fc^{+/0}$, attributed to the second one-electron reduction of the macrocycle. In the oxidation window, a reversible process at +0.93 V *vs.* $Fc^{+/0}$ is observed, attributed to porphyrin oxidation. These results are comparable with the previous examples reported by us (see also Chapter 2) and literature data.[51]

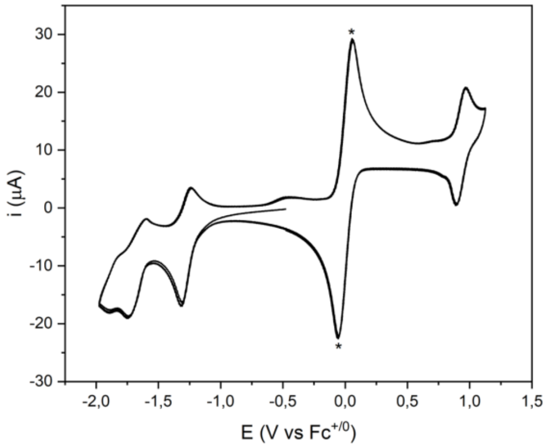

Figure 3.2.5. Cyclic voltammetry of **5** (1 mM CH_2Cl_2). CV recorded at 0.1 V/s with 0.1 M $TBAPF_6$ as supporting electrolyte under inert atmosphere using a glassy carbon as working electrode, a platinum wire as a counter electrode, Ag/AgCl (3 M KCl) as reference and ferrocene as internal standard.

An alternative synthetic strategy for the obtainment of **5** was also pursued (Scheme 3.2.2), Starting with the N- Fmoc C-O*t*Bu protected *L*-glutamic acid, and following similar methods as the ones described above, it was possible to isolate **7** (the free-base analogue of **5**) in only two steps. Briefly, **1** was conjugated to the N-Fmoc and C-O*t*Bu protected-amino acid (Fmoc-GluO*t*Bu) using the classical EDC mediated amide coupling, yielding conjugate **6** in 98% yield. The *t*Bu-ester was then hydrolyzed with TFA using a slightly modified literature procedure,[52] yielding the free-base porphyrin **7** in 75% yield, after column purification, to remove unreacted material.

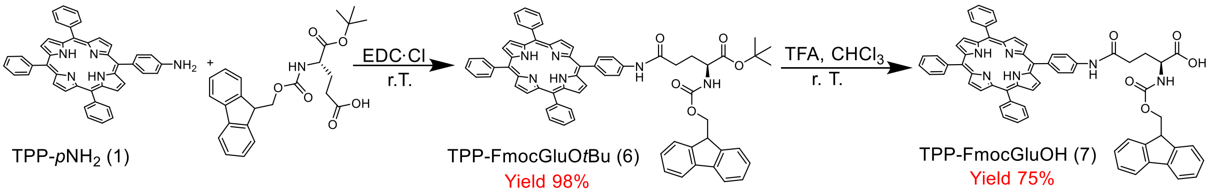

Scheme 3.2.2 Synthetic scheme followed for the obtainment of compound **7** (free-base analogue of **5**).

In Figure 3.2.6 the ^1H NMR spectrum (dmso-d_6) of **6** and **7** are reported. Complete proton assignments were done by combining signal integration, multiplicity and correlation peaks in the 2D spectra, and will not be discussed in detail here (see Figure S22 – S33 in Appendix B).

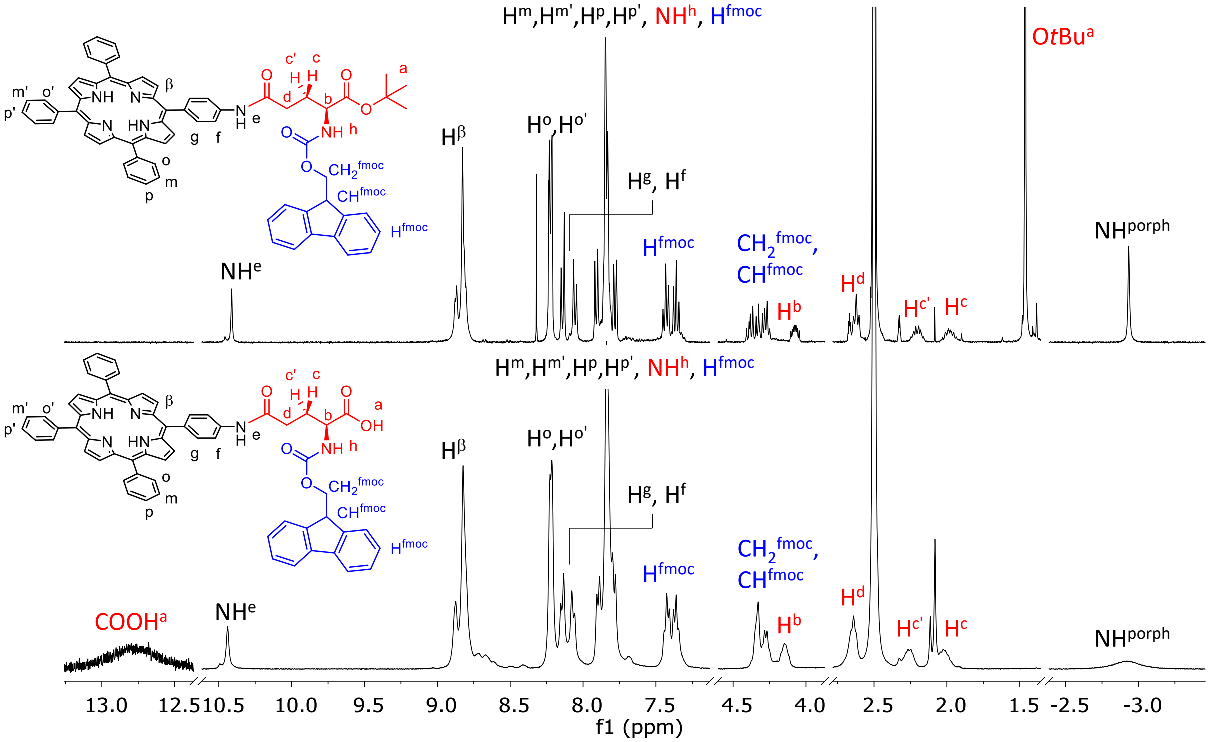

Figure 3.2.6. Comparison of the ^{1}H NMR spectra (dmso-d_6, 298 K) of **6** (top) and **7** (bottom). The –COOH proton signal in the ^{1}H NMR spectrum of **7** is partly magnified.

Efficient hydrolysis of **6** is confirmed by the disappearance of the singlet relative to the O*t*Bu group and the appearance of a (broad) resonance at $\delta = 12.7$ ppm corresponding to the –COOH proton. It must be noted that, during the isolation of compound **7**, TFA is neutralized by addition of a saturated aqueous solution of $NaHCO_3$. Under these conditions $NaHCO_3$ is basic enough to deprotonate the α-carboxylic group of glutamic acid, (pK_a ~ 2), affording the corresponding Na^+ salt. Subsequent acidification with HCl is required to re-protonate of the carboxylate group and thereby yield the desired compound. Therefore, the final step must be done with great care to avoid any concomitant protonation of the porphyrin inner pyrroles. From product **7** to the desired Sn^{IV}-porphyrin conjugate **5**, the metalation step is needed. Unfortunately, the strong basic environment required for complete insertion of Sn^{4+} ion in the porphyrin core, would also lead to the cleavage of the Fmoc protecting group (Fmoc deprotection typically occurs under basic conditions, *e.g.* 20% piperidine in DMF). Therefore, derivative **7** was for the moment stocked as a valuable precursor for future alternative metallo-porphyrin building blocks, for which the metal-insertion step occurs in milder conditions (*e.g.* Zn^{2+} or Co^{2+}).

3.2.2. Modelling of the Sn^{IV}-porphyrin/peptide conjugate.

To identify the optimal insertion site for the chromophore within the modified $YALP_{23}$ sequence, initial molecular modelling of the Sn^{IV}-porphyrin/peptide conjugate embedded in a lipid membrane was performed using YASARA (www.yasara.org, see also Experimental Section).[53] The two terminal glycine residues were replaced by histidines, and the unnatural amino acid (E with a pendant metallo-porphyrin) was introduced at four possible different positions along the peptide sequence, as reported in Table 3.2.1. A simplified model by which the $SnCl_2$-porphyrin was replaced by a simpler Zn^{II}-porphyrin analogue was employed, for data base availability reasons. The resulting structures were energy-minimised with the YASARA force field, and their folding within the membrane was subsequently evaluated. After 250 ps of simulation time (applying the macro run_membrane) each thermalised structure was analysed to determine the most promising site for the incorporation of the unnatural amino acid (EZnP).

Table 3.2.1. Sequence and naming of the modelled peptides. EZnP is the Zn^{II}-porphyrin analogue of Sn^{IV}-porphyrin building block **5**.

Compound name	**Peptide sequence**
P7	HYYLA-EZnP-ALALALALALALALYYH
P8	HYYLAL-EZnP-LALALALALALALYYH
P9	HYYLALA-EZnP-ALALALALALALYYH
P10	HYYLALAL-EZnP-ALALALALALYYH

Two parameters were taken into consideration: (i) the relative orientation and distance of the tyrosine residues with respect to the chromophore, and (ii) the distances between the $His_1/Tyr_2/Tyr_3$ residues. In fact, for an efficient photoinduced electron transfer to occur (or photoinduced PCET), it is crucial that the amino acids involved in the process are positioned sufficiently close to the chromophore and to each other. It was already reported that for protons typical tunnelling distances are around ~1 Å, whereas electron tunnelling can occur over tens of Å.[54] The peptide models **P7** – **P10** are shown in Figure 3.2.7.

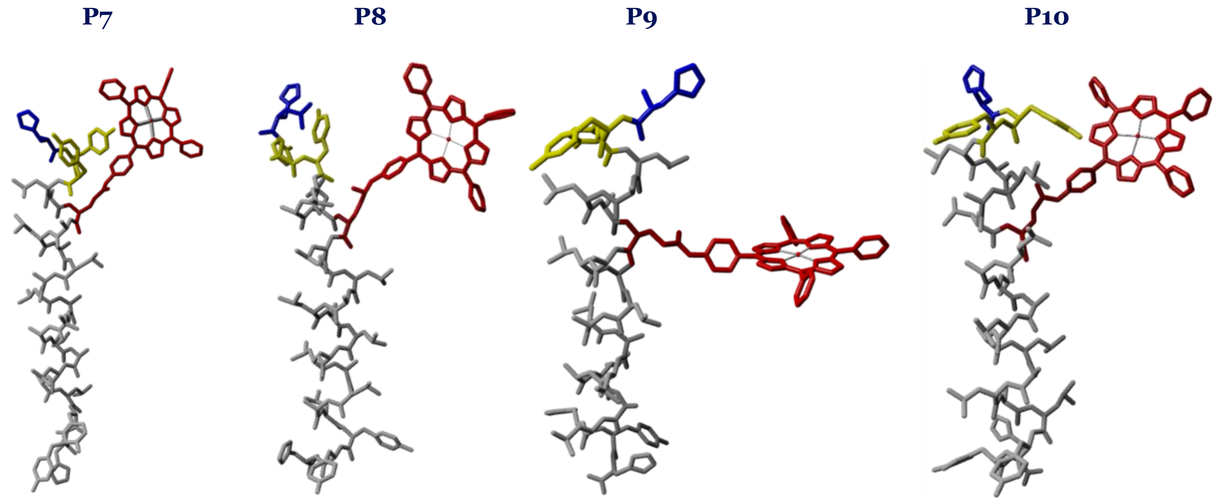

Figure 3.2.7. Models of the Zn^{II}-porphyrin/YALP peptides **P7-P10** obtained with YASARA by introducing the unnatural amino acid EZnP at different positions of the sequence. Hydrogen atoms are omitted for clarity. The peptide skeleton is depicted in grey; the pendant Zn^{II}-porphyrin unit is shown in red, the terminal His$_1$ in blue, and Tyr$_2$/Tyr$_3$ in yellow.

As illustrated in Figure 3.2.7, for **P8** and **P9** (*i.e* when the modified glutamic acid is located at positions 7 or 8), the residues Tyr$_2$/Tyr$_3$ and the chromophore are found to be oriented on opposite sides of the α-helical structure, and therefore far too distant (see also Table 3.2.2), ruling out the possibility of fast electron transfer between the tyrosine residues and the excited state of the porphyrin. In contrast, models **P7** and **P10** present the chromophore and Tyr$_2$ on the same side of the α-helix. Nonetheless, the distances between His$_1$/Tyr$_3$ and those between Tyr$_3$/Tyr$_2$ seem more favourable when EZnP is in position 6 (see also Table 3.2.2). Overall, the **P7** isomer was selected, as the key evaluated parameters are within the expected range for potential fast proton and electron transfer.

Table 3.2.2. Selected distances (in Å) evaluated in the models peptides **P7-P10**.

Model	His$_1$-Tyr$_3$ (N···O)[a]	Tyr$_2$-Tyr$_3$ (O···O)[b]	Tyr$_2$-βH (O···C)[c]
P7	5.1	6.4	3.9
P8	3.8	5.1	15.4
P9	15.1	10.3	19.3
P10	14.7	12.2	5.4

[a] Distance between the nitrogen atom of the NH group in His$_1$ and the phenolic oxygen in Tyr$_3$. [b] Distance between the two phenolic oxygen atoms in Tyr$_2$ and Tyr$_3$. [c] Distance between the phenolic oxygen atom in Tyr$_2$ and the closest β-pyrrolic carbon of the porphyrin macrocycle.

It should be noted, however, that these models need to be taken with some care for several reasons: (i) the lipid membrane used in the simulations (PEA) differs from the experimental one (DPPC); (ii) the pendant chromophore lacks the (potentially bulky and non-innocent) axial methoxy ligands on the metal centre; (ii) the peptide sequences were equilibrated in the membrane for only 250 ps, while longer simulation times in the ns-ms regime may be required to obtain more refined indications.

As already anticipated above, the actual Sn^{IV}-porphyrin/peptide **P2**, homologous of **P7**, was designed for lipid bilayer embedding and activation of photoinduced transmembrane electron transfer or, even more ambitiously, photoinduced transmembrane PCET. More in detail, it was foreseen that a certain fraction of the peptides would form antiparallel dimers within the membrane, bringing thus two porphyrin units in a face-to-face orientation, as schematically depicted in Figure 3.1.11 above. This scenario was also modeled with YASARA, by positioning two antiparallel **P7** in the desired dimerized fashion and then by equilibrating this **P7** couple in the membrane with the same conditions used above. The resulting model is presented in Figure 3.2.8

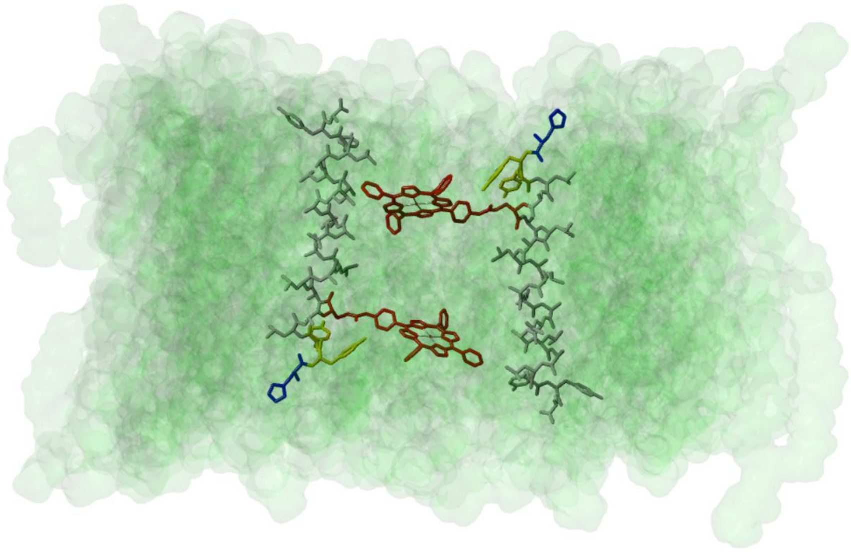

Figure 3.2.8. Model of the antiparallel dimer formed by two antiparallel **P7** peptides obtained with YASARA equilibrating the constructed membrane (in transparent green) for 250 ps. Hydrogen atoms are omitted for clarity; the peptide skeletons are depicted in grey; the pendant Zn^{II}-porphyrin units are shown in red, the terminal His_1 in blue, and Tyr_2/Tyr_3 in yellow.

On the occurring of these peptide dimer formation, and in coehistence with monomeric conjugates (which inevitably will orient the chromophore either closer to the inner compartment or to the bulk aqueous phase, depending on the strand orientation), a photoinduced transmembrane electron transfer may be achieved, by a sequence of short and fast electron transfer steps, as very schematically depicted in Figure 3.2.9. The proposed mechanism is the following: first, light absorption by a chromophore will populate the SnP^* excited state of the PS, in the monomeric embedded strands. Next oxidative quenching process of some SnP^* chromophores by the electron acceptor located in the external aqueous phase may occur, leading to the formation of oxidized photosensitizers ($PS^{\cdot+}$) at the outer monolayer (Figure 3.2.9A). Simultaneously, reductive quenching of other SnP^* chromophores by the electron donor in the internal aqueous phase may form some reduced photosensitizers ($PS^{\cdot-}$) at the inner monolayer (Figure 3.2.9B). The (partial) occurring of dimerization will couple reduced ($PS^{\cdot-}$) and oxidized ($PS^{\cdot+}$) photosensitizers and restore the ground state by charge recombination, thus finalizing the intended unidirectional transmembrane electron transfer (Figure 3.2.9C). Additionally, for the reductive quenching, our design makes that PCET might take place: once the chromophore is excited, the presence of a terminal histidine and tyrosine residues at short distances is conceived to accompany electron transfer from tyrosine to the Sn^{IV}-porphyrin macrocycle by a concomitant deprotonation of the phenol by the histidine. This process should result in a longer lifetime for the state where the tyrosine is oxidized and the photosensitizer is reduced ($PS^{\cdot-}$). Ultimately, charge recombination with $PS^{\cdot+}$ in the outer monolayer regenerates the ground state of the photosensitizer, but this process is less favorable in absence of the proton, hence with PCET (see also Figure 3.1.11, above). Alternatively, an external base with an appropriate pK_a may be added in the inner compartment to promote proton abstraction from the oxidized Tyr residues, or to move the proton further from the His residue.

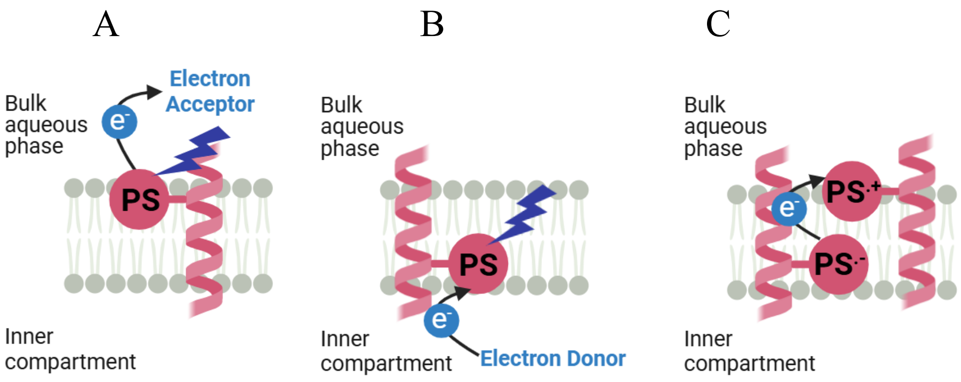

Figure 3.2.9. Schematic representations of the possible photoinduced intercomponent processes in asymmetric liposomes embedded with **P2**.

3.2.3. Synthesis and characterization of peptides.

In this project two longer and two shorter peptides were synthesized in 50 µmol scale (see also Figures 3.1.10, 3.1.11 and 3.1.12 above): a 23-AA peptide **P2** and its porphyrin-free analogue

P3 and a 7-AA peptide **P5** and its porphyrin-free analogue **P6**. In all cases the conjugation of natural amino acids was done using the well-known Solid Phase Peptide Synthesis (SPPS) method, while the unnatural amino acid with the pendant chromophore was manually coupled. A representative synthetic scheme of the entire procedure is reported in Scheme 3.2.3. Briefly, the deprotection of the Fmoc-protected amino acids was done using piperidine in DMF; to facilitate the coupling DIC (as activator) and Oxyma (as base) were used; acetic anhydride was employed for the acetylation of the N-terminus before the cleavage from the resin was performed using TFA (see Experimental Section for more details).

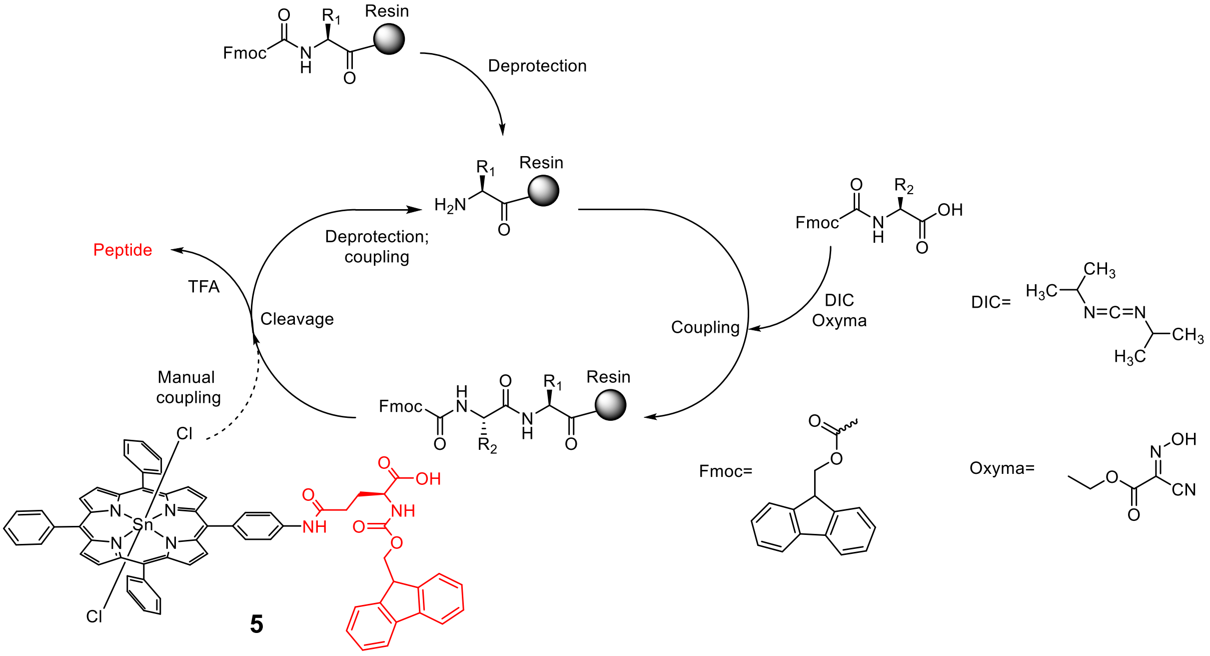

Scheme 3.2.3. Schematic representation of the Sn^{IV}-porphyrin/peptide synthesis.

Both model peptides with only natural amino acid-containing sequences were purified by standard HPLC using a C_{18} column and a H_2O:CH_3CN:*t*BuOH eluent, affording **P3** and **P6** in in 10% and 25% yield, respectively. In contrast, the purification of the Sn^{IV}-porphyrin/peptide conjugates proved to be much more challenging. The strong hydrophobic character of these molecules, arising both from the presence of apolar amino acid residues and from the porphyrin chromophore, prevented the successful use of standard reverse-phase HPLC methods. Several column/solvent combinations were tested, including:

- C_{18} column with H_2O:CH_3CN:*t*BuOH;
- C_4 column with H_2O:CH_3CN:*t*BuOH;
- C_4 column with CH_3CN:*i*PrOH;
- diphenyl column with CH_3CN:*i*PrOH.

The only effective purification method was found to be Size Exclusion Chromatography (SEC), using Sephadex LH-20 as stationary phase and methanol as eluent. As already stated, given the purification conditions and the experimental NMR evidence below, only reference to the di-methoxy Sn^{IV}-porphyrin/peptide conjugates will be given (**P2** and **P5**), with neglection of the dichloro Sn^{IV}-porphyrin/peptides analogues (**P1** and **P4**). After purification, all peptides were preliminarily characterized by LC-MS (ESI) on a C_{18} column. For the **P3** and **P6**, the main signals corresponded either to the doubly charged peptide or the singly charged one (see also Experimental Part and Appendix B). On the other hand, the LC-MS analysis performed on the two Sn^{IV}-porphyrin-functionalized peptides showed in both cases a main peak corresponding to the doubly charged species without apical ligands on the tin center (see also Chapter 1 and 2). The molecular identities of **P3**, **P5** and **P6** were further confirmed by HRMS (see Experimental Section and Appendix B), while for **P2** no signals in the HRMS spectrum were detected. In general, the mass analysis confirmed that in the isolated product the main species were the desired ones. Impurities mainly derived from the non 100% efficient coupling of the amino acids, the amount of these impurities was not estimated. NMR characterization in solution was also performed. The resulting NMR spectra proved quite complicated to be interpreted, as expected for large peptides made of a repetition of similar residues, as they may adopt different conformations in solution and/or form unpredictable dimers/trimers or higher aggregates. NMR experiments were first performed on the two heptapeptides in methanol and then compared to the spectra of the corresponding full-length peptides (CD_3OD was chosen due to the poor solubility of **P2** in most tested solvents). The simplest case of **P6** will be now discussed. In the ^{1}H NMR spectrum of **P6** signal integration and multiplicity were found consistent with the expected structure (Figure 3.2.10). Phenolic and amidic protons are not observed due to exchange process with methanol or residual water. Full assignment was realized with multiple 1D and 2D NMR techniques: the two singlets at $\delta = 8.68$ and $\delta = 7.15$ ppm are attributed to the aromatic protons of the terminal histidine, while the four doublets at $\delta = 7.08 - 6.65$ ppm pertain to the aromatic protons of the tyrosine residues. In the aliphatic region, the resonances at $\delta = 4.60 - 4.27$ ppm correspond to the CH$^{\alpha}$ protons of the peptide chain (^{1}H-^{1}H COSY analysis allow to distinguish between the CH$^{\alpha}$ signals of His and Tyr and those of Ala and Leu residues, at higher and lower ppm values, respectively). The multiplets centered around $\delta = 3.00$ ppm are attributed to the diasterotopic protons of aromatic side chains, distinguished from those of the *iso*-propyl groups, which resonate between 1.71 – 1.54 ppm.

The leucine and alanine side-chain protons were also distinctly assigned (aside for a partial overlap with the methyl resonance of N-acetylated histidine).

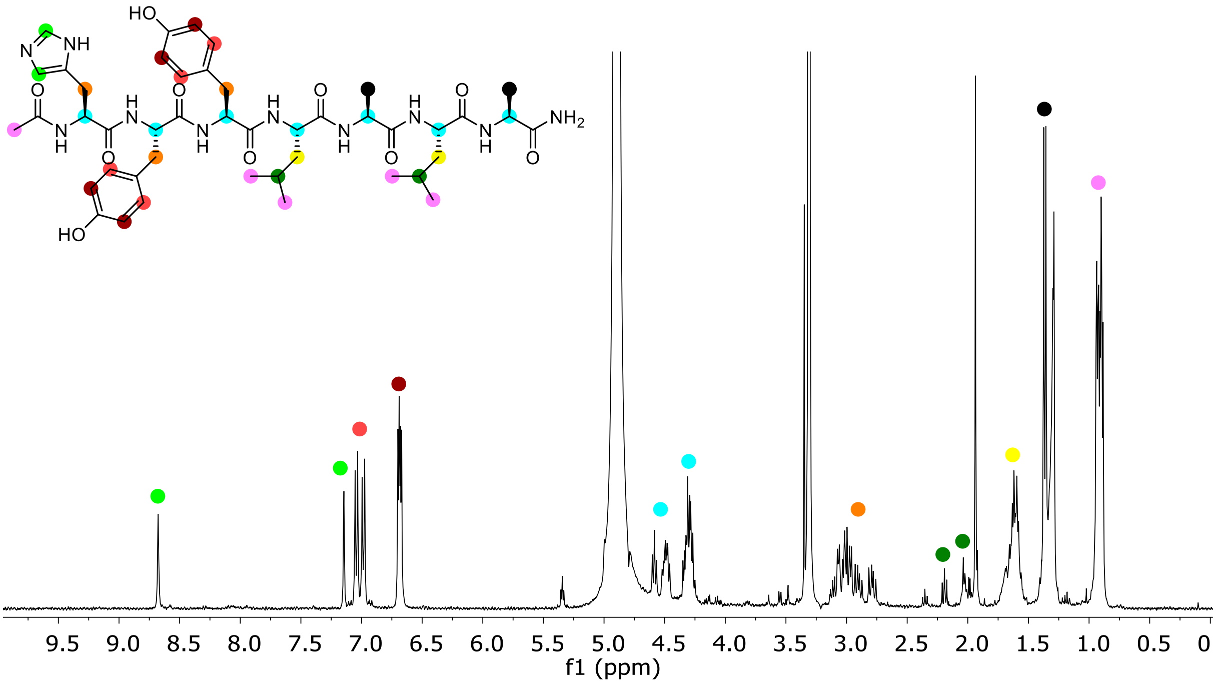

Figure 3.2.10. ^{1}H NMR spectrum (CD_3OD, 298 K) of **P6**, with color labeling scheme.

For **P5**, the presence of the pendant metallo-porphyrin was confirmed by a ^{1}H-^{119}Sn HMBC experiment. As discussed in Chapter 1 and 2, the tin center is oxophylic, therefore in methanol solution the axial chlorides rapidly exchange with methoxy groups. Indeed, in the heteronuclear 2D spectrum one main and one very minor species were identified, based on the ^{119}Sn chemical shifts (Figure 3.2.11), and also by comparison with literature values.[50,55,56] The major derivative correspond to the $Sn(OCH_3)_2$-porphyrin peptide **P5**, while the very minor one correspond to the $SnCl_2$-porphyrin peptide **P4** analogue ($\delta(^{119}Sn) = -565$ ppm and $\delta(^{119}Sn) = -590$ ppm, respectively).

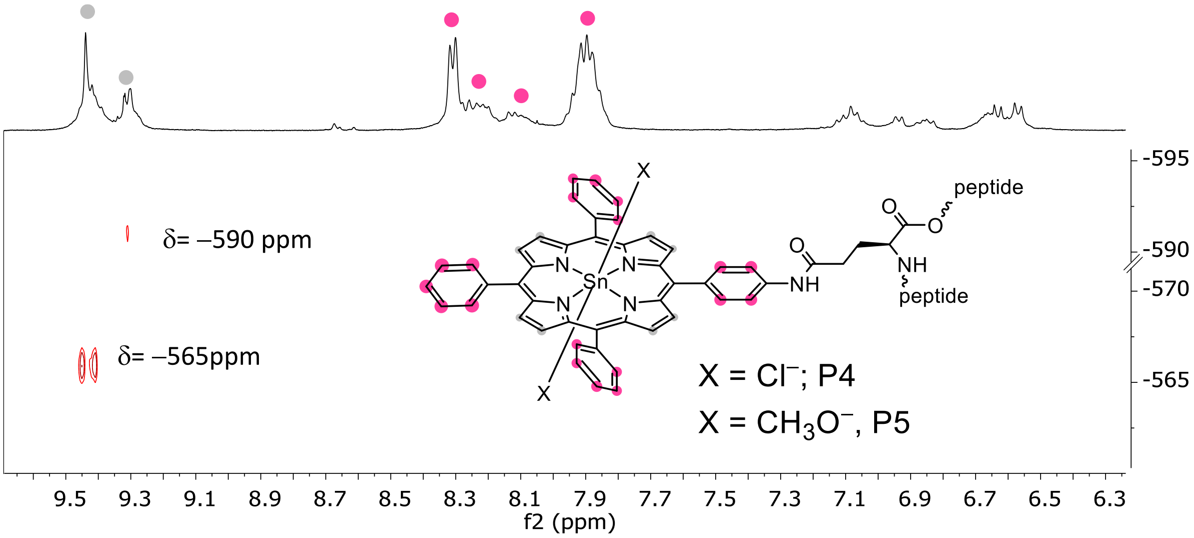

Figure 3.2.11. Aromatic region of the ^{1}H-^{119}Sn HMBC-spectrum (CD$_3$OD, 298 K) of a mixture of **P4** and **P5**.

On the other hand, complete analysis of the ^{1}H NMR spectrum was hampered given the generally broad and poorly resolved signals. Nonetheless, by comparing the ^{1}H NMR spectra of **P6** and **P5**, some qualitative assignments were possible (Figure 3.2.12). In particular, the β-pyrrolic and phenyl protons of the porphyrin macrocycles (grey and pink respectively) as well as the protons of the aromatic His/Tyr residues were assigned and distinguished from those of the peptide main chain and aliphatic residues.

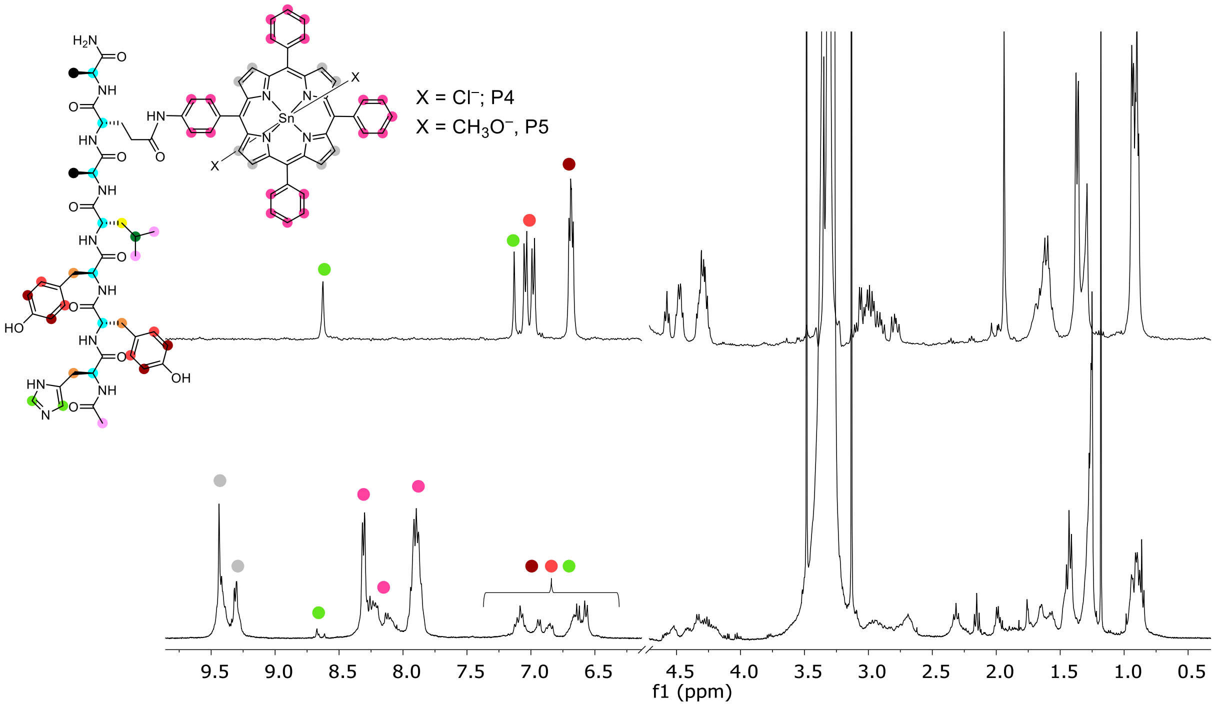

Figure 3.2.12. ^{1}H-NMR spectrum (CD$_3$OD, 298 K) of **P6** (top) and mixture of **P4** and **P5** (bottom), with color labeling scheme.

To study the target **P2** peptide, in analogy with the two simpler peptides discussed above, the porphyrin-free model **P3** was characterized first. The first significant difference between **P3** (Figure 3.2.13) and **P6** (Figure 3.2.10) is the appearance of a set of signals in the range of δ = 8.43 – 7.83 ppm belonging to the NH amide protons, and of an increased number of doublets pertaining to the tyrosine aromatic protons (four for **P6** and eight for **P3**). Given the intrinsic directionality of **P3**, the four tyrosine residues are not chemically equivalent, and therefore eight doublets may be expected for the corresponding aromatic protons. However, the distinct chemical shifts and their distribution cannot be unequivocally explained by the local chemical inequivalence. Instead, these observations may suggest that (at least in methanol solution) peptide **P3** is engaged in some kind of secondary interactions/folding, that both slows down exchange of the -NH amide protons, and produces some local magnetic anisotropy. Further NMR experiments, for instance by changing the nature of the solvent or varying the temperature, are planned to better elucidate this aspect.

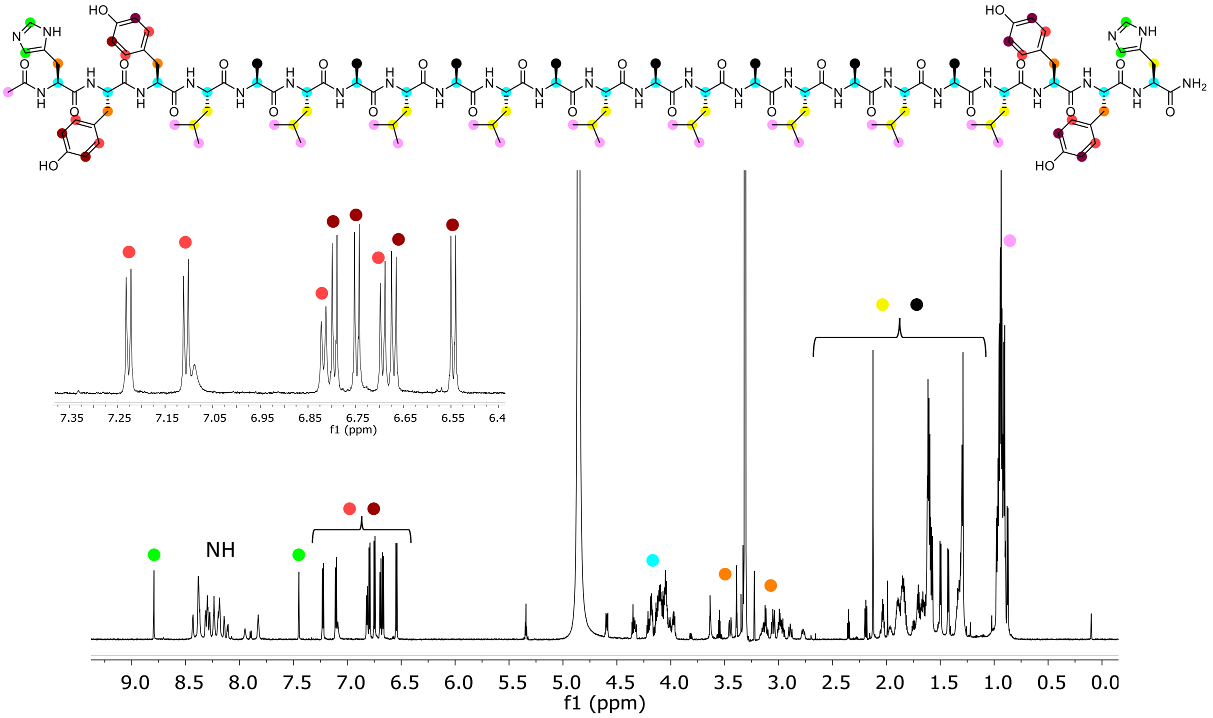

Figure 3.2.13. ^{1}H NMR spectrum (CD$_3$OD, 298 K) of **P3** with color labeling scheme. Inset: enlargement of the tyrosine aromatic resonances.

In the case of **P2** the use of an 850 MHz spectrometer equipped with a cryo-probe was necessary to obtain an acceptable signal-to-noise ratio, due to the very poor solubility of this conjugate. Still, the overall broadness of the ^{1}H-NMR spectrum did not allow for complete attribution. By comparing the ^{1}H-NMR spectra of **P3** and **P2**, and from 2D experiments, it was possible to identify the resonances corresponding to the β-pyrrolic as well as the *ortho*, *meta*, and *para* protons of the porphyrin macrocycle (indicated in gray and pink, respectively in Figure 3.2.14), confirming the incorporation of the pendant Sn^{IV}-porphyrin within the peptide sequence. The ^{1}H-^{119}Sn HMBC experiment was not recorded. Also in this case, further experiments (including the use of solid-state NMR analysis) are planned.

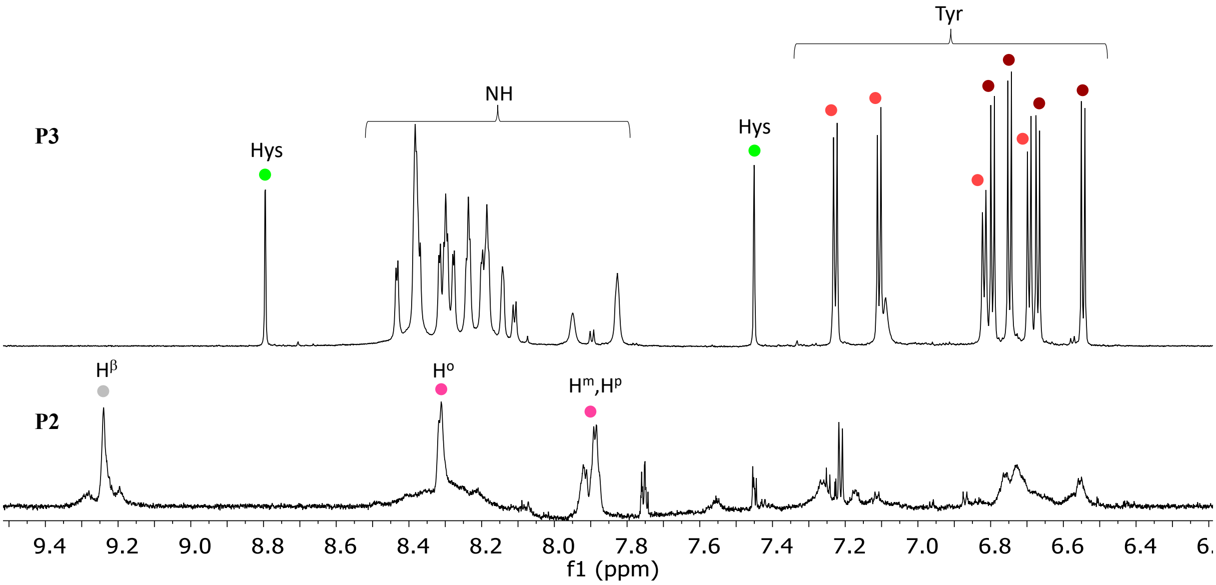

Figure 3.2.14. Aromatic region of the ^{1}H NMR spectra (CD_3OD, 298 K) of **P3** (top) and **P2** (bottom), with selected color labeling.

To evaluate whether the various isolated peptides adopt a secondary structure in solution, and more specifically the α-helical folding typical of the YALP/WALP sequences, CD spectra were recorded. All measurements were performed in 25 μM methanol solutions, a solvent known to promote α-helix formation. Both the 23-amino acid long peptides **P3** and **P2** present a spectra typical of an α-helical conformation , with two CD bands at ~208 and ~222 nm (Figure 3.2.15, left).[57] Moreover, for **P2**, an induced CD signal was observed in the visible region corresponding to the Soret band of the porphyrin unit. This signal supports the hypothesis that the porphyrin moiety was incorporated in a chiral peptide structure. In contrast, the behavior of the shorter heptapeptides proved different. While the model compound **P6** exhibits the expected α-helical signature, the CD spectrum of **P5**, lacks the features indicative of a α-helical folding, while maintaining the induced CD signal in the visible region (Figure 3.2.15, right). This may suggest that for this shorter peptide the presence of the pendant chromophore perturbs the intramolecular interactions required for helix stabilization.

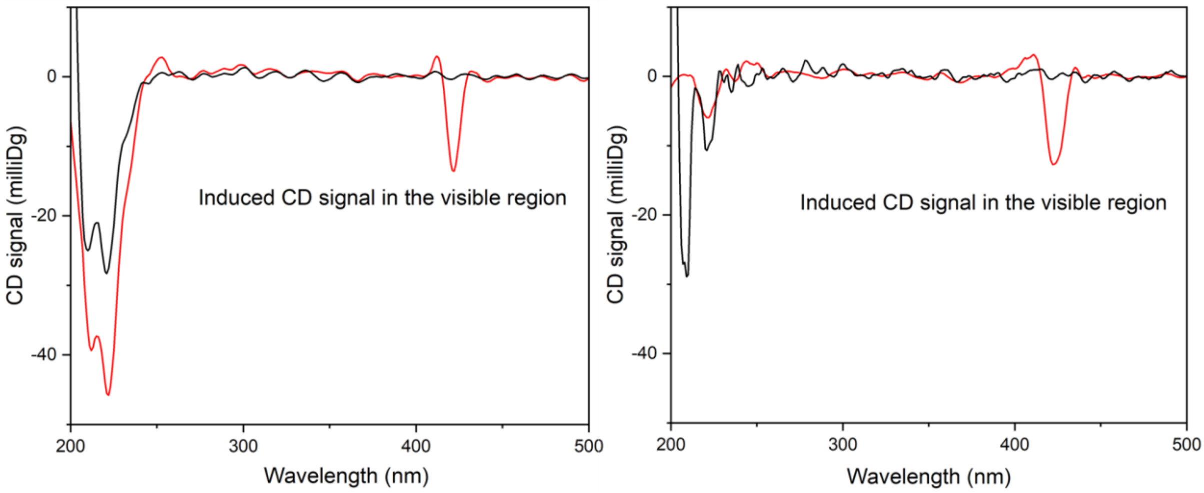

Figure 3.2.15. CD spectra (CH_3OH, 25 μM) of: **P2** (red) and **P3** (black) in the left frame; **P5** (red) and **P6** (black) in the right frame.

To conclude, the in-solution characterization of **P2**, **P3** and **P5**, **P6**, UV-Vis absorption and fluorescence emission spectra were recorded in 25 μM methanol solutions. As expected, the characteristic absorption profile of a Sn^{IV}-TPP porphyrin, consisting of a strong Soret band and two weaker Q-bands, was observed both for **P5** and **P2** (for details on the ε calculated values for **P5** see Appendix B). It is worth noting that for **P2** the light scattering is found to be higher than usual (Figure 3.2.16, left), thus impeding the determination of a precise ε value (Figure S45 in Appendix B). This light scattering may also reflect the occurring of some aggregation phenomena or, alternatively, it may be related to the very poor solubility of this conjugate and the presence of a very fine dispersion. In the UV region the characteristic absorption profile of the aromatic amino acid residues is observed (see overlap of the spectra of **P2** and **P5** in Figure 3.2.16, left, and Appendix B). Fluorescence measurements were coherent with the UV-Vis data: both Sn^{IV}-containing peptides exhibited the typical tin-porphyrin emission spectrum, with two distinct bands with maxima at 606 and 658 nm (Figure 3.2.16, right and Appendix B for additional pictures). Electrochemical CV measurements will be required to complete the present study and evaluate the redox potential of the porphyrin ground and excited states (new batches of materials need to be synthetized).

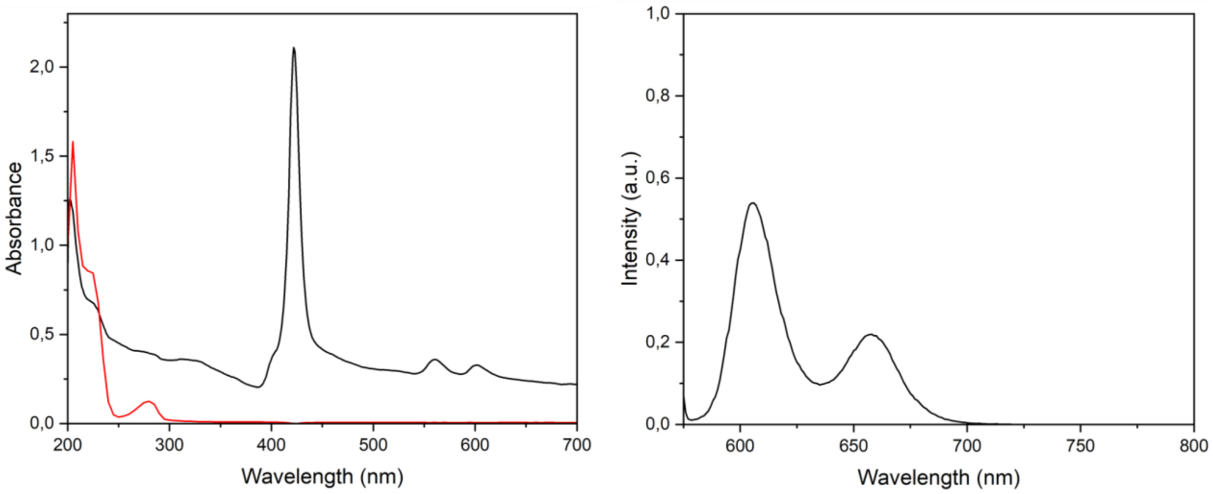

Figure 3.2.16. Left: UV-Vis absorption spectra (CH_3OH, 25 µM) of **P2** and **P3** (black and red traces, respectively). Right: Emission spectrum (CH_3OH, 25 µM, $\lambda_{irr} = 560$ nm) of **P2**.

3.2.4. Preliminary photophysical studies.

Crucial to the occurring of one of the above discussed unidirectional photoinduced process (see Section 3.2.2) is the choice of both the electron donor/base scavenger and the sacrificial electron acceptor. Based on the spectroscopic and electrochemical data presented in Section 3.2.1, it was possible to calculate the excited-state redox potentials of the pendant tin-porphyrin, in the assumption that the conjugation of **5** to the peptide did not perturb its ground-state features. In general, ground-state redox potentials were obtained by cyclic voltammetry referenced to the ferrocene/ferrocenium couple and subsequently converted to potentials relative to the saturated calomel electrode. Conversion was done by adding to the redox potential *vs.* $Fc^{+/0}$ 0.4 V, as reported in the literature.[58] The excited-state energy (E_{00}, in V) corresponds to the energy difference between the vibrational ground level of the first electronically excited state, and that of the electronic ground state. In practice, E_{00} (2.11 V) was derived from the 0-0 transition, determined from the intersection of the normalized absorption and emission spectra recorded in the same solvent. By combining electrochemical and spectroscopic data, the excited-state redox potentials in CH_2Cl_2, were calculated to be $E^*_{ox}\,(PS^*/PS^+) = -0.72$ V and $E^*_{red}\,(PS^-/PS^*) = +1.29$ V *vs.* SCE, according to the following equations:

$$E^*_{ox}\,(PS^*/PS^+) = E_{ox}\,(PS/PS^+) - E_{00} \qquad (1)$$

$$E^*_{red}\,(PS^-/PS^*) = E_{red}\,(PS^-/PS) + E_{00} \qquad (2)$$

The redox potentials were then compared with those of a variety of electron donors/acceptors reported in the literature, and in particular EDTA (in the $HEDTA^{3-}$ form), TEOA and TEA for the electron donor compartment, and WST1$^-$ for the electron acceptor part, using the energy level diagram reported in Figure 3.2.17.[11]

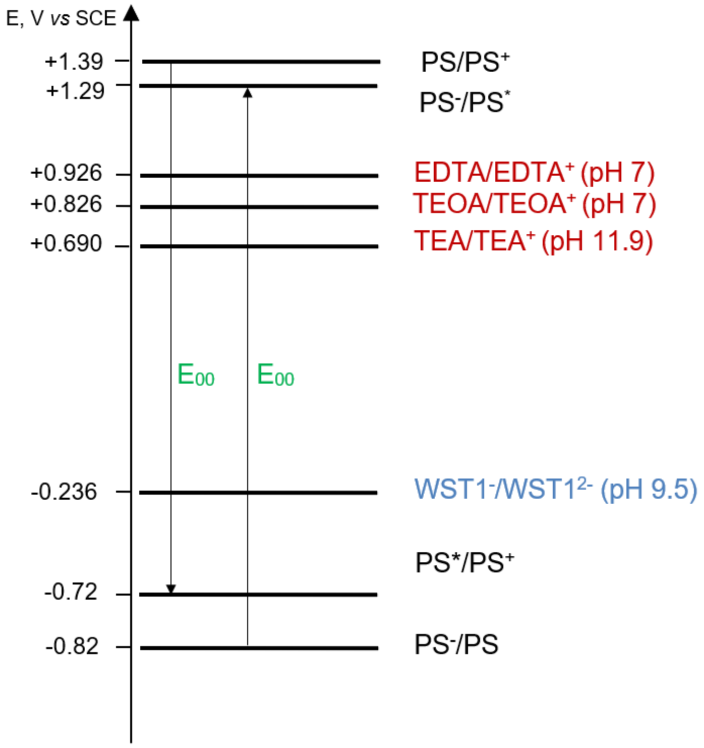

Figure 3.2.17. Redox potentials of different redox couples, taken from references 11 and 59, with respect to those calculated for the tin-porphyrin photosensitizer in **5**.

Theoretically to have an efficient and spontaneous photoinduced electron transfer it is necessary to have a thermodynamically favored process, (*i.e.* the overall ΔG of the various steps should be negative). Following the Rhem-Weller equation,[60] the standard free energy of the process can be summarized as:

$$\Delta G° = E_{ox}\,(D/D^{+}) - E_{red}(A/A^{-}) - E_{00} \qquad (3)$$

Or, given equation 1 and 2:

$$\Delta G° = E^{*}_{ox}(PS^{*}/PS^{+}) - E_{red}(A/A^{-}) \text{ for the reductive quenching} \qquad (4)$$

$$\Delta G° = E_{ox}(D/D^{+}) - E^{*}_{red}(PS^{-}/PS^{*}) \text{ for the oxidative quenching} \qquad (5)$$

In principle, the considered combinations of electron acceptor (WST1$^-$), paired to each one of the electron donors considered (EDTA, TEOA, TEA) and to the PS, should be able to promote thermodynamically favored (ΔG° < 0) photoinduced electron transfers, as reported in Table 3.2.3.

Table 3.2.3. ΔG° values for the possible couples of ED or EA and the Sn^{IV}-porphyrin photosensitizer.

PS redox couple	**ED or EA considered**	**ΔG°**
PS^{-}/PS^{*}	EDTA	−0.364
PS^{-}/PS^{*}	TEOA	−0.464
PS^{-}/PS^{*}	TEA	−0.600
PS^{*}/PS^{+}	$WST1^{-}$	−0.956

Some preliminary studies on the fluorescence quenching of **P5** in different solvents and with different electron donors/bases were performed. Quenching studies were initially done in methanol. Subsequently, owing to the limited solubility of EDTA in methanol, a 2:1 $CH_3OH:H_2O$ mixture was employed. Finally, for comparison with the data reported in Chapter 2, 30:1 $CH_2Cl_2:CH_3OH$ solutions were used – the tendency of **P5** to aggregate in pure H_2O or pure CH_2Cl_2 (as shown in the absorption spectra in Figure S49, Appendix B) required the addition of small aliquots of methanol. The emission spectra of **P5** in pure methanol and a 2:1 $CH_3OH:H_2O$ mixture are comparable with that of **5**. This observation confirmed that, at least in these conditions, no photoinduced intramolecular electron transfer from the Tyr residue to the excited SnP^{*} occurs (in line with what found for the previous SnP/Tyrosine conjugates discussed in Chapter 2) and rules out the possibility that the histidine residue acts as internal base for proton abstraction. It is worth noticing that instead the emission intensity of **P5** in a 30:1 $CH_2Cl_2:CH_3OH$ mixture is found to be lower than that observed in pure methanol, despite the two solutions having almost the same absorbance (Figure S50 in Appendix B). The possible explanations for this observation are: (i) residual aggregation phenomena leading to self-quenching of the emission; (ii) intramolecular PCET processes consequent to proton abstraction from the tyrosine by the histidine residue in the more apolar solvent mixture; (iii) intramolecular quenching through other photoinduced intercomponent pathways.

The first tested ED/base for the quenching studies was TEA in pure methanol: no emission quenching was observed with progressive addition of this donor (Figure S51 in Appendix B). Then, the emission of **P5** was measured in presence of increasing concentrations of EDTA in a 2:1 $CH_3OH:H_2O$ mixture. When increasing amounts of an aqueous EDTA solution (at pH = 8.50 to preserve its $HEDTA^{3-}$ electron donor properties) were progressively added to a 25 μM solution of **P5**, emission quenching took place initially (Figure 3.2.18), but then the emission intensity reached a plateau, above 0.010 M EDTA. Additional studies are ongoing to explore EDTA concentrations between 0.00 and 0.010 M.

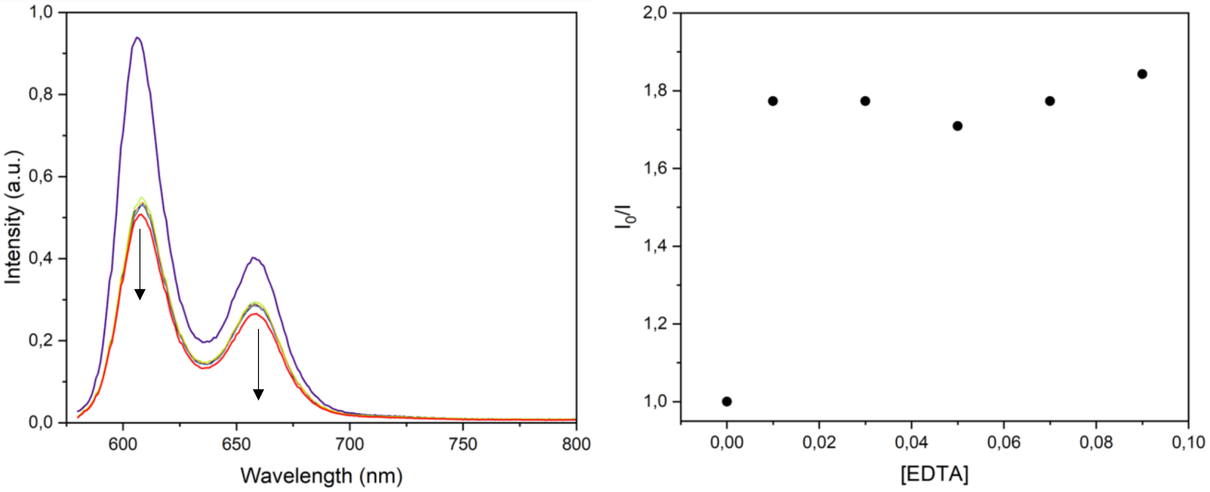

Figure 3.2.18. Left: emission spectra (λ_{irr} = 558 nm) of $CH_3OH:H_2O$ 2:1 containing 25 μM of **P5** and increasing amounts of $EDTA_{(aq)}$ at pH = 8.5 from 0.00 M (purple trace) to 0.090 M (red trace). Right: corresponding intensity Stern-Volmer plot.

Quenching studies with pyrrolidine were also performed, considering the ability of this cyclic amine to deprotonate the phenolic proton of the tyrosine residue and activate a photoinduced PCET in Sn^{IV}-porphyrin/tyrosine conjugates, as discussed in Chapter 2.[40,41] First these studies were done in pure CH_3OH, then in 30:1 $CH_2Cl_2:CH_3OH$ solutions. Addition of pyrrolidine to a CH_3OH solution of **P5** was found to have a negligible effect on the emission intensity (Figure 3.2.19, left). In a 30:1 $CH_2Cl_2:CH_3OH$ solution, upon addition of pyrrolidine, an initial decrease in the emission intensity of the Sn^{IV}-porphyrin unit was observed, which then reached a plateau. Addition of pyrrolidine also induces a slight red shift of the emission bands and an increase in background light scattering (Figure 3.2.19).

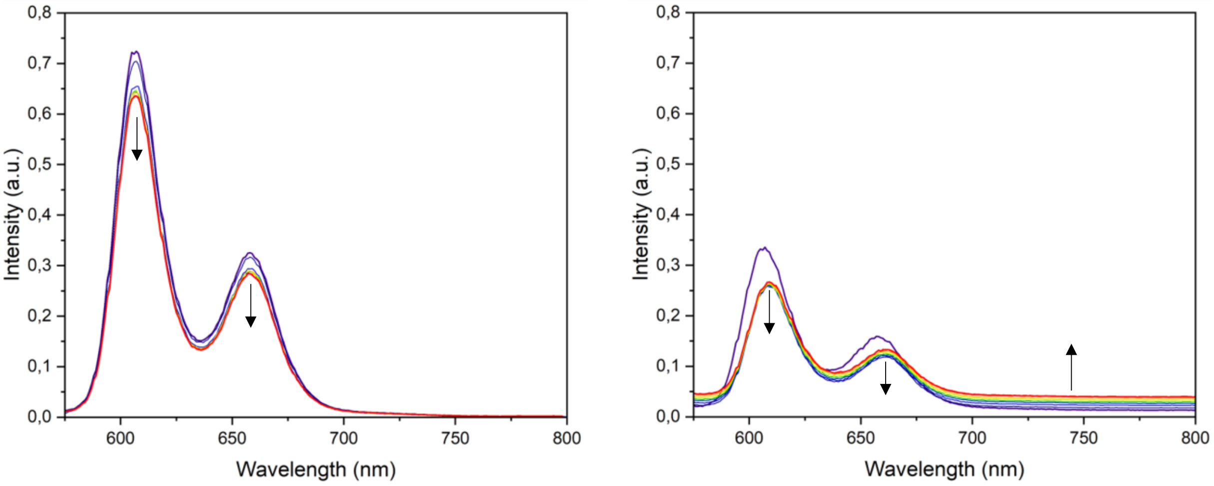

Figure 3.2.19. Left: Emission spectra (λ_{irr} = 558 nm) of CH_3OH solutions containing 25 μM of **P5** and increasing amounts of pyrrolidine from 0.00 M (purple trace) to 0.096 M (red trace). Right: Emission spectra (λ_{irr} = 558 nm) of CH_2Cl_2:CH_3OH (30:1) solution containing 25 μM of **P5** and increasing amounts of pyrrolidine from 0.00 M (purple trace) to 0.096 M (red trace).

The different behavior observed for pyrrolidine in distinct solvents will be further investigated (also by monitoring pyrrolidine concentrations in the interval between 0.00 to 0.012M). The differences may arise from various phenomena, such as distinct secondary structures in different solvents, but also from residual aggregates at high concentration of dichloromethane. From these preliminary data it was possible to conclude that, at least in part, both pyrrolidine and EDTA may act as ED/external base for **P5** in (organic) solution. Further titrations and more in-depth studies (*i.e.* electrochemical measurements, measure of the singlet excited state lifetimes in the presence and absence of external ED/base; laser flash photolysis to monitor triplet excited states, and else) are required to progress with this study and get more reliable insights. Not least, quenching studies in organic solutions using the selected EA ($WST1^-$) has also to be done to assess the ability of this system to effectively quench, *via* reductive pathway, the emission intensity of the tin-porphyrin unit in **P5**.

3.2.5. Liposome preparation and characterization.

To begin with, to verify that the 23-residue peptides can be effectively embedded in a membrane, as suggested by molecular modeling, and for characterization purposes, symmetric liposomes functionalized with **P2** were prepared (**SL1** – **SL3**) (see Experimental Section for the preparation method). Liposomes were formulated from DPPC and 1% of NaDSPE-PEG2K, which prevents liposome aggregation,[9] with different percentages of **P2** (1%, 0.6%, or 0.2%)

to determine the optimal peptide incorporation ratio (see Experimental Part for detailed procedures). The liposome solutions used are reported in Table 3.2.4.

Table 3.2.4. Compositions of liposome sampled used in this study.

Sample	**[P2]** (μM)	**[P3]** (μM)	**[EDTA]** (mM)	**[WST1$^-$]** (mM)	**[Zn^{2+}]** (mM)
SL1 – SL3[a]	25 – 15 – 5	–	–	–	–
AL1[b]	15	–	0.125	0.33	–
AL2[b]	15	–	0.125	0.33	5
AL3[b]	–	15	0.125	0.33	–
AL4[b]	–	15	0.125	0.33	5
HS	–	–	0.125	0.33	–

[a]Liposome composition: [DPPC] = 2.5 mM; [NaDSPE-PEG2K] = 25 μM in 0.1 M NH_4OAc buffer (pH = 6.90). [b]Liposome composition: [DPPC] = 2.5 mM; [NaDSPE-PEG2K] = 25 μM. [EDTA] (pH = 8.01) before SEC column); WST1$^-$ in 0.1 M NH_4OAc buffer (pH = 7.01).

UV-Vis and DLS measurements were used to select the optimal working concentration of **P2**, which was found to be 15 μM methanol solution, corresponding to a bulk molar ratio of 100:1:0.6 (DPPC:NaDSPE-PEG2K:**P2**, see Experimental Section and Appendix B for more details). Higher concentrations of **P2** led to a polydisperse liposome solution (Figure S52 in Appendix B), while lower concentrations led to a lower absorbance in the UV-Vis absorption spectra (Figure S54 in Appendix B). For **SL2**, after extrusion of the liposomes, the DLS measurements showed that the liposomes had an average hydrodynamic diameter of 160.1 nm with a polydispersity index (PDI) of 0.178, corresponding to a uniform size distribution (Figure S53, Appendix B). To verify that the Sn^{IV}-porphyrin/peptide conjugate was effectively embedded in the membrane a routine procedure was followed. The liposome solution was subjected to ultracentrifugation at 80000 G for 30 minutes to generate a lipid pellet. The UV–Vis spectrum of the supernatant collected after centrifugation showed no absorption in the visible region, thus confirming the effective incorporation of **P2** in the lipid membrane (Figure S55, Appendix B). For photophysical characterization, the liposome solution was diluted five times with the same NH_4OAc buffer. UV–Vis spectra, partially affected by liposome scattering at wavelengths below 380 – 400 nm, displayed the characteristic features of a Sn^{IV}-porphyrin: an intense Soret band at 427 nm and two weaker Q bands at 559 and 601 nm (Figure 3.2.20, left). The emission spectrum of the same solution (λ_{irr} = 427 nm) exhibited (qualitatively) a lower intensity if compared to an equally concentrated methanol solution of **P2**, suggesting the occurrence of some photoinduced processes involving the chromophore under visible light irradiation (Figure 3.2.20, right). This comparison must be taken with extreme care given that the emission spectra were obtained by excitation at two different wavelengths. For **SL2**, the excitation wavelength needed to be changed due to the negligible emission intensity upon excitation at λ= 560 nm. On top of this, for the studies under continuous photoirradiation only the blue LED was available.

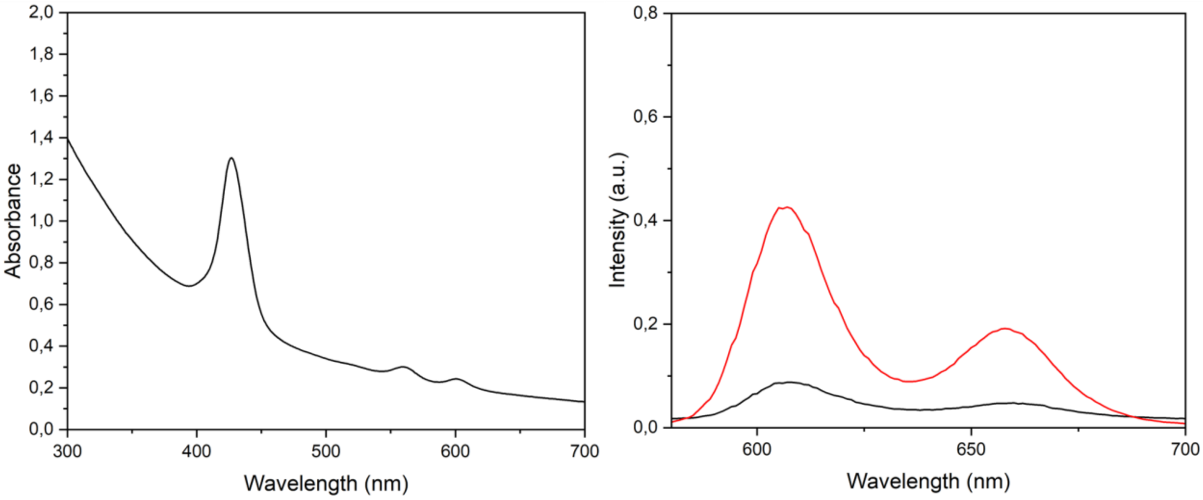

Figure 3.2.20. Left: UV-Vis absorption spectrum of **SL2**. Right: Emission spectrum (CH_3OH, 15 μM, λ_{irr} = 560 nm) of **P2** (red trace) and emission spectrum (λ_{irr} = 427 nm) of **SL2** at the same bulk porphyrin concentration (black trace).

The mechanism foreseen for photoinduced PCET in **SL2** is that of a simultaneous oxidation of the phenol via electron transfer to the excited metallo-porphyrin, and deprotonation of the same residue by the proximal histidine, with the formation of a diradical anion species, as schematically represented in the left of Figure 3.2.21.

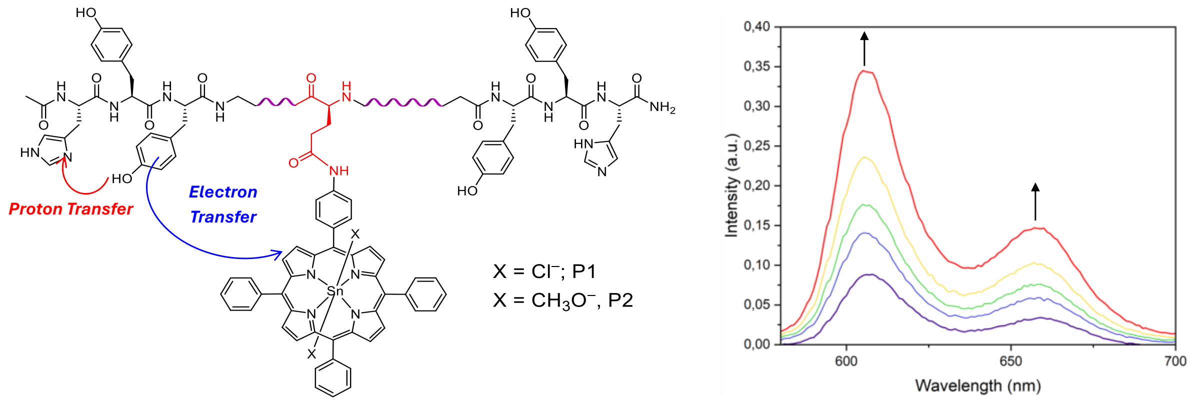

Figure 3.2.21. Left: Schematic representation of the inhibited photoinduced PCET in **P2**. Right: emission spectrum evolution (λ_{irr} = 427 nm) of **SL2** (pH 6.90 purple trace) in the presence of increasing amounts of 1 M HCl (pH down to 4.22, red trace).

To investigate whether the emission quenching observed for **SL2** may be attributed to an intramolecular photoinduced PCET, the emission spectra were recorded in the presence of increasing amounts of 1 M HCl (Figure 3.2.21, right). Acid addition is expected to progressively protonate the histidine residue ($pK_a = 5.96$),[61] yielding to a fully protonated species unable of acting as an internal base. In contrast, the tyrosine residue has a pK_a of ~10, thus is expected to be in its neutral form at the working pH. Experimentally, the addition of HCl led to a recovery of the Sn^{IV}-porphyrin emission intensity, indicating that the quenching observed at pH 6.76 may be influenced by the protonation state of the histidine residue. Dynamic light scattering (DLS) measurements, performed before and after acid addition, confirmed that the liposomes retained their structural integrity, with hydrodynamic diameters of 157.3 nm (PDI = 0.209) and 159.2 nm (PDI = 0.204), respectively (Figure S56 in Appendix B). To unequivocally establish whether the quenching mechanism in **SL2** functionalized liposomes involves a photoinduced PCET, more detailed photophysical investigations are required (*e.g.* measurement of the Sn^{IV}-porphyrin singlet and triplet lifetimes before and after the addition of HCl).

3.2.6. Dissymmetric liposome preparation and photoirradiation studies.

To survey on the possibility to promote transmembrane photoinduced unidirectional electron or PCET, dissymmetric liposomes **AL1** – **AL42** (see Table 3.2.4) were prepared. Considering the preliminary quenching studies with **P5** in organic homogeneous solution described in the previous Section, EDTA (in the form of $HEDTA^{3-}$, 0.125 M, pH 8.01, osmotic pressure 0.363 Osm) was chosen as ED for the inner compartment, and $WST1^{-}$ in NH_4OAc buffer (0.408 M, pH 7.01, osmotic pressure = 0.358 Osm) as EA for the bulk aqueous phase, as schematically represented in Figure 3.2.22.

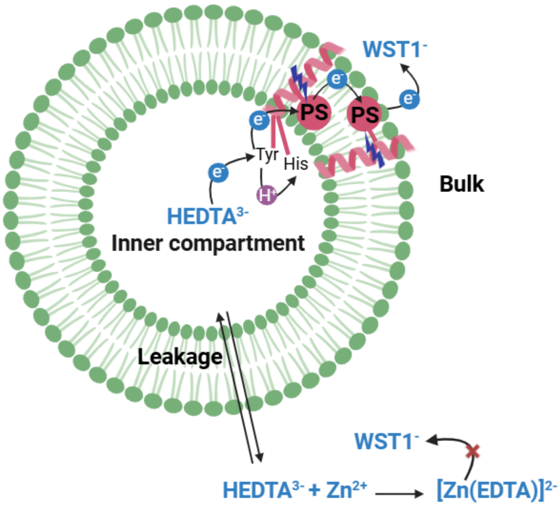

Figure 3.2.22. Schematic representation of **AL1** – **AL4** and possible electron transfer processes initiated by light irradiation.

After extrusion it is crucial to remove any residual ED that might have leaked from the inner to the outer compartment, before adding the electron acceptor. For this reason, liposomes were purified over a size-exclusion column (see Appendix B for SEC calibration run) following a reported literature procedure.[24] Finally, the liposome stock solution was diluted five times with the electron acceptor aqueous solution, before performing light irradiation studies. For **AL1** kept in the dark for 30 min, the typical absorption profile of the metallo-porphyrin was detected (see Figure S58, left in Appendix B) and no formazan production was observed, confirming the thermal stability under these conditions. By contrast, upon irradiation with blue light (λ_{irr} = 435 nm) under air, a new absorption band around 438 nm gradually appeared, together with bleaching of the Sn^{IV}-porphyrin absorption bands (Figure 3.2.23, left). This supports the formation of the reduced electron acceptor (FZ1^{2-}) and the occurrence of photoinduced electron transfer under oxygenated conditions (Figure 3.2.23, left). Additionally, bleaching of the Sn^{IV}-porphyrin absorption may also indicate the concomitant formation of the one-electron reduced form of the Sn^{IV}-porphyrin, key step for the photoinduced transmembrane electron transfer. Dynamic Light Scattering (DLS) measurements before and after the photoirradiation confirmed that the liposomes remained stable during the photoreaction (see Figure S59 in Appendix B). In parallel, control dissymmetric liposomes **AL3** were prepared under identical conditions. Here as well, the liposome solutions remained stable in the dark for 30 min (Figure S58, right in Appendix B). Unexpectedly, upon irradiation with the same light source, the characteristic formazan absorption band appeared and grew in intensity with time, indicating that electron reduction of the EA takes place (Figure 3.2.23, right). This result suggested that the Sn^{IV}-

porphyrin chromophore is not strictly required for photoinduced electron transfer. Again, DLS measurements before and after the photoirradiation confirmed that the liposomes remained stable during the photoreaction (see Figure S60 in Appendix B).

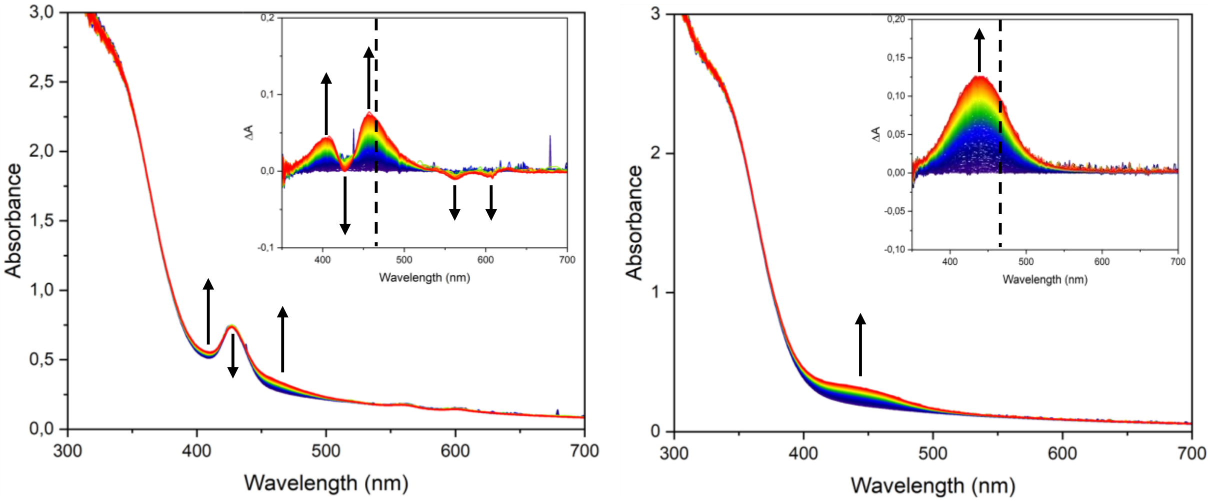

Figure 3.2.23. Evolution of the UV-Vis spectrum of **AL1** (left) and **AL3** (right) (see Table 3.2.4) under oxygenated conditions and blue light irradiation (λ_{irr} = 435 nm, P = 13.0 mW). Inset: Difference in absorbance monitored during 3h of irradiation. Dotted line showed λ = 465 nm, used for the construction of time-evolution graphs (Figure 3.2.25).

To check whether the photoinduced electron transfer proceeds through a genuine transmembrane mechanism and/or also because of partial leakage of the ED through the bilayer, followed by electron transfer to the EA on the same side of the membrane, a leakage study was performed, as already reported by Bonnet *et al.*[28] An excess of Zn^{2+} ions was added in the bulk aqueous solution before light irradiation (**AL2** and **AL4**), while maintaining the same osmolarity as that of the inner solution to avoid osmotic stress on the membrane. Any residual $HEDTA^{3-}$ molecules not carefully removed from the bulk after liposome preparation, or that may have leaked across the membrane after photoirradiation, will bind to Zn^{2+}, forming the complex $[Zn(EDTA)]^{2-}$ that cannot give electrons anymore, which thus inactivates the system, as schematically shown in Figure 3.2.22. Addition of Zn^{2+} should therefore allow to discriminate between genuine transmembrane electron transfer and leakage-mediated processes. Both **AL2** and **AL4** were stable in the dark for 30 minutes, as shown in Figure S61 in Appendix B. Upon light irradiation in the same above-mentioned conditions, **AL4** completely lose the ability to drive photoinduced electron transfer in the presence of Zn^{2+} (Figure 3.2.24, right). For **AL2** formazan production is almost completely quenched (Figure 3.2.24, left). Small quantities of $FZ1^{2-}$ were initially produced, that increased with the irradiation time (Figure S62 in Appendix B). $FZ1^{2-}$ formation was accompanied by bleaching of the porphyrin absorption bands, suggesting again the concomitant formation of the one-electron reduced form of the Sn^{IV}-porphyrin. These results indicate that for both **AL1** and **AL3** the main phenomena responsible for formazan production is the leakage of HEDTA^{3-} molecules form the inner pool to the bulk aqueous phase, followed by a photochemical reaction between the two. This hypothesis was also confirmed by a control experiment (**HS** in Table 3.2.4), in which a homogeneous mixed solution of HEDTA^{3-} and WST1^{-} was studied under identical photoirradiation conditions (Figure S63 in Appendix B). This system was stable when kept in the dark, however when irradiated (λ_{irr} = 435 nm) the characteristic absorption band of FZ1^{2-} appeared, indicating that the ED and EA can react under blue light irradiation. Most likely, by irradiating the sample with a LED at 435 nm (corresponding to the Sn^{IV}-porphyrin Soret band), part of the light is also absorbed by WST1^{-} with population of an excited state and subsequent electron transfer to the leaked HEDTA^{3-}.

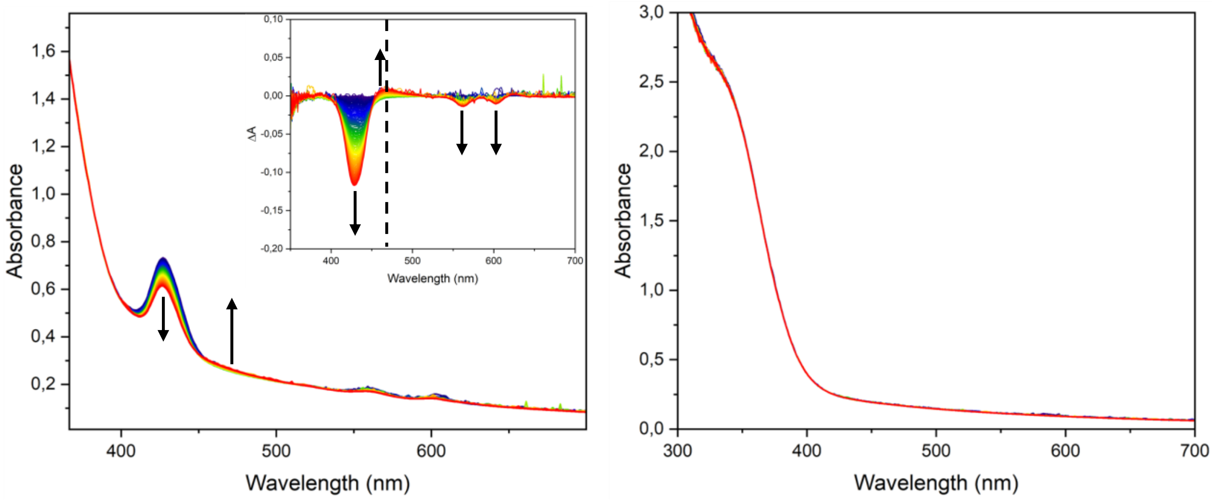

Figure 3.2.24. Evolution of the UV-Vis spectrum of **AL2** (left) and **AL4** (right) (see Table 3.2.4) under oxygenated conditions and blue light irradiation (λ_{irr} = 435 nm, P = 10.2 mW). Inset: Difference in absorbance monitored during 3h of irradiation. Dotted line showed $\lambda = 465$ nm, used for the construction of time-evolution graphs (Figure 3.2.25).

The time evolution of formazan production for **AL1** – **AL4** was evaluated by monitoring the difference in absorbance at 465 nm, chosen because at this wavelength there is no overlap with the porphyrin Soret band. The ΔA time profiles (Figure 3.2.25) show that formazan production in **AL1** – **AL4** is significantly lower than in **HS** under the same conditions (red trace in Figure 3.2.25, left). Formazan production in **AL1** and **AL3** is attributed to leakage of the electron donor, as addition of Zn^{2+} substantially block the formation of this species (for **AL2**, the very small amount of FZ1^{2-} detected can be considered within the experimental error, Figure 3.2.25, right). Moreover, the rates of FZ1^{2-} production in **AL1** and **AL3** are quite similar in the first 30 minutes of irradiation, after this time lapse **AL3** promotes faster electron transfer. Surely, these experiments need to be repeated to be gain more reliable insights. Moreover, **AL1** – **AL4**, and the control **HS**, will be also irradiated at a wavelength at which the EA surely does not absorb, *i.e.* one of the Sn^{IV}-porphyrin Q bands, to avoid any contributions deriving from the ED/EA photoreaction.

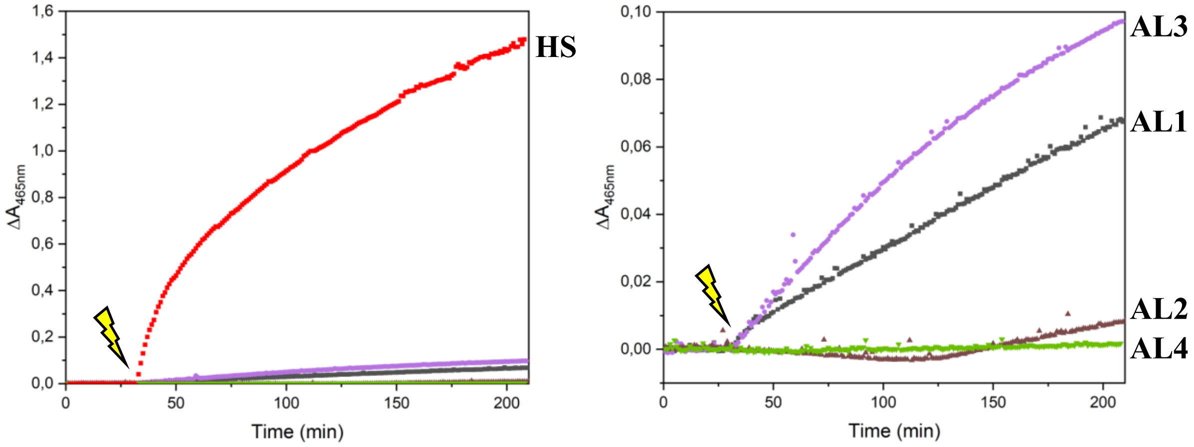

Figure 3.2.25. Left: Formation of Fz1^{2-} monitored as change in absorbance (λ_{max} = 465 nm) versus irradiation time for **AL1** – **AL4** (black, brown, purple and green traces) and for **HS** (red trace).

3.3. Conclusions and future perspectives.

In this Chapter, we have demonstrated the synthesis of a Sn^{IV}-porphyrin/peptide conjugate by combining the versatile chemistry of porphyrin derivatization with the high modularity of SPPS. This synthetic approach allowed for the generation of a set of two Sn^{IV}-porphyrin/peptide conjugates with variable peptide lengths, amino acid compositions, and numbers of Sn^{IV}-porphyrin units attached to the main peptide chain.

Specifically, we have synthesized a modified version of the YALP$_{23}$ sequence (**P2**) containing two histidine residues at positions 1 and 3, and a Sn^{IV}-porphyrin chromophore at position 6, following molecular modelling performed with the YASARA program. We envisioned that, in this conjugate, the histidine residues could act as internal bases for photoinduced PCET processes from the tyrosines of the YALP peptide. Additional model peptides, **P3**, **P5** and **P6**, were also synthesized as control without porphyrin or without the hydrophobic peptide core. Preliminary quenching studies on **P5** in homogeneous organic solutions were done prior to liposome photoirradiation experiments. Various bases and electron donors have been tested in different solvents. Among the tested conditions, pyrrolidine in CH_2Cl_2 and EDTA in 2:1 CH_3OH:H_2O (pH = 8.5) effectively quenched the fluorescence emission of the Sn^{IV}-porphyrin, supporting the use of EDTA as the preferred electron donor/base for subsequent liposome studies. Measurements of the singlet excited state lifetimes in the various tested conditions are currently undergoing.

The 23-residue peptides were then embedded into symmetric and dissymmetric lipid bilayers. We demonstrated that **P2** can be effectively embedded within the lipid bilayer (**SL2**), showing a pH-dependent fluorescence behaviour: the emission intensity was almost quenched at pH ~ 6 and was restored upon addition of 1 M HCl. These results suggested that a photoinduced PCET mechanism may be active in this system, although further experimental analysis, and in particular determination of the singlet excited state lifetime in the initial intermediate and final conditions, are required. In asymmetric liposomes containing $HEDTA^{3-}$ inside and $WST1^{-}$ outside (**AL1** – **AL4**), the formazan production in **AL1** – **AL4** is attributed to a photoinduced leakage of the electron donor from the inner compartment to the outer bulk aqueous phase followed by photoreaction between the electron donor and acceptor. For **AL3**, the (low) detected formazan production most likely arises from a combination of genuine transmembrane electron transfer and partial donor leakage, which subsequently leads to photoreduction in the bulk solution. On the other hand, formazan photo-production in **AL4** seems to derive exclusively from light-induced donor leakage and subsequent photoelectron transfer in the bulk. Future experiments are undergoing to clarify the role of oxygen in this process and determine whether electron transfer is indeed coupled to proton transfer, thereby confirming the occurrence of a PCET mechanism.

3.4. Experimental section.

Materials and reagents:

All solvents and reagents were obtained from commercial sources and used without further purification, unless otherwise stated. Deuterated solvents $CDCl_3$, CD_3OD and dmso-d_6 were purchased from Sigma-Aldrich. Thin layer chromatography (TLC) was performed using analytical silica gel on aluminium foil with fluorescent indicator 254 nm or aluminium oxide 60, activate neutral with fluorescent indication 254 nm. Silica Gel (Supelco, pore size 60 Å, mesh 230-400 μm) was used for the chromatographic purification of the porphyrins. The starting porphyrin **TPP-*p*NH$_2$** was synthesized and purified as described in literature.[47–49] TPP was available in Prof. Iengo's laboratory. The Sn^{IV} insertion reaction was done adapting known literature procedures.[50] SPPS was performed using a Liberty Blue Microwave assisted automated peptide synthesizer by Drs. Nico Meeuwenoord. Sephadex LH-20 was purchased from VWR International B. V. DPPC was obtained from Avanti Polar Lipids while NaDSPE-PEG2K was purchased from Lipoid and both were stored at –20°C. The Avanti Mini-Extruder including polycarbonate extrusion filter (pore size 400 nm, diameter 19 mm) and the filter supports (10 mm) were purchased from Avanti Polar Lipids.

Instrumentation:

NMR. Mono- and bi-dimensional experiments (^{1}H; ^{1}H-^{1}H COSY; ^{1}H-^{13}C HSQC; ^{1}H-^{13}C HMBC; ^{13}C-APT; ^{1}H-^{119}Sn HMBC) were recorded on a Bruker Avance 400 MHz or *Bruker Avance 850 MHz* equipped with a cryo-probe at 25 °C unless otherwise indicated. *Bruker Avance 400* operates at 400 MHz (^{1}H), 101 MHz (^{13}C), 149 MHz (^{119}Sn) while *Bruker Avance 850* operates at 850 MHz (^{1}H) and 214 MHz (^{13}C). Resonances are expressed in ppm (δ) and are referenced to the peak of the residual non-deuterated solvents: $\delta = 7.26$ ppm (^{1}H) and 77.16 ppm (^{13}C) for $CDCl_3$; 3.31 ppm (^{1}H) and 49.00 ppm (^{13}C) for CD_3OD; 2.50 ppm (^{1}H) and 39.52 ppm (^{13}C) for dmso-d_6. ^{119}Sn chemical shift is referenced to $Sn(OH)_2TPP$ ($\delta = -568$ ppm), available in Prof. Iengo’s laboratory. Processing was done using MestReNova© program. Multiplicity of the signals is expressed as follows: s = singlet; br. s = broad signal; d = doublet; t = triplet; m = multiplet; dd = doublet of doublets.

UV-Vis Absorption Spectroscopy. All absorption spectra of the porphyrins and Sn^{IV}-porphyrins were recorded in CH_2Cl_2 (25 μM) at 298 K using a 3 mL quartz cuvette (light path: 1 cm) and *Agilent Technologies Cary 60 UV-Vis* spectrophotometer equipped with *Cary Single Cell Peltier Accessory* for temperature control. The absorption spectra of all the peptides were recorded on the same instrument using 25 μM methanol solutions.

Emission Spectroscopy. The emission spectra of the Sn^{IV}-porphyrin conjugate, peptides as well as liposome solutions were recorded in dichloromethane or methanol at room temperature using 3 mL quartz cuvette (light path: 1 cm) and a *JASCO J-1500 CD Spectrometer*. For the Sn^{IV}-porphyrin building block 562 nm and 558 nm were used as excitation sources in CH_3OH and CH_2Cl_2, respectively. For **P5** and **P6** a 558 nm was used as excitation source while for **P2** and **P3** a 560 nm. All reported emission spectra have been corrected for the wavelength dependent phototube response.

Mass Spectrometry. The regular mass spectra (ESI-MS) were recorded on *Shimadzu LCMS-2020* (ESI-Q) using 1 mg/mL methanol solutions. The high-resolution mass spectra (HRMS) were recorded on a *ThermoFinnigan LTQ Orbitrap* with electrospray ionisation using a mother

1 mM CH_3OH solution that is then diluted 100 times in a CH_3CN:H_2O mixture at Leiden University or on a *ThermoScientific OrbitrapExploris 240* with electrospray ionisation using a mother 1 mg/mL methanol solution, then diluted 100 times in methanol at University of Trieste.

Circular Dichroism. Circular dichroism spectra of both the Sn^{IV}-porphyrin building block and all peptides were recorded in CH_3OH at room temperature using a 3 mL quartz cuvette (light path: 1 cm) and a *MOS500-Spectropolarimeter* equipped with an *ALX-300* power supply form *BioLogic*.

Cyclic Voltammetry. Electrochemical measurements were done in a home-build three-electrode electrochemical cell in a 1 mM Ar-purged dichloromethane solution. All the redox potentials are referred to the $Fc^{+/0}$ couple, used as internal standard. Potentials referred to the $Fc^{+/0}$ couple were converted in potentials vs. SCE by adding 0.4 V, accordingly to the literature.[58] The assembly of the measurement is a conventional three-electrode system with a Glassy Carbon (3 mm diameter PEEK (polyether ether ketone) encapsulated GC disk from *Methrom*) as working electrode, a Pt wire as a counter electrode and Ag/AgCl (3 M KCl) as a reference electrode. All measurements were done using an *Autolab PGSTAT 204* potentiostat equipped with an Antulab NOVA 2 software. The glassware (cell, glass connectors, glass adaptors and stoppers) was well cleaned before using, by boiling the glassware for 2 h then rinsing it 5 – 10 times before drying overnight. The working electrode was polished (200 rpm for 1.5 min) before the measurement (DiaPro 1.0 mm diamond suspension and OP-S NonDry 0.25 mm silica polishing suspension, both from Stuers) using a Struers LaboPol-30 polishing machine equipped with 200 mm diameter Struers MD Dur polishing pads. After polishing, the working electrodes were submerged in Milli-Q water and sonicated for 10 – 15 min.

Osmotic pressure. The osmolarity of aqueous solution for liposome preparation was measured on a *Micro-Osmometer Autocal Type 13* from Roebling.

Dynamic Light Scattering. Size distribution and polydispersity index (PDI) of liposomes were measured on a *Zetasizer Nano-S* from Malvern operating at 632.8 nm, at 25 °C.

Ultra-centrifuge. 1.2 mL of the symmetric liposome sample were ultra-centrifuged on a *Beckman culter OPTIMA MAX-XP Ultracentrifuge* with a TLA-100 rotor for 30 min at 80000G.

Synthesis.

TPP-BocGluOMe (**2**):

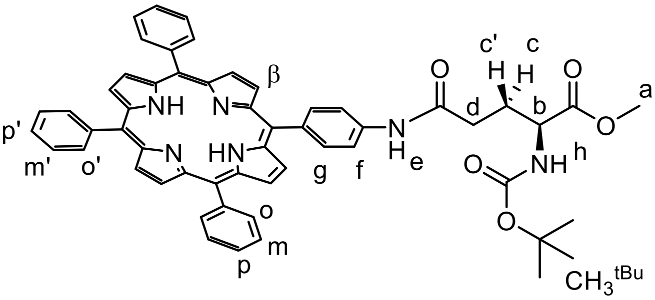

(S)-4-((tert-Butoxycarbonyl)amino)-5-methoxy-5-onopentanoic acid (Boc-GluOMe) (41.5 mg, 0.159 mmol, 2.00 eq) and 1-(3-Dimethylaminopropyl)-3-ethylcarbodiimide hydrochloride (30.5 mg, 0.159 mmol, EDC·Cl, 2.00 eq) were dissolved in dry pyridine (5 mL) in an oven dried round bottom flask. The solution was stirred for 10 min at room temperature under argon atmosphere. **TPP-*p*NH$_2$** (**1**) (50.0 mg, 0.0794 mmol, 1.00 eq) was added and the system was maintained under stirring at room temperature. The reaction was monitored by TLC (silica, first elution Hexane, second elution $CHCl_3$). After 5 h, 10 mL of $CHCl_3$ were added and the organic phase was washed with distilled water (6×50 mL). The solvent was removed under reduced pressure, and the purple solid was washed via sonication with distilled water (3×50 mL, 10 minutes per cycle). The product was collected by filtration and dried under reduced pressure. Yield 65.0 mg (93%).

^{1}H NMR (δ, 400 MHz, $CDCl_3$): 9.13 ppm (s, 1H, NH^{e}), 8.93 – 8.83 ppm (m, 8H, H$^{\beta}$), 8.26 – 8.15 ppm (m, 8H, H^{o}, H$^{o'}$), 8.18 ppm (d, J = 8.0 Hz, 2H, H^{g}), 8.02 ppm (d, J = 8.0 Hz, 2H, H^{f}), 7.83 – 7.71 ppm (m, 9H, H^{m}, H$^{m'}$, H^{p}, H$^{p'}$), 5.51 ppm (d, J = 8.2 Hz, 1H, NH^{h}), 4.59 ppm (br. s, 1H, H^{b}), 3.84 ppm (s, 3H, CH_3^{a}), 2.69 – 2.60 ppm (m, 2H, H^{d}), 2.48 ppm (br. s, 1H, H$^{c'}$), 2.06 ppm (br. s, 1H, H^{c}), 1.55 ppm (s, 9H, CH_3^{tBu}), −2.78 ppm (s, 2H, NH^{porphyrin}). ^{13}C from ^{1}H-^{13}C HSQC (δ, 101 MHz, $CDCl_3$): 135.1 ppm (C^{g}), 133.6 ppm (C^{o}, C$^{o'}$), 127.7 – 126.7 ppm (C^{m}, C$^{m'}$, C^{p}, C$^{p'}$), 117.9 ppm (C^{f}), 52.8 ppm (C^{b}), 52.7 ppm (CH_3^{a}), 34.3 ppm (C^{d}), 30.8 ppm (C^{c}, C$^{c'}$), 28.4 ppm (CH_3^{tBu}). UV–Vis (λ_{max}, nm, CH_2Cl_2): 418, 515, 552, 591, 646. HRMS: (*m/z*) (positive mode) for $C_{55}H_{49}N_6O_5$ ($[M + H]^+$) calculated 873.37590, found 873.37711.

$SnCl_2$TPP-BocGluOMe (3):

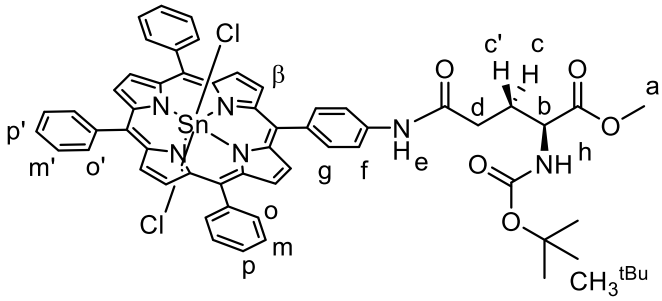

TPP-BocGluOMe (**2**) (40.0 mg, 0.0458 mmol, 1.00 eq) was dissolved in 5 mL of pyridine. $SnCl_2 \cdot 2H_2O$ (26.0 mg, 0.115 mmol, 2.50 eq) was added to the solution and the reaction mixture was refluxed at T = 115 °C. The reaction was monitored both by TLC (aluminum oxide, first elution with *n*-hexane, second elution with $CHCl_3$) and UV-Vis absorption spectroscopy (reduction of the number of the Q bands upon metalation due to increased symmetry of the system, see also Chapter 1). After 2 h the reaction mixture was cooled to room temperature and quenched with 50 mL of distilled water. The purple precipitate was filtered and washed several times with water to remove excess $SnCl_2 \cdot 2H_2O$ and pyridine. The product was dissolved in chloroform, dried over $MgSO_4$ and isolated via precipitation with *n*-hexane. Yield 43.7 mg (90%).

^{1}H NMR (δ, 400 MHz, CD_3OD): 9.44 – 9.22 ppm (m, 8H, H^{β}), 8.37 – 8.24 ppm (m, 8H, H^{o}, $H^{o'}$, H^{g}), 8.11 ppm (d, *J* = 8.4 Hz, 2H, H^{f}), 7.96 – 7.86 ppm (m, 9H, H^{m}, $H^{m'}$, H^{p}, $H^{p'}$), 4.33 ppm (m, 1H, H^{b}), 3.80 ppm (s, 3H, CH_3^{a}), 2.68 ppm (t, *J* = 7.3 Hz, 2H, H^{d}), 2.36 ppm (m, 1H, $H^{c'}$), 2.13 ppm (m, 1H, H^{c}), 1.50 ppm (s, 9H, CH_3^{tBu}). ^{13}C from ^{1}H-^{13}C HSQC (δ, 101 MHz, CD_3OD): 136.0 ppm (C^{g}), 135.5 ppm (C^{o}, $C^{o'}$), 133.6 ppm (C^{β}), 127.7 ppm (C^{m}, $C^{m'}$, C^{p}, $C^{p'}$), 119.7 ppm (C^{f}), 54.1 ppm (C^{b}), 52.2 ppm (CH_3^{a}), 33.5 ppm (C^{d}), 28.0 ppm (CH_3^{tBu}), 27.7 ppm ($C^{c'}$, C^{c}). ^{119}Sn from ^{1}H-^{119}Sn HMBC (δ, 149 MHz, CD_3OD): −564 ppm ($Sn(OCH_3)_2$TPP-BocGluOMe), −575 ppm ($Sn(OCH_3)(Cl)$TPP-BocGluOMe). UV–Vis (λ_{max}, nm, CH_2Cl_2): 427, 562, 603. HRMS: (*m/z*) (positive mode) for $C_{55}H_{47}N_6O_6Sn$ ($[M - 2Cl + OH]^+$) calculated 1007.25864, found 1007.25958.

SnCl₂TPP-BocGluOH (**4**):

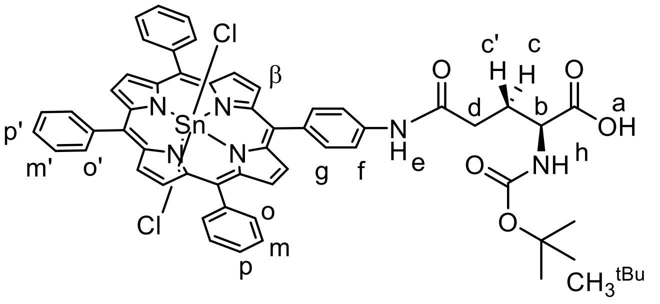

SnCl₂TPP-BocGluOMe (**3**) (58.0 mg, 0.0547 mmol, 1.00 eq) was dissolved in 20 mL THF and 0.438 mL of NaOH 1M (0.438 mmol, 8.00 eq) were added. The system was stirred at 40 °C and monitored with TLC (aluminum oxide, $CHCl_3$:CH_3OH 98:2). After 24 h the mixture was cooled to room temperature and acidified with HCl 1 M to pH 2-3. The organic phase was washed with water (3×50 mL) after addition of 20 mL of $CHCl_3$. The organic phase was evaporated to dryness and dried in vacuum. Yield 54.3 mg (95%).

^{1}H NMR (δ, 400 MHz, dmso-*d₆*): 12.63 ppm (s, 1H, COOH^a), 10.49 ppm (s, 1H, NH^e), 9.38 – 9.19 ppm (m, 8H, H^β), 8.31 ppm (dd, *J* = 7.7, 2.2 Hz, 6H, H^o, H$^{o'}$), 8.24 ppm (d, *J* = 8.3 Hz, 2H, H^g), 8.15 ppm (d, *J* = 8.3 Hz, 2H, H^f), 8.00 – 7.91 ppm (m, 9H, H^m, H$^{m'}$, H^p, H$^{p'}$), 7.26 ppm (d, *J* = 8.2 Hz, 1H, NH^h), 4.05 ppm (td, *J* = 8.9, 4.9 Hz, 1H, H^b), 2.62 ppm (t, *J* = 7.7 Hz, 2H, H^d), 2.19 ppm (m, 1H, H$^{c'}$), 1.95 ppm (m, 1H, H^c), 1.44 ppm (s, 9H, CH_3^{tBu}). ^{13}C from ^{1}H-^{13}C HSQC (δ, 101 MHz, dmso-*d₆*): 135.4 ppm (C^g), 134.8 ppm (C^o, C$^{o'}$), 133.0 – 132.6 ppm (C^β), 127.4 ppm (C^m, C$^{m'}$, C^p, C$^{p'}$), 117.8 ppm (C^f), 53.1 ppm (C^b), 32.7 ppm (C^d), 27.9 ppm (CH_3^{tBu}), 26.2 ppm (C$^{c'}$, C^c). ^{119}Sn from ^{1}H-^{119}Sn HMBC (δ, 149 MHz, dmso-*d₆*): −590 ppm (SnCl₂TPP-BocGluOH). UV–Vis (λ_{max}, nm, CH_2Cl_2): 427, 562, 603. HRMS: (*m/z*) (positive mode) for $C_{54}H_{45}N_6O_6Sn$ ($[M - 2Cl + OH]^+$) calculated 993.24232, found 993.24362.

$SnCl_2$TPP-FmocGluOH (**5**):

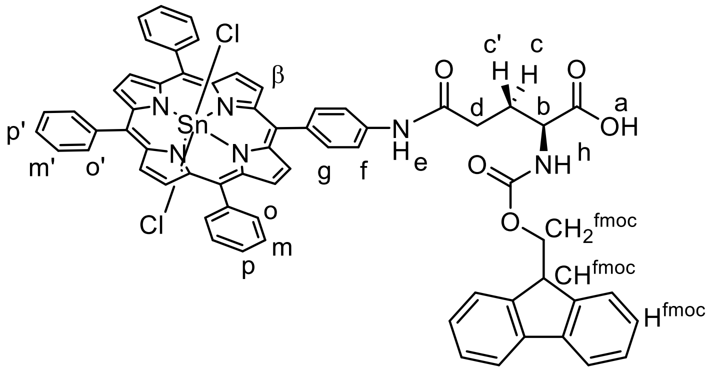

$SnCl_2$TPP-BocGluOH (**4**) (152.8 mg, 0.146 mmol, 1.00 eq) was dissolved in 3.00 mL of CH_2Cl_2. The solution was cooled at 0 °C and 0.600 mL of TFA were added. The reaction mixture was stirred at room temperature and monitored by TLC (silica, $CHCl_3$:CH_3OH 8:2). After 2 h the TFA was neutralized with a saturated aqueous solution of $NaHCO_3$. The solution was extracted with chloroform, in combination with 1 M HCl to break the emulsion. The organic phase was washed with water (2×50 mL), evaporated to dryness, and the solid dried under vacuum was used for the next synthetic step without further purifications. The deprotected intermediate was dissolved in 10 mL of THF:H_2O (9:1) brought to 0 °C followed by addition of DIPEA (0.150 mL, 0.876 mmol, 6.00 eq) and Fmoc-OSu (0.161 mmol, 54.3 mg, 1.10 eq). The reaction mixture was then stirred at room temperature and monitored by TLC (silica, $CHCl_3$:CH_3OH 8:2). After 2 h the THF was removed under reduced pressure, and the aqueous phase was extracted with $CHCl_3$. The organic phase was washed with water (3×20 mL), then concentrated to ~2 mL and washed with HCl 1 M (2×30 mL). The product was isolated as a purple solid via precipitation from a $CHCl_3$:acetone 1:1 solution by addition of *n*-hexane solution. Yield 145.0 mg (85%).

^{1}H NMR (δ, 400 MHz, dmso-d_6): 12.79 ppm (s, 1H, COOH^a), 10.52 ppm (s, 1H, NH^e), 9.35 – 9.17 ppm (m, 8H, H^β), 8.33 – 8.27 ppm (m, 6H, H^o, H$^{o'}$), 8.23 ppm (d, J = 8.7 Hz, 2H, H^g), 8.16 (d, J = 8.5 Hz, 2H, H^f), 8.02 – 7.88 (m, 11H, H^m, H$^{m'}$, H^p, H$^{p'}$, H^{fmoc}), 7.84 (d, J = 8.1 Hz, 1H, NH^h), 7.79 (d, J = 7.4 Hz, 2H, H^{fmoc}), 7.48 – 7.33 (m, 4H, H^{fmoc}), 4.41 – 4.24 (m, 3H, CH_2^{fmoc}, CH^{fmoc}), 4.15 (m, 1H, H^b), 2.66 (m, 2H, H^d), 2.26 (m, 1H, H$^{c'}$), 2.01 (m, 1H, H^c). ^{13}C from ^{1}H-^{13}C HSQC (δ, 101 MHz, dmso-d_6): 135.3 ppm (C^g), 134.8 ppm (C^o, C$^{o'}$), 133.5 – 133.0 ppm (C^β), 127.8 – 127.4 ppm (C^{fmoc}), 127.7 ppm (C^m, C$^{m'}$, C^p, C$^{p'}$), 125.5 ppm (C^{fmoc}), 120.4 ppm (C^{fmoc}), 117.7 ppm (C^f), 65.9 ppm (CH_2^{fmoc}), 53.5 ppm (C^b), 46.7 ppm (CH^{fmoc}), 33.2 ppm (C^d), 26.7 ppm (C$^{c'}$, C^c). ^{119}Sn from ^{1}H-^{119}Sn HMBC (δ, 149 MHz, dmso-d_6): −590 ppm ($SnCl_2$TPP-

FmocGluOH).UV–Vis (λ_{max}, nm, CH_2Cl_2): 428, 562, 603. HRMS: (*m/z*) (positive mode) for $C_{64}H_{47}N_6O_6Sn$ ($[M - 2Cl + OH]^+$) calculated 1115.25823, found 1115.25932.

TPP-FmocGluO*t*Bu (6):

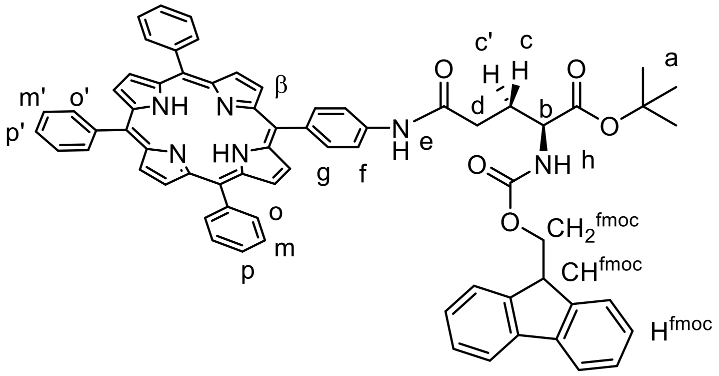

(S)-4-((((9H-Fluoren-9-yl)methoxy)carbonyl)amino)-5-(tert-butoxy)-5-oxopentanoic acid (Fmoc-GluO*t*Bu) (67.6 mg, 0.159 mmol, 2.00 eq) and 1-(3-Dimethylaminopropyl)-3-ethylcarbodiimide hydrochloride (30.5 mg, 0.159 mmol, 2.00 eq, EDC·Cl) were dissolved in dry pyridine (5 mL) in an oven dried round bottom flask. The solution was stirred for 10 min at room temperature under argon atmosphere. **TPP-*p*NH₂** (**1**) (50.0 mg, 0.0794 mmol, 1.00 eq) was added and the system was maintained under stirring at room temperature. The reaction was monitored by TLC (silica, first elution Hexane, second elution $CHCl_3$). After 4 h, 50 mL of distilled water were added, the purple precipitate was filtered and washed several times with distilled water to remove excess of pyridine. The solid was re-dissolved in 50 mL of $CHCl_3$, the solvent evaporated under reduced pressure and the product was collected via precipitation with *n*-hexane. Yield 81.3 mg (98%).

^1H NMR (δ, 400 MHz, dmso-d_6): 10.41 ppm (s, 1H, NH^e), 8.87 – 8.81 ppm (m, 8H, H^β), 8.27 – 8.19 ppm (m, 6H, , H^o, $H^{o'}$), 8.13 ppm (d, *J* = 8.4 Hz, 2H, H^g), 8.05 ppm (d, J = 8.4 Hz, 2H, H^f), 7.91 ppm (d, *J* = 7.4 Hz, 2H, H^{fmoc}), 7.89 – 7.80 ppm (m, 10H, H^m, $H^{m'}$, H^p, $H^{p'}$, NH^h), 7.84 – 7.75 ppm (d, 2H, *J* = 7.4 Hz, H^{fmoc}), 7.42 (q, *J* = 7.6 Hz, 2H, H^{fmoc}), 7.40 – 7.32 ppm (m, 2H, H^{fmoc}), 4.43 – 4.23 ppm (m, 3H, CH_2^{fmoc}, CH^{fmoc}), 4.08 ppm (td, *J* = 9.1, 4.9 Hz, 1H, H^b), 2.62 ppm (t, *J* = 7.6 Hz, 2H, H^d), 2.25 – 2.16 ppm (m, 1H, $H^{c'}$), 2.03 – 1.93 ppm (m, 1H, H^c), 1.46 ppm (s, 9H, $OtBu^a$), –2.93 ppm (s, 2H, $NH^{porphyrin}$).

^1H NMR (δ, 400 MHz, $CDCl_3$): 8.87 – 8.81 ppm (m, 8H, H^β), 8.26 – 8.17 ppm (m, 6H, H^o, $H^{o'}$), 8.21 – 8.13 ppm (m, 2H, H^g), 8.01 ppm (d, *J* = 8.1 Hz, 2H, H^f), 7.80 – 7.73 ppm (m, 11H, H^m, $H^{m'}$, H^p, $H^{p'}$, H^{fmoc}), 7.75 – 7.63 ppm (m, 2H, H^{fmoc}), 7.41 ppm (d, *J* = 7.4 Hz, 2H, H^{fmoc}), 7.34

ppm (tt, J = 7.3, 1.4 Hz, 2H, H^{fmoc}), 5.73 ppm (d, J = 8.1 Hz, 1H, NH^{h}), 4.60-4.52 ppm (m, 2H, CH_2^{fmoc}), 4.47 ppm (m, 1H, H^{b}), 4.28 ppm (t, J = 6.8 Hz, 1H, CH^{fmoc}), 2.60 – 2.49 ppm (m, 2H, H^{d}), 2.46 ppm (m, 1H, $H^{c'}$), 2.05 ppm (m, 1H, H^{c}), 1.55 ppm (s, 9H, O*t*Bu^{a}), −2.78 ppm (s, 2H, $NH^{porphyrin}$). ^{13}C from ^{1}H-^{13}C HSQC (δ, 101 MHz, $CDCl_3$): 134.6 ppm (C^{o}, $C^{o'}$, C^{g}), 131.0 ppm (C^{β}), 128.0 – 120.0 ppm (C^{m}, $C^{m'}$, C^{p}, $C^{p'}$, C^{fmoc}), 117.8 ppm (C^{f}), 67.2 ppm (CH^{fmoc}), 53.5 ppm (C^{b}), 47.2 ppm (CH_2^{fmoc}), 34.2 ppm (C^{d}), 30.0 ppm ($C^{c'}$, C^{c}), 28.0 ppm (O*t*Bu^{a}). UV–Vis (λ_{max}, nm, CH_2Cl_2): 418, 515, 551, 592, 646. ESI-MS (*m/z*) (positive mode) for $C_{68}H_{57}N_6O_5$ ([M + H]$^+$) calculated 1037.43850, found 1037.47.

TPP-FmocGluOH (7):

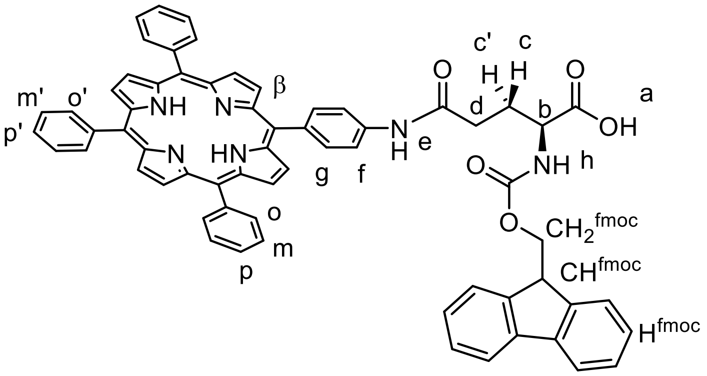

TPP-FmocGluO*t*Bu (**6**) (81.3 mg, 0.0783 mg, 1.00 eq) was dissolved in 2 mL of a 3:1 CH_2Cl_2:TFA mixture and allowed to react at room temperature under constant stirring. The reaction was monitored via TLC (silica gel, $CHCl_3$:CH_3OH 95:5). After 6 h the reaction mixture was diluted with 10 mL of CH_2Cl_2 and washed with a $NaHCO_3$ saturated aqueous solution (2×50 mL). The organic phase was acidified with HCl 1 M to pH ~3, then the organic phase was washed twice with 50 mL of distilled water. The product was purified via column chromatography (silica, $CHCl_3$:CH_3OH 9:1) to remove unreacted **6**, then isolated via precipitation from a chloroform/*n*-hexane mixture. Yield 57.4 (75%).

^{1}H NMR (δ, 400 MHz, dmso-d_6): 12.77 ppm (s, 1H, $COOH^{a}$), 10.44 (s, 1H, NH^{e}), 8.88 – 8.82 ppm (m, 8H, H^{β}), 8.30 – 8.17 ppm (m, 6H, H^{o}, $H^{o'}$), 8.14 (d, J = 8.3 Hz, 2H, H^{g}), 8.07 ppm (d, J = 8.6 Hz, 2H,H^{f}), 7.89 ppm (d, J = 7.4 Hz, 2H, H^{fmoc}), 7.94 – 7.73 ppm (m, 10H, H^{m}, $H^{m'}$, H^{p}, $H^{p'}$, NH^{h}), 7.80 ppm (t, J = 7.6 Hz, 2H, H^{fmoc}), 7.47 – 7.32 ppm (m, 4H, H^{fmoc}), 4.38 – 4.23 ppm (m, 3H, CH_2^{fmoc}, CH^{fmoc}), 4.15 ppm (td, J = 8.9, 4.9 Hz, 1H, H^{b}), 2.63 ppm (t, J = 7.6 Hz, 2H, H^{d}), 2.31– 2.20 ppm (m, 1H, $H^{c'}$), 2.06 – 1.94 ppm (m, 1H, H^{c}), −2.92 ppm (s, 2H, $NH^{porphyrin}$). ^{13}C from ^{1}H-^{13}C HSQC (δ, 101 MHz, dmso-d_6): 134.7 ppm (C^{g}), 134.3 ppm (C^{o}, $C^{o'}$), 131.0 ppm (C^{β}), 127.5 – 126.6 ppm (C^{fmoc}),126.7 – 119.7 ppm (C^{m}, $C^{m'}$, C^{p}, $C^{p'}$), 117.4 ppm (C^{f}), 65.8 ppm (CH^{fmoc}), 53.5 ppm (C^b), 46.7 ppm (CH_2^{fmoc}) , 33.0 ppm (C^d), 26.3 ppm ($C^{c'}$, C^c). UV–Vis (λ_{max}, nm, CH_2Cl_2): 418, 515, 551, 592, 646. ESI-MS (*m/z*) (positive mode) for $C_{64}H_{48}N_6O_5$ ($[M + H]^+$) calculated 981.37590, found 981.46.

Peptide design (preliminary MD studies).

The x, y, z coordinated of the α-helical $YALP_{23}$ peptide (Ac-HYYLAEALALALALALALALYYH-carboxamide, where E is the Sn^{IV}-porphyrin/glutamic acid conjugate **5**) were initially generated using PyMol. YASARA, www.yasara.org (Yet Another Scientific Artificial Reality Application) was used as modelling program to replace the amino acid glycine in position 1 and 23 with two histidine and to introduce the unnatural amino acid (**5**) in the desired positions of the peptide (6, 7, 8 and 9). Instead of using Sn^{IV} which is not known by the program a Zn^{II} metal centre was used inside the porphyrin. All the generated structures were first optimized by using energy minimization (using the YASARA force field).[53] Their behaviour in the membrane was then simulated by running the YASARA macro run membrane allowing the system to equilibrate for 250 ps at 298 K. The optimized structure was analysed to evaluate the relative position between the metallo-porphyrin and one of the two tyrosine residues. We chose to synthesize **P3** with the chromophore in position 6 and 9 (not synthesized yet for time reasons).

Peptide synthesis.

During the peptide synthesis all the natural amino acids (H, Y, A, L) were coupled as Fmoc-protected amino acids using SPPS, while the unnatural one (Sn^{IV}-porphyrin building block) was coupled using a manual coupling. Synthesis was performed at 50 µmol scale, using Fmoc-L-His-Wang resin as the solid support. The Fmoc deprotection was achieved using 20% piperidine in DMF, and coupling was done using DIC as a coupling agent and Oxyma as a base. The coupling process was done using the "double deprotection-double coupling" procedure. For the manual coupling of the chromophore the peptide (ALALALALALALALYYH-resin in the case of **P2**, or the natural amino acid Fmoc-L-Ala-Wang resin for **P5**) bound to the resin was transferred to a 10 mL syringe with a filter and washed with DMF. Then a solution of **5** (87.6 mg, 75 µmol), DIC and Oxyma in DMF was added to the syringe and left to react for 24h on a rocking platform. After 24h the efficiency of the coupling was checked via LC-MS, then a DMF solution with other 25 µmol (29.2 mg), DIC and Oxyma was added to the reaction vessel and left to react on a rocking platform for other 24h. The reaction mixture was then washed with

DMF before being transferred again to the reaction vessel of the solid phase peptide sensitizer to couple the last five amino acids (HYYLA). Afterwards the peptide was transferred again to a 10 mL syringe to acetylate the N-terminus (using acetic anhydride, working at room temperature for 24h on a rocking platform). Finally, the peptide was cleaved from the resin using TFA:water:Triisopropyl silane (TIPS) (95%:2.5%:2.5%) mixture. Sn^{IV}-porphyrin/peptides were purified via size-exclusion chromatography (Sephadex LH-20 and methanol as eluent) while the chromophore-free peptides were purified via HPLC (High Pressure Liquid Chromatography using a C_{18} Column and H_2O:CH_3CN:*t*BuOH 1:1:1 as eluent). All intermediates and final peptides were analysed via LC-MS to monitor the progress of the peptide synthesis. Purified peptides were characterized via HRMS, mono- and bidimensional NMR spectroscopy, UV-Vis absorption and emission spectroscopy.

P2 (20.2 mg, 13% yield). LC-MS (ESI) (*m/z*) $[M - 2Cl]^{2+}$ calculated 1658.3, found 1658.8; $[M + 2H]^{2+}$ calculated 1694.3, found 1693.9. UV–Vis (λ_{max}, nm, CH_3OH): 422, 560, 601. ^1H NMR (δ, 850 MHz, CD_3OD), tentative assignments: 9.22 ppm (H^{β}), 8.30 – 7.73 ppm (H^o, $H^{o'}$, H^m, $H^{m'}$, H^p, $H^{p'}$).

P3 (12.6 mg, 10% yield): LC-MS (ESI) (*m/z*) $[M + 2H]^{2+}$ calculated 1287.2, found 1287.3. HRMS (ESI) (*m/z*) (positive mode) for $C_{128}H_{195}N_{28}O_{28}$ ($[M + H]^+$) calculated 2573.47237, found 2573.4503; for $C_{128}H_{196}N_{28}O_{28}$ ($[M + 2H]^{2+}$) calculated 1287.23982, found 1287.2398; for $C_{128}H_{197}N_{28}O_{28}$ ($[M + 3H]^{3+}$) calculated 858.49564, found 858.4954. UV–Vis (λ_{max}, nm, CH_3OH) (ε, M^{-1} cm^{-1}): 280 (5.45×10^3). ^1H NMR (δ, 850 MHz, CD_3OD), tentative assignments: 8.80 ppm (H^{his}), 8.43 – 7.83 ppm (NH), 7.45 ppm (H^{his}), 7.23 – 6.55 ppm (H^{tyr}), 4.43 – 3.96 ppm (H^{α}), 3.74 – 2.77 ppm (CH_2^{tyr}, CH_2^{his}), 2.35 – 1.30 ppm (CH^{leu}, CH_2^{leu}, CH_3^{ala}), 0.93 ppm (CH_3^{leu}, $CH_3^{N\text{-terminus}}$).

P5 (10.1 mg, 14% yield): LC-MS (ESI) (*m/z*) $[M - 2Cl + H]^+$ calculated 1635.5, found 1634.3. HRMS: (*m/z*) (positive mode) for $C_{87}H_{85}N_{15}O_{11}Sn$ ($[M - 2Cl]^{2+}$) calculated 817.77934, found 817.77933. UV–Vis (λ_{max}, nm, CH_3OH) (ε, M^{-1} cm^{-1}): 227 (3.72×10^4), 313 (1.54×10^4), 422 (35.1×10^4), 558 (1.53×10^4), 599 (1.09×10^4). ^1H NMR (δ, 400 MHz, CD_3OD), tentative assignments: 9.50 – 9.22 ppm (H^{β}), 8.41 – 7.76 ppm (H^o, $H^{o'}$, H^m, $H^{m'}$, H^p, $H^{p'}$), 7.07 – 6.56 ppm (H^{tyr}). ^1H-^{119}Sn HMBC (δ, 149 MHz, CD_3OD): −590 ppm (**P4**), −565 ppm (**P5**).

P6 (11.5 mg, 25% yield): LC-MS (ESI) (*m/z*) $[M + H]^+$ calculated 891.4, found 891.0. HRMS: (*m/z*) (positive mode) for $C_{44}H_{63}N_{10}O_{10}$ ($[M + H]^+$) calculated 891.47231, found 891.47260; for $C_{44}H_{62}N_{10}O_{10}Na$ ($[M + Na]^+$) calculated 913.454260, found 913.45473. UV–Vis (λ_{max}, nm, CH_3OH) (ε, M^{-1} cm^{-1}): 280 (3.6×10^3 M^{-1}). ^{1}HNMR (δ, 400 MHz, CD_3OD), tentative assignments: 8.68 ppm (H^{his}), 7.08 – 6.65 ppm (H^{tyr}), 4.60 – 4.27 ppm (H^{α}), 3.15 – 2.72 ppm (CH_2^{tyr}, CH_2^{his}), 2.19 – 1.95 ppm (CH^{leu}, CH_2^{leu}), 1.36 ppm (CH_3^{ala}), 0.91 ppm (CH_3^{leu}, $CH_3^{N\text{-}terminus}$).

Liposome preparation for characterization.

All liposome formulations were prepared by the classical hydration-extrusion method. DPPC lipids and NaDSPE-PEG2K in chloroform, together with one of the peptides (**P2** or **P3**) dissolved in methanol, were added to a pressure-resistant tube. The solvent was evaporated under reduced pressure to form a thin lipid film, which was further dried under vacuum for at least 1h to remove any residual solvent. The film was then hydrated with 1 mL of NH_4OAc buffer (0.1 M, pH 6.90), followed by 10 freeze-thaw cycles between liquid N_2 and a 50 °C water bath, with a brief sonication step applied between the first and second cycle. The resulting vesicles were extruded 11 times through a 400 nm polycarbonate membrane at 55 °C using an Avanti Polar Lipids Mini-Extruder. Assuming no losses during preparation, the liposome stock solution contained DPPC:NaDSPE-PEG2K:peptide in a molar ratio of 100:1:0.6, corresponding to bulk concentrations of 12.5 mM for DPPC, 0.125 mM for NaDSPE-PEG2K, and 0.075 mM for the peptide. Liposome samples were stored at room temperature and used within three days. For DLS, ultracentrifugation, and spectroscopic characterization, the stock solution was diluted five times with NH_4OAc buffer.

Liposome preparation for photoirradiation studies.

DPPC lipids and NaDSPE-PEG2K dissolved in chloroform, together with one of the peptides in methanol, were added to a pressure-resistant tube. The solvent was evaporated under reduced pressure to form a thin lipid film, which was further dried under vacuum for at least 1 h to remove residual solvent. The film was then hydrated with 1 mL of Na_3HEDTA buffer (0.125 M, pH = 8.01, Osmotic pressure = 0.363 Osm), followed by 10 freeze-thaw cycles between liquid N_2 and a 50 °C water bath, with a brief sonication step applied between the first and second cycle. The resulting vesicles were extruded 11 times through a 400 nm polycarbonate membrane at 55 °C using an Avanti Polar Lipids Mini-Extruder. After extrusion, liposomes were purified from the residual electron donor present in the bulk aqueous phase by size-exclusion chromatography (GE Healthcare Illustra^{TM} NAP^{TM}-25 column from Cytiva) using an isotonic NH_4OAc buffer (3.5 mL, 0.1 M, pH = 7.01, Osmotic pressure = 0.360 Osm). Liposome fractions were collected from vials 7-10 (~1.6 mL) according to the SEC calibration run, as previously described by Bonnet *et. al* (see Figures S52 in Appendix B).[24] Assuming no losses during preparation, the liposome stock solution contained DPPC:NaDSPE-PEG2K:peptide in a molar ratio of 100:1:0.6, corresponding to bulk concentrations of 12.5 mM for DPPC, 0.125 mM for NaDSPE-PEG2K, and 0.075 mM for the peptide. Liposome samples were stored at room temperature and used within three days. For DLS, ultracentrifugation, and spectroscopic characterization, the stock solution was diluted five times with NH_4OAc buffer containing $WST1^-$ (0.41 mM, pH = 7.01, Osmotic pressure = 0.358 Osm). All photoirradiation studies were performed under oxygenated conditions and constant stirring. A blue LED (λ_{irr} = 435 nm, OSRAM Opto Semiconductors), equipped with a water-cooling system for temperature control, was positioned on top of the cuvette. The time dependence of the absorbance was measured horizontally (light path: 1 cm), at 25 °C: first every minute in the dark for 30 min, and subsequently under continuous light irradiation for 3 h (vertical beam, light path: 3 cm).

3.5. References.

(1) Fang, X.; Kalathil, S.; Reisner, E. *Chem. Soc. Rev.* **2020**, *49*, 4926.

(2) Lubitz, W.; Ogata, H.; Rüdiger, O.; Reijerse, E. *Chem. Rev.* **2014**, *114*, 4081.

(3) Meyer, T. J.; Huynh, M. H. V.; Thorp, H. H. *Angew. Chem. Int. Ed.* **2007**, *46*, 5284.

(4) Keijer, T.; Bouwens, T.; Hessels, J.; Reek, J. N. H. *Chem. Sci.* **2021**, *12*, 50.

(5) Kobayashi, A.; Takizawa, S.; Hirahara, M. *Coord. Chem. Rev.* **2022**, *467*, 214624.

(6) Pannwitz, A.; Klein, D. M.; Rodríguez-Jiménez, S.; Casadevall, C.; Song, H.; Reisner, E.; Hammarström, L.; Bonnet, S. *Chem. Soc. Rev.* **2021**, *50*, 4833.

(7) Troppmann, S.; König, B. *Chem. – Eur. J.* **2014**, *20*, 14570.

(8) Ikuta, N.; Takizawa, S.; Murata, S. *Photochem. Photobiol. Sci.* **2014**, *13*, 691.

(9) Limburg, B.; Wermink, J.; Van Nielen, S. S.; Kortlever, R.; Koper, M. T. M.; Bouwman, E.; Bonnet, S. *ACS Catal.* **2016**, *6*, 5968.

(10) Armstrong, F. A.; Hirst, J. *Proc. Natl. Acad. Sci.* **2011**, *108*, 14049.

(11) Pellegrin, Y.; Odobel, F. *Comptes Rendus Chim.* **2016**, *20*, 283.

(12) Ucar, D.; Zhang, Y.; Angelidaki, I. *Front. Microbiol.* **2017**, *8*.

(13) Ishiyama, M.; Shiga, M.; Sasamoto, K.; Mizoguchi, M.; He, P. *Chem. Pharm. Bull. (Tokyo)* **1993**, *41*, 1118.

(14) Sutherland, M. W.; Learmonth, B. A. *Free Radic. Res.* **1997**, *27*, 283.

(15) Hansen, M.; Li, F.; Sun, L.; König, B. *Chem. Sci.* **2014**, *5*, 2683.

(16) Tsvetkov, I. M.; Buyanova, E. R.; Lymar, S. V.; Parmon, V. N. *React. Kinet. Catal. Lett.* **1983**, *22*, 159.

(17) Troppmann, S.; Brandes, E.; Motschmann, H.; Li, F.; Wang, M.; Sun, L.; König, B. *Eur. J. Inorg. Chem.* **2016**, *2016*, 554.

(18) Klein, D. M.; Passerini, L.; Huber, M.; Bonnet, S. *ChemCatChem* **2022**, *14*, e202200484.

(19) Moser, C. C.; Keske, J. M.; Warncke, K.; Farid, R. S.; Dutton, P. L. *Nature* **1992**, *355*, 796.

(20) Robinson, J. N.; Cole-Hamilton, D. J. *Chem. Soc. Rev.* **1991**, *20*, 49.

(21) Altamura, E.; Milano, F.; Tangorra, R. R.; Trotta, M.; Omar, O. H.; Stano, P.; Mavelli, F. *Proc. Natl. Acad. Sci.* **2017**, *114*, 3837.

(22) Milano, F.; Trotta, M.; Dorogi, M.; Fischer, B.; Giotta, L.; Agostiano, A.; Maróti, P.; Kálmán, L.; Nagy, L. *J. Bioenerg. Biomembr.* **2012**, *44*, 373.

(23) Stikane, A.; Hwang, E. T.; Ainsworth, E. V.; Piper, S. E. H.; Critchley, K.; Butt, J. N.; Reisner, E.; Jeuken, L. J. C. T *Faraday Discuss.* **2019**, *215*, 26.

(24) Limburg, B.; Bouwman, E.; Bonnet, S. *Chem. Commun.* **2015**, *51*, 17128.

(25) Gust, D.; Moore, T. A.; Moore, A. L. *Acc. Chem. Res.* **1993**, *26*, 198.

(26) Bhosale, S.; Sisson, A. L.; Talukdar, P.; Fürstenberg, A.; Banerji, N.; Vauthey, E.; Bollot, G.; Mareda, J.; Röger, C.; Würthner, F.; Sakai, N.; Matile, S. *Science* **2006**, *313*, 84.

(27) Sinambela, N.; Jacobi, R.; Sorsche, D.; González, L.; Pannwitz, A. *Angew. Chem. Int. Ed.* **2025**, *64*, e202423393.

(28) Klein, D. M.; Li, X.; Boyle, A. L.; Van Der Pol, R.; Tsina, V. E.; Sevink, G. J. A.; Brouwer, A. M.; Bonnet, S. *Artif. Photosynth.* **2025**, *1*, 188.

(29) Steinberg-Yfrach, G.; Liddell, P. A.; Hung, S.-C.; Moore, A. L.; Gust, D.; Moore, T. A. *Nature* **1997**, *385*, 239.

(30) Steinberg-Yfrach, G.; Rigaud, J.-L.; Durantini, E. N.; Moore, A. L.; Gust, D.; Moore, T. A. *Nature* **1998**, *392*, 479.

(31) Killian, J. A.; Salemink, I.; Greathouse, D. V. *Biochemistry* **1996**, *35*, 1037.

(32) De Planque, M. R. R.; Killian, J. A. *Mol. Membr. Biol.* **2003**, *20*, 271.

(33) Killian, J. A.; Nyholm, T. K. *Curr. Opin. Struct. Biol.* **2006**, *16*, 473.

(34) Krieger, E.; Darden, T.; Nabuurs, S. B.; Finkelstein, A.; Vriend, G. *Proteins Struct. Funct. Bioinforma.* **2004**, *57*, 678.

(35) Krieger, E.; Nielsen, J. E.; Spronk, C. A. E. M.; Vriend, G. *J. Mol. Graph. Model.* **2006**, *25*, 481.

(36) Sinambela, N.; Nau, M.; Haug, G.; Linseis, M.; Koblischek, P.; F. Winter, R.; Pannwitz, A. *Sustain. Energy Fuels* **2025**, *9*, 2302.

(37) Rinia, H. A.; De Kruijff, B. *FEBS Lett.* **2001**, *504*, 194.

(38) Strandberg, E.; Morein, S.; Rijkers, D. T. S.; Liskamp, R. M. J.; Van Der Wel, P. C. A.; Killian, J. A. *Biochemistry* **2002**, *41*, 7190.

(39) Rinia, H. A.; Boots, J.-W. P.; Rijkers, D. T. S.; Kik, R. A.; Snel, M. M. E.; Demel, R. A.; Killian, J. A.; Van Der Eerden, J. P. J. M.; De Kruijff, B. *Biochemistry* **2002**, *41*, 2814.

(40) Natali, M.; Amati, A.; Demitri, N.; Iengo, E. *Chem. Commun.* **2018**, *54*, 6148.

(41) Natali, M.; Amati, A.; Merchiori, S.; Ventura, B.; Iengo, E. *J. Phys. Chem. C* **2020**, *124*, 8514.

(42) Pathak, P.; Zarandi, M. A.; Zhou, X.; Jayawickramarajah, J. *Front. Chem.* **2021**, *9*, 764137.

(43) Biron, E.; Voyer, N. *Chem. Commun.* **2005**, *37*, 4652.

(44) Biron, E.; Voyer, N. *Org. Biomol. Chem.* **2008**, *6*, 2507.

(45) Capasso, S. *Thermochim. Acta* **1996**, *286*, 41.

(46) Konuklar, F. A. S.; Aviyente, V. *Org. Biomol. Chem.* **2003**, *1*, 2290.

(47) Bettelheim, A.; White, B. A.; Raybuck, S. A.; Murray, R. W. *Inorg. Chem.* **1987**, *26*, 1009.

(48) Luguya, R.; Jaquinod, L.; Fronczek, F. R.; Vicente, M. G. H.; Smith, K. M. *Tetrahedron* **2004**, *60*, 2757.

(49) Gianferrara, T.; Bratsos, I.; Iengo, E.; Milani, B.; Oštrić, A.; Spagnul, C.; Zangrando, E.; Alessio, E. *Dalton Trans.* **2009**, *48*, 10742.

(50) Arnold, D. P.; Blok, J. *Coord. Chem. Rev.* **2004**, *248*, 299.

(51) Ou, Z.; E, W.; Zhu, W.; Thordarson, P.; Sintic, P. J.; Crossley, M. J.; Kadish, K. M. *Inorg. Chem.* **2007**, *46*, 10840.

(52) Bätz, T.; Enke, M.; Zechel, S.; Hager, M. D.; Schubert, U. S. *Macromol. Chem. Phys.* **2021**, *222*, 2100295.

(53) Krieger, E.; Vriend, G. *Bioinformatics* **2014**, *30*, 2981.

(54) Tyburski, R.; Liu, T.; Glover, S. D.; Hammarström, L. *J. Am. Chem. Soc.* **2021**, *143*, 560.

(55) Arnold, D. P.; Bartley, J. P. *Inorg. Chem.* **1994**, *33*, 1486.

(56) Amati, A.; Cavigli, P.; Demitri, N.; Natali, M.; Indelli, M. T.; Iengo, E. *Inorg. Chem.* **2019**, *58*, 4399.

(57) Toniolo, C.; Formaggio, F.; Woody, R. W. *Comprehensive Chiroptical Spectroscopy*; Berova, N., Polavarapu, P. L., Nakanishi, K., Woody, R. W., Eds.; Wiley, 2012; 499.

(58) Connelly, N. G.; Geiger, W. E. *Chem. Rev.* **1996**, *96*, 877.

(59) Oritani, T.; Fukuhara, N.; Okajima, T.; Kitamura, F.; Ohsaka, T. *Inorganica Chim. Acta* **2004**, *357*, 436.

(60) Manke, A.-M.; Geisel, K.; Fetzer, A.; Kurz, P. *Phys Chem Chem Phys* **2014**, *16*, 12029.

(61) Leberman, R.; Rabin, B. R. *Trans. Faraday Soc.* **1959**, *55*, 1660.

Appendix B.

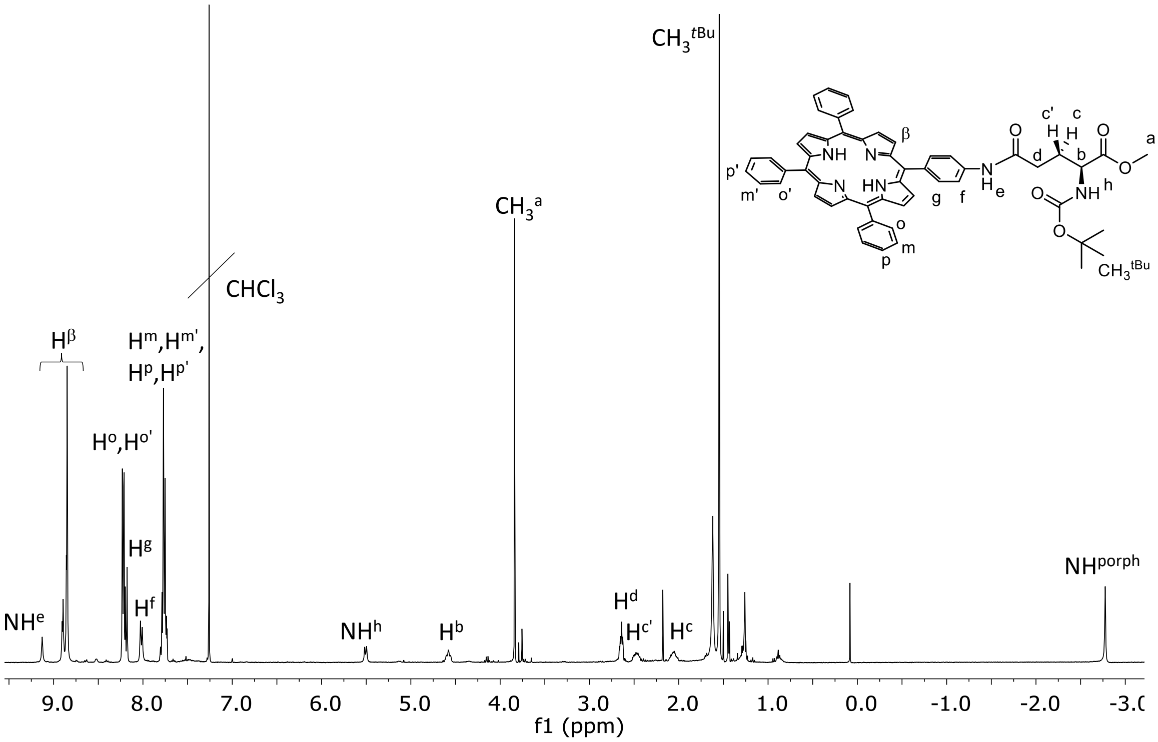

Figure S1. ^{1}H NMR spectrum (CDCl$_3$, 298 K) of **TPP-BocGluOMe** (**2**).

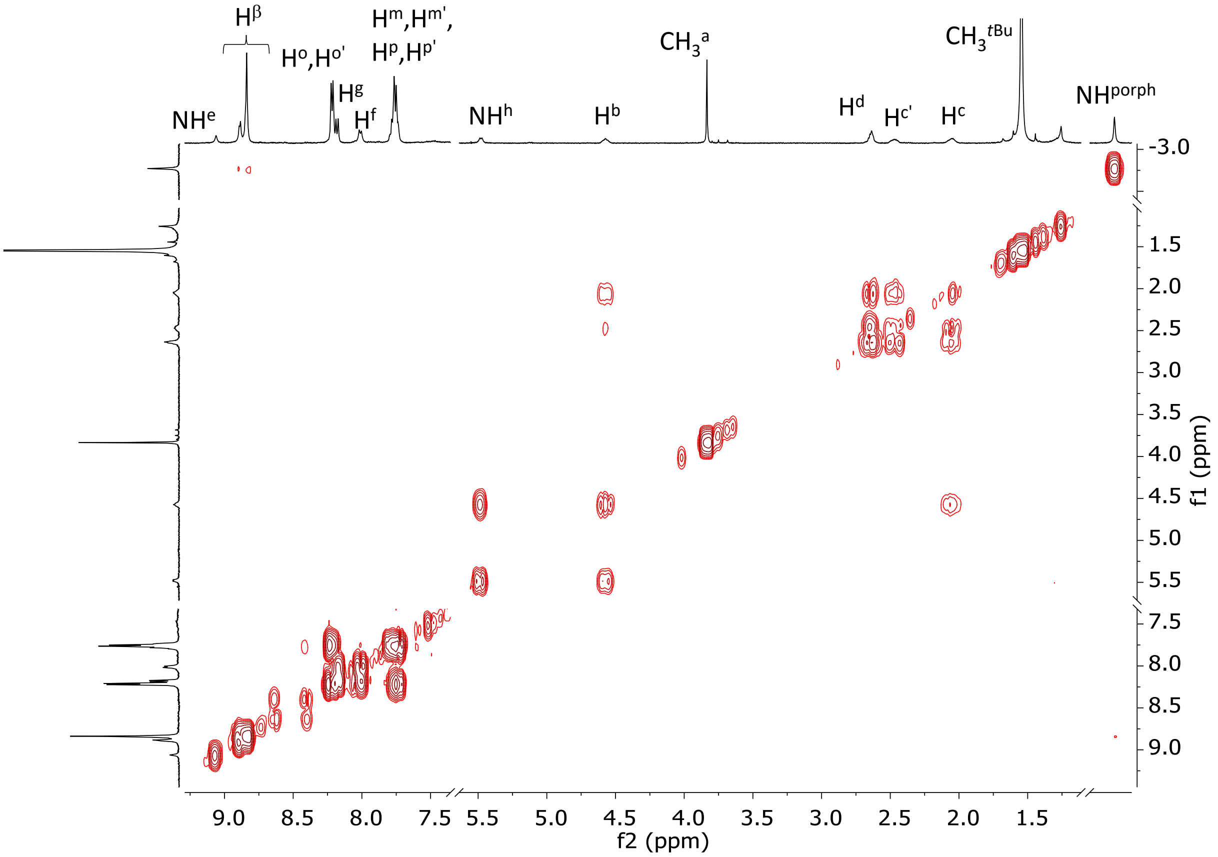

Figure S2. ^{1}H-^{1}H COSY spectrum (CDCl$_3$, 298 K) of **2**.

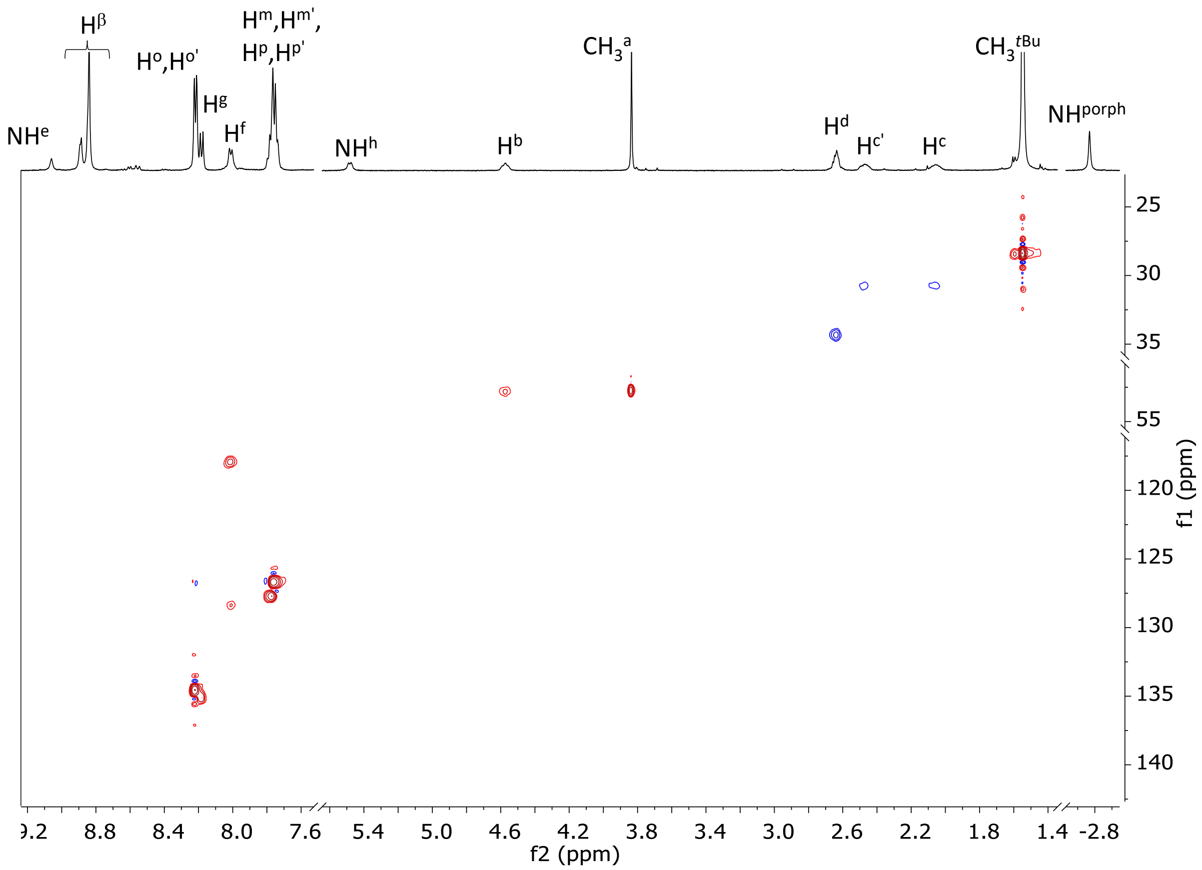

Figure S3. ^{1}H-^{13}C HSQC spectrum (CDCl$_3$ 298 K) of **2**.

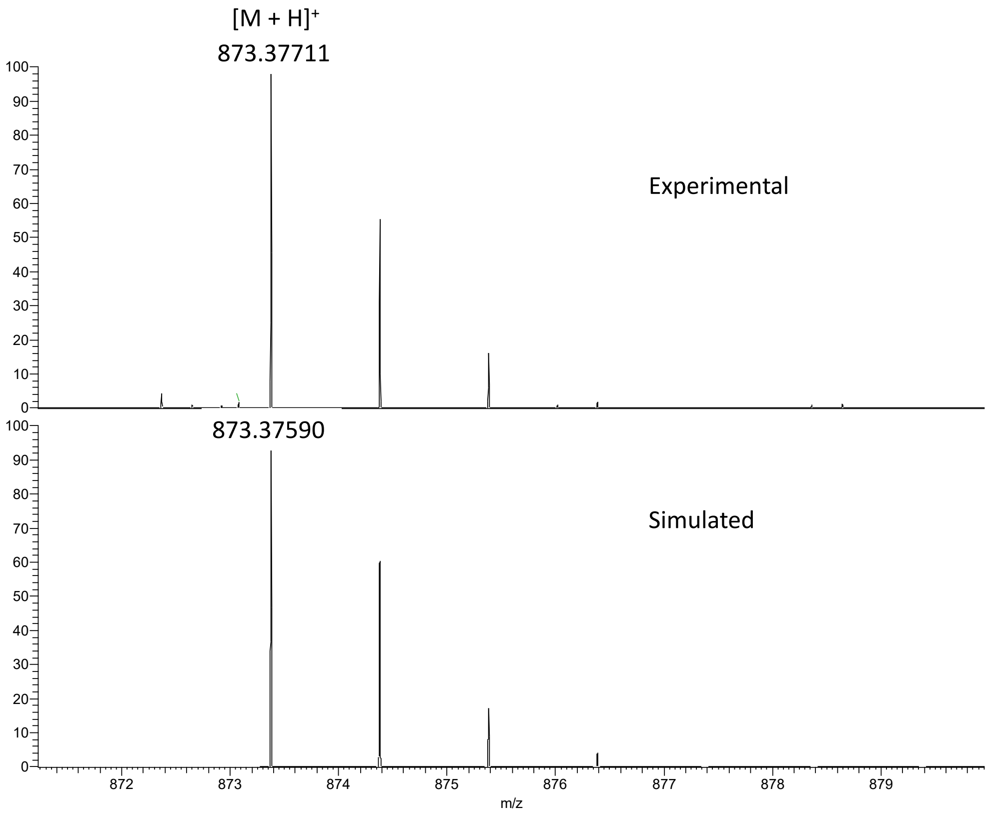

Figure S4. HRMS of **2** in CH$_3$CN:H$_2$0 1:1, experimental (top) and simulated (bottom).

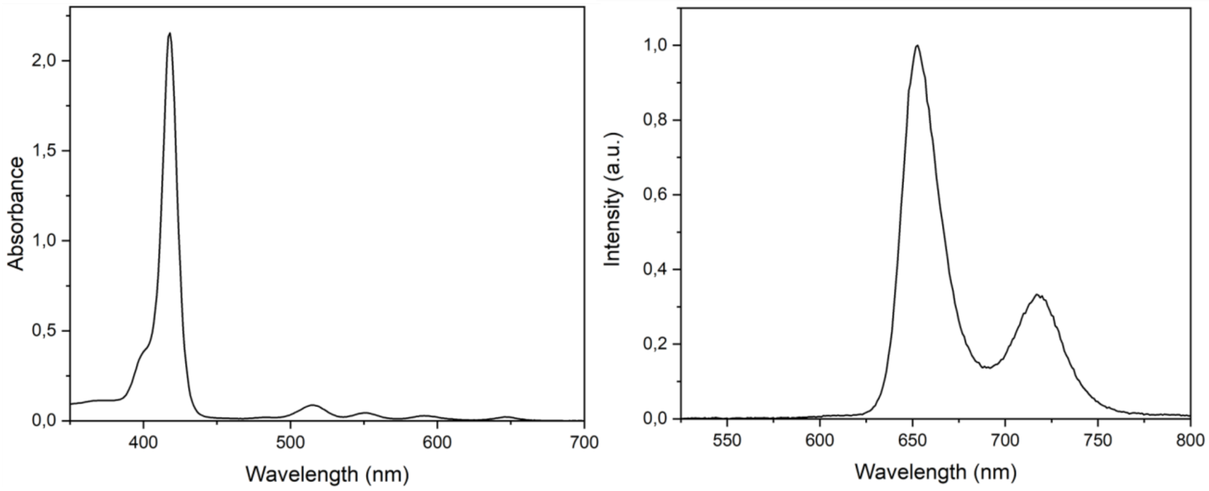

Figure S5. Left: UV-Vis absorption spectrum (CH_2Cl_2, 5 μM) of **2**. Right: Emission spectrum (CH_2Cl_2, 5 μM, λ_{irr} = 515 nm) of **2**.

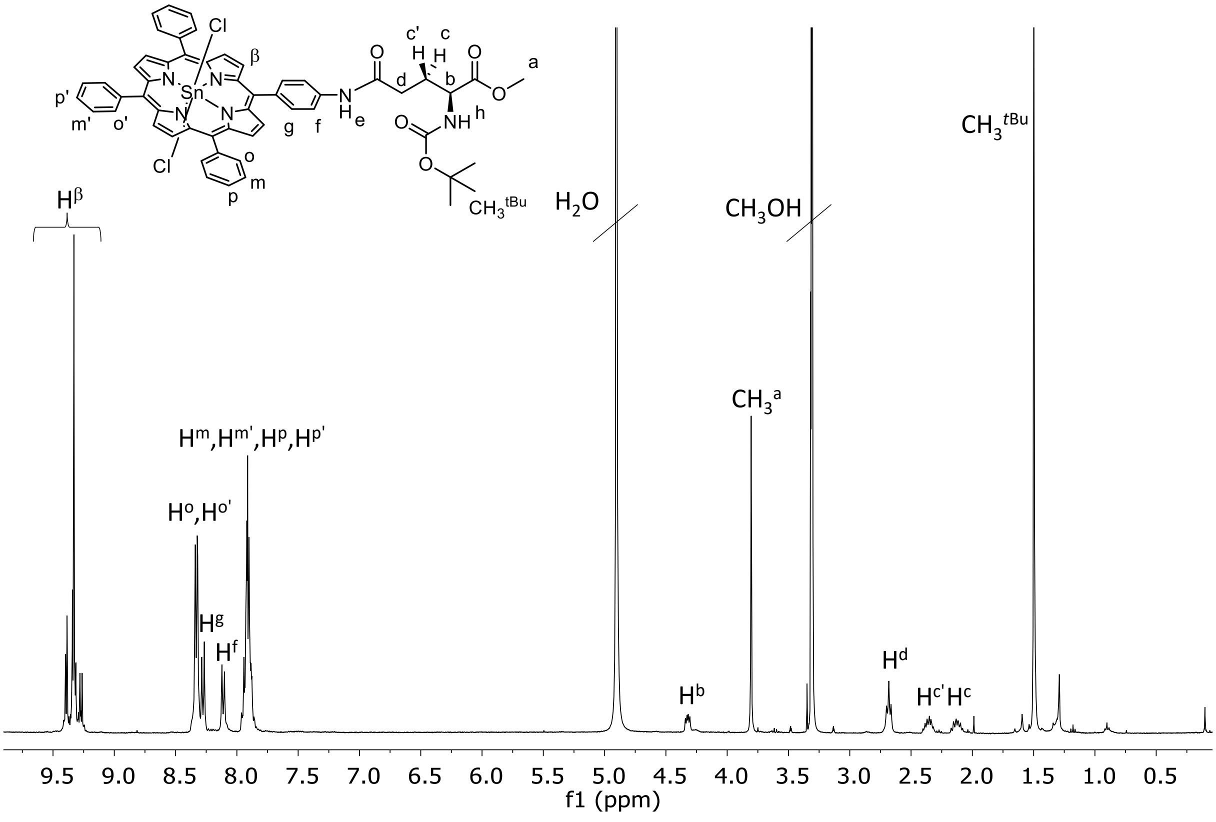

Figure S6. ^{1}H NMR spectrum (CD_3OD, 298 K) of **SnCl₂TPP-BocGluOMe** (**3**).

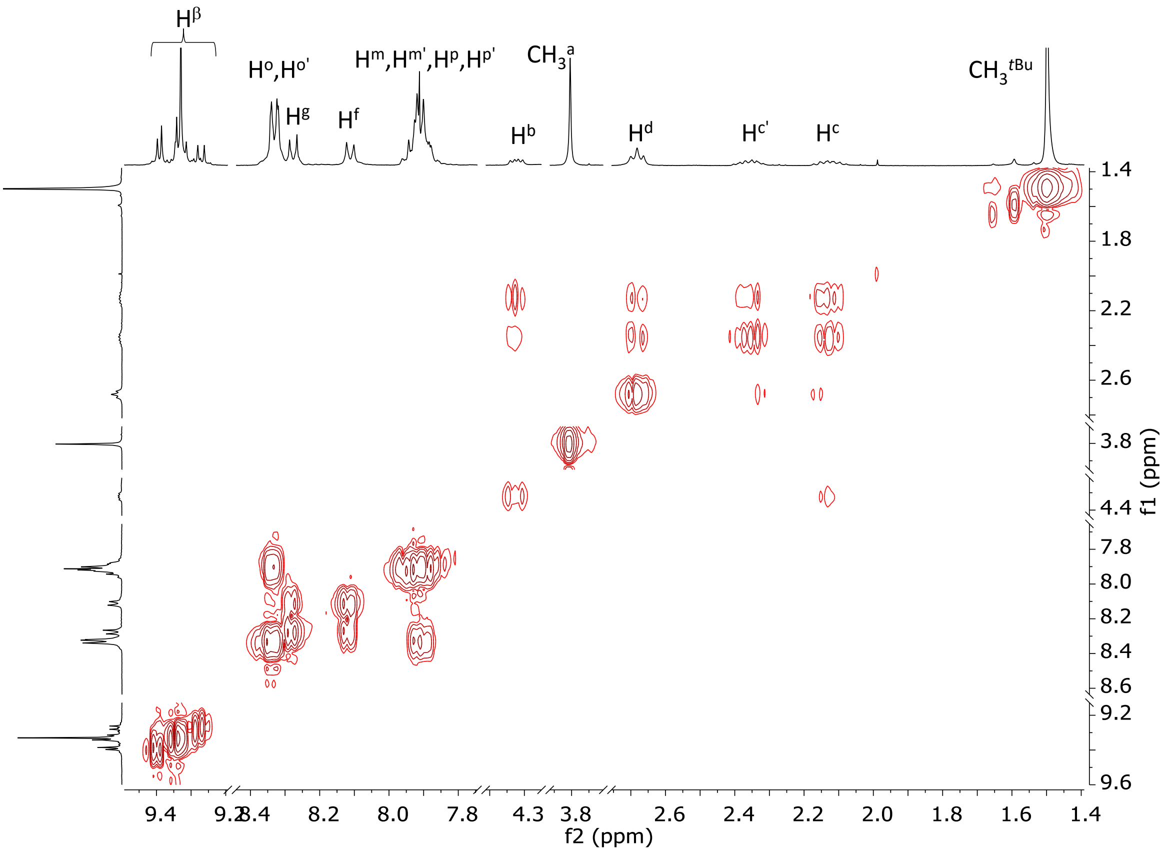

Figure S7. ^{1}H,^{1}H-COSY spectrum (CD$_3$OD, 298 K) of **3**.

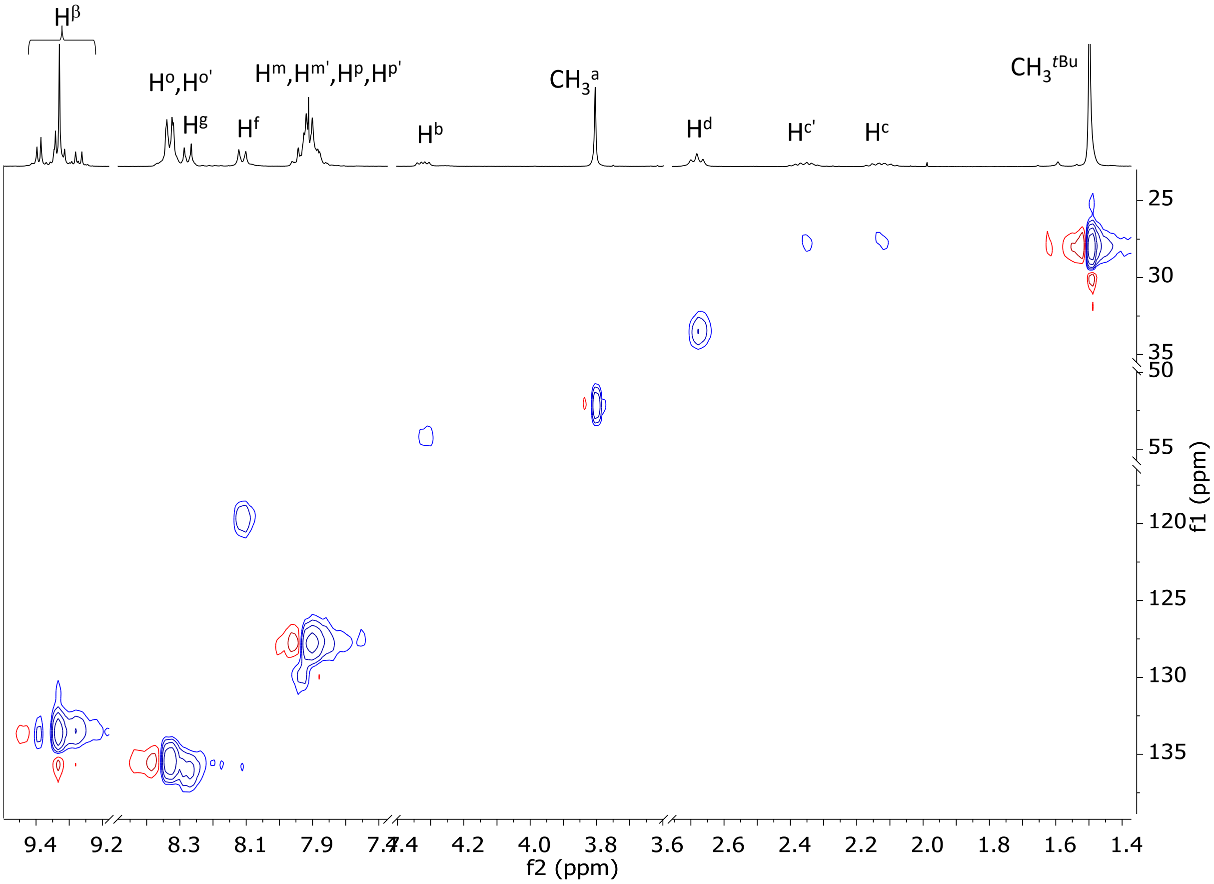

Figure S8. ^{1}H-^{13}C HSQC spectrum (CD$_3$OD, 298 K) of **3**.

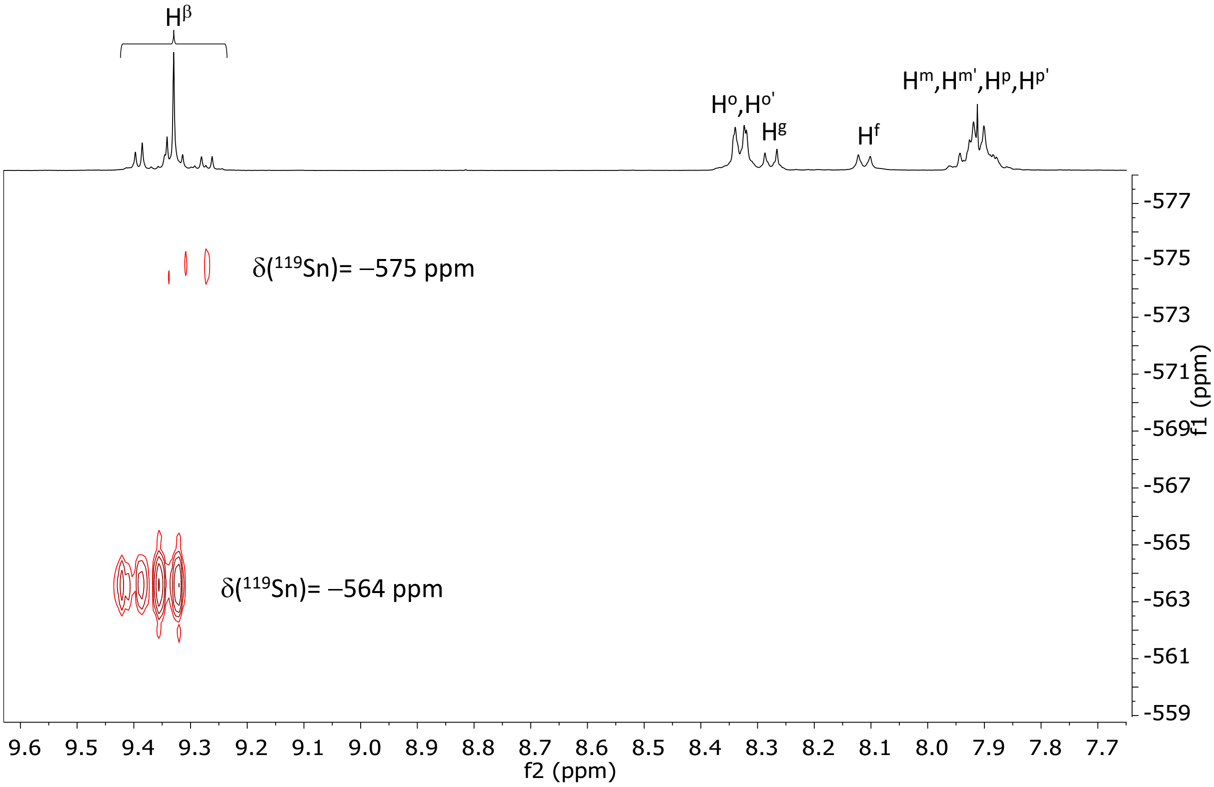

Figure S9. Aromatic region of the ^{1}H-^{119}Sn HMBC spectrum (CD_3OD, 289K) of **3**.

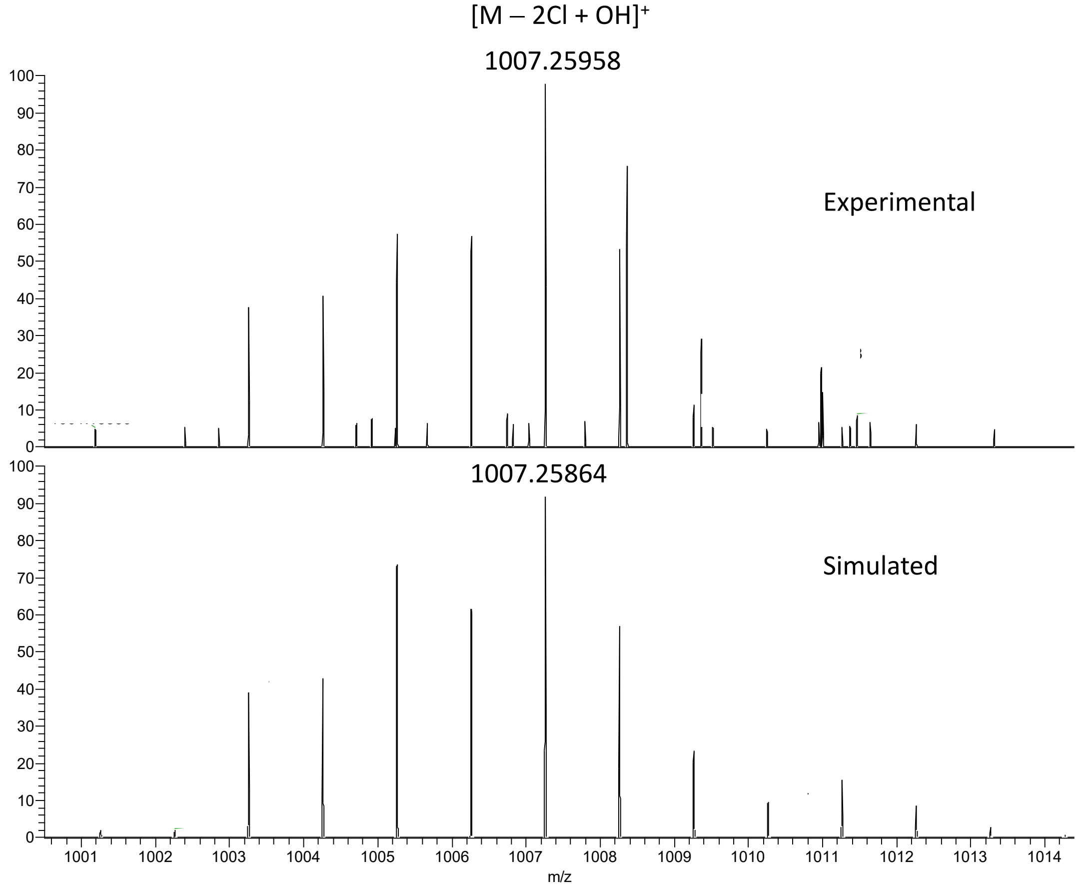

Figure S10. HRMS of **3** in CH_3CN:H_20 1:1, experimental (top) and simulated (bottom).

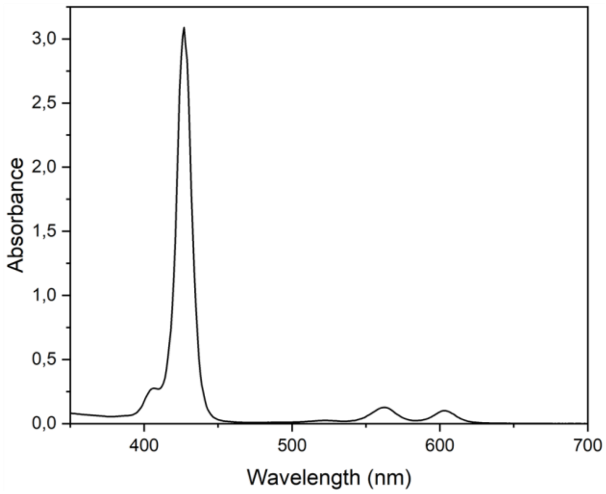

Figure S11. UV-Vis absorption spectrum (CH_2Cl_2, 5 μM) of **3**.

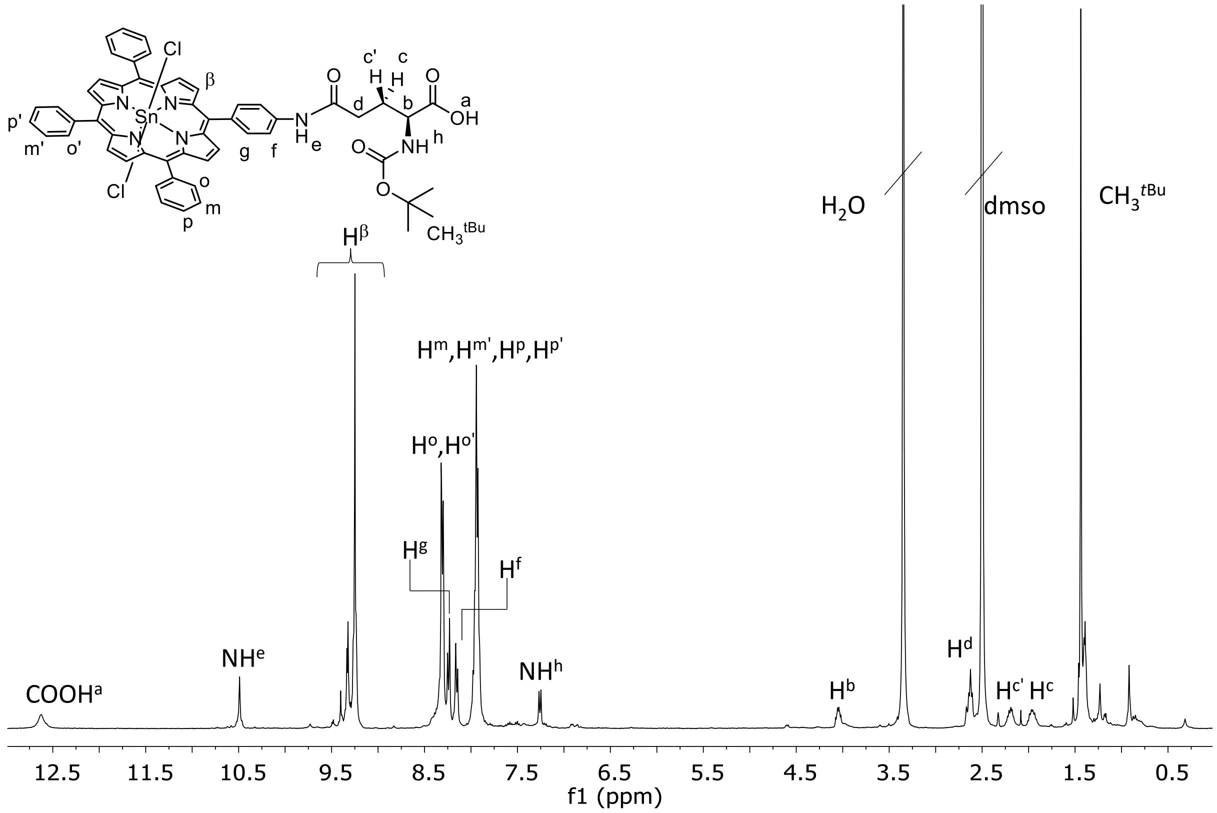

Figure S12. ^{1}H NMR spectrum (dmso-d_6, 298 K) of **$SnCl_2$TPP-BocGluOH** (**4**).

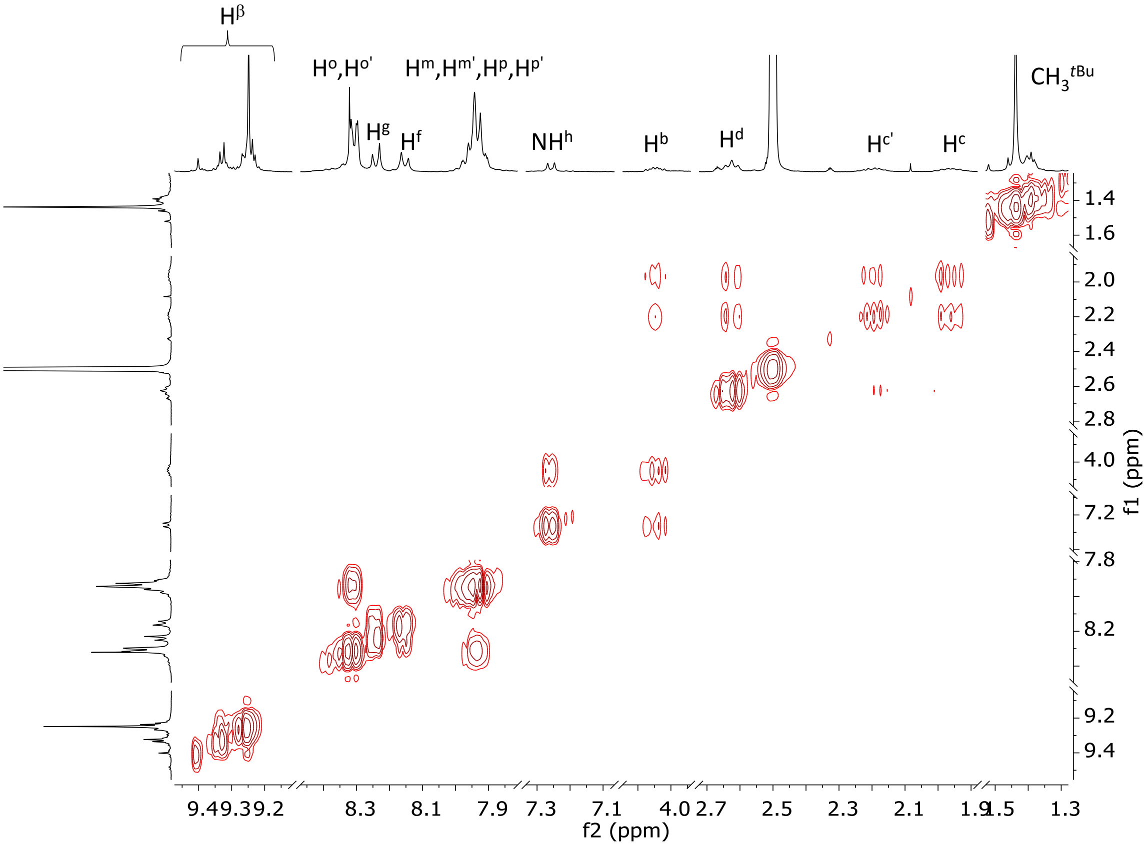

Figure S13. ^{1}H-^{1}H COSY spectrum (dmso-d_6, 298 K) of **4**.

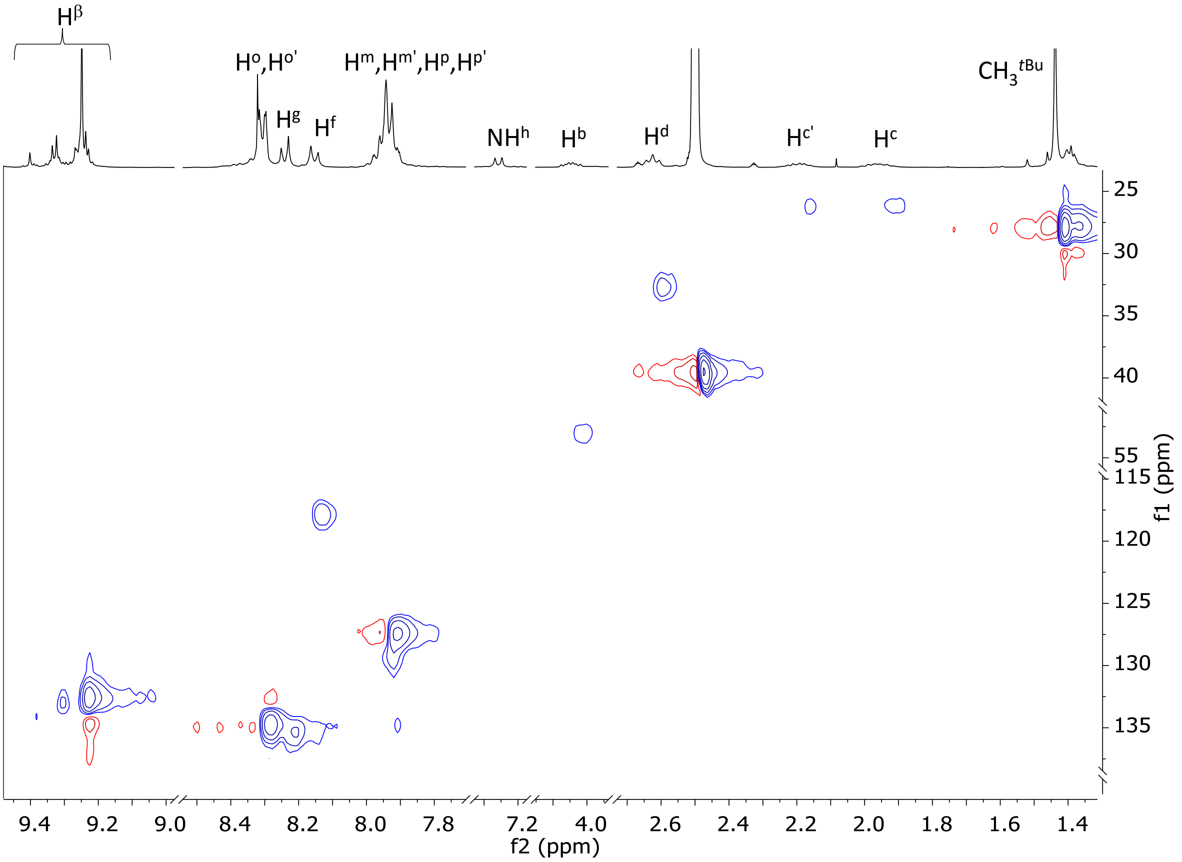

Figure S14. ^{1}H-^{13}C HSQC spectrum (dmso-d_6, 298 K) of **4**.

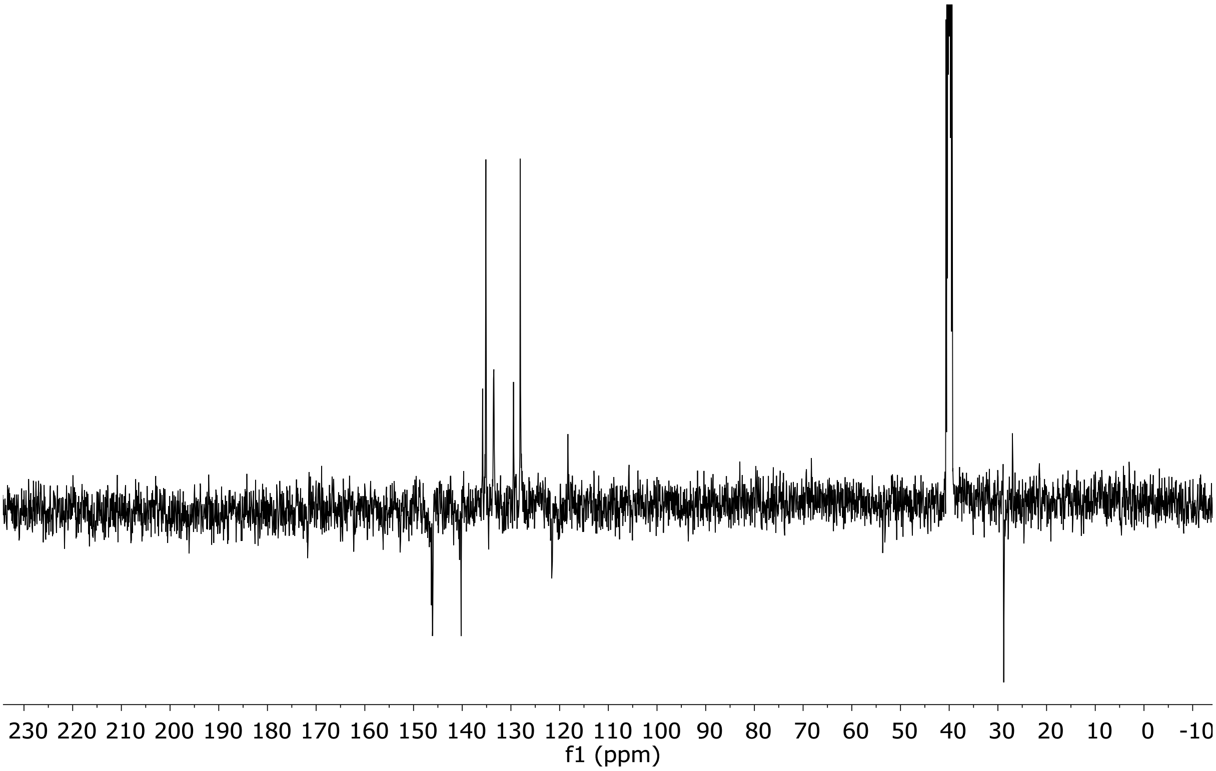

Figure S15. ^{13}C-APT NMR spectrum (dmso-d_6, 298 K) of **4**.

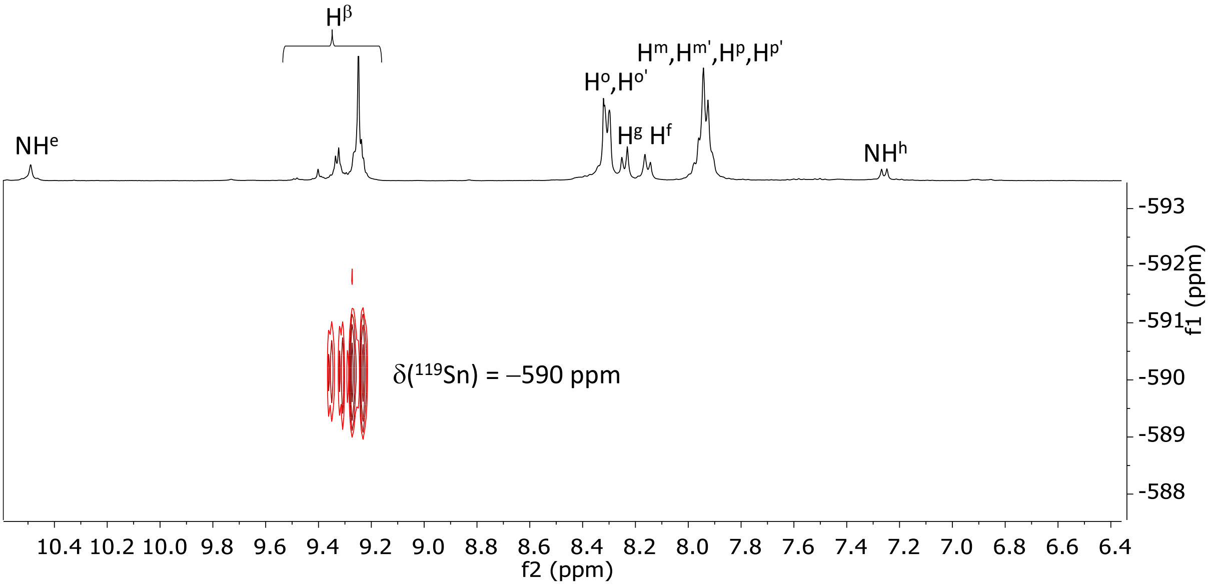

Figure S16. Aromatic region of the ^{1}H-^{119}Sn HMBC spectrum (dmso-d_6, 298 K) of **4**.

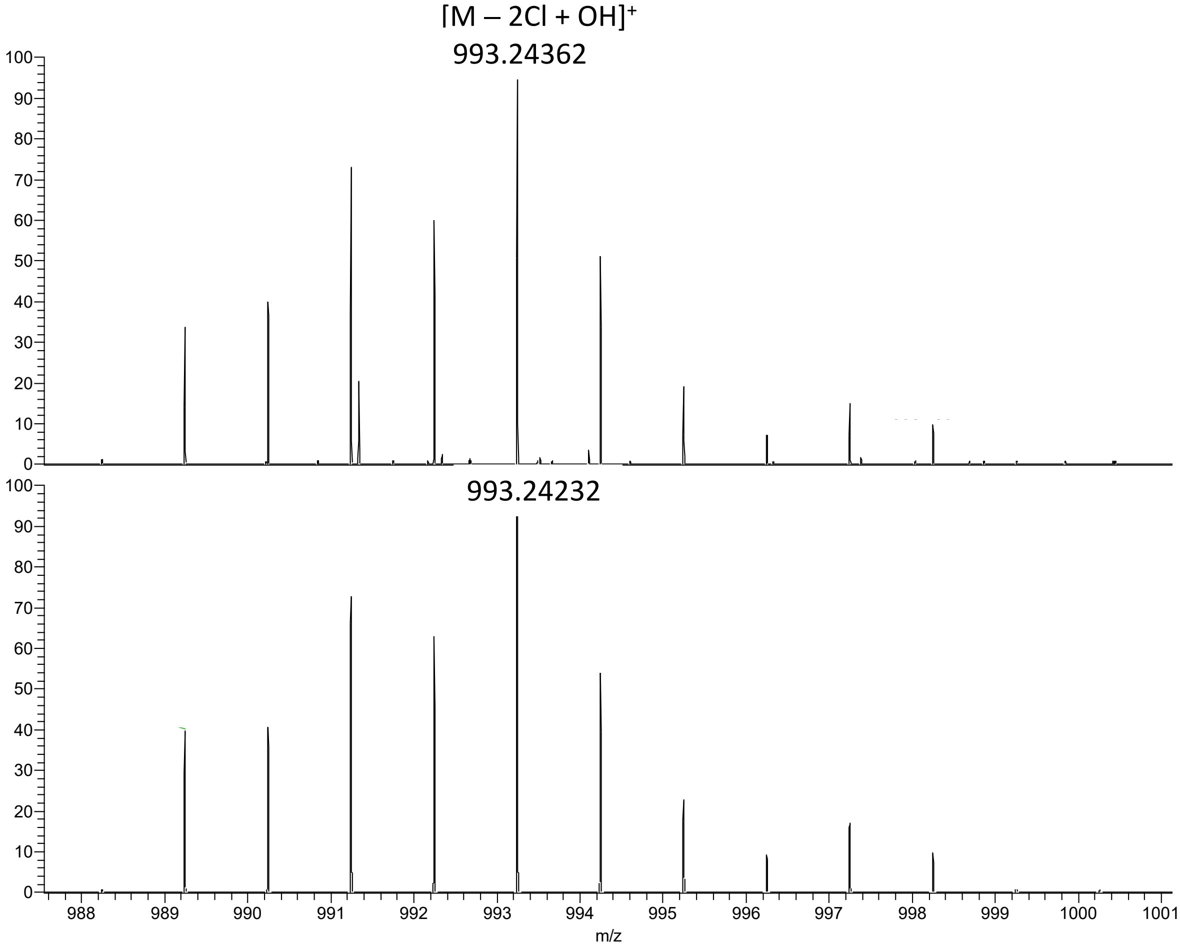

Figure S17. HRMS of **4** in $CH_3CN:H_20$ 1:1, experimental (top) and simulated (bottom).

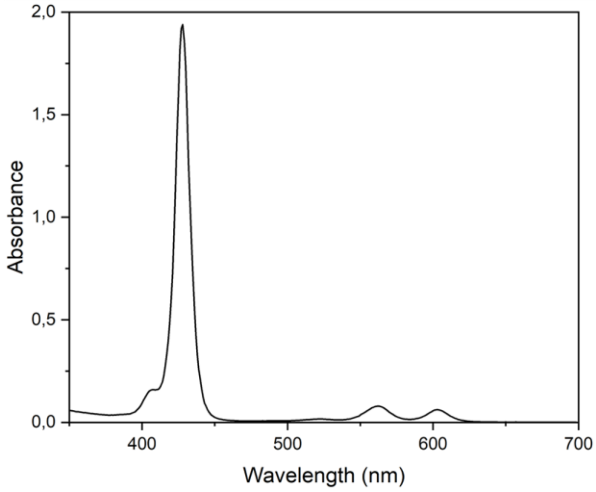

Figure S18. UV-Vis absorption spectrum (CH_2Cl_2, 5 μM) of **4**.

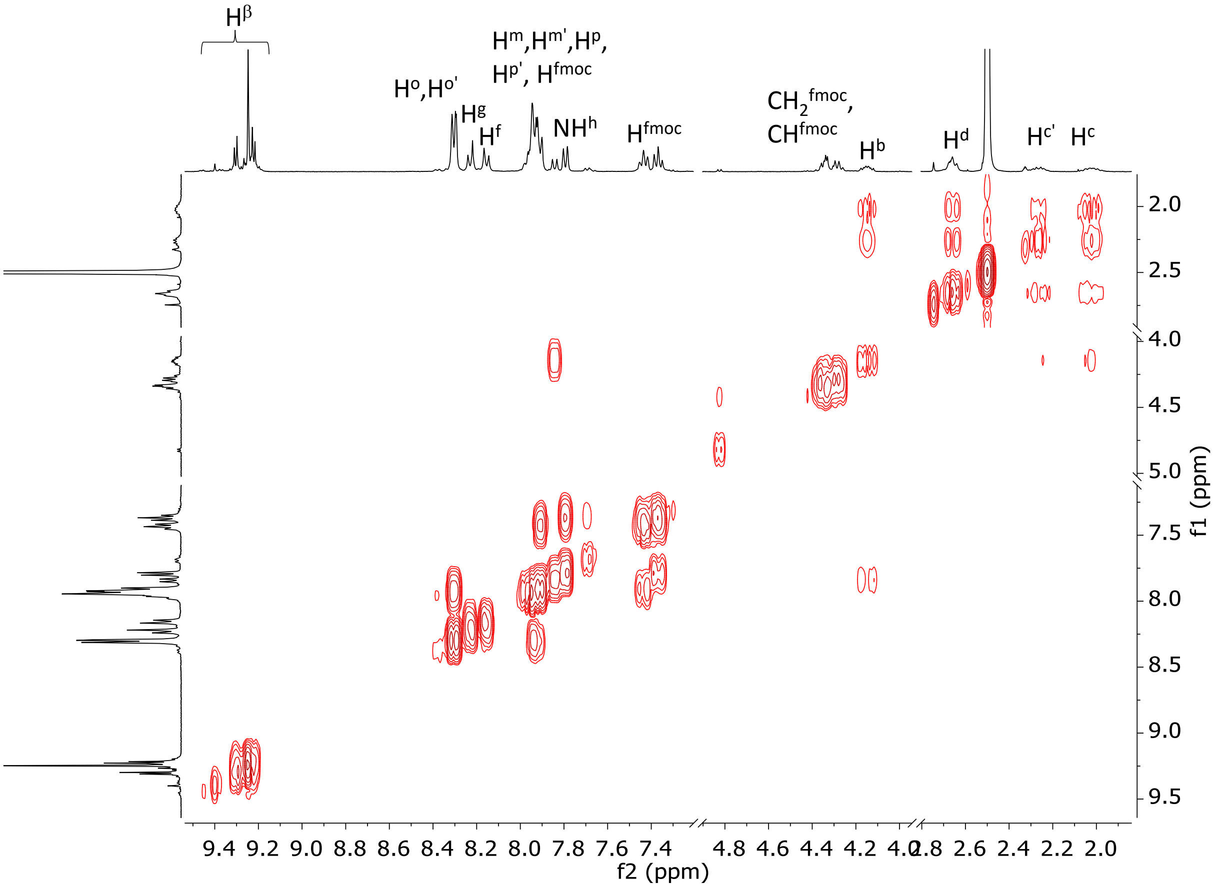

Figure S19. ^1H-^1H COSY spectrum (dmso-d_6, 298 K) of **SnCl₂TPP-FmocGluOH** (**5**). For proton labelling see Experimental Section.

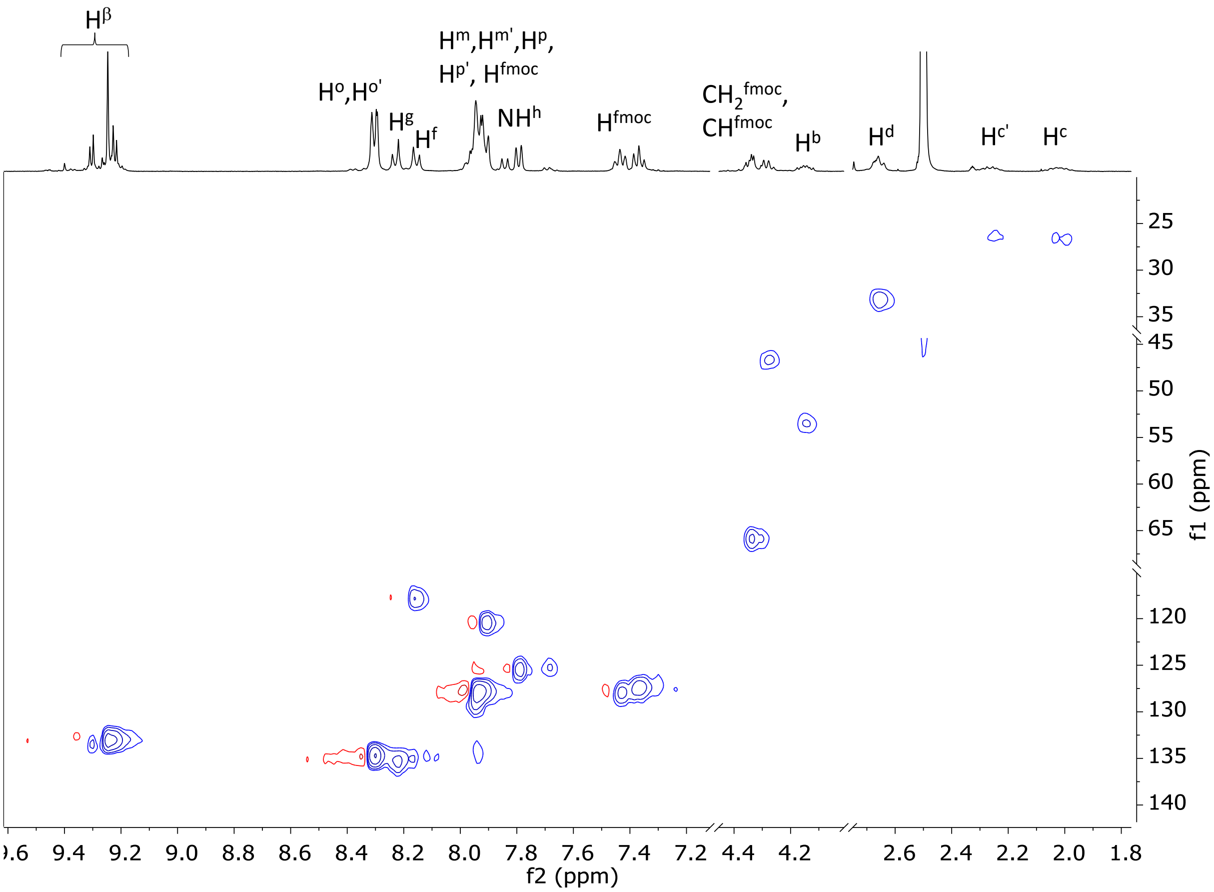

Figure S20. ^{1}H-^{13}C HSQC spectrum (dmso-d_6, 298 K) of **5**.

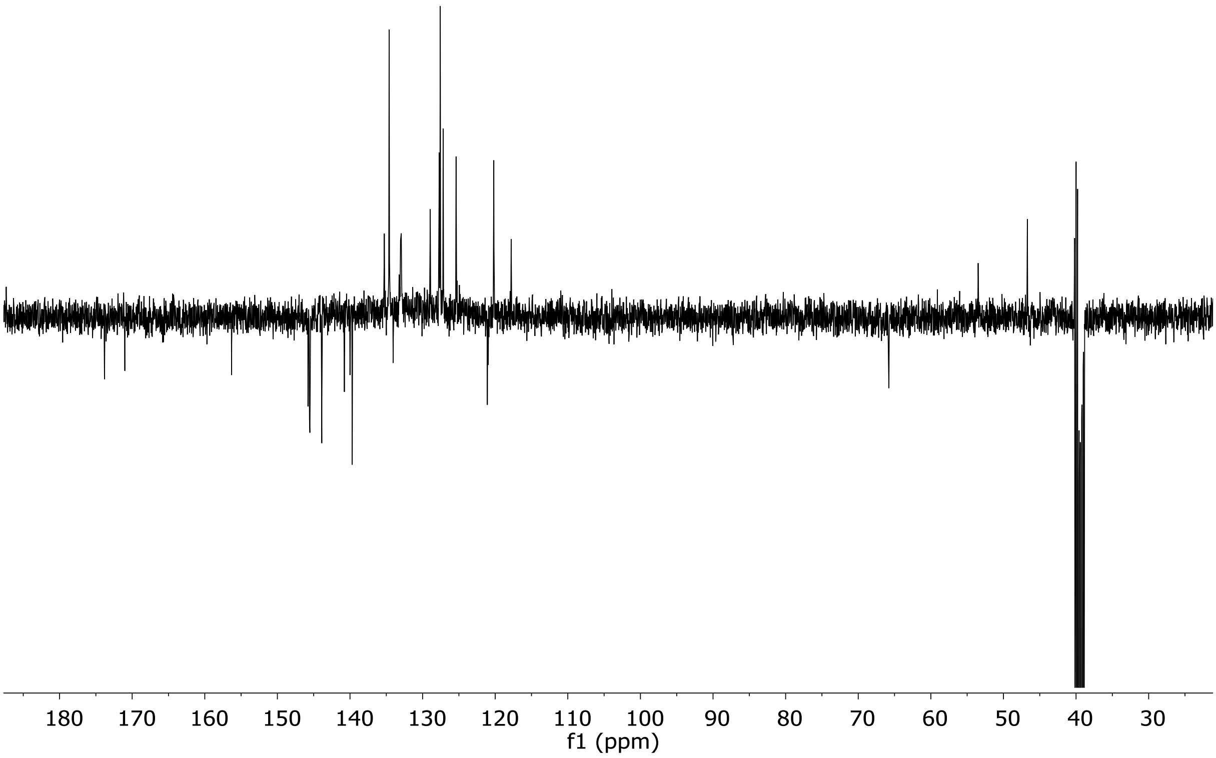

Figure S21. ^{13}C-APT NMR spectrum (dmso-d_6, 298 K) of **5**.

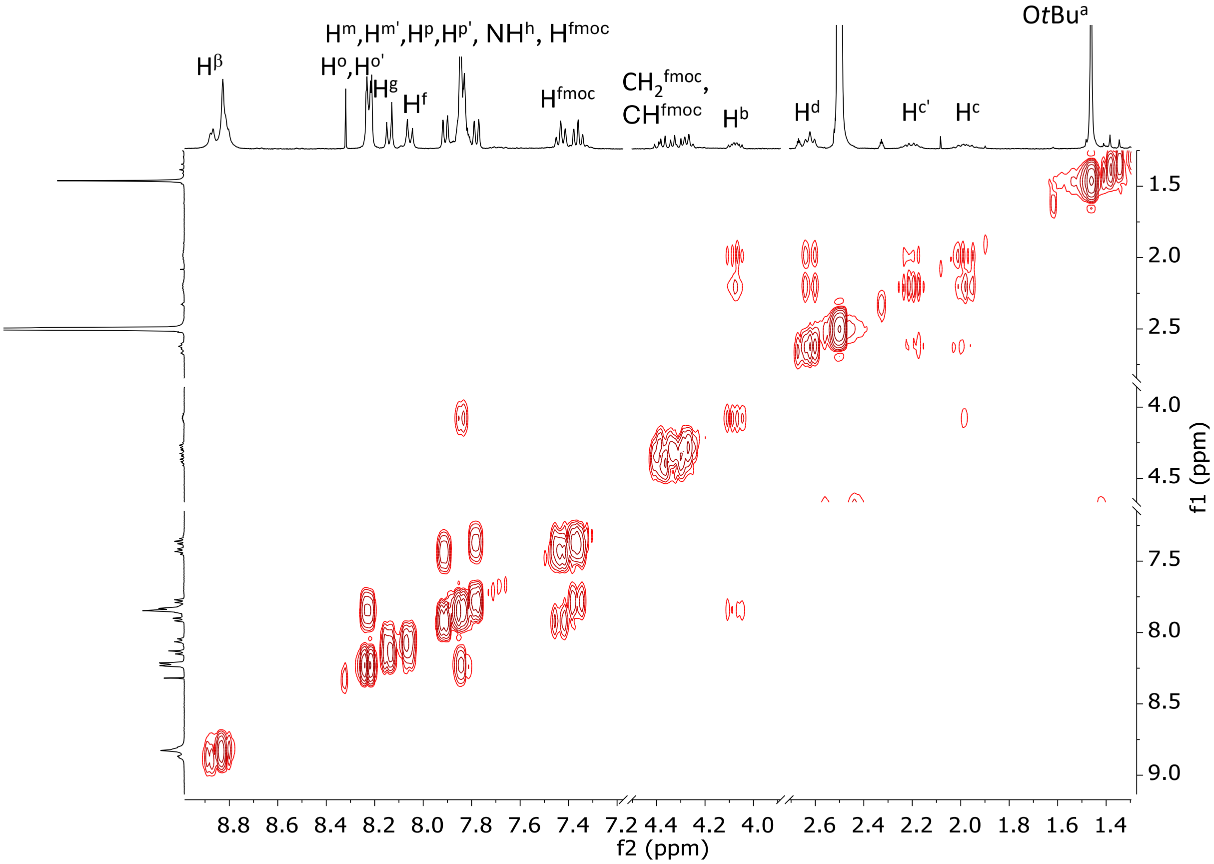

Figure S22. ^{1}H-^{1}H COSY spectrum (dmso-*d*$_6$, 298 K) of **6**. For proton labelling see Experimental Section.

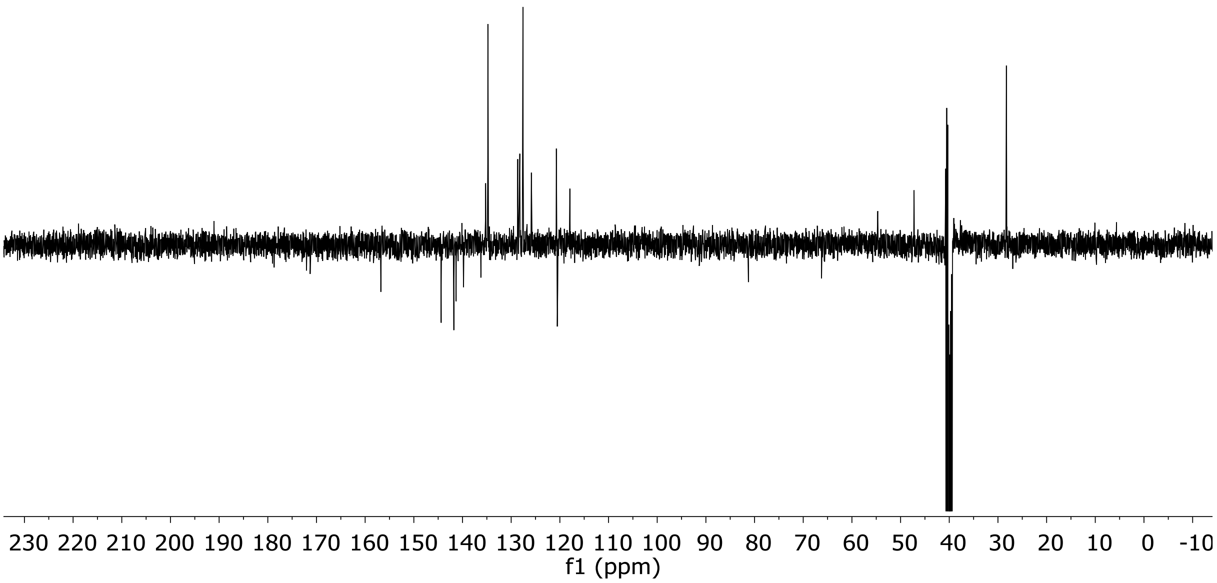

Figure S23. ^{13}C-APT NMR spectrum (dmso-*d*$_6$, 298 K) of **6**.

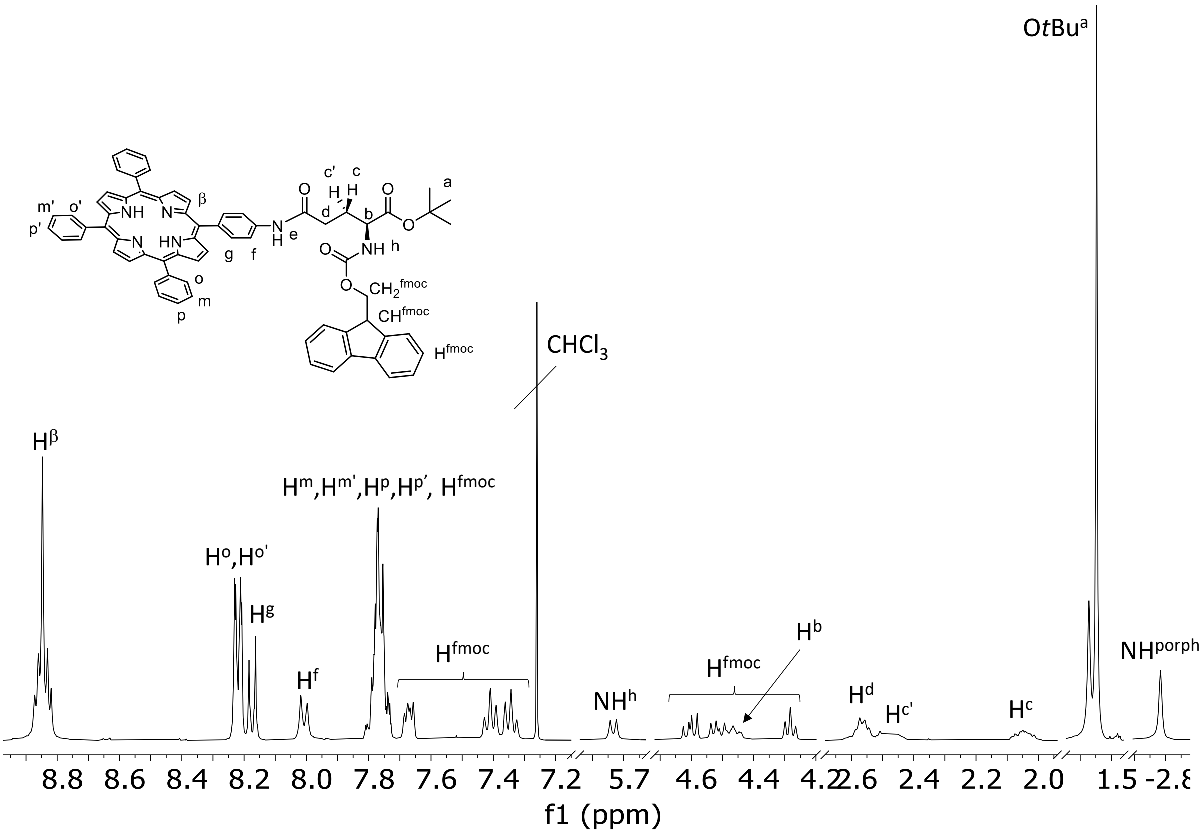

Figure S24. ^{1}H NMR spectrum (CDCl$_3$, 298 K) of **TPP-FmocGluO*t*Bu** (**6**).

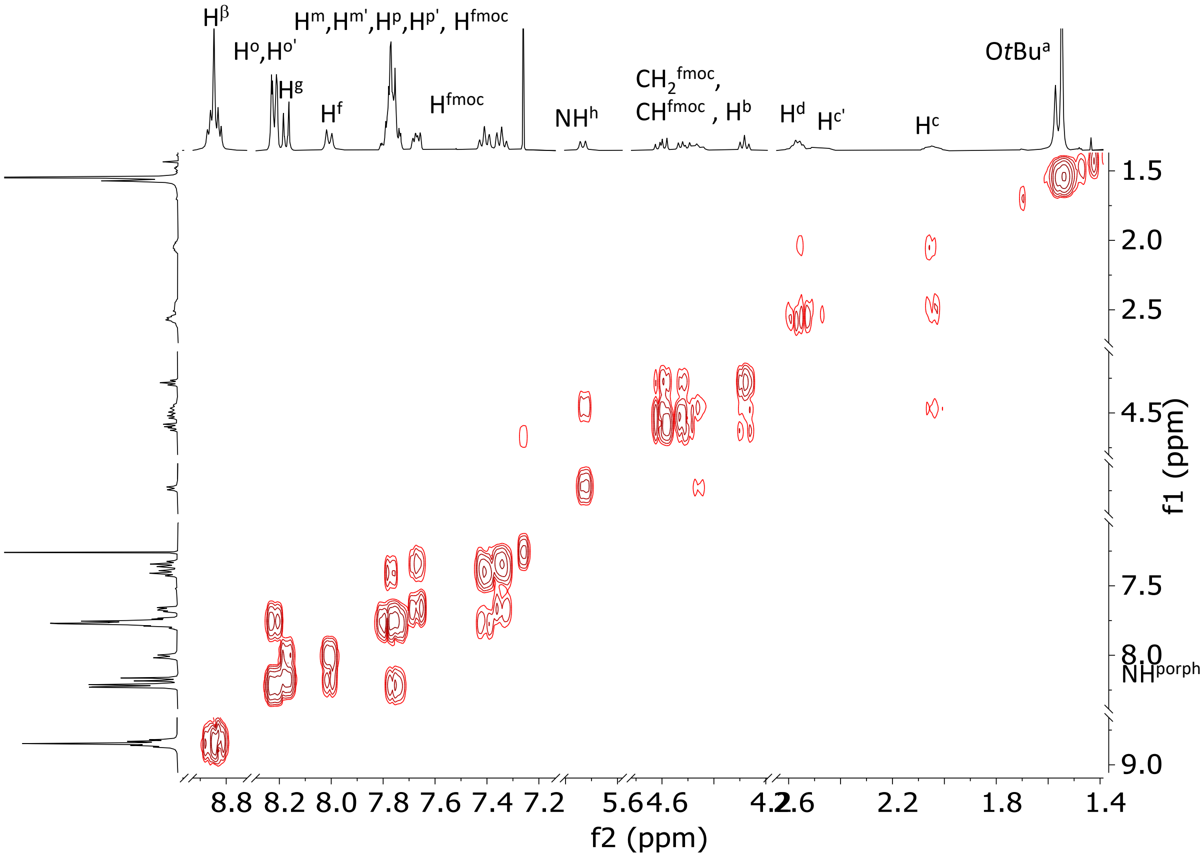

Figure S25. ^{1}H-^{1}H COSY spectrum (CDCl$_3$, 298 K) of **6**.

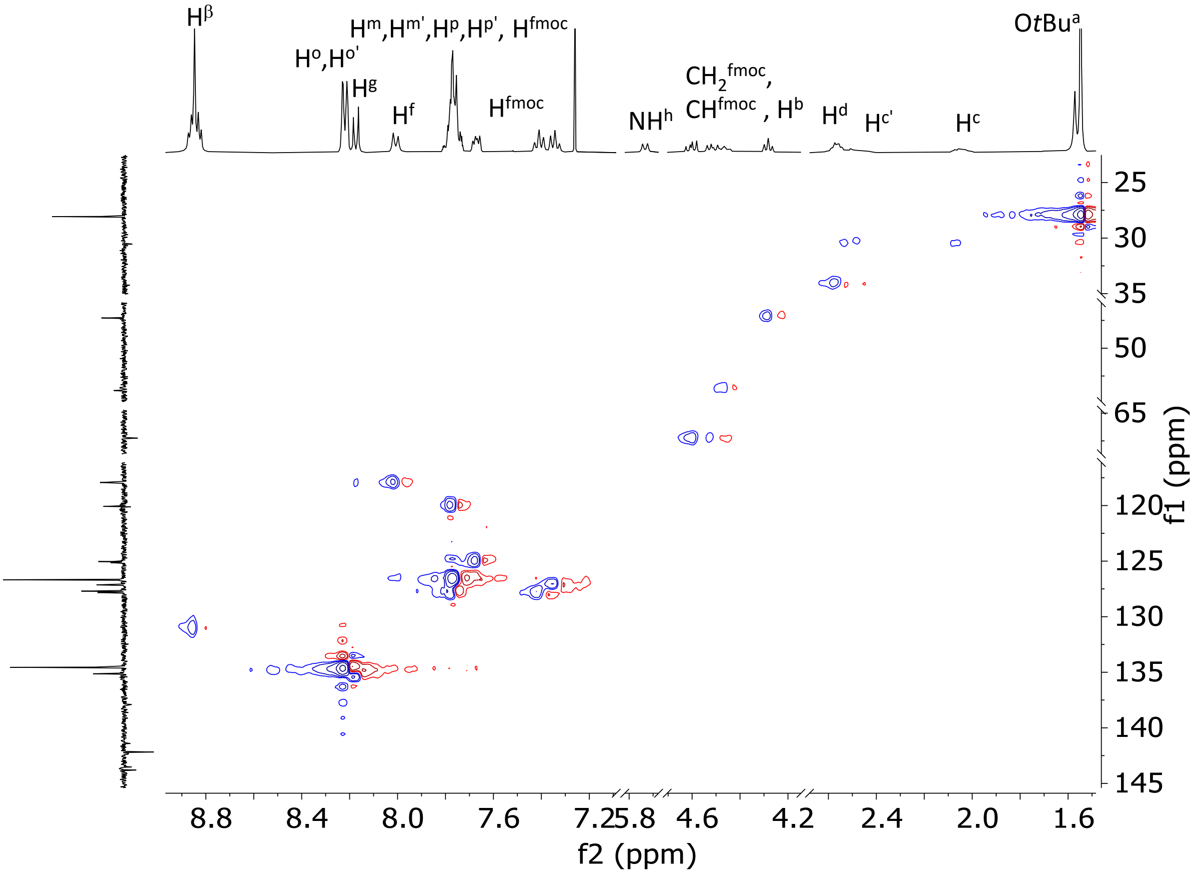

Figure S26. ^{1}H-^{13}C HSQC spectrum ($CDCl_3$, 298 K) of **6**.

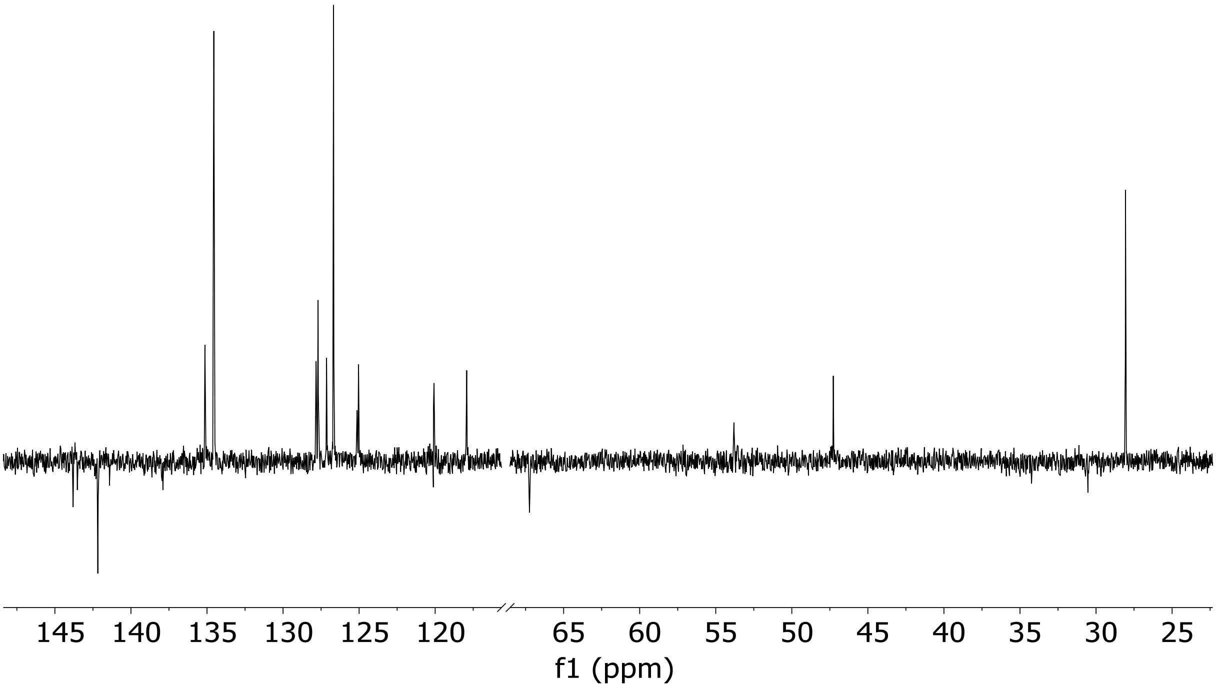

Figure S27. ^{13}C-APT NMR spectrum (dmso-d_6, 298 K) of **6**.

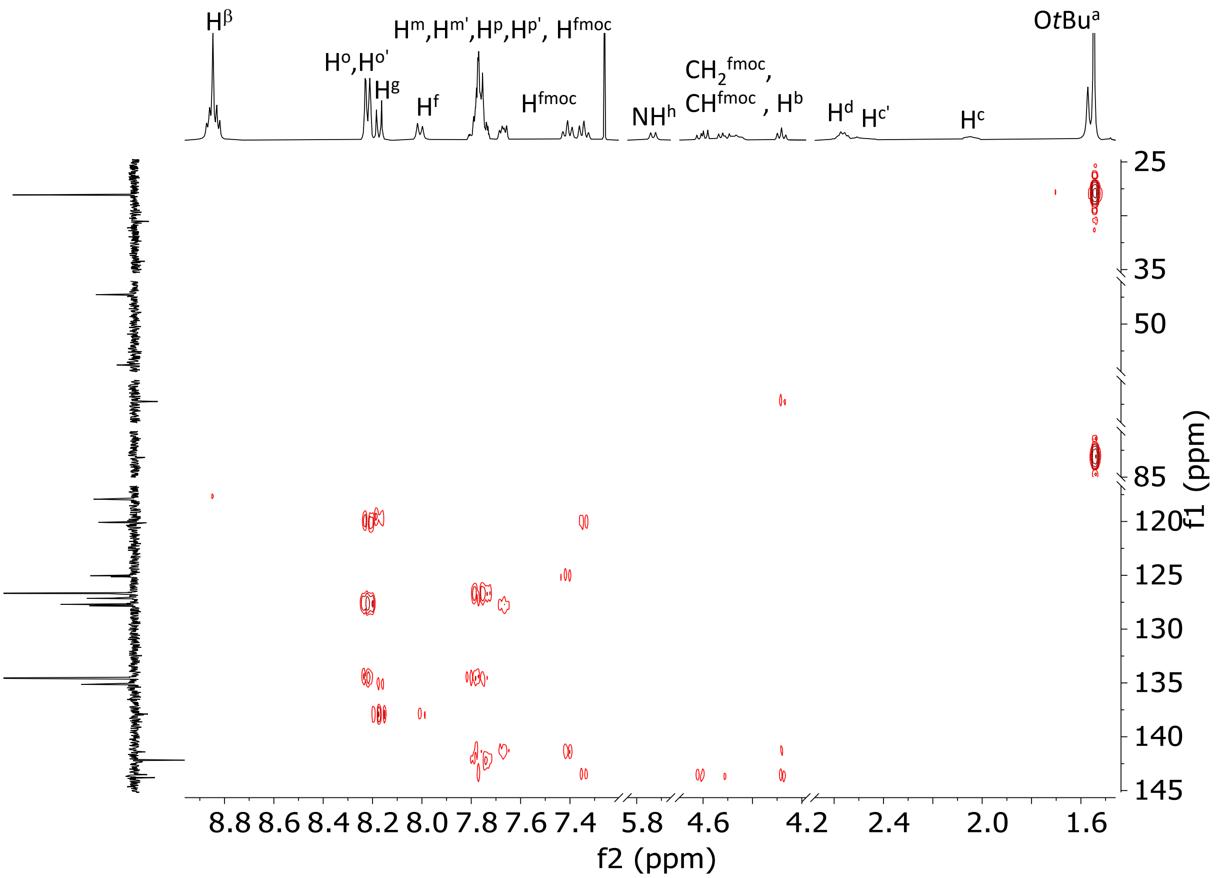

Figure S28. ^{1}H-^{13}C HMBC spectrum (CDCl$_3$, 298 K) of **6**.

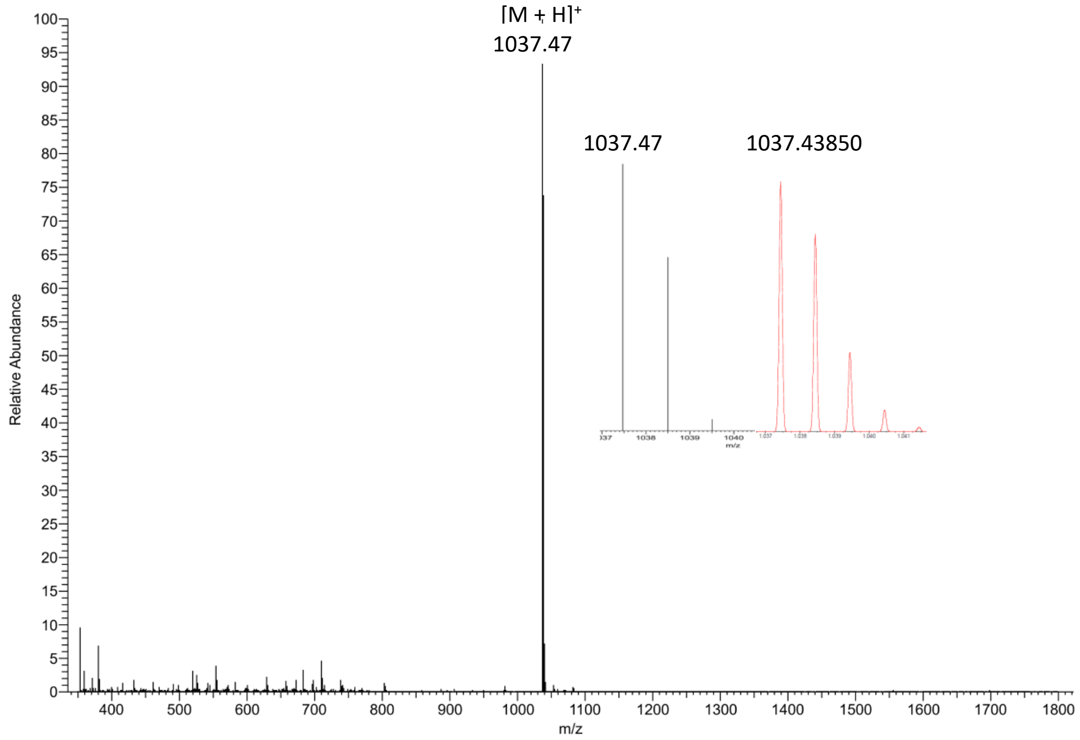

Figure S29. ESI-MS of **6** in CH$_3$OH, experimental (black) and simulated (red).

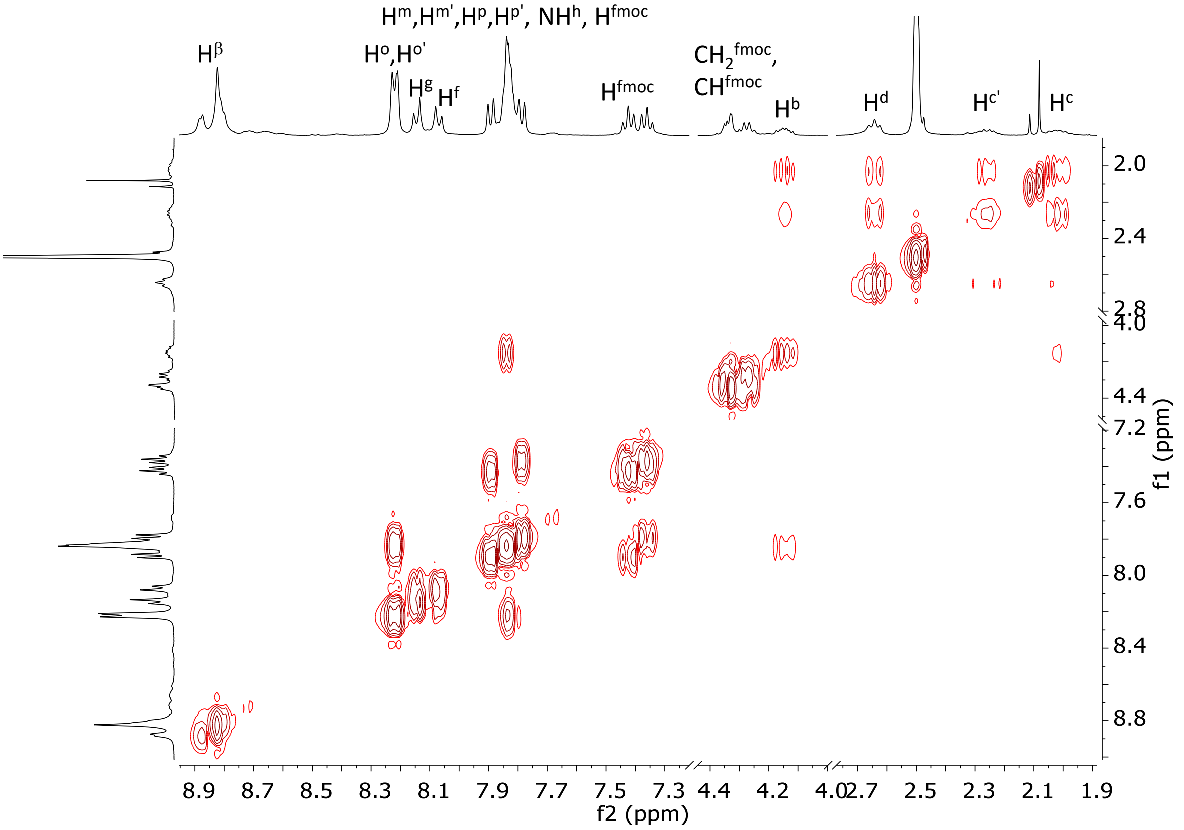

Figure S30. ^{1}H-^{1}H COSY spectrum (dmso-d_6, 298 K) of **TPP-FmocGluOH** (**7**). For proton labelling see Experimental Section.

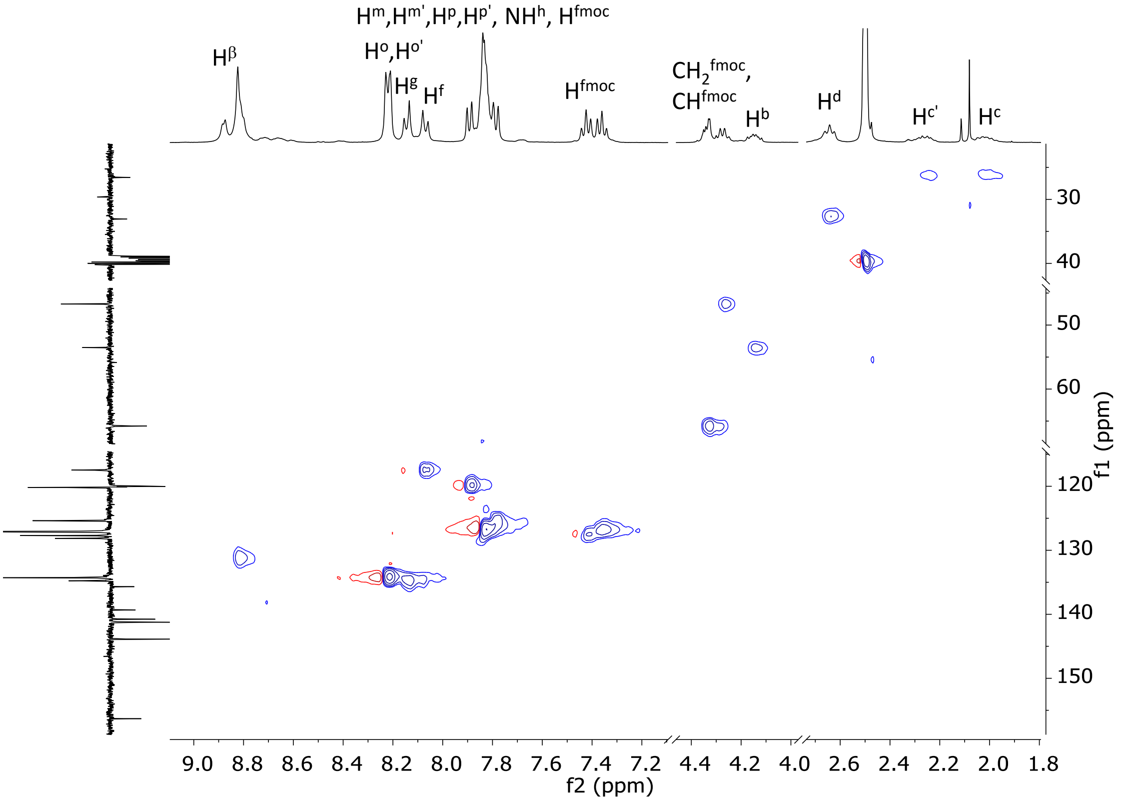

Figure S31. ^{1}H-^{13}C HSQC spectrum (dmso-d_6, 298 K) of **7**.

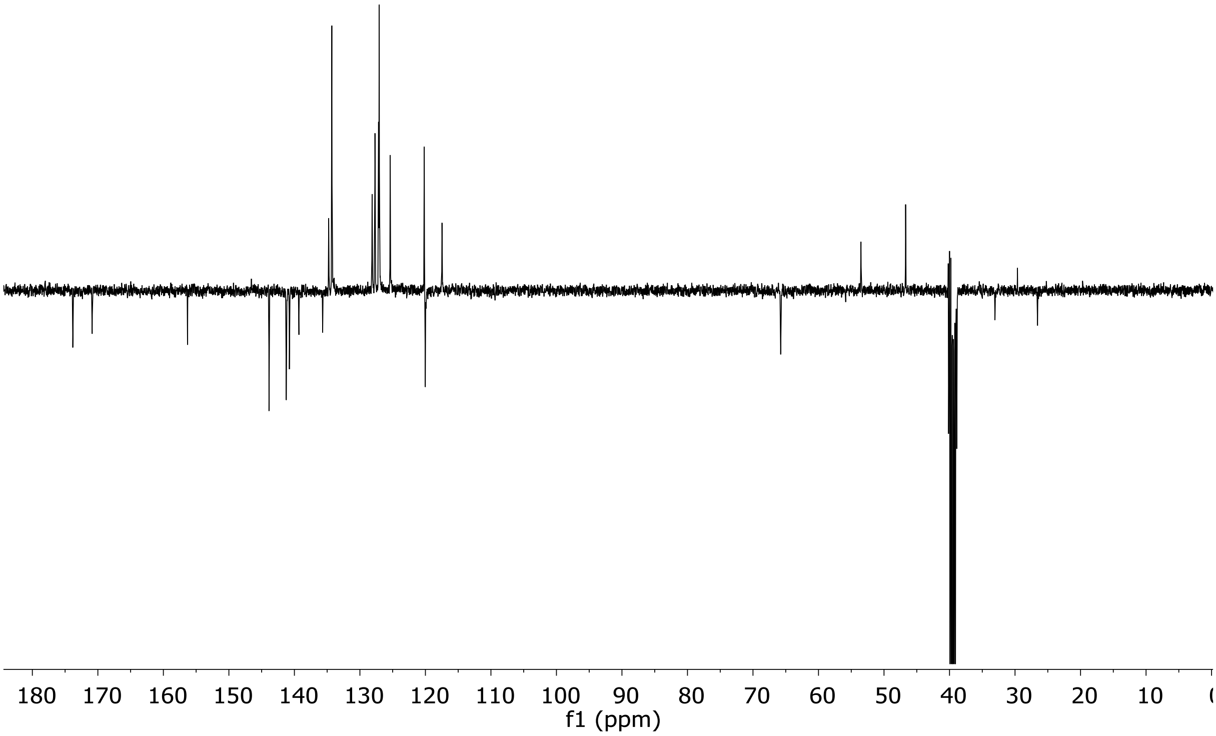

Figure S32. ^{13}C-APT NMR spectrum (dmso-*d*$_6$, 298 K) of **7**.

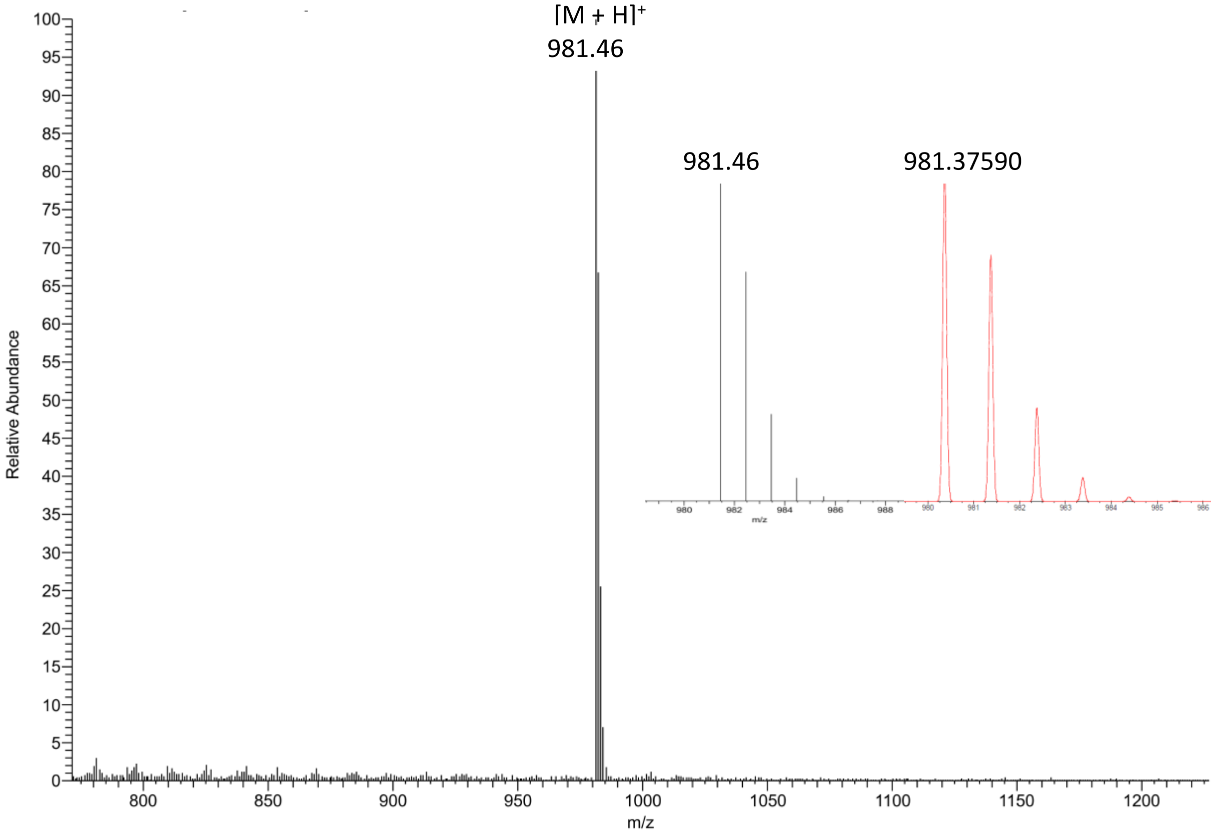

Figure S33. ESI-MS of **7** in CH_3OH, experimental (black) and simulated (red).

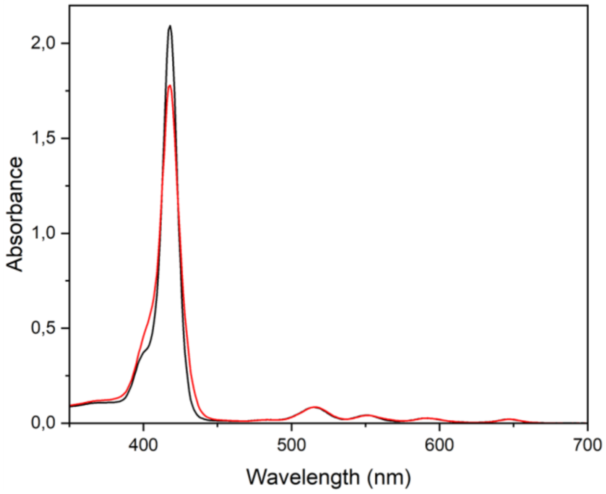

Figure S34. UV-Vis absorption spectra (CH_2Cl_2, 5 μM) of **6** and **7** (black and red traces, respectively).

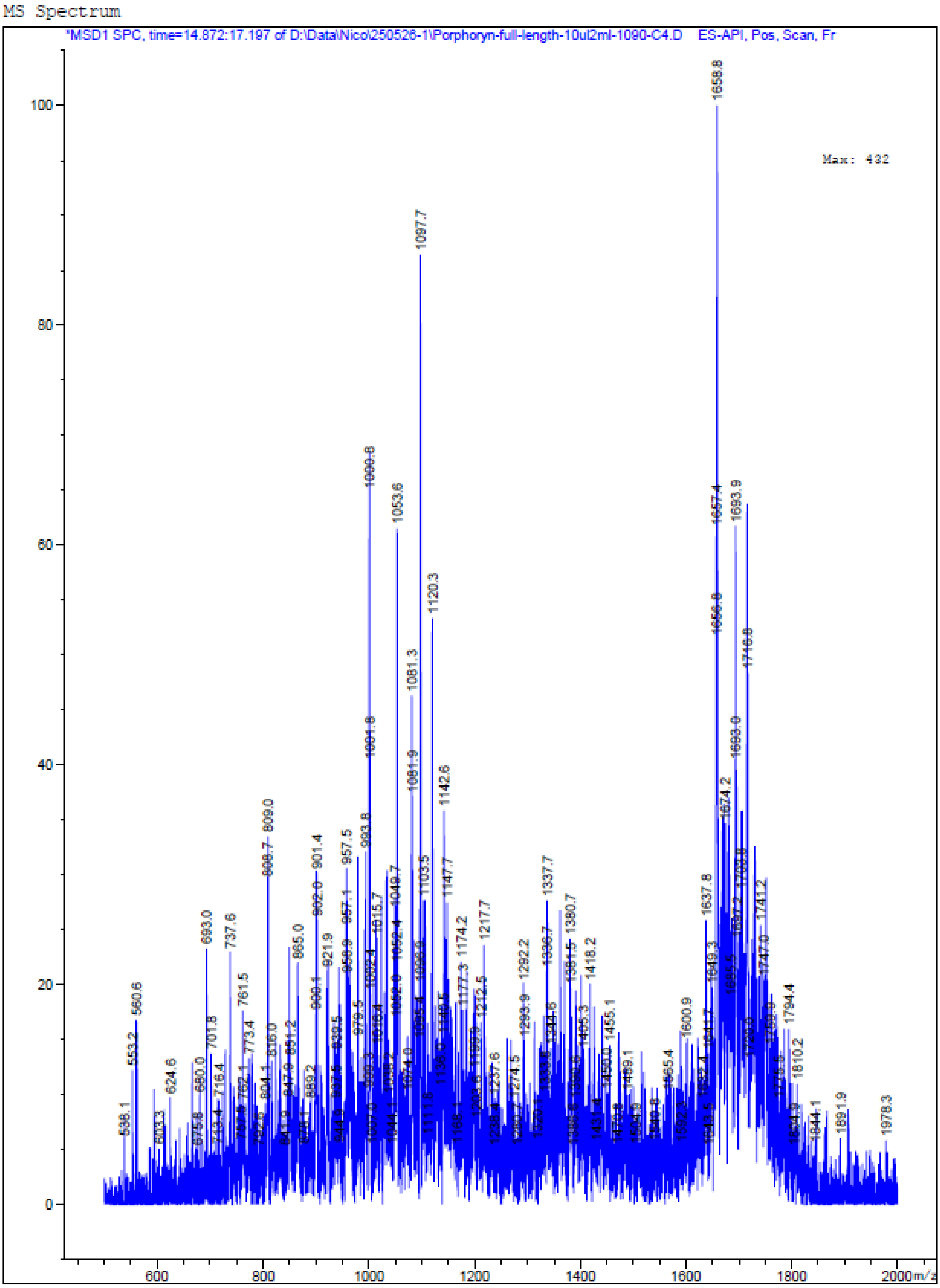

Figure S35. LC-MS of **P2** H_2O:CH_3CN:tBuOH 1:1:1. $[M - 2Cl]^{2+}$ calculated 1658.3, found 1658.8; $[M + 2H]^{2+}$ calculated 1694.3, found 1693.9.

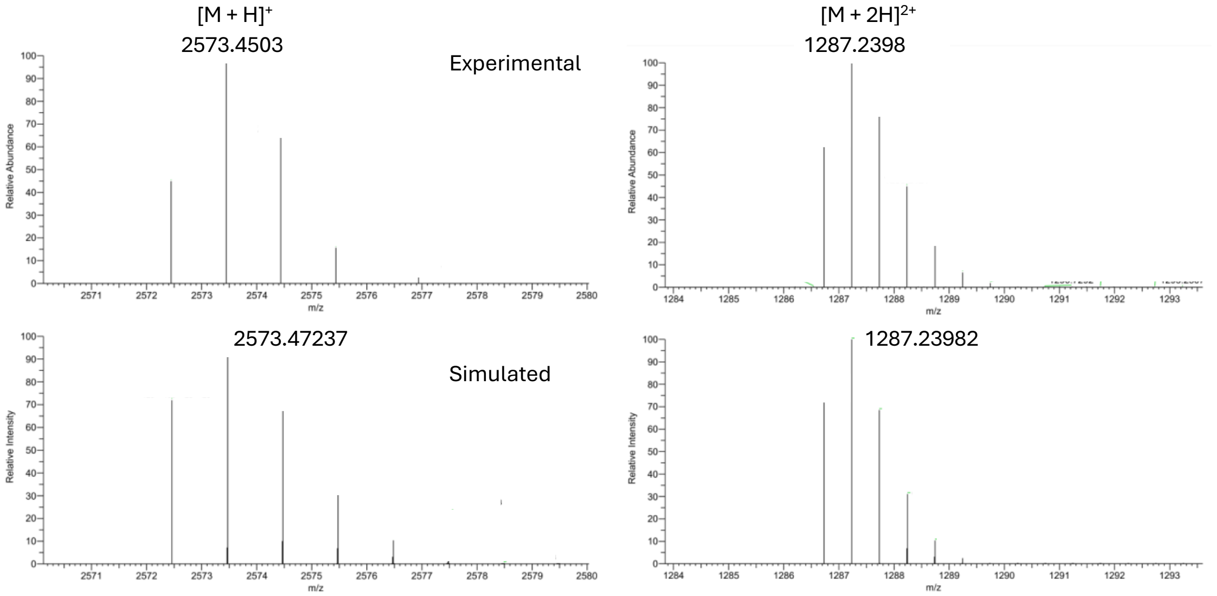

Figure S36. HRMS of **P3** in $CH_3CN:H_2O$ 1:1, experimental (top) and simulated (bottom).

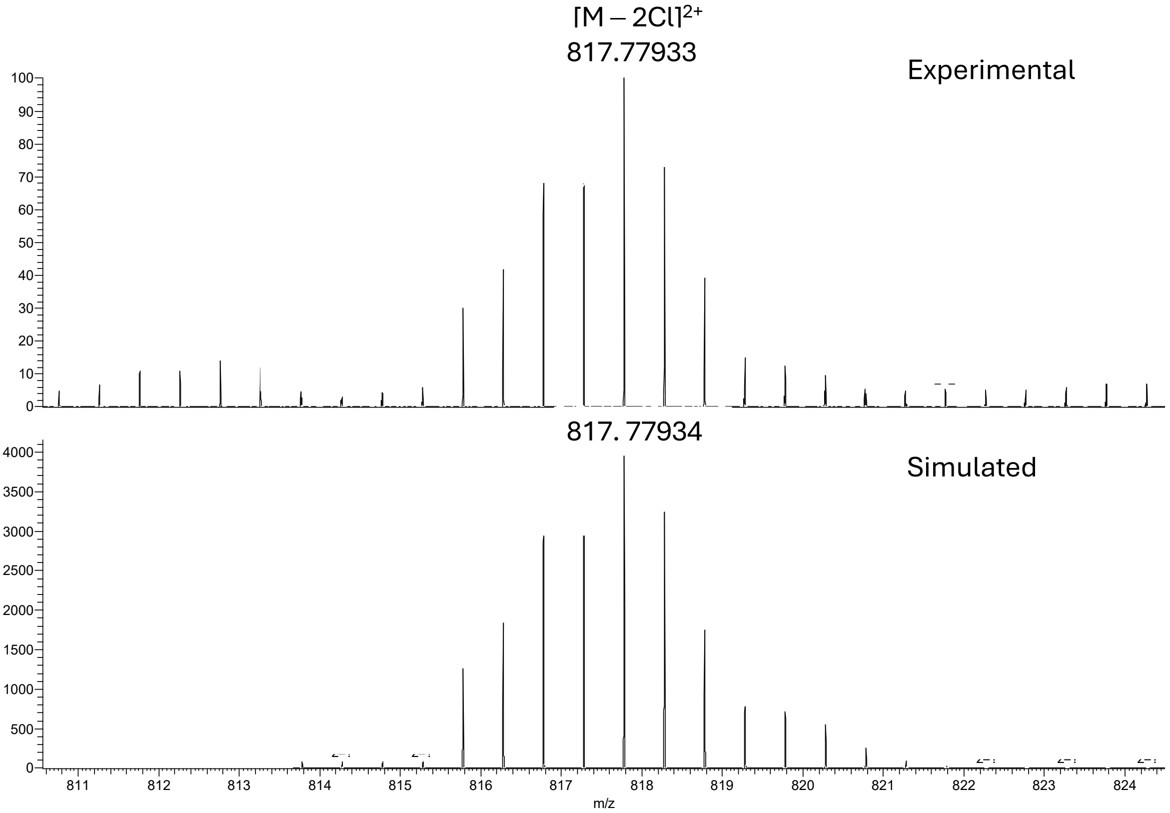

Figure S37. HRMS of **P5** in $CH_3CN:H_2O$ 1:1, experimental (top) and simulated (bottom).

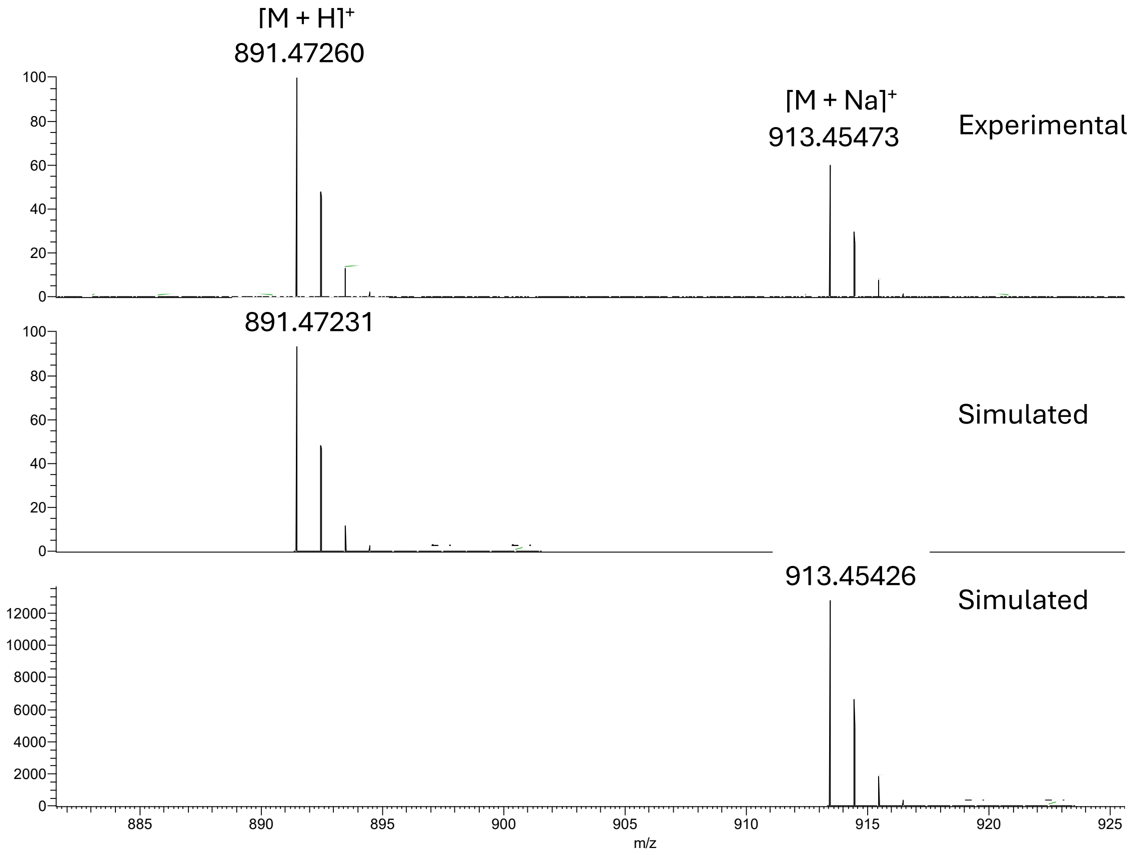

Figure S38. HRMS of **P6** in CH_3CN:H_2O 1:1, experimental (top) and simulated (bottom).

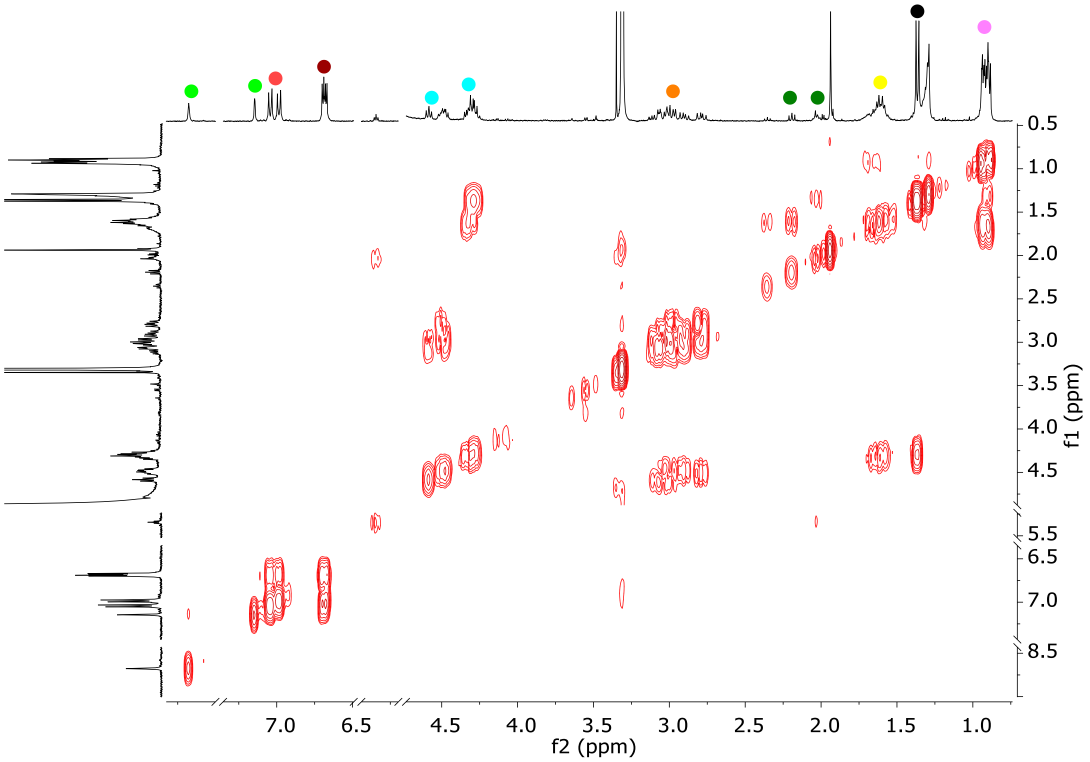

Figure S39. ^{1}H-^{1}H COSY spectrum (CD_3OD, 298 K) of **P6**. For colour labelling scheme see main text.

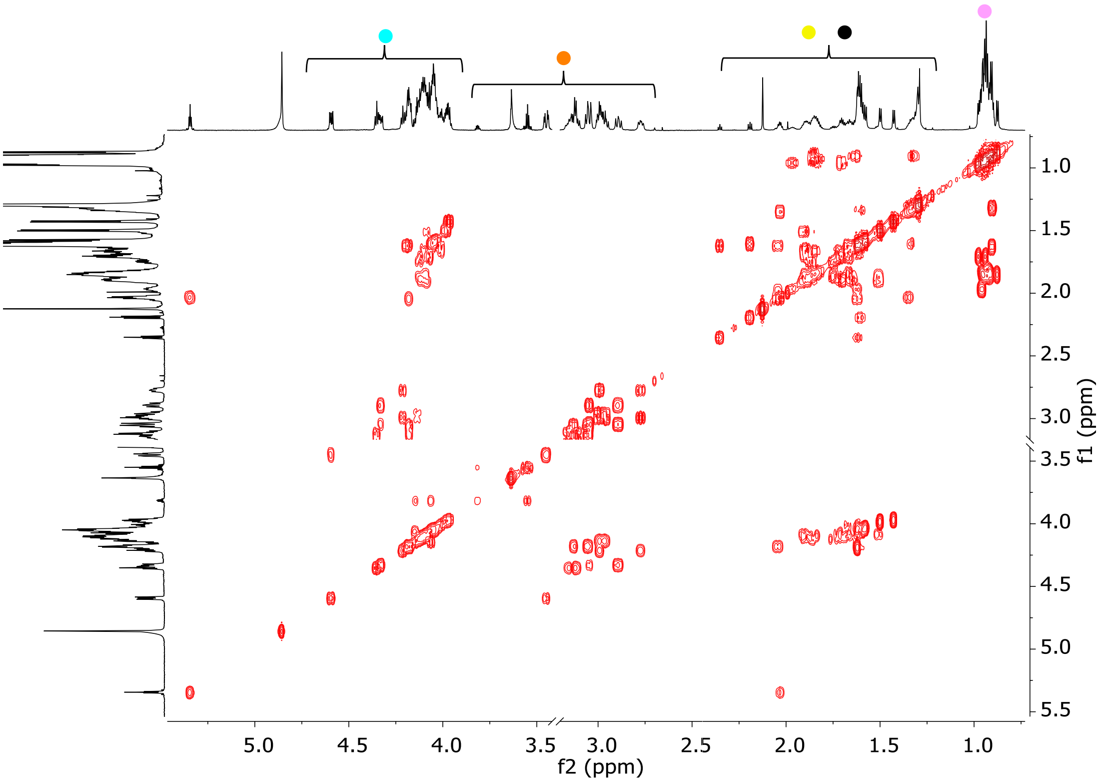

Figure S40. Aliphatic region of the ^{1}H-^{1}H COSY spectrum (CD$_3$OD, 298 K) of **P3**. CH$^\alpha$ and diasterotopic region partially magnified. For colour labelling scheme see main text.

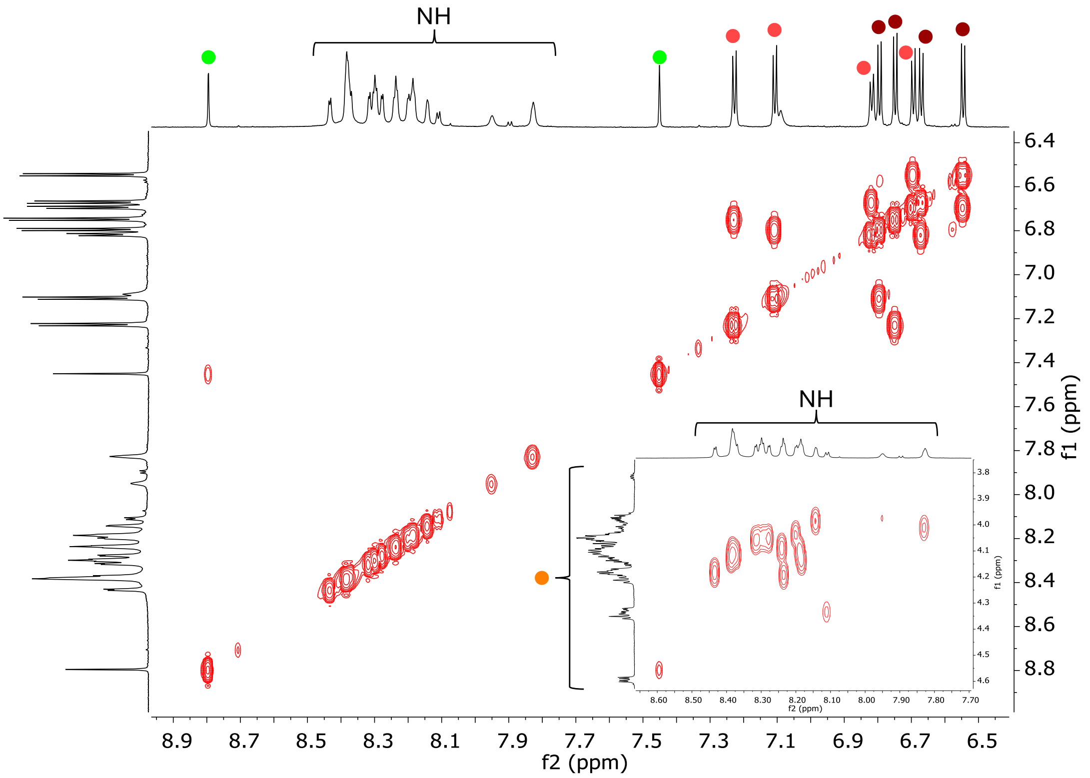

Figure S41. Aromatic region of the ^{1}H-^{1}H COSY spectrum (CD$_3$OD, 298 K) of **P3**. Inset: coupling between CH$^\alpha$ and NH protons.

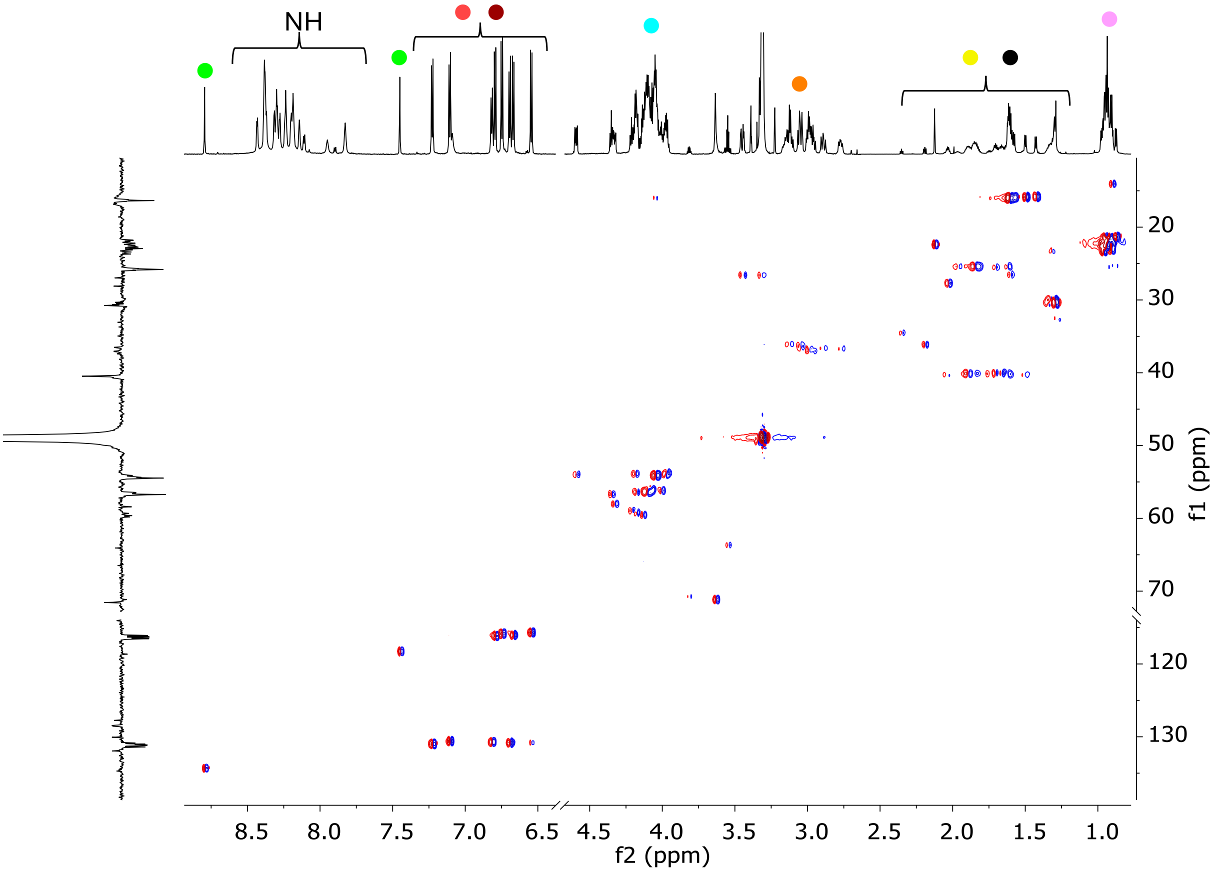

Figure S42. ^1H-^{13}C HSQC spectrum (CD_3OD, 298 K) of **P3**. Region from 2.5 to 9.0 ppm partially magnified.

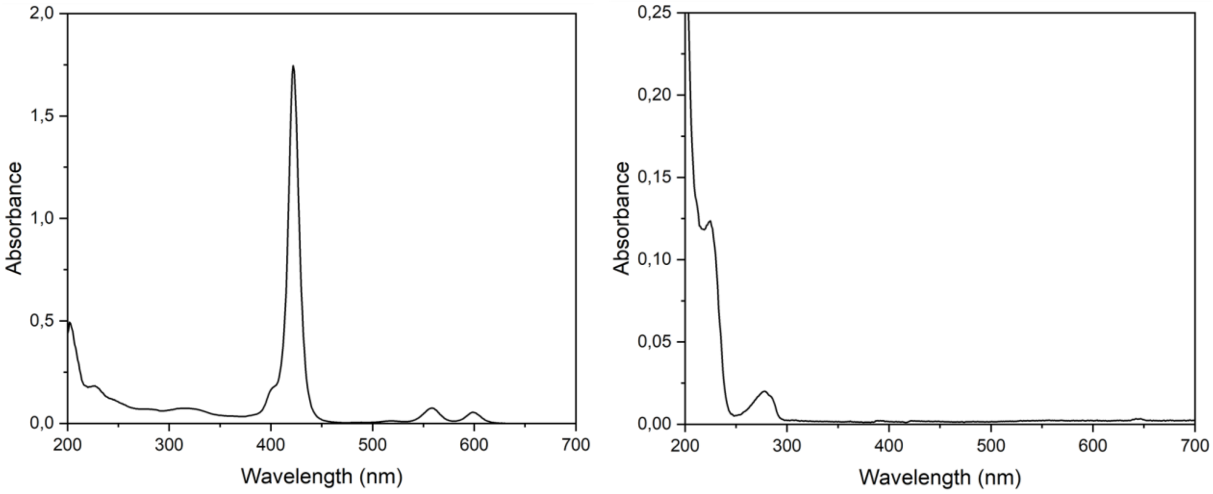

Figure S43. UV-Vis absorption spectra (CH_3OH, 5 µM) of **P5** (left) and **P6** (right).

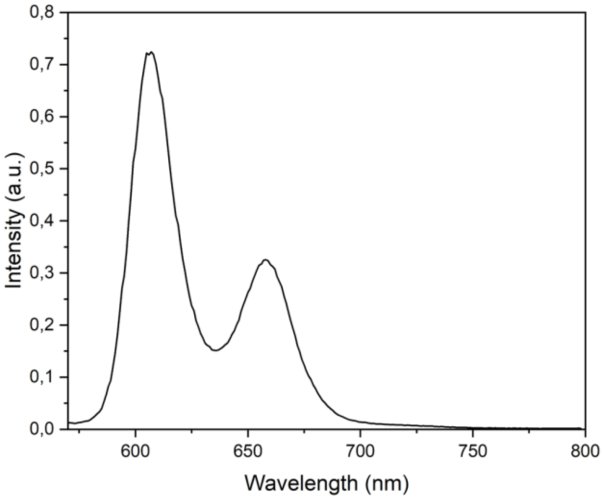

Figure S44. Emission spectrum (CH₃OH, 25 µM, λ_{irr} = 558 nm) of **P5**.

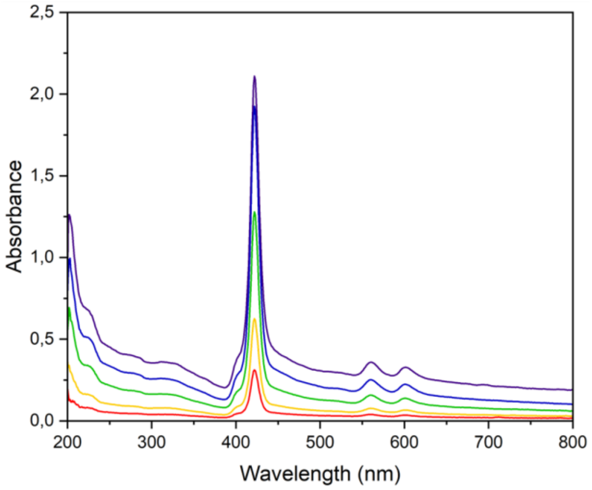

Figure S45. UV-Vis absorption spectra (CH₃OH) of **P2** at five different concentrations, from 2.5 µM (red trace) to 25 µM (purple trace).

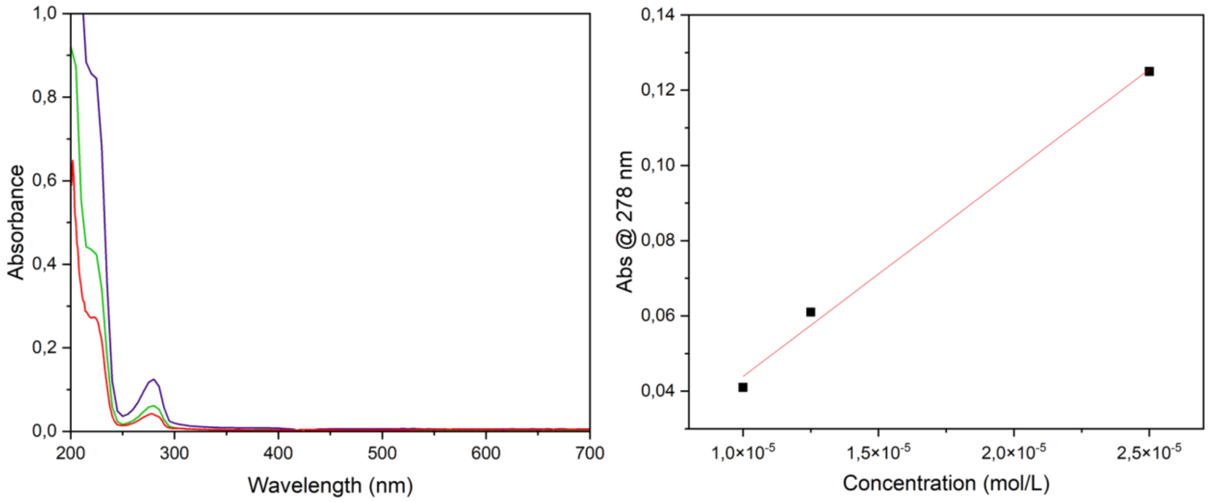

Figure S46. UV-Vis absorption spectra (CH_3OH) of **P3** at three different concentrations: from 10 μM (red trace) to 25 μM (purple trace) (left) and determination of the molar absorption coefficient: ε = 5.45 × 10^3 M^{-1} cm^{-1} (R^2 = 0.9946) at λ = 278 nm (right).

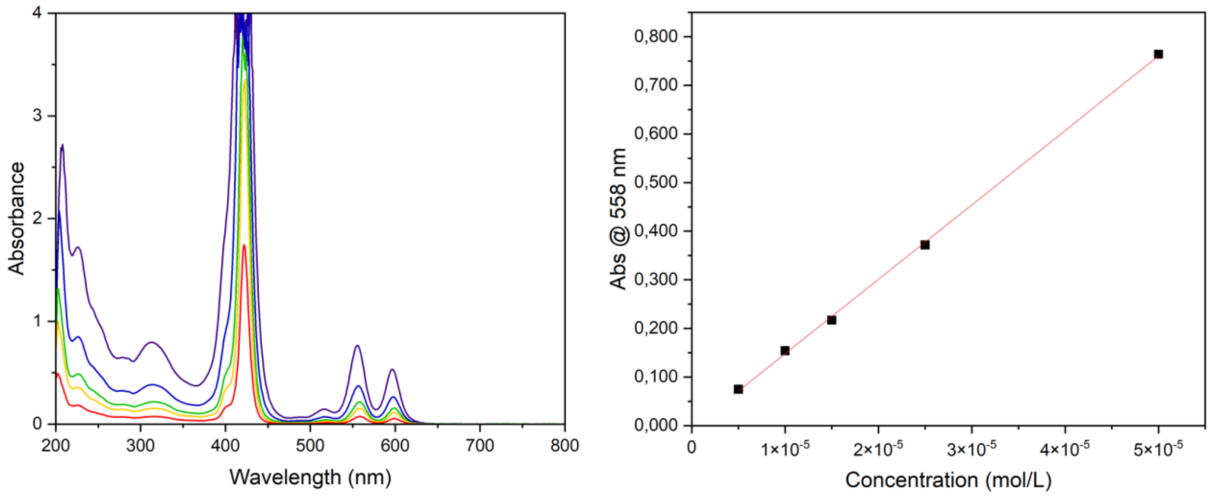

Figure S47. UV-Vis absorption spectra (CH_3OH) of **P5** at five different concentrations, from 5 μM (red trace) to 50 μM (purple trace) (left) and determination of the molar absorption coefficient: ε = 1.53 × 10^4 M^{-1} cm^{-1} (R^2 = 0.9995) at λ = 558 nm (right).

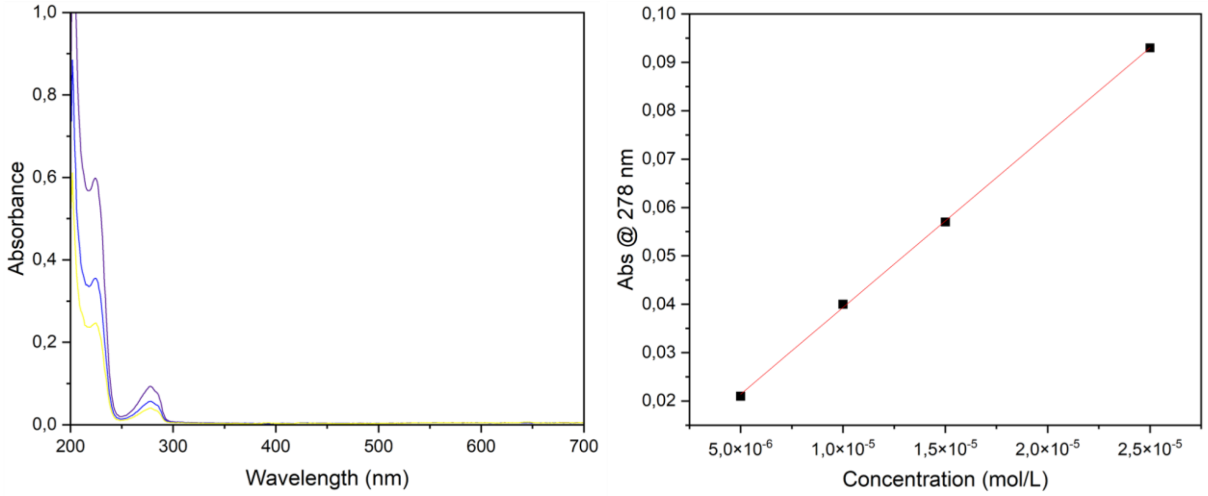

Figure S48. UV-Vis absorption spectra (CH_3OH) of **P6** at four different concentrations: from 10 μM (yellow trace) to 25 μM (purple trace) (left) and determination of the molar absorption coefficient: $\varepsilon = 3.6 \times 10^3\ M^{-1}\ cm^{-1}$ ($R^2 = 0.9998$) at $\lambda = 278$ nm (right).

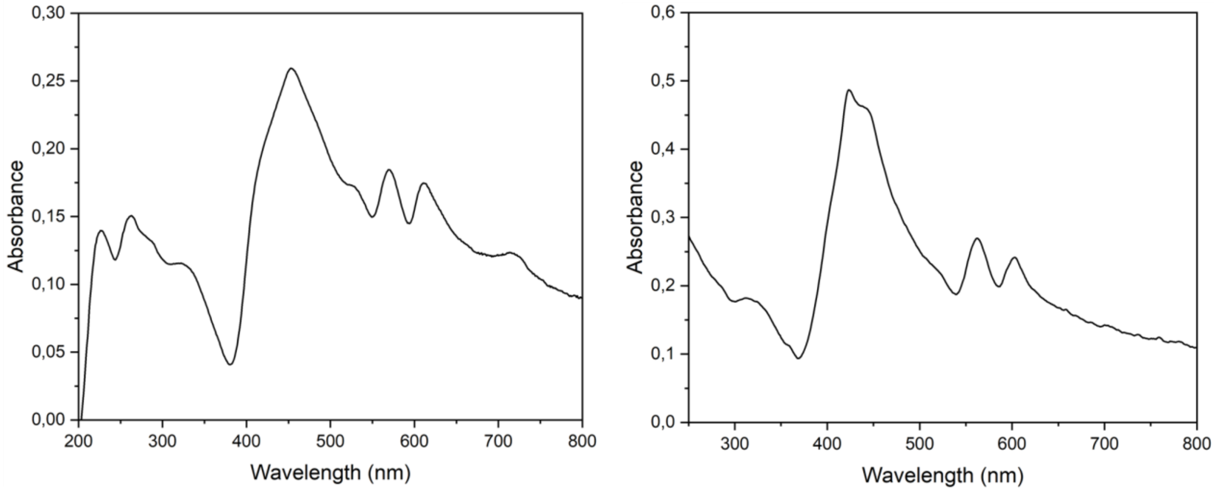

Figure S49. UV-Vis absorption spectra (25 μM) of **P5** in pure H_2O (left) and pure CH_2Cl_2 (right).

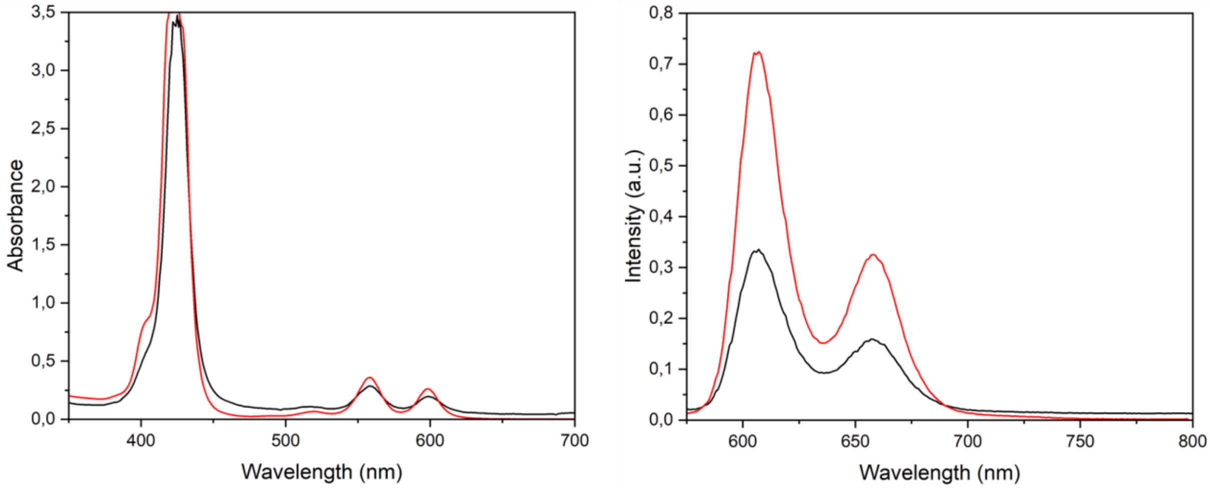

Figure S50. Left: UV-Vis absorption spectra of **P5**, and right: Emission spectra ($\lambda_{irr} = 560$ nm); red trace pure CH_3OH; black trace 30:1 CH_2Cl_2:CH_3OH mixture.

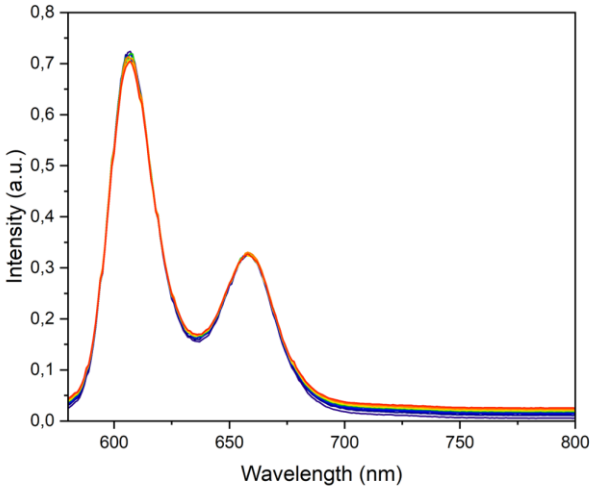

Figure S51. Emission spectra (λ_{irr} = 558 nm) of CH_3OH solutions containing 25 μM of **P5** and increasing amounts of TEA, from 0.00 M (purple trace) to 0.096 M (red trace) TEA.

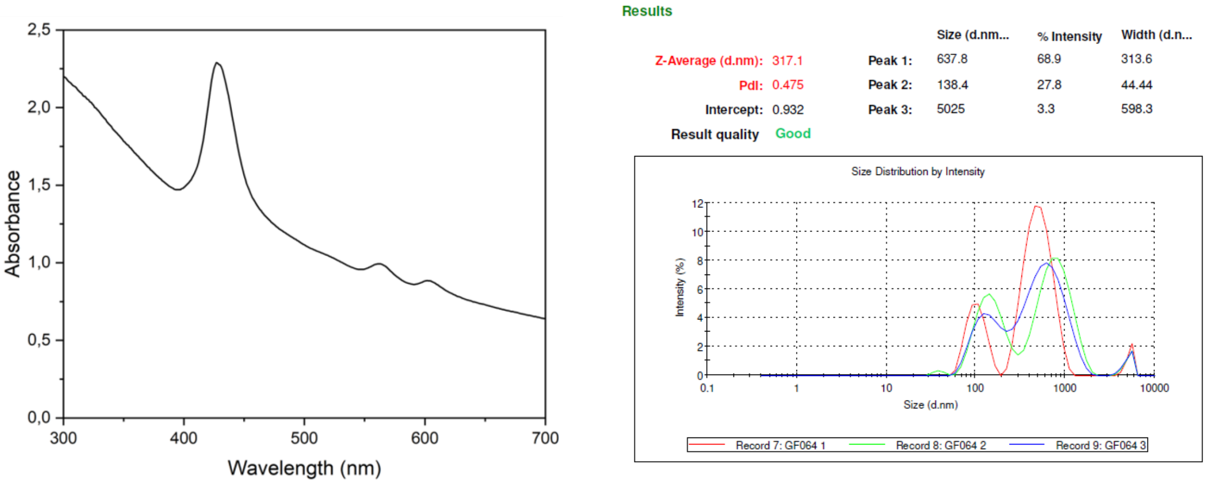

Results

Z-Average (d.nm): 317.1
PdI: 0.475
Intercept: 0.932
Result quality Good

	Size (d.nm...	% Intensity	Width (d.n...
Peak 1:	637.8	68.9	313.6
Peak 2:	138.4	27.8	44.44
Peak 3:	5025	3.3	598.3

Figure S52. UV-Vis absorption (left) and DLS (Z-average 317.1 nm, PDI = 0.475) (right) spectra of **SL1** (see Main Text for liposome composition).

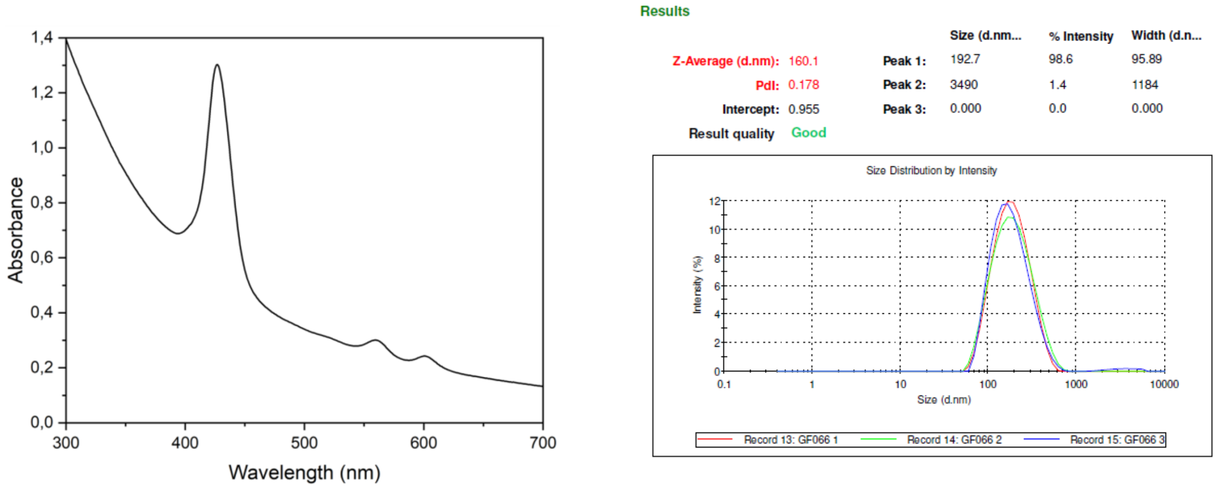

Results

			Size (d.nm...	% Intensity	Width (d.n...
Z-Average (d.nm):	160.1	Peak 1:	192.7	98.6	95.89
PdI:	0.178	Peak 2:	3490	1.4	1184
Intercept:	0.955	Peak 3:	0.000	0.0	0.000
Result quality	Good				

Figure S53. UV-Vis absorption (left) and DLS (Z-average 160.1 nm, PDI = 0.178) (right) spectra of **SL2** (see Main Text for liposome composition).

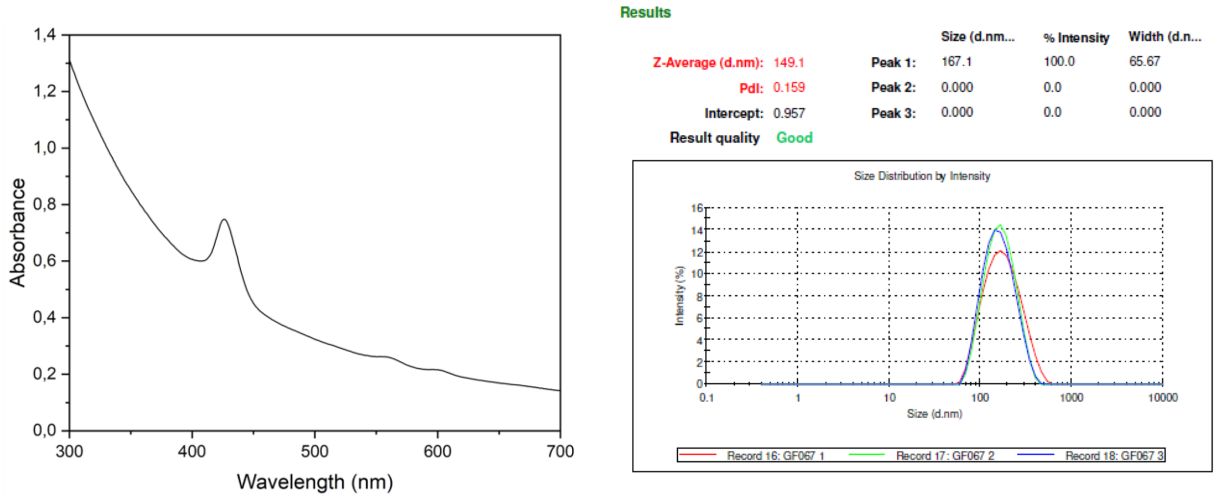

Results

			Size (d.nm...	% Intensity	Width (d.n...
Z-Average (d.nm):	149.1	Peak 1:	167.1	100.0	65.67
PdI:	0.159	Peak 2:	0.000	0.0	0.000
Intercept:	0.957	Peak 3:	0.000	0.0	0.000
Result quality	Good				

Figure S54. UV-Vis absorption (left) and DLS (Z-average 1149.1 nm, PDI = 0.159) (right) spectra of **SL3** (see Main Text for liposome composition).

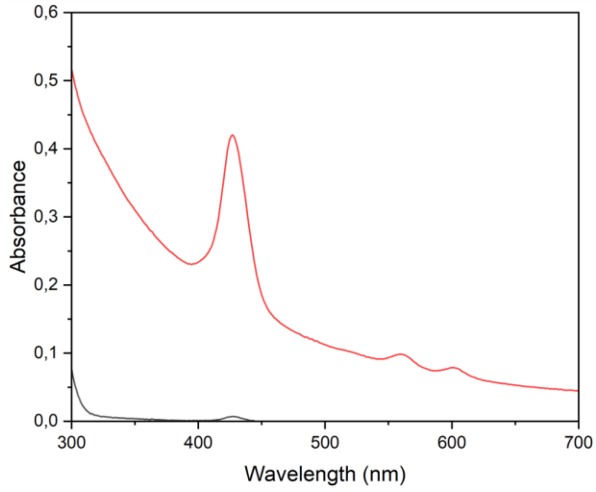

Figure S55. UV-Vis absorption spectra of **SL2** before (red) and after (black) ultracentrifugation.

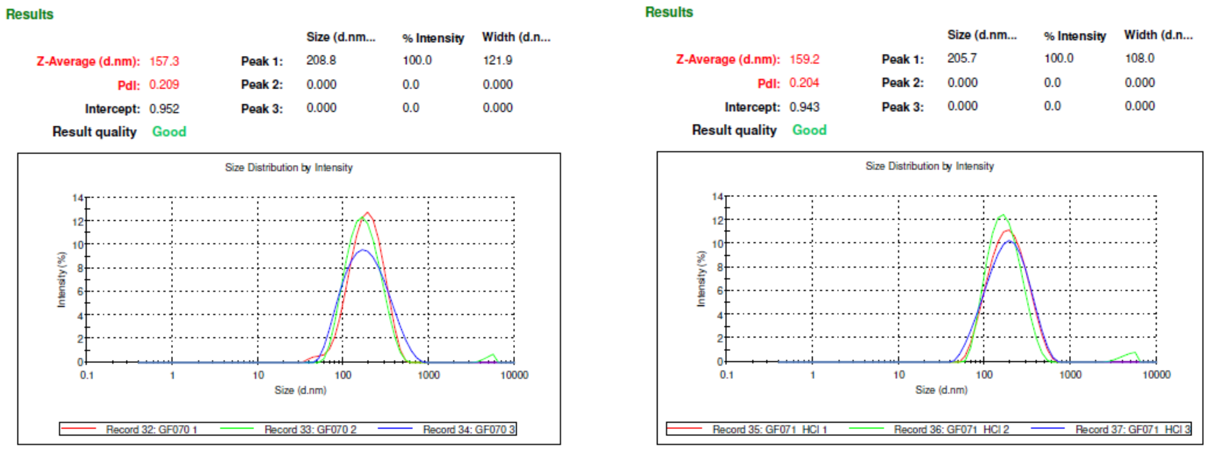

Results

			Size (d.nm...	% Intensity	Width (d.n...
Z-Average (d.nm):	157.3	Peak 1:	208.8	100.0	121.9
PdI:	0.209	Peak 2:	0.000	0.0	0.000
Intercept:	0.952	Peak 3:	0.000	0.0	0.000
Result quality	Good				

Results

			Size (d.nm...	% Intensity	Width (d.n...
Z-Average (d.nm):	159.2	Peak 1:	205.7	100.0	108.0
PdI:	0.204	Peak 2:	0.000	0.0	0.000
Intercept:	0.943	Peak 3:	0.000	0.0	0.000
Result quality	Good				

Figure S56. DLS measurement of **SL2** before (left) and after (right) addition of HCl. Before: Z-average 157.3 nm, PDI = 0.209; after: Z-average 159.2 nm, PDI = 0.204.

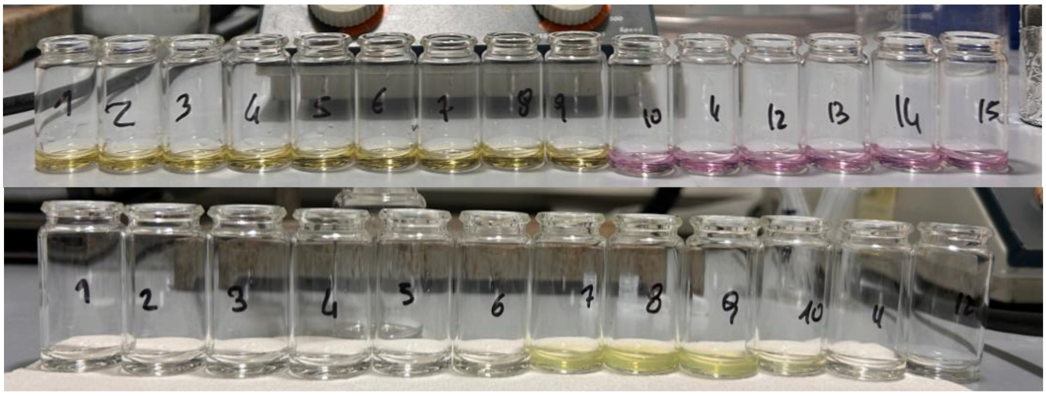

Figure S57. Visual representation of the fractions from the size exclusion column for the purification of HEDTA^{3-} encapsulation liposomes. Top: the fraction from HEDTA^{3-} calibration run: HEDTA^{3-} elutes from fraction 10 and further. Bottom: the fractions from the **AL1** purification run (fractions 6 – 9 were collected for next measurements).

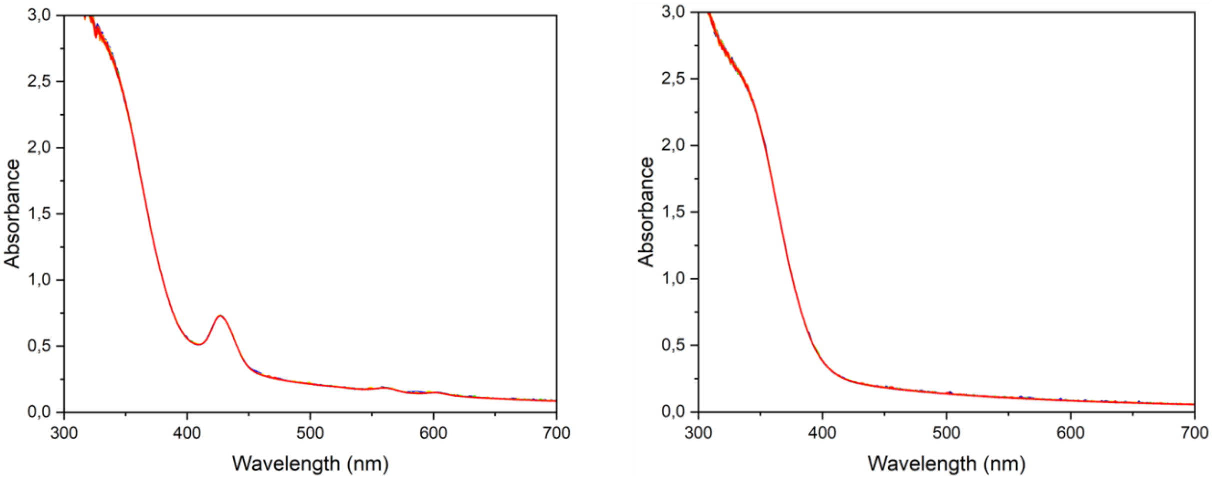

Figure S58. Evolution of the UV-Vis spectrum of **AL1** (left) and **AL3** (right) (see Main Text for the liposome composition) monitored for 30 minutes in the dark.

Results

			Size (d.nm...	% Intensity	Width (d.n...
Z-Average (d.nm):	171.3	Peak 1:	198.1	96.3	95.16
PdI:	0.231	Peak 2:	4407	3.7	918.6
Intercept:	0.931	Peak 3:	0.000	0.0	0.000
Result quality	Good				

Results

			Size (d.nm...	% Intensity	Width (d.n...
Z-Average (d.nm):	166.8	Peak 1:	217.6	100.0	127.1
PdI:	0.232	Peak 2:	0.000	0.0	0.000
Intercept:	0.967	Peak 3:	0.000	0.0	0.000
Result quality	Good				

Figure S59. DLS measurement of **AL1** before (left) and after (right) 3h irradiation. Before: Z-average 171.3 nm, PDI = 0.231; after: Z-average 166.8 nm, PDI = 0.232.

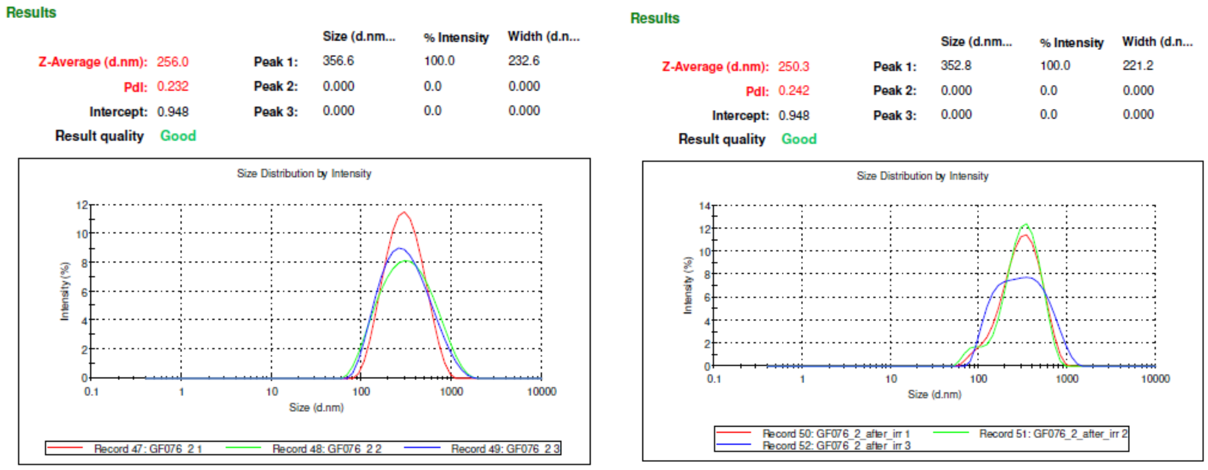

Results

			Size (d.nm...	% Intensity	Width (d.n...
Z-Average (d.nm):	256.0	Peak 1:	356.6	100.0	232.6
PdI:	0.232	Peak 2:	0.000	0.0	0.000
Intercept:	0.948	Peak 3:	0.000	0.0	0.000
Result quality	Good				

Results

			Size (d.nm...	% Intensity	Width (d.n...
Z-Average (d.nm):	250.3	Peak 1:	352.8	100.0	221.2
PdI:	0.242	Peak 2:	0.000	0.0	0.000
Intercept:	0.948	Peak 3:	0.000	0.0	0.000
Result quality	Good				

Figure S60. DLS measurement of **AL3** before (left) and after (right) 3h irradiation. Before: Z-average 256.0 nm, PDI = 0.232; after: Z-average 250.3 nm, PDI = 0.242.

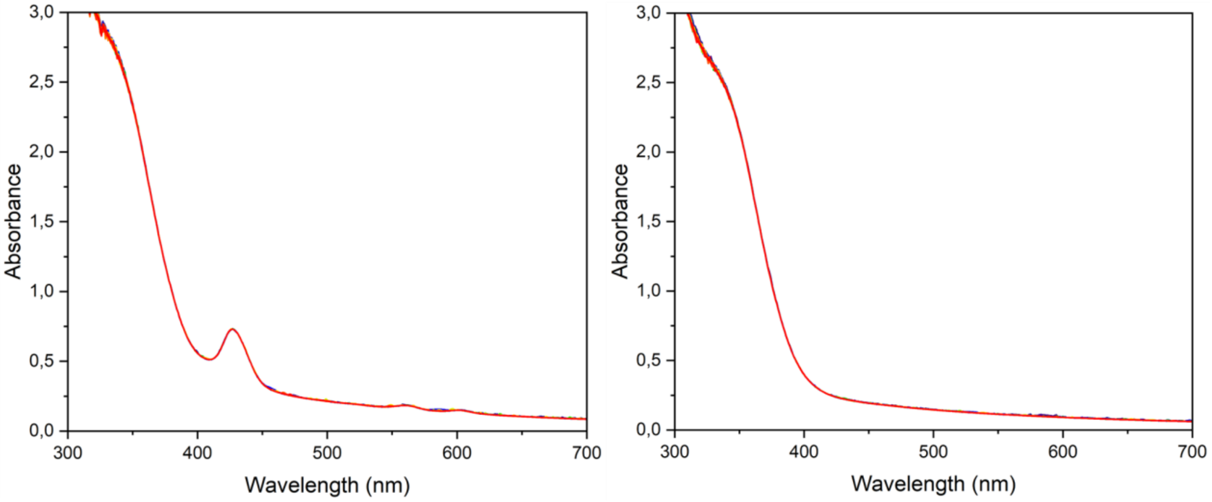

Figure S61. Evolution of the UV-Vis spectrum of **AL2** (left) and **AL4** (right) (see Main Text for the liposome composition) monitored for 30 minutes in the dark.

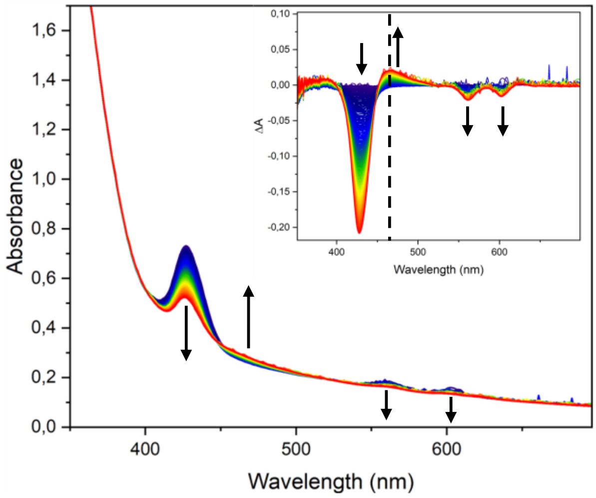

Figure S62. Evolution of the UV-Vis spectrum of **AL3** (see Main Text for liposome composition) under oxygenated conditions and blue light irradiation (λ_{irr} = 435 nm, P = 10.2 mW). Inset: Difference in absorbance monitored during 6h of irradiation. Dotted line showed λ = 465 nm, used for the construction of time-evolution graphs.

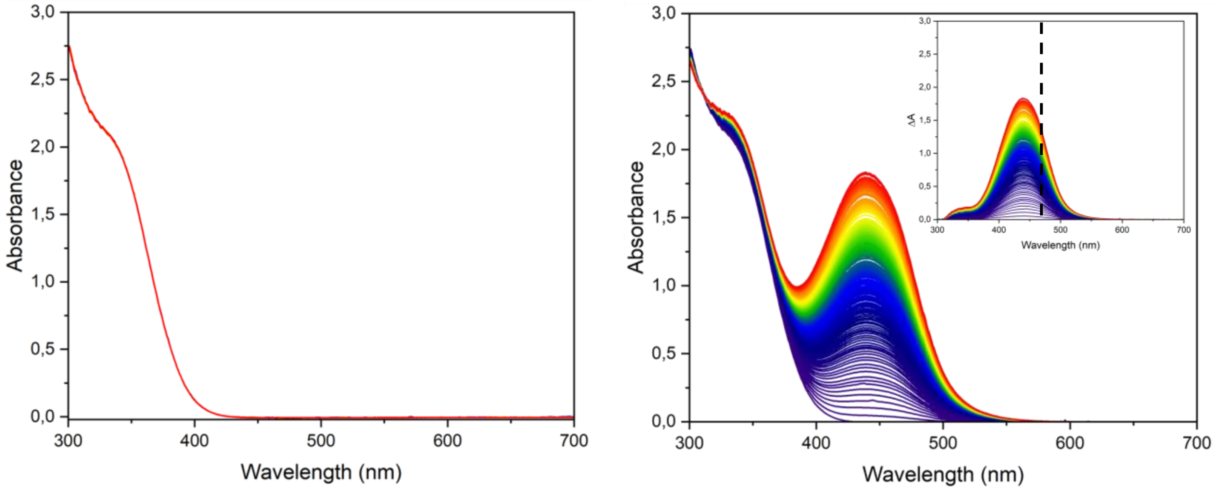

Figure S63. Evolution of the UV-Vis spectrum of **HS** under oxygenated conditions monitored for 30 minutes in the dark (left) and under blue light irradiation (λ_{irr} = 435 nm, P = 10.2 mW), right. Inset: Difference in absorbance monitored during 3h of irradiation. Dotted line showed λ = 465 nm, used for the construction of time-evolution graphs.

CHAPTER 4

Overview

This Chapter presents the design, synthesis, and surface characterization of a series of functionalized porphyrins aimed at forming tunable two-dimensional metal organic networks (2D-MONs) for single-atom catalysis. Three benzamide-substituted free-base porphyrins and their corresponding cobalt derivatives were synthesized to mimic selected features of enzymatic second coordination spheres. Their structural and photophysical properties were comprehensively determined in solution by 1D and 2D NMR spectroscopy, high-resolution mass spectrometry, and UV-Vis spectroscopy. To investigate the ability of these conjugates to form ordered supramolecular architectures on surfaces, the free-base porphyrin versions were deposited under ultrahigh-vacuum conditions on graphene/Ir(111) and Au(111) substrates using electrospray ionization beam deposition. The resulting layers were analyzed by a combination of IR-visible sum-frequency generation spectroscopy (IR-Vis SFG) and scanning tunneling microscopy (STM). These techniques provided detailed insight into molecular adsorption geometries, thermal stability, intermolecular interactions, and vibrational fingerprints associated with the benzamide functional groups, paving the way for the deposition of the metallo-porphyrin analogues and next studies on the metal single-atom reactivity towards small substrates.

The work presented in this Chapter was done in collaboration with the group of Prof. Erik Vesselli, University of Trieste (IT). The STM measurements were done in collaboration with Dr. Kelvin Anggara, Max Planck Institute for Solid State Research in Stuttgart (DE).

List of abbreviations.

SACs = Single-Atom Catalysis

MONs = Metal-Organic Networks

OER = Oxygen Evolution Reaction

ORR = Oxygen Reduction Reaction

UHV = Ultra-High Vacuum

NAP = Near Ambient Pressure

TPP = 5,10,15,20-(phenyl)porphyrin

Gr = graphene

TPyP = 5,15,10,20-tetra- (4-pyridyl)-porphyrin

TPP-*o*NH$_2$ = (5-(2'-aminophenyl)-10,15,20-triphenylporphyrin)

EDC = N-(3-Dimethylaminopropyl)-N'ethylcarbodiimide hydrochloride

TPP-*p*NH$_2$ = (5-(4'-aminophenyl)-10,15,20-triphenylporphyrin)

4.1. Introduction.

Supported metal nanoclusters are key catalysts in industrial sectors ranging from petroleum refining to chemical manufacturing and energy conversion. Their catalytic behavior, however, is strongly dependent on cluster size.[1] Extensive research shows that shrinking metal clusters can boost activity through size-dependent effects, but this also increases surface free energy, making the clusters more prone to sintering and ultimately leading to catalyst deactivation. In addition, conventional supported nanocluster systems typically feature wide distributions in particle size and morphology, resulting in heterogeneous active sites that complicate the control and optimization of catalytic performance. A promising way to overcome these limitations is the use of caged Single-Atom Catalysts (SACs), which maximize the use of isolated, uniform, and highly active metal centers. Yet, single atoms are intrinsically unstable due to their elevated surface free energy and tend to aggregate. One effective stabilization strategy is to anchor individual atoms within an organic framework, thereby preventing their mobility and sintering. This concept underpins Metal-Organic Networks (2D-MONs): ordered, two-dimensional layers composed of metal centers coordinated to organic ligands and supported on a substrate (Figure 4.1.1).[2,3] 2D-MONs belong to the broader class of atomically thin materials, consisting of one or several stacked molecular layers. They are typically formed *via* the co-deposition of metal atoms or ions and organic linkers onto a surface, followed by self-assembly driven by coordination chemistry.[3]

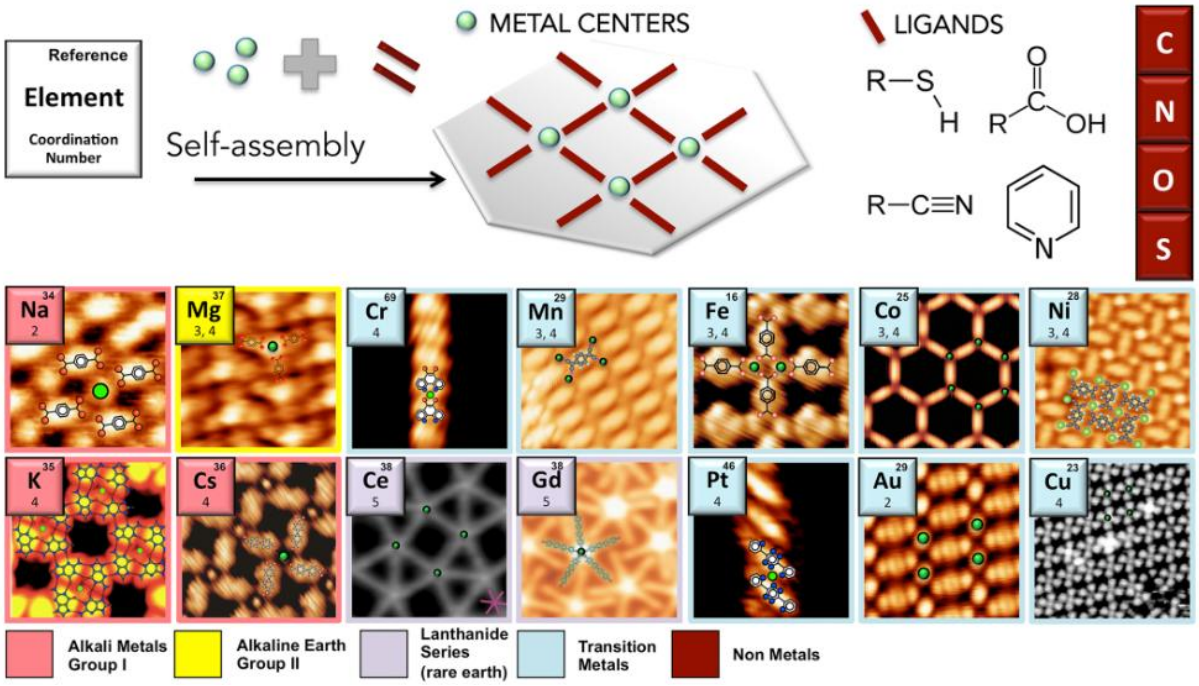

Figure 4.1.1. STM images of metal-organic networks incorporating different metal centers. Typical functional groups of the most common ligands are listed at the bottom. Figure taken from ref. 4.

These networks offer extraordinary chemical and structural tunability, high thermal stability, large surface area, and high porosity to fine-tune their electrical and chemical properties through the suitable choice of metals, substrates and organic linkers. Typically, the metal is selected based on the intended catalytic reaction to promote. The supporting substrate also plays a fundamental role as it acts as a proximal ligand, thus altering the absorption environment of the metal centers through the surface *trans* effect,[5] modulating charge transfer between the surface and the active site and thereby tuning the catalyst's electronic structure and reactivity. Finally, the organic ligand must promote the self-assembly process on the surface. Typical ligands used to self-assemble 2D-MONs are porphyrins and phthalocyanines.[6,7] In general, tetrapyrrole macrocycles have an impressive variety of functional properties that have been exploited in natural and artificial systems (see also previous Chapters). Their ability to chelate different metal cations within the inner tetradentate core and the possibility of tailoring the substituents on the macrocycle make them interesting candidates for the obtainment of 2D-MONs. Several examples of porphyrin systems used to self-organize single metal atoms on a surface have been reported.[8–10] Thus, thanks to this versatility, 2D-MONs have emerged as promising materials for applications spanning heterogeneous catalysis, sensing, biomedicine, energy storage, and gas adsorption and separation. Importantly, they have already shown exceptional performance in electrocatalytic processes such as oxygen evolution and oxygen reduction reactions (OER and ORR). Gaining a deeper understanding of these reactions at the atomic scale is crucial for advancing next-generation energy technologies, including bifunctional electrodes for rechargeable metal-air batteries and catalysts for water-splitting systems. Molecular self-assembly at surfaces is governed by a fine balancing between intermolecular and molecule-surface interactions. The adsorbed molecules experience, indeed, the potential energy surface of the templating substrate and surface mobility is a key parameter for the assembly process. The strength and nature of the competing molecule-molecule lateral interactions are similarly important. Finally, thermal energy governs the level of ordering within both energetic and kinetic constraints. Both covalent and non-covalent bonding can be exploited to bind molecular tectons in 2D ordered superstructures.[11] Under UHV conditions, covalent synthesis or coupling can be achieved by means of the thermal activation of building blocks and their subsequent chemical reaction at predefined connection points. This can be obtained with mainly two approaches. In the first one, molecular building blocks are pre-deposited on a surface, where they get successively activated by dissociation of the substituent atoms upon annealing. In the second case, instead, activation occurs in the thermal evaporator and the already activated molecules are deposited on the substrate. The non-covalent synthesis under UHV conditions exploits instead planar π-tectons with peripheral functional groups that adsorb, on appropriate substrates, in flat-lying geometry, thus favoring lateral group recognition. The cooperative geometrical complementarity (zwitterionic coupling), promoting the formation of multiple weak linkages (H-bonding, Van der Waals interactions), is an important factor in 2D supramolecular engineering. Moreover, hydrogen-bonded networks assembled at low temperatures on a surface can be transformed into metal-organic arrangements by exploiting the catalytic activity of the substrates upon annealing. Hydrogen bonding provides selectivity and directionality, while coordination to transition metals to tailored ligands at surfaces provides an alternative, versatile approach for the synthesis of highly organized molecular arrangements. The relatively high metal-ligand bond energies yield robust structures and the same stabilizing metal atoms bestow specific electronic, magnetic, or catalytic functions. Among all the reported systems, in this Chapter focus will be given on the use of (metallo)porphyrins as molecular systems to organize single atoms on a surface. Porphyrins (and more in general organic layers) deposition can be achieved mainly by using two different techniques. In the first one, powder of the desired organic molecule is thermally sublimed from a crucible. This method requires high working temperatures (above 300 °C for metalated molecules), thus making this deposition method unsuitable for thermally labile molecules. The second one, named Electrospray Ionization Beam Deposition (ESIBD), is a deposition technique used to deposit molecules on surfaces under UHV conditions, starting from a liquid solution.[12–16] In the 90s, John Fenn demonstrated through mass spectroscopy that electrospray could be used to obtain gas-phase molecular ions without fragmenting them,[17] paving the way to ESIBD as a deposition method in the field of self-assembled nanostructures at surfaces, enabling the deposition of complex building blocks *via* electrospray. The vast choice of available building blocks, the possibility of coupling ESIBD with mass spectrometry, together with the tools offered by surface science to probe the local and non-local properties of surfaces, enables the synthesis of new functional 2D materials with tailored properties.[18] In this scenario, ESIBD expands the range of available building blocks by enabling the deposition of large, thermally labile and non-volatile systems, such as inorganic clusters and organic molecules. ESIBD is based on Electrospray Ionization, a soft-ionization technique used to convert solution-phase macromolecules into gas-phase ions. It has been successfully applied to the deposition of a variety of analytes, such as ionized polymers, nucleic acids, peptides and proteins, with molecular masses in the range ~1-10^9 Daltons. Once the gas-phase ions are obtained, differential pumping stages establish a pressure gradient that accelerates the ions towards the UHV preparation chamber, where the sample is placed. The substrate could be based on a metal-interacting surface or on a non-interacting material (*e.g.* graphene) grown on a metal support. The choice of the surface substrate can significantly influence the properties of the 2D-MON as it can affect the catalytic properties of the deposited molecules and single atoms. For tetrapyrrole systems it is reported that they adapt their conformation to the local environment, both by deformations of the macrocycle and by reorientations of the substituents.[6] Adsorption of porphyrins on atomic lattices frequently induces distortions that are triggered by molecule-substrate interactions, detectable by *e.g.* Scanning Tunneling Microscopy (STM). Furthermore, the absorption-induced deformation may sensitively affect the intermolecular interactions and thus the self-assembly of porphyrin architectures. Additionally, the underlying substrate can assume the role of an extended ligand, sensitively affecting the coordination properties of both the tetrapyrrolic unit and the coordinated metal through the above-mentioned surface *trans* effect. Once the porphyrin organic layer is deposited, the obtainment of the 2D-MON is achieved by metalation of the free-base porphyrin. This process can be done by means of several different techniques. In-situ metalation of deposited porphyrins under UHV conditions represents a valuable route for the synthesis of metal-organic active complexes.[11] Several methods can be exploited at surfaces in UHV, including physical vapor deposition (PVD), self-metalation, tip manipulation and chemical vapor deposition (CVD). For the PVD, both free-base porphyrins and single metal atoms are deposited on a supporting surface, and temperature-dependent metalation occurs, in some cases even at room temperature. Since strong molecule-substrate interactions are to be avoided in this case, relatively inert surfaces are preferred, like in the case of Ag(111) and Au(111). This method often needs an annealing process of the molecular layers, thus making PVD metalation inefficient for thermally labile molecules. Therefore, on-surface metalation is limited by the chemical/thermal stability of the molecular species. Self-metalation consists of the deposition of the tetrapyrroles in vacuo on a metal termination, followed by a thermal treatment that induces the incorporation of a surface metal atom of the underlying surface into the tetrapyrrolic cage. Strong kinetic limitations contribute and may even prevail over the thermodynamic energy balance in this method. Local tip manipulation by means of an STM can also be exploited to induce metalation. It was reported that Ag(I) insertion in a phthalocyanine can be achieved with this method. If the in-situ metalation process does not work, it is possible to directly deposit the metalated version of the desired porphyrin. This approach requires a previous in-solution metalation of the free-base porphyrin, which is then deposited on the desired substrate. Several experimental techniques can be used for the characterization of the obtained 2D-MON. To gain information about both the electronic and vibrational structure of the system under investigation, as well as the successful deposition of the desired molecule, Infrared-Visible Sum-Frequency Generation (IR-Vis SFG) spectroscopy is often used. IR-Vis SFG is a surface-sensitive, photon-in photon-out vibronic technique. It is based on sum-frequency generation, a coherent, second-order optical process.[19,20] The long mean free path of both probes and signal, combined with the fact that IR-Vis SFG can’t occur in non-centrosymmetric materials, makes this technique suitable for studying solid-vacuum, solid-liquid, solid-gas and liquid-gas interfaces under both UHV and near ambient pressure (NAP) conditions.[21] Being a second-order process, pulsed laser beams, which typically yield high intensities, are required to generate detectable IR-Vis SFG intensities. Here the case of **TPP** deposited on a graphene/Ir(111) substrate will be briefly discussed as it turns useful for the next discussion.[22] **TPP** molecules were deposited by PVD on graphene/Ir(111) at sub-monolayer coverage. Then, to investigate also solvent resonances in the IR-Vis SFG spectra, pure ethanol was electrosprayed on the pristine **TPP**/Gr/Ir(111) layer. The molecules yielded several vibrational features in the following ranges: 1050 – 1380 cm^{-1}, 1400 – 1700 cm^{-1}, 2740 – 3130 cm^{-1} and 3300 – 3400 cm^{-1}, which include characteristic vibrational modes of the macrocycle and the ligands. The IR-Vis spectra were recorded in UHV conditions at room temperature, in a *ppp* polarization combination, both before and after annealing the sample at 425 K, to investigate the temperature influence on the layer ordering. IR-Vis SFG spectra are reported in Figures 4.1.2 and 4.1.3, together with the best fit and the deconvolution of the spectral components. Each resonance was assigned to a specific vibrational mode based on simulated and experimental Raman and IR **TPP** spectra available in the literature.[23–28] Accordingly to the reported literature values, the 1050 – 1380 cm^{-1} region mainly contains resonances associated with vibrational modes of the phenyl ring, predominantly at low energies, while the higher energy peaks above 1300 cm^{-1} are associated with macrocycle modes (Figure 4.1.2). After annealing at 425 K, small band shifts (~ 1 – 10 cm^{-1}) are observed. The latter can be attributed to thermal excitation, which, combined with the high mobility of porphyrins on graphene, may induce reorientation of the molecules, changing the local environment of the probed dipoles. The 1400 – 1700 cm^{-1} region mainly contains resonances associated with porphyrin skeletal symmetric and asymmetric C_α–C_m and C_β–C_β vibrations, as well as pyrrole quarter and half-ring stretch vibration model within the macrocycle. Minor contributions belonging to the phenyl rings are present. The feature at 1606 cm^{-1} is attributed to the graphene substrate.[29] After annealing at 425 K, two new bands appeared due to thermally induced molecular reorientation with respect to the surface, which may lead to previously SFG-inactive dipoles to become active.[22]

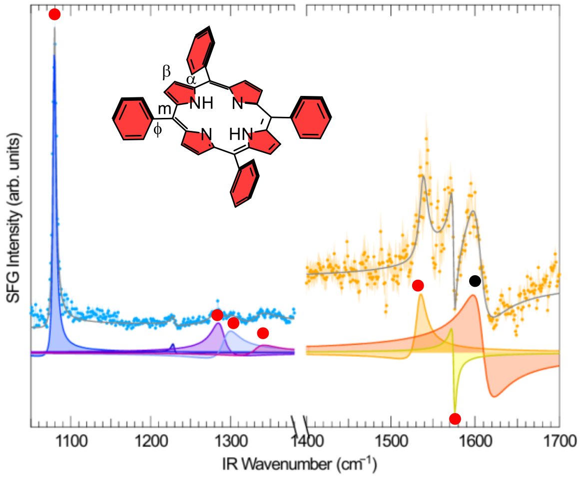

Figure 4.1.2. IR-Vis SFG spectra in the 1050 – 1380 and 1400 – 1700 cm^{-1} regions, together with the best fit functions and deconvolution spectral components of **TPP**/Gr/Ir(111) at sub-monolayer coverage for the pristine sample. The spectra were acquired in *ppp* polarization configuration. Red dots indicate porphyrin resonances, black ones graphene resonances.

Moving to higher wavenumber regions, the 2740 – 3130 cm^{-1} range exhibits a single resonance at 3060 cm^{-1}, attributed to the C_β–H stretching vibrations of the porphyrin ring (Figure 4.1.3, left).[23] On the other hand, the 3300 – 3400 cm^{-1} region contains a stretching mode corresponding to the pyrrolic N–H bonds. Upon annealing, no significant band or phase shifts are observed. Finally, the solvent contribution to the IR-Vis SFG spectra was determined as four additional bands to the **TPP** band at 3060 cm^{-1} as shown in Figure 4.1.3, right.

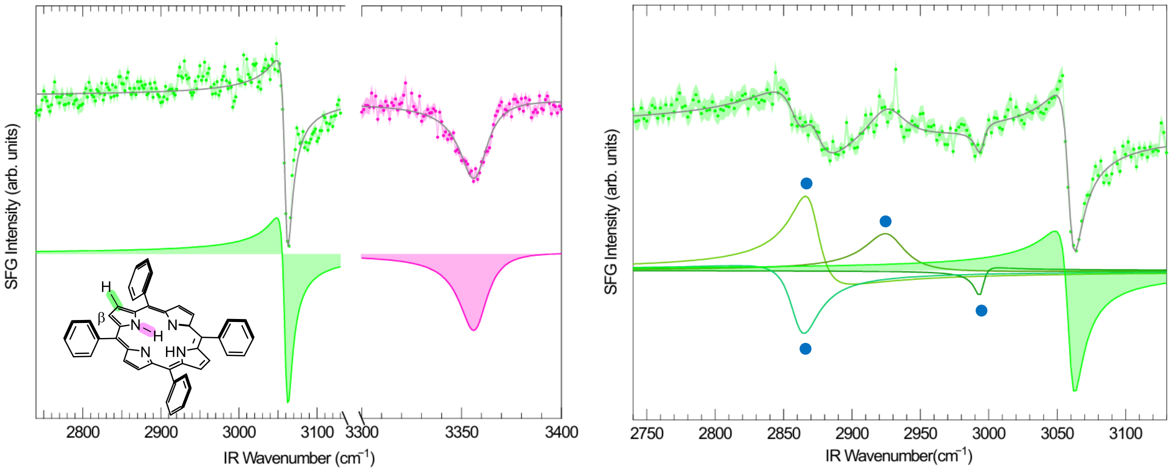

Figure 4.1.3. Left: IR-Vis SFG spectra in the 2740 – 3130 and 3300 – 3400 cm^{-1} regions, together with the best fit functions and deconvolution spectral components of **TPP**/Gr/Ir(111) at sub-monolayer coverage for the pristine sample. The spectra were acquired in *ppp* polarization configuration. Right: ethanol contribution (blue dots) to the IR-Vis SFG spectra.

To gain information on the topological and electronic structure of a 2D-MON with atomic resolution, the most commonly used technique is STM.[30,31] Additionally, STM images gain insights into the relative organization of the organic layers and metal atoms deposited on the surface. To do this, a sharp metallic tip is used to probe the sample's surface. The tip and the sample are close enough in such a way that their wave functions overlap, decaying exponentially into the gap. If a bias voltage is applied between the tip and the sample, a tunneling current, whose intensity depends on the tip-sample distance, is established. A recent STM image of **TPP** deposited on an Au(111) surface is reported in Figure 4.1.4.[32]

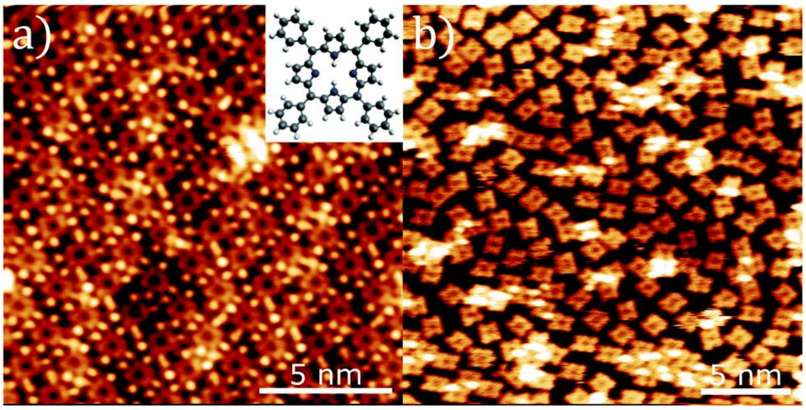

Figure 4.1.4. STM images of **TPP**/Au(111) measured at constant current mode (I = 5 pA) of: a) monolayer close-packed phase with inset of the **TPP** chemical structure and b) diffuse phase, formed by annealing a monolayer of **TPP** to 580K. Figure adapted from ref. 32.

Finally, quantitative information about the chemical identity of the surface species and their electronic structure can be obtained by X-Ray Photoelectron Spectroscopy (XPS) as well as

Near-Edge X-Ray Absorption Fine Structure Spectroscopy (NEXAFS). XPS is a photon-in/electron-out surface science technique that presents element sensitivity. Additionally, XPS allows gaining information about the chemical environment of an atom, structural dishomogeneities, lifetime of the excited state induced by photoemission processes, and metallicity. XPS is furthermore a surface-sensitive technique due to the high cross-section of electrons for inelastic scattering with matter. On the other hand, NEXAFS is nowadays a routinely exploited technique in surface science, allowing for the obtainment of information about the geometric and electronic structure of molecules deposited on surfaces. The combination of IR-Vis SFG spectroscopy, STM imaging, XPS and NEXAFS techniques allows for a complete characterization of a 2D-MON. Single-atom catalytic activity of 2D-MONs formed by (metallo)porphyrin has been extensively studied by Vesselli *et al.* Some selected examples of the ligation and/or activation of simple small molecules such as H_2O, O_2, and CO will be briefly discussed here. In 2022, they reported an example of a 2D-MON formed by deposition of **CoTPyP** on a Gr/Ir(111) substrate for the ORR.[8] Graphene was selected as it is almost unreactive under the used mild experimental conditions, completely passivating the underlying Ir termination. Additionally, for the graphene-supported network, the surface *trans* effect is quenched as the π-mediated weaker interaction between molecules and graphene precludes the formation of a direct bond between the substrate and the metal centers. ORR can follow two different and competing pathways; direct reduction to -OH groups via the $4e^-$ mechanism ($O_2 + 2H_2O + 4e^- \rightarrow 4OH^-$), or indirect reduction through hydrogen peroxide ($O_2 + H_2O + 2e^- \rightarrow HO_2^- + OH^-$; $HO_2^- + OH^- + 2e^- \rightarrow 3OH^-$; $2HO_2^- \rightarrow O_2 + 2OH^-$) according to the $2e^-$ pathway. By working at room temperature, they explored the single-atom catalyst activity of **CoTPyP**/Gr/Ir(111) at NAP. In particular, by means of a combination of in-situ measurements and theoretical methods, they have demonstrated that a cobalt-single atom biomimetic model catalyst, based on a self-assembled monolayer of **CoTPyP**, stabilizes a hydroperoxyl-water cluster at room temperature in $O_2 + H_2O$ atmosphere. Additionally, the authors observed that the majority of the single-atom Co sites host the water and hydroperoxyl ligands. The detection of the hydroperoxyl intermediate is associated with its stabilization by a surprising combination of charge transfer, dipole and chemical H-bonding with physiosorbed water. A similar mechanism was found in heme enzymatic reaction centers. In hemoglobin and myoglobin, an imidazole group of the protein histidine residue provides a stabilizing H-bonded network for the Fe-peroxo intermediate so that, by artificially engineering the H-bonding structure of myoglobin, the protein can be modified to promote O_2 reduction to water via the

4e⁻ mechanism. These findings lead to the possibility of controlling the selectivity of the ORR pathways. In a previous work from 2020,[9] they have reported on the employment of **CoTPyP**/Au(111) 2D-MON for the stabilization and possible activation of molecular O_2, which is probably a fundamental step in the ORR. Using UHV and NAP IR-Vis SFG spectroscopy, they observed that by exposing the layer to O_2 at room temperature, this gas is first adsorbed on Co single metal atoms, then the O–O stretching frequency lowers due to the weakening of the intramolecular bond associated with the charge transfer, a molecular dipole is formed and a 15% decrease in the porphyrin magnetization is observed, thus indicating stabilization and initial activation of the O_2 molecule. The adsorption geometry of O_2 on the Co metal atoms closely resembles the one observed in biological systems, with the O_2 molecule sitting on-top of the Co atom and the molecular axis tilted by 118°. The ligand configuration lies between the oxo- and the superoxo species. Finally, in a very recent example from 2024, it was reported on a homo bimetallic **CoTPyPCo**/graphene/Ir(111) self-assembled 2D-MON.[10] The peculiarity of **TPyP** MONs is that, in contrast with porphyrin without functional groups on the *meso*-aryl rings, in addition to the metal atom coordinated into the inner cavity of the porphyrin macrocycle, a second metal ion can be embedded in the fourfold coordination sites formed by the pyridinic nitrogen atoms of neighboring molecules. Here, the authors demonstrated the effect of coordination on local and non-local electronic structure through a combination of experimental techniques and ab-initio calculations in a homo bimetallic **CoTPyPCo**/Gr/Ir(111). By STS (scanning tunnelling spectroscopy) it was proved that for **CoTPyP**/Gr/Ir(111) the adsorbed molecules assemble into a close-packed lattice with a rectangular unit cell, optimizing the interaction between the electronegative N-atoms of the pyridyl groups and the peripheral H-atoms of the neighbouring pyrrole moieties. This arrangement is typical of pyridyl-substituted porphyrins when the interaction with the substrate is weaker than the intermolecular forces, as observed on gold or silver. Upon post-evaporation of Co adatoms, a rearrangement of the porphyrins network occurs to accommodate the single Co species. In this configuration, each single Co adatom is tetra-coordinated by the pyridinic terminations of adjacent **CoTPyP**. Using XPS spectroscopy, it was seen that the Co atom in the inner core of the porphyrin macrocycle, in a +2 oxidation state in **CoTPyP**/Gr/Ir(111) 2D-MON, changes its oxidation state to +3 upon addition of the second Co centre. Additionally, the “external” Co atom presents the unusual +1 oxidation state, confirmed also by DFT simulations. This leads to the growth of a 2D-MON with two metals with non-equivalent chemical activity. The Co(I) species is known to be active for CO_2 activation, thus making this heterometallic 2D-MON interesting for further catalytic applications. Here, the reactivity of the

2D-MONs was studied only with CO. The results indicate that CO ligation occurs exclusively at the (external) **CoTPyPCo(I)** site, relevant for practical catalytic applications, including CO oxidation, water gas-shift, or CO methanation. These experimental results are supported by DFT calculations showing that the favourable binding site for CO is Co(I) with a calculated binding energy of 1.3 eV *vs.* a binding energy of 0.4 eV in the case of the porphyrin-inserted Co(III). It should be mentioned that only a selection of representative examples has been discussed here, while numerous other homo- and hetero-bimetallic 2D-MONs based on **TPyP** have been reported in the literature.[33–35] The possibility of readily varying both the organic ligand and the metal centre enables the straightforward synthesis of 2D-MONs with finely tuned properties, which can be exploited to mimic the reactivity observed in natural (metallo)porphyrins. As an illustrative example of a natural catalytic system based on a molecular metallo-porphyrin, the case of cytochrome P450 will be described here (Figure 4.1.5).

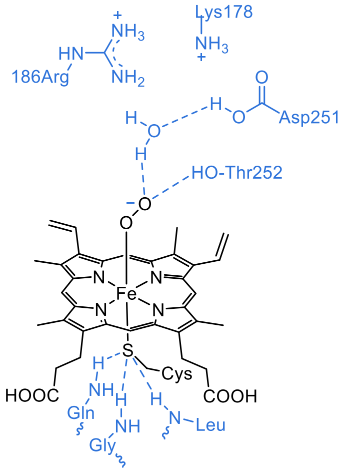

Figure 4.1.5. Active site of cytochrome P450. First coordination sphere is shown in black while second coordination sphere in blue. Figure adapted from ref. 36.

This enzyme is a heme-containing monooxygenase that catalyses the heterolytic cleavage of molecular oxygen in processes such as drug and xenobiotic metabolism, as well as the biosynthesis of steroid hormones and lipids.[36] Cytochrome P450 contains a Fe^{II}-porphyrin core, in which a cysteine residue occupies the fifth coordination site, thereby modulating oxygen binding and activation at the vacant sixth site. The catalytic activity of cytochrome P450 is influenced not only by the central metal ion and its first coordination sphere, but also by its second coordination sphere. Here, the second coordination sphere of a metal complex is defined as the set of non-coordinated atoms or molecules that interact weakly with the first coordination sphere. A key factor in tuning the reactivity of the central Fe atom through the second coordination sphere is the hydrogen-bond network established between the bound molecular oxygen, amino acid residues in the surrounding protein scaffold, and water molecules acting as solvent. This hydrogen-bond network functions as a proton-transfer channel, essential for oxygen activation in cytochrome P450. The Asp251 residue interacts with Lys178 and Arg186 in a way that restricts the conformational flexibility of Thr252 and of nearby water molecules, thereby creating a rigid proton channel that promotes protonation of the distal oxygen atom and its subsequent activation through the catalytic cycle intermediates. On the opposite side of the porphyrin plane, the thiolate axial ligand provided by the cysteine residue is surrounded by the amide groups of leucine, glycine, and glutamine residues. Hydrogen bonding between these amide groups and the sulphur atom affects the charge distribution within the Fe-S bond, contributing both to the stabilization of the thiolate ligand and to enhanced electron donation to the central metal ion, ultimately facilitating oxygen activation. With the goal of mimicking the catalytic activity found in natural enzymes, several molecular systems based on metallo-porphyrins bearing functionalized ligands that can mimic the enzyme second coordination sphere have been reported. Some selected examples based on Fe- or Co- porphyrins will briefly be discussed. In 2021 Dey *et al.* reported the use of iron-porphyrins with pendant N-based ligands as electrocatalysts for hydrogen production (Figure 4.1.6).[37] The authors demonstrated that the simple **Fe^{II}TPP** is able to catalyse hydrogen production (HER) through intermolecular protonation of a Fe^{III}-H^{-} intermediate generated from the protonation of a Fe^{I}-state, in the presence of an external acid source. However, when pendant amine groups were introduced sufficiently close to the metal centre (**FeTPP^{NH}** or **FeTPP^{pyr}** in Figure 4.1.6), the mechanism shifts to intramolecular proton transfer with the protonated amine becoming the local source of protons. Linear free-energy relationships reveal that the protonated amines decrease the dependence of HER kinetics with the pK_a of the bulk acid. Yet, the inclusion of too many pendant groups (**FeTPP^{F}** in Figure 4.1.6) leads to a decrease in the HER activity due to the higher proton binding affinity that slows the proton transfer process. These results highlight the need for a finely tuned balance between proton affinity and proton mobility within the second coordination sphere of molecular catalysts.

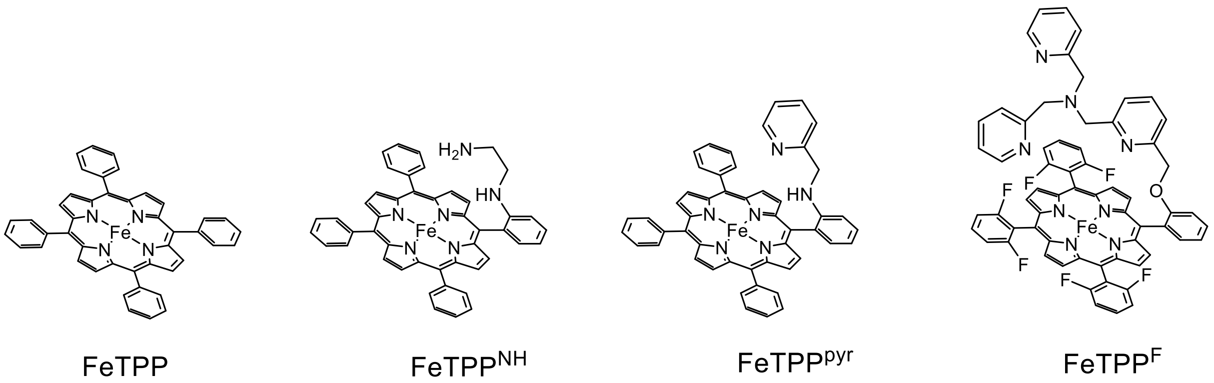

Figure 4.1.6 Schematic representation of the iron-porphyrins electrocatalysts reported by Dey *et al.*[37]

Similarly, in 2022 Chang *et al.* reported that the second coordination sphere has a significant effect on the electrochemical reduction of CO_2 by iron porphyrins.[38] These authors introduced one urea group in *ortho* position of FeP macrocycle (**FeTPP^{urea}** in Figure 4.1.7), and showed a template binding of bicarbonate, a species that is often present in organic electrolytes and that can act as an internal proton donor. Bicarbonate binding *via* two hydrogen bonds to a urea moiety places the anion precisely above the Fe-CO_2 adduct and increases its acidity, thereby facilitating rapid proton transfer to CO_2-derived intermediates. Spectrophotometric titrations, NMR binding studies, and DFT calculations support the formation of these templated complexes and explain the significant catalytic enhancement observed experimentally. Further insight into the interplay between local acidity and electrocatalytic efficiency towards CO_2 reduction has been obtained from a recent study reported by Nichlos *et al.* where they have employed amide-functionalized iron-porphyrins with tunable pK_a (**FeTPP^{OMe}**, **FeTPP^{H}**, **FeTPP^{OCF3}** and **FeTPP^{CF3}** in Figure 4.1.7).[39] By varying both the acidity of the amide side groups and the acidity of external proton donors, it was possible to evaluate contributions of the second coordination sphere and to obtain mechanistic insights into CO_2 reduction as function of pK_a. Linear free-energy relationships reveal that catalytic rates become dependent to changes in second-sphere acidity when stronger external acids are used, and more sensitive to external acid pK_a when the second sphere is made more acidic. These results illustrate that the rational tuning of secondary coordination sphere proton transfer driving forces is a crucial design strategy for enhancing the performance of molecular CO_2 reduction catalysts.

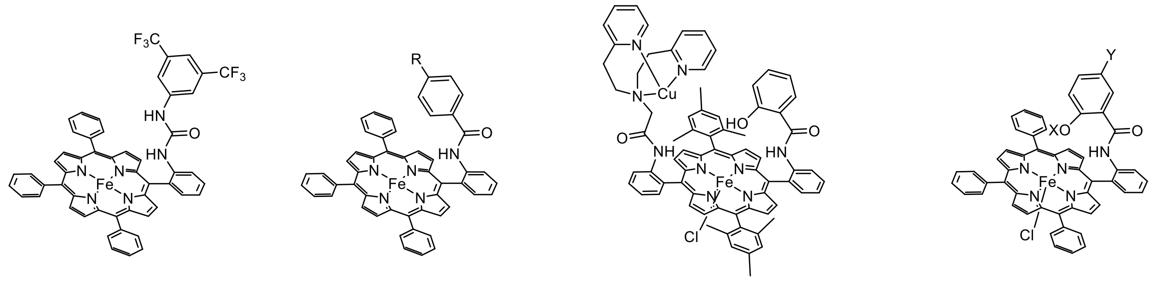

FeTPP^{urea}

R = OMe FeTPP^{OMe}
R = H FeTPP^{H}
R = OCF_3 FeTPP^{OCF3}
R = CF_3 FeTPP^{CF3}

FeTPP^{Cu}

X = Y = H FePh
X = H; Y = OH $FeQH_2$

Figure 4.1.7. Schematic representation of iron-porphyrins reported by Cheng *et al.* (**FeTPP^{urea}**),[38] Nichols *et al.* (**FeTPP^{OMe} – FeTPP^{CF3}**),[39] Coutsolesos *et al.* (**FeTPP^{Cu}**),[40] and Dey *et al.* (**FePh** and **$FeQH_2$**).[41]

Second-sphere modifications have also proven essential in tailoring porphyrins for the OER. Synthetic heme/Cu models inspired by cytochrome *C* oxidase, reported by Coutsolelos *et al.* (**FeTPP^{Cu}** in Figure 4.1.7), have demonstrated that the presence of a copper site placed on the top of the porphyrin plane, combined with a phenolic moiety mimicking the enzyme's tyrosine residue, allows the formation and stabilization of key intermediates in O_2 reduction.[40] These systems bind O_2 and CO, display photochemical reactivity, and catalyse the reduction of O_2 to water, although their stability is limited. Still, this study has provided insights into how proton and electron transfers may be orchestrated cooperatively in a biomimetic framework. An elegant example of iron porphyrins functionalized with covalently linked phenol or quinol groups have been reported in 2020 by Dey *et al.* (**FePh** and **$FeQH_2$** respectively in Figure 4.1.7).[41] In this work it was shown that both types of complexes can reduce O_2 electrochemically with high selectivity for the four-electron/four-proton pathway, *albeit* with distinct mechanisms. Phenol-bearing porphyrins promote a Proton Coupled Electron Transfer mechanism, because of stabilization of a highly reactive intermediate by hydrogen bonding and therefore by lowering the inner-sphere reorganization energies of the PCET process. For the quinol-bearing analogues the O_2 reduction proceed *via* two sequential hydrogen-atom transfer (HAT) events because of the lower reduction potential of the quinol unit with respect to the phenol one. These observations show how small differences in the redox properties related to the different second coordination sphere can significantly influence the energy profiles for O_2 activation.

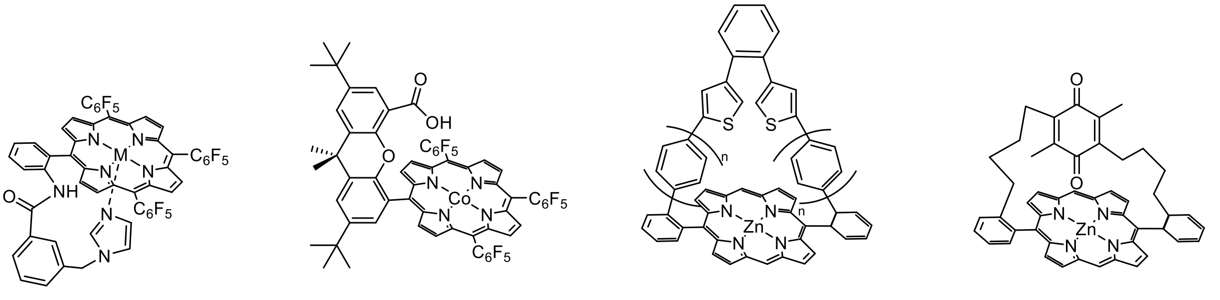

M = Fe; FepFP^{Im}
M = Co; CopFP^{Im}

CoHP

n = 0; Zn-DTE-1
n = 1; Zn-DTE-2

Zn^{SP}

Figure 4.1.8 Schematic representation of metallo-porphyrins reported by Cao *et al.* (**FepFP^{Im}**),[42] Nam *et al.* (**CopFP^{Im}**),[43] Nocera *et al.* (**CoHP**),[44] and the three strapped zinc-porphyrins described in the main text (**Zn-DTE-1**, **Zn-DTE-2** and **ZnPQ**).[45,46]

Cao *et al.* in 2021 reported an enzyme-inspired iron-porphyrin featuring a tethered imidazole group (**FepFP^{Im}**, Figure 4.1.8).[42] This system exhibits significantly improved performance in both electrochemical ORR and OER relative to the corresponding imidazole-free counterpart. Computational studies suggest that the imidazole ligand directs reactivity by stabilizing the correct intermediate for the O–O bond formation while preventing the formation of intermediates less competent for O–O formation. The same porphyrin skeleton, bearing cobalt(II) in the porphyrin core in place of the iron(II) cation was reported in 2022 by Nam *et al.* (**CopFP^{Im}**, Figure 4.1.8).[43] In this work the authors have demonstrated that the second coordination sphere can significantly influence both the stoichiometric and the catalytic O_2 reduction pathways. In the presence of strong acids, the imidazole gets protonated and form an imidazolinium species that participates directly in a PCET mechanism for oxygen reduction, while in the absence of acid the simple electron transfer is promoted. Kinetic analysis and identification of reactive intermediates have confirmed the central importance of the pendant arm in these transformations. The group of Nocera in 2010 successfully embedded a carboxylic group in the second coordination sphere of a Co^{II}-porphyrin through a rigid xanthene spacer, thus positioning the -COOH group correctly above the metal centre offering hydrogen bonding to the metal centre *via* the so-called "hangman effect"(**CoHP**, Figure 4.1.8).[44] The carboxylic group acting as a proton donor and the electronegative -C_6F_5 residues on the periphery of the macrocycle were shown to be successful structural variations to promote the four-electron reduction of oxygen to water, previously observed only with bimetallic systems. The same hangman porphyrin also showed catalytic activity for hydrogen evolution. Both the oxygen reduction and hydrogen evolution reactions require the proton transfer from the carboxylic group embedded in the second coordination sphere to the metal site. Examples of porphyrins with a functionalized second coordination sphere without hydrogen bonding patterns include strapped zinc-porphyrins featuring a dithienylethene bridge linked to the porphyrin *meso* phenyl rings in *trans* positions *via* benzene linkers (**Zn-DTE-1** and **Zn-DTE-2** in Figure 4.1.8) or a strapped zinc-porphyrin featuring a quinone bridge for which the linkers are simple alkyl chains (**ZnPQ**, Figure 4.1.8).[45,46] **Zn-DTE-1** and **Zn-DTE-2** exhibit totally different but reversible binding capacity and fluorescence intensity when irradiated by different light wavelengths, potentially exploitable as multi-controlled molecular switch or logic gate.[45] **ZnPQ** was found to undergo ultrafast electron transfer processes from the metallo-porphyrin to the quinone group upon photoexcitation of the chromophore, which are believed to play important roles in biological photoinduced electron transfer processes and also for the design of artificial photoelectric devices.[46] Taken together, the above discussed studies highlight a common principle: the reactivity of metallo-porphyrins in complex redox transformations is governed not only by the structure of the first coordination sphere, but to an equal or greater extent also by the careful design of the second coordination sphere. This secondary environment influences proton and electron delivery, modulates reaction energetics, stabilizes highly reactive intermediates, influences mechanistic pathways, and imparts selectivity by shaping the microenvironment of the substrate and the metal centre. The emerging ability to control electronic structure, local acidity, proton mobility, and hydrogen-bonding topology (by synthetic tailoring of the porphyrin macrocycle) makes porphyrin-based systems ideal platforms for applications in energy conversion, sustainable catalysis, and the modelling of enzymatic redox processes. Inspired by these observations, the goal of the present study was that of preparing and characterizing the one-armed porphyrins **2** – **6** bearing benzamide pendant ligands with different substitution patterns, and either no metal or Co^{II} in the macrocyclic core (Figure 4.1.9).

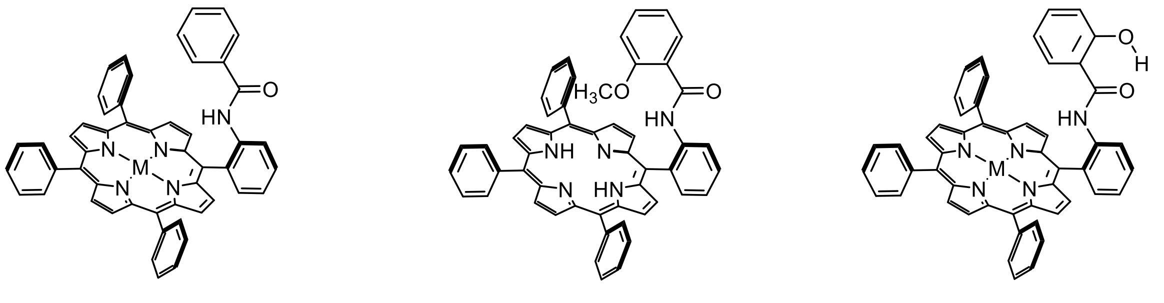

M = H_2; TPP-*o*BA (2)
M = Co; CoTPP-*o*BA (5)

TPP-*o*MeOBA (3)

M = H_2; TPP-*o*OHBA (4)
M = Co; CoTPP-*o*OHBA (6)

Figure 4.1.9 Chemical structures of the free-base (**2** – **4**) and Co^{II}-porphyrins (**5** and **6**) synthesized and described in this Chapter.

The presence of benzamide moieties orthogonal to the porphyrin macrocycle was designed to reproduce the second coordination environment of natural enzymes. The introduction of a $-OCH_3$ or $-OH$ group at the peripheral phenyl group should vary the possible effects of the second sphere. After a through solution characterization, an initial selection of these systems was used to grow metal-organic layers. The 2D-MONs were characterized in UHV conditions by IR-Vis SFG on Gr/Ir(111) and by STM on Au(111). Further characterization by and NEXAFS at a dedicated Synchrotron beamline will soon be undertaken. In parallel, reactivity of the metallo-porphyrin 2D-MONs on Gr/Ir(111) by exposure to various gases such as CO, O_2 and H_2O, is under study in UHV and by means of XPS.

4.2. Results and Discussion.

*4.2.1. Synthesis and characterization of **2** – **4**.*

2 – **4** were synthesized starting from the same porphyrin precursor, 5-(2'aminophenyl)-10,15,20-triphenylporphyrin, **TPP-*o*NH$_2$** (**1**). **1** was obtained according to literature procedures, following the classical Adler-Longo method (see also Chapter one).[38,47] Freshly distilled pyrrole was added to a propionic acid solution containing benzaldehyde and 2-nitrobenzaldehyde (in a 2:1:1 ratio) and allowed to react at 145 °C for 2h. After cooling the reaction mixture to room temperature, cold methanol was added to induce porphyrin precipitation. The resulting purple solid was filtered, washed with methanol and used for the next synthetic step without further purification. The mixture of **TPP** and nitro-porphyrin regioisomers (by TLC analysis the presence of TPP, mono-, di- (*cis* and *trans*) and tris-nitro porphyrin was detected) was reduced in concentrated HCl in the presence of $SnCl_2$, with conversion of the nitro groups to amino groups. Compound **1** was obtained as a purple solid after purification by column chromatography, as shown in Scheme 4.2.1.

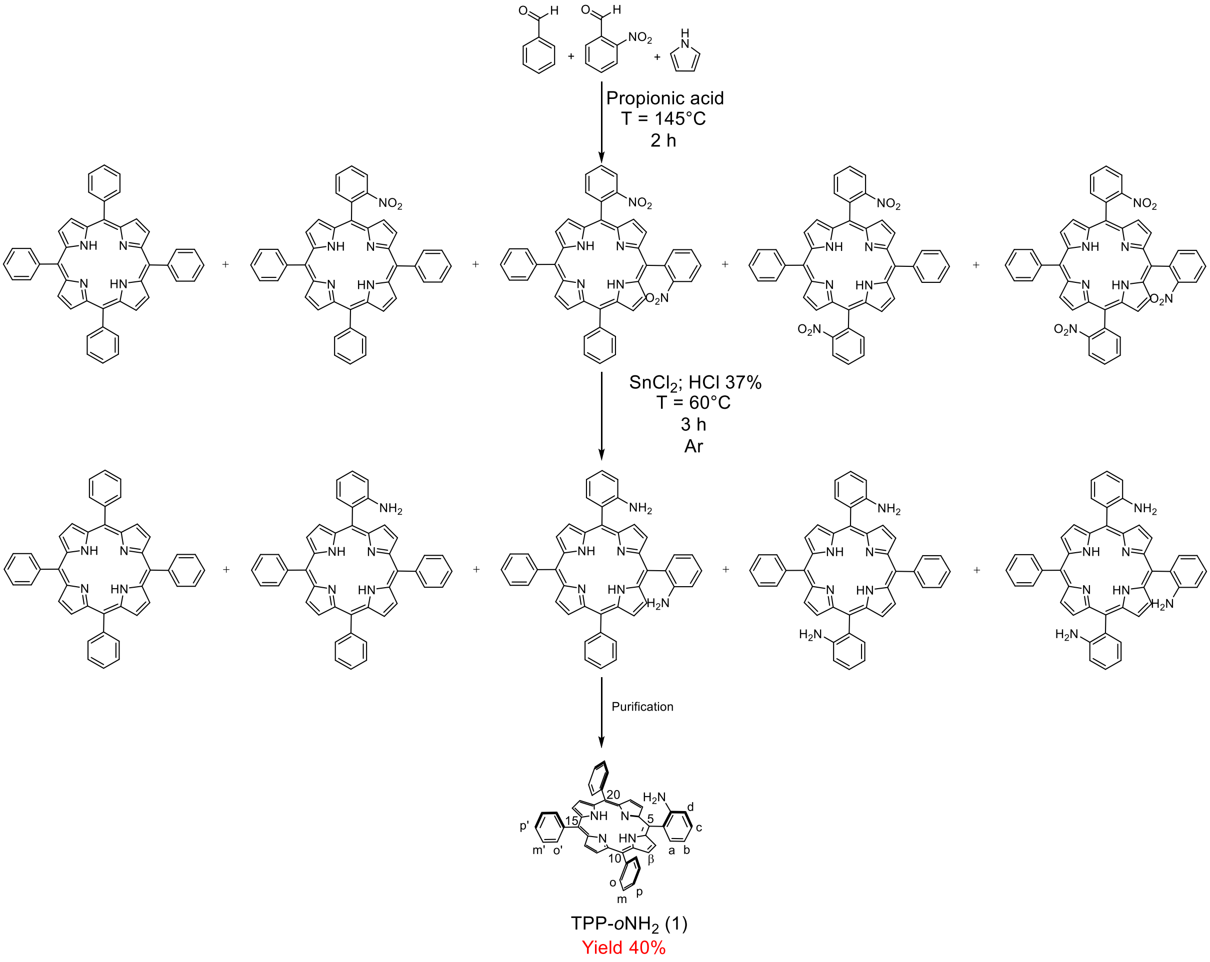

Scheme 4.2.1. Synthetic strategy for the obtainment of **TPP-*o*NH$_2$ (1)**.

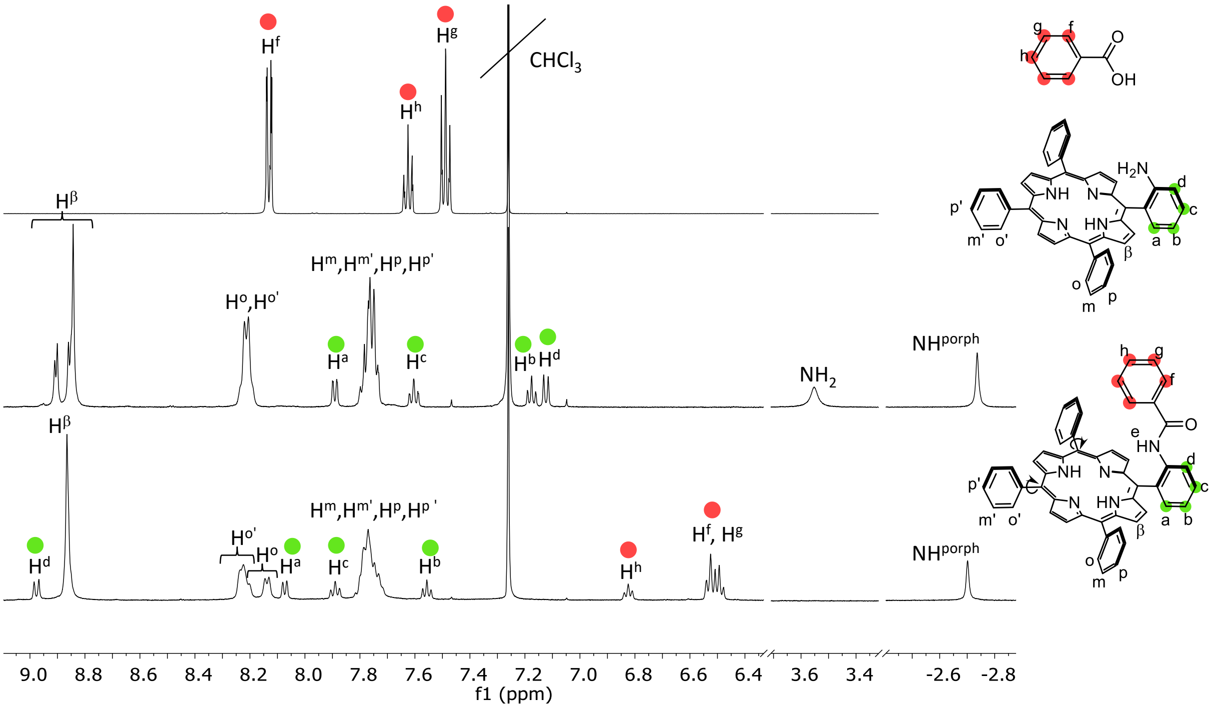

Figure 4.2.1. ^{1}H NMR spectrum (CDCl$_3$, 298 K) of benzoic acid (top), **1** (middle) and **2** (bottom); the arrows refer to the slow rotation on the NMR time scale of the porphyrin *meso* aryl rings.

1 was characterized in solution by 1D and 2D NMR spectroscopy. The ^{1}H NMR spectrum of **1** is reported in Figure 4.2.1. The presence of a single set of signals indicates that only one species is present in solution. Complete signal-proton assignment was done using 2D NMR experiments (^{1}H-^{1}H COSY, ^{1}H-^{13}C HSQC and ^{1}H-^{13}C HMBC, see Appendix C). Relative integration values, signal multiplicity and cross-peaks observed in 2D NMR spectra confirm the structure of the desired porphyrin **1**. The nature of **1** was further validated by ESI-MS analysis (Figure S4 in Appendix C). For the preparation of **TPP-*o*BA** (**2**) initially **1** was reacted with benzoic acid in pyridine using the classical EDC-mediated amide coupling method (see also Chapters 2 and 3). After 24 hours, TLC analysis showed only the presence of unreacted precursor **1**. The different reactivity of **TPP-*o*NH$_2$** and **TPP-*p*NH$_2$** can be attributed to the steric hindrance generated by the porphyrin macrocycle over the amino group. Compounds **TPP-*o*BA** (**2**) and **TPP-*o*MeOBA** (**3**) were then successfully synthesized by reacting **1** with the corresponding benzoyl chlorides in dry CH_2Cl_2, under Ar atmosphere for 20h for **2** or 4h for **3**, as shown in Scheme 4.2.2.[41]

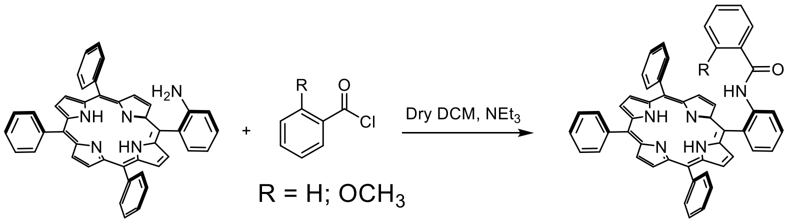

TPP-*o*NH$_2$ (1)

TPP-*o*BA (2): R = H; Yield 74%
TPP-*o*MeOBA (3): R = OCH$_3$ Yield 78%

Scheme 4.2.2. Schematic representation of the synthesis of **TPP-*o*BA** (**2**) and **TPP-*o*MeOBA** (**3**).

2 and **3** were obtained as purple solids in 74% and in 78% yield, respectively, after purification by column chromatography. The ^{1}H NMR spectrum of **2** is reported in Figure 4.2.1. Full signal-proton assignment was done using 2D NMR experiments (^{1}H-^{1}H COSY, ^{1}H-^{13}C HSQC, ^{1}H-^{13}C HMBC and ^{1}H-^{1}H ROESY, see Appendix C). Formation of **2** is confirmed by the disappearance of the amine proton signal at $\delta = 3.55$ ppm (the resonance of the -NH amide proton in **2** can be observed only in the ^{1}H NMR spectrum in dmso-d_6, as a singlet at $\delta = 9.53$ ppm, Figure S9 in Appendix C). The signals of the conjugated benzoyl moiety (triplet at $\delta = 6.82$ ppm for H^h and multiplet at $\delta = 6.54 – 6.48$ ppm for H^f and H^g) are found all upfield shifted compared to free benzoic acid (Figure 4.2.1). This observation agrees with the fact that the pendant phenyl ring is positioned above the shielding cone of the porphyrin macrocycle, as represented in Figure 4.2.1. On the other hand, the significant downfield shift observed for the doublet pertaining to H^d ($\Delta\delta = + 1.83$ ppm relative to **1**) likely derives from the proximity of this proton to the carbonyl group, thus offering an indication on the average disposition of the amide moiety relative to the porphyrin phenyl ring in *meso* position 5. Also, the signals of *ortho* protons pertaining to the other porphyrin *meso* phenyl rings (positions 10, 15 and 20) are partly split into two resonances of comparable intensity. In general, the porphyrin *meso* aryl substituents are in slow rotation on the NMR time scale and stay in average perpendicular to the macrocyclic plane. In the present case, the introduction of the pendant arm correspond to the loss of symmetry on the two sides of the plane containing the macrocycle, with magnetic distinction between the *ortho* protons pointing above or below this plane (exchange cross-peaks are found in the ^{1}H-^{1}H ROESY spectrum for the resolved split resonances, Figure S8, Appendix C). The nature of **2** was further confirmed by HRMS analysis, with two main peaks detected, corresponding to the mono- and di-cationic molecular ions (Figure 4.2.2).

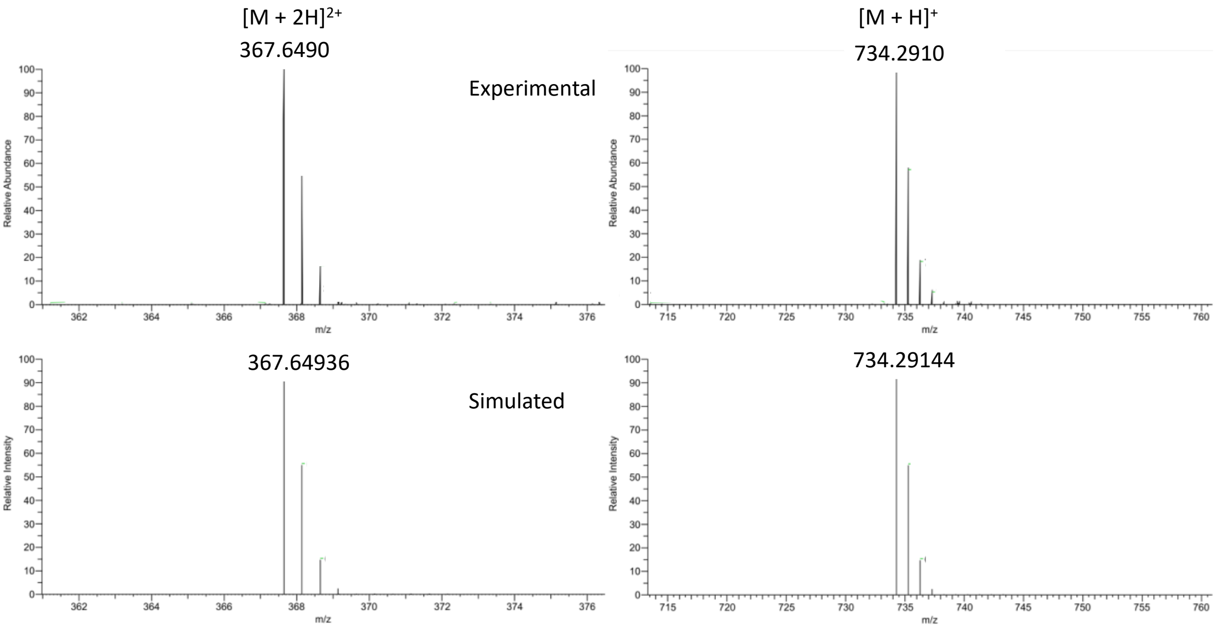

Figure 4.2.2. HRMS of **2** in CH_3OH, experimental (top) and simulated (bottom).

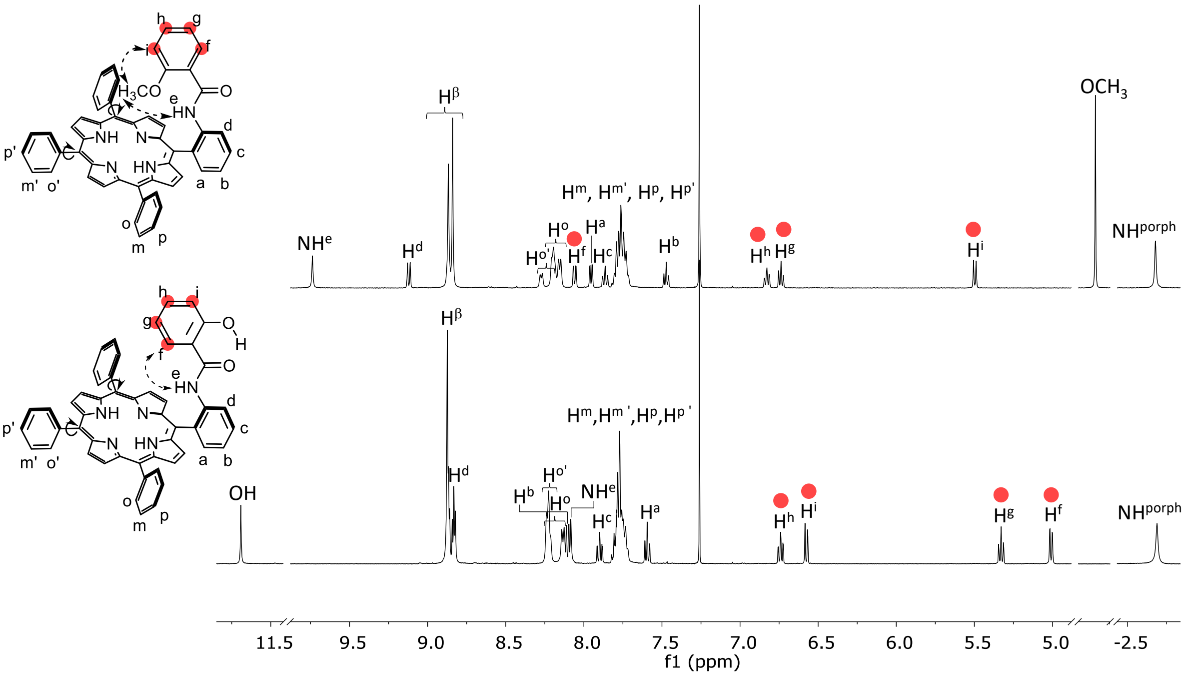

Figure 4.2.3. ^1H NMR spectrum ($CDCl_3$, 298 K) of **3** (top) and **4** (bottom). The full arrows refer to the slow rotation on the NMR time scale of the porphyrin *meso* aryl rings, while the dotted arrows refer to some useful nOe cross peaks found in the ^1H-^1H ROESY spectrum (see Appendix C).

The ^1H NMR spectrum of conjugate **3** is reported in Figure 4.2.3, top. Integration and multiplicity of the NMR signals confirm the presence of a single species in solution. Signal assignments were done using 2D NMR experiments (^1H-^1H COSY, ^1H-^{13}C HSQC, ^1H-^{13}C HMBC, and ^1H-^1H ROESY, Figures S10 – S13 in Appendix C). Observation of the resonances of the -NH amide group and of the protons of pendant methoxy-benzoyl residue confirm the successful conjugation. As already observed for compound **2**, here more marked, splitting of the doublets of the porphyrin *ortho* phenyl protons ring (in *meso* positions 10, 15 and 20) results from the loss of symmetry with respect to the macrocyclic plane (exchange peaks found in the ^1H-^1H ROESY spectrum are in line with this, Figure S13 in Appendix C). The chemical shift distribution and spatial connections of some signals offer clear indication on the orientation of the pendant 2-methoxy-benzoylamide arm, providing key information relevant to the subsequent surface studies discussed later in this Chapter (see below). In particular, the presence of a singlet, integrating for three protons, at $\delta = -0.16$ ppm, assigned to the $-OCH_3$, indicates that this substituent lays above the porphyrin shielding cone. The downfield shifted singlet of the –NH amide group ($\delta = 9.74$) likely results from an intramolecular hydrogen bond between the same group and the oxygen of the methoxy residue, confirmed also by the nOe observed in the ^1H-^1H ROESY spectrum. Accordingly, the doublet of H^i is shifted at lower ppm values as compared to the signal of the analogous H^g proton in compound **2** ($\Delta\delta = 1.04$). All the other signals are assigned as follows: a comparison with the ^{1}H NMR spectrum of **2** (Figure 4.2.2) assigns the doublet at δ = 9.12 ppm to H^d. Based on cross-peaks in the ^{1}H-^{1}H COSY spectrum, H^c, H^b, and H^a are assigned to the triplet at δ = 7.86 ppm, the triplet of doublets at δ = 7.47 ppm, and the doublet of doublets at δ = 7.95 ppm, respectively. For the pendant phenyl ligand, the doublet at δ = 5.50 ppm is attributed to H^i, according to the nOe with the –OCH$_3$ singlet observed in the ^{1}H-^{1}H ROESY spectrum. The remaining aromatic protons were assigned primarily through ^{1}H-^{1}H COSY correlations: H^h resonates as a multiplet at δ = 6.83 ppm, H^g as a triplet of doublets at δ = 6.74 ppm, and H^f as a doublet of doublets at δ = 8.06 ppm. The porphyrin *meta* and *para* phenyl protons (in *meso* positions 10, 15, and 20) are all contributing to a multiplet at δ = 7.79 – 7.70 ppm, while the signals of the non-equivalent β-protons appear collapsed into two broad singlets (each integrating for four protons) at δ = 8.87 and δ = 8.84 ppm. Finally, the inner pyrrolic NH protons of the macrocycle resonate as a sightly broad singlet at δ = –2.68 ppm. The nature of **3** was confirmed by HRMS mass analysis (Figure 4.2.4).

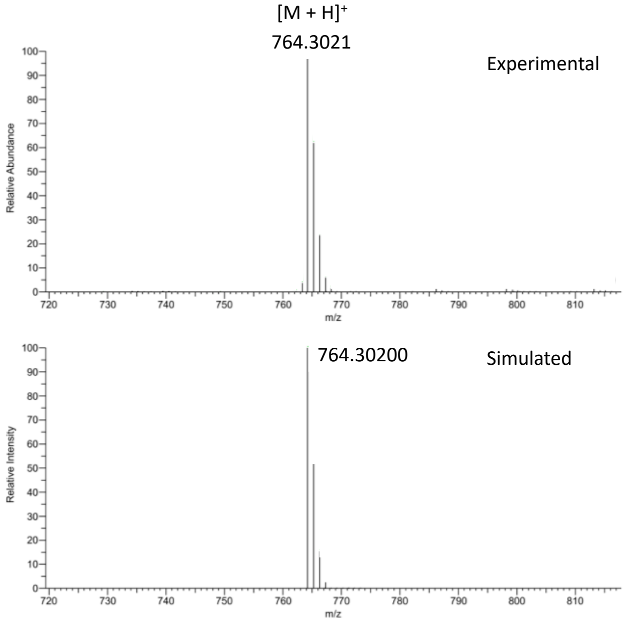

Figure 4.2.4. HRMS of **3** in CH$_3$OH, experimental (top) and simulated (bottom).

Compound **3** served as a precursor for the synthesis of derivative **TPP-*o*OHBA** (**4**). The reaction was done by adapting reported literature procedures. The hydrolysis of the methyl ether to give the phenol was achieved using boron tribromide as dealkylating agent, in dry CH$_2$Cl$_2$ under Ar atmosphere at low temperature as shown in Scheme 4.2.3.[40] **4** was isolated as a purple solid in 75% yield after purification by column chromatography. The ^{1}H NMR spectrum of **4** is reported in Figure 4.2.3, bottom.

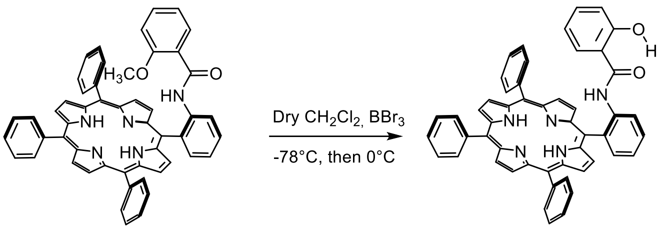

TPP-*o*MeOBA (3)

TPP-*o*OHBA (4)
Yield 75%

Scheme 4.2.3. Schematic representation of the synthesis of **TPP-*o*OHBA** (**4**).

The presence of a single set of signals indicates that only one species is present in solution. Full signal-proton assignments were done using 2D NMR experiments (^{1}H-^{1}H COSY; ^{1}H-^{13}C HSQC; ^{1}H-^{13}C HMBC; ^{1}H-^{1}H ROESY, Figure S14 – S17 in Appendix C). The signals integration and multiplicity confirmed the formation of the desired product. In particular, the effective hydrolysis of the methyl ether is confirmed by the disappearance of the $-OCH_3$ singlet and by the presence of a new singlet at $\delta = 11.71$ ppm, attributed to the –OH phenol proton (this assignment was done according to the absence of ^{1}J-coupling with carbon atoms in the ^{1}H-^{13}C HSQC spectrum, and the presence of an exchange cross peak with residual water in the ^{1}H-^{1}H ROESY spectrum, Figure S17 in Appendix C). The not resolved resonances at $\delta = 8.89 - 8.80$ ppm are assigned to the β-pyrrolic protons, partly overlapping with the doublet of H^{d}. Based on ^{1}H-^{1}H COSY correlations, the signals of the porphyrin aryl ring in *meso* position 5 are assigned as follows: the triplet at $\delta = 7.90$ ppm to H^{c}, the triplet of doublets at $\delta = 7.59$ ppm to H^{b}, and the doublet of doublets at $\delta = 8.14 - 8.08$ ppm to H^{a}, squeezed between the resonance of the –NH amide singlet and the broad doublet of two porphyrin *ortho* protons (likely the ones pointing upwards of the two phenyl rings in *meso* positions 10 and 15). The remaining *meta* and *para* protons of the porphyrin aryl rings resonate as a multiplet at $\delta = 7.84 - 7.70$ ppm, integrating for nine protons. For what concern the pendant moiety, the spatial correlation observed in the ^{1}H-^{1}H ROESY spectrum between the amide proton signal and the doublet of doublets at $\delta = 5.01$ ppm allows the assignment of the latter to H^{f}, thus also suggesting that the hydroxy ligand is oriented toward the outer side of the porphyrin macrocycle. Finally, based on the ^{1}H-^{1}H COSY correlations, the remaining aromatic protons of the pendant arm are assigned as follows: $\delta = 5.33$ ppm (H^{g}), $\delta = 6.74$ ppm (H^{h}), and $\delta = 6.58$ ppm (H^{i}). The chemical shift distribution of some signals further supports the just proposed orientation of the pendant 2-hydroxy-benzoylamide arm. In fact, the strong upfield shift observed for the signal of H^{f} compared to the same proton in **3** ($\Delta\delta = -3.06$ ppm), indicates that this proton resides above the shielding cone of the macrocycle. The downfield shift observed for the –OH singlet (compared to a free phenol, typically resonating around δ = 5 ppm values) is in line with the presence of an intramolecular hydrogen bond between this proton and the amide carbonyl group. In conclusion, **4** likely present the pendant aromatic residue flipped by 180 ° with respect to **3** (in the analysed conditions). The HRMS spectrum of **4** shows one main peak relative to the mono-cationic molecular ion (Figure 4.2.5).

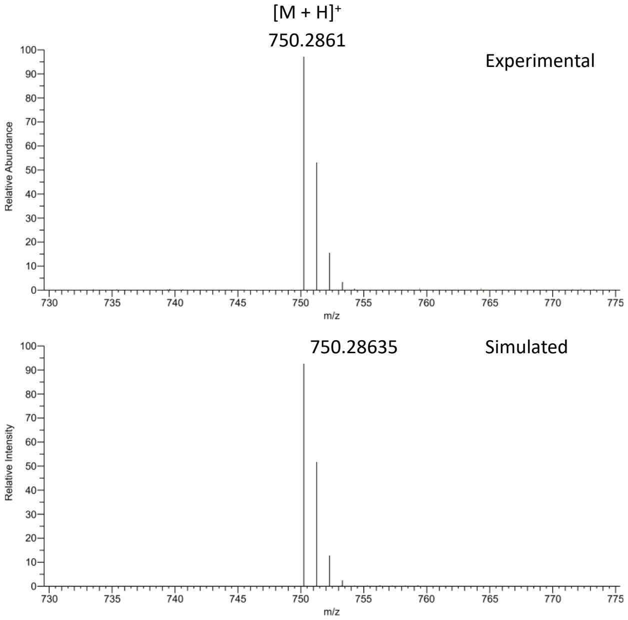

Figure 4.2.5. HRMS of **4** in CH_3OH, experimental (top) and simulated (bottom).

The UV-vis absorption and emission spectra of **2** – **4** shows the typical absorption profiles and intensities of a free-base tetraphenyl porphyrin (see below and Figure S18, Appendix C).

Free-base porphyrins **2** and **4** were metalated with $Co(CH_3COO)_2{\cdot}4H_2O$ using adapted literature procedures (Scheme 4.2.4, see also Experimental Part).[48]

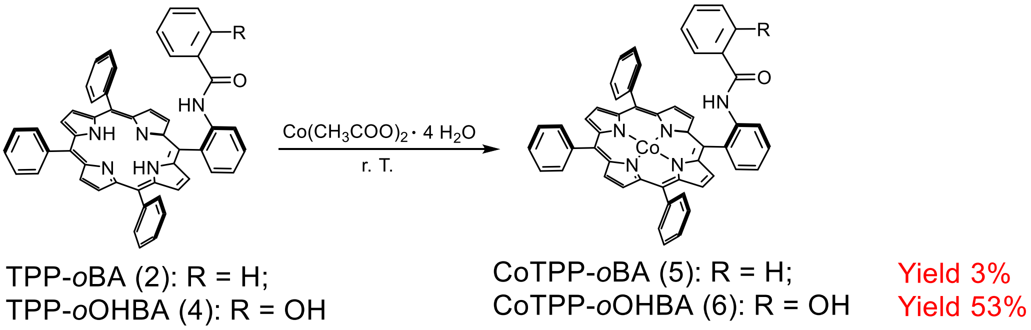

Scheme 4.2.4. Schematic representation of the preparation of **CoTPP-*o*BA** (**5**) and **CoTPP-*o*OHBA** (**6**).

Depending on the free-base precursors a different reactivity was observed. For **2** the reaction proceeded very slowly, yielding after 24h a mixture of free-base and Co^{II}-porphyrin, as confirmed by the UV-Vis absorption analysis and mass spectrometry (Figure S19 in Appendix

C). Few attempts were made to purify the reaction mixture by chromatography without success. A small amount of pure **5** was, for the moment, isolated by selective precipitation (see Experimental Section). In contrast, metalation of **4** proceeded much faster and efficiently, leading to full conversion within approximately 2h. A first fraction of pure **6** was isolated via precipitation from a chloroform/*n*-hexane solution. Due to the paramagnetic nature of **5** and **6** the in-solution NMR characterization is hampered for these derivatives. In-solution characterization was performed by UV-Vis absorption spectroscopy (Figure 4.2.6) and HRMS analysis (Figure 4.2.7). The four Q bands observed in the UV-Vis absorption spectra of the free-base porphyrin precursors (Figure S18 in Appendix C) collapse into one Q band upon metalation, while concomitantly the Soret band is blue shifted by 7 nm for **5** and **6** compared to **2** and **4**. These features confirm the successful metal insertion.

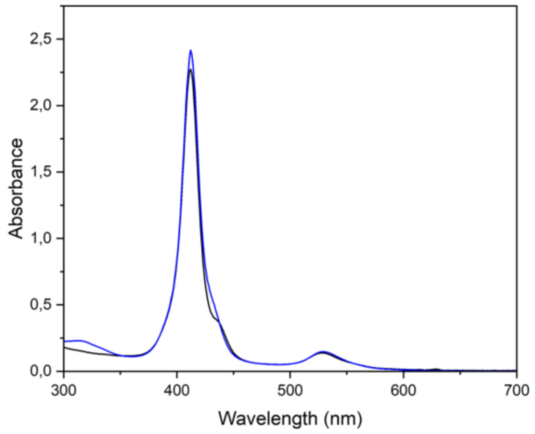

Figure 4.2.6. UV-Vis (CH_2Cl_2, 25 μM) absorption spectra. **5** and **6** (black and blue traces respectively).

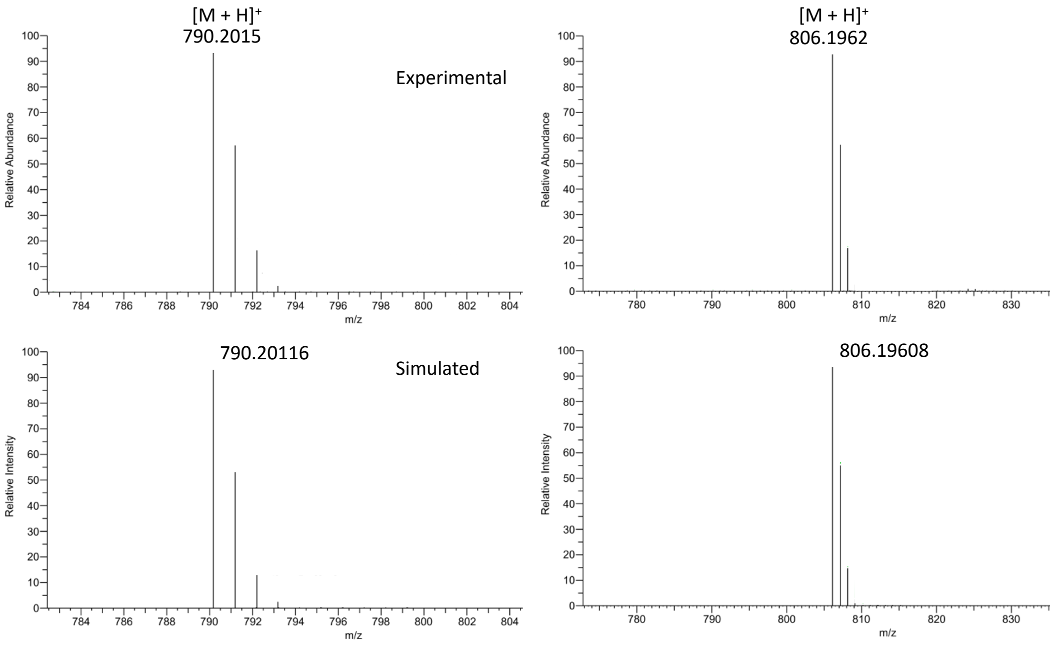

Figure 4.2.7. HRMS of **5** (left) and **6** (right) in CH_3OH, experimental (top) and simulated (bottom).

4.2.2. IR-Vis SFG characterization.

ESIBD deposition, as well as the characterization *via* IR-Vis SFG in UHV conditions was done by the group of Prof. Erik Vesselli (Department of Physics, University of Trieste, Italy). Here, the IR-Vis SFG spectra of **2** – **4** layers grown on Gr/Ir(111) will be briefly discussed. The spectral regions in which the resonances have been registered are the following: 1050 – 1380 cm^{-1}, 1400 – 1700 cm^{-1}, 2740 – 3130 cm^{-1} and 3300 – 3400 cm^{-1} and will be compared to those of the model **TPP** layer, described in the Introduction. The aim is to characterize the vibrational fingerprints of the differently functionalized benzamide moiety for each compound. The resonance peaks assignment was done by comparison with experimental and theoretical IR and Raman spectra of benzamide derivatives reported in the literature.[22,49–52] The IR-Vis SFG spectra of **2** – **4** sub-monolayers deposited on Gr/Ir(111), collected at room temperature, are reported in Figures 4.2.8, 4.2.9 and 4.2.10 respectively. All spectra indicate the successful deposition of the free-base porphyrins on the desired substrate.

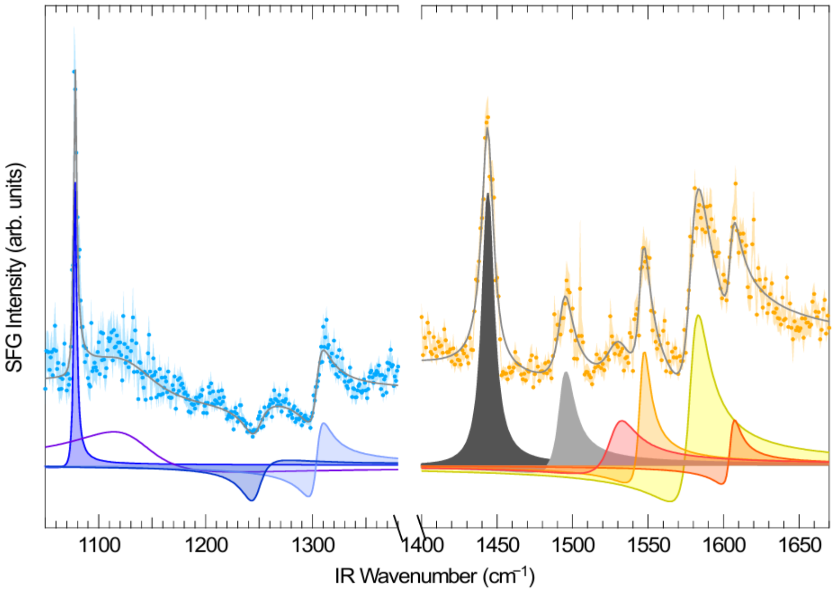

Figure 4.2.8. IR-Vis SFG spectra in the 1050 – 1380 and 1400 – 1700 cm^{-1} regions, together with the fit and deconvolution spectral components of **2**/Gr/Ir(111) at sub-monolayer coverage. The spectra were acquired in *ppp* polarization configuration. Resonances of the benzamide moiety are colored in black and grey.

TPP-*o*BA (**2**) displays a very similar IR-Vis SFG spectra to that of **TPP**/Gr/Ir(111) in the 1050 – 1380 cm^{-1} region (Figure 4.1.2), despite some slight band shifts, attributable to the presence of the benzamide moiety that affects the electronic structure and geometric conformation of the macrocycle. In the 1400 – 1700 cm^{-1} region, two new resonances (1444 cm^{-1} and 1494 cm^{-1}) were observed, assigned respectively to the stretching of the C–C bonds within the phenyl ring of the functionalized benzamide moiety and to the in-plane bending of the C–H bonds. Thus, these two resonances (respectively colored in black and grey in Figure 4.2.8) may constitute a vibrational fingerprint of the conjugated pendant ligand.

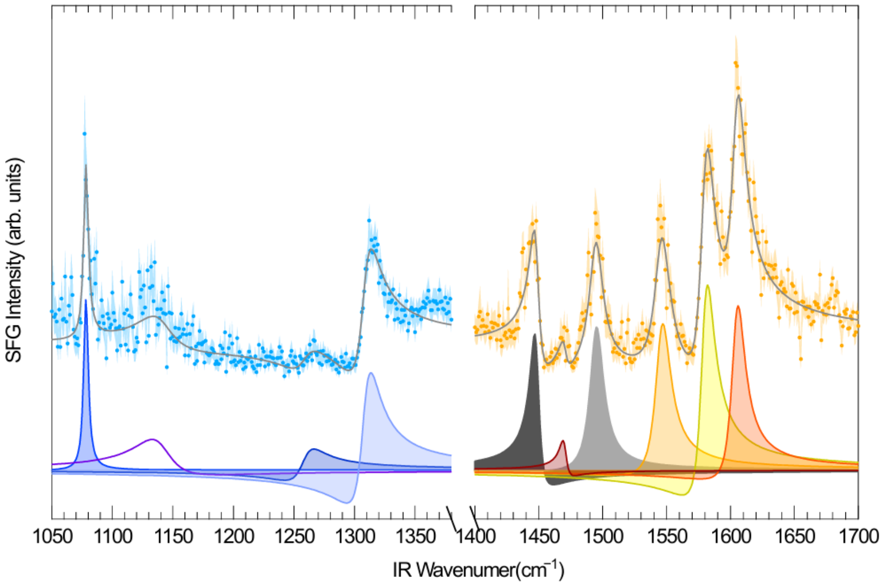

Figure 4.2.9. IR-Vis SFG spectra in the 1050 – 1380 and 1400 – 1700 cm^{-1} regions, together with the fit and deconvolution spectral components of **3**/Gr/Ir(111) at sub-monolayer coverage. The spectra were acquired in *ppp* polarization configuration. Resonances of the benzamide moiety are colored in black and grey.

The IR-Vis SFG spectra of **TPP-*o*MeOBA** (**3**) (Figure 4.2.9) show a different intensity ratio between the spectral components observed for **2**. These variations are accompanied by a phase shift attributed to a different charge transfer between **3** and the surface substrate. The two resonances attributed to the benzamide moiety are slightly shifted compared to **2** (1448 *vs.* 1444 cm^{-1} and 1495 *vs.* 1494 cm^{-1}). A phase shift of ~60° was observed for the component at 1448 cm^{-1}. The two benzamide resonances are again colored black and grey in Figure 4.2.9.

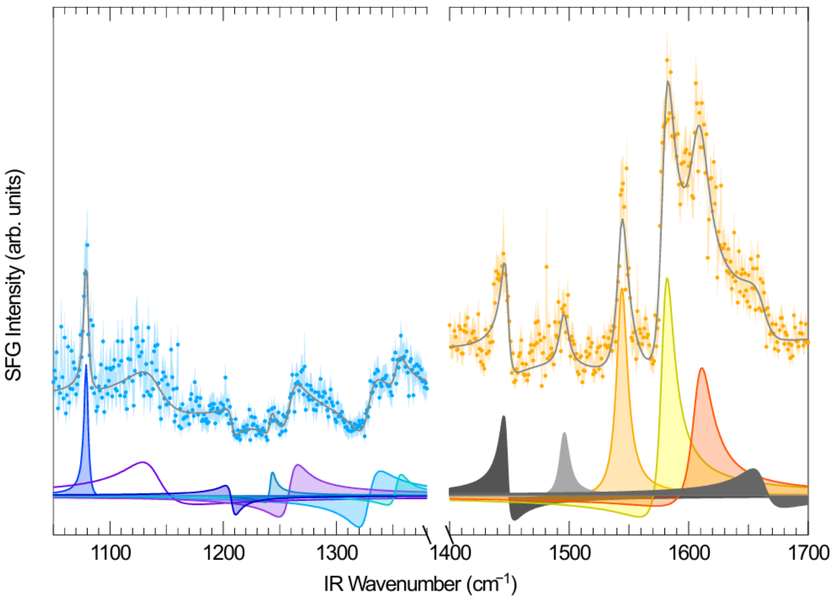

Figure 4.2.10. IR-Vis SFG spectra in the 1050 – 1380 and 1400 – 1700 cm^{-1} regions, together with the fit and deconvolution spectral components of **4**/Gr/Ir(111) at sub-monolayer coverage. The spectra were acquired in *ppp* polarization configuration. Resonances of the benzamide moiety are colored in black and grey.

The IR-Vis SFG spectra of **TPP-*o*OHBA** (**4**) (Figure 4.2.10) showed, besides the common components present in the IR-Vis SFG spectra of **2** and **3**, new components arising in the 1200 – 1380 cm^{-1} region. The resonance at 1208 cm^{-1} is attributed to the rocking of N–H bonds within the macrocycle and the benzamide moiety. Additionally, the features at 1328 and 1354 cm^{-1} are associated to symmetric stretching and bending modes of the pyrrole rings. The 1400 – 1700 cm^{-1} region presents the same bands observed for **2** and **3**, in which the different phases and intensity ratios are assigned, again, to a different charge transfer between **4** and the substrate. The spectrum of **4** presents an additional resonance at 1662 cm^{-1}, assigned to the stretching mode of the carbonyl group of the amide group. In the 2740 – 3130 and 3300 – 3400 cm^{-1} regions, the IR-Vis SFG spectra of **2** – **4** share the same features, apart from small band shifts of the order of a few cm^{-1}. As an example, the IR-Vis SFG spectra of **2** (Figure 4.2.11) will be here discussed. Resonances were also assigned by comparison with the IR-Vis SFG spectra of **TPP** on Gr/Ir(111), reported in the Section 4.1. The region 2740 – 3130 cm^{-1} is dominated by the stretching modes of the C–H bonds due to the co-presence of ethanol molecules, which did not desorb completely upon the electrospray deposition. In the 3300 – 3400 cm^{-1} region, the resonances are attributed to the stretching of the N–H bonds within the macrocycle with a contribution from the same vibrational modes within the benzamide moiety.

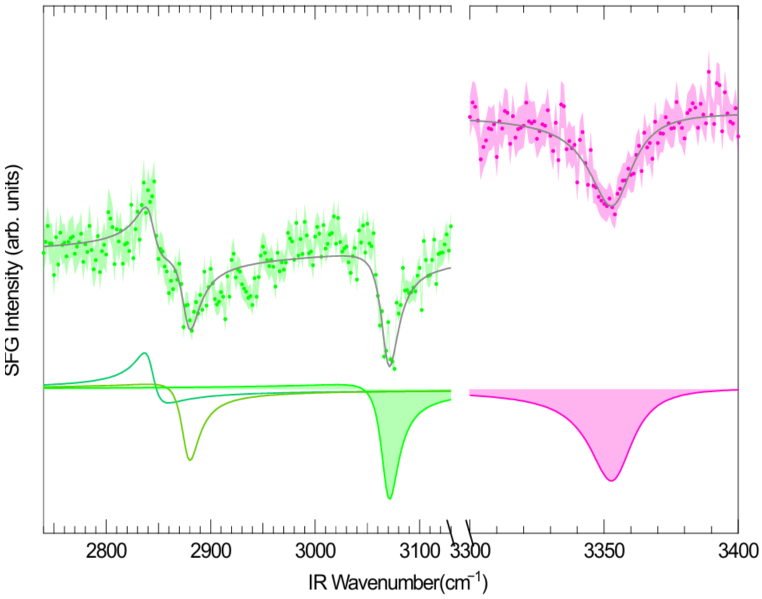

Figure 4.2.11. IR-Vis SFG spectra in the 2740 – 3130 and 3300 – 3400 cm^{-1} regions, together with the fit and deconvolution spectral components of **2**/Gr/Ir(111) at sub-monolayer coverage. The spectra were acquired in *ppp* polarization configuration.

Temperature stability of each molecular layer was determined by acquiring the IR-Vis SFG spectra after annealing of the **2**/Gr/Ir(111), **3**/Gr/Ir(111) and **4**/Gr/Ir(111) samples (Figures S20 – S25 in Appendix C). For **2**, temperature stability was investigated by stepwise annealing, heating the sample to 375, 425, 475, 525, and 600 K. The analysis showed that the effect of heating the sample up to 475 K is both that of ordering of the molecular layer (suggested by the increased intensity of most of the vibrational resonances), and that of reorienting the molecules over the surface substrate (observed by the change in the intensity ratio of the resonances attributed to the macrocycle and the phenyl rings attached to it).[22] Heating the samples above 475 K leads to competing fragmentation and desorption processes, likely accompanied by a disordering of the molecular layer induced by the thermal annealing. This hypothesis is supported by the disappearance of the vibrational bands when reaching 600 K. It should be mentioned that for all the tested free-base porphyrins, resonances attributed to the benzamide moiety are still present after annealing at 475 K, suggesting thermal stability of the amidic bond up to these temperatures. Since **2** is stable up to 475 K, **3** and **4** have been annealed to 425 K, to promote ordering and reorientation of the molecules, along with solvent evaporation, without compromising their integrity. As found for **2**, it was seen that annealing at 425 K of **3**/Gr/Ir(111) and **4**/Gr/Ir(111) led to a more ordered structure due to diffusion and molecular reorientation. In addition, a dramatic increase in the intensity of the vibrational bands was observed after a second annealing of **4**, showing that the different benzamide residues change some of the properties of the molecule. Finally, some considerations about IR-Vis SFG spectra of **4**/Gr/Ir(111) will be made. It was seen that, after exposure of the sample to 6×10^{-9} mbar of water, a slight increase in the spectral intensity was detected (Figure 4.2.12), suggesting that water exposure induces the assembling into a more ordered phase of the adsorbed molecules. The hypothesis is that some H_2O molecules bind the terminal –OH group of **4** *via* formation of H-bonds. If the hypothesis is correct, this would imply the presence of some constraints on the possible orientations that both the macrocycle and the pendant benzamide moiety can assume with respect to the surface, thus leading to an increase in the IR-Vis SFG response of the layer.

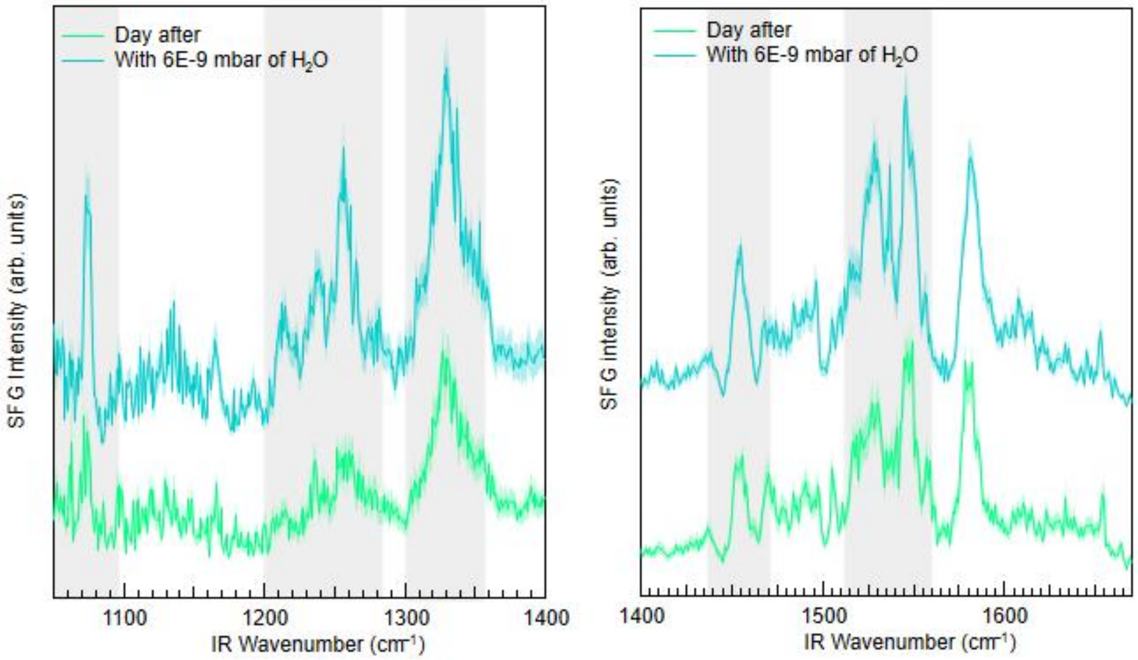

Figure 4.2.12. Normalized IR-Vis SFG spectra in the 1050 – 1380 cm^{-1} (left) and 1050 – 1380 cm^{-1} (right) regions for the **4**/Gr/Ir(111) layer the day after the first annealing at 455 K and while exposing the sample to 6×10^{-9} mbar of H_2O (green and blue traces respectively). All the spectra were acquired in *ppp* polarization configuration.

4.2.3. STM characterization.

STM imaging was done in collaboration with Dr. Kelvin Anggara from the Max Planck Institute for Solid State Research in Stuttgart (Germany). **TPP-*o*BA** (**2**) or **TPP-*o*OHBA** (**4**) have been deposited on a Au(111) surface using an electrospray source coupled with a mass selector. This laboratory is one of the rare facilities equipped with such an integrated setup. This setup allows for the fine selection of the *m/z* ratio of the molecules to be deposited on the surface, enabling the precise deposition of the desired species with a high degree of accuracy, even in the presence of very minor amounts of impurities (for instance deriving form electrospray fragmentation).

Additionally, when probing highly mobile molecules adsorbed on surfaces, as in the case of porphyrins, it is necessary to cool the sample down to the liquid He temperature to minimize the thermal drift of the adsorbates over time-scaled comparable with the characteristic STM acquisition times. Figure 4.2.13 shows the STM image of a sub-monolayer of **2** molecules deposited on Au(111). The images were acquired in constant-current mode at 11 K. Figure 4.2.13 shows that molecules do not form large-scale ordered islands. Instead, they dimerize in a planar configuration, with the synthetic benzamide moieties of neighbouring molecules standing on top in a "handshake" configuration, suggesting a specific interaction of the pendant ligands. Two different dimer configurations are observed: in one, the benzamide moieties of each molecule faces directly toward each other as shown in Figure 4.2.13 right and by the dimer circled in blue in Figure 4.2.13 middle. In the other, the molecules are offset, with their pendant ligands displaced relative to one another, as shown by the dimer circled in yellow in Figure 4.2.13 middle.

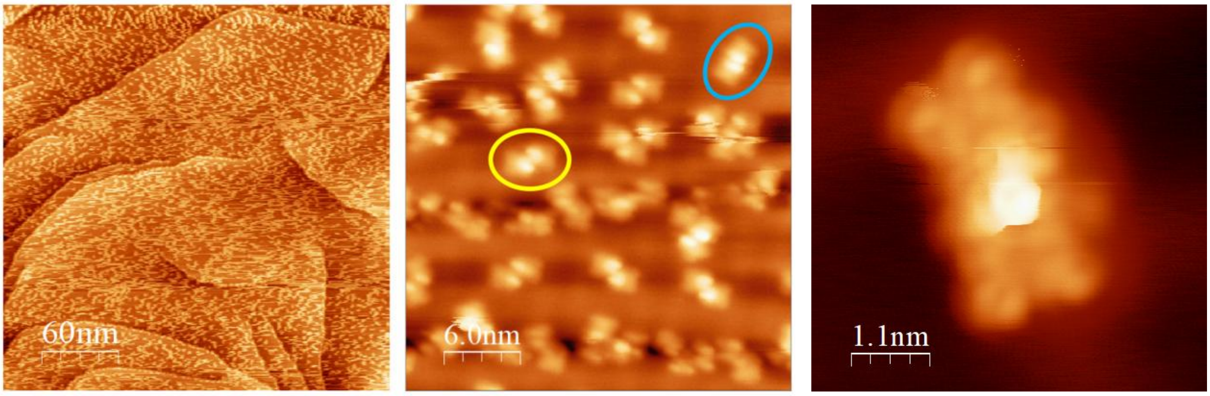

Figure 4.2.13. STM images of **TPP-*o*BA** (**2**)/Au(111), collected in constant-current mode at T = 11 K, V = 20 mV, I = 0.3 pA.

TPP-*o*OHBA (**4**) was also characterized by STM after ESIBD deposition on Au(111) surface and characterized using same conditions described above (Figure 4.2.14). For **4** a lower coverage compared to **2** was observed. As already seen for **2**, also **4** do not form large-scale ordered islands. In place both dimers (yellow circle in Figure 4.2.14) and trimers (blue circle in Figure 4.2.14) with the phenol ligand of neighboring molecules in a "handshake" configuration. Dimers are found to be more mobile compared to trimers, thus making their imaging more challenging. The differences in the STM images of **2** and **4** deposited on Au(111) indicate that the presence of the phenol substituent is certainly crucial in the distinct type of surface ordering observed for the two derivatives. Deposition of the cobalt-porphyrin **CoTPP-*o*BA** (**5**) and **CoTPP-*o*OHBA** (**6**) on Au(111) is in current progress.

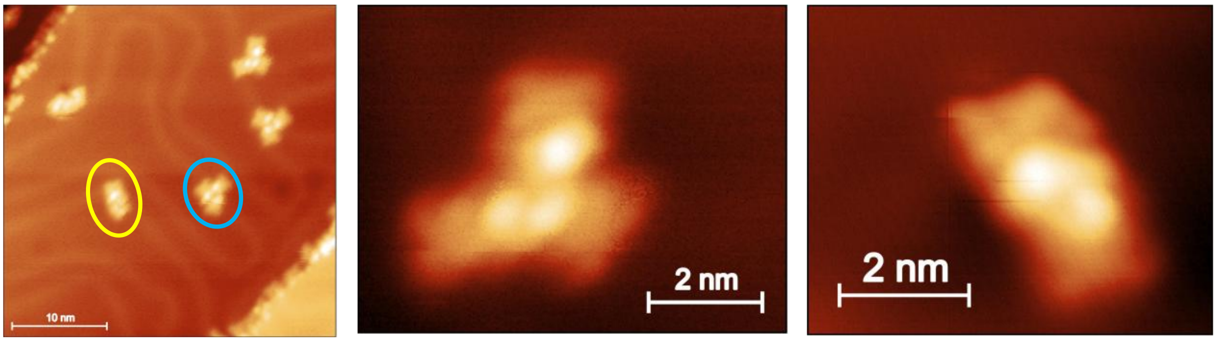

Figure 4.2.14. STM images of **TPP-*o*OHBA** (**4**)/Au(111), collected in constant-current mode at T = 11 K, V = 1.5 V, I = 0.1 pA.

4.3. Conclusions and future perspectives.

In this Chapter, three new benzamide *ortho*-functionalized porphyrins (**2** – **4**), and two Co^{II}-porphyrins corresponding derivatives (**5** and **6**) were successfully synthesized and comprehensively characterized with the aim of exploiting the pendant ligand as mimic of enzymes second coordination sphere. The presence of a substituent orthogonal to the porphyrin macrocycle should influence the molecular structure, surface organization and reactivity of the derived 2D-MONs. For **2** – **4** the presence of the benzamide moiety on the top of the porphyrin macrocycle was confirmed by 1D and 2D NMR analysis, with a different orientation of the pendant phenyl found for the two derivatives - in **3** the $-OCH_3$ group is positioned on the top of the porphyrin core, while in **4** the –OH group is facing the external part of the macrocycle. **2** – **4** were then deposited on a Gr/Ir(111) surface by electrospray deposition in collaboration with the group of Prof. Erik Vesselli (Department of Physics, University of Trieste, IT). Each of the porphyrin was deposited at room temperature under UHV conditions by ESIBD. Following deposition, the obtained layers were characterized by IR-Vis SFG spectroscopy, also after annealing at different temperatures to study their thermal stability. The first interesting result is the efficient deposition of **2** – **4**, as evident from the different vibrational bands observed for the pristine samples at characteristic wavenumber regions. The second promising result was the detection of vibrational fingerprints attributed to the pendant benzamide ligand for each compound. In all cases thermal annealing induces reorientation of the molecules over the surface substrate and reorganization of the layer. Above 475 K desorption and partial fragmentation processes were observed. Importantly, vibrational features associated with the pendant arm were detected up to 475 K, indicating remarkable thermal robustness. For compound **4**, exposure to water resulted in a certain enhancement of spectral intensity, suggesting a water-induced supramolecular ordering, probably occurring with the formation a network of H-bonds. Further investigations with the use of complementary techniques (*e.g.* NEXAFS, XPS) are required to understand this phenomenon. Additionally, for **2** and **4** real-space characterization was also done by STM imaging in collaboration with the group of Dr. Kelvin Anggara (Max Planck Institute for Solid State Research, Stuttgart, DE). **2** and **4** were successfully deposited on Au(111) by ESIBD. In both cases it was seen that the molecules organize on the surface without forming large islands. Instead, the molecules form dimers (both for **2** and **4**) or trimers (for **4**) by interaction between their pendant benzamide moieties. Ligands of a neighbouring molecules, placed on top of the porphyrin cores, interact with each other in a "handshake" manner. Current efforts are devoted to the surface deposition, and characterization by IR-Vis SFG and STM, of the two Co^{II}-porphyrins (**5** and **6**), followed by studies on the catalytic reactivity of the layers by exposure to O_2, CO, CO_2 and H_2O in UHV. Very soon a characterization of the geometry of some of the 2D-MONs on Gr/Ir(111) will be done by XPS and NEXAFS at the dedicated beamline of the MAX IV Synchrotron facility of Lund (Sweden). Possibility to obtain additional beamtime at the same Synchrotron facility to explore the reactivity of the cobalt-porphyrin layers at NAP conditions is also programmed.

4.4. Experimental Section.

Materials and reagents:

All reagents were obtained from commercial sources and used without further purification, unless otherwise stated. Deuterated solvents $CDCl_3$ and dmso-d_6 were purchased from *Sigma-Aldrich* while CD_2Cl_2 from *Cambridge Isotope Laboratories* (CIL). Silica Gel (*Supelco*, pore size 60 Å, mesh 230-400) was used for the chromatographic purification of the porphyrins. **TPP-*o*NH$_2$**, **1**, was synthesized and purified as described in literature.[38] The Porphyrin conjugates **2-4** were obtained by adapted literature procedures, se below.[40,41]

Instrumentation:

NMR. 1D and 2D experiments (^{1}H; ^{1}H-^{1}H COSY; ^{1}H-^{13}C HSQC; ^{1}H-^{13}C HMBC; ^{1}H-^{1}H ROESY) were recorded on a *Varian Inova* 500 spectrometer at 25 °C unless otherwise indicated. Varian 500 operates at 500 MHz (^{1}H), 126 MHz (^{13}C). Resonances are expressed in ppm (δ) and are referenced to the peak of the residual non-deuterated solvents: δ=7.26 ppm (^{1}H) and 77.16 ppm (^{13}C) for $CDCl_3$; 2.50 ppm (^{1}H) and 39.52 ppm (^{13}C) for dmso-d_6; 5.32 ppm (^{1}H) and 53.84 ppm (^{13}C) for CD_2Cl_2. Processing was done using MestreNova© program. Multiplicity of the signals is expressed as follows: s = singlet; d = doublet; t = triplet; m =

multiplet; dd = doublet of doublets; td = triplet of doublets; br. s = broad signal; ddd = doublet of doublets of doublets.

UV-Vis Absorption Spectroscopy. All absorption spectra were recorded in CH_2Cl_2. The spectra were recorded at room temperature using standard 3 mL quartz cuvette (light path: 1 cm) and an Agilent Technologies spectrophotometer.

Emission Spectroscopy. Photoluminescence spectra were recorded in CH_2Cl_2. The spectra were recorded at 298K using standard 3 mL quartz cuvette (light path: 1 cm) and a Varian Cary Eclipse Fluorescence Spectrophotometer equipped with a Cary Single Cell Peltier Accessory for temperature control. All reported emission spectra have been corrected for the wavelength dependent phototube response.

Mass Spectrometry. Electrospray ionization mass spectrometry (ESI-MS) measurements were performed always starting from a 1 mg/mL $CHCl_3$ solution of each compound, then diluted 100 times in CH_3OH. Experiments were performed using an electrospray ionization (ESI) source and a Thermo Scientific Orbitrap Exploris 250 Instrument by Dr. Fabio Hollan, Department of Chemical and Pharmaceutical Sciences, University of Trieste (IT).

SFG. SFG measurements have been done at the Visible and Infrared Spectroscopy Laboratory by the group of Prof. Erik Vesselli (VISPLab, Department of Physics, University of Trieste (IT)). Measurements were done via a customized SFG Spectrometer purchased from the Lithuanian laser manufacturing company EKSPLA. Samples were prepared in a UHV chamber and SFG spectra were acquired in a high-pressure cell (although all the following experiments have been done in UHV). The UHV chamber and the high-pressure cell communicate through a gate valve. Pulsed laser radiation was used to reach the high intensities required for the SFG technique. The setup consists of a green laser beam at 532 nm and a tunable infrared beam in the range ~2300-10000 nm. The signals are generated from the 1064 nm fundamental of the laser, and they overlap in space and time at the sample's surface, generating the SFG signal. Its intensity is measured by a photomultiplier as a function of the infrared beam wavenumber, in cm^{-1}. A class IV PL2230 Series Laser is used to generate the fundamental infrared pulsed radiation at 1064 nm. The pulses are 28 ± 3 ps long with a repetition rate of 50 Hz and a maximum pulse energy of 25 mJ. The peak power of the fundamental radiation is ~1 GW and the mean power is ~1.25 W. The beam diameter is ~6 mm, with a beam divergence < 0.7 mrad. Harmonic Unit SFGH500-H/2H is employed to convert the fundamental radiation of PL2230 laser into the second harmonic radiation at 532 nm.

ESIBD (Electrospray Ionization Beam Deposition). The ESIBD setup used at VISPLab in Trieste consists of a UHV-4i modular electrospray deposition source purchased from Molecularspray Ltd., a syringe pump purchased from Molecularspray Ltd., a MV5 high-voltage power supply and a stainless steel 1 m long arm which connects the electrospray source to the UHV preparation chamber. The solution to be deposited is contained in a 10 ml syringe, placed on the syringe pump. The liquid is transported from the syringe barrel to the electrospray head by a polymer tubing. A nonconducting PEEK microtee ensures safe delivery of the high voltage directly to the liquid, which passes through the electrospray head to the emitter. The emitter is a stainless-steel metal tip with an internal diameter of 30 μm, and it is held in the microtee through a microtight sleeve. The entrance capillary is a 5 cm long stainless-steel capillary with an internal diameter of 0.25 mm, and it can be eventually heated by a heater mounted internally on the vacuum side of the entrance flange, to aid the evaporation of the remaining solvent as the ESI droplets travel into the vacuum system. The spot size of the jet at 20 cm from the exit aperture is specified by the manufacturer to be ~2 mm. The spot size at the sample is estimated to be ~4 - 6 mm. The stability of the jet can be monitored by looking at the pressure measured before being deposited. The ion current reaching the main chamber was measured by a gold flag placed below the sample. Its intensity can be used as a measure of the molecular flux reaching the sample, while the time-integrated charge represents an estimation of the deposited quantity of molecules.

ESIBD-STM. The ESIBD setup at the Max Planck Institute for Solid State Research in Stuttgart consists of four main parts: i) electrospray ionization; ii) mass selection; iii) soft landing deposition; iv) STM. For the ESIBD, a glass emitter of ~1 − 2 μm diameter was used. The solution was pumped by a back-pressure at pumping rates on the order of μL/hr. The emitter is coated with Pt to deliver the high voltage to the conducting solution. For an emitter of a few μm of aperture, typical voltages are ∼ 0.5 − 1.5 kV. An ion funnel is employed to collect all the ions at the exit of the inlet capillary without losing flux, as is the case when using skimmer cones, allowing to reach ion currents of ∼ 10^2 pA. Mass selection was done through two quadrupole mass selectors. Mass selection results were analysed through an orthogonal extraction linear Time Of Flight Mass Spectrometer (TOF-MS). Soft landing deposition was achieved by applying a retarding potential to the surface to decelerate the incoming ions as their kinetic energy is transformed into electrostatic potential. ESIBD apparatus is coupled to a Omicrom Fermi SPM from ScientaOmicron operating at 15 – 400 K, under ultra-high vacuum conditions (~10^{-10} mbar). Low temperatures were obtained by cooling down the sample through liquid He cryostat.

Synthesis.

TPP-*o*NH$_2$ (1):

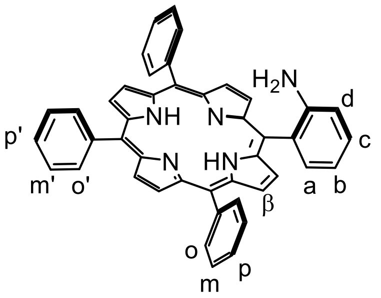

2-nitrobenzaldeide (7.56 g, 50.0 mmol, 1.00 eq) and benzaldehyde (5.31 g, 50.0 mmol, 1.00 eq) were dissolved in 200 mL of propionic acid at 80 °C. The solution was stirred for 10 min before adding pyrrole dropwise (6.71g, 100 mmol, 2.00 eq). The reaction mixture was kept under stirring at 145 °C for 2h. After cooling to room temperature, 100 mL of cold CH_3OH were added and the mixture of nitro-porphyrin regioisomers was collected as a purple solid by filtration. The collected product was used for the next synthetic step without further purification. 250.0 mg of the porphyrin mixture were dissolved in 20.0 mL of concentrated HCl under Ar atmosphere and the solution was heated at 65 °C. $SnCl_2 \cdot 2H_2O$ (512 mg, 2.27 mmol) was added and the reaction mixture was allowed to react under stirring for 3h protected from light. After cooling to room temperature, the mixture was neutralized to pH 8 with 6 M KOH, followed by extraction with $CHCl_3$. The organic layer was dried over anhydrous Na_2SO_4 and purified by column chromatography (silica, CH_2Cl_2:*n*-hexane 9:1, the desired product is collected as second eluted band). Yield: 95.4 mg (40%).

^{1}H NMR (δ, 500 MHz, $CDCl_3$): 8.91 – 8.85 ppm (m, 8H, H^{β}), 8.21 ppm (d, J = 7.5 Hz, 6H, H^{o}, $H^{o'}$), 7.89 ppm (dd, J = 7.4, 1.5 Hz, 1H, H^{a}), 7.82 – 7.71 ppm (m, 9H, H^{m}, $H^{m'}$, H^{p}, $H^{p'}$), 7.64 – 7.57 ppm (m, 1H, H^{c}), 7.18 ppm (td, J = 7.4, 1.2 Hz, 1H, H^{b}), 7.15 – 7.10 ppm (m, 1H, H^{d}), 3.55 ppm (s, 2H, NH_2), −2.74 ppm (s, 2H, $NH^{porphyrin}$). ^{13}C from ^{1}H-^{13}C HSQC (δ, 126 MHz, $CDCl_3$): 134.5 ppm (C^{d}), 134.2 ppm (C^{o}, $C^{o'}$), 129.3 ppm (C^{c}), 127.4 – 126.4 ppm (C^{m}, $C^{m'}$, C^{p}, $C^{p'}$), 117.2 ppm (C^{b}), 114.2 ppm (C^{b}).

TPP-*o*BA (2):

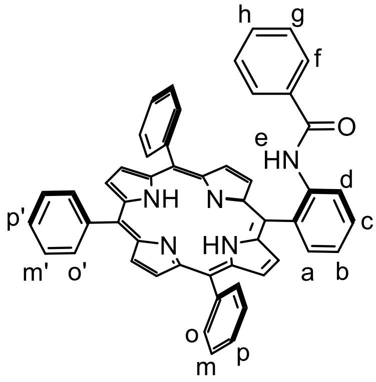

TPP-*o*NH$_2$ (**1**) (40.0mg, 0.0635 mmol, 1.00 eq) was dissolved in distilled CH_2Cl_2 in an oven-dried flask under Ar atmosphere. Triethylamine (18.0 μL, 2.00 eq) was added followed by addition of benzoyl chloride (7.50 μL, 1.00 eq). The solution was heated at 40 °C under stirring and monitored by TLC (silica gel, CH_2Cl_2:*n*-hexane 8:2). After 20h the organic phase was extracted with distilled water (3 ×10 mL), dried over anhydrous Na_2SO_4 and purified by column chromatography (silica, CH_2Cl_2:*n*-hexane 9:1, the desired product is collected as second eluted band). Yield 34.5 mg (74%).

^{1}H NMR (δ, 500 MHz, $CDCl_3$): 8.98 ppm (d, *J* = 8.5 Hz, 1H, H^d), 8.86 ppm (m, 8H, H^{β}), 8.21 ppm (br. s, 4H, H^o, $H^{o'}$), 8.14 ppm (br. s, *J* = 7.4 Hz, 2H, H^o, $H^{o'}$), 8.07 ppm (d, *J* = 7.4 Hz, 1H, H^a), 7.89 ppm (t, *J* = 8.0 Hz, 1H, H^c), 7.85 – 7.65 ppm (m, 9H, H^m, $H^{m'}$, H^p, $H^{p'}$), 7.56 ppm (t, *J* = 7.5 Hz, 1H, H^b), 6.82 ppm (t, *J* = 7.2 Hz, 1H, H^h), 6.54 – 6.48 ppm (m, 4H, H^f, H^g), –2.70 ppm (s, 2H, $NH^{porphyrin}$). ^{13}C from ^{1}H-^{13}C HSQC (δ, 126 MHz, $CDCl_3$): 134.9 ppm (C^a), 134.5 ppm (C^o, $C^{o'}$), 130.9 ppm (C^f), 129.7 ppm (C^c), 127.9 – 126.1 ppm (C^g, C^h), 127.8 – 126.7 ppm (C^m, $C^{m'}$, C^p, $C^{p'}$), 122.9 ppm (C^b), 120.5 ppm (C^d). ^{1}H NMR (δ, 500 MHz, dmso-d_6): 9.53 ppm (s, 1H, NH^e), 8.89 – 8.75 ppm (m, 8H, H^{β}), 8.22 – 7.70 ppm (m, 19H, H^o, $H^{o'}$, H^a, H^c, H^m, $H^{m'}$, H^p, $H^{p'}$, H^b), 6.97 – 6.94 ppm (m, 1H, H^h), 6.73 – 6.66 ppm (m, 4H, H^f, H^g), –2.88 ppm (s, 2H, $NH^{porphyrin}$). ^{13}C from ^{1}H-^{13}C HSQC (δ, 126 MHz, dmso-d_6): 135.5 – 124.4 ppm (C^o, $C^{o'}$, C^h, C^c, C^m, $C^{m'}$, C^p, $C^{p'}$, C^b), 130.4 ppm (C^h), 127.1 – 126.8 ppm (C^f, C^g). UV–Vis (λ_{max}, nm, CH_2Cl_2): 419, 516, 549, 589, 646. ESI-MS: (*m/z*) (positive mode) for $C_{51}H_{37}N_5O$ $[M + 2H]^{2+}$ calculated 367.6493 found 367.6490; for $C_{51}H_{36}N_5O$ $[M + H]^+$ calculated 734.2911 found 734.2910.

TPP-*o*MeOBA (**3**):

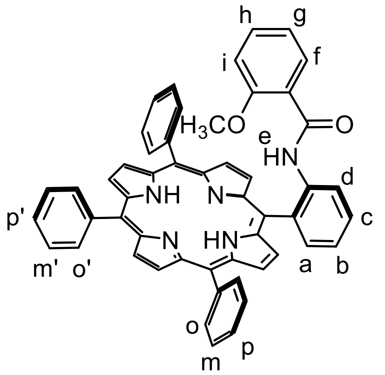

TPP-*o*NH$_2$ (**1**) (80.0 mg, 0.127 mmol, 1.00 eq) was dissolved in distilled CH_2Cl_2 in an oven-dried flask under Ar atmosphere. Triethylamine (17.6 µL, 1.00 eq) was added followed by addition of 2-metoxybenzoyl chloride (9.4 µL, 0.50 eq). The solution was heated to 40 °C under stirring and the reaction was monitored by TLC (silica gel, CH_2Cl_2:*n*-hexane 9:1). After 2 h a second portion of triethylamine (17.6 µL, 1.00 eq) and 2-metoxybenzoyl chloride (9.4 µL, 0.50 eq) was added. After 2 h the reaction mixture was cooled to room temperature and the organic phase was washed with distilled water (3×10 mL), dried over anhydrous Na_2SO_4 and purified by column chromatography (silica, CH_2Cl_2:*n*-hexane 9:1, the desired product is collected as second eluted band). Yield 75.7 mg (78%).

^{1}H NMR (δ, 500 MHz, $CDCl_3$): 9.74 ppm (s, 1H, NH^e), 9.12 ppm (d, J = 8.0 Hz, 1H, H^d), 8.85 ppm (m, 8H, H$^\beta$), 8.27 – 8.13 ppm (m, 6H, H^o, H$^{o'}$), 8.06 ppm (dd, J = 8.0, 1.9 Hz, 1H, H^f), 7.95 ppm (dd, J = 7.5, 1.6 Hz, 1H, H^a), 7.86 ppm (t, J = 7.1 Hz, 1H, H^c), 7.79 – 7.70 ppm (m, 9H, H^m, H$^{m'}$, H^p, H$^{p'}$), 7.47 ppm (td, J = 7.5, 1.2 Hz, 1H, H^b), 6.83 ppm (td, J = 7.1, 1.8 Hz, 1H, H^h), 6.74 ppm (td, J = 7.1, 1.0 Hz, 1H, H^d), 5.50 ppm (d, J = 8.8 Hz, 1H, H^i), −0.16 ppm (s, 3H, OCH_3), −2.68 ppm (s, 2H, NH^{porphyrin}). ^{13}C from ^{1}H-^{13}C HSQC (δ, 126 MHz, $CDCl_3$): 134.7 ppm (C^a), 134.5 – 134.3 ppm (C^o, C$^{o'}$), 132.4 ppm (C^h), 132.0 ppm (C^f), 129.5 ppm (C^c), 128.0 – 126.5 ppm (C^m, C$^{m'}$, C^p, C$^{p'}$), 122.2 ppm (C^b), 120.9 ppm (C^d), 110.1 ppm (C^i), 52.9 ppm (OCH_3). UV–Vis (λ_{max}, nm, CH_2Cl_2): 419, 514, 548, 589, 644. ESI-MS: (*m/z*) (positive mode) for $C_{52}H_{38}N_5O_2$ [M + H]$^+$ calculated 764.30200 found 764.3021.

TPP-*o*OHBA (4):

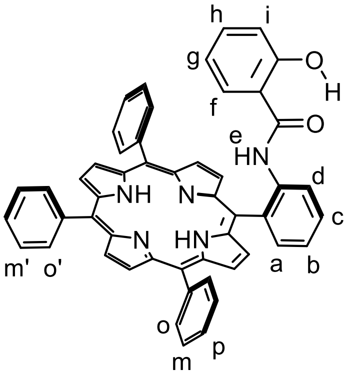

TPP-*o*NH₂ (**1**) (40.0 mg, 0.052 mmol, 1.00 eq) was dissolved in anhydrous CH_2Cl_2 in an oven-dried flask under Ar atmosphere. A solution of BBr_3 (1.0 M, 0.52 mL, 0.52 mmol, 10.0 eq) in dry CH_2Cl_2 was added and the reaction mixture was stirred under argon at −78°C for 1 h and after that at 0 °C for 30 minutes. The solution was then brought to room temperature, neutralized with a saturated aqueous solution of $NaHCO_3$ and the organic phase was washed with water (2×20 mL), dried over anhydrous Na_2SO_4 and purified by column chromatography (silica, CH_2Cl_2:*n*-hexane 9:1, the desired product is collected as first eluted band). Yield 75.7 mg (75%).

^{1}H NMR (δ, 500 MHz, $CDCl_3$): 11.71 ppm (s, 1H, OH), 8.89 – 8.80 ppm (m, 9H, H^{β}, H^{d}), 8.24 – 8.21 ppm (br. s, 4H, H^{o}, $H^{o'}$), 8.14 – 8.08 ppm (br. s, 2H, H^{o}, $H^{o'}$; dd, 1H, H^{a}; br. s, 1H, NH^{e}), 7.90 ppm (ddd, J = 8.6, 7.9, 1.6 Hz, 1H, H^{c}), 7.84 – 7.70 ppm (m, 9H, H^{m}, $H^{m'}$, H^{p}, $H^{p'}$), 7.59 ppm (td, J = 7.6, 1.2 Hz, 1H, H^{b}), 6.74 ppm (ddd, J = 8.7, 7.4, 1.6 Hz, 1H, H^{h}), 6.58 ppm (dd, J = 8.2, 1.2 Hz, 1H, H^{i}), 5.33 ppm (ddd, J = 8.3, 7.4, 1.2 Hz, 1H, H^{g}), 5.01 ppm (dd, J = 8.1, 1.6 Hz, 1H, H^{f}), −2.69 ppm (s, 2H, $NH^{porphyrin}$). ^{13}C from ^{1}H-^{13}C HSQC (δ, 127 MHz, $CDCl_3$): 134.9 ppm (C^{a}), 134.5 ppm (C^{o}, $C^{o'}$), 133.7 ppm (C^{h}), 129.7 ppm (C^{c}), 128.0 – 126.8 ppm (C^{m}, $C^{m'}$, C^{p}, $C^{p'}$), 124.3 ppm (C^{f}), 123.6 ppm (C^{b}), 121.0 ppm (C^{d}), 118.2 ppm (C^{g}), 118.1 ppm (C^{i}). UV–Vis (λ_{max}, nm, CH_2Cl_2): 419, 516, 550, 589, 647. ESI-MS: (*m/z*) (positive mode) for $C_{51}H_{36}N_5O_2$ $[M + H]^+$ calculated 750.28635 found 750.2861.

CoTPP-*o*BA (**5**):

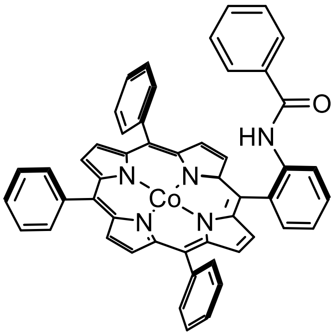

Free-base porphyrin **TPP-*o*BA** (**2**) (22.0 mg, 0.028 mmol, 1.00 eq) was dissolved in 15.0 mL of $CHCl_3$. A 3.00 mL CH_3OH solution of $Co(CH_3COO)_2 \cdot 4H_2O$ (17.7 mg, 0.071 mmol, 2.50 eq) was added and the solution was allowed to react under stirring at room temperature, protected from light, for 24 h. The reaction was monitored both by TLC (silica, CH_2Cl_2:petroleum ether 1:1) and UV-Vis absorption spectroscopy. After 24 h the solvent was removed under reduced pressure, and the solid washed with 2×20.0 mL of distilled water, under sonication. Porphyrin mixture was extracted with $CHCl_3$ (3×15.0 mL), dried over anhydrous Na_2SO_4 and collected as a pure solid by precipitation from a $CHCl_3$/*n*-hexane solution containing 1% of CH_3OH. Yield: 3.2 mg (3%).

UV–Vis (λ_{max}, nm, CH_2Cl_2): 412, 528. HRMS: (*m/z*) (positive mode) for $C_{51}H_{33}N_5OCo$ $[M + H]^+$ calculated 790.20116, found 790.2015.

CoTPP-*o*OHBA (**6**):

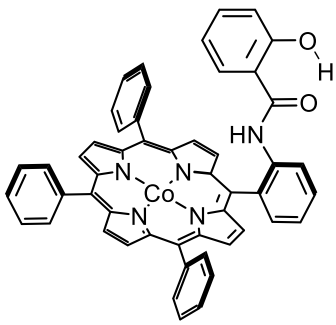

Free-base porphyrin **TPP-*o*OHBA** (**3**) (23.0 mg, 0.031 mmol, 1.00 eq) was dissolved in 15.0 mL of $CHCl_3$. A 3.00 mL CH_3OH solution of $Co(CH_3COO)_2 \cdot 4H_2O$ (17.6 mg, 0.077 mmol, 2.50 eq) was added and the solution was allowed to react under stirring at room temperature, protected from light, for 24 h. The reaction was monitored both by TLC (silica, CHCl3:*n*-hexane 1:1) and UV-Vis absorption spectroscopy. After 24 h the solvent was removed under reduced pressure, and the solid washed with 2×20.0 mL of distilled water under sonication. The

product was extracted with $CHCl_3$ (3×15.0 mL), dried over anhydrous Na_2SO_4 and collected as a pure solid by precipitation from a $CHCl_3$/*n*-hexane solution. Yield 13.2 mg (53%).
UV–Vis (λ_{max}, nm, CH_2Cl_2): 412, 528. HRMS: (*m/z*) (positive mode) for $C_{51}H_{33}N_5O_2Co$ $[M + H]^+$ calculated 806.19608, found 806.1962.

SFG measurements - Choice of the substrate and Sample preparation.

For the SFG measurements the Gr/Ir(111) substrate has been used. The Ir(111) sample was cleaned by repeated cycles of Ar^+ sputtering at 2 keV and annealing at 1275 K. Graphene monolayer was synthesized by chemical vapor deposition (CVD) until a self-limiting monolayer is completed. The Ir(111) was held at 1275 K and exposed to 5×10^{-8} mbar of C_2H_4 for 2 minutes and the to 3×10^{-7} mbar for additional 2 minutes. After the exposure, temperature was gradually reduced while restoring the UHV conditions.

TPP/Gr/Ir(111)

After graphene formation, TPP molecules, purchased from Frontier Scientific, were deposited via thermal sublimation using a boron nitride crucible (I = 1.9 A, V = 3.22 V). Before deposition, molecules were extensively outgassed at 350 – 400 K to remove organic residuals and gas contaminants. Sublimation was performed at 525 K with a deposition rate of approximately 0.05 mL/min, to achieve a sub-monolayer coverage in about 20 – 25 minutes. A Quartz Microbalance was used for the deposition rate calibration while Auger Electron Spectroscopy (AES) was used to estimate the molecular coverage.

2/Gr/Ir(111)

2 was deposited over the Gr/Ir(111) substrate by ESIBD. A $CHCl_3$:EtOH (1:25) 4.5×10^{-5} M solution of **2** was pumped with a rate or 1 mL/h and a voltage at the emitter capillarity of ~1.7 – 1.8 kV. The measured current at the Au flag was ~6 – 8 pA and the pressure in the main chamber was $1.7 - 2 \times 10^{-7}$ mbar during deposition. AES was then employed to check the molecular coverage by comparing the N spectrum to a N sub-monolayer coverage spectrum acquired in previous experiments.

3/Gr/Ir(111)

Same procedure described for **2** was used for deposition of **3**, starting with a $CHCl_3$:EtOH (1:25) 4.3×10^{-5} M solution. The pumping rate was varied between 0.4 and 0.6 mL/h with an applied emitter voltage of ~1.5 – 1.6 kV. The measured current at the Au flag was ~25 – 35 pA and the pressure in the main chamber lies in the 5 – 7 × 10^{-7} mbar range during deposition. **4/Gr/Ir(111)** Same procedure described for **2** was used for deposition of **4**, starting with a $CHCl_3$:EtOH (1:25) 4.4 × 10^{-5} M solution. The pumping rate was varied between 0.4 and 0.7 mL/h with an applied emitter voltage of ~1.3 kV. The measured current at the Au flag was ~6 – 8 pA and the pressure in the main chamber lied in the 3 – 6 × 10^{-7} mbar range during deposition.

Au(111)

The Au(111) single crystal has been employed as substrate for the preliminary characterization of **2** performed at the Max Planck Institute for Solid State Research in Stuttgart. The sample was cleaned by repeated cycles of Ar^+ sputtering at 0.86 keV for 20 minutes and annealing at ~ 400 – 450 °C for 10 minutes before deposition.

2/Au(111)

2 was deposited on Au(111) via ESIBD at the Max Planck Institute for Solid State Research in Stuttgart. A $CHCl_3$:EtOH (1:25) 4.5 × 10^{-5} M solution of **2** was pumped with 1 mL of formic acid to increase the beam intensity was used. The solution was electrosprayed via ESI in positive mode. The voltage applied at the emitter was 1.2 kV. The U/V ratio at the quadrupoles was set at 11 to have the mass selection. The deposition beam energy was measured to be 50 ± 3 eV, with a retarding voltage of 49 V applied to the surface. The coverage, estimated by the time-integrated current arriving at the sample, was 30 pAh STM images showed sub-monolayer coverage.

4/Au(111)

4 was deposited on Au(111) via ESIBD following the same deposition procedure used for 2, using a $CHCl_3$:EtOH (1:25) 4.4 × 10^{-5} M solution.

4.5. References.

(1) Yang, X.-F.; Wang, A.; Qiao, B.; Li, J.; Liu, J.; Zhang, T. *Acc. Chem. Res.* **2013**, *46*, 1740.

(2) Li, D.; Yadav, A.; Zhou, H.; Roy, K.; Thanasekaran, P.; Lee, C. *Glob. Chall.* **2024**, *8*, 2300244.

(3) Wang, Y.; Ma, J.; Jin, F.; Li, T.; Javanmardi, N.; He, Y.; Zhu, G.; Zhang, S.; Xu, J.-D.; Wang, T.; Feng, Z.-Q. *Small Sci.* **2024**, *4*, 2400132.

(4) Gutzler, R.; Stepanow, S.; Grumelli, D.; Lingenfelder, M.; Kern, K. *Acc. Chem. Res.* **2015**, *48*, 2132.

(5) Hieringer, W.; Flechtner, K.; Kretschmann, A.; Seufert, K.; Auwärter, W.; Barth, J. V.; Görling, A.; Steinrück, H.-P.; Gottfried, J. M. T. *J. Am. Chem. Soc.* **2011**, *133*, 6206.

(6) Auwärter, W.; Écija, D.; Klappenberger, F.; Barth, J. V. *Nat. Chem.* **2015**, *7*, 105.

(7) Gottfried, J. M. *Surf. Sci. Rep.* **2015**, *70*, 259.

(8) Armillotta, F.; Bidoggia, D.; Baronio, S.; Biasin, P.; Annese, A.; Scardamaglia, M.; Zhu, S.; Bozzini, B.; Modesti, S.; Peressi, M.; Vesselli, E. *ACS Catal.* **2022**, *12*, 7950.

(9) Armillotta, F.; Pividori, A.; Stredansky, M.; Seriani, N.; Vesselli, E. *Top. Catal.* **2020**, *63*, 1585.

(10) Armillotta, F.; Bidoggia, D.; Baronio, S.; Sala, A.; Costantini, R.; dell'Angela, M.; Cojocariu, I.; Feyer, V.; Morgante, A.; Peressi, M.; Vesselli, E. *Adv. Funct. Mater.* **2024**, *34*, 2408200.

(11) Vesselli, E. *J. Phys. Mater.* **2020**, *3*, 022002.

(12) Kavadiya, S.; Biswas, P. *J. Aerosol Sci.* **2018**, *125*, 182.

(13) Kebarle, P.; Verkerk, U. H. *Mass Spectrom. Rev.* **2009**, *28*, 898.

(14) Konermann, L.; Ahadi, E.; Rodriguez, A. D.; Vahidi, S. *Anal. Chem.* **2013**, *85*, 2.

(15) Temperton, R. H. PhD Thesis; University of Nottingham, **2018**.

(16) Temperton, R. H.; O'Shea, J. N.; Scurr, D. J. *Chem. Phys. Lett.* **2017**, *682*, 15.

(17) Morse, M. D. *Experimental Methods in the Physical Sciences* **1996**, *29*, 21.

(18) Wu, X.; Kumar, D.; Ham, J.; Huang, S.; Anggara, K. *Soft Landing Mass-Selected Ions for Single Molecule Imaging*; American Chemical Society **2025**.

(19) Lambert, A. G.; Davies, P. B.; Neivandt, D. J. *Appl. Spectrosc. Rev.* **2005**, *40*, 103.

(20) Wang, H.-F.; Velarde, L.; Gan, W.; Fu, L. *Annu. Rev. Phys. Chem.* **2015**, *66*, 189.

(21) Humbert, C.; Noblet, T.; Humbert, C.; Noblet, T. *Symmetry* **2021**, *13*.

(22) Formentin, S.; Master Thesis; University of Trieste, **2025**.

(23) Saini, G. S. S.; Sharma, S.; Kaur, S.; Tripathi, S. K.; Mahajan, C. G. *Spectrochim. Acta. A. Mol. Biomol. Spectrosc.* **2005**, *61*, 3070.

(24) Aydin, M. *Vib. Spectrosc.* **2013**, *68*, 141.

(25) Aydin, M. C. *Molecules* **2014**, *19*, 20988.

(26) Wan, J.; Wang, H.; Wu, Z.; Shun, Y. C.; Zheng, X.; Phillips, D. L. *Phys. Chem. Chem. Phys.* **2011**, *13*, 10183.

(27) Stein, P.; Ulman, A.; Spiro, T. G. *J. Phys. Chem.* **1984**, *88*, 369.

(28) Andersson, L. A.; Loehr, T. M.; Thompson, R. G.; Strauss, S. H. *Inorg. Chem.* **1990**, *29*, 2142.

(29) Chen, J.-H.; Cullen, W. G.; Jang, C.; Fuhrer, M. S.; Williams, E. D. *Phys. Rev. Lett.* **2009**, *102*, 236805.

(30) Besenbacher, F. *Rep. Prog. Phys.* **1996**, *59*, 1737.

(31) Binnig, G.; Rohrer, H.; Gerber, Ch.; Weibel, E. *Phys. Rev. Lett.* **1982**, *49*, 57.

(32) Edmondson, M. *Chem. Commun.* **2022**, *58*, 6247.

(33) Baronio, S.; De Col, M.; Yadav, A.; Roondhe, B.; Mischke, V.; Resel, O.; Bidoggia, D.; Namar, A.; Vinogradov, N.; Scardamaglia, M.; Valvidares, M.; Gargiani, P.; Cinchetti, M.; Zamborlini, G.; Giannozzi, P.; Vesselli, E. *Nanoscale* **2025**, *17*, 16946.

(34) Bidoggia, D.; Armillotta, F.; Sala, A.; Vesselli, E.; Peressi, M. *J. Phys. Chem. C* **2024**, *128*, 1737.

(35) Armillotta, F.; Bidoggia, D.; Biasin, P.; Annese, A.; Cossaro, A.; Verdini, A.; Floreano, L.; Peressi, M.; Vesselli, E. *Cell Rep. Phys. Sci.* **2023**, *4*, 101378.

(36) Zhao, M.; Wang, H.-B.; Ji, L.-N.; Mao, Z.-W. *Chem. Soc. Rev.* **2013**, *42*, 8360.

(37) Bhunia, S.; Rana, A.; Hematian, S.; Karlin, K. D.; Dey, A. *Inorg. Chem.* **2021**, *60*, 13876.

(38) Derrick, J. S.; Loipersberger, M.; Nistanaki, S. K.; Rothweiler, A. V.; Head-Gordon, M.; Nichols, E. M.; Chang, C. J. *J. Am. Chem. Soc.* **2022**, *144*, 11656.

(39) Teindl, K.; Patrick, B. O.; Nichols, E. M. *J. Am. Chem. Soc.* **2023**, *145*, 17176.

(40) Ladomenou, K.; Charalambidis, G.; Coutsolelos, A. G. *Polyhedron* **2013**, *54*, 47.

(41) Singha, A.; Mondal, A.; Nayek, A.; Dey, S. G.; Dey, A. *J. Am. Chem. Soc.* **2020**, *142*, 21810.

(42) Xie, L.; Zhang, X.; Zhao, B.; Li, P.; Qi, J.; Guo, X.; Wang, B.; Lei, H.; Zhang, W.; Apfel, U.; Cao, R. *Angew. Chem. Int. Ed.* **2021**, *60*, 7576.

(43) Yang, J.; Li, P.; Li, X.; Xie, L.; Wang, N.; Lei, H.; Zhang, C.; Zhang, W.; Lee, Y.; Zhang, W.; Cao, R.; Fukuzumi, S.; Nam, W. *Angew. Chem.* **2022**, *134*, e202208143.

(44) McGuire Jr., R.; Dogutan, D. K.; Teets, T. S.; Suntivich, J.; Shao-Horn, Y.; Nocera, D. G. *Chem. Sci.* **2010**, *1*, 411.

(45) Jin, P.; Liu, M.; Cao, F.; Luo, Q. *Dyes Pigments* **2016**, *132*, 151.

(46) Dreuw, A.; Worth, G. A.; Cederbaum, L. S.; Head-Gordon, M. U. *J. Phys. Chem. B* **2004**, *108*, 19049.

(47) Adler, A. D.; Longo, F. R.; Finarelli, J. D.; Goldmacher, J.; Assour, J.; Korsakoff, L. *J. Org. Chem.* **1967**, *32*, 476.

(48) Natali, M.; Luisa, A.; Iengo, E.; Scandola, F. *Chem. Commun.* **2014**, *50*, 1842.

(49) Yoshida, S. *Chemical & Pharmaceutical Bulletin* **1963**, *11*, 628.

(50) Brittain, H. G. *Cryst. Growth Des.* **2009**, *9*, 2492.

(51) Arjunan, V.; Mythili, C. V.; Mageswari, K.; Mohan, S. *Spectrochim. Acta. A. Mol. Biomol. Spectrosc.* **2011**, *79*, 245.

(52) Krishnakumar, V.; Murugeswari, K.; Surumbarkuzhali, N. *Spectrochim. Acta. A. Mol. Biomol. Spectrosc.* **2013**, *114*, 410.

Appendix C.

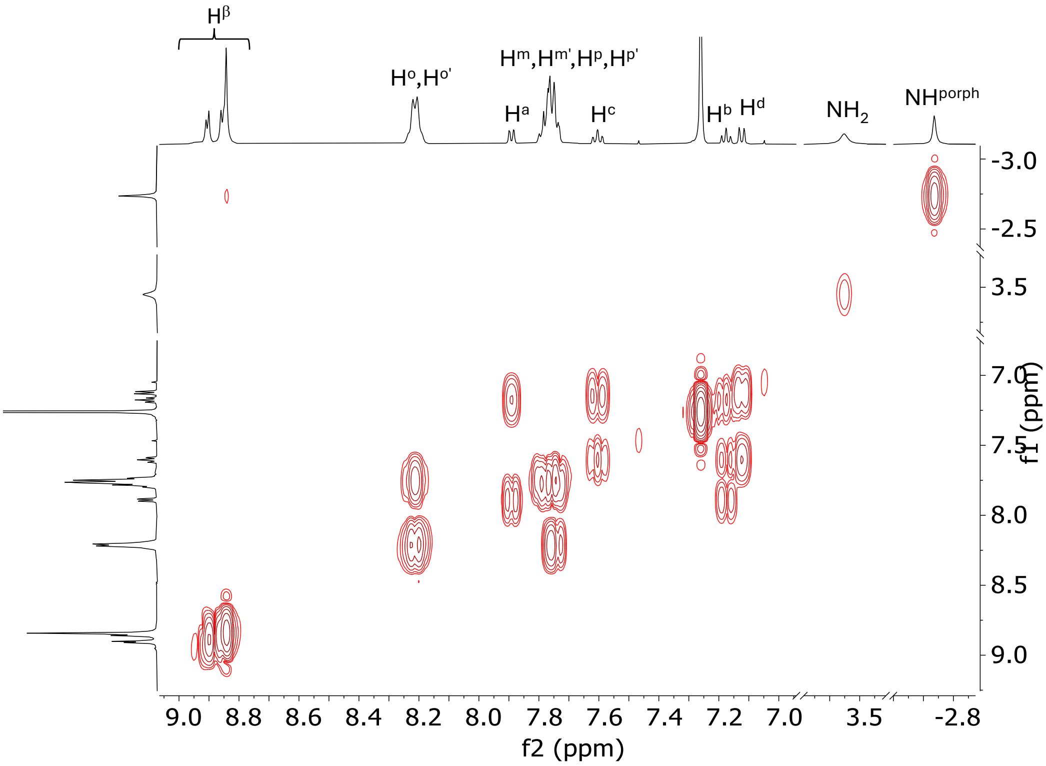

Figure S1. ^{1}H-^{1}H COSY spectrum (CDCl$_3$, 298 K) of **TPP-*o*NH$_2$** (**1**). For proton labelling see Experimental Section.

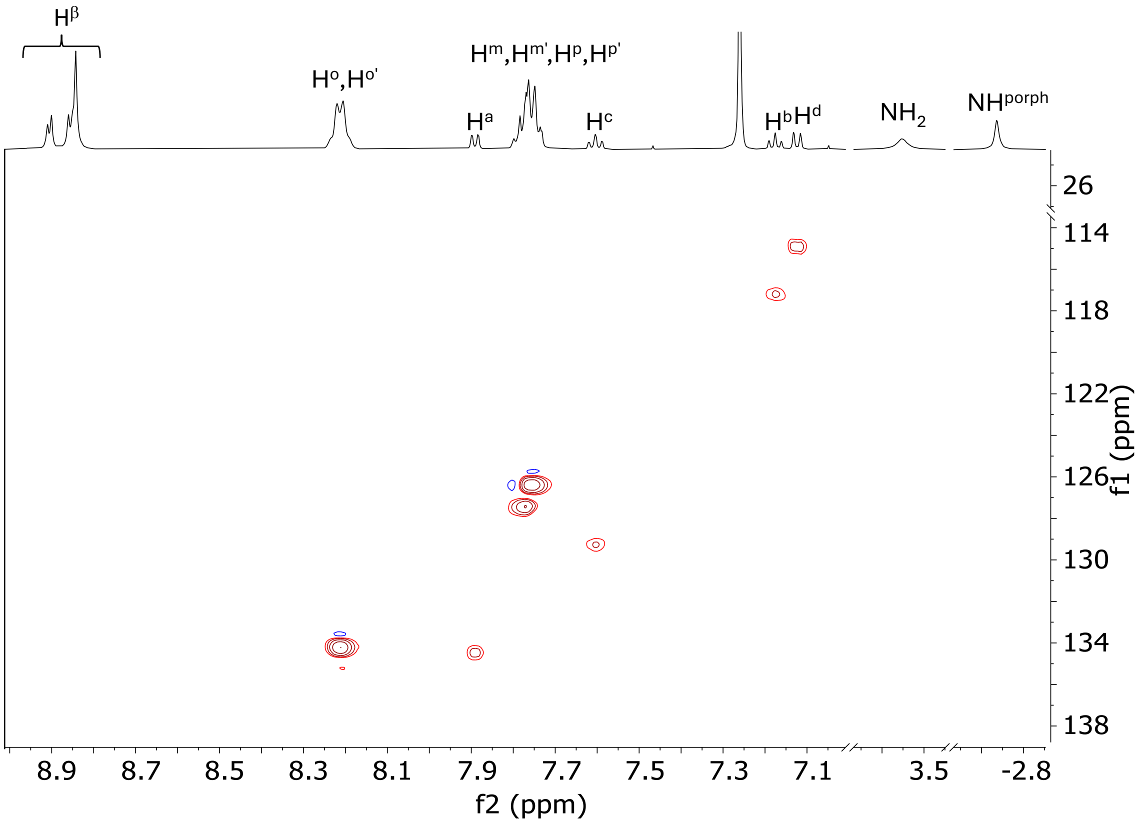

Figure S2. ^{1}H-^{13}C HSQC spectrum (CDCl$_3$, 298 K) of **1**.

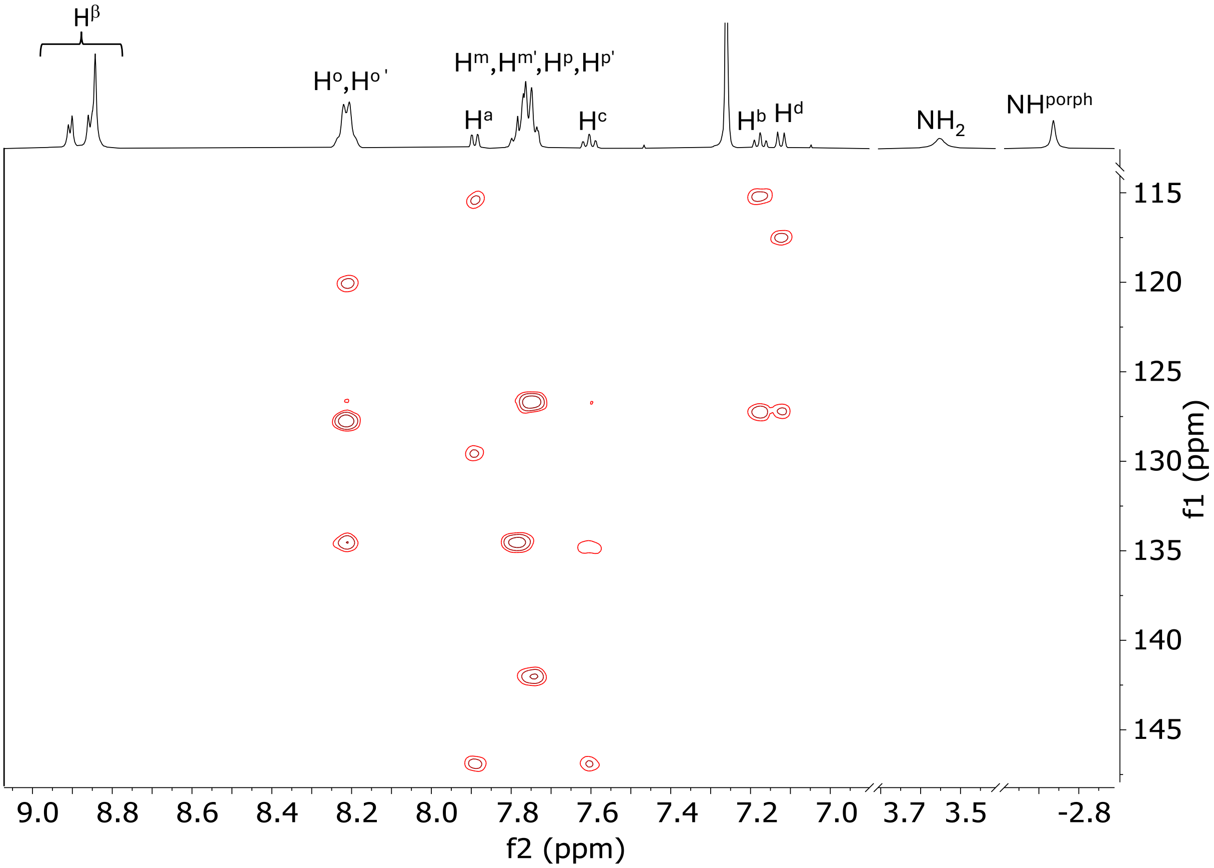

Figure S3. ^{1}H-^{13}C HMBC spectrum (CDCl$_3$, 298 K) of **1**. For proton labelling see main text.

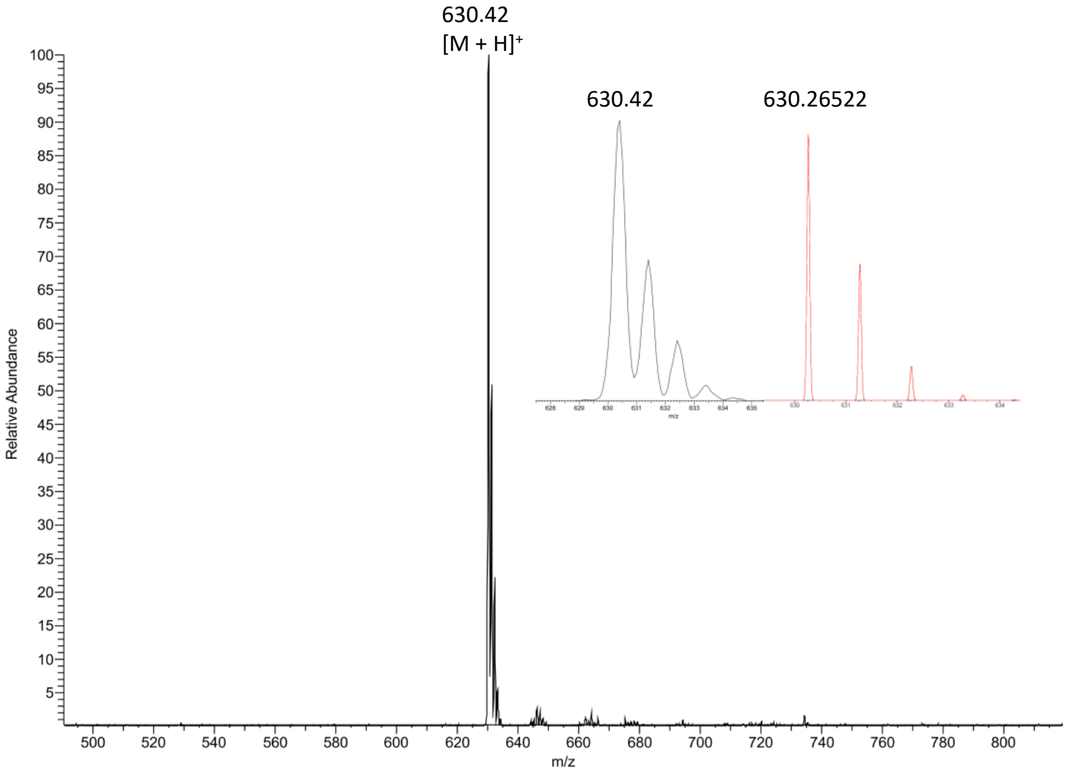

Figure S4. ESI-MS of **1** in CH$_3$OH, experimental (black) and simulated (red).

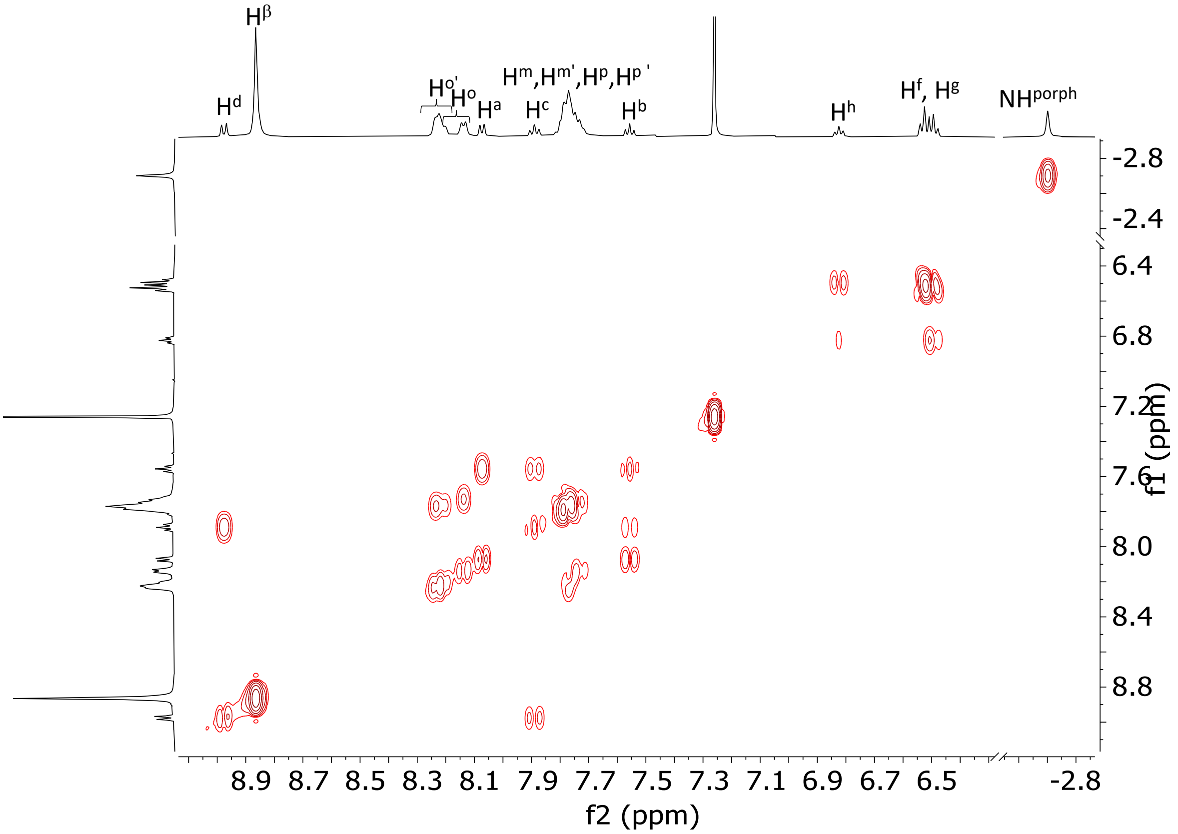

Figure S5. ^{1}H-^{1}H COSY spectrum (CDCl$_3$, 298 K) of **TPP-*o*BA** (**2**). For proton labelling see Experimental Section.

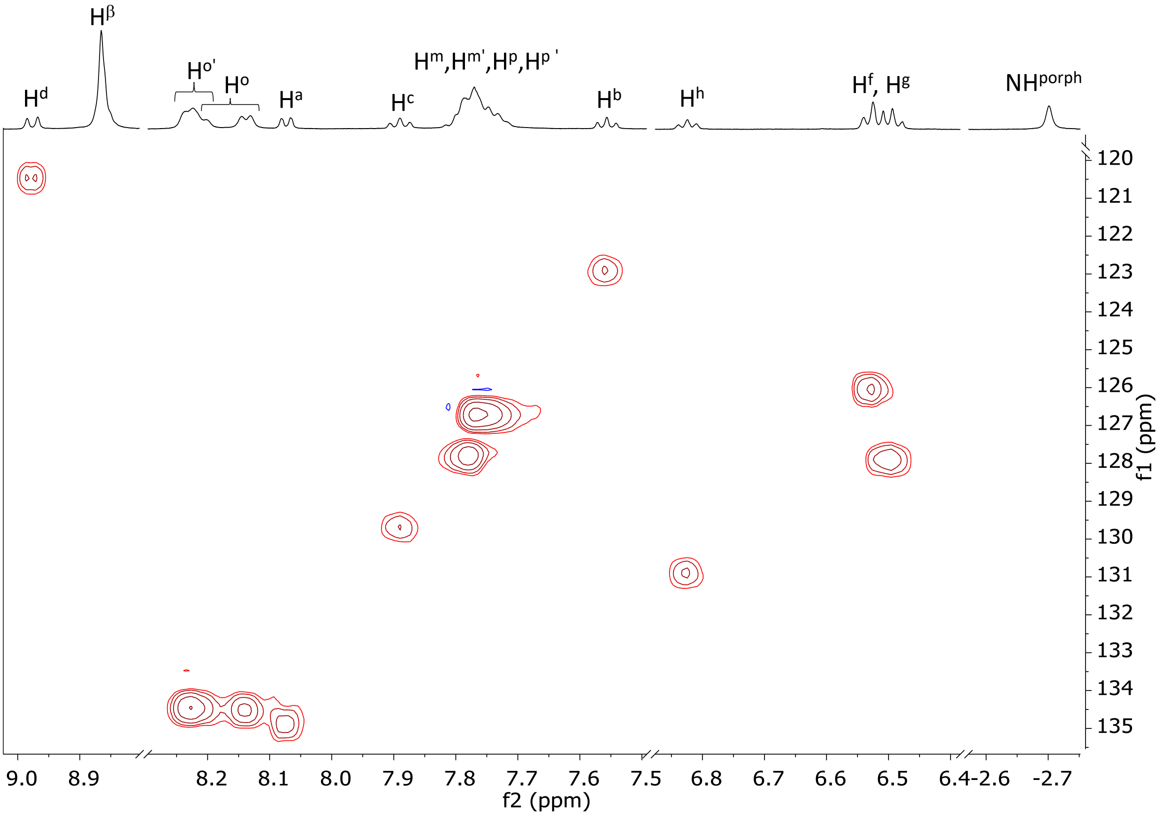

Figure S6. ^{1}H-^{13}C HSQC spectrum (CDCl$_3$, 298 K) of **2**.

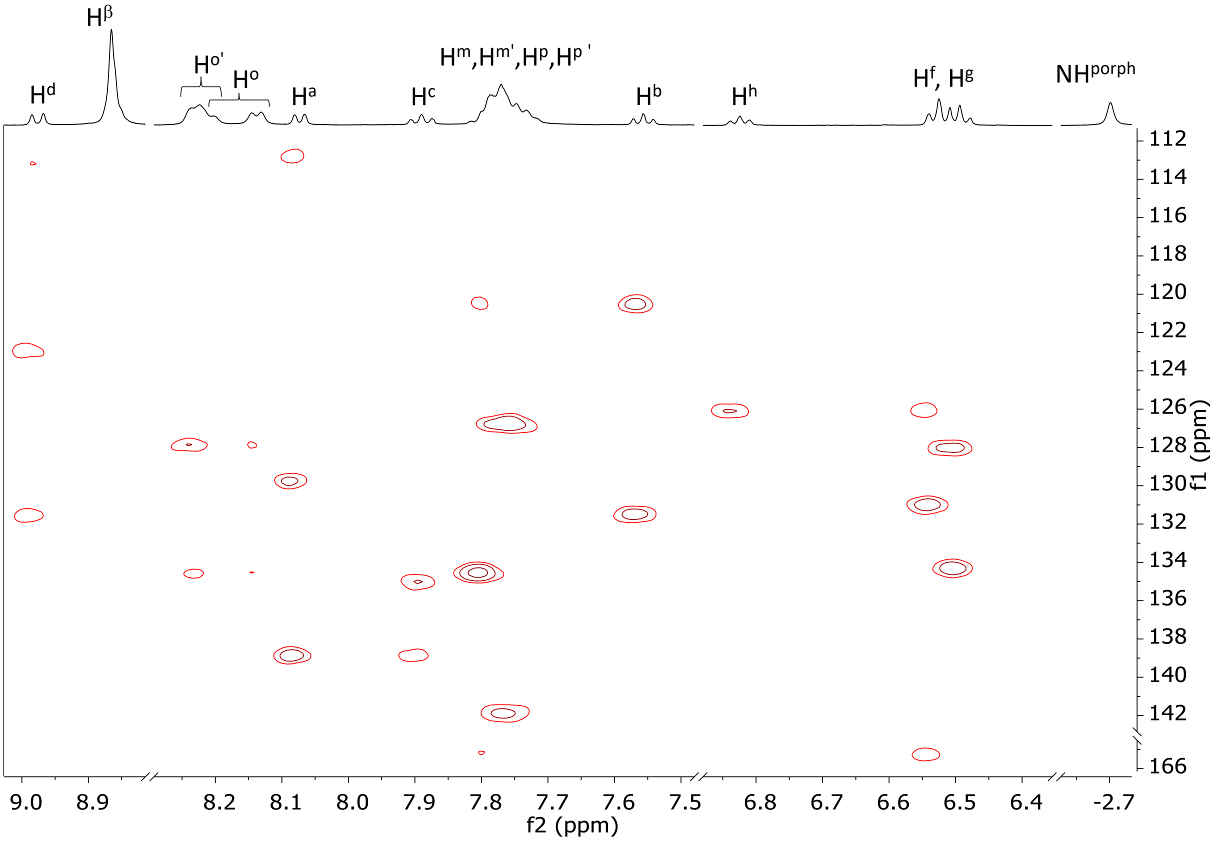

Figure S7. ^{1}H-^{13}C HMBC spectrum ($CDCl_3$, 298 K) of **2**.

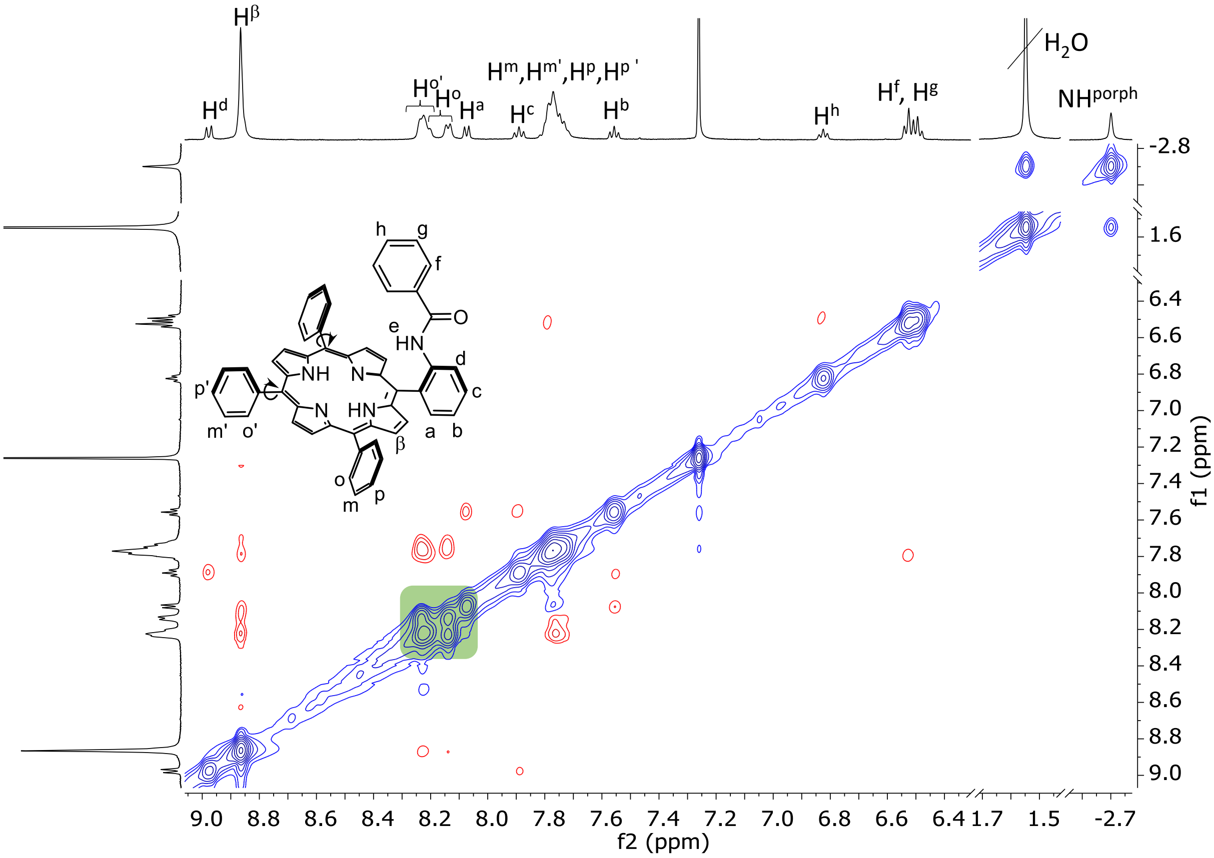

Figure S8. ^{1}H-^{1}H ROESY spectrum ($CDCl_3$, 298 K) of **2**. Exchange peaks are highlighted in green.

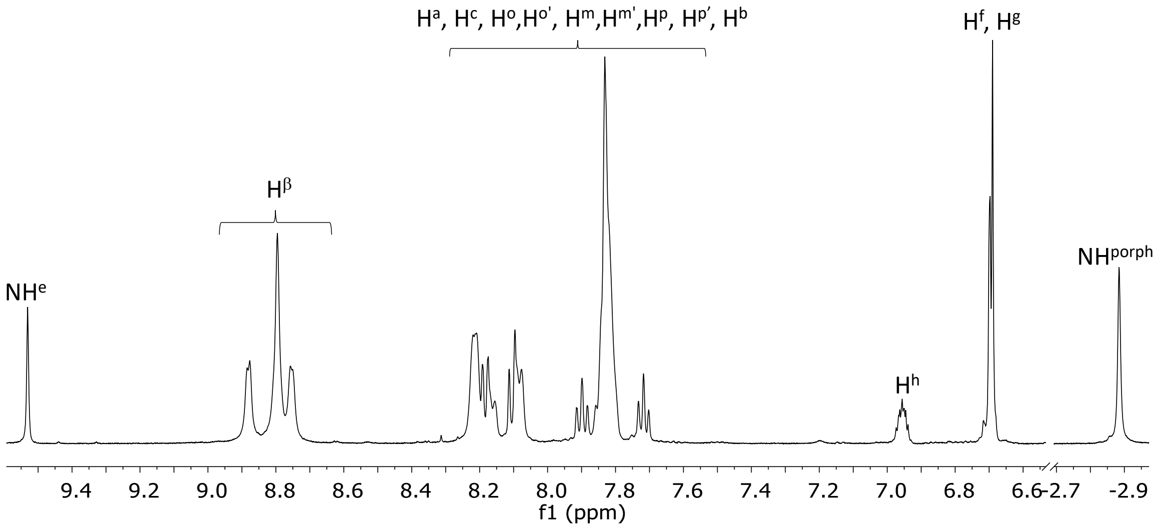

Figure S9. ^{1}H NMR spectrum (dmso-d_6, 298 K) of **2**.

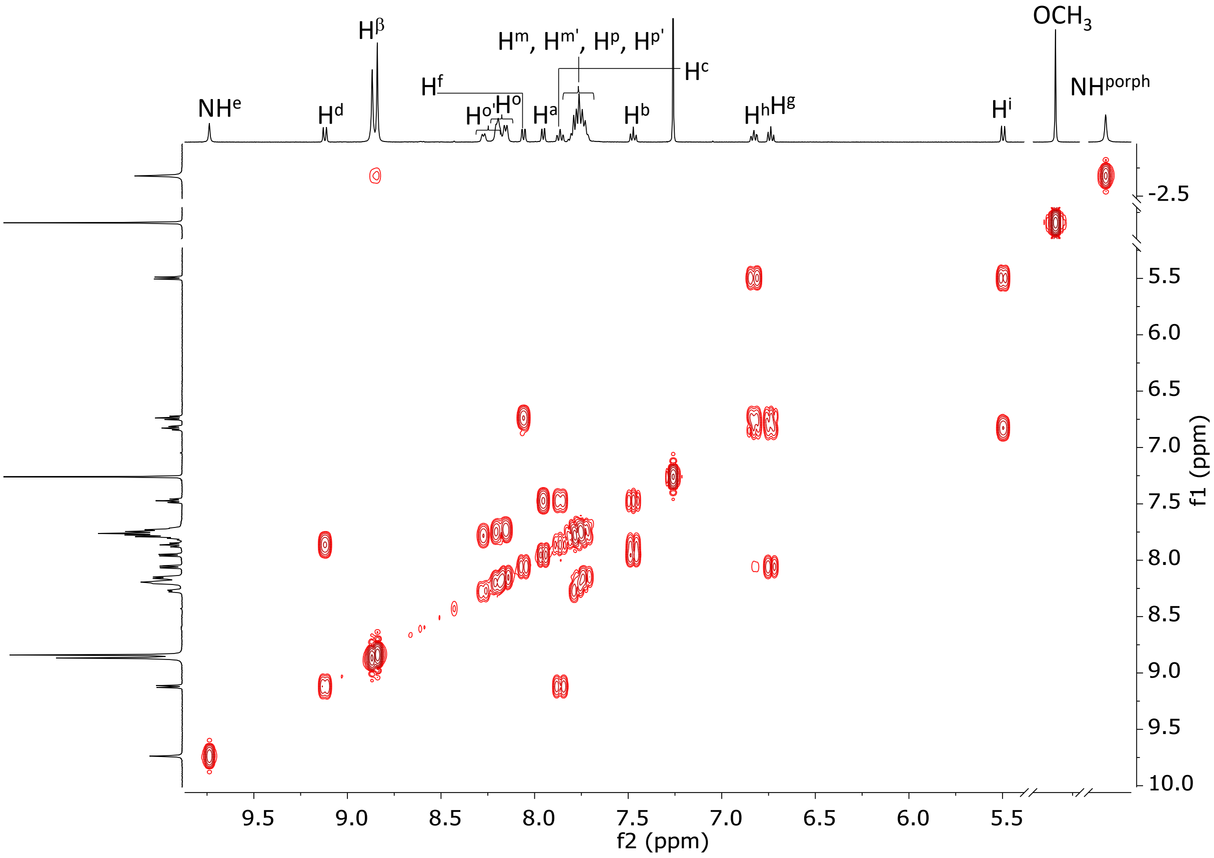

Figure S10. ^{1}H-^{1}H COSY spectrum (CDCl$_3$, 298 K) of **TPP-*o*MeOBA** (**3**). For proton labelling see Experimental Section.

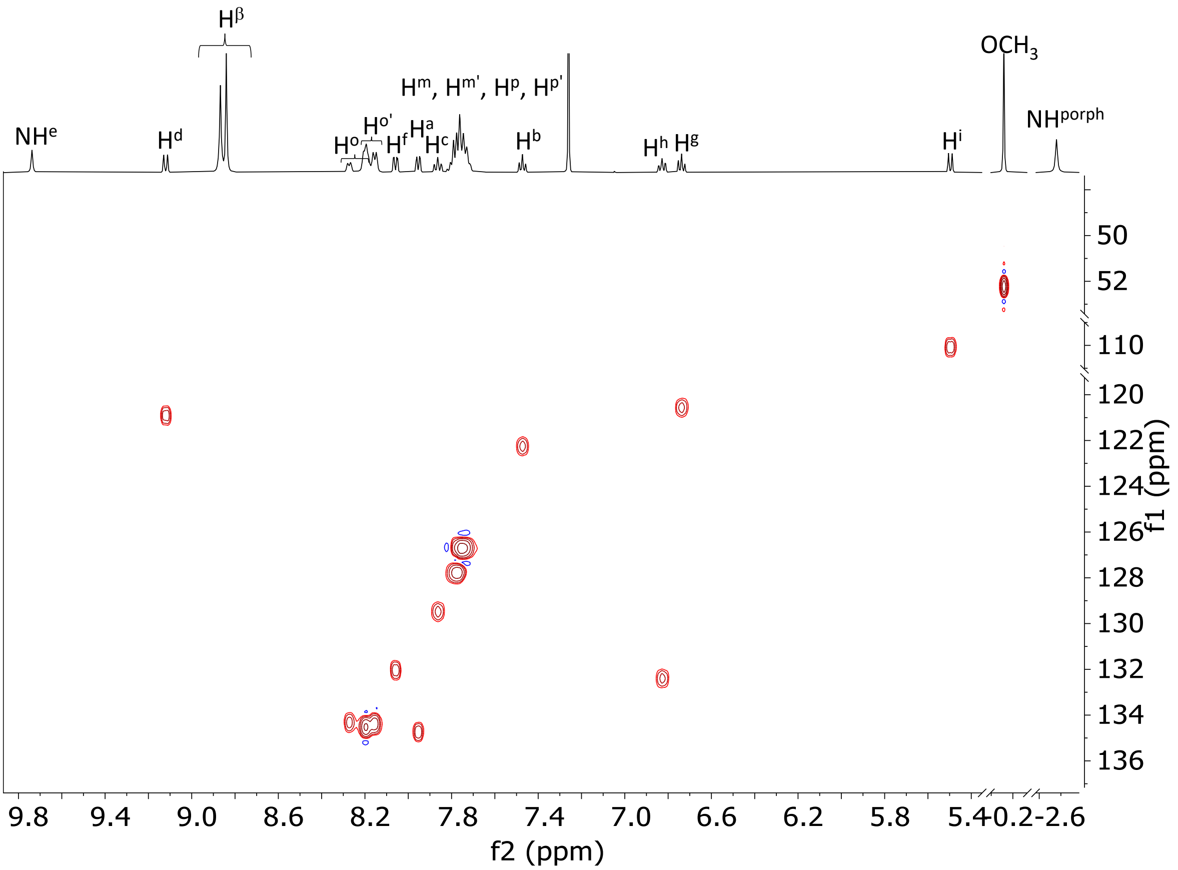

Figure S11. ^{1}H-^{13}C HSQC spectrum (CDCl$_3$, 298 K) of **3**.

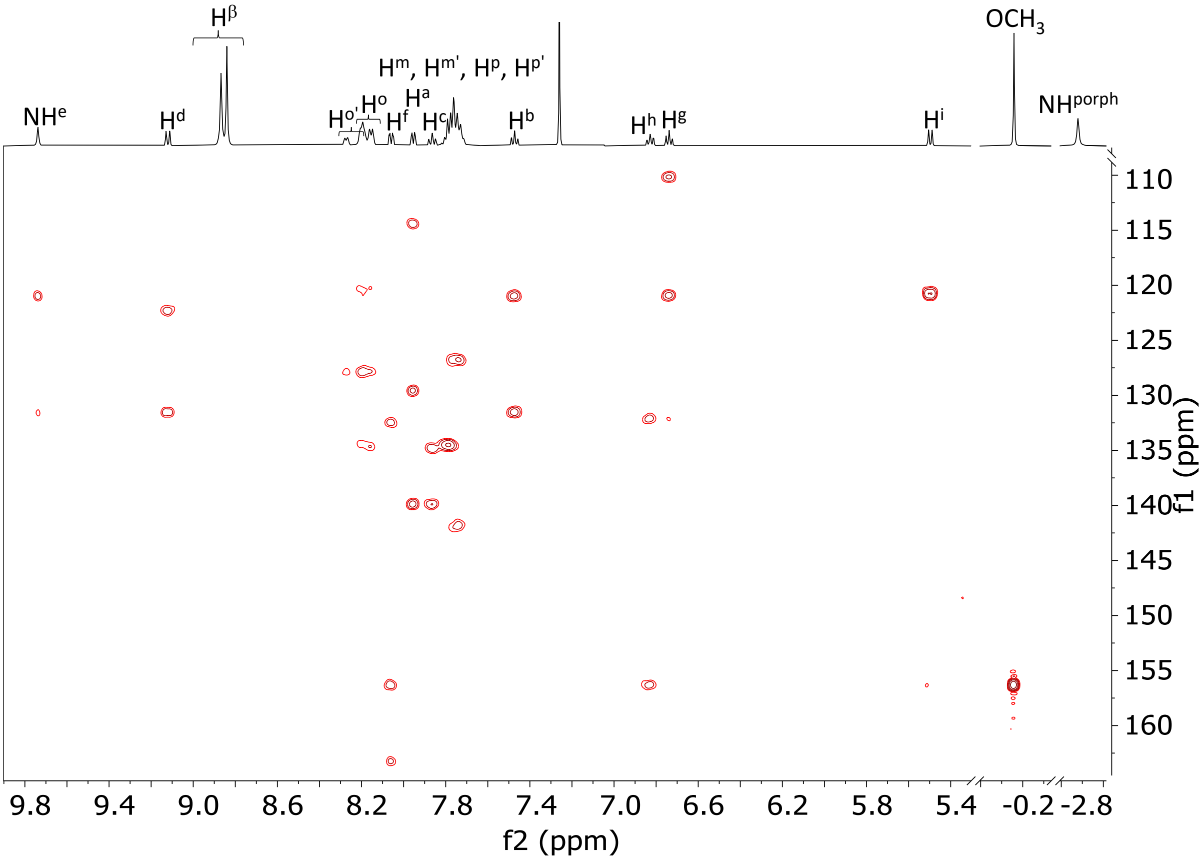

Figure S12. ^{1}H-^{13}C HMBC spectrum (CDCl$_3$, 298 K) of **3**.

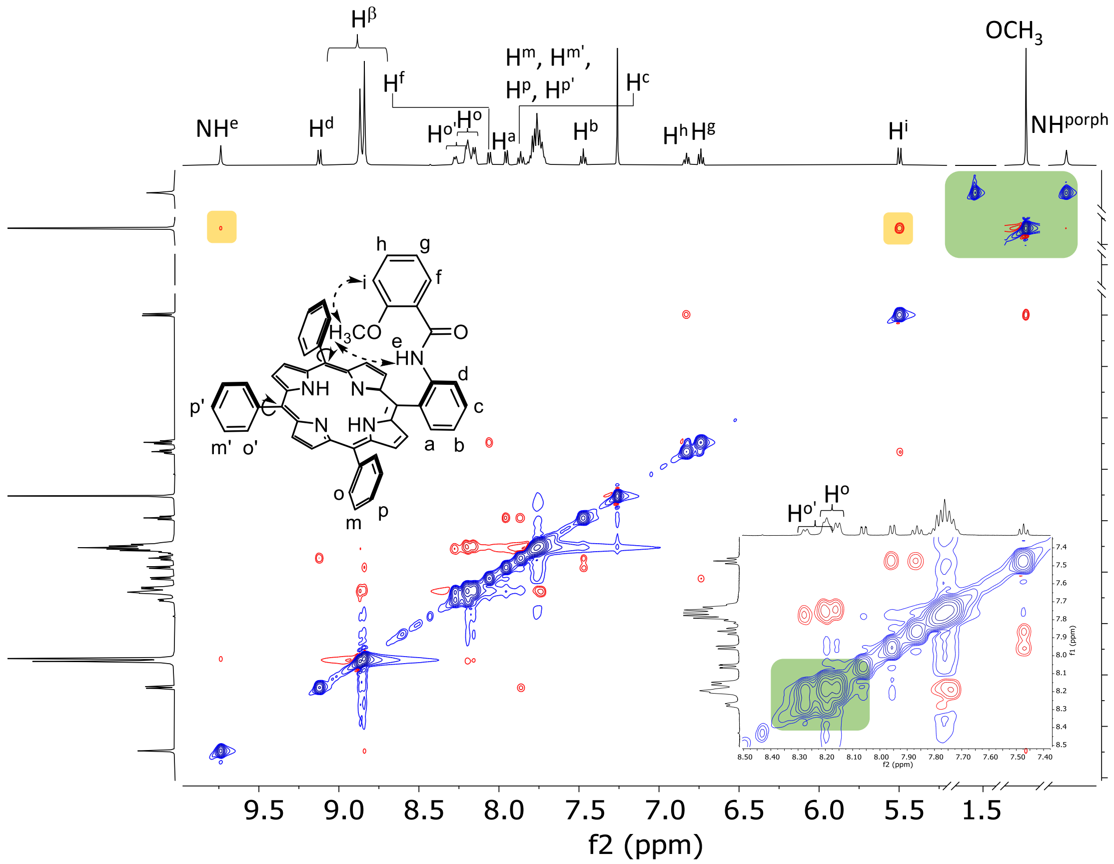

Figure S13. ^{1}H-^{1}H ROESY spectrum (CDCl$_3$, 298 K) of **3**. Exchange peaks are highlighted in green, nOe peaks are highlighted in yellow.

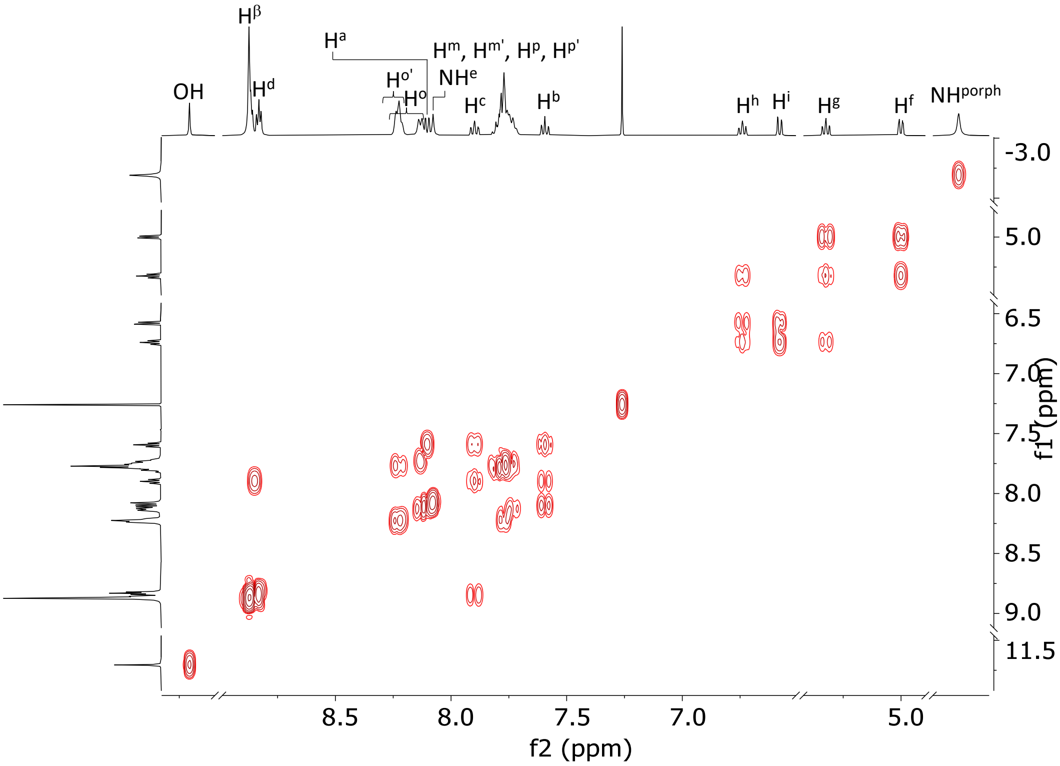

Figure S14. ^{1}H-^{1}H COSY spectrum (CDCl$_3$, 298 K) of **TPP-*o*OHBA (4)**. For proton labelling see Experimental Section.

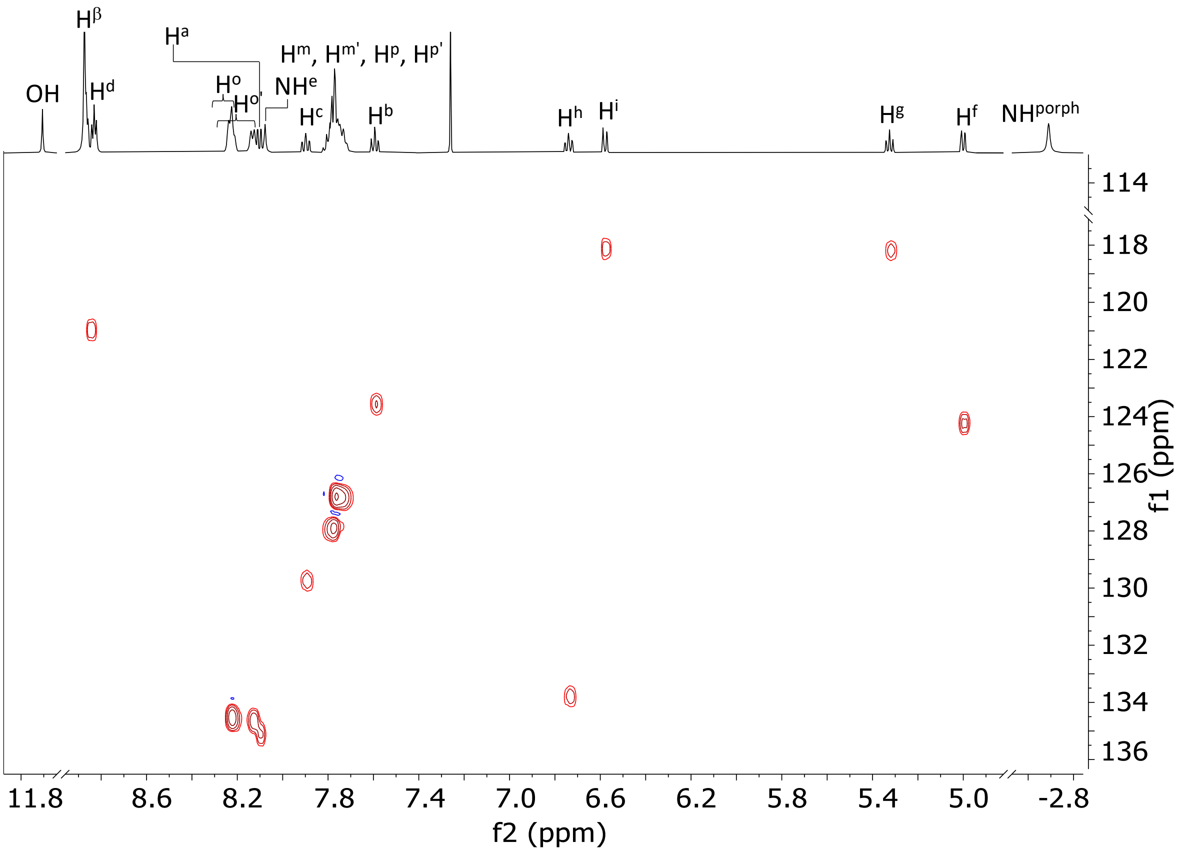

Figure S15. ^{1}H-^{13}C HSQC spectrum (CDCl$_3$, 298 K) of **4**.

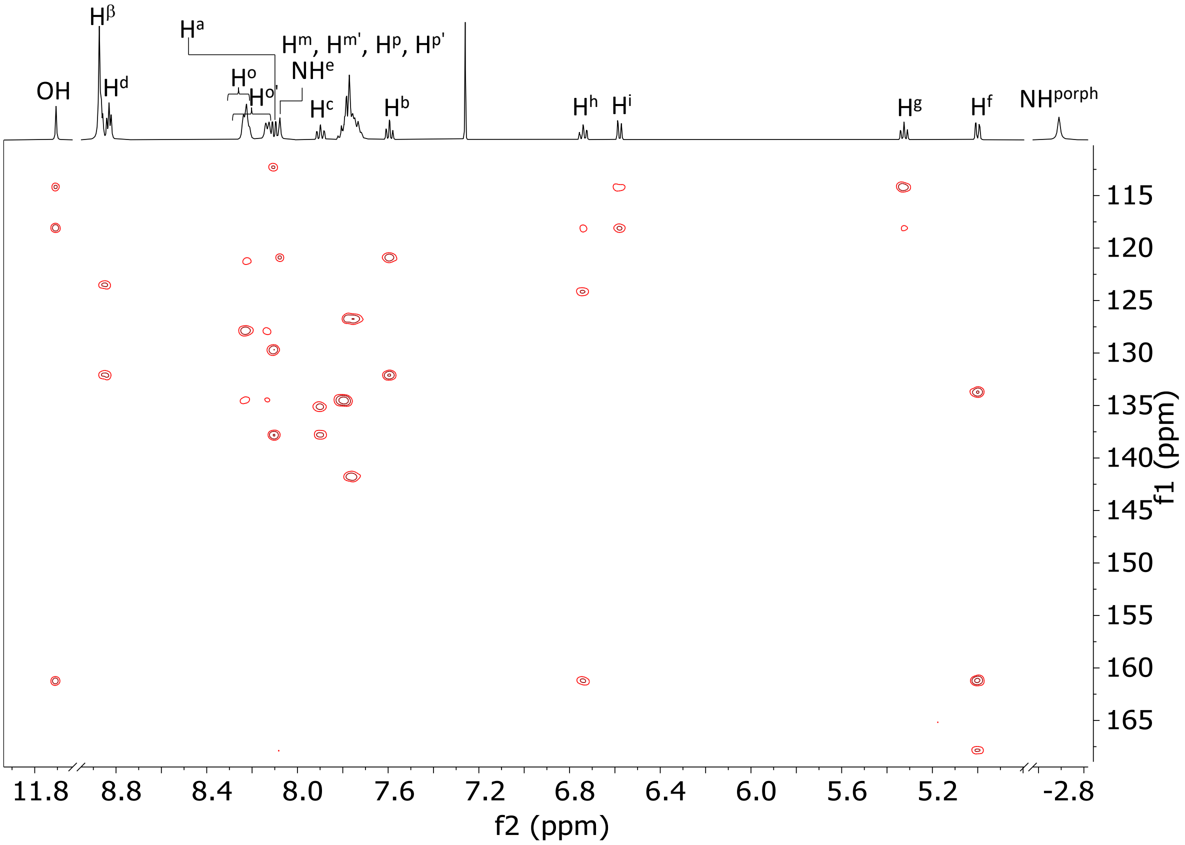

Figure S16. ^{1}H-^{13}C HMBC spectrum (CDCl$_3$, 298 K) of **4**.

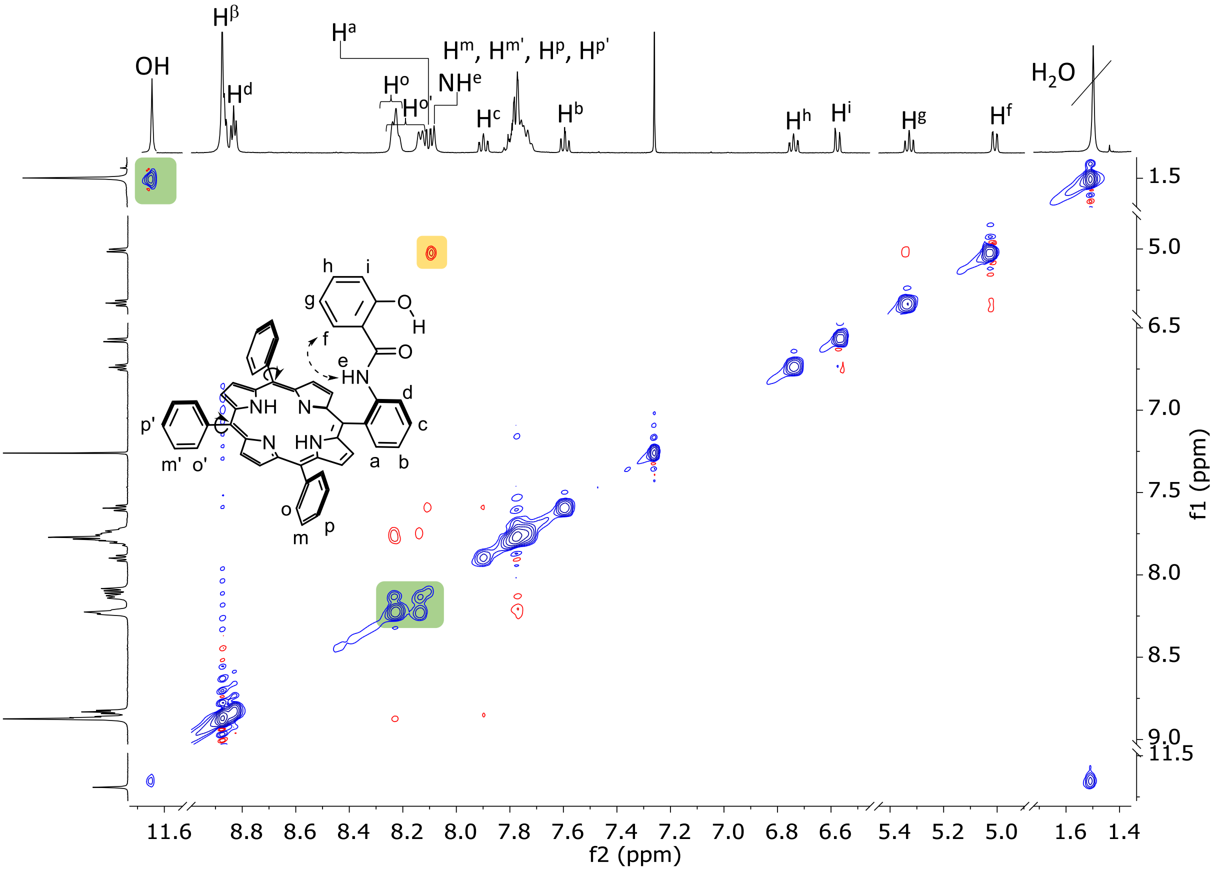

Figure S17. ^{1}H-^{1}H ROESY spectrum (CDCl$_3$, 298 K) of **4**. Exchange peaks are highlighted in green, nOe peaks are highlighted in yellow.

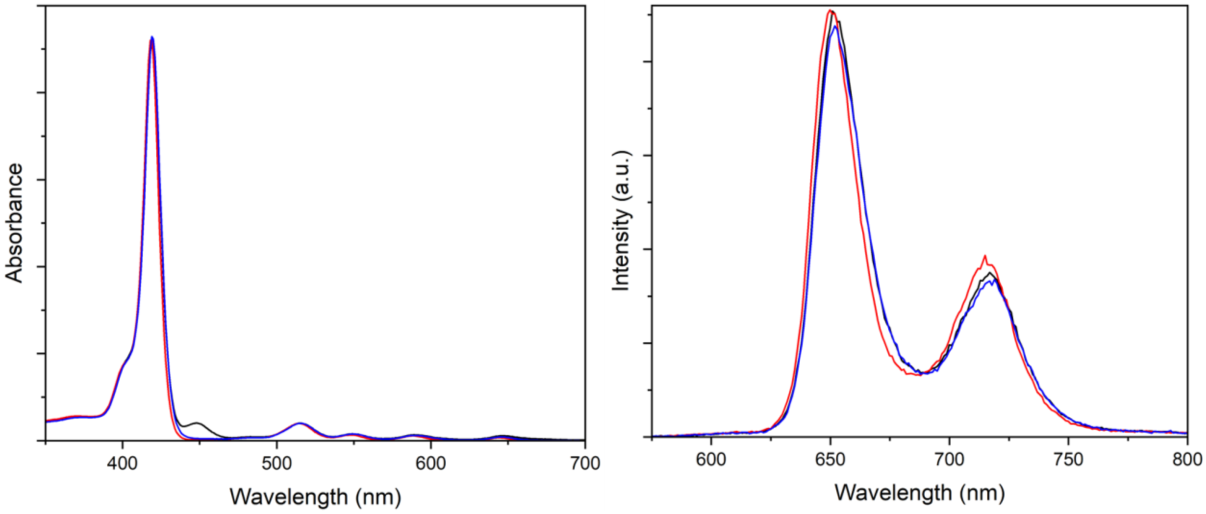

Figure S18. Left: UV-Vis absorption spectra (CH$_2$Cl$_2$, 5 µM); right: Emission spectra (CH$_2$Cl$_2$, 5 µM, λ_{irr} = 515 nm) of **2** – **4** (black, red and blue traces respectively).

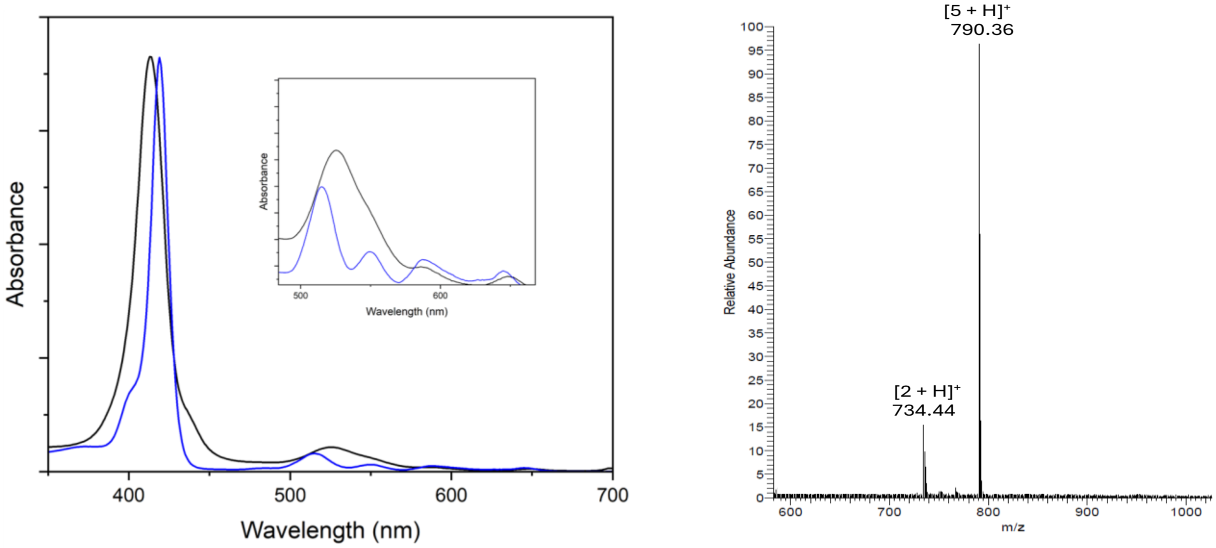

Figure S19. Left: UV-Vis absorption spectra (CH_2Cl_2) of the reaction mixture of **2** at t = 0 min (blue trace) and t = 24h (black trace). Inset: Enlargement of the Q bands region. Right: ESI-MS of the reaction mixture after 24 h of reaction in CH_3OH.

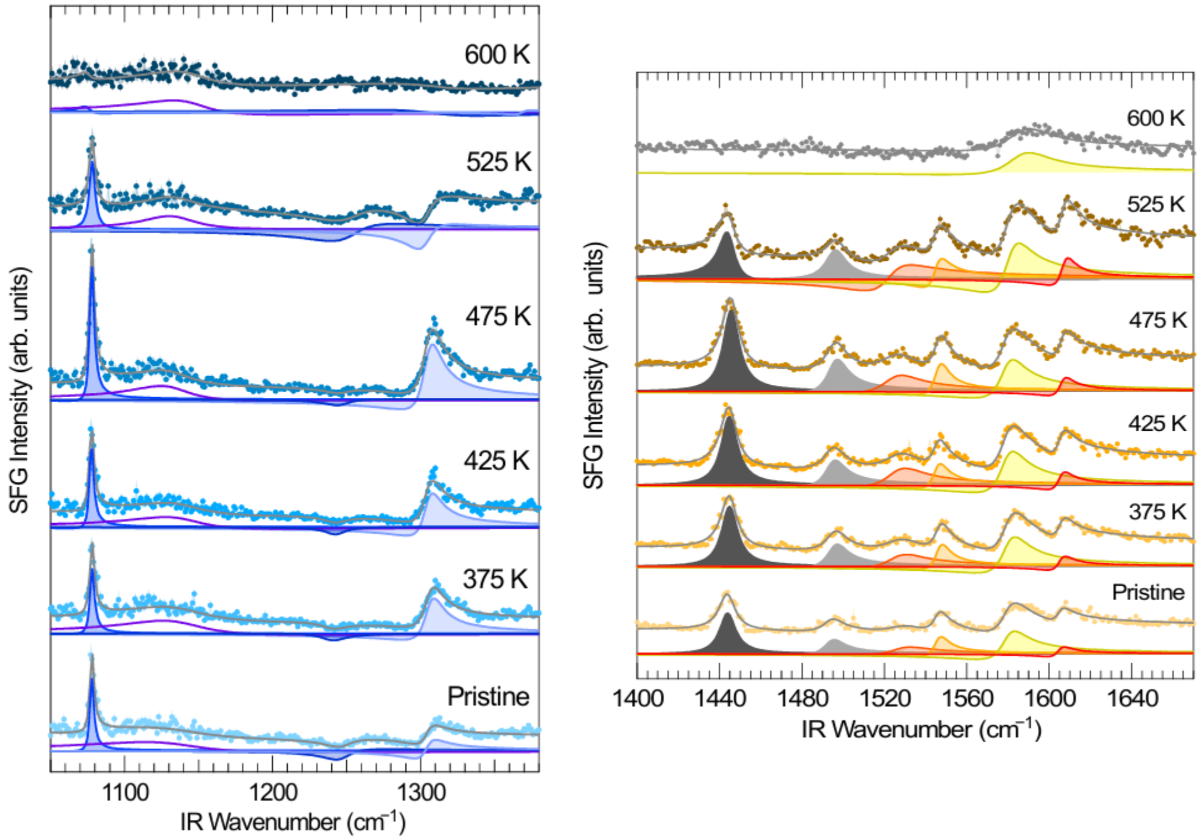

Figure S20. IR-Vis SFG spectra in the 1050 – 1380 and 1400 – 1700 cm^{-1} regions, together with the fit and deconvolution spectral components of **2**/Gr/Ir(111) at sub-monolayer coverage for the pristine sample and after annealing to 375, 425, 475, 525 and 600 K. The spectra were acquired in *ppp* polarization configuration.

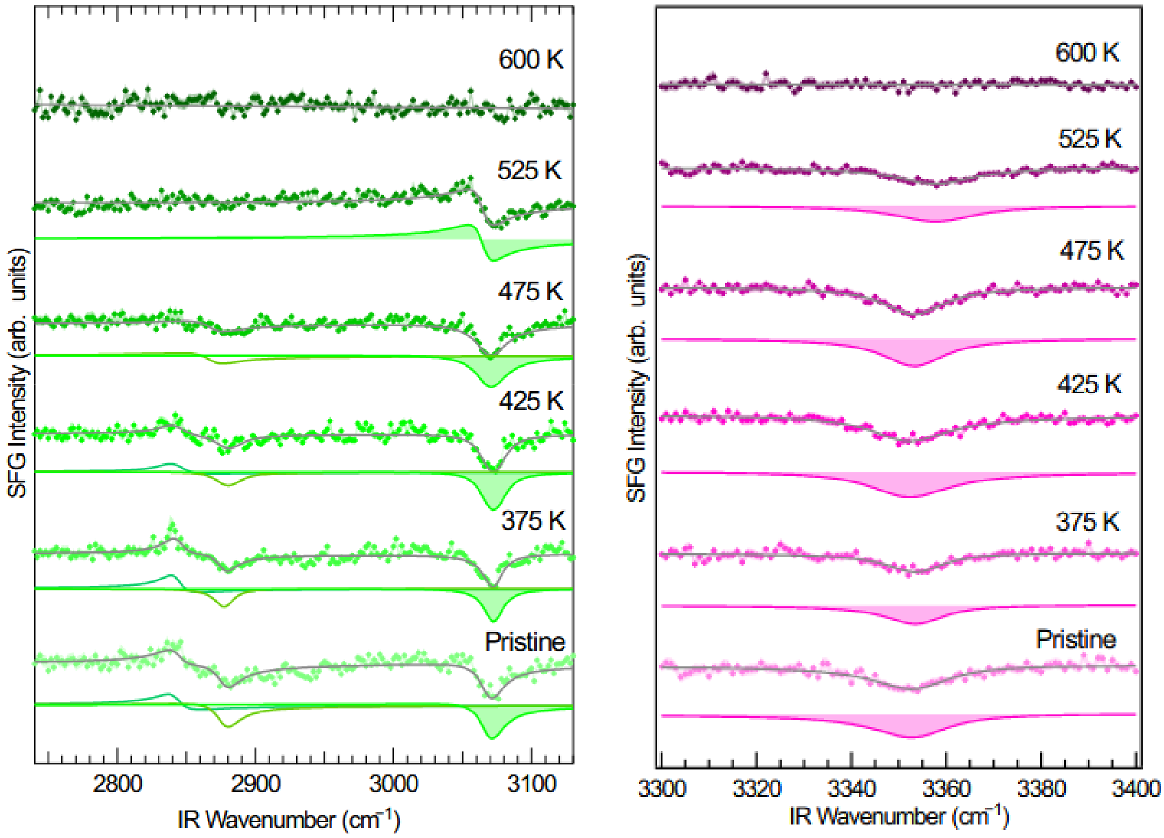

Figure S21. IR-Vis SFG spectra in the 2740 – 3130 and 3300 – 3400 cm^{-1} regions, together with the fit and deconvolution spectral components of **2**/Gr/Ir(111) at sub-monolayer coverage for the pristine sample and after annealing to 375, 425, 475, 525 and 600 K. The spectra were acquired in *ppp* polarization configuration.

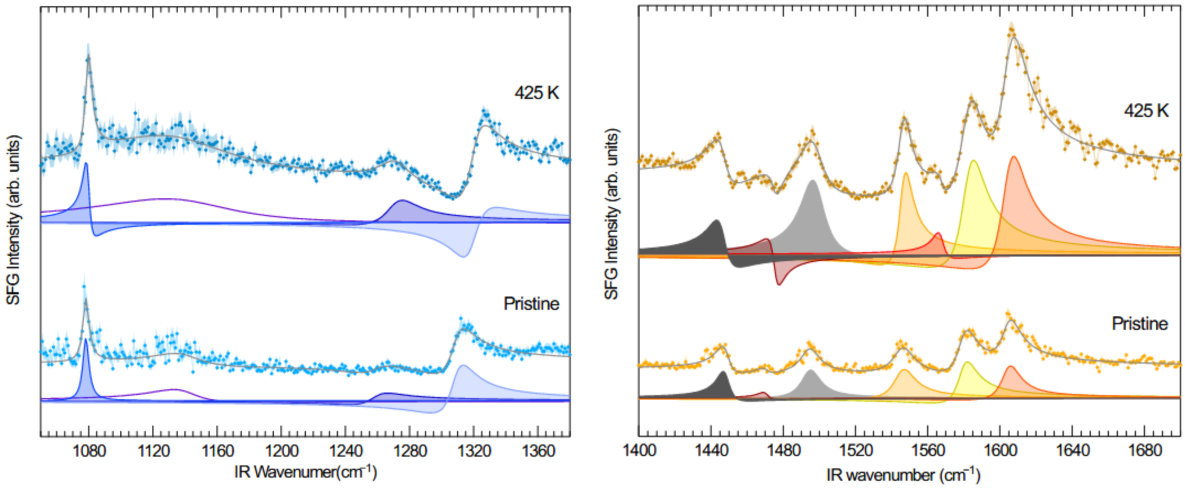

Figure S22. IR-Vis SFG spectra in the 1050 – 1380 and 1400 – 1700 cm^{-1} regions, together with the fit and deconvolution spectral components of **3**/Gr/Ir(111) at sub-monolayer coverage for the pristine sample and after annealing to 425 K. The spectra were acquired in *ppp* polarization configuration.

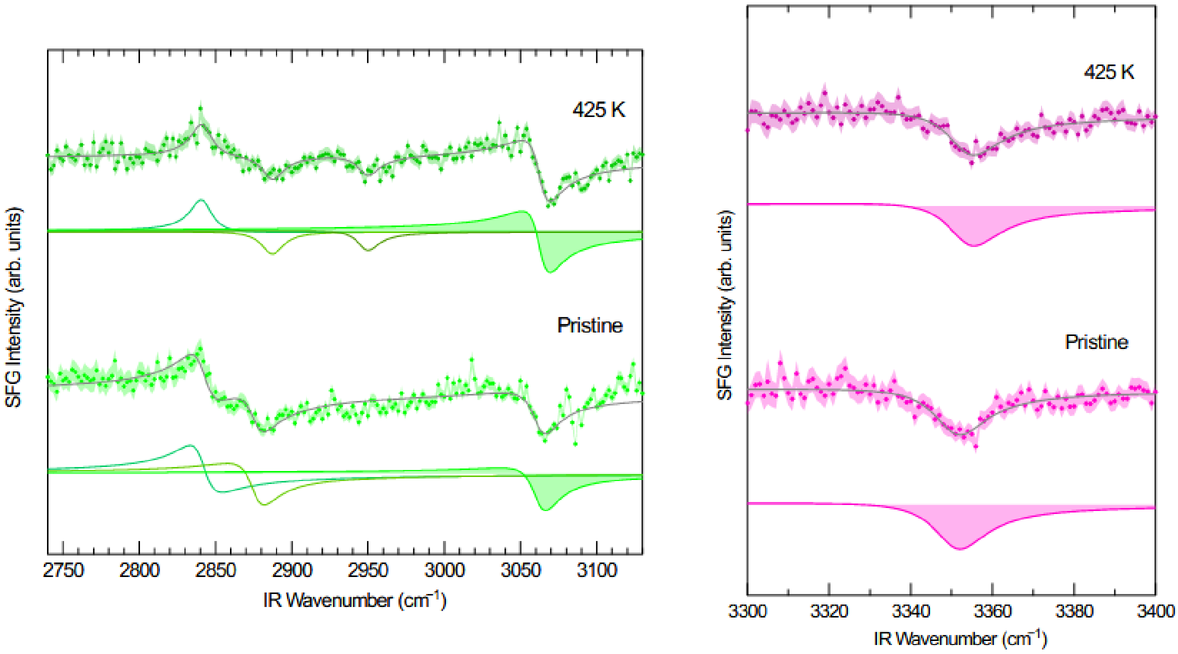

Figure S23. IR-Vis SFG spectra in the 2740 – 3130 and 3300 – 3400 cm^{-1} regions, together with the fit and deconvolution spectral components of **3**/Gr/Ir(111) at sub-monolayer coverage for the pristine sample and after annealing to 425 K. The spectra were acquired in *ppp* polarization configuration.

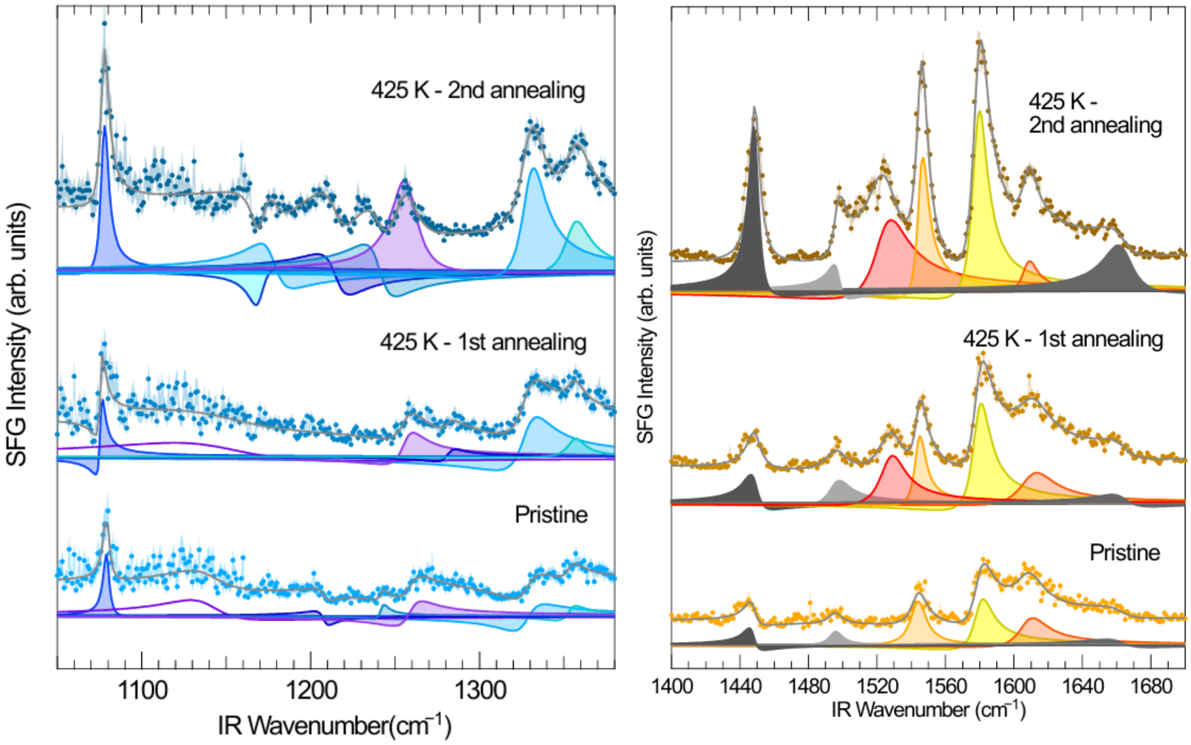

Figure S24. IR-Vis SFG spectra in the 1050 – 1380 and 1400 – 1700 cm^{-1} regions, together with the fit and deconvolution spectral components of **4**/Gr/Ir(111) at sub-monolayer coverage for the pristine sample and after annealing to 425 K, for two times. The spectra were acquired in *ppp* polarization configuration.

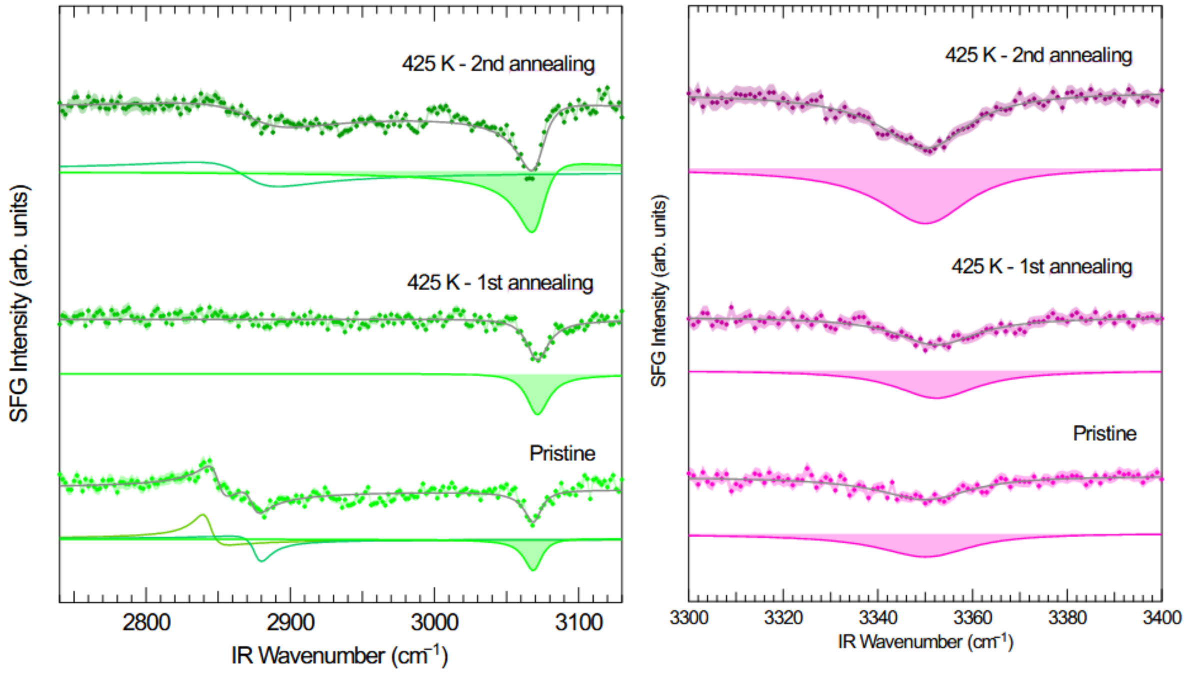

Figure S25. IR-Vis SFG spectra in the 2740 – 3130 and 3300 – 3400 cm^{-1} regions, together with the fit and deconvolution spectral components of **4**/Gr/Ir(111) at sub-monolayer coverage for the pristine sample and after annealing to 425 K, for two times. The spectra were acquired in *ppp* polarization configuration.

ACKNOWLEDGEMENTS

Financial supports from the European Union – NextGenerationEU- Piano Nazionale di Ripresa e Resilienza, Missione 4 – Componente 1 – Investimento 4.1 CUP J92B22000930007 and European Union – NextGeneration UE P2022ZSPWF PRIN Project are gratefully acknowledged.

The research project of this PhD Thesis involves some collaborations related to specific aspects. In particular, I want to thank:
My supervisor and my co-supervisor, Prof. Elisabetta Iengo and Prof. Sylvestre Bonnet (Leiden University, NL).
Prof. Mirco Natali and Dr. Federico Droghetti (University of Ferrara, IT) for the photophysical measurements described in Chapter 2.
Dr. Gabriele Balducci (University of Trieste, IT) for the X-ray structure analysis reported in Chapter 2.
Prof. Federico Berti (University of Trieste, IT) for the DFT calculations shown in Chapter 2.
Dr. Dmitri Filippov and Drs. Nico Meeuwenoord (Leiden University, NL) for the peptide synthesis described in Chapter 3.
Prof. Erik Vesselli, Michela De Col and Simone Formentin (University of Trieste, IT) for the deposition and on-surface studies described in Chapter 4.
Dr. Kelvin Anggara (Max Plank Institute for Solid State Research, Stuttgart, DE) for the STM images reported in Chapter 4.

UNIVERSITÀ
DEGLI STUDI
DI TRIESTE

Università
Ca'Foscari
Venezia

La borsa di dottorato è cofinanziata con risorse dell'Unione europea, NextGeneration EU - Piano Nazionale di Ripresa e Resilienza, Missione4 – Componente 1 – Investimento 4.1 CUP J92B22000930007

Finanziato
dall'Unione europea
NextGenerationEU

Ministero
dell'Università
e della Ricerca

Italiadomani
PIANO NAZIONALE
DI RIPRESA E RESILIENZA

UNIVERSITÀ
DEGLI STUDI
DI TRIESTE